frontiers | Research Topics

Tissue and organ decellularization strategies in regenerative medicine; recent advances, current translational challenges, and future directions

Edited by
Kamal Hany Hussein, Sotirios Korossis and Laura Iop

Published in
Frontiers in Bioengineering and Biotechnology

FRONTIERS EBOOK COPYRIGHT STATEMENT

The copyright in the text of individual articles in this ebook is the property of their respective authors or their respective institutions or funders. The copyright in graphics and images within each article may be subject to copyright of other parties. In both cases this is subject to a license granted to Frontiers.

The compilation of articles constituting this ebook is the property of Frontiers.

Each article within this ebook, and the ebook itself, are published under the most recent version of the Creative Commons CC-BY licence. The version current at the date of publication of this ebook is CC-BY 4.0. If the CC-BY licence is updated, the licence granted by Frontiers is automatically updated to the new version.

When exercising any right under the CC-BY licence, Frontiers must be attributed as the original publisher of the article or ebook, as applicable.

Authors have the responsibility of ensuring that any graphics or other materials which are the property of others may be included in the CC-BY licence, but this should be checked before relying on the CC-BY licence to reproduce those materials. Any copyright notices relating to those materials must be complied with.

Copyright and source acknowledgement notices may not be removed and must be displayed in any copy, derivative work or partial copy which includes the elements in question.

All copyright, and all rights therein, are protected by national and international copyright laws. The above represents a summary only. For further information please read Frontiers' Conditions for Website Use and Copyright Statement, and the applicable CC-BY licence.

ISSN 1664-8714
ISBN 978-2-8325-2183-0
DOI 10.3389/978-2-8325-2183-0

About Frontiers

Frontiers is more than just an open access publisher of scholarly articles: it is a pioneering approach to the world of academia, radically improving the way scholarly research is managed. The grand vision of Frontiers is a world where all people have an equal opportunity to seek, share and generate knowledge. Frontiers provides immediate and permanent online open access to all its publications, but this alone is not enough to realize our grand goals.

Frontiers journal series

The Frontiers journal series is a multi-tier and interdisciplinary set of open-access, online journals, promising a paradigm shift from the current review, selection and dissemination processes in academic publishing. All Frontiers journals are driven by researchers for researchers; therefore, they constitute a service to the scholarly community. At the same time, the *Frontiers journal series* operates on a revolutionary invention, the tiered publishing system, initially addressing specific communities of scholars, and gradually climbing up to broader public understanding, thus serving the interests of the lay society, too.

Dedication to quality

Each Frontiers article is a landmark of the highest quality, thanks to genuinely collaborative interactions between authors and review editors, who include some of the world's best academicians. Research must be certified by peers before entering a stream of knowledge that may eventually reach the public - and shape society; therefore, Frontiers only applies the most rigorous and unbiased reviews. Frontiers revolutionizes research publishing by freely delivering the most outstanding research, evaluated with no bias from both the academic and social point of view. By applying the most advanced information technologies, Frontiers is catapulting scholarly publishing into a new generation.

What are Frontiers Research Topics?

Frontiers Research Topics are very popular trademarks of the *Frontiers journals series*: they are collections of at least ten articles, all centered on a particular subject. With their unique mix of varied contributions from Original Research to Review Articles, Frontiers Research Topics unify the most influential researchers, the latest key findings and historical advances in a hot research area.

Find out more on how to host your own Frontiers Research Topic or contribute to one as an author by contacting the Frontiers editorial office: frontiersin.org/about/contact

Tissue and organ decellularization strategies in regenerative medicine; recent advances, current translational challenges, and future directions

Topic editors

Kamal Hany Hussein — Assiut University, Egypt

Sotirios Korossis — Loughborough University, United Kingdom

Laura Iop — University of Padua, Italy

Citation

Hussein, K. H., Korossis, S., Iop, L., eds. (2023). *Tissue and organ decellularization strategies in regenerative medicine; recent advances, current translational challenges, and future directions*. Lausanne: Frontiers Media SA.

doi: 10.3389/978-2-8325-2183-0

Table of contents

05 Editorial: Tissue and organ decellularization strategies in regenerative medicine; recent advances, current translational challenges, and future directions
Kamal Hussein, Sotirios Korossis and Laura Iop

09 Engineering Functional Vasculature in Decellularized Lungs Depends on Comprehensive Endothelial Cell Tropism
Ifeolu Akinnola, Daniel R. Rossi, Carolyn Meyer, Ashley Lindsey, Douglas R. Haase, Samuel Fogas, Michael J. Ehrhardt, Rachel E. Blue, Andrew. P. Price, Max Johnson, Diego F. Alvarez, Doris A. Taylor and Angela Panoskaltsis-Mortari

22 Decellularized Whole-Organ Pre-vascularization: A Novel Approach for Organogenesis
Ibrahim Fathi, Takehiro Imura, Akiko Inagaki, Yasuhiro Nakamura, Ayman Nabawi and Masafumi Goto

34 A Pulmonary Vascular Model From Endothelialized Whole Organ Scaffolds
Yifan Yuan, Katherine L. Leiby, Allison M. Greaney, Micha Sam Brickman Raredon, Hong Qian, Jonas C. Schupp, Alexander J. Engler, Pavlina Baevova, Taylor S. Adams, Mehmet H. Kural, Juan Wang, Tomohiro Obata, Mervin C. Yoder, Naftali Kaminski and Laura E. Niklason

52 Decellularization Following Fixation of Explanted Aortic Valves as a Strategy for Preserving Native Mechanical Properties and Function
Manisha Singh, Clara Park and Ellen T. Roche

61 Decellularized Tissues for Wound Healing: Towards Closing the Gap Between Scaffold Design and Effective Extracellular Matrix Remodeling
Víctor Alfonso Solarte David, Viviana Raquel Güiza-Argüello, Martha L. Arango-Rodríguez, Claudia L. Sossa and Silvia M. Becerra-Bayona

87 Can Heart Valve Decellularization Be Standardized? A Review of the Parameters Used for the Quality Control of Decellularization Processes
F. Naso and A. Gandaglia

102 Applications of Tissue Decellularization Techniques in Ventricular Myocardial Biofabrication
Aravind Krishnan, Hanjay Wang and John Ward MacArthur

109 Decellularization Strategies for Regenerating Cardiac and Skeletal Muscle Tissues
Yong How Tan, Haylie R. Helms and Karina H. Nakayama

132 Novel Decellularization Method for Tissue Slices
Maria Narciso, Anna Ulldemolins, Constança Júnior, Jorge Otero, Daniel Navajas, Ramon Farré, Núria Gavara and Isaac Almendros

145 Bioprinting of Decellularized Porcine Cardiac Tissue for Large-Scale Aortic Models
Beu P. Oropeza, Jason R. Adams, Michael E. Furth, Jack Chessa and Thomas Boland

154 Re-Endothelialization of Decellularized Liver Scaffolds: A Step for Bioengineered Liver Transplantation
Kewei Li, Mohammad Tharwat, Ellen L. Larson, Philipp Felgendreff, Seyed M. Hosseiniasl, Anan Abu Rmilah, Khaled Safwat, Jeffrey J. Ross and Scott L. Nyberg

164 Photooxidation and Pentagalloyl Glucose Cross-Linking Improves the Performance of Decellularized Small-Diameter Vascular Xenograft *In Vivo*
Yuhong Liu, Chunyang Chen, Xinlong Xie, Haoyong Yuan, Zhenjie Tang, Tao Qian, Yalin Liu, Mingzhe Song, Sixi Liu, Ting Lu and Zhongshi Wu

181 Decellularization in Tissue Engineering and Regenerative Medicine: Evaluation, Modification, and Application Methods
Afarin Neishabouri, Alireza Soltani Khaboushan, Faezeh Daghigh, Abdol-Mohammad Kajbafzadeh and Masoumeh Majidi Zolbin

202 Decellularization of Porcine Carotid Arteries: From the Vessel to the High-Quality Scaffold in Five Hours
Maria Stefania Massaro, Petra Kochová, Richard Pálek, Jáchym Rosendorf, Lenka Červenková, Uta Dahmen, Václav Liška and Vladimíra Moulisová

220 Decellularized blood vessel development: Current state-of-the-art and future directions
Xinyu Wang, Vincent Chan and Peter R. Corridon

239 Modified nanofat grafting: Stromal vascular fraction simple and efficient mechanical isolation technique and perspectives in clinical recellularization applications
Paul Girard, Joelle Dulong, Jerome Duisit, Camille Mocquard, Simon Le Gallou, Benoit Chaput, Elise Lupon, Eric Watier, Audrey Varin, Karin Tarte and Nicolas Bertheuil

253 Ventricular stabilization with a customized decellularized cardiac ECM-based scaffold after myocardial infarction alters gene expression in a rodent LAD-ligation model
Hug Aubin, Lenard Rath, Alexandra Vey, Vera Schmidt, Mareike Barth, Elvira Weber, Artur Lichtenberg and Payam Akhyari

266 Development of a dual-component infection-resistant arterial replacement for small-caliber reconstructions: A proof-of-concept study
Sonia Zia, Adrian Djalali-Cuevas, Michael Pflaum, Jan Hegermann, Daniele Dipresa, Panagiotis Kalozoumis, Artemis Kouvaka, Karin Burgwitz, Sofia Andriopoulou, Alexandros Repanas, Fabian Will, Karsten Grote, Claudia Schrimpf, Sotiria Toumpaniari, Marc Mueller, Birgit Glasmacher, Axel Haverich, Lucrezia Morticelli and Sotirios Korossis

frontiers | Frontiers in Bioengineering and Biotechnology

TYPE Editorial
PUBLISHED 12 April 2023
DOI 10.3389/fbioe.2023.1201041

Check for updates

OPEN ACCESS

EDITED AND REVIEWED BY
Hasan Uludag,
University of Alberta, Canada

*CORRESPONDENCE
Kamal Hussein,
kamalhussein1986@gmail.com

RECEIVED 05 April 2023
ACCEPTED 07 April 2023
PUBLISHED 12 April 2023

CITATION
Hussein K, Korossis S and Iop L (2023), Editorial: Tissue and organ decellularization strategies in regenerative medicine; recent advances, current translational challenges, and future directions.
Front. Bioeng. Biotechnol. 11:1201041.
doi: 10.3389/fbioe.2023.1201041

COPYRIGHT
© 2023 Hussein, Korossis and Iop. This is an open-access article distributed under the terms of the Creative Commons Attribution License (CC BY). The use, distribution or reproduction in other forums is permitted, provided the original author(s) and the copyright owner(s) are credited and that the original publication in this journal is cited, in accordance with accepted academic practice. No use, distribution or reproduction is permitted which does not comply with these terms.

Editorial: Tissue and organ decellularization strategies in regenerative medicine; recent advances, current translational challenges, and future directions

Kamal Hussein[1]*, Sotirios Korossis[2] and Laura Iop[3]

[1]Department of Surgery, Anaesthesiology and Radiology, College of Veterinary Medicine, Assiut University, Assiut, Egypt, [2]Cardiopulmonary Regenerative Engineering (CARE) Group, Centre for Biological Engineering (CBE), Wolfson School of Mechanical, Electrical and Manufacturing Engineering, Loughborough University, Loughborough, United Kingdom, [3]Department of Cardiac Thoracic Vascular Sciences and Public Health, University of Padua, Padua, Italy

KEYWORDS

decellularization, scaffold, recellularization, extracellular matrix, reendothelialization, tissue engineering, regenerative medicine

Editorial on the Research Topic
Tissue and organ decellularization strategies in regenerative medicine; recent advances, current translational challenges, and future directions

Several different scaffolds of either synthetic or biological origin have been utilized in regenerative medicine for the engineering of tissues and organs. The ideal scaffold should be biocompatible, non-immunogenic, and easily fabricated. In addition, it should provide mechanical stability, mimicking the role of the natural ECM, whilst providing appropriate microstructure for cellular growth. A variety of different methods have been used over the past few years to fabricate synthetic scaffolds, including electrospinning (Amoroso et al., 2012), knitting (Moreira et al., 2014), and 3D printing (Mosadegh et al., 2015), with a view to creating porous structures that would facilitate cellular infiltration and colonization. Ideally, the scaffold would be degraded by the colonizing cells, which will synthesize their own ECM.

The most commonly used polymers in scaffold fabrication are polylactic acid and polyglycolic acid. However, a variety of different polymers have been used in the field over the years. The main reported advantage of polymeric scaffolds was that they can be fabricated in a well-controlled and reproducible manner that reflects their consistency in terms of mechanical properties, degradation rates, pore size, and surface topographies (McClelland et al., 2012). On the other hand, identifying the correct balance between degradation rates and ECM synthesis, as well as imitating the complex histoarchitectural and biomechanical properties of the native ECM, remain significant challenges in synthetic scaffold fabrication.

Biological scaffolds have been fabricated using reconstituted proteins or other structural components of the native ECM. Such scaffolds have been produced using fibrin (Kaminski et al., 2011; Syedain et al., 2015), collagen (Shi and Vesely, 2003), and hyaluronan (Masters et al., 2005). These biopolymers have been prepared as gels in which cells were suspended (Moreira et al., 2014) prior to forming the scaffold geometry. Although such biological scaffolds have an advantage over synthetic ones due to the natural origin of their constitutive

components, source-related immunogenicity, inadequate mechanical properties, and absence of natural histoarchitecture remain grossly unsolved issues.

Decellularized tissue represents the current state-of-the-art in scaffold fabrication, featuring natural histoarchitecture and mechanical integrity, similar to the native tissue. Nevertheless, source-related immunogenicity remains an important hurdle for the wide adoption of decellularized tissue scaffolds in the clinical setting, especially in the case of xenogeneic tissue scaffolds. Decellularization is aimed at removing the cellular and nuclear components, and antigens from the tissue, while minimizing the alterations in the composition, histoarchitecture, biological activity, and mechanical integrity of the remaining ECM (Gilbert et al., 2006). Xenogeneic or allogeneic cellular antigens are recognized as foreign by the host and, therefore, trigger an inflammatory response, which can result in immune-mediated graft rejection. Moreover, although the ECM components are well conserved among species and tolerated by the immune system of the host, even when xenogeneic tissue is used (Gilbert et al., 2006), antigens that can trigger an inflammatory response and immune-mediated graft rejection are not only localized in the cells, but have also been reported to reside within the ECM (Galili, 2001; Galili, 2015). Therefore, decellularization alone might not be sufficient for rendering the tissue completely non-immunogenic. On the other hand, harsh treatments for removing antigens from within the ECM can damage the integrity of the ECM proteins.

In the saga of finding efficacious therapies for the treatment of cardiovascular disease, tissue engineering and/or tissue-guided regeneration approaches based on decellularized scaffolds have the potential to provide excellent clinical alternatives to non-viable devices, especially in the field of heart valve replacement. Nevertheless, there are a number of hurdles that still remain in for the wide clinical translation of decellularized scaffolds in cardiovascular surgery.

The decellularization strategies so far developed for cardiac and skeletal muscles were reviewed by Tan et al., pointing out the key requisites for an effective regenerative medicine therapy to tackle cardiovascular disease and musculoskeletal pathologies. The identification of the right balance between effective cell removal and retention of the original biochemical and biomechanical properties of the native tissue remains a challenging task for many tissues and organs. Focusing on ventricular myocardium, Krishnan et al. discussed the components, methods, and obstacles for its biofabrication, describing the wide variety of cell types that have been proposed for a personalized regenerative medicine approach. Aubin et al. reported on an approach that implanted a decellularized myocardial sleeve onto the surface of an infarcted rat heart model. As early as 4 weeks, the sleeve activated a pro-regenerative genetic program, culminating in scaffold repopulation and integration and, ultimately, improvement in overall cardiac function.

The generation of a competent vascular substitute is one of the challenges in cardiovascular bioengineering. Wang et al. reported that the ideal blood vessel replacement should exhibit several characteristics, such as biodegradability, biocompatibility, ability to integrate and bear typical physiologic conditions, while being able to adapt to somatic growth, and can be manufactured at reasonable cost. Bioengineered large blood vessels are a clinical reality, with mainly bovine-derived decellularized arteries and veins. Oropeza et al. reported on a bioengineered ascending aorta, obtained by bioprinting with a viscous ink that was generated by lyophilized and powdered decellularized hearts and human aortic smooth muscle cells. This bioprinted scaffold was reported to possess biomechanical properties similar to those of an immature, growing aorta and, therefore, has the potential to be used as a pediatric aortic model *in vitro*.

The generation of a small-caliber vascular substitute remains a challenging problem, which has been addressed in this Research Topic. Maintenance of patency *in vivo* is the main issue for arteries with a caliber smaller than 6 mm. In order to overcome this issue, Liu et al. proposed the use of crosslinking with photooxidation and penta-galloyl glucose with a view to increasing the biomechanical and biochemical stability of the decellularized internal mammary artery. The treated acellular bovine-origin was grafted in rabbit models of subcutaneous implantation and abdominal aorta transposition, and demonstrated a 4-month overall patency, no stenosis or calcification, null immune response, good biocompatibility, and cellular repopulation. Surgical intervention for small-caliber arterial substitution is frequently urgent, as in the case of coronary bypass after an ischemic heart attack. Most of the current protocols for the preparation of decellularized tubular scaffolds are generally time-consuming and unable to readily address the immediate clinical demand. In order to bridge this temporal gap, Massaro et al. developed a 5-h decellularization protocol for porcine carotid arteries. *In vitro* tests revealed biomechanical integrity and biocompatibility with rat endothelial cells and human umbilical vein endothelial cells (HUVECs), provided that efficient removal of the decellularization detergent (sodium dodecyl sulfate; SDS) was reached. Sterilization and preservation methodologies for small-caliber arterial grafts still need to be optimized, since decellularization protocols might introduce alterations in the treated tissues. Zia et al. investigated the effects of peracetic acid (PAA) and gamma irradiation and reported depletion of collagen IV and overall deterioration of the decellularized tibial artery scaffold using PAA, while both methods reduced the glycosaminoglycan content. This study demonstrated for the first time the feasibility of combining the decellularized scaffold with an electrospun PCL/PEG sleeve that endowed antimicrobial properties and mechanical stability to the graft.

As mentioned above, decellularized heart valves have been among the first scaffolds to reach the clinical setting. Many protocols have been developed to manufacture decellularized heart valve replacements, but yet, decellularization efficiency has been evaluated following not univocal parameters. Naso and Gandaglia emphasized the need to standardize decellularization procedures and recommended a checklist for quality control of heart valve replacements generated with these treatments. Singh et al. proposed a novel application for decellularization treatments. Aldehyde-treated human hearts that are preserved in anatomopathological tissue banks, have been shown to stiffen and might be less informative in medical education and training. Decellularization could restore the original native biomechanical properties of heart valves for high fidelity *in vitro* simulation.

The generation of whole functional solid organs, including liver, kidney, lungs, or heart, which have an inherent sophisticated structure, still faces a number of challenges that need to be

addressed (Hussein et al., 2020). Vascular reconstruction or reendothelialization is the main obstacle to avoiding coagulation and guaranteeing continuous blood flow through the transplanted organ (Hussein et al., 2016). Li et al. reviewed the different techniques that have been developed to enhance the reendothelialization efficiency, promote cell seeding of parenchymal cells, and improve graft functionality during both *in vitro* and *in vivo* perfusion of the bioengineered liver. Fathi et al. investigated an alternative way to overcome the reendothelialization problem through an axial pre-vascularization approach of the decellularized liver and evaluated its suitability for pancreatic islet transplantation. They reported that both fresh bone marrow preparation or adipose-derived stem cell-seeded scaffolds showed superior vascularization and graft function compared to the acellular scaffold in streptozotocin-diabetic rats. Using a novel method to enhance endothelial cell coverage in whole lung scaffolds, Yuan et al. developed a culture protocol with the presence of Rho-associated protein kinase (ROCK) inhibitor (Y27632). They investigated the effect of decellularized whole lung scaffolds on reseeded endothelial phenotypes and functions using single-cell RNA-sequencing analysis. This sequencing analysis demonstrated that primary rodent pulmonary microvascular or human-induced pluripotent stem cell-derived endothelium started to regain the native endothelial phenotypes after transitioning from expansion on culture plates into the decellularized lung scaffold.

Akinnola et al. demonstrated that endothelial cells may exhibit selective tropism during reendothelialization. They reseeded the blood vessels of decellularized mouse lung with rat pulmonary microvascular endothelial progenitor cells (RMEPCs), pulmonary arterial endothelial cells (PAECs), or microvascular endothelial cells (MVECs). They reported that PAECs and MVECs possessed selective tropism for larger vessels or microvasculature, respectively, while RMEPCs lacked site preference and were located to all vascular segments. Additionally, they reported that cells with selective tropism were suboptimal for functional reendothelialization of the vasculature within the whole organ.

Cell sourcing for recellularization has been identified as another challenge for the application of decellularized tissues and organs. Girard et al. obtained stromal vascular fractions by 20 inter-syringe passages and suggested that could be applicable to reseed decellularized tissues. These cells are considered a large source of autologous progenitor cells that can be harvested during liposuction or lipectomies that are classically used in plastic and aesthetic surgery.

Neishabouri et al. highlighted and summarized the different decellularization and sterilization methods, testing decellularization efficiency, and the current challenges and prospects of decellularization.

As another application of decellularized tissues, Narciso et al. used different decellularizing agents to develop a fast and efficient decellularization technique for lung tissue slices attached to a glass slide. This work could be an important tool for cancer research studies on scarce and valuable samples/clinical biopsies as well as to use the decellularized extracellular matrix as a cell culture substrate. Last but not least, Solarte David et al. discussed the natural decellularized ECM, obtained from different tissues, as a promising approach for wound healing. These ECMs could provide a convenient microenvironment through its constituents of cytokines, proteins, and growth factors that could coordinate inflammation, re-epithelialization, and remodelling processes.

This Research Topic presents a snapshot at the cutting edge of tissue and organ decellularization and subsequent recellularization, particularly focusing on the hurdles and unresolved issues that need to be overcome towards the engineering of tissues and organs for clinical transplantation in the near future. The associate editors would like to thank the editors of Frontiers in Bioengineering and Biotechnology for hosting this Research Topic, the reviewers for their valuable help in assessing the contributions, and the authors for contributing their high-quality studies to this Research Topic. The editors hope that their Research Topic will be interesting and useful to the readers and researchers in the fields of tissue engineering and regenerative medicine.

Author contributions

All authors listed have made a substantial, direct, and intellectual contribution to the work and approved it for publication.

Conflict of interest

The authors declare that the research was conducted in the absence of any commercial or financial relationships that could be construed as a potential conflict of interest.

Publisher's note

All claims expressed in this article are solely those of the authors and do not necessarily represent those of their affiliated organizations, or those of the publisher, the editors and the reviewers. Any product that may be evaluated in this article, or claim that may be made by its manufacturer, is not guaranteed or endorsed by the publisher.

References

Amoroso, N. J., D'Amore, A., Hong, Y., Rivera, C. P., Sacks, M. S., and Wagner, W. R. (2012). Microstructural manipulation of electrospun scaffolds for specific bending stiffness for heart valve tissue engineering. *Acta Biomater.* 8, 4268–4277. doi:10.1016/j.actbio.2012.08.002

Galili, U. (2015). Avoiding detrimental human immune response against Mammalian extracellular matrix implants. *Tissue Eng. Part B Rev.* 21, 231–241. doi:10.1089/ten.teb.2014.0392

Galili, U. (2001). The α-gal epitope (Galα1-3Galβ1-4GlcNAc-R) in xenotransplantation. *Biochimie* 83, 557–563. doi:10.1016/s0300-9084(01)01294-9

Gilbert, T. W., Sellaro, T. L., and Badylak, S. F. (2006). Decellularization of tissues and organs. *Biomaterials* 27, 3675–3683. doi:10.1016/j.biomaterials.2006.02.014

Hussein, K. H., Park, K. M., Kang, K. S., and Woo, H. M. (2016). Heparin-gelatin mixture improves vascular reconstruction efficiency and hepatic function in bioengineered livers. *Acta Biomater.* 38, 82–93. doi:10.1016/j.actbio.2016.04.042

Hussein, K. H., Park, K. M., Yu, L., Song, S. H., Woo, H. M., and Kwak, H. H. (2020). Vascular reconstruction: A major challenge in developing a functional whole solid organ graft from decellularized organs. *Acta Biomater.* 103, 68–80. doi:10.1016/j.actbio.2019.12.029

Kaminski, A., Klopsch, C., Mark, P., Yerebakan, C., Donndorf, P., Gäbel, R., et al. (2011). Autologous valve replacement-CD133+ stem cell-plus-fibrin composite-based sprayed cell seeding for intraoperative heart valve tissue engineering. *Tissue Eng. Part C Methods* 17, 299–309. doi:10.1089/ten.tec.2010.0051

Masters, K. S., Shah, D. N., Leinwand, L. A., and Anseth, K. S. (2005). Crosslinked hyaluronan scaffolds as a biologically active carrier for valvular interstitial cells. *Biomaterials* 26, 2517–2525. doi:10.1016/j.biomaterials.2004.07.018

Mcclelland, R. E., Dennis, R., Reid, L. M., Stegemann, J. P., Palsson, B., and Macdonald, J. M. (2012). "Chapter 6 - tissue engineering," in *Introduction to biomedical engineering*. Editors J. D. ENDERLE and J. D. BRONZINO (Boston: Academic Press).

Moreira, R., Gesche, V. N., Hurtado-Aguilar, L. G., Schmitz-Rode, T., Frese, J., Jockenhoevel, S., et al. (2014). TexMi: Development of tissue-engineered textile-reinforced mitral valve prosthesis. *Tissue Eng. Part C Methods* 20, 741–748. doi:10.1089/ten.tec.2013.0426

Mosadegh, B., Xiong, G., Dunham, S., and Min, J. K. (2015). Current progress in 3D printing for cardiovascular tissue engineering. *Biomed. Mater* 10, 034002. doi:10.1088/1748-6041/10/3/034002

Shi, Y., and Vesely, I. (2003). Fabrication of mitral valve chordae by directed collagen gel shrinkage. *Tissue Eng.* 9, 1233–1242. doi:10.1089/10763270360728143

Syedain, Z., Reimer, J., Schmidt, J., Lahti, M., Berry, J., Bianco, R., et al. (2015). 6-month aortic valve implantation of an off-the-shelf tissue-engineered valve in sheep. *Biomaterials* 73, 175–184. doi:10.1016/j.biomaterials.2015.09.016

frontiers in Bioengineering and Biotechnology

ORIGINAL RESEARCH
published: 16 August 2021
doi: 10.3389/fbioe.2021.727869

Engineering Functional Vasculature in Decellularized Lungs Depends on Comprehensive Endothelial Cell Tropism

*Ifeolu Akinnola[1], Daniel R. Rossi[2], Carolyn Meyer[2], Ashley Lindsey[3], Douglas R. Haase[4], Samuel Fogas[2], Michael J. Ehrhardt[2], Rachel E. Blue[4], Andrew. P. Price[2], Max Johnson[2], Diego F. Alvarez[3], Doris A. Taylor[5] and Angela Panoskaltsis-Mortari[2,6]**

[1]MSTP, University of Minnesota Medical School, Minneapolis, MN, United States, [2]Pediatric Blood and Marrow Transplantation and Cell Therapy, University of Minnesota, Minneapolis, MN, United States, [3]Internal Medicine and Center for Lung Biology, College of Medicine, University of South Alabama, Mobile, AL, United States, [4]University of Minnesota Medical School, Minneapolis, MN, United States, [5]RegenMedix, Houston, TX, United States, [6]Pulmonary, Allergy, Critical Care and Sleep Medicine, University of Minnesota, Minneapolis, MN, United States

OPEN ACCESS

Edited by:
Laura Iop,
University of Padua, Italy

Reviewed by:
Zaozao Chen,
Southeast University, China
Jun Liao,
University of Texas at Arlington, United States

***Correspondence:**
Angela Panoskaltsis-Mortari
panos001@umn.edu

Specialty section:
This article was submitted to Biomaterials, a section of the journal Frontiers in Bioengineering and Biotechnology

Received: *20 June 2021*
Accepted: *02 August 2021*
Published: *16 August 2021*

Citation:
Akinnola I, Rossi DR, Meyer C, Lindsey A, Haase DR, Fogas S, Ehrhardt MJ, Blue RE, Price AP, Johnson M, Alvarez DF, Taylor DA and Panoskaltsis-Mortari A (2021) Engineering Functional Vasculature in Decellularized Lungs Depends on Comprehensive Endothelial Cell Tropism. Front. Bioeng. Biotechnol. 9:727869. doi: 10.3389/fbioe.2021.727869

Tissue engineering using decellularized whole lungs as matrix scaffolds began as a promise for creating autologous transplantable lungs for patients with end-stage lung disease and can also be used to study strategies for lung regeneration. Vascularization remains a critical component for all solid organ bioengineering, yet there has been limited success in generating functional re-endothelialization of most pulmonary vascular segments. We evaluated recellularization of the blood vessel conduits of acellular mouse scaffolds with highly proliferating, rat pulmonary microvascular endothelial progenitor cells (RMEPCs), pulmonary arterial endothelial cells (PAECs) or microvascular endothelial cells (MVECs). After 8 days of pulsatile perfusion, histological analysis showed that PAECs and MVECs possessed selective tropism for larger vessels or microvasculature, respectively. In contrast, RMEPCs lacked site preference and repopulated all vascular segments. RMEPC-derived endothelium exhibited thrombomodulin activity, expression of junctional genes, ability to synthesize endothelial signaling molecules, and formation of a restrictive barrier. The RMEPC phenotype described here could be useful for identifying endothelial progenitors suitable for efficient vascular organ and tissue engineering, regeneration and repair.

Keywords: endothelial progenitors, decellularization, extracellular matrix, tissue engineering, bioscaffold recellularization

INTRODUCTION

The treatment of end-stage lung diseases requires lung transplantation, yet there is a severe shortage of available lungs for transplant. Roughly 20% of patients on lung transplant lists are removed before receiving a new lung due to death or becoming too ill to undergo the procedure (Ahya and Diamond, 2019). Tissue engineering using decellularized whole lungs as scaffolding might provide an opportunity to generate functional lungs for autologous transplant in patients for whom there is no other therapeutic alternative. Despite some advancements in lung tissue engineering (Petersen et al., 2010; Song et al., 2011; Calle et al., 2014; Ren et al., 2015; Balestrini et al., 2016), to date, the

establishment of a functioning vasculature with low thrombogenicity and adequate barrier function has proven to be difficult, resulting in lung failure. Although synthetic vascular grafts are utilized clinically for simple vessels (Deutsch et al., 2009) current synthetic materials can mimic neither the anatomical placement of cells interacting at the air-liquid interface, the native mechanical properties of the lung, nor the complex organ compositional and micro-environmental cues needed for geospatial branching. Perfusion-based decellularization provides an alternative approach that preserves the lung's native architecture and extracellular matrix composition, overcoming these challenges (Price et al., 2010; Daly et al., 2012). Decellularized lungs provide the ideal biomimetic cues for appropriate cell localization, differentiation, and function. Such three-dimensional niches are conducive to physiological cell-matrix and cell-cell crosstalk, potentially enhancing the functionality and stability of engineered, transplantable organs.

Whole complex solid organ regeneration, while still in the early stages, has rapidly matured since the initial demonstration for the heart (Ott et al., 2008; Gilpin et al., 2016). Bioengineered lungs implanted in rats showed evidence of successful gas exchange for up to 7 days (Song et al., 2011), and a similar method is being developed using a nonhuman primate model (Bonvillain et al., 2012). Bioengineered lungs have also been successfully implanted into large, non-primate mammals lasting up to 2 months, without acute rejection, where the implanted lung displayed continued growth and restoration of native microbiota (Nichols et al., 2018). While the longevity of a lung transplant depends on many different factors, the functionality of engineered grafts has faltered primarily from their susceptibility to thrombus formation and barrier leakiness (Petersen et al., 2010; Kurobe et al., 2012; Balestrini et al., 2016; Liu et al., 2018). In native tissues, the endothelium regulates hemostasis and thrombosis, forming a functional barrier that allows for selective permeability (Feletou and Vanhoutte, 2006; Aird, 2007). The primary goal of this study was to determine the endothelial cell specification necessary to generate functional, patent pulmonary vasculature using acellular whole lung matrices in bioreactor conditions. We show the identification of a pulmonary endothelial cell population from a single source that can overcome selective tropism, recellularize all vascular areas of an acellular lung scaffold, and provide a functional barrier.

METHODS

Animals: Male B10.BR mice were bred in-house at the University of Minnesota Research Animal Resources facility and used at 8–12 weeks of age. Sprague Dawley rats were purchased from Charles River Laboratory, housed at University of South Alabama and used at 4 months of age. All experiments were approved by the Institutional Animal Care and Use Committees of the respective institutions.

Perfusion based decellularization of whole mouse lungs: Mouse lungs were decellularized as previously published (Price et al., 2010). Lungs were excised *en bloc* with the trachea and heart, and were perfused with sequential solutions of deionized water, 0.1% Triton X-100, 1% 3α,12α-dihydroxy-5β-cholanic acid sodium salt (Na deoxycholate), 1 M NaCl, then 30 mg/ml porcine pancreatic DNase in 1.3 mM $MgSO_4$ and 2 mM $CaCl_2$, followed by a final rinse with sterile, deionized water. Cell removal was verified via 4′,6-diamidino-2-phenylindole (DAPI) immunofluorescence (Vector Labs) confocal microscopy (Olympus FV500) on cryosections of representative lungs processed at the same time for quality control purposes, as well as DNA quantitation using the PicoGreen Assay (Price et al., 2015). Decellularized scaffolds were maintained at 4°C in PBS containing pen/strep to maintain sterility.

Isolation and culture of rat endothelial cells: PAECs, MVECs, and RMEPCs were isolated from Sprague-Dawley rats and cultured as previously described (King et al., 2004; Alvarez et al., 2008). For PAECs, the main pulmonary artery was dissected from the root to a second vessel generation and under sterile conditions placed in a 60 mm dish containing ice-cold DMEM (GIBCO). The vessels were inverted, the intima was scraped, and the collected cells were strained with a 20 μm filter (BD Biosciences). Harvested cells were transferred to a T75 flask, supplemented with DMEM enriched with 20% FBS (Hyclone) and 100 U/ml penicillin-100 μg/ml streptomycin (GIBCO) and were incubated at 37°C with 5% CO_2-21% O_2. For MVECs, the distal lung parenchyma was sliced, and the subjacent tissue was carefully dissected and placed in a 60-mm dish containing cold DMEM (4°C). Tissue was digested with type II collagenase (Worthington), rinsed with DMEM, transferred to a T75 flask, and incubated as described for PAECs. Cell culture medium was replaced with DMEM + 10% FBS and 1% penicillin/streptomycin and passages 5–7 were used for consecutive experiments. Cells were selected for homogeneity based on morphological appearance and tested by flow cytometry as described below. For RMEPCs, cells were selected after subjecting MVECs to a single-cell clonogenic assay as described (Alvarez et al., 2008). All cells were screened for *mycoplasma* (Lonza #LT07) and found to be negative.

Flow cytometry characterization of rat endothelial cells: PAECs, MVECs, RMEPCs were characterized by flow cytometry using a FACSCalibur (BD Biosciences) and analyzed with Cyflogic software. Cells were phenotyped using antibodies to rat CD31 (Abcam #ab28364), CD34 (BD Biosciences #341071), CD62P (Takara Bio #M062), CD104 (Millipore #AB 1922), CD146 (R&D Systems #FAB3250P), eNOS (Santa Cruz #sc654), VE-Cadherin (Santa Cruz #sc9989), VEGF (Santa Cruz #sc507), vWF (Affinity Biologicals #SARTW), and lectins from *Griffonia simplicifolia I and II* (GSI and GSII, EY Laboratories #F-2401-B-1 and #R2402-2), and *Helix pomatia* (HP, EY Laboratories #R3601-1 and F3601-1).

Gene expression: mRNA from recellularized lungs and cells grown in tissue culture flasks was analyzed using the RT2 Profiler PCR Array for Rat Tight Junctions (Qiagen, Valencia, CA). cDNA was generated using the RT2 First Strand Kit (Qiagen) following the product insert. Quantitative real-time PCR was performed on an ABI 7500 Real Time PCR System using the RT2

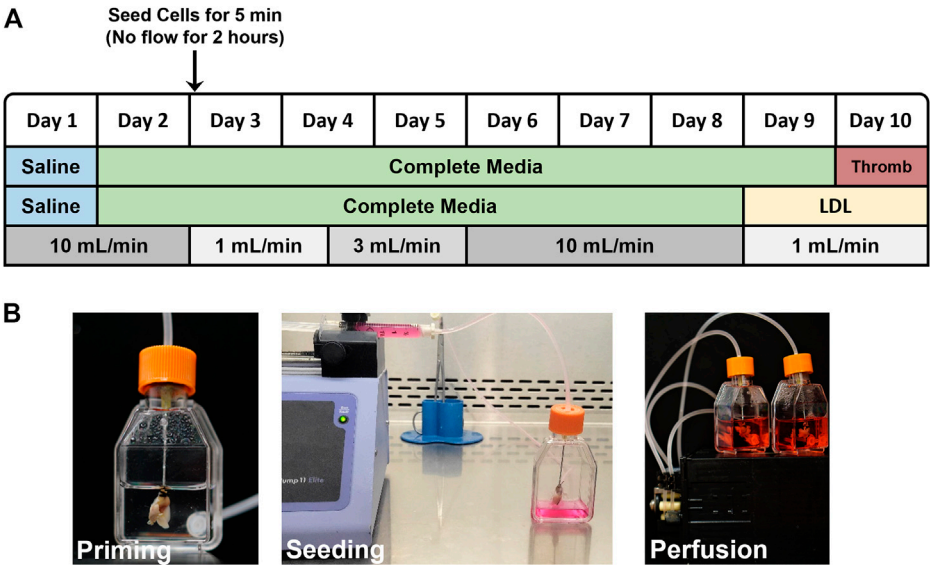

FIGURE 1 | (A) Flow chart outlining the reseeding protocol. LDL-uptake and Thrombogenicity assays were conducted on day 9 and 10, respectively. **(B)** Photographs showing assembled, modified tissue culture flask bioreactor with attached acellular mouse lung scaffold during priming with saline **(left)**, injector pump seeding ECs into acellular scaffold via right ventricle **(middle)**, and reseeded lung scaffolds with 25 ml of media in a closed loop system, attached to pulsatile pump **(right)**.

SYBR Green ROX qPCR MasterMix (Qiagen). Results were entered into the Ingenuity pathway analysis program (Ingenuity Systems, Inc.). Relative gene expression analyses of LDL-receptor, scavenger receptors and integrins was done by isolating total RNA from cells with TRIzol (Invitrogen, Carlsbad, CA), generating cDNA using the Superscript III First Strand RT PCR kit (Life Technologies), and qRT-PCR done using Taqman Universal PCR Mastermix (Life Technologies). For analysis, samples were only used in comparison if they met our cutoff criteria (i.e. CT values ≤ 35 and dCT Std Err ≤0.25). The probes used for these analyses were ordered from Life Technologies (Grand Island, NY) and listed in **Supplementary Table S5**. For analysis of LDL-receptor and scavenger gene expression, samples from each cell line underwent serum starvation overnight prior to obtaining total RNA.

In vitro tube formation assay: Tube formation assays were performed as previously published (Chung-Welch et al., 1989). PAECs, MVECs, and RMEPCs were seeded at 4×10^4 cells per well, in triplicate, of a 24-well plate coated with 100 µl/cm^2 BD Matrigel (BD Biosciences) and incubated at 37°C, 5% CO_2. Cultures were imaged with a phase-contrast microscope (Leica) 2, 4, 8, and 24 h post-seeding.

Assessment of endothelial function: Dil-Ac LDL (1,1′-dioctacecyl-1,3,3,3′3-tetramethyl-indocarbocyanine perchlorate acetylated low density lipoprotein) uptake in PAECs, MVECs, and RMEPCs was measured in confluent cultures using previously published methods (Chang et al., 2009). Cultured cells were incubated with 10 µg/ml Dil-Ac LDL (ThermoFisher) for 4 h before analyzing for fluorescence at 550 nm (Leica). For reseeded lung scaffolds, 10 µg/ml Dil-Ac LDL was added to the bioreactor media 7 days after seeding to assess uptake. To prepare for histological analysis, lung constructs were inflated with PBS:OCT (1:3 ratio), embedded in OCT, frozen in liquid nitrogen and stored at -80°C. Cryosections (7 µm) were air dried, fixed with methanol (4°C) for 10 min and air dried for 30 min. Slides were then rinsed twice with PBS for 3 min, then with PBS-Tween 20 (0.2 M PBS, 0.05% Tween 20, pH 7.4) twice for 2 min before coverslipping with VectaShield mounting medium (Vector Labs) containing nucleic acid stain 4′,6-diamidino-2-phenylindole (DAPI) and imaged using a confocal microscope (Olympus FV500).

Bioreactor assembly: T-25 flasks were modified in sterile conditions. Holes were created through the vented filter cap and on the bottom of one wall just large enough to allow passage of 2 mm outer diameter Puri-Flex tubing (Masterflex) through both holes. This allowed for continuous circulation of liquid out from the bottom of the bioreactor, through an adjustable Masterflex pump, and back in through the cap, terminating with a 20 gauge x 1 ½″ disposable murine gavage needle (Cadence Science) serving as a cannula for the heart/lung bloc. A hole was created in the right ventricular wall to allow insertion of the rubberized gavage needle tip to access the pulmonary trunk (main pulmonary artery).

Reseeding decellularized lungs with endothelial cells: The bioreactor set up, cell seeding protocol and assay endpoints are shown in **Figure 1A**. Decellularized lungs were perfused in a humidified bioreactor at 37°C/5%CO_2/21%O_2 with 25 ml PBS for 1 day (24 h), then with 25 ml of DMEM containing 10% FBS and 1% penicillin-streptomycin (complete media) for 1 day (24 h) prior to reseeding. Endothelial cells were washed with PBS and lifted from theirz tissue culture dish via 0.05% trypsin/EDTA, centrifuged for 5 min at ×2,000 g, and resuspended at 1×10^7 cells/ml. The cell suspension was filtered using a 40 µm pore mesh and loaded in a 3 ml luer lock syringe, for a total

of 3×10^7 cells injected into each pair of decellularized lungs. The 20 gauge x 1 ½″ disposable gavage needle cannulating the decellularized heart/lung bloc was then attached to the syringe and placed in an automated syringe pump set at 0.6 ml/min. During the 5 min cell infusion, a 15 ml conical tube was placed under the lungs to collect flow for a final cell count and viability analysis. 25ml of fresh complete media was then added to each flask. After cell infusion, the gavage needle was removed from the luer lock syringe and attached to the bioreactor tubing. Air bubbles were avoided by priming the tubing before connections were made. The reseeded lungs were incubated in a humidified chamber at 37°C/5%CO_2/21% O_2 for 2 h prior to beginning vascular perfusion. Flow rates began at 1 ml/min on Day 3 (for 36 h), increased to 3 ml/min on Day 4 (for 36 h), increased again to 10 ml/min on Day 6 (for 72 h), and then slowed to 1 ml/min on Day 9 prior to the start of the acetylated LDL uptake or thrombogenicity assays. Media was replaced 24 h after cell seeding and then every 48 h thereafter. The lungs were then removed from the bioreactor to be frozen. Frozen lungs were rinsed with PBS, infused with PBS:OCT (1:3 ratio), embedded in OCT, flash frozen in liquid N_2 and stored at −80°C.

H&E and Immunofluorescence staining of reseeded lungs: Frozen lung cryosections (7 μm) were prepared as described above. Sections were blocked with 10% normal horse serum for 30 min at room temp and incubated in the dark overnight at 4°C with 1 μg/ml rabbit-anti- VEGF (Santa Cruz #sc507) and sheep-anti-vWF (Affinity Biologicals #SARTW) primary antibodies. Sections were rinsed with PBS-Tween 20 before incubating 30 min at room temp with 1:1,000 Goat Anti-Rabbit IgG TRITC (Jackson #111-025-003) and Donkey Anti-Sheep IgG FITC (R&D Systems #F012F) secondary antibodies, then rinsed 3 times with PBS-Tween 20 for 2 min before coverslipping with VectaShield mounting medium (Vector Labs) containing DAPI. Absence of mouse cells was confirmed by negative PCR for murine GAPDH as described (Price et al., 2010).

Thrombomodulin activity assay: Measuring function of thrombomodulin (CD141) on endothelial cells was adapted from previously published studies (Calnek and Grinnell, 1998; Ibrahim and Ramamurthi, 2008; Robertson et al., 2014). Positive control lungs were excised from euthanized (sodium pentobarbital, 50 mg/kg ip) adult male B10.BR mice with the trachea and heart attached; after exsanguination via the right ventricle, the heart-lung bloc was perfused with PBS. After 7 days in bioreactor (Day 10), all lung (controls and reseeded) constructs were perfused for 15 min at 3 ml/min with 25 ml phenol red-free DMEM/F12. They were then perfused for 45 min at 1 ml/min with 4 ml phenol red-free DMEM/F12 plus human α-thrombin (0.1 U/ml) and human protein C (12 μg/ml). In triplicate, 100 μl was transferred to a 96-well plate and incubated for 5 min at 37°C with excess hirudin (6 U/ml) to inactivate the α-thrombin. S-2366 (Chromogenix) was added for a final concentration of 0.75 mM and incubated at room temperature for 5min before measuring absorbance at λ = 410 nm and λ = 490 nm (BIORAD Model 550). The relative absorbance was calculated by subtracting the mean acellular absorbance (λ = 410 nm from λ = 490 nm) from each sample.

Vascular permeability assay: To assess vascular barrier function in recellularized lungs, Evans blue (EB)-tagged bovine serum albumin (BSA) was perfused through the vasculature and measured using a near-infrared spectrophotometry method adapted from previously published studies (Lowe et al., 2010; von Drygalski et al., 2012). Decellularized and recellularized, and exsanguinated control mouse lung/heart blocs were weighed and perfused for 5 min with phenol red-free DMEM, then for 15 min with 0.4% EB-tagged BSA (EB-BSA) in phenol red-free DMEM, followed by a 5 min perfusion with 4% BSA in PBS before immersing and gently shaking in PBS as a final rinse. The hearts were then removed and weighed to obtain accurate lung weights for data normalization. EB-BSA content of each lung was then analyzed immediately using a Li-COR Odyssey scanner reading at 700 nm at a resolution of 169 μm and "Intensity" = 2. The lungs were scanned at three distinct focal planes (2, 3, and 4 mm) and the average of the three planes was then normalized to lung weight for a final measure of EB-BSA permeability.

In addition to evaluating EB-BSA permeability of recellularized lungs, isogravimetric and lung perfusion methods were used to recorded absolute change in weight of RMEPC-recellularized, decellularized and native mouse lungs. Gavage needles were inserted though the right ventricles in order to use the heart as conduit to the pulmonary vasculature. The trachea was then attached to an isometric force transducer (Harvard Apparatus) with a suture. 2 mm OD Masterflex tubing submerged in a 50 ml conical filled with PBS was primed and connected to the gavage needle while a P75 Hugo Sachs Elektronik pressure transducer (Harvard Apparatus) was added inline. A peristaltic pump was turned on to begin perfusion of the pulmonary vasculature with PBS. Every 5 min, measurements from the pressure and force transducers were taken, followed by an increase in flow rate. This process continued until maximum flow rate from the pump was achieved. Data Acquisition ActiveX™ (DTx-EZ, Quick DataAcq) was used to record measurements from the pressure transducer. Results were recorded into Microsoft Excel, where average slope of each sample ($\Delta V_{Force}/\Delta V_{Pressure}$) and the average for each group was calculated.

Cytokine assays: Supernatants from endothelial cell cultures and effluent collected from decellularized and recellularized lungs (48 h collections) were assessed for levels of cytokines and soluble mediators that have been shown to play roles in angiogenesis, vascular integrity and permeability. Samples were evaluated for CXCL1, TIMP1, PAI1, and VEGF via the Luminex platform (Austin, TX) using rat-specific bead sets from Millipore (Billerica, MA) and data analyzed with BioPlex software (BioRad, Hercules, CA).

Statistics

Statistical significance comparisons between control, decellularized, and recellularized lungs were analyzed by using one-way ANOVA using Tukey as a post-hoc test (R x64 2.15.0 statistical software). $p < 0.05$ was considered significant.

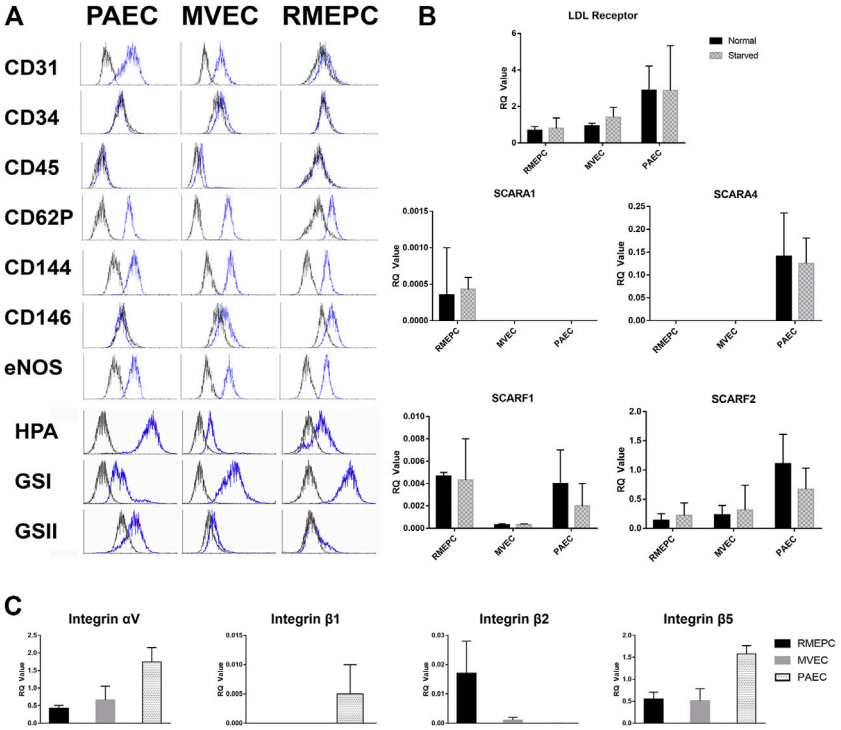

FIGURE 2 | PAEC, MVEC, and RMEPC express representative endothelial cell associated markers and lectin binding properties as assessed via flow cytometry **(A)**. In addition, gene expression of LDL-receptor, selected scavenger receptors, and selected integrin chains were assessed via qPCR **(B,C)**. For qPCR data, $n = 3$ for each sample/condition.

RESULTS

Characterization of Pulmonary Endothelial Cells

All cultured rat pulmonary endothelial cells used in these studies were capable of *in vitro* tube formation in Matrigel (**Supplementary Figure S1A**) as previously demonstrated (Alvarez et al., 2008). Functionality of the cultured rat endothelial cells was confirmed *in vitro* by demonstrating uptake of Dil-Ac LDL (**Supplementary Figure S1B**). In addition, PAECs, MVECs, and RMEPCs were assessed by flow cytometry to confirm the phenotypes perfused into the decellularized lungs. RMEPCs were negative for CD31 (PECAM-1), whereas PAECs and MVECs stained positively (**Figure 2**). RMEPCs expressed less CD62P (P-selectin), and more CD146 (MUC18) when compared to PAECs and MVECs. Consistent with their endothelial phenotype, all cells displayed high levels of CD144 (VE-Cadherin) and eNOS, and lacked expression of CD34 (mucosialin) and CD45 (leukocyte common antigen). RMEPCs and MVECs were differentiated from their PAEC counterpart by their higher binding to lectins GSI, with low or negative binding to GSII and HPA, consistent with our previous report (Alvarez et al., 2008).

Gene expression of LDL-receptor, multiple scavenger receptors, as well as multiple integrin chains were assessed within PAECs, MVECs, and RMEPCs via qPCR within 2D cell culture. Fold change of genes for LDL-receptor and selected scavenger receptors (i.e. Scara1, Scara4, Scarf1 and Scarf2) were measured in both normal and serum starved conditions. Within both normal and serum starved conditions, all three pulmonary endothelial cell types had measurable expression of LDL-receptor, scavenger receptor class F, member 1 (Scarf1) and class F, member 2 (Scarf2). RMEPCs were the only cell type with measurable expression of Scara1 while PAECs were the only cell type with measurable expression of Scara4. For expression of selected integrin chains (i.e. αv, β1, β2, and β5), PAECs displayed the highest relative expression of αv, β1and β5. RMEPCs had the highest relative expression of β2 and virtually no expression of β1. Reported RQ values were normalized to fresh rat lung, which is comprised of multiple cell types, thus accounting for seemingly lower RQ values amongst some of our target genes.

From the assessment of endothelial markers and gene expression, we have established the overall phenotype of our RMEPCs as $CD31^{-}$, $CD45^{-}$, $CD144^{+}$, $eNOS^{+}$, $CD62P^{lo}$ cells with strong and weak binding to GSI and HPA, respectively. In addition, they have relatively higher gene expression of Scara1 and Itg-β2, compared to PAECs and MVECs.

Selective populations of endothelial cells and progenitor cells are necessary for segment-specific revascularization of decellularized lungs

PAECs, MVECs and RMEPCs were infused into the lung vasculature via the pulmonary artery trunk. Remarkably, when cells of arterial origin (PAECs) were used to reseed the tissue, only

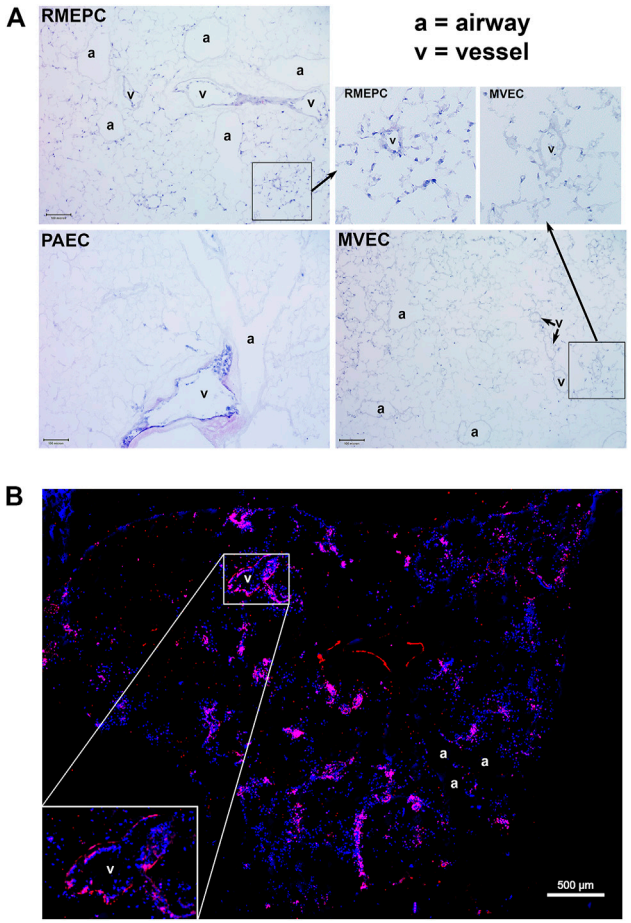

FIGURE 3 | (A) MVEC and PAEC show selective tropism to their *in vivo* point of origin whereas RMEPC exhibit pan-tropism to *ex vivo* decellularized ECM vascular conduits. Representative H&E-stained cryosections (5 um) of decellularized whole lungs re-seeded with progenitor enriched microvascular cells (RMEPC), pulmonary arterial endothelial cells (PAEC), and microvascular (MVEC). All images are at ×100 magnification (×10 objective). Scale bar indicates 100 µm. Arrows indicate zoomed-in areas comparing engraftment of RMPEC to microvasculature and larger vessel, whereas MVEC engraftment is only in microvasculature. **(B)** Immunofluorescent image of a decellularized mouse lung lobe seeded with RMEPCs. Cryosection was stained for VE-Cadherin (red). Multiple images taken at ×40 objective magnification and stitched together. DAPI used to label cell nuclei (blue).

extra-capillary vessels were recellularized. In contrast, areas of lung that originally housed microvascular endothelium remained acellular. The reverse was seen when cells of microvascular origin (MVECs) were used to re-endothelialize the vasculature: cells were observed in microvasculature (capillaries) whereas extra-capillary vessels remained acellular. Interestingly, progenitor enriched endothelial cells (RMEPCs) had tropism for both larger vessel (i.e. extra-capillary) and microvascular (capillary) ECM and showed more matrix coverage when compared to lungs reseeded with PAECs or MVECs alone (**Figure 3A**). Importantly, RMEPCs displayed attachment within both extra-capillary and capillary vessels when compared to PAECs and MVECs after 8 days of incubation (**Figure 3A**). RMEPCs displayed widespread expression of VE-Cadherin/CD144–a major protein in establishing membrane permeability (**Figure 3B**). The detection of VE-Cadherin supports the use of RMEPCs to recreate a functional barrier membrane throughout the decellularized vasculature. Together, the data indicate that endothelial cells derived from the microvascular segments and enriched for progenitors can revascularize all pulmonary segments.

Revascularized Lung Scaffolds Retain Endothelial Cells that Maintain Functional Attributes

In **Figure 4A**, decellularized mouse lungs reseeded with RMEPCs showed positive staining for PECAM-1 (CD31) and cytosolic vWF and VEGF after 8 days of incubation. This indicates that RMEPC possess the capacity to adopt a mature endothelial phenotype and retaining fundamental molecular cues for their functional

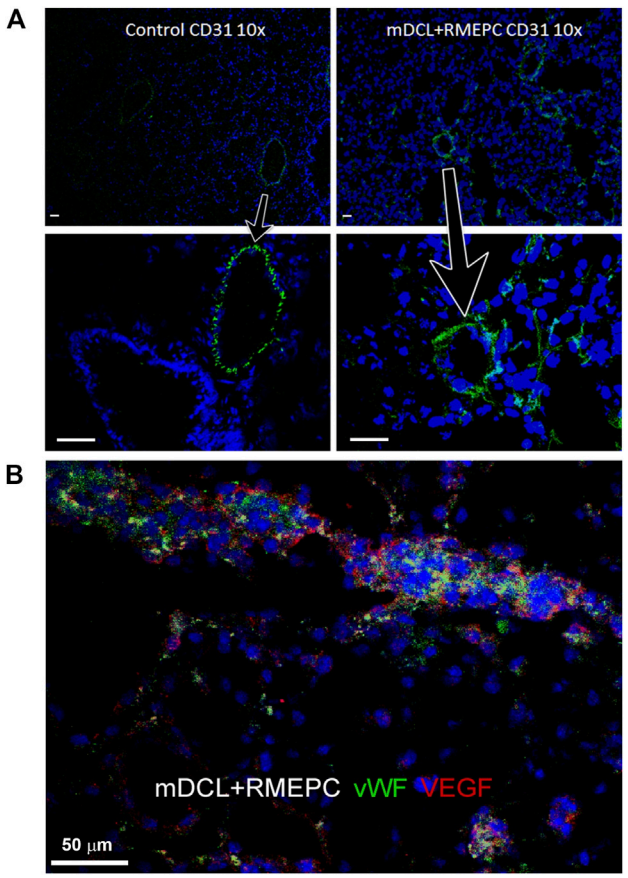

FIGURE 4 | RMEPC express endothelial markers after reseeding on decellularized mouse lungs. **(A)** PECAM-1 (CD31) expression in rat lung control and recellularized lungs. Images taken at ×100 magnification, ×10 objective; DAPI nuclear stain in blue. Arrows point to zoomed areas. **(B)** Immunofluorescence of representative image of RMEPC-recellularized lungs at ×630 magnification (×63 objective) showing expression of von Willebrand factor (vWF) and vascular endothelial growth factor (VEGF). DAPI nuclear stain in blue. Scale bars set to 50 µm in each panel.

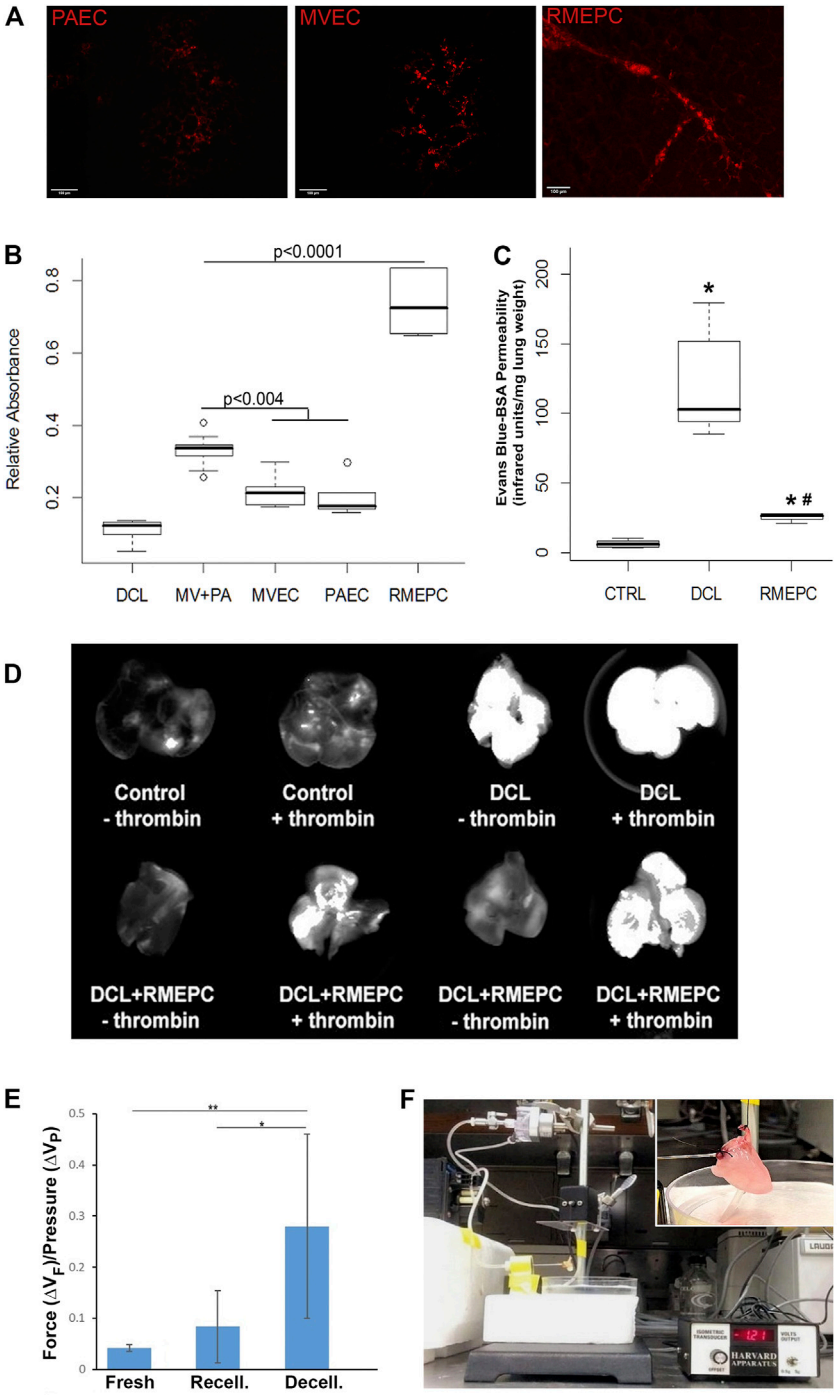

FIGURE 5 | Recellularized lungs are functional and maintain endothelial barrier integrity. **(A)** Uptake of Dil-Ac LDL in revascularized lungs. Cryosections (5 μm) viewed via confocal microscopy (Left–PAEC, Middle–MVEC, Right–RMEPC). **(B)** Thrombomodulin activity assay of recellularized lungs after 45 min perfusion with α-thrombin and protein C colorimetric activity was normalized to whole mouse lung controls ($n = 6$) and compared to decellularized lungs (DCL, $n = 6$), all other groups $n = 3$. **(C)** Vascular permeability of RMEPC-recellularized lungs ($n = 4$) compared to mouse lung controls (CTRL, $n = 8$) and decellularized lungs (DCL, $n = 8$) measured by near-infrared spectrophotometry of perfused Evans-blue-tagged albumin (EB-BSA). $^{*}p < 0.0000004$ vs. control; $^{*\#}p < 0.0004$ vs. decellularized lungs. **(D)** Representative whole lung near-infrared spectrophotometry of EB-BSA showing barrier integrity of RMEPC-recellularized lungs and increased permeability in response to thrombin (+). **(E)** Comparison of the average change in force (ΔV_F) gained per increase in pressure (ΔV_P) for native-fresh ($n = 4$), decellularized ($n = 7$), and RMEPC-recellularized ($n = 6$) mouse lungs (* indicates a p-value <0.05; ** indicates a p-value < 0.001). **(F)** Setup of isogravimetric experiment and insert of a close-up of heart/lung *en bloc*.

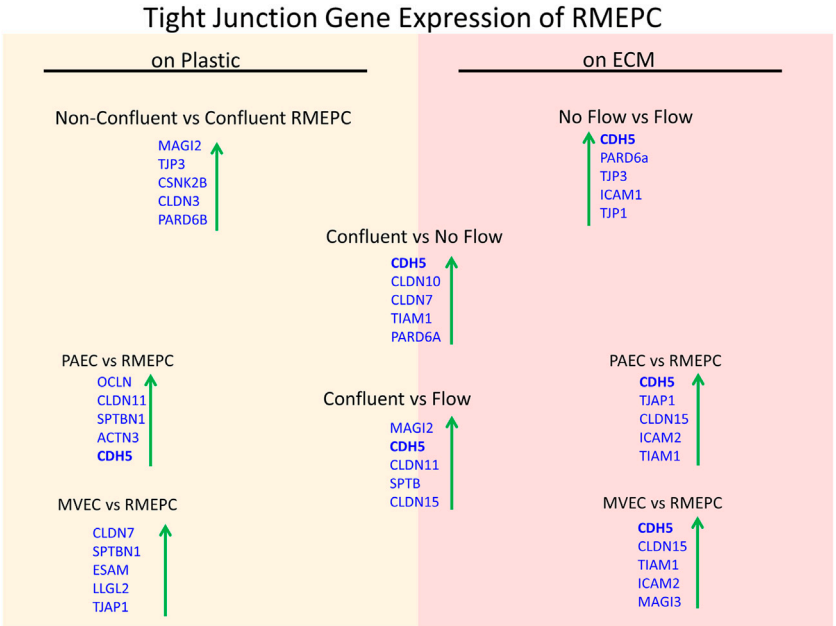

FIGURE 6 | Confluency, extracellular matrix and no-flow conditions promote the highest expression of tight junction genes by RMEPCs. Top left shows the top upregulated tight junction genes in response to confluency on RMEPCs cultured on plastic. Bottom left shows the increase in genes in confluent RMEPCs compared to confluent PAECs and MVECs cultured on plastic. The right-hand side (red) shows day 7 gene expression when seeded by perfusion on decellularized mouse lung ECM. The bottom right shows the top tight junction genes upregulated in RMEPCs vs. PAECs and MVECs on ECM (with flow) after 7 days. The middle portion shows the increases in tight junction genes in RMEPC in conditions vascular flow and no-flow for 7 days compared to confluency on plastic. The far top right compares no-flow vs. flow of RMEPCs on ECM.

behavior. Binding to GSI and HPA lectins could not be used to distinguish endothelial subtypes since these lectins could also bind to decellularized lung ECM (**Supplementary Figure S2**).

Figure 5A shows that decellularized mouse lungs reseeded and incubated for 7 days with rat PAECs, MVECs, or RMEPCs could take up Acetylated LDL. Thrombomodulin activity, relative to non-decellularized mouse lung controls (**Figure 5B**), was significantly increased in decellularized mouse lungs reseeded with RMEPCs compared with lungs reseeded with MVECs or PAECs or a combination of MVEC and PAECs (MV + PA). Collectively, these data demonstrate the extraordinary capacity of RMEPCs to generate endothelium barriers with functional behaviors.

RMEPCs-reseeded decellularized lung scaffolds display enhanced repopulation and functional barrier properties

To demonstrate that decellularized lungs reseeded with rat RMEPCs could maintain a functional barrier, lungs (after 8 days incubation) were perfused with EB-tagged BSA for 5 min. After clearing the vasculature with PBS, lungs were imaged for near-infrared fluorescence that can detect any albumin-conjugated-Evans Blue dye leaking into the pulmonary interstitium and airway space. As shown in **Figure 5C**, intact control lungs displayed marginal vascular leak as evidenced by the low detection of extra-vascular albumin. In contrast, decellularized lungs exhibited substantial vascular leak as evidenced by the high levels of extra-vascular albumin detected. Decellularized lungs reseeded with RMEPCs demonstrated low vascular leak approximating that exhibited by intact control lungs, indicating significant re-endothelialization of the lung scaffold. Importantly, **Figure 5D** shows that lungs reseeded with RMEPCs respond to α-thrombin with an increase in vascular permeability, albeit higher than the response of intact normal lungs. Therefore, lungs re-endothelialized with RMEPCs not only generated barriers that restrict the movement of fluid and solutes from the vascular to the interstitial space, but formed a barrier that responds to a circulating agonist known to increase permeability.

Further evidence of tight barrier formation was obtained by measuring expression of tight junction and cell adhesion genes by qRT-PCR. Comparisons were made for RMEPCs grown to confluence vs. non-confluence in 2D tissue culture, those grown on decellularized lung ECM scaffolds versus 2D tissue culture, and versus rat PAEC and MVEC cells in 2D and on decellularized lung ECM in pulsatile flow conditions. **Figure 6** and **Supplementary Table S1** show the top upregulated mRNAs in RMEPCs grown to confluence on plastic, with the highest being MAGI2, a gene that encodes for membrane-associated guanylate kinase inverted two protein. MAGI2 was further upregulated when RMEPC were grown on decellularized lungs under flow conditions. Growth on lung ECM also caused upregulation of several claudins as well as cadherin 5 (**Supplementary Tables S2, S3**). Since endothelial cells also respond to fluid flow and shear stress, mRNA expression of RMEPCs reseeded in decellularized lungs were compared in conditions of flow vs. no-flow (**Supplementary Table S4**). In

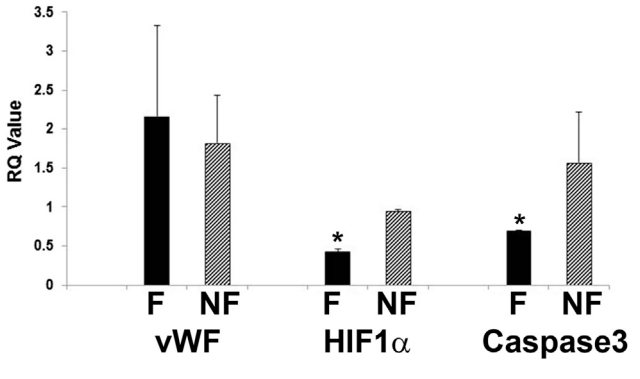

FIGURE 7 | Decreased apoptosis and hypoxic signal in RMEPC on ECM after 1 week in flow conditions. qRT-PCR for vWF, HIF-1a and caspase-3 are shown. F = flow, NF = no flow. *p=<0.05 for F vs. NF (n = 3/group).

flow conditions, expression of many tight junction genes was downregulated compared to no-flow conditions (i.e. they were higher in no-flow), a finding that is consistent with the formation of mature junctions *in vivo*. **Figure 7** shows that in conditions of flow, expression of HIF-1a and caspase-3 mRNAs were decreased compared to no-flow conditions when RMEPCs were seeded on decellularized ECM, indicating that flow decreases apoptosis and hypoxia in the endothelial cells as expected.

To further evaluate the function of reseeded cells, effluents from PAEC-, MVEC- or RMEPC-infused matrices were examined for secreted vascular factors. **Figure 8A** shows that RMEPC-seeded matrices secreted higher levels of PAI-1, TIMP-1 and VEGF-A compared to those seeded with MVECs, PAECs, or MVECs + PAECs. RMEPC-seeded lung scaffolds secreted levels of CXCL1 similar to PAEC-seeded scaffolds and were higher than those seeded with MVECs or MVECs + PAECs. Analysis of cell culture supernatants of these cells grown in tissue culture flasks (**Figure 8B**) showed that, within 2D culture, RMEPCs had the highest production of VEGF-A and TIMP-1, while levels of PAI-1 and CXCL1 were similar between RMEPCS and PAECs (and higher than MVECs). The discrepancies seen between cells grown in culture flasks versus those in reseeded lung scaffolds highlight the effect of ECM on signaling cytokine production in the three endothelial cell populations.

DISCUSSION

We have described a pulmonary endothelial cell population generated from microvasculature that can functionally recellularize heterogeneous vascular segments of decellularized lung scaffolds. Perfusion of the vasculature with a pulsatile flow of endothelial populations enriched with progenitor cells assembles functional pulmonary vasculatures using a xenogeneic reseeding approach. Moreover, infused mature pulmonary microvascular endothelial cells consistently display selective tropism for their vascular segment of origin, whereas PAECs prefer to repopulate larger vessel conduits. Along with work conducted by other groups (Marcu et al., 2018; Scarritt et al., 2018), this observation indicates that engraftment into specific vascular segments is dependent on the endothelial cell phenotype when using mature endothelial cells. Importantly, infused endothelial progenitor cells were stable for up to 10 days' post initial infusion and, under the flow conditions utilized, they retained functional endothelial attributes and developed functional restrictive barriers. Our findings provide the basis necessary for developing functional, autologous, transplantable lungs capable of gas exchange, proper hemodynamics, and incorporation into the host's circulatory system without thrombogenicity. In addition, the phenotypic characterization of cells capable of such re-endothelialization could be useful for identifying endothelial progenitors suitable for efficient vascular organ and tissue engineering, regeneration and repair.

Endothelial cells lining the pulmonary arteries, veins, and alveolar capillaries exhibit remarkable heterogeneity both in structure and in function. Ultrastructural analysis indicate that endothelial cells derived from the pulmonary artery (PAECs) reside in thicker basement membranes, display a bulging-like phenotype and possess cell to cell borders that are clearly distinguishable (King et al., 2004; Aird, 2012; Przysinda et al.,

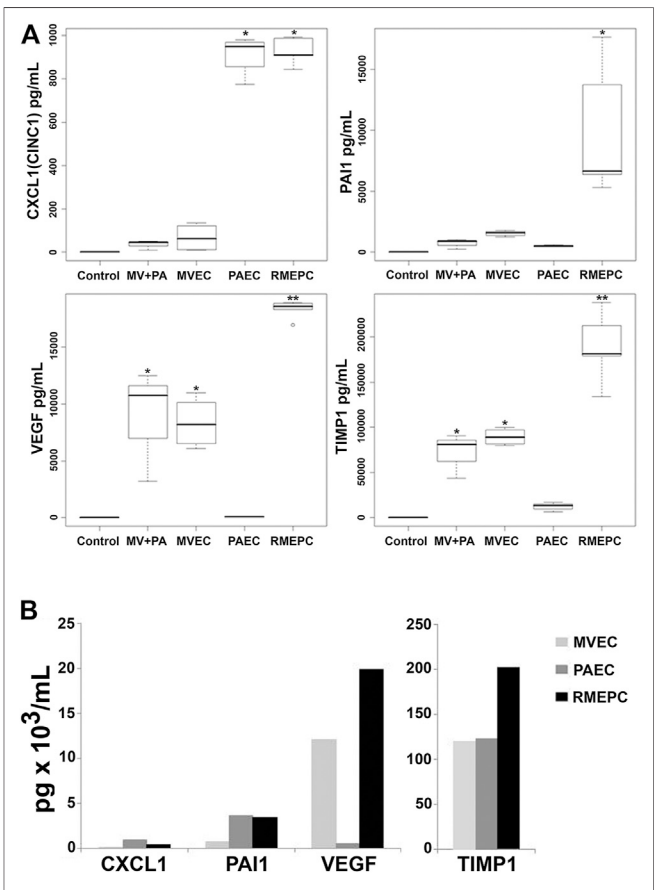

FIGURE 8 | (A) Secretion of endothelial cell mediators from perfusate of decellularized lungs reseeded with RMEPC, MVEC, PAEC, or both MVEC and PAEC ("MV + PA"). "Control" indicates complete culture medium alone. Perfusates were sampled from reseeded constructs at 48 h post-seeding. * Single asterisk indicates p < 0.05 versus non asterisk, and double asterisk (**) groups. For all samples, n = 8, except for RMEPC where n = 10. **(B)** *In vitro* production of endothelial cell mediators after 48 h of 2D tissue culture in flasks. These single samples were run in duplicate with CV < 15%.

2020). In contrast, pulmonary microvascular endothelial cells (MVECs) reside in thinner basement membranes, display a flatter phenotype, and overlap at the border with nearby cells forming what appear to be stronger junctional complexes when compared to their conduit vessel-residing relatives (King et al., 2004; Aird, 2012). The structural differences are accompanied by significant differences in stress responses most of which have been studied in the context of inflammation and barrier restrictive properties. The clearly identifiable heterogeneity existing within the pulmonary circulation has been attributed to both environmental factors and epigenetic modifications. Exposure to high PCO_2, low PO_2 and relatively higher vascular pressure (when compared to other pulmonary vascular segments) demand unique adaptive processes in the endothelium lining pulmonary arteries while reciprocal exposures are seen in microvascular regions where gas exchange occurs (Aird, 2007). In addition, several epigenetic imprints have been described, in particular those which explain, at least in part, the enhanced replication competence of the microvascular endothelial cells when compared to their conduit-derived pulmonary artery counterparts (Alvarez et al., 2008; Clark et al., 2008).

Populations of resident endothelial cells enriched with progenitor cells have been previously described in the pulmonary circulation (RMVECs) (Alvarez et al., 2008). Compared to PAECs and MVECs, RMEPCs have longer telomeres, and a higher proliferative capacity without evidence of transformation transelectrical membrane resistance. Furthermore, they exhibited the highest transepithelial membrane resistance (Alvarez et al., 2008). Our results demonstrated that those progenitor cells do not exhibit selective tropic abilities as shown by PAECs or MVECs but display a capacity to seed in any vascular segment. Considering our use of similar perfusion conditions, the data indicates that unique physical properties of the cells, specific expression of integrins, or other matrix-recognizing molecules are determinants for recognition of distinctive scaffold components that lure cells towards specific segments of the circulation. Similar work conducted with PAECs and MVECs, as well with HUVECs and pulmonary venous ECs, has shown similar limitations in vascular coverage and the need for combination seeding in order to achieve maximal coverage, including distal areas (Ren et al., 2015; Gilpin et al., 2016; Scarritt et al., 2018). Importantly, RMEPCs displayed an enhanced replicative competence (Alvarez et al., 2008) and/or enhanced adhesive ability which explains their remarkable vascular repopulation. Consequently, infusion of RMEPCs under the flow conditions described was able to generate a restrictive barrier with limited permeability for large solutes and detectable VE-cadherin, a major endothelial adhesion molecule, without the need for combination seeding.

Flow-seeding technology is necessary to perfuse the complete vasculature of decellularized whole organs (Walluscheck et al., 1996). Flow also induces physiological shear stress responses, which induces endothelium to shift from cobblestone morphology to align with the direction of flow, stabilizing endothelial-endothelial cell communications and promoting remodeling of focal adhesion sites (Davies et al., 1994; Malek and Izumo, 1996; Chiu and Chien, 2011; Adamson et al., 2013). While this technology is necessary for restoration of functional vasculature, there are numerous obstacles that are associated with seeding cells within acellular tissue and should be consider by any research group studying tissue decellularization or recellularization. Harsh decellularization as well as improper storage (i.e. freezing, thawing) of acellular scaffolds can lead to disruption of components and architecture (Calle et al., 2016; Feng et al., 2020). During cell seeding of pulmonary vasculature, positioning of the scaffold (supine vs. prone vs. upright) and the physiological distribution of blood flow within the pulmonary vascular tree greatly affect distribution of cells within lobes (Stabler et al., 2016). In order to prevent clots from disrupting complete organ decellularization and subsequent vascular recellularization, anticoagulants and thrombolytics are commonly employed to prevent and dissolve clots, respectively (Price et al., 2015; Doi et al., 2017). The method of seeding is another crucial factor in achieving high vascular coverage within acellular scaffolds. Recent reviews have stated the importance of using low cellular concentrations within large volumes, choosing gravity-dependent infusion over pump-dependent infusion, as well as seeding cells with both antegrade and retrograde perfusion to attain greater coverage throughout the entire vasculature of the acellular scaffold (Ohata and Ott, 2000; Robertson et al., 2014; Leiby et al., 2020). While we used pump-driven seeding in only the antegrade direction, we did not experience the seeding issues described above. This might be explained by our inclusion of priming the scaffolds with 24 h each of saline and media alone, and filtering of cell suspensions prior to reseeding to prevent clumping.

Our data show that, under continuous pulsatile flow, a significant proportion of RMEPCs was able to form a stable barrier for up to 8 days post initial infusion. Another benefit in the use of flow–perfusing conditions is the removal of any potentially thrombogenic gas nuclei within the lung tissue, as hydrostatic pressure has been shown to reduce the thrombogenicity of polytetrafluoroethylene vascular grafts (Ritter et al., 1989). Our data suggest that using native lung scaffolds as a substrate for cell attachment provides sufficient binding to withstand pulsatile flow through the vasculature. We recognize that further hemodynamic studies are necessary for determining the optimal infusion conditions (rate, time, pressures) to obtain a pulmonary barrier similar to that observed *in vivo*.

Our results demonstrate that endothelial heterogeneity is required for bioengineering functional vasculature, consistent with *in vivo* findings (Belloni and Tressler, 1990; Sieminski et al., 2005; Verhamme and Hoylaerts, 2006; Stevens, 2011; Scarritt et al., 2018). All endothelial cells used for this study were able to attach and function on decellularized lung matrices, although RMEPC showed significantly greater attachment, maintenance of functional endothelial attributes (e.g. thrombomodulin activity, VEGF production), barrier restrictive properties, and a reduction of apoptotic signals in the presence of flow. Interestingly, RMEPC showed less CD31 expression than PAEC or MVEC *in vitro*. This may be explained, in part, by the heterogeneous nature of this particular primary endothelial lineage, which is enriched with progenitor cells not yet expressing migration adhesion molecules. In fact, among the tight junction and adhesion molecules we looked into (see **Supplementary Table S3**), there were only a few that had a relatively higher gene expression within our RMEPCs. RMEPC

have enhanced adherence to and maturation within multiple regions compared to PAEC and MVEC, apparently without much need for CD31 as seen in **Figure 2**. These data collectively lend evidence toward utilizing a single source-derived endothelial population that, after enrichment with progenitor cells, favors revascularization of each segment of the pulmonary circulation.

The qPCR results indicate that there are differences in the expression of genes for LDL-receptor and selected scavenger receptors (other proteins that play a role in the uptake of LDL) amongst the 3 cell types we studied. Based on information from public databases created from compiled murine endothelial cell transcriptomes (Goveia et al., 2020; Kalucka et al., 2020), it was expected that similar expressions of genes for LDL-receptor, Scarf1, and Scarf2 would be found since LDL is an important nutrient for endothelial cells, and the class F scavenger receptors are classified as endothelial-specific (Patten, 2018). While public databases show a mixed expression of genes for αv, β1, β2, and β5 among all endothelial cell types, we found that the PAECs had relatively higher expression of all but β2, whereas our RMEPCs had the highest expression of β2, an integrin that forms adhesion proteins by binding to CD11 a-d and primarily seen amongst leukocytes (Fagerholm et al., 2019). While outside the scope of this study, more work is needed in both understanding the expression of these important proteins as they will further our understanding of supplying cells with proper nutrients during recellularization and insight into what sites they will be able to adhere to during the seeding step of regenerating tissue.

While differential tropism might indicate a difference in expression of integrins responsible for attachment to the ECM, we do not yet understand the molecular determinants that resulted in the endothelial cell recognition of specific vascular segments within the pulmonary circulation. Canonical homo- and hetero-topic interactions are ascribed to the engagement of integrins and the contribution of the endothelial cell glycocalyx. Based on our flow cytometry data of our markers of interest, there is little differential expression of cell surface adhesion molecules, though we were able to detect P-selectin, which is important for ECs and platelets during an inflammatory response. While GAGs play a role in cell adhesion to implantable grafts (Ibrahim and Ramamurthi, 2008), they may also allow for anatomically relevant attachment to decellularized native ECM, by providing native geospatial cues. This could be facilitated by glycosphingolipids, glycoproteins, or proteoglycans, which have all been documented as modulators of cell localization. If so, these terminal sugar residues would shift cell-matrix binding toward common glycosylation motifs, instead of canonical integrin/collagen or laminin binding protein (LBP) within focal adhesions (that GAGs also modulate by conferring steric hindrance). Differential expression of saccharide-binding receptors, such as P-selectin, may explain the increased binding of the RMEPC. Alternatively, binding domains within ECM proteins favor a particular endothelial glycocalyx. Growth factors, cytokines, and chemokines trapped within native matrix may impact origin-specific endothelial cell-matrix binding. As with most physiological systems, there is likely a dynamic balance between these influences on cell adhesion and subsequent intracellular signal transduction through anchor proteins (Burgess et al., 2006; Schultz and Wysocki, 2009; Ishihara et al., 2018; Mammoto and Mammoto, 2019).

In summary, we have identified a single cell source that is capable of re-endothelializing the lung in a comprehensive manner providing a functional barrier. Furthermore, we have determined that endothelial cells that exhibit selective tropism are suboptimal for functional re-endothelialization of acellular lungs. Along with recent studies published by others we conclude that it is vital to include endothelial progenitors, such as RMEPCs, in the seeding process of decellularized lung scaffolds in order to improve endothelial function, barrier permeability, and coverage throughout the entire pulmonary vasculature (Ren et al., 2015; Nagao et al., 2016; Scarritt et al., 2018). Although future studies will help us understand the mechanism of the stochastic nature of lung microvascular EPCs in recellularizing the lung vascular extracellular matrix, it is apparent that our findings warrant moving ahead on determining their translational capacity for bioengineering, therapeutic applications, and understanding regeneration and repair for lungs and other vascularized organs.

DATA AVAILABILITY STATEMENT

The original contributions presented in the study are included in the article/**Supplementary Materials**, further inquiries can be directed to the corresponding author.

ETHICS STATEMENT

The animal study was reviewed and approved by the Institutional Animal Care and Use Committees at the University of Minnesota and at University of South Alabama.

AUTHOR CONTRIBUTIONS

IA and DR designed experiments, analyzed data and wrote the paper; CM, AL, DH, SF, ME, RB, AP, and MJ performed experiments and analyzed data; DA, DT, and AP-M conceptualized and designed the study, interpreted data and edited the paper.

FUNDING

This study was supported by funding awarded to APM (NHLBIR01HL108627), DFA (NHLBI R01HL066299), and IA (T32GM113846-09:PI R, Perlingeiro, MSTP T32 GM008244:PI Y. Shimizu, and The Dinnaken Fellowship).

SUPPLEMENTARY MATERIAL

The Supplementary Material for this article can be found online at: https://www.frontiersin.org/articles/10.3389/fbioe.2021.727869/full#supplementary-material

REFERENCES

Adamson, R. H., Sarai, R. K., Altangerel, A., Clark, J. F., Weinbaum, S., and Curry, F. E. (2013). Microvascular Permeability to Water Is Independent of Shear Stress, but Dependent on Flow Direction. *Am. J. Physiology-Heart Circulatory Physiol.* 304, H1077–H1084. doi:10.1152/ajpheart.00956.2012

Ahya, V. N., and Diamond, J. M. (2019). Lung Transplantation. *Med. Clin. North America* 103, 425–433. doi:10.1016/j.mcna.2018.12.003

Aird, W. C. (2012). Endothelial Cell Heterogeneity. *Cold Spring Harbor Perspect. Med.* 2, a006429. doi:10.1101/cshperspect.a006429

Aird, W. C. (2007). Phenotypic Heterogeneity of the Endothelium. *Circ. Res.* 100, 158–173. doi:10.1161/01.RES.0000255691.76142.4a

Alvarez, D. F., Huang, L., King, J. A., ElZarrad, M. K., Yoder, M. C., and Stevens, T. (2008). Lung Microvascular Endothelium Is Enriched with Progenitor Cells that Exhibit Vasculogenic Capacity. *Am. J. Physiology-Lung Cell Mol. Physiol.* 294, L419–L430. doi:10.1152/ajplung.00314.2007

Balestrini, J. L., Gard, A. L., Gerhold, K. A., Wilcox, E. C., Liu, A., Schwan, J., et al. (2016). Comparative Biology of Decellularized Lung Matrix: Implications of Species Mismatch in Regenerative Medicine. *Biomaterials* 102, 220–230. doi:10.1016/j.biomaterials.2016.06.025

Belloni, P. N., and Tressler, R. J. (1990). Microvascular Endothelial Cell Heterogeneity: Interactions with Leukocytes and Tumor Cells. *Cancer Metast Rev.* 8, 353–389. doi:10.1007/bf00052608

Bonvillain, R. W., Danchuk, S., Sullivan, D. E., Betancourt, A. M., Semon, J. A., Eagle, M. E., et al. (2012). A Nonhuman Primate Model of Lung Regeneration: Detergent-Mediated Decellularization and Initial *In Vitro* Recellularization with Mesenchymal Stem Cells. *Tissue Eng. A* 18, 2437–2452. doi:10.1089/ten.TEA.2011.0594

Burgess, J. K., Ge, Q., Poniris, M. H., Boustany, S., Twigg, S. M., Black, J. L., et al. (2006). Connective Tissue Growth Factor and Vascular Endothelial Growth Factor from Airway Smooth Muscle Interact with the Extracellular Matrix. *Am. J. Physiology-Lung Cell Mol. Physiol.* 290, L153–L161. doi:10.1152/ajplung.00287.2005

Calle, E. A., Ghaedi, M., Sundaram, S., Sivarapatna, A., Tseng, M. K., and Niklason, L. E. (2014). Strategies for Whole Lung Tissue Engineering. *IEEE Trans. Biomed. Eng.* 61, 1482–1496. doi:10.1109/tbme.2014.2314261

Calle, E. A., Hill, R. C., Leiby, K. L., Le, A. V., Gard, A. L., Madri, J. A., et al. (2016). Targeted Proteomics Effectively Quantifies Differences between Native Lung and Detergent-Decellularized Lung Extracellular Matrices. *Acta Biomater.* 46, 91–100. doi:10.1016/J.ACTBIO.2016.09.043

Calnek, D. S., and Grinnell, B. W. (1998). Thrombomodulin-Dependent Anticoagulant Activity Is Regulated by Vascular Endothelial Growth Factor. *Exp. Cel Res.* 238, 294–298. doi:10.1006/excr.1997.3812

Chang, E. I., Bonillas, R. G., El-ftesi, S., Chang, E. I., Ceradini, D. J., Vial, I. N., et al. (2009). Tissue Engineering Using Autologous Microcirculatory Beds as Vascularized Bioscaffolds. *FASEB j.* 23, 906–915. doi:10.1096/fj.08-114868

Chiu, J.-J., and Chien, S. (2011). Effects of Disturbed Flow on Vascular Endothelium: Pathophysiological Basis and Clinical Perspectives. *Physiol. Rev.* 91, 327–387. doi:10.1152/physrev.00047.2009

Chung-Welch, N., Patton, W. F., Yen-Patton, G. P. A., Hechtman, H. B., and Shepro, D. (1989). Phenotypic Comparison between Mesothelial and Microvascular Endothelial Cell Lineages Using Conventional Endothelial Cell Markers, Cytoskeletal Protein Markers and *In Vitro* Assays of Angiogenic Potential. *Differentiation* 42, 44–53. doi:10.1111/j.1432-0436.1989.tb00606.x

Clark, J., Alvarez, D. F., Alexeyev, M., King, J. A. C., Huang, L., Yoder, M. C., et al. (2008). Regulatory Role for Nucleosome Assembly Protein-1 in the Proliferative and Vasculogenic Phenotype of Pulmonary Endothelium. *Am. J. Physiology-Lung Cell Mol. Physiol.* 294, L431–L439. doi:10.1152/ajplung.00316.2007

Daly, A. B., Wallis, J. M., Borg, Z. D., Bonvillain, R. W., Deng, B., Ballif, B. A., et al. (2012). Initial Binding and Recellularization of Decellularized Mouse Lung Scaffolds with Bone Marrow-Derived Mesenchymal Stromal Cells. *Tissue Eng. Part A* 18, 1–16. doi:10.1089/ten.TEA.2011.0301

Davies, P. F., Robotewskyj, A., and Griem, M. L. (1994). Quantitative Studies of Endothelial Cell Adhesion. Directional Remodeling of Focal Adhesion Sites in Response to Flow Forces. *J. Clin. Invest.* 93, 2031–2038. doi:10.1172/jci117197

Deutsch, M., Meinhart, J., Zilla, P., Howanietz, N., Gorlitzer, M., Froeschl, A., et al. (2009). Long-term Experience in Autologous *In Vitro* Endothelialization of Infrainguinal ePTFE Grafts. *J. Vasc. Surg.* 49, 352–362. doi:10.1016/j.jvs.2008.08.101

Doi, R., Tsuchiya, T., Mitsutake, N., Nishimura, S., Matsuu-Matsuyama, M., Nakazawa, Y., et al. (2017). Transplantation of Bioengineered Rat Lungs Recellularized with Endothelial and Adipose-Derived Stromal Cells. *Sci. Rep.* 7, 8447. doi:10.1038/s41598-017-09115-2

Fagerholm, S. C., Guenther, C., Llort Asens, M., Savinko, T., and Uotila, L. M. (2019). Beta2-Integrins and Interacting Proteins in Leukocyte Trafficking, Immune Suppression, and Immunodeficiency Disease. *Front. Immunol.* 10, 254. doi:10.3389/fimmu.2019.00254

Félétou, M., and Vanhoutte, P. M. (2006). Endothelial Dysfunction: a Multifaceted Disorder (The Wiggers Award Lecture). *Am. J. Physiology-Heart Circulatory Physiol.* 291, H985–H1002. doi:10.1152/ajpheart.00292.2006

Feng, H., Xu, Y., Luo, S., Dang, H., Liu, K., and Sun, W. Q. (2020). Evaluation and Preservation of Vascular Architectures in Decellularized Whole Rat Kidneys. *Cryobiology* 95, 72–79. doi:10.1016/J.CRYOBIOL.2020.06.003

Gilpin, S. E., Charest, J. M., Ren, X., and Ott, H. C. (2016). Bioengineering Lungs for Transplantation. *Thorac. Surg. Clin.* 26, 163–171. doi:10.1016/j.thorsurg.2015.12.004

Goveia, J., Rohlenova, K., Taverna, F., Treps, L., Conradi, L.-C., Pircher, A., et al. (2020). An Integrated Gene Expression Landscape Profiling Approach to Identify Lung Tumor Endothelial Cell Heterogeneity and Angiogenic Candidates. *Cancer Cell* 37, 21–36. doi:10.1016/j.ccell.2019.12.001

Ibrahim, S., and Ramamurthi, A. (2008). Hyaluronic Acid Cues for Functional Endothelialization of Vascular Constructs. *J. Tissue Eng. Regen. Med.* 2, 22–32. doi:10.1002/term.61

Ishihara, J., Ishihara, A., Fukunaga, K., Sasaki, K., White, M. J. V., Briquez, P. S., et al. (2018). Laminin Heparin-Binding Peptides Bind to Several Growth Factors and Enhance Diabetic Wound Healing. *Nat. Commun.* 9. doi:10.1038/s41467-018-04525-w

Kalucka, J., de Rooij, L. P. M. H., Goveia, J., Rohlenova, K., Dumas, S. J., Meta, E., et al. (2020). Single-Cell Transcriptome Atlas of Murine Endothelial Cells. *Cell* 180, 764–779. doi:10.1016/j.cell.2020.01.015

King, J., Hamil, T., Creighton, J., Wu, S., Bhat, P., McDonald, F., et al. (2004). Structural and Functional Characteristics of Lung Macro- and Microvascular Endothelial Cell Phenotypes. *Microvasc. Res.* 67, 139–151. doi:10.1016/j.mvr.2003.11.006

Kurobe, H., Maxfield, M. W., Breuer, C. K., and Shinoka, T. (2012). Concise Review: Tissue-Engineered Vascular Grafts for Cardiac Surgery: Past, Present, and Future. *Stem Cell Transl Med* 1, 566–571. doi:10.5966/sctm.2012-0044

Leiby, K. L., Raredon, M. S. B., and Niklason, L. E. (2020). Bioengineering the Blood-gas Barrier. *Compr. Physiol.* 10, 415–452. doi:10.1002/CPHY.C190026

Liu, G., Wu, R., Yang, B., Deng, C., Lu, X., Walker, S. J., et al. (2018). Human Urine-Derived Stem Cell Differentiation to Endothelial Cells with Barrier Function and Nitric Oxide Production. *STEM CELLS Translational Med.* 7, 686–698. doi:10.1002/sctm.18-0040

Lowe, K., Alvarez, D. F., King, J. A., and Stevens, T. (2010). Perivascular Fluid Cuffs Decrease Lung Compliance by Increasing Tissue Resistance*. *Crit. Care Med.* 38, 1458–1466. doi:10.1097/CCM.0b013e3181de18f0

Malek, A. M., and Izumo, S. (1996). Mechanism of Endothelial Cell Shape Change and Cytoskeletal Remodeling in Response to Fluid Shear Stress. *J. Cel Sci* 109 (Pt 4), 713–726. doi:10.1242/jcs.109.4.713

Mammoto, A., and Mammoto, T. (2019). Vascular Niche in Lung Alveolar Development, Homeostasis, and Regeneration. *Front. Bioeng. Biotechnol.* 7. doi:10.3389/fbioe.2019.00318

Marcu, R., Choi, Y. J., Xue, J., Fortin, C. L., Wang, Y., Nagao, R. J., et al. (2018). Human Organ-specific Endothelial Cell Heterogeneity. *iScience* 4, 20–35. doi:10.1016/j.isci.2018.05.003

Nagao, R. J., Ouyang, Y., Keller, R., Nam, S. Y., Malik, G. R., Emelianov, S. Y., et al. (2016). Ultrasound-guided Photoacoustic Imaging-Directed Re-endothelialization of Acellular Vasculature Leads to Improved Vascular Performance. *Acta Biomater.* 32, 35–45. doi:10.1016/j.actbio.2015.12.029

Nichols, J. E., La Francesca, S., Niles, J. A., Vega, S. P., Argueta, L. B., Frank, L., et al. (2018). Production and Transplantation of Bioengineered Lung into a Large-Animal Model. *Sci. Transl. Med.* 10, eaao3926. doi:10.1126/scitranslmed.aao3926

Ohata, K., and Ott, H. C. (2020). Human-scale Lung Regeneration Based on Decellularized Matrix Scaffolds as a Biologic Platform. *Surg. Today* 50, 633–643. doi:10.1007/s00595-020-02000-y

Ott, H. C., Matthiesen, T. S., Goh, S.-K., Black, L. D., Kren, S. M., Netoff, T. I., et al. (2008). Perfusion-decellularized Matrix: Using Nature's Platform to Engineer a Bioartificial Heart. *Nat. Med.* 14, 213–221. doi:10.1038/nm1684

Patten, D. A. (2018). SCARF1: a Multifaceted, yet Largely Understudied, Scavenger Receptor. *Inflamm. Res.* 67, 627–632. doi:10.1007/s00011-018-1154-7

Petersen, T. H., Calle, E. A., Zhao, L., Lee, E. J., Gui, L., Raredon, M. B., et al. (2010). Tissue-engineered Lungs for *In Vivo* Implantation. *Science* 329, 538–541. doi:10.1126/science.1189345

Price, A. P., England, K. A., Matson, A. M., Blazar, B. R., and Panoskaltsis-Mortari, A. (2010). Development of a Decellularized Lung Bioreactor System for Bioengineering the Lung: the Matrix Reloaded. *Tissue Eng. Part A* 16, 2581–2591. doi:10.1089/ten.TEA.2009.0659

Price, A. P., Godin, L. M., Domek, A., Cotter, T., D'Cunha, J., Taylor, D. A., et al. (2015). Automated Decellularization of Intact, Human-Sized Lungs for Tissue Engineering. *Tissue Eng. C: Methods* 21, 94–103. doi:10.1089/TEN.TEC.2013.0756

Przysinda, A., Feng, W., and Li, G. (2020). Diversity of Organism-wide and Organ-specific Endothelial Cells. *Curr. Cardiol. Rep.* 22, 19. doi:10.1007/s11886-020-1275-9

Ren, X., Moser, P. T., Gilpin, S. E., Okamoto, T., Wu, T., Tapias, L. F., et al. (2015). Engineering Pulmonary Vasculature in Decellularized Rat and Human Lungs. *Nat. Biotechnol.* 33, 1097–1102. doi:10.1038/nbt.3354

Ritter, E. F., Vann, R. D., Wyble, C., Barwick, W. J., and Klitzman, B. (1989). Hydrostatic Pressure Reduces Thrombogenicity of Polytetrafluoroethylene Vascular Grafts. *Am. J. Physiology-Heart Circulatory Physiol.* 257, H1076–H1081. doi:10.1152/ajpheart.1989.257.4.H1076

Robertson, M. J., Dries-Devlin, J. L., Kren, S. M., Burchfield, J. S., and Taylor, D. A. (2014). Optimizing Recellularization of Whole Decellularized Heart Extracellular Matrix. *PLoS One* 9, e90406. doi:10.1371/journal.pone.0090406

Scarritt, M. E., Pashos, N. C., Motherwell, J. M., Eagle, Z. R., Burkett, B. J., Gregory, A. N., et al. (2018). Re-endothelialization of Rat Lung Scaffolds through Passive, Gravity-driven Seeding of Segment-specific Pulmonary Endothelial Cells. *J. Tissue Eng. Regen. Med.* 12, e786–e806. doi:10.1002/term.2382

Schultz, G. S., and Wysocki, A. (2009). Interactions between Extracellular Matrix and Growth Factors in Wound Healing. *Wound Repair Regen.* 17, 153–162. doi:10.1111/j.1524-475X.2009.00466.x

Sieminski, A. L., Hebbel, R. P., and Gooch, K. J. (2005). Improved Microvascular Networkin Vitroby Human Blood Outgrowth Endothelial Cells Relative to Vessel-Derived Endothelial Cells. *Tissue Eng.* 11, 1332–1345. doi:10.1089/ten.2005.11.1332

Song, J. J., Kim, S. S., Liu, Z., Madsen, J. C., Mathisen, D. J., Vacanti, J. P., et al. (2011). Enhanced *In Vivo* Function of Bioartificial Lungs in Rats. *Ann. Thorac. Surg.* 92, 998–1006. doi:10.1016/j.athoracsur.2011.05.018

Stabler, C. T., Caires, L. C., Mondrinos, M. J., Marcinkiewicz, C., Lazarovici, P., Wolfson, M. R., et al. (2016). Enhanced Re-endothelialization of Decellularized Rat Lungs. *Tissue Eng. Part C: Methods* 22, 439–450. doi:10.1089/ten.tec.2016.0012

Stevens, T. (2011). Functional and Molecular Heterogeneity of Pulmonary Endothelial Cells. *Proc. Am. Thorac. Soc.* 8, 453–457. doi:10.1513/pats.201101-004MW

Verhamme, P., and Hoylaerts, M. F. (2006). The Pivotal Role of the Endothelium in Haemostasis and Thrombosis. *Acta Clinica Belgica* 61, 213–219. doi:10.1179/acb.2006.036

von Drygalski, A., Furlan-Freguia, C., Mosnier, L. O., Yegneswaran, S., Ruf, W., and Griffin, J. H. (2012). Infrared Fluorescence for Vascular Barrier Breach In Vivo--a Novel Method for Quantitation of Albumin Efflux. *Thromb. Haemost.* 108, 981–991. doi:10.1160/th12-03-0196

Walluscheck, K. P., Steinhoff, G., and Haverich, A. (1996). Endothelial Cell Seeding of De-endothelialised Human Arteries: Improvement by Adhesion Molecule Induction and Flow-Seeding Technology. *Eur. J. Vasc. Endovasc Surg.* 12, 46–53. doi:10.1016/s1078-5884(96)80274-7

Conflict of Interest: The authors declare that the research was conducted in the absence of any commercial or financial relationships that could be construed as a potential conflict of interest.

Publisher's Note: All claims expressed in this article are solely those of the authors and do not necessarily represent those of their affiliated organizations, or those of the publisher, the editors and the reviewers. Any product that may be evaluated in this article, or claim that may be made by its manufacturer, is not guaranteed or endorsed by the publisher.

Copyright © 2021 Akinnola, Rossi, Meyer, Lindsey, Haase, Fogas, Ehrhardt, Blue, Price, Johnson, Alvarez, Taylor and Panoskaltsis-Mortari. This is an open-access article distributed under the terms of the Creative Commons Attribution License (CC BY). The use, distribution or reproduction in other forums is permitted, provided the original author(s) and the copyright owner(s) are credited and that the original publication in this journal is cited, in accordance with accepted academic practice. No use, distribution or reproduction is permitted which does not comply with these terms.

frontiers in Bioengineering and Biotechnology

ORIGINAL RESEARCH
published: 19 October 2021
doi: 10.3389/fbioe.2021.756755

Decellularized Whole-Organ Pre-vascularization: A Novel Approach for Organogenesis

Ibrahim Fathi[1,2], *Takehiro Imura*[1], *Akiko Inagaki*[1], *Yasuhiro Nakamura*[3], *Ayman Nabawi*[2] *and Masafumi Goto*[1,4]*

[1]Division of Transplantation and Regenerative Medicine, Tohoku University, Sendai, Japan, [2]Department of Surgery, University of Alexandria, Alexandria, Egypt, [3]Division of Pathology, Faculty of Medicine, Tohoku Medical and Pharmaceutical University, Sendai, Japan, [4]Department of Surgery, Tohoku University, Sendai, Japan

Introduction: Whole-organ decellularization is an attractive approach for three-dimensional (3D) organ engineering. However, progress with this approach is hindered by intra-vascular blood coagulation that occurs after *in vivo* implantation of the re-cellularized scaffold, resulting in a short-term graft survival. In this study, we explored an alternative approach for 3D organ engineering through an axial pre-vascularization approach and examined its suitability for pancreatic islet transplantation.

Methods: Whole livers from male Lewis rats were decellularized through sequential arterial perfusion of detergents. The decellularized liver scaffold was implanted into Lewis rats, and an arteriovenous bundle was passed through the scaffold. At the time of implantation, fresh bone marrow preparation (BM; $n = 3$), adipose-derived stem cells (ADSCs; $n = 4$), or HBSS ($n = 4$) was injected into the scaffold through the portal vein. After 5 weeks, around 2,600 islet equivalents (IEQs) were injected through the portal vein of the scaffold. The recipient rats were rendered diabetic by the injection of 65 mg/kg STZ intravenously 1 week before islet transplantation and were followed up after transplantation by measuring the blood glucose and body weight for 30 days. Intravenous glucose tolerance test was performed in the cured animals, and samples were collected for immunohistochemical (IHC) analyses. Micro-computed tomography (CT) images were obtained from one rat in each group for representation.

Results: Two rats in the BM group and one in the ADSC group showed normalization of blood glucose levels, while one rat from each group showed partial correction of blood glucose levels. In contrast, no rats were cured in the HBSS group. Micro-CT showed evidence of sprouting from the arteriovenous bundle inside the scaffold. IHC analyses showed insulin-positive cells in all three groups. The number of von-Willebrand factor-

OPEN ACCESS

Edited by:
Kamal Hany Hussein, Assiut University, Egypt

Reviewed by:
Hiroshi Yagi, Keio University School of Medicine, Japan
Katsuhiro Hosoyama, Iwate Prefectural Central Hospital, Japan

***Correspondence:**
Masafumi Goto
masafumi.goto.c6@tohoku.ac.jp

Specialty section:
This article was submitted to Biomaterials, a section of the journal Frontiers in Bioengineering and Biotechnology

Received: *11 August 2021*
Accepted: *04 October 2021*
Published: *19 October 2021*

Citation:
Fathi I, Imura T, Inagaki A, Nakamura Y, Nabawi A and Goto M (2021) Decellularized Whole-Organ Pre-vascularization: A Novel Approach for Organogenesis. Front. Bioeng. Biotechnol. 9:756755. doi: 10.3389/fbioe.2021.756755

Abbreviations: ADSCs, adipose-derived stem cells; AUC, area under the curve; AV, arteriovenous; BM, bone marrow; BrdU, 5-bromo-2′-deoxyuridine; CNTF, ciliary neurotrophic factor; CT, computed tomography; DLM, decellularized liver; DW, distilled water; ECM, extracellular matrix; ECV, extracellular vesicles; EGF, epidermal growth factor; HA hepatic artery; HBSS, Hank's balanced salt solution; HGF, hepatocyte growth factor; IEQ, islet equivalent; Ins1, insulin 1; IVC, inferior vena cava; IVGTT, intravenous glucose tolerance testi.p., intraperitoneal; MI, myocardial infarction; MSCs, mesenchymal stem cells; PBS, phosphate buffered saline; Pdx1, pancreatic and duodenal homeobox; 1PV, portal vein; RPMI, Roswell Park Memorial Institute; SDS, sodium dodecyl sulphate; SIS, small intestinal submucosa; STZ, streptozotocin; TNF, tumor necrosis factor; Vegfa, vascular endothelial growth factor; WF, von-Willebrand factor.

positive cells in the islet region was higher in the BM and ADSC groups than in the HBSS group. The number of 5-bromo-2′-deoxyuridine-positive cells was significantly lower in the BM group than in the other two groups.

Conclusions: Despite the limited numbers, the study showed the promising potential of the pre-vascularized whole-organ scaffold as a novel approach for islet transplantation. Both BM- and ADSCs-seeded scaffolds were superior to the acellular scaffold.

Keywords: whole-liver decellularization, arteriovenous, pancreatic islet, extracellular matrix, axial vascularization

INTRODUCTION

Pancreatic islet transplantation is a promising therapy for type 1 diabetes. However, the current standard site for islet transplantation, intraportal transplantation, has several shortcomings. For instance, a large proportion of the injected islets are lost during or shortly after the implantation (Bennet et al., 2000) as a result of instant blood-mediated inflammatory responses, invasion by natural killer cells and low oxygen tension (Smink et al., 2013). Furthermore, the ability of the transplanted cells to maintain tight glycemic control is not sustained in the long term (Hering, 2005). The transplanted islets are also not accessible for follow-up or subsequent removal, which is a concern if regenerative approaches are applied. Therefore, a more suitable alternative site for islet transplantation is desirable and has been the focus of many investigations (Merani et al., 2008; Smink et al., 2013).

Whole-organ decellularization is an approach in which the cellular content of an organ is removed, commonly through vascular perfusion of detergents, leaving an intact extracellular matrix (ECM) that can be recellularized using the native vascular system of the scaffold. This seeded scaffold can then be transplanted using vascular anastomosis techniques. Hypothetically, the merits of this approach include the removal of the antigenic cellular elements from the organ in order to prevent host adverse immune response to the scaffold; using the natural three-dimensional (3D) architecture of the organ formed by the ECM proteins with the incorporated growth factors as a scaffold for cell seeding, seeding cells with a better immunological profile towards the recipient; and using the natural vascular network to deliver oxygen and nutrients to the complex 3D scaffold after anastomosing it to the recipient vasculature (Fathi et al., 2017).

Due to the complex architecture of the liver and its rich vascular supply, such an approach has proven attractive for liver bioengineering. However, despite the evident progress and refinement of this approach over the last 2 decades, a major hurdle remains. The de-endothelialization of the vascular network during decellularization allows for the direct contact of the recipient's blood and the ECM of the blood vessels after vascular anastomosis in the host. ECM proteins include collagen and laminin, which can initiate the blood coagulation cascade (Bao et al., 2015; Bruinsma et al., 2015), thereby resulting in vascular occlusion due to thrombosis. Indeed, the first trials of *in vivo* transplantation of decellularized or recellularized liver scaffolds were associated with a short-term graft survival (Uygun et al., 2010; Bao et al., 2011; Bruinsma et al., 2015; Ko et al., 2015).

Several research groups have sought to prevent intravascular coagulation through different approaches, including re-endothelialization of the graft to prevent direct contact of blood with ECM (Ko et al., 2015; Kojima et al., 2018); heparin immobilization on the ECM of the scaffold through covalent binding, end-point immobilization, or layer-by-layer techniques (Bao et al., 2015; Bruinsma et al., 2015); and coating the vascular network with heparin-gelatin (Hussein et al., 2016). However, while these approaches did result in the significant prolongation of the graft survival and improved vascular patency to different extents, the long-term survival of a functioning graft has not yet been reported.

Several groups have conversely sought to bypass this hurdle by directly implanting either pieces of the seeded scaffold under the kidney capsule (Wang et al., 2014) or in the subcutaneous tissue (Citro et al., 2019) or the intact seeded scaffold into the peritoneal cavity (Vishwakarma et al., 2019) and relying on peripheral vascularization to supply this relatively small scaffold, sacrificing the native vascular network. In such cases, the ECM scaffold was shown capable of supporting the cell function. However, the problem with this maneuver is the difficulty in scaling it to a clinically meaningful size.

In the present study, we sought an alternative approach to circumvent the current obstacles through scaffold pre-vascularization. Our approach relies on axial vascularization, where a ligation-type arteriovenous (AV) bundle is used for the pre-vascularization of the scaffold while maintaining the natural vascular cues of the graft for cell transplantation and graft modulation (**Figure 1**).

We herein report our preliminary results of this technique and compare the pre-vascularization of acellular scaffold and seeded scaffold containing either fresh bone marrow preparation (BM) or cultured adipose-derived stem cells (ADSCs), as demonstrated through the function of transplanted pancreatic islets.

MATERIALS AND METHODS

Animals

Lewis rats were purchased from Japan SLC Inc (Shizuoka, Japan). For all experiments, scaffold recipients were 14–16 weeks old, scaffold and pancreatic islet donors were 10–12 weeks old, and BM and ADSC donors were 8 weeks old. Except for the BM donors, all of the rats used in this study were males. All animals had free access to a standard diet and water.

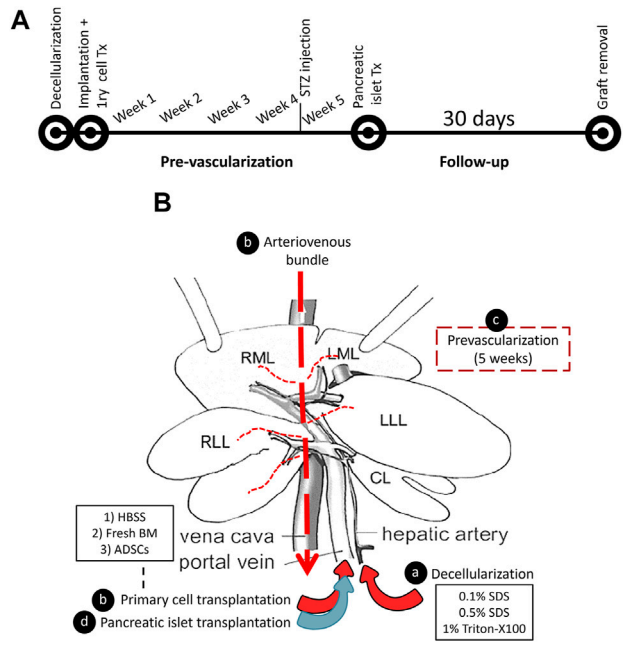

FIGURE 1 | A schematic representation of the decellularized liver pre-vascularization study. **(A)** A timeline representing the flow of the study. **(B)** The graft modulation during the study: **(A)** the rat liver was decellularized by detergent perfusion through the HA, **(B)** the decellularized scaffold was implanted into the recipient, and an AV bundle was threaded through the inferior vena cava using a tube that was placed in the IVC. Then, either fresh BM or ADSC or HBSS vehicle was infused through the PV of the scaffold, **(C)** a five-week period was allowed for pre-vascularization, and **(D)** syngeneic pancreatic islets were transplanted through the PV.

The experiments were approved by the local ethics committee (approved protocol 2019MdA-104) and performed in accordance with national and institutional regulations. Animals were maintained in a specific-pathogen-free environment. All surgeries were performed under anesthesia, and all efforts were made to minimize suffering.

Rat Whole-Liver Decellularization

Livers were obtained from male Lewis rats after cannulation of the portal vein (PV) and hepatic artery (HA) with a 22-G venflon cannula, and a tube (TOP X2-100 extension tube, TOP Co., Tokyo, Japan) was placed in the infra-hepatic inferior vena cava (IVC-tube).

The liver was decellularized following the protocol described by Vishwakarma et al. (2019). In brief, after washing out the blood, the liver was sequentially perfused with 0.1% w/v sodium dedocylsulphate (SDS; Wako, Osaka, Japan) for 2 h, SDS 0.5% w/v for 18 h, distilled water for 10 min, 1% Triton X-100 v/v (Wako) for 30 min, and finally distilled water (DW) for 30 min to wash out the detergents. Perfusion was performed through the HA cannula at a flow rate of 1 ml/min using a peristaltic pump (Perista AC-2110; ATTO Corporation, Tokyo, Japan). The decellularized liver (DLM) was kept in 100 ml of DW containing 1% (1,000 U) heparin sodium (Mochida, Tokyo, Japan) and 1% penicillin/streptomycin (Thermo Fisher Scientific, Waltham, MA, United States) in a sterile container at 4°C until the time of implantation (**Figure 2**).

All procedures were performed using sterile techniques and sterile DW. Detergent perfusion was performed in a laminar flow cabinet. After completion of decellularization protocol, 0.5 × 0.5-cm samples were excised and fixed in 4% paraformaldehyde for the histological assessment of the decellularization in selected samples.

ADSC Isolation and Culture

ADSCs were isolated from male Lewis rats as described previously (Ohmura et al., 2010), with a few modifications. In brief, adipose tissue was obtained from the inguinal fat pad and cut into fine pieces before being placed in ice-cold phosphate-buffered saline (PBS; Sigma-Aldrich, St. Louis, MO, United States) and then in Hank's balanced salt solution (HBSS; Sigma-Aldrich) containing 1 mg/ml collagenase II (Sigma-Aldrich) and 1% penicillin/streptomycin, at 37°C for 30 min with gentle agitation. The digested tissue was filtered through a sterile 70-μm cell-strainer, centrifuged at 400 *g* for 5 min at room temperature, and resuspended. This process was repeated twice. ADSCs were seeded into T-75 cell culture flasks (Thermo Fisher Scientific) in ADSC-1 medium (Kohjin Bio Co., Ltd., Sakado, Japan) containing 10% fetal bovine serum (Thermo Fisher Scientific) and 1% penicillin/streptomycin (**Figure 3**). Passage 2 cells were cryopreserved after resuspension in CELL BANKER® 1plus (Takara Bio Inc., Kusatsu, Japan).

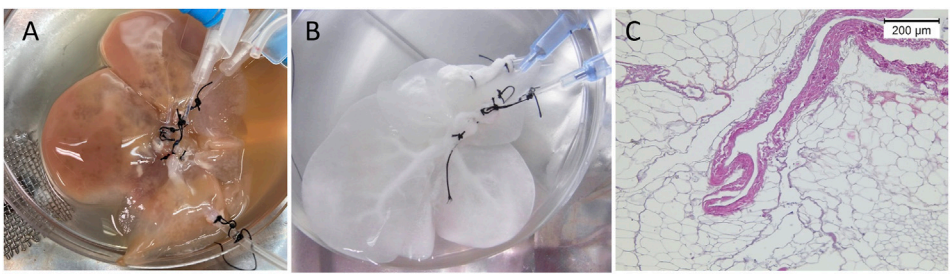

FIGURE 2 | Rat liver decellularization. **(A)** The liver during perfusion of detergents, **(B)** transparent DLM after completion of the decellularization protocol, **(C)** DLM histology showing preservation of the native honeycomb appearance of the liver ECM.

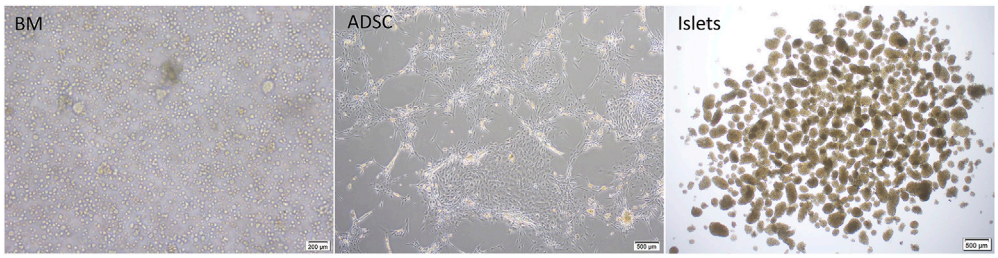

FIGURE 3 | Cell preparations used in the study; BM: fresh rat bone marrow, ADSCs: rat adipose-derived stem cells.

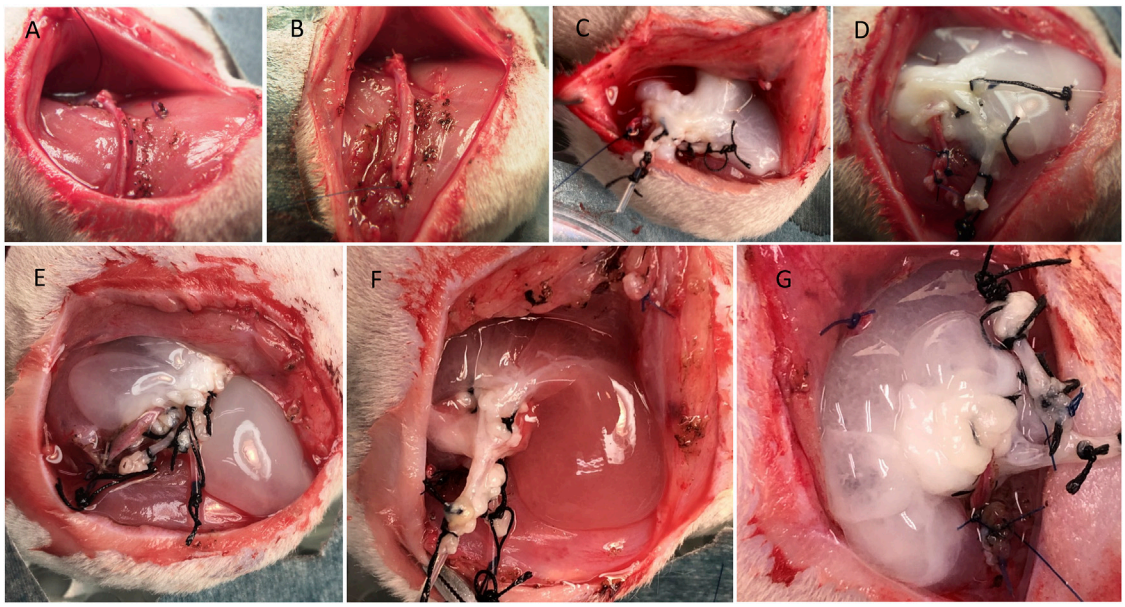

FIGURE 4 | Steps of the DLM implantation. **(A)** AV bundle dissection, **(B)** ligation of the AV bundle, **(C)** implantation of the liver in the left thigh region of Lewis rat and passage of AV bundle, **(D)** the final configuration of the DLM and AV bundle, **(E, F, G)** injection of HBSS, fresh BM, or ADSCs into the scaffold through the portal vein, respectively.

Decellularized Scaffold Implantation Surgery

Fourteen-to 16-week-old male Lewis rats were used as recipients (315–370 g). Induction of anesthesia was achieved using 3–4% isoflurane inhalation, and 1.5% isoflurane was used for maintenance during surgery. After hair clipping, the skin of the lower abdomen and left thigh region was prepared with 70% alcohol, and a sterile surgical drape was sutured around the location. A curved skin incision was performed, and the saphenous vessels were dissected using microsurgical techniques and electrocautery. Heparin sodium (100 U) was injected intravenously, followed by ligation of the arteriovenous (AV) bundle at the knee level (before bifurcation). The liver was placed inside the subcutaneous pouch, and the AV bundle was threaded through the scaffold's IVC to enter from the supra-hepatic IVC and exit through the infra-hepatic IVC by passing the AV bundle ligation thread through the IVC tube. The IVC tube was then removed, and the AV bundle was fixed to the muscle using 5/0 nylon sutures. The scaffold was oriented, and a drop of Viti-bond glue (3M, St. Paul, MN, United States) was used to keep the scaffold in place (**Figures 4A–D**). The cannulas to the PV and HA were cut and kept inside the subcutaneous pocket for future use. Hemostasis was checked, and the wound was closed in 2 layers using 4/0 Nylon sutures. Saline (5 ml) containing 100 µL of 30% glucose was injected subcutaneously for rehydration. Rats were kept in a warm cage until complete recovery.

Before wound closure, 2.5 ml of HBSS (Thermo Fisher Scientific) was injected through the PV cannula using a butterfly 23-G needle containing no cells (HBSS group; $n = 4$), freshly obtained BM preparation (BM group; $n = 3$), or ADSCs (ADSC group; $n = 3$). Injection was manually performed at a rate of 1 ml/min (**Figures 4E–G**).

Fresh BM Collection and Transplantation

BM was collected from the femur of female Lewis rats after decontamination with 1% Isodine solution (Mundipharma,

Tokyo, Japan). Using sterile instruments, the femur was cut near its end, and BM was extruded onto a cell culture plate using HBSS. The process was repeated for the other femur (5 ml total). The collected crude BM was then gently aspirated using a 25-G butterfly cannula for mechanical dispersion to produce a single-cell suspension and collected into a sterile 5-ml Eppendorf tube (**Figure 3**). A 2.5-ml aliquot of the single-cell suspension was injected into the decellularized scaffold through the PV. Cell counting was then performed using a hemocytometer.

ADSC Collection and Transplantation

The cryopreserved ADSCs were thawed at 37°C, resuspended in 10 ml of ADSC-1 medium, and centrifuged at 400 *g* for 5 min at 4°C. The supernatant was discarded, and the pellet was resuspended in medium. The cells were cultured in T-75 flasks. The medium was changed every two to 3 days. Before the time of transplantation, the ADSCs from passage 3 or 4 were collected after detachment with 0.05% trypsin/EDTA (Thermo Fisher Scientific) and washed. A total of 4×10^6 cells were then suspended in 2.5 ml of HBSS, and the 2.5-ml cell suspension was injected into the decellularized scaffold through the PV. The ADSCs used in this study belong to the same lot (from the same isolation).

Follow-up During the Pre-Vascularization Period

After surgery, the rats were followed up by body weight measurements until day 3 and then weekly for 4 weeks. Four weeks after surgery, streptozotocin (STZ; Sigma-Aldrich) was injected intravenously through the penile vein (65 mg/kg). The blood glucose was monitored using a portable glucometer (Freestyle; ABBOTT, Tokyo, Japan). Rats were considered diabetic if 2 consecutive measures of blood glucose were >400 mg/dl.

Pancreatic Islet Isolation and Transplantation

Pancreatic islets were isolated from male Lewis donors as described previously (Saitoh et al., 2021). In brief, rats were anesthetized by isoflurane inhalation (Abbott Japan Co., Ltd., Tokyo, Japan). The bile duct was identified and clamped at the papilla of Vater. Cold HBSS (10 ml) containing 1 mg/ml collagenase (Sigma type V; Sigma Chemicals, St. Louis, MO, United States) was injected into the common bile duct leading to the pancreas. The pancreas was removed and incubated in a water bath at 37°C for 12 min before being digested, and the cell suspension was washed 3 times in cold HBSS and centrifuged for 1 min. Density-gradient centrifugation was performed for 10 min using a Histopaque-1119 (Sigma Diagnostics, St. Louis, MO, United States) and LymphoprepTM (Axis-Shiled, Oslo, Norway) to isolate pancreatic islets. The islets were cultured in Roswell Park Memorial Institute Medium 1640 (RPMI-1640) (Thermo Fisher Scientific) containing 5.5 mmol/L glucose, 10% fetal bovine serum (Thermo Fisher Scientific), and 1% penicillin/streptomycin (Thermo Fisher Scientific) at 37°C in 5% CO_2 and humidified air (**Figure 3**).

One day after isolation, the islets were collected for transplantation. Anesthesia and surgical site preparation were performed as described earlier. The previous incision was re-opened, and the scaffold was exposed and carefully dissected from the overlying fibrofatty tissue. The cannula to the PV was exposed, and 300 µL of normal saline was injected using a 25-/23-G butterfly needle connected to a 1-ml syringe to test the patency. A total of 2,600 islet equivalents (IEQs; approximately 8 IEQs/g of rat weight) were then transferred to 100 µL of saline and aspirated using the butterfly needle. The islets were slowly injected into the scaffold through the PV in a total volume of 0.5–1 ml of saline and at a rate of 1 ml/min (manually). Occasional slight leakage of clear fluid out of the scaffold was considered acceptable.

The wound was then closed, and the rat was allowed to recover as described earlier. In one extra rat, both islets and hepatocytes (freshly isolated from male Lewis rats as described previously (Saitoh et al., 2021)) were injected, and the scaffold was retrieved immediately after injection to check the distribution of cells at day 0.

Follow-up after Islet Transplantation

The rats were followed up for 30 days (±2 days) after transplantation for their general condition and correction of hyperglycemia. Rats were considered cured if 2 consecutive glucose measures were below 200 mg/dl. In cured animals and those with partial correction of hyperglycemia, an intravenous glucose tolerance test (IVGTT) was performed on day 28, and the scaffold was removed to confirm recurrence of hyperglycemia. The scaffold was fixed in 4% paraformaldehyde overnight and used for immunohistochemical analyses. 5-bromo-2′-deoxyuridine (BrdU; Abcam, Cambridge, United Kingdom) was injected intraperitoneally (i.p.) on days -4, -3, and -2 relative to the scaffold removal day (dose = 500 mg/kg). In one rat per group, micro-computed tomography (micro-CT) was performed at the study end-point to evaluate the AV bundle, as described later.

IVGTT

The IVGTT was performed as described previously (Jimbo et al., 2014; Inagaki et al., 2021). In brief, after fasting for 14 h with free access to water, the BW and BGL were measured, and 1 g/kg glucose was injected intravenously. The blood glucose was measured at 5, 10, 20, 30, 60, 90, and 120 mins, and the blood glucose curve was generated. The area under the curve (AUC) was then used for comparisons.

Ex Vivo Micro-CT

Micro-CT was performed in one rat per group as described previously (Eweida et al., 2018a), with a few modifications. The abdominal aorta was cannulated with a 22-G venflon cannula, and 100 ml of normal saline containing 100 U of heparin sodium per mL was perfused using gravity to wash out the blood. A total of 20 ml of Microfil® (MV-122; Flow Tech Inc., Carver, MA, United States) with 0.6 ml of curing agent was then injected using a 30-ml syringe through the cannula. After 90 min, the implanted scaffold was dissected and carefully removed. The scaffold was then imaged using a

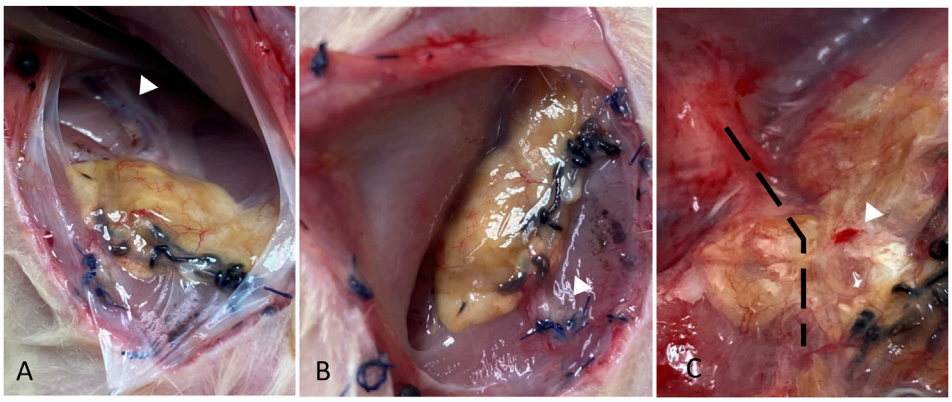

FIGURE 5 | Gross morphology of the liver at the study end-point showing the AV bundle proximal and distal to the scaffold (white arrowheads in **A** and **B**, respectively), surface vascularization, and bleeding on touch (white arrowhead in **C**). The location of AV bundle in (**C**) is marked by a dashed line.

LaTheta™ LCT-200 (Hitachi Aloka Medical Ltd., Tokyo, Japan). The VGSTUDIO MAX™ software program (version 3.0) (Volume Graphics, Heidelberg, Germany) was used for the 3D reconstruction and video acquisition.

Immunohistochemistry

Removed scaffolds were fixed in 4% paraformaldehyde, dehydrated, and embedded in paraffin blocks. In brief, 4-μm sections were incubated with rabbit anti-von-Willebrand factor (anti-vWF;Sigma Aldrich, ab7356), rabbit anti-insulin (Abcam, ab181547), and rat anti-BrdU antibody-HRP (Abcam, ab220507). Rabbit Envision and goat anti-rabbit-HRP (4003; DAKO, Glostrup, Denmark) were used as secondary antibodies for anti-vWF and anti-insulin staining, respectively. Either methylene green or Hematoxylin was used for nuclear staining. Hematoxylin-Eosin (HE) staining was also performed. Six to 8 sections with equal intervals (250 μm) were evaluated per sample and scored by a pathologist in a blinded manner. The positive cells for vWF and BrdU were counted, and the total islet area was measured in each section. Then, we calculated the number of positive cells for vWF and BrdU per μm^2 of islet area (number/μm^2) in each section. The resulting scores were used for statistical comparison.

Statistical Analyses

Data for histological scoring are expressed as the mean ± standard error of mean (SEM). All statistical analyses were performed using the JMP pro 15 software program (SAS institute Inc., Carry, NC, United States). For histological scoring, a one-way analysis of variance (ANOVA) was used to compare the means, and the Tukey-Kramer test was used for the post hoc analysis. A student t-test was used to compare the means of AUC from the IVGTT results. p values of <0.05 were considered to indicate statistical significance.

RESULTS

Gross Morphology

At the end of the decellularization protocol, the DLM demonstrated a whitish, transparent appearance (**Figure 2B**). With adequate dissection of the subcutaneous plane up to the inguinal ligaments, placement of the whole-liver decellularized scaffold was possible. At the time of islet transplantation, no significant adhesion or fibrous capsule was observed, and the scaffold was easily visualized. A considerable yet expected decrease in size and change in shape was noted at this point. Injection of pancreatic islets into the scaffold was feasible with minimal leakage.

At the time of scaffold retrieval, the size of the scaffold was comparable to the size at islet transplantation. Vascularization of the scaffold surface was visible in most specimens. The AV bundle above and below the scaffold was clearly seen, and pulsation was frequently observed through the scaffold (**Figure 5** and **Supplementary Video 1**). Cut sections through the scaffold showed an intact AV bundle, and the intra-graft vasculature was observed in silicon-injected samples.

Blood Glucose Level

Two rats in the BM group and 1 in the ADSC group showed normalization of blood glucose, (blood glucose <200 mg/dl on 2 consecutive measurements). One rat in each group showed partial correction of glucose level. No rats were cured in the HBSS group. After graft removal, hyperglycemia recurred, confirming the function of the graft. In one rat in the BM group, hyperglycemia did not completely recur after scaffold removal. **Figure 6** shows the blood glucose levels of the rats during the study period.

The IVGTT was performed in rats with improved blood glucose levels (n = 6), and the results are shown in **Figure 7**. The AUC in rats with functioning grafts were significantly lower than values in diabetic rats (n = 3), p = 0.002, while significantly higher compared to normal Lewis rats (n = 6), p < 0.001.

Micro-CT

In all three groups, there was evidence of vascular sprouting from the AV bundle inside the scaffold. **Figure 8** shows representative micro-CT 3D reconstruction images. The micro-CT examination also confirmed the patency of the AV bundle in samples from the three groups (HBSS, BM, and ADSC). A representative video

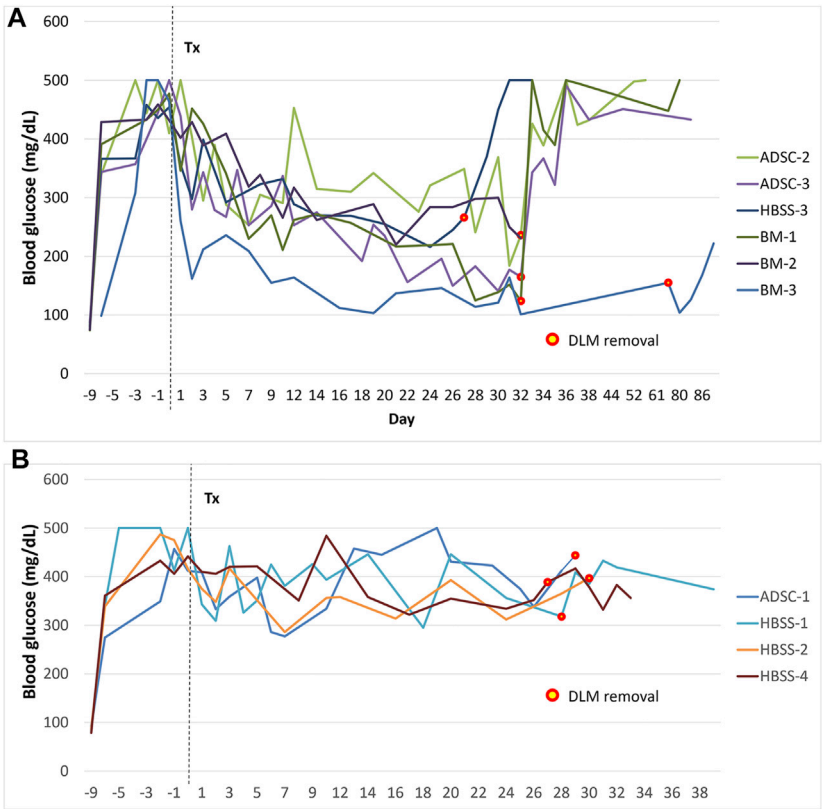

FIGURE 6 | Blood glucose levels during follow-up after transplantation. **(A)** animals with improvement of blood glucose levels, **(B)** animals that did not show improvement of blood glucose levels. The mark signifies the time of graft removal. *The graft was removed after 81 days in the first rat of the study to check for long-term adverse effects (BM group, this graft was not included in histological or vascularization assessments).

through the axial scans can be found in the supplementary data (**Supplementary Video 2**).

Immunohistochemistry

Histological examination showed insulin-positive cells in all three study groups (**Figure 9**). However, intact islets were more frequently encountered in the BM and ADSC groups than in the acellular scaffolds. The number of vWF-positive cells was higher within the islet region in the ADSC and BM groups than in the HBSS group (p = 0.08 and 0.10, respectively). BrdU + cells were significantly less frequent in the BM group than in both the ADSC and acellular groups (p = 0.003 for both), with no significant difference noted between the HBSS and ADSC groups.

The AV bundle was intact and patent in all analyzed samples with evident sprouting into the scaffold (**Figure 10**). No evidence of fibrosis or capsule formation was noted. A honeycomb appearance of the empty DLM was noted in some regions, while evidence of resorption could also be seen at other locations.

DISCUSSION

Decellularized ECM scaffolds were shown to support the islet function *in vitro* (Napierala et al., 2017; Guruswamy Damodaran and Vermette, 2018; Citro et al., 2019). In addition, transplanting islets with a decellularized lung scaffold was functionally superior to islets-only when transplanted in the subcutaneous tissue (Citro et al., 2019). In another report (Yu et al., 2018), a recellularized pancreas scaffold improved the blood glucose levels when anastomosed to diabetic rat vessels, although the graft survival was short. A decellularized pancreatic scaffold accelerated the insulin gene expression in induced pluripotent stem cell-derived β-cell-like cells (Wan et al., 2017). In the present proof-of-concept study, we showed that decellularized whole liver can allow for islet engraftment and the graft survival in a rat model. The choice of the subcutaneous location, known for its low vascularity and oxygen tension, and islets, with their high oxygen demand, allowed us to examine the potential utility of this approach for cell transplantation.

Several studies have demonstrated the utility of the axial vascularization concept in tissue-engineered constructs and its ability to promote vascularized tissue formation (Eweida et al., 2018a; Eweida et al., 2018b; Wong et al., 2019). However, few studies have examined the suitability of axially vascularized chambers for islet transplantation in the form of an AV shunt (Maki et al., 1996; Brown et al., 2006) or bundle (Knight et al.,

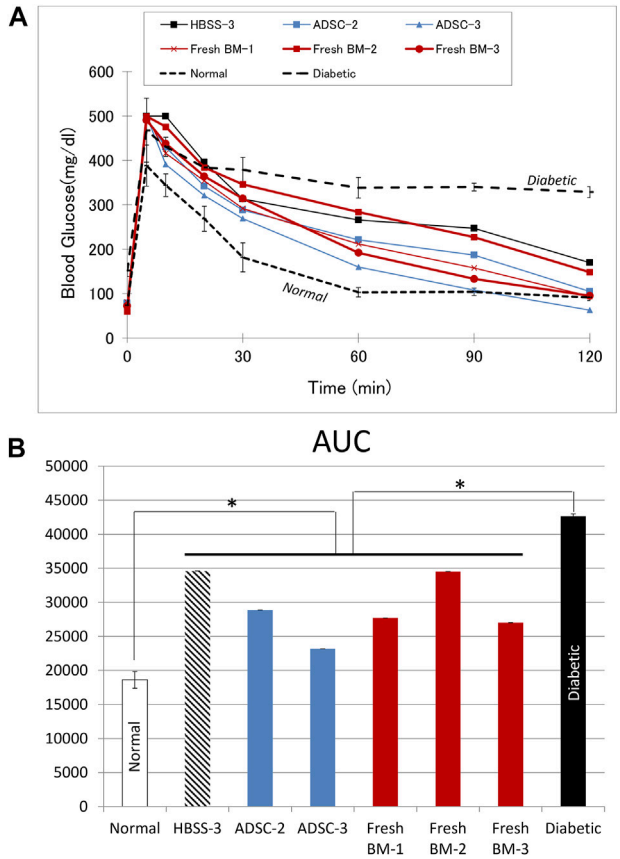

FIGURE 7 | Intravascular glucose tolerance test (IVGTT). **(A)** The blood glucose curve in animals with improved blood glucose levels. **(B)** The corresponding area under the curve (AUC). Average data from diabetic ($n = 3$) or normal ($n = 6$) Lewis rats are provided for comparison. In comparison to diabetic rats, AUC was significantly lower ($p = 0.002$) in the treatment group with functioning graft, while it was significantly higher ($p < 0.001$) in comparison to values from normal rats.

2006). Results have shown an improved glycemic control compared to diabetic controls (Maki et al., 1996; Knight et al., 2006) as well as evidence of intact islets on histology (Brown et al., 2006). Tanaka et al. (Tanaka et al., 2003) compared the AV bundle to AV shunt and found a significantly higher rate of new tissue formation in cases with an AV shunt. However, excessive vascular sprouting was noted in both the AV shunt and bundle (ligation type) groups. Because of its simplicity and suitability for the scaffold size and orientation, a ligation-type AV bundle was chosen for the present study.

Both micro-CT and the histological assessment showed intact AV bundles more than 65 days after the initial scaffold implantation. Furthermore, sprouting from the AV bundle was clearly seen on histology and micro-CT. Branching along the native IVC tributaries and, to a lesser extent, direct penetration through the IVC-ECM could be seen during the histological examination (**Figure 10**). The AV bundle was passed through the IVC for two reasons: because the grossly multi-lobular nature of the rat liver makes it difficult to pass the bundle through all the lobes, and to avoid damaging the integrity of the scaffold to allow for seeding through the PV later. The histological assessment showed that more vWF-positive vessels were found in the BM and ADSC groups than HBSS group, while no superiority was noted with regard to BrdU staining, suggesting that the improvement in the function was likely due to better islet vascularization.

The subcutaneous location offers many advantages for islet transplantation including easy accessibility, low invasiveness, and monitoring feasibility. However, due to its poor vascularization, a pre-vascularization approach is usually necessary in order to achieve an islet function comparable to that with intra-portal transplantation (Uematsu et al., 2018a; Uematsu et al., 2018b). In this approach, a device is placed in the subcutaneous tissue to induce a vascular capsule, and then islets are transplanted inside this capsule after a certain period. This device is either made of material that induces neovascularization or loaded with angiogenic growth factors (Uematsu et al., 2018a; Uematsu et al., 2018b). In the present study, we examined the effect of ECM alone compared with seeded ECM with fresh BM or ADSCs to induce vascularization of the scaffold.

Several studies have demonstrated the angiogeneic potential of both ADSCs and BM-derived mesenchymal stem cells (BM-MSCs) (reviewed in (Mazini et al., 2019; Liu and Holmes,

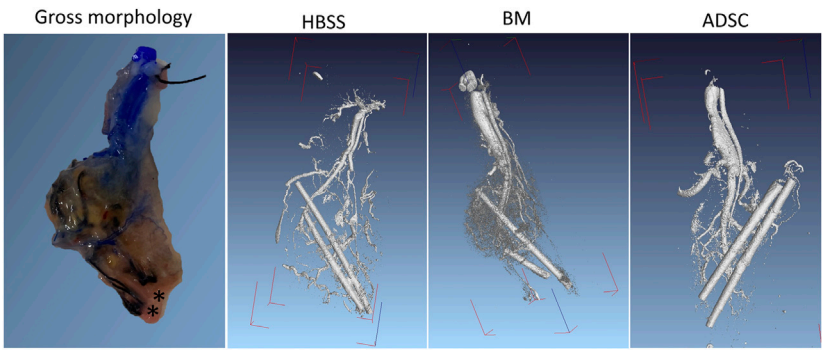

FIGURE 8 | *Ex vivo* micro-CT imaging. *Ex vivo* micro-CT was performed in one rat per group after injecting Microfil through the abdominal aorta. The DICOM files were reconstructed using a visual studio software program. The PV and HA cannulas were left in place for orientation (radioopaque). The gross morphology of the graft after Microfil injection is provided for anatomical correlation (the asterixis mark the cannulas' location).

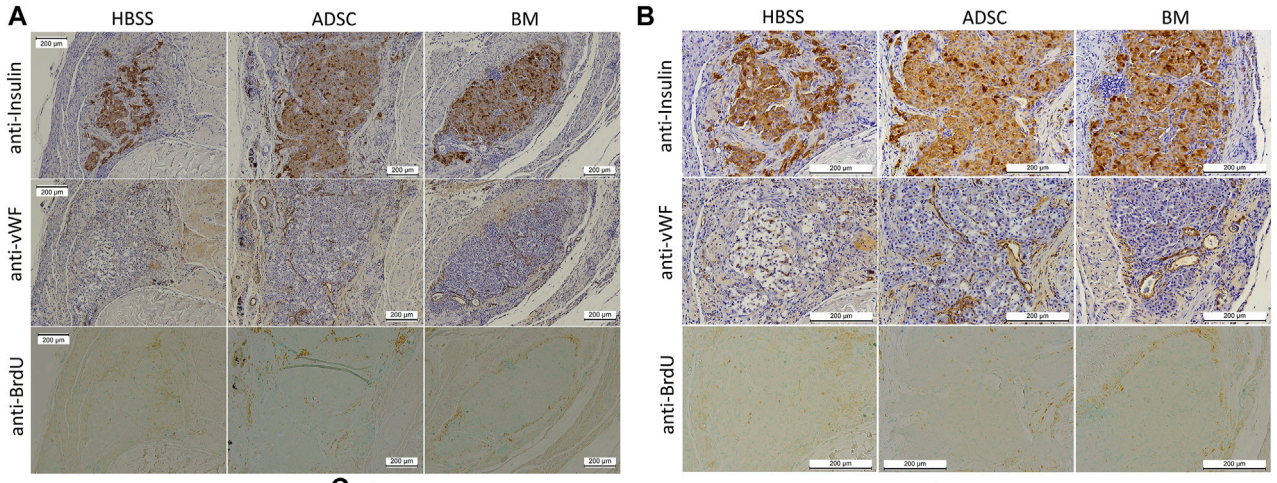

C

Islet area	HBSS	ADSCs	BM
vWF⁺ (mean±SEM)	89.0 ± 57.1	231.3±31.4	227.3±34.1
BrdU⁺ (mean±SEM)	207.1±38.2	176.5±27.6	45.8±27.0

FIGURE 9 | Representative images of the immunohistochemical staining of the scaffold showing anti-insulin **(upper panel),** anti-Von-Willebrand factor **(middle panel),** and anti-BrdU **(lower panel)** staining of the islet region [**(A)** low magnification (100x) and **(B)** high magnification (200x)]. **(C)** There were more vWF + cells in the islet region in the ADSC and BM groups than in the HBSS group, while the numbers of BrDU + cells were significantly lower in the BM group than in the other two groups.

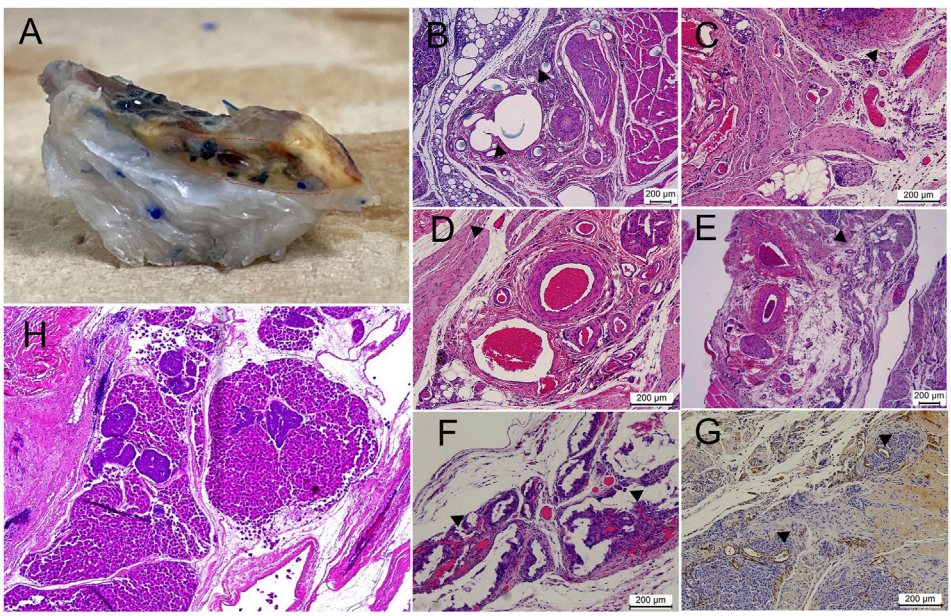

FIGURE 10 | Vascularity of the implanted scaffold at the end of the study. **(A)** Large vessels inside the scaffold, shown by injection of colored dye (region encircled by dashed red line). B-G) Different patterns of vascularization seen on a histological examination, with the following findings marked with black arrowheads: **(B)** direct sprouting from the main vein of the AV bundle, **(C)** vessels observed inside the scaffold in close association with the AV bundle, **(D,E)** sprouting of vessels along the native scaffold inferior vena cava tributaries, **(F)** remarkable intra-scaffold vascularization in association with scaffold resorption regions, **(G)** anti-Von-Willebrand staining of neovascularization inside the islet graft. **(H)** Day 0 specimen after combined injection of both pancreatic islets and hepatocytes; islets frequently failed to reach the intra-scaffold location compared with smaller hepatocytes.

2021)) and their ability to improve the islet function (Jung et al., 2011; Chen et al., 2013; Lee et al., 2020; Yamashita et al., 2021). One study demonstrated a better vascularization after ADSC implantation than with BM-MSCs in a myocardial infarction (MI) model (Paul et al., 2013). Extracellular vesicles (ECVs) from ADSCs also had a superior effect compared to those from BM-MSCs in an MI model (Xu et al., 2020). In contrast, in two separate studies involving a brain-ischemia model, ECVs from BM-MSCs resulted in a 4-fold increase in the endothelial cell number (Doeppner et al., 2015) compared to a 1.5-fold increase in the other study utilizing ADSCs (Chen et al., 2016). While a direct comparison between BM-MSCs and ADSCs was not the target of the present study, with these cells instead compared to an acellular scaffold, our findings suggest that ADSCs did not offer any particular advantage over fresh BM (MSCs ≈0.004–0.009% of nucleated cells in murine BM (Meirelles and Nardi, 2003)) with regard to the islet function or number of newly formed vessels. Co-transplantation of either cell type alone without a pre-vascularization device was not reported to be successful in allowing the islet function in the subcutaneous tissue, although transplantation with ADSC-sheets showed promising results (Lee et al., 2020; Yamashita et al., 2021). *In vitro,* ADSC-sheet + islets co-culture media showed significantly higher concentration of IL-8 compared to control (Yamashita et al., 2021). A previous report showed that transplanting islets with decellularized small intestine submucosa (SIS) or with SIS + BM-MSCs resulted in significantly lower blood glucose levels, although the latter showed significantly higher blood insulin levels (Wang et al., 2017). The study showed that co-culturing with BM-MSCs significantly increased vascular endothelial growth factor A (Vegfa) expression and CD31 mean fluorescence intensity in islets compared to islets-only and islets + SIS groups *in vitro*. The co-culture media also had significantly higher concentrations of ciliary neurotrophic factor (CNTF), epidermal growth factor (EGF), hepatocyte growth factor (HGF) (Wang et al., 2017).

In addition to improving islet revascularization, BM-MSCs (Chen et al., 2013; Wang et al., 2017; He et al., 2018) and ADSCs (Lee et al., 2020; Yamashita et al., 2021) were shown to improve islet viability and stimulated insulin secretion *in vitro*. BM-MSCs also significantly upregulated insulin 1 (Ins1) and pancreatic and duodenal homeobox 1 (Pdx1) expression in islets (Wang et al., 2017). BM-MSCs co-culture protected the islets against endoplasmic reticulum stress-induced apoptosis in another study (He et al., 2018). The concentration of tumor necrosis factor (TNF), in BM-MSC + islets co-culture media (Wang et al., 2017), and IL-16, in ADSCs + islets co-culture media (Yamashita et al., 2021), were significantly lower in comparison to islets-only medium.

The merits of the present approach include its functionality in the subcutaneous location, feasibility of repeated transplantation and drug delivery, accessibility for removal or re-implantation through the AV bundle without animal sacrifice, allowance for ECM material modifications after decellularization, and suitability for studying cell-ECM interactions. However, the main demerit of this approach is the active ECM resorption, although this can be considered a part of the remodeling process. Therefore, the balance between the pre-vascularization period and the expected ECM resorption should be tuned according to the size of the scaffold. In addition, a day 0 assessment showed that not all islets could reach an intraparenchymal location, and some got stuck at the terminal portal venules. This finding is supported by a previous report (Fu et al., 2017) and justifies the transplantation of many islets in this study. Accordingly, this model might be more suitable for single-cell preparations (e.g., hepatocytes or disintegrated beta cells) or small organoids (small islets or hepatocyte spheroids). If the challenges associated with upscaling could be overcome, this model can be a promising alternative site for clinical cell transplantation and a novel approach for organ bioengineering.

In conclusion, despite the limited sample size, the study demonstrated the potential utility of the pre-vascularized whole-organ scaffold as a novel approach for islet transplantation. Both BM- and ADSCs-seeded scaffolds were superior to the acellular scaffold with regard to the vascularization and graft function.

DATA AVAILABILITY STATEMENT

All data generated or analyzed in the present study were included in this published article and its supporting files.

ETHICS STATEMENT

The animal study was reviewed and approved by the Tohoku University, Graduate School of Medicine, Animal experimentation ethics committee (approved protocol 2019MdA-104).

AUTHOR CONTRIBUTIONS

IF planned and conducted the study and wrote the article. TI shared in the pancreatic islet isolation. AI performed the adipose-derived stem cell isolation. YN performed the semi-quantitative analysis of histology. AN shared in the conception of the study and revised the article. MG supervised the work, performed the statistical analysis, and revised the article. All authors read, and approved the submitted version.

FUNDING

This study was supported by a Japanese Grant-in-Aid for Scientific Research (A) (Grant Number 18H04056) from the Japan Society for the Promotion of Science. The founders played no role in the study design, the collection and analysis of the data, the decision to publish, or the preparation of the article.

ACKNOWLEDGMENTS

The authors thank Kozue Imura and Megumi Goto (Division of Transplantation and Regenerative Medicine, Tohoku University) for their excellent technical assistance. The authors also acknowledge the support of the Biomedical Research Core of Tohoku University, Graduate School of Medicine and TAMRIC (Tohoku Advanced Medical Research and Incubation Center).

SUPPLEMENTARY MATERIAL

The Supplementary Material for this article can be found online at: https://www.frontiersin.org/articles/10.3389/fbioe.2021.756755/full#supplementary-material

Supplementary Video 1 | Arterial pulsations.

Supplementary Video 2 | Micro-CT.

REFERENCES

Bao, J., Wu, Q., Sun, J., Zhou, Y., Wang, Y., Jiang, X., et al. (2015). Hemocompatibility Improvement of Perfusion-Decellularized Clinical-Scale Liver Scaffold through Heparin Immobilization. *Sci. Rep.* 5 (1), 1–13. doi:10.1038/srep10756

Bao, J., Shi, Y., Sun, H., Yin, X., Yang, R., Li, L., et al. (2011). Construction of a portal Implantable Functional Tissue-Engineered Liver Using Perfusion-Decellularized Matrix and Hepatocytes in Rats. *Cel Transpl.* 20 (5), 753–766. doi:10.3727/096368910x536572

Bennet, W., Groth, C.-G., Larsson, R., Nilsson, B., and Korsgren, O. (2000). Isolated Human Islets Trigger an Instant Blood Mediated Inflammatory Reaction: Implications for Intraportal Islet Transplantation as a Treatment for Patients with Type 1 Diabetes. *Upsala J. Med. Sci.* 105 (2), 125–133. doi:10.1517/03009734000000059

Brown, D. L., Meagher, P. J., Knight, K. R., Keramidaris, E., Romeo-Meeuw, R., Penington, A. J., et al. (2006). Survival and Function of Transplanted Islet Cells on an *In Vivo*, Vascularized Tissue Engineering Platform in the Rat: A Pilot Study. *Cel Transpl.* 15 (4), 319–324. doi:10.3727/000000006783981909

Bruinsma, B. G., Kim, Y., Berendsen, T. A., Ozer, S., Yarmush, M. L., and Uygun, B. E. (2015). Layer-by-layer Heparinization of Decellularized Liver Matrices to Reduce Thrombogenicity of Tissue Engineered Grafts. *J. Clin. Transl Res.* 1 (1), 48–56.

Chen, J., Ye, Y., Liao, L., Cai, J., Huang, L., Yang, S., et al. (2013). Mesenchymal Stem Cells Promote Islet Survival *In Vitro* and Function *In Vivo*. *CellR4.* 1 (2), e382.

Chen, K.-H., Chen, C.-H., Wallace, C. G., Yuen, C.-M., Kao, G.-S., Chen, Y.-L., et al. (2016). Intravenous Administration of Xenogenic Adipose-Derived Mesenchymal Stem Cells (ADMSC) and ADMSC-Derived Exosomes Markedly Reduced Brain Infarct Volume and Preserved Neurological Function in Rat after Acute Ischemic Stroke. *Oncotarget* 7 (46), 74537–74556. doi:10.18632/oncotarget.12902

Citro, A., Moser, P. T., Dugnani, E., Rajab, T. K., Ren, X., Evangelista-Leite, D., et al. (2019). Biofabrication of a Vascularized Islet Organ for Type 1 Diabetes. *Biomaterials* 199, 40–51. doi:10.1016/j.biomaterials.2019.01.035

Doeppner, T. R., Herz, J., Görgens, A., Schlechter, J., Ludwig, A.-K., Radtke, S., et al. (2015). Extracellular Vesicles Improve Post-Stroke Neuroregeneration and Prevent Postischemic Immunosuppression. *Stem Cell translational Med.* 4 (10), 1131–1143. doi:10.5966/sctm.2015-0078

Eweida, A., Fathi, I., Eltawila, A. M., Elsherif, A. M., Elkerm, Y., Harhaus, L., et al. (2018). Pattern of Bone Generation after Irradiation in Vascularized Tissue Engineered Constructs. *J. Reconstr. Microsurg* 34 (02), 130–137. doi:10.1055/s-0037-1607322

Eweida, A., Frisch, O., Giordano, F. A., Fleckenstein, J., Wenz, F., Brockmann, M. A., et al. (2018). Axially Vascularized Tissue-Engineered Bone Constructs Retain Their *In Vivo* Angiogenic and Osteogenic Capacity after High-Dose Irradiation. *J. Tissue Eng. Regen. Med.* 12 (2), e657–e68. doi:10.1002/term.2336

Fathi, I., and Eltawila, A. (2017). "Whole-Liver Decellularization: Advances and Insights into Current Understanding," in *Xenotransplantation: New Insights*. Editor S. Miyagawa (Suita, Japan: Osaka University), 139.

Fu, H., Qiu, K., Jiang, X., Chen, X., Xu, F., Zhao, Y., et al. (2017). Islet Distribution in Decellularized Liver Bioscaffolds by Infusion through the Portal Vein. *J Biomater. Tissue Eng.* 7 (5), 348–354. doi:10.1166/jbt.2017.1582

Guruswamy Damodaran, R., and Vermette, P. (2018). Decellularized Pancreas as a Native Extracellular Matrix Scaffold for Pancreatic Islet Seeding and Culture. *J. Tissue Eng. Regen. Med.* 12 (5), 1230–1237. doi:10.1002/term.2655

He, Y., Zhang, D., Zeng, Y., Ma, J., Wang, J., Guo, H., et al. (2018). Bone Marrow-Derived Mesenchymal Stem Cells Protect Islet Grafts against Endoplasmic Reticulum Stress-Induced Apoptosis during the Early Stage after Transplantation. *Stem Cells* 36 (7), 1045–1061. doi:10.1002/stem.2823

Hering, B. J. (2005). Achieving and Maintaining Insulin independence in Human Islet Transplant Recipients. *Transplantation* 79 (10), 1296–1297. doi:10.1097/01.tp.0000157321.55375.86

Hussein, K. H., Park, K.-M., Kang, K.-S., and Woo, H.-M. (2016). Heparin-gelatin Mixture Improves Vascular Reconstruction Efficiency and Hepatic Function in Bioengineered Livers. *Acta Biomater.* 38, 82–93. doi:10.1016/j.actbio.2016.04.042

Inagaki, A., Imura, T., Nakamura, Y., Ohashi, K., and Goto, M. (2021). The Liver Surface Is an Attractive Transplant Site for Pancreatic Islet Transplantation. *Jcm* 10 (4), 724. doi:10.3390/jcm10040724

Jimbo, T., Inagaki, A., Imura, T., Sekiguchi, S., Nakamura, Y., Fujimori, K., et al. (2014). A Novel Resting Strategy for Improving Islet Engraftment in the Liver. *Transplantation* 97 (3), 280–286. doi:10.1097/01.tp.0000437557.50261.b9

Jung, E.-J., Kim, S.-C., Wee, Y.-M., Kim, Y.-H., Choi, M. Y., Jeong, S.-H., et al. (2011). Bone Marrow-Derived Mesenchymal Stromal Cells Support Rat Pancreatic Islet Survival and Insulin Secretory Function *In Vitro*. *Cytotherapy* 13 (1), 19–29. doi:10.3109/14653249.2010.518608

Knight, K. R., Uda, Y., Findlay, M. W., Brown, D. L., Cronin, K. J., Jamieson, E., et al. (2006). *Vascularized Tissue-engineered chambers Promote Survival and Function of Transplanted Islets and Improve Glycemic Control*. Hoboken, New Jersey, United States: Wiley Online Library.

Ko, I. K., Peng, L., Peloso, A., Smith, C. J., Dhal, A., Deegan, D. B., et al. (2015). Bioengineered Transplantable Porcine Livers with Re-endothelialized Vasculature. *Biomaterials* 40, 72–79. doi:10.1016/j.biomaterials.2014.11.027

Kojima, H., Yasuchika, K., Fukumitsu, K., Ishii, T., Ogiso, S., Miyauchi, Y., et al. (2018). Establishment of Practical Recellularized Liver Graft for Blood Perfusion Using Primary Rat Hepatocytes and Liver Sinusoidal Endothelial Cells. *Am. J. Transpl.* 18 (6), 1351–1359. doi:10.1111/ajt.14666

Lee, Y. N., Yi, H.-J., Kim, Y. H., Lee, S., Oh, J., Okano, T., et al. (2020). Evaluation of Multi-Layered Pancreatic Islets and Adipose-Derived Stem Cell Sheets Transplanted on Various Sites for Diabetes Treatment. *Cells* 9 (9), 1999. doi:10.3390/cells9091999

Liu, Y., and Holmes, C. (2021). Tissue Regeneration Capacity of Extracellular Vesicles Isolated from Bone Marrow-Derived and Adipose-Derived Mesenchymal Stromal/stem Cells. *Front. Cel Developmental Biol.* 9, 308. doi:10.3389/fcell.2021.648098

Maki, T., Otsu, I., O'Neil, J. J., Dunleavy, K., Mullon, C. J., Solomon, B. A., et al. (1996). Treatment of Diabetes by Xenogeneic Islets without Immunosuppression: Use of a Vascularized Bioartificial Pancreas. *Diabetes* 45 (3), 342–347. doi:10.2337/diab.45.3.342

Mazini, L., Rochette, L., Amine, M., and Malka, G. (2019). Regenerative Capacity of Adipose Derived Stem Cells (ADSCs), Comparison with Mesenchymal Stem Cells (MSCs). *Ijms* 20 (10), 2523. doi:10.3390/ijms20102523

Meirelles, L. d. S., and Nardi, N. B. (2003). Murine Marrow-Derived Mesenchymal Stem Cell: Isolation,in Vitroexpansion, and Characterization. *Br. J. Haematol.* 123 (4), 702–711. doi:10.1046/j.1365-2141.2003.04669.x

Merani, S., Toso, C., Emamaullee, J., and Shapiro, A. M. J. (2008). Optimal Implantation Site for Pancreatic Islet Transplantation. *J. Br. Surg.* 95 (12), 1449–1461. doi:10.1002/bjs.6391

Napierala, H., Hillebrandt, K. H., Haep, N., Tang, P., Tintemann, M., Gassner, J., et al. (2017). Engineering an Endocrine Neo-Pancreas by Repopulation of a Decellularized Rat Pancreas with Islets of Langerhans. *Sci. Rep.* 7 (1), 1–12. doi:10.1038/srep41777

Ohmura, Y., Tanemura, M., Kawaguchi, N., Machida, T., Tanida, T., Deguchi, T., et al. (2010). Combined Transplantation of Pancreatic Islets and Adipose Tissue-Derived Stem Cells Enhances the Survival and Insulin Function of Islet Grafts in Diabetic Mice. *Transplantation* 90 (12), 1366–1373. doi:10.1097/tp.0b013e3181ffba31

Paul, A., Srivastava, S., Chen, G., Shum-Tim, D., and Prakash, S. (2013). Functional Assessment of Adipose Stem Cells for Xenotransplantation Using Myocardial Infarction Immunocompetent Models: Comparison with Bone Marrow Stem Cells. *Cell Biochem Biophys* 67 (2), 263–273. doi:10.1007/s12013-011-9323-0

Saitoh, Y., Inagaki, A., Fathi, I., Imura, T., Nishimaki, H., Ogasawara, H., et al. (2021). Improvement of Hepatocyte Engraftment by Co-transplantation with Pancreatic Islets in Hepatocyte Transplantation. *J. Tissue Eng. Regen. Med.* 15 (4), 361–374. doi:10.1002/term.3170

Smink, A. M., Faas, M. M., and de Vos, P. (2013). Toward Engineering a Novel Transplantation Site for Human Pancreatic Islets. *Diabetes* 62 (5), 1357–1364. doi:10.2337/db12-1553

Tanaka, Y., Sung, K.-C., Tsutsumi, A., Ohba, S., Ueda, K., and Morrison, W. A. (2003). Tissue Engineering Skin Flaps: Which Vascular Carrier, Arteriovenous Shunt Loop or Arteriovenous Bundle, Has More Potential for Angiogenesis and Tissue Generation?. *Plast. Reconstr. Surg.* 112 (6), 1636–1644. doi:10.1097/01.prs.0000086140.49022.ab

Uematsu, S., Inagaki, A., Nakamura, Y., Imura, T., Igarashi, y., Fathi, I., et al. (2018). A Novel Subcutaneous Pancreatic Islet Transplantation Method Using the New Device of Recombinant Peptide Containing Human Type I Collagen Material with RGD Motif (Arg-Gly-Asp). *Transplantation* 102, S73. doi:10.1097/01.tp.0000542652.41619.4a

Uematsu, S. S., Inagaki, A., Nakamura, Y., Imura, T., Igarashi, Y., Fathi, I., et al. (2018). The Optimization of the Prevascularization Procedures for Improving Subcutaneous Islet Engraftment. *Transplantation* 102 (3), 387–395. doi:10.1097/tp.0000000000001970

Uygun, B. E., Soto-Gutierrez, A., Yagi, H., Izamis, M.-L., Guzzardi, M. A., Shulman, C., et al. (2010). Organ Reengineering through Development of a Transplantable Recellularized Liver Graft Using Decellularized Liver Matrix. *Nat. Med.* 16 (7), 814–820. doi:10.1038/nm.2170

Vishwakarma, S. K., Bardia, A., Lakkireddy, C., Raju, N., Paspala, S. A. B., Habeeb, M. A., et al. (2019). Intraperitoneal Transplantation of Bioengineered Humanized Liver Grafts Supports Failing Liver in Acute Condition. *Mater. Sci. Eng. C* 98, 861–873. doi:10.1016/j.msec.2019.01.045

Wan, J., Huang, Y., Zhou, P., Guo, Y., Wu, C., Zhu, S., et al. (2017). Culture of iPSCs Derived Pancreatic β-like Cells *In Vitro* Using Decellularized Pancreatic Scaffolds: a Preliminary Trial. *Biomed. Research International* 2017, 1–14. doi:10.1155/2017/4276928

Wang, D., Ding, X., Xue, W., Zheng, J., Tian, X., Li, Y., et al. (2017). A New Scaffold Containing Small Intestinal Submucosa and Mesenchymal Stem Cells Improves Pancreatic Islet Function and Survival *In Vitro* and *In Vivo*. *Int. J. Mol. Med.* 39 (1), 167–173. doi:10.3892/ijmm.2016.2814

Wang, X., Cui, J., Zhang, B.-Q., Zhang, H., Bi, Y., Kang, Q., et al. (2014). Decellularized Liver Scaffolds Effectively Support the Proliferation and Differentiation of Mouse Fetal Hepatic Progenitors. *J. Biomed. Mater. Res.* 102 (4), 1017–1025. doi:10.1002/jbm.a.34764

Wong, R., Donno, R., Leon-Valdivieso, C. Y., Roostalu, U., Derby, B., Tirelli, N., et al. (2019). Angiogenesis and Tissue Formation Driven by an Arteriovenous Loop in the Mouse. *Sci. Rep.* 9 (1), 1–11. doi:10.1038/s41598-019-46571-4

Xu, H., Wang, Z., Liu, L., Zhang, B., and Li, B. (2020). Exosomes Derived from Adipose Tissue, Bone Marrow, and Umbilical Cord Blood for Cardioprotection after Myocardial Infarction. *J. Cel Biochem* 121 (3), 2089–2102. doi:10.1002/jcb.27399

Yamashita, M., Adachi, T., Adachi, T., Ono, S., Matsumura, N., Maekawa, K., et al. (2021). Subcutaneous Transplantation of Engineered Islet/adipose-Derived Mesenchymal Stem Cell Sheets in Diabetic Pigs with Total Pancreatectomy. *Regenerative Ther.* 16, 42–52. doi:10.1016/j.reth.2020.12.005

Yu, H., Chen, Y., Kong, H., He, Q., Sun, H., Bhugul, P. A., et al. (2018). The Rat Pancreatic Body Tail as a Source of a Novel Extracellular Matrix Scaffold for Endocrine Pancreas Bioengineering. *J. Biol. Eng.* 12 (1), 6–15. doi:10.1186/s13036-018-0096-5

Conflict of Interest: The authors declare that the research was conducted in the absence of any commercial or financial relationships that could be construed as a potential conflict of interest.

Publisher's Note: All claims expressed in this article are solely those of the authors and do not necessarily represent those of their affiliated organizations, or those of the publisher, the editors and the reviewers. Any product that may be evaluated in this article, or claim that may be made by its manufacturer, is not guaranteed or endorsed by the publisher.

Copyright © 2021 Fathi, Imura, Inagaki, Nakamura, Nabawi and Goto. This is an open-access article distributed under the terms of the Creative Commons Attribution License (CC BY). The use, distribution or reproduction in other forums is permitted, provided the original author(s) and the copyright owner(s) are credited and that the original publication in this journal is cited, in accordance with accepted academic practice. No use, distribution or reproduction is permitted which does not comply with these terms.

frontiers in Bioengineering and Biotechnology

ORIGINAL RESEARCH
published: 19 November 2021
doi: 10.3389/fbioe.2021.760309

A Pulmonary Vascular Model From Endothelialized Whole Organ Scaffolds

*Yifan Yuan[1,2], Katherine L. Leiby[1,3,4], Allison M. Greaney[1,3], Micha Sam Brickman Raredon[1,3,4], Hong Qian[1,2], Jonas C. Schupp[5,6], Alexander J. Engler[1,3], Pavlina Baevova[1,2], Taylor S. Adams[5], Mehmet H. Kural[1,2], Juan Wang[1,2], Tomohiro Obata[1,2], Mervin C. Yoder[7], Naftali Kaminski[5] and Laura E. Niklason[1,2,3]**

[1]Vascular Biology and Therapeutics Program, Yale University School of Medicine, New Haven, CT, United States, [2]Department of Anesthesiology, Yale University, New Haven, CT, United States, [3]Department of Biomedical Engineering, Yale University, New Haven, CT, United States, [4]Medical Scientist Training Program, Yale University, New Haven, CT, United States, [5]Section of Pulmonary, Critical Care, and Sleep Medicine, Yale School of Medicine, New Haven, CT, United States, [6]Department of Respiratory Medicine, Hannover Medical School and Biomedical Research in End-stage and Obstructive Lung Disease Hannover, German Lung Research Center (DZL), Hannover, Germany, [7]Indiana Center for Regenerative Medicine and Engineering, Indiana University School of Medicine, Indianapolis, IN, United States

OPEN ACCESS

Edited by:
Kamal Hany Hussein,
Assiut University, Egypt

Reviewed by:
Gabor Foldes,
Imperial College London,
United Kingdom
Amiq Gazdhar,
Bern University Hospital, Switzerland
Axel Haverich,
Hannover Medical School, Germany

***Correspondence:**
Laura E. Niklason
laura.niklason@yale.edu

Specialty section:
This article was submitted to Biomaterials, a section of the journal Frontiers in Bioengineering and Biotechnology

Received: 18 August 2021
Accepted: 27 October 2021
Published: 19 November 2021

Citation:
Yuan Y, Leiby KL, Greaney AM, Raredon MSB, Qian H, Schupp JC, Engler AJ, Baevova P, Adams TS, Kural MH, Wang J, Obata T, Yoder MC, Kaminski N and Niklason LE (2021) A Pulmonary Vascular Model From Endothelialized Whole Organ Scaffolds. Front. Bioeng. Biotechnol. 9:760309. doi: 10.3389/fbioe.2021.760309

The development of an *in vitro* system for the study of lung vascular disease is critical to understanding human pathologies. Conventional culture systems fail to fully recapitulate native microenvironmental conditions and are typically limited in their ability to represent human pathophysiology for the study of disease and drug mechanisms. Whole organ decellularization provides a means to developing a construct that recapitulates structural, mechanical, and biological features of a complete vascular structure. Here, we developed a culture protocol to improve endothelial cell coverage in whole lung scaffolds and used single-cell RNA-sequencing analysis to explore the impact of decellularized whole lung scaffolds on endothelial phenotypes and functions in a biomimetic bioreactor system. Intriguingly, we found that the phenotype and functional signals of primary pulmonary microvascular revert back—at least partially—toward native lung endothelium. Additionally, human induced pluripotent stem cell-derived endothelium cultured in decellularized lung systems start to gain various native human endothelial phenotypes. Vascular barrier function was partially restored, while small capillaries remained patent in endothelial cell-repopulated lungs. To evaluate the ability of the engineered endothelium to modulate permeability in response to exogenous stimuli, lipopolysaccharide (LPS) was introduced into repopulated lungs to simulate acute lung injury. After LPS treatment, proinflammatory signals were significantly increased and the vascular barrier was impaired. Taken together, these results demonstrate a novel platform that recapitulates some pulmonary microvascular functions and phenotypes at a whole organ level. This development may help pave the way for using the whole organ engineering approach to model vascular diseases.

Keywords: whole lung tissue engineering, endothelium, pulmonary vasculature, *in vitro* disease modeling, single-cell RNA-sequencing

1 INTRODUCTION

Diseases of the lung vasculature, including primary pulmonary hypertension, capillary leak syndrome/acute respiratory distress syndrome (ARDS), inhalation injury, and the novel coronavirus disease-19 (COVID-19), are difficult to study *in vitro* due to the lack of functional *ex vivo* models (Huertas et al., 2018; Ackermann et al., 2020). Typical culture systems do not recapitulate lung macro- and micro-vascular structure, and the phenotype of cultured endothelium on plastic differs dramatically from that of native (Pampaloni et al., 2007; Schupp et al., 2020; Schupp et al., 2021). Pulmonary vascular diseases can be characterized by remodeling and loss of microvessels, processes which are often attributed to pathological responses in vascular endothelium (Mélot and Naeije, 2011).

Vascular niche characteristics, such as paracrine factors, hemodynamics, extracellular matrix (ECM), and cell-cell crosstalk, are crucial for regulating endothelial maturation and maintaining vascular homeostasis. Recently, organoid and microfluidics-based *in vitro* culture systems have emerged as tools for modeling vascular diseases (Tsai et al., 2012; Qiu et al., 2018; Wimmer et al., 2019; Monteil et al., 2020). These systems typically involve culturing differentiated or mature endothelial cells in polydimethylsiloxane (PDMS) or hydrogel-based structures under some degree of perfusion (Tsai et al., 2012; Qiu et al., 2018; Wimmer et al., 2019). However, these systems only recapitulate a very few physiological properties, such as shear stress, while failing to mimic important other aspects of organ physiology such as appropriate substrate stiffness, physiological mechanical stretch, and co-culture with other cell types of the airway or alveolar niche (Tsai et al., 2012; Qiu et al., 2018). Further, microfluidic systems fail to reconstitute the structural, compositional, and biological features of native ECM, which are critical for intracellular regulation within the vascular compartment. Native lung tissues derived from humans or animals that are cultured as whole organs *ex vivo* rapidly lose cell viability and barrier function during organ culture, and cannot be maintained in a reproducible way for extended time periods. As a result, no *in vitro* platform exists that can simulate native pulmonary vascular phenotypes and functions for long time periods and in a controlled fashion.

Whole organ decellularization opens a door to developing a construct that can recapitulate a complete vascular structure. Unlike native whole organs, acellular matrices can be repopulated with controlled cell numbers and cell types, and cellular viability can be maintained for many days since cells accommodate to the *in vitro* environment. But while repopulation of acellular lung matrices has been reported by several groups (Petersen et al., 2010; Ren et al., 2015; Le et al., 2017), evaluation of endothelial and microvascular functionality and phenotypes in these model systems has heretofore been fairly limited.

Protocols for the characterization of decellularized lung scaffolds have been published previously (Balestrini et al., 2016; Calle et al., 2016). ECM components remaining after decellularization in rat, and human lungs have been examined by quantitative proteomics, showing that a decellularization technique employing Triton detergent and sodium deoxycholate (SDC) results in an intact vascular architecture and near-native retention of laminins, proteoglycans, and other basement membrane and ECM-associated proteins (Calle et al., 2016; Li et al., 2016). Additionally, the decellularized matrix itself immobilizes soluble and insoluble cues, including VEGF, FGF, BMP, HGF, and PDGF that drive pulmonary cell regeneration (Booth et al., 2012; Gilpin et al., 2014; Ullah et al., 2019). Therefore, the decellularized lung scaffold represents a potential platform to recapitulate physiological niches in the lung parenchyma, by virtue of retained matrix protein composition, soluble and insoluble cues, 3-dimensional structure, and mechanical properties.

In this study, we explored the impact of decellularized whole lung scaffolds on endothelial cell phenotype and functions in the biomimetic bioreactor system (**Supplementary Figure S1**). As evaluated by single cell RNA sequencing (scRNAseq), primary rodent pulmonary microvascular or human induced pluripotent stem cell-derived endothelium showed a dramatic shift back to phenotypes resembling native after transitioning from expansion on tissue culture plates, into the lung matrix scaffold. After introduction of lipopolysaccharide (LPS) into endothelial-repopulated lung matrices, the endothelium was actively responsive, showing increased pro-inflammatory and matrix degradation characteristics, and decreased barrier function at the whole organ level, similar to the effect in native lungs (**Figure 1**). Thus, this study shows the potential of using the bioengineered whole organ as a platform for pulmonary vascular disease modeling.

2 RESULTS

2.1 Reendothelialization of Decellularized Whole Lung Scaffolds

The isolation of pulmonary microvascular endothelial cells (PMECs) was performed as previously described (Alphonse et al., 2015). Endothelial cells were isolated from the distal parenchyma of the lung in postnatal day 7 rats by CD31-labeled magnetic bead selection (**Supplementary Figure S2A**). PMECs became morphologically homogenous as early as passage 1, with no evident mesenchyme contamination (data not shown). Flow cytometry data confirmed that PMECs at passage 1 contain 99.5 ± 0.3% CD31 and 99.6 ± 0.2% CD144 positive cells while having low or no expression of CD90 and CD45 (**Supplementary Figure S2B**). These PMECs were rapidly proliferative—with an average doubling time of ~26.6 h across passages—and displayed key endothelial characteristics including expression of CD31, vWF, VE-Cadherin, eNOS, and Griffonia simplicifolia lectin, as well as acLDL uptake (**Supplementary Figures S2C,D**).

We cultured PMECs in decellularized lung scaffolds in a biomimetic bioreactor, as previously described (Yuan et al., 2019; Engler et al., 2019). Acellular lung scaffolds were produced by decellularizing adult native rat lungs using Triton and SDC detergents, followed by copious washing with PBS and sterilization with antibiotics. Lung scaffolds were then seeded with 50 million P4 PMECs at a concentration of 250,000 cells/mL into the pulmonary vein, followed by seeding another 50 million

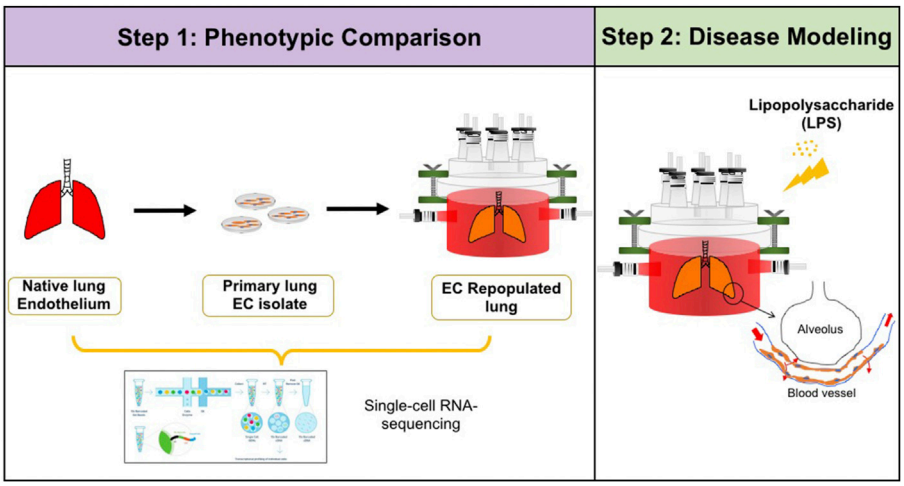

FIGURE 1 | Schematic of experimental design. Step 1: single-cell RNA-sequencing analysis was performed to compare the phenotypic and functional signals among native pulmonary endothelium, primary pulmonary endothelium cultured on tissue culture plastic, and in whole lung scaffolds. Step 2: Lipopolysaccharide (LPS) was introduced into endothelialized whole lung scaffolds to simulate inflammation.

cells into the pulmonary artery. Cultures were maintained with a flow of medium delivered via the pulmonary artery under laminar flow. The trachea and pulmonary vein were cannulated to monitor real-time fluid flows and pressures during the culture process.

Seeding of cultured endothelial cells into acellular organ microvasculature has proven difficult in prior studies, in part because the cytoplasmic volume of cultured endothelium is much larger than that of native cells (Pugacheva et al., 2006). Prior studies have shown that cultured EC can lodge in arteriolar and venular structures immediately after seeding into the pulmonary vasculature (Le et al., 2017). The physically large cell bodies may be blocked from ingress into small decellularized capillary lumens having diameters of 5–8 microns or less (Townsley, 2012). We therefore investigated whether an exogenous agent that can impact EC cytoplasmic organization could affect the ability of cells to transit or migrate into small capillary lumens. Rho-associated protein kinases (ROCK) inhibitor (Y27632) can re-organize the actin cytoskeleton, and further remodel overall cell morphology (Amano et al., 2010). Additionally, ROCK inhibition could potentially provide pro-survival signals to support EC survival and growth in decellularized lung scaffolds (Watanabe et al., 2007). We therefore applied 10 μM Y27632 to endothelial-containing lung cultures for 7 days, to determine the impact on endothelial repopulation and cell spreading in the lung matrix.

In control lungs, cells had a round morphology, with limited repopulation throughout the lung vasculature especially in microvasculature, and no or minimal patent lumens were visible (**Figure 2A**). Interestingly, after treatment with Y27632, PMECs appeared to repopulate extensively throughout the large and small vasculature of the lung matrix (**Supplementary Figure S3A**). Endothelial cells had a native-like and flattened morphology in the vasculature, and also formed observable patent lumens in the small vessels throughout the repopulated organs (**Figure 2B**). Consistently, transmission electron microscopy (TEM) images of the repopulated lungs cultured with Y27632 treatment show patent lumens in the alveolar-capillary network, with flattened cytoplasmic processes covering the inner surface of the vessel, similar to those seen in native lungs (**Figures 2D,E**), whereas such lumens were not present under control conditions (**Figure 2C**). Immunostaining for PECAM1, Laminin, VE-Cadherin, vWF, eNOS, ZO1, and Lectin GS confirmed that PMECs remained inside of the vasculature and maintained their expression of endothelial markers after 7 days of lung culture (**Figures 2F–K**). Additionally, representative TEM images demonstrate the formation of tight junctions between cells, suggesting that the vascular barrier is starting to reconstruct in our repopulated lungs (**Figure 2L**). Since the repopulated lungs without ROCK inhibitor have limited EC repopulation throughout the organ, we have therefore only analyzed the vascular functions and transcriptomic information in lungs supplied with ROCK inhibitor in subsequent studies.

To determine whether PMEC could establish measurable barrier function within the repopulated lungs, we applied a non-invasive mechanical measurement that was previously developed (Engler et al., 2019) to monitor the pressure changes generated by fluid flowing across the alveolar basement membrane (from the repopulated capillaries, into the alveolar air sacs (tracheal outflow) and within the vasculature (venous outflow) (**Figure 2M**). These non-invasive pressure measurements allow the inference of alveolar barrier function during culture. Measurement of average internal pressures (capillary entry pressure, and capillary exit pressure) is accomplished by briefly shutting off flow into or out of the organ, and measuring transient pressures at the end-organ level using piezoelectric pressure sensors situated within the bioreactor system (Engler et al., 2019).

In endothelial repopulated lungs, measurements of pressures, and of fluid translocation across the alveolar membrane and

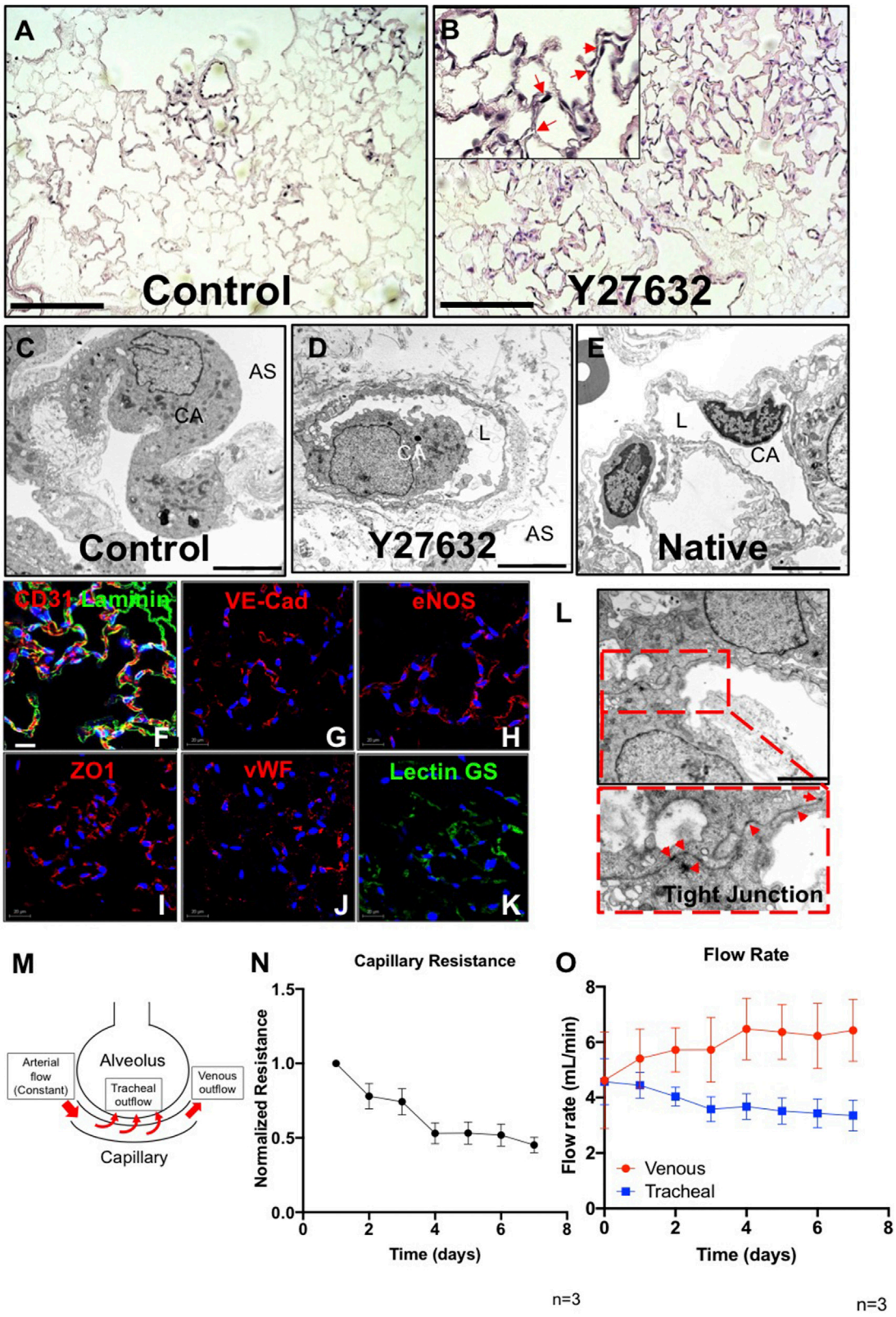

FIGURE 2 | Characterization of PMEC-repopulated lungs. **(A,B)** H/E image of a representative section in control **(A)** and Y27632-treated repopulated lungs **(B)**. Scale bars 150 μm, arrows point to reconstituted capillary lumens. **(C,D,E)** TEM images of control, Y27632-treated repopulated lungs, and native lungs, respectively.

(*Continued*)

FIGURE 2 | Scale bars 5 μm, CA: Capillary; AS: Alveolar Space; L: Lumen. **(F–K)** Immunostaining for CD31, VE-Cad, eNOS, ZO1, vWF, and lectin GS in repopulated lungs, scale bar 20 μm. **(L)** Representative TEM image of tight junctions in repopulated lungs. Arrowheads indicate tight junctions, scale bar 2 μm. **(M)** Schematic description of the flow paths in decellularized lung vasculature. **(N,O)** Non-invasive measurements were performed daily to assess the mechanical characteristics in repopulated lungs. **(N)** Capillary resistances to fluid flow within the vascular bed, versus time. **(O)** Flow rates: venous (red), and tracheal (blue) outflows versus time. "n" indicates experimental replicates. There were three independent experiments performed for each condition.

exiting the trachea, revealed that capillary resistances to fluid flow through the vascular bed gradually decreased over the 7-days culture period (**Figure 2N**). This may indicate that endothelial cells, which initially occlude arterioles and venules at the time of cell seeding (**Supplementary Figure S3B**), may migrate into capillaries and form patent lumens that can then conduct vascular flow, while increasing overall coverage throughout the vasculature. Evidence to support this supposition is seen in H&E histology (**Figure 2B**; **Supplementary Figure S3A**). Measurement of fluid translocation over time indicates that there are increasing trends of outflows in the pulmonary vein, indicating increasing flow rate exiting the vasculature (as opposed to leaking across the alveolar barrier and into the airways) over time. Similarly, flow exiting the trachea, which is indicative of net fluid leak across the alveolar barrier, decreased over time in endothelial-repopulated lungs, implying functional barrier formation by cultured PMECs (**Figure 2O**). Since repopulated lungs lack alveolar epithelium, which is a significant component of native physiological barrier, we did not anticipate a full reconstitution of native levels of alveolar barrier. However, the ability to detect some barrier function conferred by cultured endothelium is a reflection of functional competency of the cells. In here, we have optimized our protocol by adding ROCK inhibitor and determined that the cultured endothelium could form a functional monolayer that partially reconstructs vascular barrier function in whole lung scaffolds.

2.2 PMECs Cultured in Lung Scaffolds Regain Native-Like Functional Endothelial Character Compared to PMEC on Tissue Culture Plastic

To understand the evolving phenotype of PMECs in lung scaffolds, postnatal day 7 rodent native whole lung tissues (13,619 cells), pre-seeded PMECs grown in tissue culture flasks (9,321 cells), and PMEC-repopulated engineered lungs (6,188 cells) were processed through single-cell transcriptomic analysis. Whole lung tissues were harvested from three male and three female rats, and the native endothelial populations were sub-clustered by selecting for VE-cadherin (*Cdh5*) positive cells while excluding cells expressing *Col1a1* (mesenchyme), *Epcam* (epithelium), and *Ptprc* (leukocyte). We then merged, scaled, and compared the transcriptomic information among native lung endothelium, pre-seeded PMECs, and PMEC-repopulated lungs datasets. The gene ontology analysis (DAVID) of the top differentially expressed genes (DEGs) between native endothelium and cultured PMECs revealed that during expansion, PMECs markedly lost native molecular signals that are related to angiogenesis (e.g., *Acvrl1*, *Nrp1*, and *Egfl7*) (Nichol and Stuhlmann, 2012; Kofler and Simons, 2015; Rochon et al., 2016), cell adhesion (e.g., *Itgb1*, *Fbln5*, and *Itga6*) (Preis et al., 2006), ECM synthesis (e.g., *Col15a1*, *Eln*, *Col4a1*, and *Lamb2*), and cell junctions (*Cxcr4*, *Cldn5*, and *Prx*) (Wang et al., 2018) (**Figure 3A**; **Supplementary Table S1**). After culturing in acellular whole lung scaffolds for 7 days under arterial perfusion, intriguingly, many of the molecular signals that are related to angiogenesis, cell adhesion, cell junctions, and ECM synthesis were increased (**Figure 3B**; **Supplementary Table S2**). Many of the increased genes are associated with angiogenesis, cell adhesion, ECM synthesis, and cell junctions, including *Acvrl1*, *Nrp1*, *Egfl7*, *Itga6*, *Itga3*, *Col4a1*, *Eln*, *Cxcr4*, and *Gja4* (**Figure 3C**). Consistent with the findings from scRNAseq, the levels of Itga6, Itgb1, Acvrl1, Eln, and Col4a1 evaluated by western blotting or qRT-PCR were significantly increased in cells extracted from repopulated lungs, as compared to pre-seeded PMECs, across at least three independent experiments (**Supplementary Figure S4**). We have additionally studied the expression level of glycocalyx-associated genes such as syndecan, glypican, perlecan, and biglycan in ECs before and after culturing in lung scaffolds. Only biglycan (gene name: bgn) was found to be higher in repopulated lung as compared to pre-seeded cells (**Supplementary Table S2**). Hence, the global comparisons among PMEC before and after culturing in lung scaffolds, and native lung endothelium, suggest that the microenvironmental cues in lung scaffolds, including ECM components and structure, insoluble or soluble cues, and shear stress, could potentially induce the endothelial cells to regain some aspects of the native functional phenotype that is lost during *in vitro* expansion on tissue culture plastic.

2.3 PMECs Partially Regain Native Heterogeneous Endothelial Phenotypes in Repopulated Lungs

To characterize heterogenous endothelial phenotypes expressed within PMECs before and after culturing in lung scaffolds, we first determined the molecular signatures of the various endothelial phenotypes present in native lungs. Based on top DEGs, we identified 7 major endothelial clusters in native rat lung at postnatal day 7: general capillary (gCap); aerocyte capillary (aCap); arterial; pulmonary venous; systemic venous; cycling; and lymphatic (Lymph) endothelium (**Figure 4A**). The general capillary (gCap), aerocyte capillary (aCap), arterial, pulmonary venous, systemic venous, cycling, and lymphatic clusters expressed canonical endothelial markers of their respective sub-types, including *Aplnr*, and *Kit* for gCap (Kalucka et al., 2020; Travaglini et al., 2020); *Car4* and *Prx* for aCap (Gillich et al., 2020; Kalucka et al., 2020; Travaglini et al., 2020); *Gja5*, and *Cxcl12* for arterial ECs (Kalucka et al., 2020; Travaglini et al.,

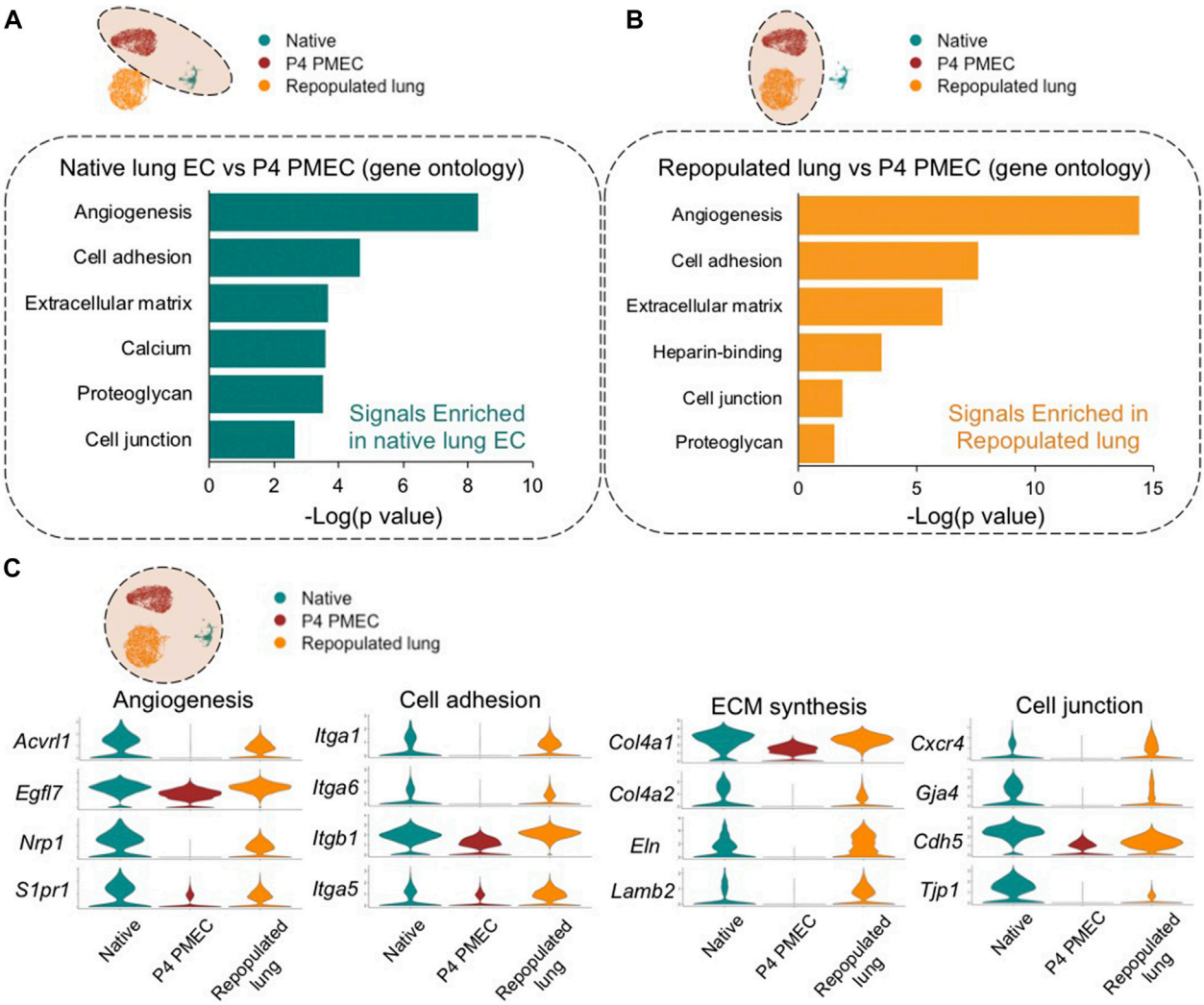

FIGURE 3 | Global comparison amongst Native, P4 PMEC, and Repopulated lung. **(A,B)** Gene ontology analysis shows the top upregulated signals based on the top DEGs of comparisons between Native endothelium and P4 PMEC **(A)**, and between Repopulated lung and P4 PMEC **(B)**. **(C)** VlnPlots of representative genes of angiogenesis, cell adhesion, ECM synthesis, and cell junction in the merged dataset of Native, P4 PMEC, and Repopulated lung samples.

2020); *Vegfc*, and *Vcam1* for pulmonary venous ECs (Kalucka et al., 2020; Travaglini et al., 2020); *Vwa1*, and *Ebf1* for systemic venous ECs (Schupp et al., 2020); *Mki67*, and *Top2a* for cycling ECs; *Prox1*, and *Ccl21* for lymph ECs (Kalucka et al., 2020; Travaglini et al., 2020) (**Figure 4B**). Since the systemic venous EC cluster is a tiny population in native rodent lung (Verloop, 1949; Parent, 2015), it was excluded in further comparisons. To confirm protein expression in various native EC populations, we selected two specific genes amongst the DEGs for each cell type. Immunostaining of native rat lung shows protein expression of Connexin 40 (*Gja5*) and Cxcl12 in arterial ECs; Vcam1 and Coup-TFII (*Nr2f2*) in venous ECs; and Aplnr, Kit, Prx, and Car4 in small capillaries, but not in large vessels (**Supplementary Figure S5**). Taken together, the scRNAseq analysis and the immunostaining of whole lung tissues confirm that endothelium in rodent pulmonary vasculature exhibits molecular heterogeneity that is consistent with recent published reports (Schupp et al., 2020; Travaglini et al., 2020; Schupp et al., 2021).

To examine the similarities and differences between engineered and native samples, we applied the "Merge" function in Seurat and combined native lung endothelium, P4 PMECs (pre-seeded and grown on tissue culture plastic), and PMEC-repopulated lungs into a single dataset. P4 PMECs were a homogenous endothelial population, with an overall phenotype quite different from that of any of the native endothelial clusters observed in this study. In contrast, and unlike the pre-seeded PMEC population, the ECs in repopulated lungs were a mixture of arterial-like, venous-like, and also a small population of lymph-like endothelium (**Supplementary Figure S6**). Arterial-like cells (Repopulated Arterial) expressed canonical arterial (e.g., *Cxcr4*, *Gja4*, and *Kcne3*) markers (Su et al., 2018; Kalucka et al., 2020; Schupp et al., 2020). In contrast, venous-like endothelium (Repopulated Venous) expressed venous (e.g., *Ackr3*, *Nr2f2*,

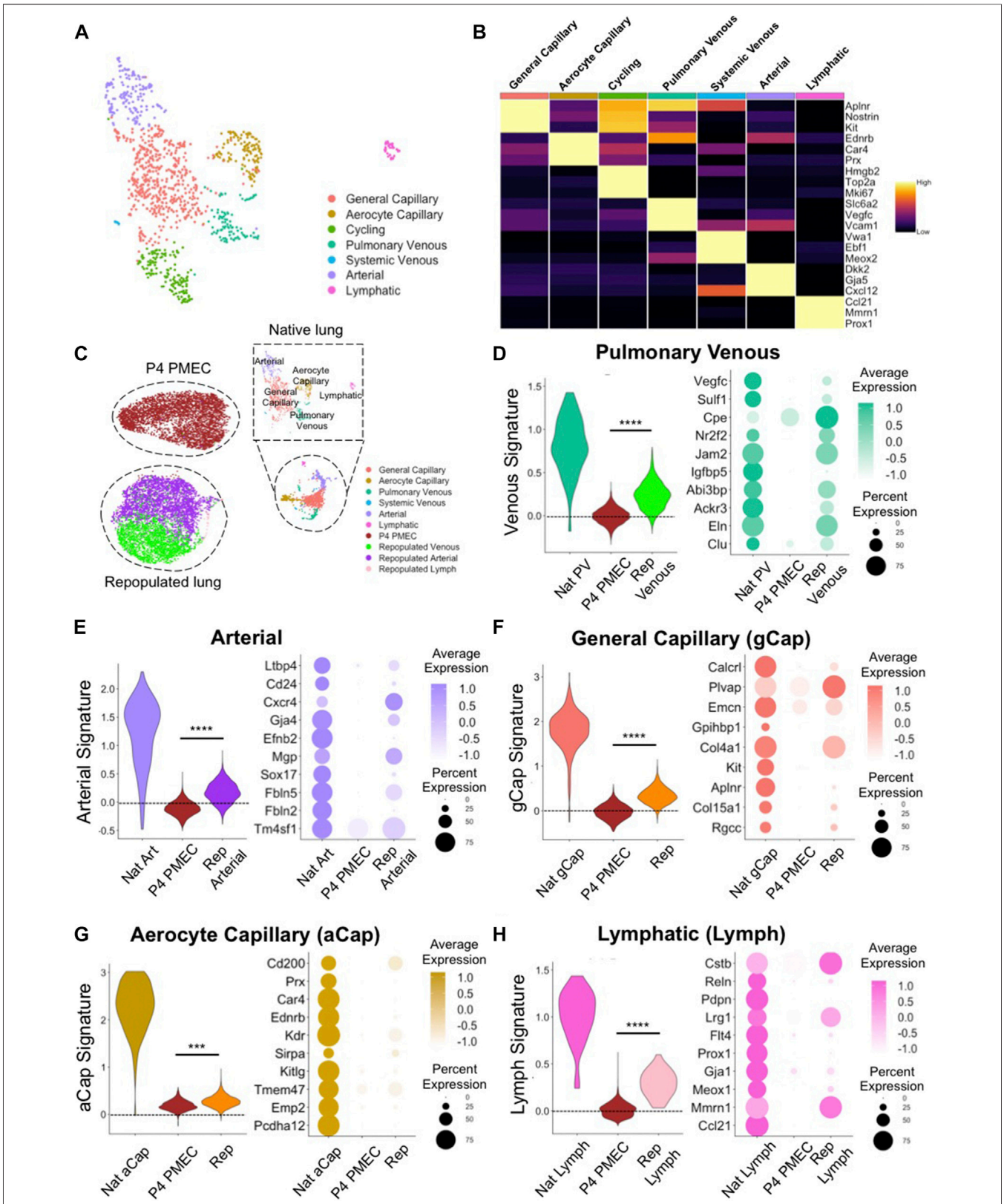

FIGURE 4 | scRNAseq evaluation of native and engineered rat pulmonary endothelium. **(A)** Uniform Manifold Approximation and Projection (UMAP) of the native pulmonary endothelial clusters. **(B)** Heatmap of top 3 DEGs for each cluster. **(C)** UMAPplots of merged object of native pulmonary endothelial clusters, pre-seeded

(*Continued*)

FIGURE 4 | PMECs, and repopulated lungs. **(D–H)** Dotplots and Module scores for **(D)** pulmonary venous, **(E)** arterial, **(F)** gCap, **(G)** aCap, and **(H)** lymph endothelium amongst native and engineered endothelium. Dot plots show the comparison for top 10 select markers of each native lung EC subtype. Samples were merged and re-scaled. Module scores were calculated based on the top 20 DEGs of each native lung EC subtypes in each engineered EC dataset at single cell level. Violin plots represent the distribution of module score for each EC subtype among native endothelium, P4 PMEC, and repopulated lung datasets. Scores >0 indicate enriched expression, compared to random control gene sets. ***, and **** indicate $p < 0.001$, and $p < 0.0001$, respectively.

and *Jam2*) markers (You et al., 2005; dela Paz and D'Amore, 2009; Schupp et al., 2020). A small population of lymph-like endothelium (Repopulated Lymph) expressed lymph marker (e.g., *Prox1*) (Wigle et al., 2002) (**Supplementary Figure S6**).

We further used "Addmodulescore" function in Seurat and calculated module scores for each cell type/cluster amongst different datasets, using the top 20 DEGs identified from each native lung EC subtype (**Supplementary Table S3**). Cells in the venous cluster in the repopulated lungs (Repopulated Venous) expressed higher levels of markers for native venous endothelium, such as *Nr2f2*, *Cpe* (Schupp et al., 2020), *Ackr3* (Schupp et al., 2020), and *Eln*, and received significantly higher scores for gene signatures of pulmonary venous endothelium, as compared to pre-seeded PMEC (**Figure 4D**). Similarly, cells in the arterial cluster in repopulated lungs expressed higher levels of markers for native arterial endothelium *Cxcr4*, *Fbln5* (Noda et al., 2013), *Cd24*, *Gja4*, *Efnb2* (Su et al., 2018), and *Sox17* (Corada et al., 2013), and received significantly higher scores for gene signatures of native arterial endothelium, as compared to pre-seeded cells (**Figure 4E**). Immunostaining confirmed the protein presence of Fbln5, Eln, and Nr2f2 in repopulated lungs (**Supplementary Figure S7B**).

Interestingly, repopulated lungs also expressed many specific markers for gCap endothelium (e.g., *Aplnr*, *Col4a1*, *Plvap*, *Rgcc*, and *Col15a1*) (Gillich et al., 2020; Kalucka et al., 2020; Schupp et al., 2020; Travaglini et al., 2020) and for aCap endothelium (e.g., *Kdr*, *Sirpa*, and *Ednrb*) (Gillich et al., 2020; Schupp et al., 2020; Travaglini et al., 2020), and received significantly higher scores for gene signatures of both native cell subtypes, as compared to cells cultured on tissue culture plastic (**Figures 4F,G**). Furthermore, there are some native capillary endothelial markers which appear to be completely silenced during EC growth on plastic (e.g., *Aplnr*, *Rgcc*, *Ednrb*, and *Sirpa*), that are regained after culture on the decellularized lung matrix (**Figures 4F,G**). Immunostaining for these previously silenced markers, including Sirpa, and Ednrb, confirmed their presence in repopulated lungs (**Supplementary Figure S7B**). While expression of these key genes was not fully restored to native levels in engineered lungs, these trends imply that functional pulmonary endothelial phenotypes are supported and encouraged by a physiological lung matrix substrate and biomimetic bioreactor culture conditions.

There was a tiny, but detectable, population of lymphatic endothelium in EC-repopulated lungs that expressed high level of lymphatic markers (e.g., *Mmnr1*, and *Prox1*), suggesting either a leftover of lymphatic cells and progenitors from the starting passaged population, or a limited differentiation effect of the lung matrix scaffold, since all of the endothelium was seeded into the blood, rather than into the lymphatic, vasculature (**Figure 4H**). Consistent with the findings from scRNAseq, the levels of *Gja4*, *Fbln5*, *Nr2f2*, *Eln*, *Aplnr*, *Rgcc*, *Ednrb*, and *Sirpa*, as evaluated by qRT-PCR were significantly increased in cells from three independent repopulated lungs as compared to pre-seeded PMECs (**Supplementary Figure S7A**). These pairwise comparisons indicate that PMECs are changing phenotypes to more resemble the native complement of ECs when cultured in the decellularized lung scaffolds in a bioreactor system.

2.4 Human iPSC-ECFCs Start to Gain Human Lung Endothelial Phenotypes in Repopulated Lungs

To develop a modeling system to study pulmonary vascular diseases, we explored the phenotypic changes of human induced pluripotent stem cell-derived endothelial colony-forming cells (iPSC-ECFCs) in acellular whole lung scaffolds. We seeded 25 million iPSC-ECFCs into the pulmonary vein, followed by seeding another 25 million cells into the pulmonary artery. Cultures were maintained with a flow of medium delivered via the pulmonary artery. After culturing human iPSC-ECFCs in the decellularized lungs with Y27632 for 6 days, endothelial cells appeared to repopulate extensively throughout the lung vasculature (**Figure 5A**), while patent vascular lumens were appreciable (**Figure 5B**). The iPSC-ECFCs maintained their endothelial phenotype within lung scaffolds, as evidenced by expression of CD31, ZO1, eNOS, and vWF (**Figure 5E**). The venous outflows continuously increased over time (**Figure 5F**), suggesting an increased barrier formation in iPSC-ECFC repopulated lungs. From these data it appears that under current culture conditions, both rodent primary PMECs and human iPSC-ECFCs express endothelial-specific markers in repopulated lung matrix, and, over time, contribute to alveolar barrier formation in culture. Combined with observable lumen formation and decreased vascular flow resistance during culture, this implies the reconstitution of a highly functional endothelial lining within the repopulated lung constructs, that provides a vascular flow path for fluid, as well as increasing barrier function within the alveolar compartment.

To understand the phenotypic changes of iPSC-ECFCs in acellular whole lung scaffolds, we processed 7,089 cells that were pre-seeded, cultured iPSC-ECFCs; and 5,591 cells from iPSC-ECFC repopulated lungs through scRNAseq. Similar to rodent primary PMECs, after culturing in acellular lung scaffolds, iPSC-ECFCs acquired markers that are related to angiogenesis, ECM/basement membrane protein synthesis, cell adhesion, and cell junctions, as compared to pre-seeded iPSC-ECFCs that had been expanded on tissue culture plastic (**Figure 5G**; **Supplementar Table S4**). We further compared the iPSC-ECFC datasets with a published human EC single-cell dataset (GEO number:

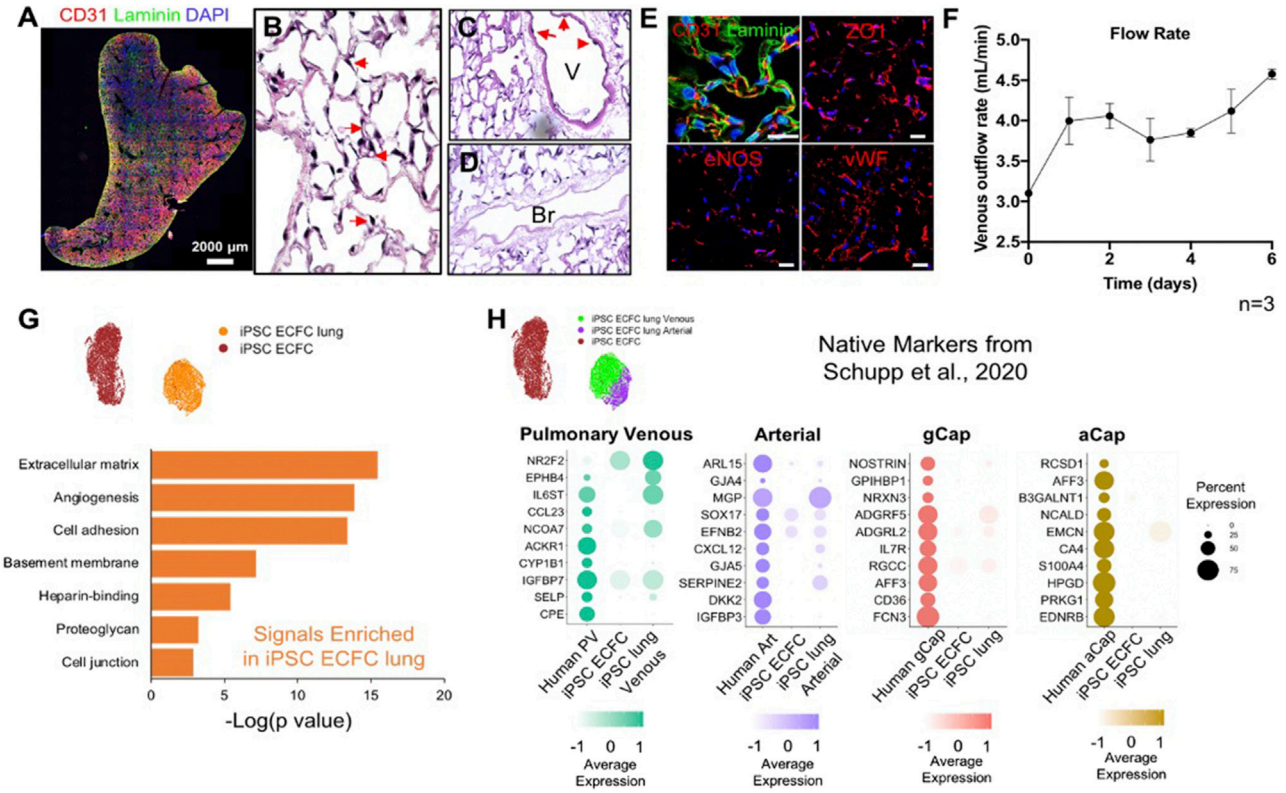

FIGURE 5 | Human iPSC-ECFCs start to gain native EC phenotype in repopulated lungs. **(A)** Immunostaining of CD31 and Laminin in iPSC-ECFC-repopulated lungs. Scale bar 2,000 μm. **(B–D)** H/E image of a representative section iPSC-ECFC repopulated lungs. Arrows in **(B)** point to reconstituted capillary lumens; arrows in **(C)** point to endothelial cells in the vasculature but not in bronchia. V: Blood Vessel; Br: Bronchi **(E)** Immunostaining for CD31, laminin, ZO1, eNOS, and vWF in repopulated lungs, scale bar 20 μm. **(F)** Venous outflows versus time, $n = 3$. **(G)** Gene ontology analysis of the top DEGs ($p < 0.05$) enriched in iPSC-ECFC lungs as compared to pre-seeded iPSC-ECFCs. **(H)** Dot plots show the comparison for top 10 select native markers of human pulmonary venous, arterial, gCap, and aCap amongst native human lung endothelium, pre-seeded iPSC-ECFCs, and iPSC-ECFC-repopulated lungs. Samples were merged and re-scaled.

GSE164829), which is comprised of over 15,000 vascular endothelial cells from 73 healthy individuals, both males and females (Schupp et al., 2020; Schupp et al., 2021). iPSC-ECFCs in repopulated lungs gained arterial-like or venous-like phenotypes. Arterial-like cells (iPSC ECFC lung Arterial) expressed canonical arterial (e.g., SERPINE2 and CXCL12) (Boulaftali et al., 2011), venous-like endothelium (iPSC ECFC lung Venous) expressed venous (e.g., IGFBP7 and NR2F2) markers (Schupp et al., 2020) (**Supplementary Figure S8**). We then compared pre-seeded iPSC-ECFCs, iPSC-ECFC-repopulated lungs, and human lung endothelium, in terms of the top markers of each native human EC subtype (Schupp et al., 2020). Cells in the venous cluster of the repopulated lungs (iPSC ECFC lung Venous) expressed a higher level of markers for native pulmonary venous endothelium, such as NR2F2, EPHB4 (Wang et al., 1998), and SELP (Thiriot et al., 2017) as compared to pre-seeded cells (**Figure 5H**). Similarly, the arterial cluster in repopulated lung expressed a higher level of SERPINE2, GJA5, CXCL12, and GJA4, than did the pre-seeded cells. Interestingly, iPSC-ECFCs in decellularized lung scaffolds also gained some recognized gCap markers, including NOSTRIN, FCN3, and ADGRF5 (Gillich et al., 2020; Schupp et al., 2020), whereas the expression of aCap markers are fairly dim, suggesting that the microenvironmental regulation of gCap and aCap phenotypes might be different. Increased expression of NOSTRIN, RGCC, CXCL12, SERPINE2, NR2F2, EPHB4, PLVAP, and COL15A1, was confirmed across multiple replicates by qRT-PCR (**Supplementary Figure S9**). Taken together, these data show that the iPSC-ECFCs start to shift their phenotype—at least partially—toward human lung EC phenotypes in acellular whole lung scaffolds, and become more native-like than pre-seeded cells.

2.5 Using Repopulated Lungs to Model Barrier Damage During Inflammation

To evaluate the repopulated lung as a disease modeling system, we first established an *ex vivo* native lung culture platform to mimic acute lung injury, as a basis of comparison with the engineered constructs. Native lungs from adult rats were mounted into the bioreactor system and cultured with DMEM medium supplemented with 0.5% FBS and 1% antibiotics/antimycotics, and perfused at 20 ml/min via the pulmonary artery. Ten minutes after initiating arterial perfusion, we introduced 6 μg/ml LPS into the bioreactor and performed

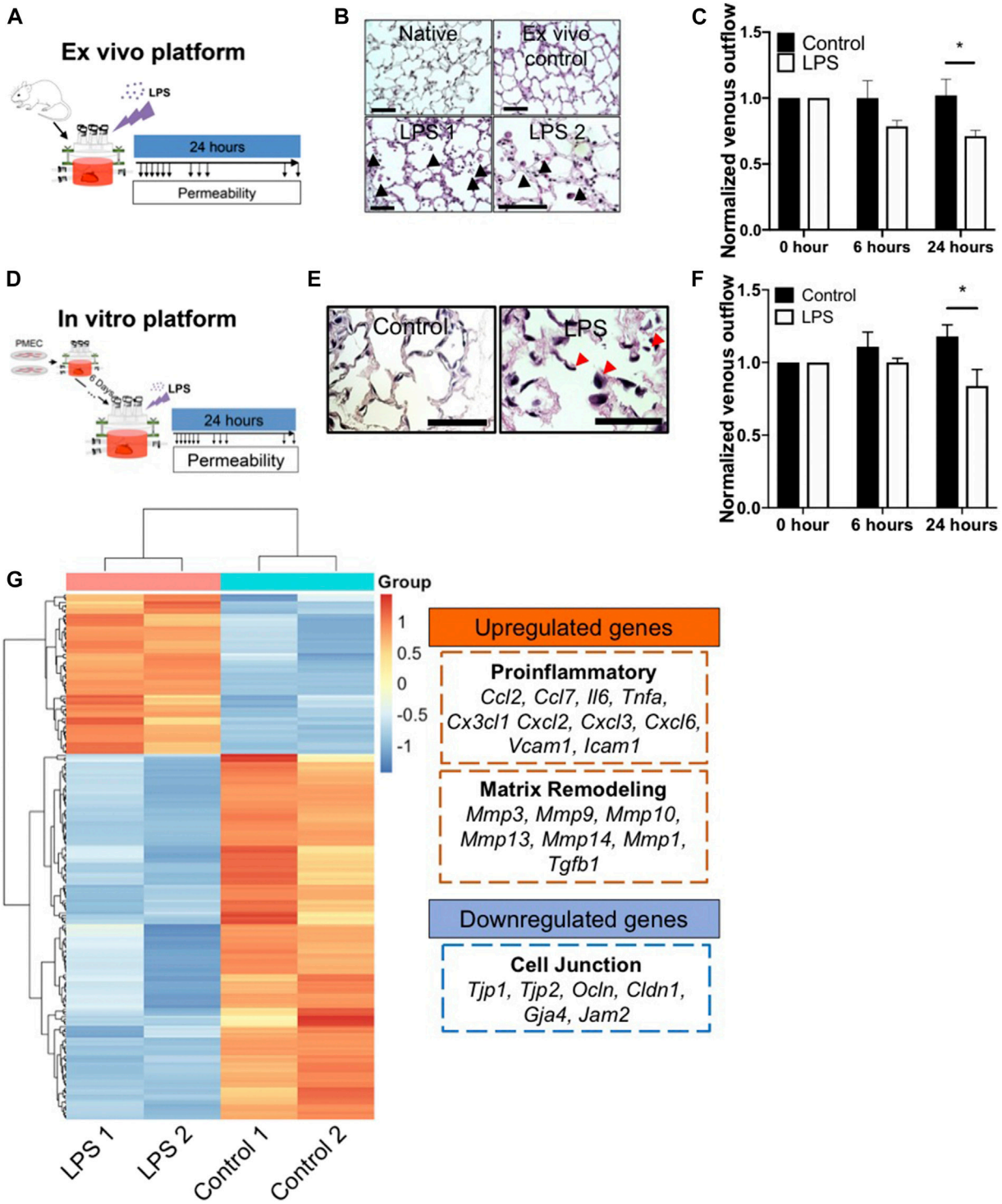

FIGURE 6 | The *ex vivo* and *in vitro* platform to model LPS-induced inflammation. **(A)** Schematic of workflow for the *ex vivo* platform. **(B)** Representative H/E images of lung tissues from native, *ex vivo* control, and *ex vivo* LPS samples. Arrows indicate cell death, matrix breakdown, and interstitial puffing. Scale bar indicate 75 μm. **(C)** Venous outflows in the *ex vivo* platform with or without LPS treatment, $n = 3$. **(D)** Schematic of workflow for the *in vitro* platform. **(E)** Representative H/E images of lung tissues from control and LPS-treated repopulated lungs. Arrows indicate cell detachment and occlusion in the pulmonary vasculature. Scale bar indicate 75 μm. **(F)** Venous outflows in the repopulated lung control, and repopulated lung LPS conditions, versus time, $n = 3$. **(G)** Heatmap of top differentially (adjusted $p < 0.05$ and log2foldchange >3 or <−3) expressed genes between control and LPS-treated repopulated lungs, normalized across each gene to show up-regulation (red) and down-regulation (blue) as compared to the other group. The representative upregulated and downregulated genes after LPS treatment as compared to control without LPS were listed. * indicate $p < 0.05$. There were 3–4 replicates performed in each sample.

non-invasive mechanical measurements to look for evidence of barrier function and capillary leak over the ensuing 24 h (**Figure 6A**). As a control, we introduced a matching volume of culture medium, rather than LPS, and monitored lung mechanics over the ensuing 24 h.

After 24 h of bioreactor culture, histochemical staining of native lung samples demonstrates that the alveolar structure remains intact, resembling the morphology of freshly harvested native lungs. In contrast, LPS induced substantial cell death and visible cell detachment within the alveolar compartment (**Figure 6B**; **Supplementary Figure S10A**). Additionally, there was a markedly increased volume in the interstitial spaces at the alveolar septa in lungs treated with LPS, possibly due to the loss of microvascular alveolar barrier and influx of fluid into the lung interstitium, while the alveolar septa in the *ex vivo* control remained thin and intact (**Figure 6B**). Non-invasive measurements of fluid flow and barrier function revealed a marked reduction of venous outflows at 6 h after the addition of LPS to the native lungs, implying an increase in alveolar barrier permeability induced by LPS in these organs. The loss of venous flow persisted throughout the experiment, while in the control lungs, the venous outflows remained high, implying retained alveolar barrier (**Figure 6C**). Interestingly, capillary resistances increased over time after LPS treatment, implying a decrease of barrier function (**Supplementary Figure S10B**). Thus, we observed that the bioreactor system could support cellular survival, maintain the physiological barrier function for *ex vivo* native lung culture, and could model key pathological findings in response to an acute inflammatory stimulus such as LPS exposure, over a 24 h period.

To determine whether EC-repopulated lungs would exhibit similar functional changes to those of native organs, PMECs were cultured in the decellularized lung scaffolds for 6 days, followed by the introduction of a single dose of 6 μg/ml LPS into the bioreactor (**Figure 6D**). Within 24 h of LPS treatment, there was a substantial increase in cell death, cell detachment, and matrix degradation, as compared to control repopulated lungs not receiving LPS (**Figure 6E**; **Supplementary Figure S10C**), similar to the response observed in native lungs. H&E staining showed the cells exposed to LPS treatment appeared round and large in size. Markedly reduced numbers of patent lumens were visible 1 day after LPS exposure, whereas in control lungs the ECs displayed a flattened morphology and maintained many observable patent lumens (**Figure 6E**). Non-invasive mechanical measurements revealed a progressively decrease of venous outflows and an increase of capillary resistances after LPS treatment as compared to control conditions, signaling a loss of barrier function as fluid escaped from the vasculature and into the interstitium or the air sacs (**Figure 6F**; **Supplementary Figure S10D**).

Gene expression patterns from control and LPS-treated, repopulated lungs were compared using bulk RNAseq. There were a total of 2,766 genes (adjusted $p < 0.05$) differently expressed between these two conditions. The top 213 differentially expressed genes (adjusted $p < 0.05$ and Log2 fold change >3 or <−3) were extracted and clustered into a heatmap (**Figure 6G**). Within the top 213 differentially expressed genes, 25% of the genes were related to inflammatory response, including *Ccl2*, *Ccl7*, *Il6*, *Csf2*, *Lcn2*, *Cx3cl1*, *Cxcl2*, *Cxcl3*, *Cxcl6*, *Vcam1*, and *Icam1*. In addition, 24% of the genes were related to immune cell trafficking, suggesting that after LPS treatment, PMECs in repopulated lungs displayed a significant increase of the pro-inflammatory gene expression (**Figure 6G**). Additionally, matrix metalloproteases (MMPs) (e.g., *Mmp3*, *Mmp9*, *Mmp10*, and *Mmp13*) were significantly upregulated in the LPS-treated group as compared to the control group, indicating an increase in matrix degradation. Evidence of matrix degradation can also be seen in the LPS-treated repopulated lung (**Figure 6E**). Signals related to endothelial barrier function including *Tjp1*, *Ocln*, *Cldn1*, and *Gja4* were significantly decreased in repopulated lungs after LPS treatment compared to control conditions, consistent with the observed increase in vascular permeability. Overall, these data demonstrate that after treatment with endotoxin/LPS, PMEC-repopulated lungs displayed significantly increased pro-inflammatory signals, matrix degradation, and permeability, that simulate endothelial dysfunction during inflammation.

Therefore, these results show that the repopulated lung platform is responsive to LPS treatment in terms of increased cell death, and upregulation of inflammation-induced endothelial dysfunction signals. Combined with reduced microvascular lumen retention and an increase in permeability during culture, these findings demonstrate that LPS treatment disrupts the previously functional endothelial lining within the repopulated lungs, in ways that mimic many aspects of endothelial dysfunction during acute lung injury.

3 DISCUSSION

Currently, there is no *in vitro* culture system that recapitulates structural and biological features of the pulmonary vasculature, especially the microvasculature, at a whole organ level. Whole organ decellularization provides a construct that preserves almost the entire vascular structure of a whole living organ. Here, leveraging single-cell RNA-sequencing analysis, we investigated the role of acellular whole lung scaffolds in regulating endothelial phenotypes and functions in a biomimetic bioreactor system. We found that both primary and iPSC-derived endothelium could create a degree of barrier function in lung scaffolds, and they partially gain native lung endothelial phenotypes.

To leverage this endothelilaized model platform for studying pulmonary vascular disease, we introduced LPS into the bioreactor to induce inflammation in the repopulated lung system. Similar to the reports of *in vivo* studies (Zheng et al., 2018), LPS treatment induced a marked loss of barrier function as well as dramatic histological modifications in the alveolar compartment in our *ex vivo* culture model. Analogously, in the repopulated *in vitro* platform, LPS treatment not only increased molecular signals relate to endothelial dysfunction during acute lung injury, but also induced a loss of functional endothelial lining in the pulmonary vasculature, in terms of decreased barrier function.

The development of *in vitro* systems to model human diseases is centered on recapitulating physiological properties and native cellular phenotypes. Endothelial phenotypes and functions are influenced by various *in vitro* culture conditions such as shear stress (reviewed in (Chistiakov et al., 2017)), oxygen tension (Funamoto et al., 2017), cytokine concentrations (reviewed in (Nomi et al., 2006)), ECM structure and components (Yuan et al., 2020), and substrate stiffness (reviewed in (Karki and Birukova, 2018)). In this study, we applied a biomimetic bioreactor system and optimized protocols by adding Y27632 to improve endothelial cell repopulation in the decellularized whole lung scaffolds to recapitulate *in vivo* conditions. Both primary rodent and human iPSC-derived endothelial cells display near-native appearance in the decellularized lung scaffolds. Vascular barrier can be partially reconstructed while the capillary lumens are appreciable. scRNAseq analysis reveals that after expansion on TCPS, most native signals in PMECs such as angiogenesis, cell adhesion, cell junction, and ECM synthesis are lost. Intriguingly, after only 7 days of culture in the acellular whole lung scaffolds in our biomimetic bioreactor system, many of molecular signals related to these functions could be partially restored, including increased gene expression of integrins, basement membrane proteins, receptors for growth factors, and cell-cell junction molecules, likely due to the combinational effect of cell-matrix interactions, matrix-bound growth factors, shear stress, physiological substrate stiffness, or the addition of Y27632 in our culture system.

scRNAseq has emerged as a powerful tool for identifying cell heterogeneity in native or engineered cellular systems (Hwang et al., 2018; Kumar et al., 2018; Greaney et al., 2020). In this study, we identified seven endothelial subpopulations in rat lungs, including the newly identified general capillary and aerocyte capillary endothelial cells, consistent to the recent work, including ours (Gillich et al., 2020; Travaglini et al., 2020; Schupp et al., 2021). We further leveraged established computational pipelines to compare native lung EC subtypes with *in vitro* counterparts (Greaney et al., 2020). Primary rodent PMECs that were cultured in decellularized lungs display two major clusters—arterial and venous EC, which have markedly increased expression of native markers of each EC subtype as compared to pre-seeded cells. Previous studies showed that the shear stress is responsible for arterial and venous endothelial phenotype determination (Sivarapatna et al., 2015) (Reviewed in (Baeyens et al., 2016)). In our system, the level of shear stress varies across the whole organ due to the changes of flow rate and vessel sizes, so the different regional shear stress may account for the phenotypic change into arterial or venous cells. Additionally, scRNAseq reveals marked upregulation of markers in small capillaries, more so for gCap cells rather than that for aCap cells, suggesting that ECM and shear stress could partially influence the gCap cell phenotypes, while aCap cell phenotypes may be controlled by factors that are not in our current systems, such as supporting cell populations, oxygen tension, cyclic stretch, or paracrine factors. Interestingly, we found that some cells that express mature arterial or venous markers (e.g., Eln, or Nr2f2) only attached in large vessels in the repopulated scaffolds, rather than in small vessels, suggesting a regional effect of the native matrix. However, we have also seen many cells randomly locate throughout the scaffold, suggesting that additional regional microenvironmental cues are needed to induce committed endothelial phenotypes. Human iPSC-ECFCs also start to gain some native human EC phenotypes, especially toward pulmonary venous and arterial endothelium, in decellularized lung scaffolds under current culture conditions. Although their phenotypic changes are not comparable to that in rodent primary endothelium, possibly due to species variation, it still indicates the beneficial influence of near-physiological microenvironmental cues supplied by our system.

Finally, we investigated the effects of endotoxin/LPS in our model system to simulate acute lung injury. Endothelial repopulated lungs not only display increased molecular signals that are related to pro-inflammation, matrix degradation, and decreased barrier function, but also show reduction of venous outflow and increase of capillary resistance after treatment with LPS, similar to the trends in *ex vivo* model. This result suggests that the established vascular barrier in our lung system is biologically active and their changes can be tracked at real-time.

There are still several limitations associated with the current system. First, endothelium alone cannot fully reconstitute the barrier function of native lung, due to the critical absence of differentiated type 1 alveolar epithelial cells. Therefore, changes in barrier must be viewed as relative within this system, though our studies show that barrier changes are still measurable and physiologically meaningful. Secondly, the endothelial phenotypes in repopulated lungs are still different from their native counterparts. Further development will include optimizations of oxygen tension, cyclic stretch, and inclusion of other supporting cells, as well as potentially improvements in culture medium composition to further enhance endothelial phenotype in repopulated organs.

Overall, this proof-of-principle study demonstrates that endothelium from various sources can partially simulate the native functions and phenotypes during both homeostatic and diseased states, when cultured in decellularized lung scaffolds and a biomimetic bioreactor. This tissue-engineered culture platform can be used to model vascular diseases, which paves the way for using the whole organ engineering approach for disease modeling applications.

4 METHODS AND MATERIALS

4.1 PMEC Isolation and Culture

All animal procedures in this study were approved by the Yale University Institutional Animal Care and Use Committee (IACUC) and complied with the NIH Guidelines for the Care and Use of Laboratory Animals. Lung extraction and cell isolation were modified based on previous literature (Alphonse et al., 2016). For all experiments, we used the species Rattus norvegicus, strain Sprague Dawley. Postnatal day 7 pups were euthanized by intraperitoneal injection of pentobarbital (Euthasol, 150 mg/kg). Lungs were extracted from the animals and the border (~1 mm) of all lobes were cut off and minced into small pieces. The lung pieces are then digested with collagenase/

TABLE 1 | Antibodies used for immunostaining and western blot.

Antigen	Antibody source	Catalog number
CD31	Abcam	ab28364
VE-Cadherin	ThermoFisher	36–1900
eNOS	Abcam	ab11575
vWF	Abcam	ab6994
Dil-ac-LDL	ThermoFisher	L3484
Alexa fluor 488 conjugated-lectin GSII	Vectorlabs	FL1211
ZO1	ThermoFisher	617300
Connexin 40	Abcam	ab16585
Cxcl12	ThermoFisher	PA1-29029
Prx	Novus biologicals	NBP1-89598
Aplnr	Abcam	ab214369
Sirpa	LifeSpan Biosciences	LS-B551
Coup_TFII	Abcam	ab41859
Eln	Abcam	ab21610
Ednrb	Novus biologicals	MAB4496
Fbln5	Abcam	ab202977
β1 integrin	Cell signaling	4706S
α6 integrin	Cell signaling	3750S
Acvrl1	Santa Cruz	sc-101556
Laminin	Abcam	ab14055
Car4	Abcam	ab239505
c-Kit	bioss	bs-10005R
SMA	Dako	M0851

dispase (Roche) solution (0.1 U collagenase and 0.8 U dispase per mL of double-distilled (dd) water) at 37°C for 1–1.5 h under continuous agitation. After digestion, quenched the lung-digestive solution mixture with DMEM (Gibco) supplemented with 10% FBS and 1% pen/strep. After serial washes with MACS buffer (PBS with 0.1% BSA) and DMEM, the cell mixture was incubated with $CD31^+$ (Roche) conjugated Dynabeads (Dynal) for 30 min at 4°C followed by magnetic selection.

The isolated cells were cultured on fibronectin-coated (2 μg/cm^2) six well-plate at a density of 5,000 cells/cm^2 in endothelial culture medium (Vasculife (VEGF) medium (Lifeline cell technology) supplemented with 10% FBS and 1.5% antibiotic/antimycotic (A/A)) for 7 days with daily complete medium change. Upon passaging, the contaminated (non-endothelial-like) cell colonies were removed by scraping using pipette tips followed by rinsing with pre-warmed PBS. Usually, no further beads selection is needed after this step. If many cell contaminants were seen after 7 days of culture, apply another $CD31^+$ selection after trypsinization. The resulting cells were then plated on fibronectin-coated (2 μg/cm^2) flasks at a density of 10,000 cells/cm^2 in endothelial culture medium.

4.2 Immunofluorescent Staining

To characterize the phenotype of PMECs, cells were cultured on fibronectin-coated coverslips at a density of 10,000 cells/cm^2. After 3 days of culture, cells were fixed with 2% paraformaldehyde (containing Ca^{2+}/Mg^{2+}) for 15 min, permeabilized with 0.1% Triton-X in PBS for 3 min, and blocked with 5% FBS PBS for 1 h at room temperature (RT). The fixed cells were then probed with primary antibodies (**Table 1**) including CD31, VE-Cadherin, eNOS, and vWF overnight at 4°C followed by staining with secondary antibodies (RT, 1 h) and DAPI (RT, 5 min). To detect acLDL uptake and griffonia simplicifolia lectin, fixed cells were directly incubated with Dil-acLDL or Alexa fluor 488 conjugated-lectin GSII for 2 h. All samples were then washed, mounted, and assessed with confocal microscopy (Leica SP5).

Re-cellularized or native lung tissues were inflation-fixed with 10% formalin for 3 h, and then embedded in paraffin. De-paraffinized tissues were soaked in antigen retrieval solution (0.05% Tween-20, 1 mM EDTA, and 10 mM Tris (pH = 9)) at 75°C for 20 min, followed by blocking (10% FBS and 0.2% Triton X-100, RT, 20 min). Re-cellularized or native lung samples were stained with antibodies overnight at 4 °C followed by staining with secondary antibodies (RT, 1 h) and DAPI (RT, 5 min). All samples were then washed, mounted, and assessed with confocal microscopy (Leica SP5).

4.3 Transmission Electron Microscopy

Native or re-cellularized lung samples were fixed in 2.5% gluteraldehyde and 2% paraformaldehyde in 0.1 M sodium cacodylate (pH 7.4) for 30 min at RT, followed by 90 min at 4°C with continuous shaking. The fixed samples were then rinsed in 0.1 M sodium cacodylate buffer 3 times with 10 min each at RT. After fixation, the sample preparation and imaging were carried out by the Yale School of Medicine Center for Cellular and Molecular Imaging (CCMI) Electron Microscopy (EM) core facility.

4.4 Quantitative Real-Time Reverse Transcription-PCR

Methods for qRT-PCR are performed as per previously described (Yuan et al., 2019). In brief, total mRNA was extracted from cells,

TABLE 2 | Primer sequences used in qRT-PCR.

Genes		Sequence
Gja4	Forward	GAAAGAGGGAGAGCTTCGGG
	Reverse	CATGGTCCAGCCGTAGAGAC
Nr2f2	Forward	CGGAGGAACCTGAGCTACAC
	Reverse	CTGCCCCTCTGTACAGCTTC
Aplnr	Forward	TGTACGCCAGTGTCTTTTGC
	Reverse	CTGTTTTCCGGGATGTCAGT
Sirpa	Forward	GTCTTCATCGGTGTGGGTGT
	Reverse	TTTGTGTCCTGGATCTGGGT
Rgcc	Forward	CGCCACTTCCACTATGAGGAG
	Reverse	TCCGTCGGAGAATTCAGCTTC
Col4a1	Forward	AATACCAGGATCCCCTGGAC
	Reverse	TGCCTTTCTCTCCCTTCTCA
Eln	Forward	AGCAGCTAAAGCAGCGAAGT
	Reverse	TGGGACCCTAACTCCTGGTC
Col15a1	Forward	GCCCCCTACTTCATCCTCTC
	Reverse	CAGTACGGACCTCCAGGGTA
Fbln5	Forward	CTCCCCTGCAGACTTGCTAC
	Reverse	TCTCAGCAGGGCACATACAG
Vcam1	Forward	GAAATGCCACCCTCACCTTA
	Reverse	GAGATCCAGGGGAGATGTCA
Icam1	Forward	AGGTATCCATCCATCCCACA
	Reverse	GCCACAGTTCTCAAAGCACA
β-actin	Forward	GCAGGAGTACGATGAGTCCG
	Reverse	ACGCAGCTCAGTAACAGTCC
NOSTRIN	Forward	TGAGGGACCCACTGACAGAT
	Reverse	TGCTTTGCTCAGCTTGCTTG
RGCC	Forward	GCCACTTCCACTACGAGGAG
	Reverse	TGAGGAGTGACAGTGGCAGA
CXCL12	Forward	AGAGCCAACGTCAAGCATCT
	Reverse	CTTTAGCTTCGGGTCAATGC
SERPINE2	Forward	CTTTGAGGATCCAGCCTCTG
	Reverse	TGCGTTTCTTTGTGTTCTCG
NR2F2	Forward	TGCCTGTGGTCTCTCTGATG
	Reverse	ATATCCCGGATGAGGGTTTC
COL15A1	Forward	GTTGTCCACCTACCGAGCAT
	Reverse	TTCGCCATGCTTCACAGTAG
PLVAP	Forward	GAGCTGGCCATCAGAAACTC
	Reverse	GGGACTCCAGGATCTTCCTC
EPHB4	Forward	TGAAGAGGTGATTGGTGCAG
	Reverse	AGGCCTCGCTCAGAAACTCAC
GAPDH	Forward	GACAACAGCCTCAAGATCATCAG
	Reverse	ATGGCATGGACTGTGGTCATGAG

native, or re-cellularized lungs using an RNA isolation kit (Qiagen) and cDNA was synthesized (Bio-Rad). The mRNA levels of rat genes including *CD31*, *Cdh5*, *Prox1*, *Ccl21*, *Pdpn*, *Aplnr*, *Sirpa*, *Rgcc*, *Col4a1*, *Eln*, *Col15a1*, *Fbln5*, and *β-actin*, and human genes including NOSTRIN, RGCC, CXCL12, SERPINE2, NR2F2, EPHB4, PLVAP, COL15A1, and GAPDH were analyzed using SYBR green primers (purchased from Yale Oligo Synthesis Resource) and a Real-Time PCR system (Bio-Rad). The sequences of each primer are listed in **Table 2**.

4.5 Western Blot

PMECs cultured on tissue culture plates were lysed in cold RIPA buffer (50 mM Tris-HCl, pH 7.4, 150 mM NaCl, 1% [v/v] Triton X-100, 0.5% [w/v] SDC, and 0.1% [w/v] sodium dodecyl sulphate (SDS)) containing 1% protease inhibitor (Sigma Aldrich, St. Louis, MO). For studies of recellularized lungs, the right middle lobes were homogenized in RIPA buffer. Protein lysate was mixed with laemmli sample buffer, reduced (DTT at 95°C 5 min), and loaded on 4–20% gradient polyacrylamide gels (Bio-Rad, Hercules, CA). Blots were run for 60 min at 120 V and the protein was transferred to PVDF membrane and blocked for 1 h at room temperature in 5% nonfat dry milk. Primary antibodies were applied overnight at 4°C in 1% nonfat dry milk in TBST buffer (0.1% Tween-20 in Tris-buffered saline) at concentrations listed in **Table 1**. After being rinsed with TBST, secondary antibodies were applied at a dilution of 1:1,000 for 1 h at room temperature. Protein was detected using enhanced chemiluminescence (Thermo Fischer Scientific).

4.6 Lung Decellularization

The decellularized lung scaffolds were prepared as per previously described (Yuan et al., 2019; Calle et al., 2011). In brief, lungs were extracted from the thorax and were perfused with antibiotics/antimycotics, and blood was cleared by additional perfusion with PBS containing heparin and sodium nitroprusside. Lungs were decellularized by serial washes with sodium deoxycholate (0.1, 0.5, and 1%) and Triton X-100 (0.0035, and 0.5%). The decellularized lungs were mounted in a sterile bioreactor and perfused with antibiotics/antimycotics for 48 h at 37°C prior to storing at 4°C. We performed H/E staining, and DNA quantification to confirm that the decellularization is complete as per previously described (Calle et al., 2016). For experiments in protein detection, we verified that the level of proteins such as integrins in decellularized lung scaffolds are under detection limit using western blot.

4.7 Human iPSC-Derived Endothelial Colony Forming Cells Culture

Human iPSC-derived endothelial colony forming cells (iPSC-ECFCs) were a general gift from Dr. Mervin Yoder's group. These cells were cultured on collagen I-coated flasks (50 μg/ml) in endothelial culture medium as per previously described (Yuan et al., 2019; Prasain et al., 2014). Cells at passage 7–10 were used in the current studies.

4.8 PMEC and iPSC-ECFC Culture in Decellularized Lung Scaffolds

Whole decellularized lungs were mounted in a sterile bioreactor containing endothelial culture medium and perfused at 20 ml/min overnight via the pulmonary artery (Yuan et al., 2019; Engler et al., 2019; Calle et al., 2011). PMECs or human iPSC-ECFCs were suspended into culture medium supplemented with 30 μM Y27632 (Cayman) at a concentration of 250,000 cells/mL. Lungs were first seeded with 50 million PMECs from the pulmonary vein followed by seeding in the same manner the rest 50 million cells into the pulmonary artery. Thereafter, arterial perfusion was initiated with a peristaltic pump at a flow rate of 4 ml/min. This perfusion rate was maintained for 4 h and was ramped up 4 ml/min every 15 min until reaching 20 ml/min. During the ensuing 7 days of culture, half of the medium (endothelial culture medium +10 μM Y27632 (Cayman)) was replaced every day. For the lipopolysaccharide (LPS) study, ROCK inhibitor was removed

by complete medium change on day 5. On day 6, a single dose of 6 μg/ml LPS (Sigma-Aldrich) was applied into the bioreactor jar in PMEC-repopulated lungs. The vascular barrier was measured and calculated by non-invasive methods as per previously described (Engler et al., 2019) for the following 24 h.

4.9 Measurement of Internal Pressures

All non-invasive flow and pressure measurements were based on our previous report (Engler et al., 2019). In brief, measurement of average internal pressures was accomplished by briefly shutting off flow into or out of the organ. To measure the average pressure at the end of the capillaries, flow out of the vein was briefly shut off. The average pressure in the alveoli is found in a comparable manner by briefly shutting off flow out of the trachea and monitoring the measured tracheal pressure immediately after the change. The average pressure at the start of the capillary is found in a comparable manner by briefly shutting off pulsatile perfusion to the whole organ and monitoring the measured arterial pressure immediately after the change.

4.10 *Ex Vivo* Lung Culture

In *ex vivo* lung culture, we used 0.25 m L/S 14 BPT tubing (Cole Parmer, PharMed) at both venous and tracheal sides. Lungs from adult rats (250–350 g) were extracted from the thorax and were perfused with antibiotics/antimycotics, and blood was cleared by additional perfusion with PBS containing heparin and sodium nitroprusside. Extracted lungs were mounted into a bioreactor system and cultured with DMEM medium supplemented with 0.5% FBS and 1% antibiotics/antimycotics and perfused at 20 ml/min via the pulmonary artery. Barrier measurements were performed as per previously described (Engler et al., 2019) for the following 24 h. To model the acute lung injury, 15 min after the start of arterial perfusion, a single dose of LPS was applied to bioreactor jar to reach a concentration of 6 μg/ml and barrier measurements were performed for the following 24 h.

4.11 10x scRNAseq Library Preparation, Sequencing, and Alignment

scRNAseq libraries were generated with the Chromium Single Cell 3' assay (10x Genomics). Samples were diluted for an expected cell recovery population of 10,000 cells per lane. Libraries sequenced on the HiSeq4000 platform to a depth of 180–500 million reads per library. Downstream processing was conducted with Cellranger 3.0.2 with the default parameters. Ensembl Rnor6.0 release 95 was used to align rat data (Raredon et al., 2019).

4.12 scRNAseq Data Filtration, Normalization, Scaling, and Clustering

Aligned data was processed using Seurat v3.1.2 under R (v3.5.0) environment. Default parameters were used for each function unless otherwise specified. After creating Seurat objects for each sample, we filtered on percent mitochondrial genes to exclude damaged and dying cells and on the number of genes and transcripts to remove debris and doublets. The gene counts were normalized to the total counts and multiplied by 10,000 scaling factor. We used Variance Stabilizing Transformation (VST) to select highly variable genes. Top 2,000 genes within the selected genes were retained for downstream analysis. Variable genes were scaled using Seurat's ScaleData function with regression on percent mitochondrial transcripts and cell cycle genes (Nestorowa et al., 2016), and subsequently were used for principal component analysis (PCA) to generate clusters. The numbers of clusters produced using PCA analysis are controlled by a resolution parameter with higher values giving more clusters and by the number of PCs. All cells across different samples were assigned into two-dimensional Uniform Manifold Approximation and Projection (UMAPs).

To sub-cluster postnatal day 7 endothelial cells, we first filtered, normalized, scaled the cells from whole lung sample. We then used SubsetData function in Seurat to select cell clusters that are positive for Cdh5 while negative for Ptprc, Col1a1, and Epcam to create a new postnatal day 7 lung EC Seurat object. We then re-normalized, re-scaled and re-clustered this EC object for downstream analysis.

4.13 Cluster Identification by Differentially Expressed Genes

The FindAllMarkers function in Seurat was applied to each sample to identify differentially expressed genes for each cluster relative to all the other clusters in the object (Greaney et al., 2020). We only chose genes that were expressed in at least 10% of cells in one of these clusters to ensure the quality of genes. These marker lists were used to apply cluster labels based on top defining genes of canonical cell types in the literature. The gene ontology analysis was performed through on-line library DAVID (Huang et al., 2009a; Huang et al., 2009b).

4.14 Combined

We performed Merge function in Seurat to combine different samples to allow for direct comparisons on gene expression without corrections on the batch-effect. Using top DEGs from native lung EC clusters, dot plots and violin plots were generated in merged objects using the DotPlot, and VlnPlot functions, respectively.

4.15 Bulk RNA Sequencing

RNA sequencing libraries were prepared by the Yale Center for Genomics Analysis using the Pair End Sequencing Prep Kit, and sequenced through NovaSeq with sequencing read length of 100 base pairs (bp). Sequenced FASTQ samples were evaluated for overrepresented sequences using FASTQC and trimmed of poly(A) sequences using Trimmomatic v 0.36 (no overrepresented adapter sequences were found in any samples). Paired sequences, all with length longer than 30 bp, were then aligned with Rsubread (Bioconductor) with the default parameters.

For RNA sequencing analysis and heatmap clustering, features were counted using Rsubread feature counts and genes were filtered to remove those with no counts across all conditions. A variance stabilizing transform was then performed on the dataset

with the count matrix using the "vst" function to remove the dependence of data variance on the mean across the entire experiment. DeSeq2 (Bioconductor) was then used to determine differentially expressed genes between the two different sample comparisons. Clustered heatmaps were generated with normalized values across each gene. Ensembl Gene IDs were converted to gene symbols using biomaRt (Bioconductor).

4.16 Statistical Analysis

Comparisons between groups were performed with Student's *t*-test or, for multi-group comparisons, by analysis of variance (ANOVA) followed by a post-hoc test. All analysis was performed with GraphPad Prism 7.0; values shown graphically are mean ± standard error.

DATA AVAILABILITY STATEMENT

Publicly available datasets were analyzed in this study. This data can be found on the Gene Expression Omnibus under the accession number GSE188425.

ETHICS STATEMENT

The animal study was reviewed and approved by Yale University Institutional Animal Care and Use Committee (IACUC).

AUTHOR CONTRIBUTIONS

Conceptualization, YY and LN, Methodology, YY, KL, AG, MR, HQ, AE, and JW, Experimentation, YY, KL, AG, MR, HQ, AE, PB, TA, MK, and TO, Writing—Original draft, YY and LN, Writing—Review and Editing, YY, KL, AG, JS, MY, NK, and LN, Funding Acquisition, LN.

FUNDING

The author(s) disclosed receipt of the following financial support for the research, authorship, and/or publication of this article: This work was supported by NIH grants R01 HL138540 (LN), R21 EB024889 (LN), CT Stem Cell grant 15-RMB-YALE-07 (LN), an unrestricted Research Gift from Humacyte, Inc. (LN), American Heart Association postdoctoral fellowships 20POST35210709 (YY), 19POST34381048 (MK), the NIH Medical Scientist Training Program Training Grant T32GM136651 (KL and MR), and German Research Foundation SCHU 3147/1-1 (JS).

SUPPLEMENTARY MATERIAL

The Supplementary Material for this article can be found online at: https://www.frontiersin.org/articles/10.3389/fbioe.2021.760309/full#supplementary-material

REFERENCES

Ackermann, M., Verleden, S. E., Kuehnel, M., Haverich, A., Welte, T., Laenger, F., et al. (2020). *Pulmonary Vascular Endothelialitis, Thrombosis, and Angiogenesis in Covid-19* 383 (20), 120–128. doi:10.1056/NEJMoa2015432

Alphonse, R. S., Vadivel, A., Zhong, S., McConaghy, S., Ohls, R., Yoder, M. C., et al. (2016). Erratum: Corrigendum: The Isolation and Culture of Endothelial colony-forming Cells from Human and Rat Lungs. *Nat. Protoc.* 11, 192. doi:10.1038/nprot0116-192c

Alphonse, R. S., Vadivel, A., Zhong, S., McConaghy, S., Ohls, R., Yoder, M. C., et al. (2015). The Isolation and Culture of Endothelial colony-forming Cells from Human and Rat Lungs. *Nat. Protoc.* 10, 1697–1708. doi:10.1038/nprot.2015.107

Amano, M., Nakayama, M., and Kaibuchi, K. (2010). Rho-kinase/ROCK: A Key Regulator of the Cytoskeleton and Cell Polarity. *Cytoskeleton* 67, 545–554. doi:10.1002/cm.20472

Baeyens, N., Bandyopadhyay, C., Coon, B. G., Yun, S., and Schwartz, M. A. (2016). Endothelial Fluid Shear Stress Sensing in Vascular Health and Disease. *J. Clin. Invest.* 126, 821–828. doi:10.1172/jci83083

Balestrini, J. L., Gard, A. L., Gerhold, K. A., Wilcox, E. C., Liu, A., Schwan, J., et al. (2016). Comparative Biology of Decellularized Lung Matrix: Implications of Species Mismatch in Regenerative Medicine. *Biomaterials* 102, 220–230. doi:10.1016/j.biomaterials.2016.06.025

Booth, A. J., Hadley, R., Cornett, A. M., Dreffs, A. A., Matthes, S. A., Tsui, J. L., et al. (2012). Acellular Normal and Fibrotic Human Lung Matrices as a Culture System forIn VitroInvestigation. *Am. J. Respir. Crit. Care Med.* 186, 866–876. doi:10.1164/rccm.201204-0754oc

Boulaftali, Y., Ho-Tin-Noe, B., Pena, A., Loyau, S., Venisse, L., François, D., et al. (2011). Platelet Protease Nexin-1, a Serpin that Strongly Influences Fibrinolysis and Thrombolysis. *Circulation* 123, 1326–1334. doi:10.1161/circulationaha.110.000885

Calle, E. A., Hill, R. C., Leiby, K. L., Le, A. V., Gard, A. L., Madri, J. A., et al. (2016). Targeted Proteomics Effectively Quantifies Differences between Native Lung and Detergent-Decellularized Lung Extracellular Matrices. *Acta Biomater.* 46, 91–100. doi:10.1016/j.actbio.2016.09.043

Calle, E. A., Petersen, T. H., and Niklason, L. E. (2011). *Procedure for Lung Engineering* 49. J Vis Exp. doi:10.3791/2651

Chistiakov, D. A., Orekhov, A. N., and Bobryshev, Y. V. (2017). Effects of Shear Stress on Endothelial Cells: Go with the Flow. *Acta Physiol.* 219, 382–408. doi:10.1111/apha.12725

Corada, M., Orsenigo, F., Morini, M. F., Pitulescu, M. E., Bhat, G., Nyqvist, D., et al. (2013). Sox17 Is Indispensable for Acquisition and Maintenance of Arterial Identity. *Nat. Commun.* 4, 2609. doi:10.1038/ncomms3609

dela Paz, N. G., and D'Amore, P. A. (2009). Arterial versus Venous Endothelial Cells. *Cell Tissue Res* 335, 5–16. doi:10.1007/s00441-008-0706-5

Engler, A. J., Raredon, M. S. B., Le, A. V., Yuan, Y., Oczkowicz, Y. A., Kan, E. L., et al. (2019). Non-invasive and Real-Time Measurement of Microvascular Barrier in Intact Lungs. *Biomaterials* 217, 119313. doi:10.1016/j.biomaterials.2019.119313

Funamoto, K., Yoshino, D., Matsubara, K., Zervantonakis, I. K., Funamoto, K., Nakayama, M., et al. (2017). Endothelial Monolayer Permeability under Controlled Oxygen Tension. *Integr. Biol.* 9, 529–538. doi:10.1039/c7ib00068e

Gillich, A., Zhang, F., Farmer, C. G., Travaglini, K. J., Tan, S. Y., Gu, M., et al. (2020). Capillary Cell-type Specialization in the Alveolus. *Nature* 586, 785–789. doi:10.1038/s41586-020-2822-7

Gilpin, S. E., Ren, X., Okamoto, T., Guyette, J. P., Mou, H., Rajagopal, J., et al. (2014). Enhanced Lung Epithelial Specification of Human Induced Pluripotent Stem Cells on Decellularized Lung Matrix. *Ann. Thorac. Surg.* 98, 1721–1729. doi:10.1016/j.athoracsur.2014.05.080

Greaney, A. M., Adams, T. S., Brickman Raredon, M. S., Gubbins, E., Schupp, J. C., Engler, A. J., et al. (2020). Platform Effects on Regeneration by Pulmonary Basal Cells as Evaluated by Single-Cell RNA Sequencing. *Cel Rep.* 30, 4250–4265. doi:10.1016/j.celrep.2020.03.004

Huang, D. W., Sherman, B. T., and Lempicki, R. A. (2009). Bioinformatics Enrichment Tools: Paths toward the Comprehensive Functional Analysis of Large Gene Lists. *Nucleic Acids Res.* 37, 1–13. doi:10.1093/nar/gkn923

Huang, D. W., Sherman, B. T., and Lempicki, R. A. (2009). Systematic and Integrative Analysis of Large Gene Lists Using DAVID Bioinformatics Resources. *Nat. Protoc.* 4, 44–57. doi:10.1038/nprot.2008.211

Huertas, A., Guignabert, C., Barberà, J. A., Bärtsch, P., Bhattacharya, J., Bhattacharya, S., et al. (2018). Pulmonary Vascular Endothelium: the Orchestra Conductor in Respiratory Diseases: Highlights from Basic Research to Therapy. *Eur. Respir. J.* 51. doi:10.1183/13993003.00745-2017

Hwang, B., Lee, J. H., and Bang, D. (2018). Single-cell RNA Sequencing Technologies and Bioinformatics Pipelines. *Exp. Mol. Med.* 50, 96. doi:10.1038/s12276-018-0071-8

Kalucka, J., de Rooij, L. P. M. H., Goveia, J., Rohlenova, K., Dumas, S. J., Meta, E., et al. (2020). Single-Cell Transcriptome Atlas of Murine Endothelial Cells. *Cell* 180, 764–779. doi:10.1016/j.cell.2020.01.015

Karki, P., and Birukova, A. A. (2018). Substrate Stiffness-dependent Exacerbation of Endothelial Permeability and Inflammation: Mechanisms and Potential Implications in ALI and PH (2017 Grover Conference Series). *Pulm. Circ.* 8, 2045894018773044. doi:10.1177/2045894018773044

Kofler, N. M., and Simons, M. (2015). Angiogenesis versus Arteriogenesis: Neuropilin 1 Modulation of VEGF Signaling. *F1000prime Rep.* 7, 26. doi:10.12703/P7-26

Kumar, M. P., Du, J., Lagoudas, G., Jiao, Y., Sawyer, A., Drummond, D. C., et al. (2018). Analysis of Single-Cell RNA-Seq Identifies Cell-Cell Communication Associated with Tumor Characteristics. *Cel Rep.* 25, 1458–1468. doi:10.1016/j.celrep.2018.10.047

Le, A. V., Hatachi, G., Beloiartsev, A., Ghaedi, M., Engler, A. J., Baevova, P., et al. (2017). Efficient and Functional Endothelial Repopulation of Whole Lung Organ Scaffolds. *ACS Biomater. Sci. Eng.* 3, 2000–2010. doi:10.1021/acsbiomaterials.6b00784

Li, Q., Uygun, B. E., Geerts, S., Ozer, S., Scalf, M., Gilpin, S. E., et al. (2016). Proteomic Analysis of Naturally-Sourced Biological Scaffolds. *Biomaterials* 75, 37–46. doi:10.1016/j.biomaterials.2015.10.011

Mélot, C., and Naeije, R. (2011). Pulmonary Vascular Diseases. *Compr. Physiol.* 1, 593–619. doi:10.1002/cphy.c090014

Monteil, V., Kwon, H., Prado, P., Hagelkrüys, A., Wimmer, R. A., Stahl, M., et al. (2020). Inhibition of SARS-CoV-2 Infections in Engineered Human Tissues Using Clinical-Grade Soluble Human ACE2. *Cell* 181, 905–913. doi:10.1016/j.cell.2020.04.004

Nestorowa, S., Hamey, F. K., Pijuan Sala, B., Diamanti, E., Shepherd, M., Laurenti, E., et al. (2016). A Single-Cell Resolution Map of Mouse Hematopoietic Stem and Progenitor Cell Differentiation. *Blood* 128, e20–e31. doi:10.1182/blood-2016-05-716480

Nichol, D., and Stuhlmann, H. (2012). EGFL7: a Unique Angiogenic Signaling Factor in Vascular Development and Disease. *Blood* 119, 1345–1352. doi:10.1182/blood-2011-10-322446

Noda, K., Dabovic, B., Takagi, K., Inoue, T., Horiguchi, M., Hirai, M., et al. (2013). Latent TGF- Binding Protein 4 Promotes Elastic Fiber Assembly by Interacting with Fibulin-5. *Proc. Natl. Acad. Sci.* 110, 2852–2857. doi:10.1073/pnas.1215779110

Nomi, M., Miyake, H., Sugita, Y., Fujisawa, M., and Soker, S. (2006). Role of Growth Factors and Endothelial Cells in Therapeutic Angiogenesis and Tissue Engineering. *Cscr* 1, 333–343. doi:10.2174/157488806778226777

Pampaloni, F., Reynaud, E. G., and Stelzer, E. H. K. (2007). The Third Dimension Bridges the gap between Cell Culture and Live Tissue. *Nat. Rev. Mol. Cel Biol* 8, 839–845. doi:10.1038/nrm2236

Parent, R. A. (2015). *Comparative Biology of the normal Lung*. Second edition. Amsterdam ; Boston: Elsevier/AP, Academic Press is an imprint of Elsevierxvii, 815.

Petersen, T. H., Calle, E. A., Zhao, L., Lee, E. J., Gui, L., Raredon, M. B., et al. (2010). Tissue-engineered Lungs for *In Vivo* Implantation. *Science* 329, 538–541. doi:10.1126/science.1189345

Prasain, N., Lee, M. R., Vemula, S., Meador, J. L., Yoshimoto, M., Ferkowicz, M. J., et al. (2014). Differentiation of Human Pluripotent Stem Cells to Cells Similar to Cord-Blood Endothelial colony-forming Cells. *Nat. Biotechnol.* 32, 1151–1157. doi:10.1038/nbt.3048

Preis, M., Cohen, T., Sarnatzki, Y., Ben Yosef, Y., Schneiderman, J., Gluzman, Z., et al. (2006). Effects of Fibulin-5 on Attachment, Adhesion, and Proliferation of Primary Human Endothelial Cells. *Biochem. Biophysical Res. Commun.* 348, 1024–1033. doi:10.1016/j.bbrc.2006.07.156

Pugacheva, E. N., Roegiers, F., and Golemis, E. A. (2006). Interdependence of Cell Attachment and Cell Cycle Signaling. *Curr. Opin. Cel Biol.* 18, 507–515. doi:10.1016/j.ceb.2006.08.014

Qiu, Y., Ahn, B., Sakurai, Y., Hansen, C. E., Tran, R., Mimche, P. N., et al. (2018). Microvasculature-on-a-chip for the Long-Term Study of Endothelial Barrier Dysfunction and Microvascular Obstruction in Disease. *Nat. Biomed. Eng.* 2, 453–463. doi:10.1038/s41551-018-0224-z

Raredon, M. S. B., Adams, T. S., Suhail, Y., Schupp, J. C., Poli, S., Neumark, N., et al. (2019). Single-cell Connectomic Analysis of Adult Mammalian Lungs. *Sci. Adv.* 5, eaaw3851. doi:10.1126/sciadv.aaw3851

Ren, X., Moser, P. T., Gilpin, S. E., Okamoto, T., Wu, T., Tapias, L. F., et al. (2015). Engineering Pulmonary Vasculature in Decellularized Rat and Human Lungs. *Nat. Biotechnol.* 33, 1097–1102. doi:10.1038/nbt.3354

Rochon, E. R., Menon, P. G., and Roman, B. L. (2016). Alk1 Controls Arterial Endothelial Cell Migration in Lumenized Vessels. *Development* 143, 2593–2602. doi:10.1242/dev.135392

Schupp, J. C., Adams, T. S., Cosme, C., Jr., Raredon, M. S. B., Yuan, Y., Omote, N., et al. (2021). *Integrated Single Cell Atlas of Endothelial Cells of the Human Lung*. Circulation. doi:10.1161/CIRCULATIONAHA.120.052318

Schupp, J. C., Adams, T. S., Cosme, C., Raredon, M. S. B., Omote, N., De Frias, S. P., et al. (2020). Integrated Single Cell Atlas of Endothelial Cells of the Human Lung. *bioRxiv* 2010, 2021347914. doi:10.1101/2020.10.21.347914

Sivarapatna, A., Ghaedi, M., Le, A. V., Mendez, J. J., Qyang, Y., and Niklason, L. E. (2015). Arterial Specification of Endothelial Cells Derived from Human Induced Pluripotent Stem Cells in a Biomimetic Flow Bioreactor. *Biomaterials* 53, 621–633. doi:10.1016/j.biomaterials.2015.02.121

Su, T., Stanley, G., Sinha, R., D'Amato, G., Das, S., Rhee, S., et al. (2018). Single-cell Analysis of Early Progenitor Cells that Build Coronary Arteries. *Nature* 559, 356–362. doi:10.1038/s41586-018-0288-7

Thiriot, A., Perdomo, C., Cheng, G., Novitzky-Basso, I., McArdle, S., Kishimoto, J. K., et al. (2017). Differential DARC/ACKR1 Expression Distinguishes Venular from Non-venular Endothelial Cells in Murine Tissues. *BMC Biol.* 15, 45. doi:10.1186/s12915-017-0381-7

Townsley, M. I. (2012). Structure and Composition of Pulmonary Arteries, Capillaries, and Veins. *Compr. Physiol.* 2, 675–709. doi:10.1002/cphy.c100081

Travaglini, K. J., Nabhan, A. N., Penland, L., Sinha, R., Gillich, A., Sit, R. V., et al. (2020). A Molecular Cell Atlas of the Human Lung from Single-Cell RNA Sequencing. *Nature* 587, 619–625. doi:10.1038/s41586-020-2922-4

Tsai, M., Kita, A., Leach, J., Rounsevell, R., Huang, J. N., Moake, J., et al. (2012). *In Vitro* modeling of the Microvascular Occlusion and Thrombosis that Occur in Hematologic Diseases Using Microfluidic Technology. *J. Clin. Invest.* 122, 408–418. doi:10.1172/jci58753

Ullah, I., Abu-Dawud, R., Busch, J. F., Rabien, A., Erguen, B., Fischer, I., et al. (2019). VEGF - Supplemented Extracellular Matrix Is Sufficient to Induce Endothelial Differentiation of Human iPSC. *Biomaterials* 216, 119283. doi:10.1016/j.biomaterials.2019.119283

Verloop, M. C. (1949). On the Arteriae Bronchiales and Their Anastomosing with the Arteria Pulmonalis in Some Rodents; a Micro-anatomical Study. *Cells Tissues Organs* 7, 1–32. doi:10.1159/000140373

Wang, H. U., Chen, Z.-F., and Anderson, D. J. (1998). Molecular Distinction and Angiogenic Interaction between Embryonic Arteries and Veins Revealed by Ephrin-B2 and its Receptor Eph-B4. *Cell* 93, 741–753. doi:10.1016/s0092-8674(00)81436-1

Wang, M. M., Zhang, X., Lee, S. J., Maripudi, S., Keep, R. F., Johnson, A. M., et al. (2018). Expression of Periaxin (PRX) Specifically in the Human Cerebrovascular System: PDZ Domain-Mediated Strengthening of Endothelial Barrier Function. *Sci. Rep.* 8, 10042. doi:10.1038/s41598-018-28190-7

Watanabe, K., Ueno, M., Kamiya, D., Nishiyama, A., Matsumura, M., Wataya, T., et al. (2007). A ROCK Inhibitor Permits Survival of Dissociated Human Embryonic Stem Cells. *Nat. Biotechnol.* 25, 681–686. doi:10.1038/nbt1310

Wigle, J. T., Harvey, N., Detmar, M., Lagutina, I., Grosveld, G., Gunn, M. D., et al. (2002). An Essential Role for Prox1 in the Induction of the Lymphatic Endothelial Cell Phenotype. *EMBO J.* 21, 1505–1513. doi:10.1093/emboj/21.7.1505

Wimmer, R. A., Leopoldi, A., Aichinger, M., Wick, N., Hantusch, B., Novatchkova, M., et al. (2019). Human Blood Vessel Organoids as a Model of Diabetic Vasculopathy. *Nature* 565, 505–510. doi:10.1038/s41586-018-0858-8

You, L.-R., Lin, F.-J., Lee, C. T., DeMayo, F. J., Tsai, M.-J., and Tsai, S. Y. (2005). Suppression of Notch Signalling by the COUP-TFII Transcription Factor Regulates Vein Identity. *Nature* 435, 98–104. doi:10.1038/nature03511

Yuan, Y., Engler, A. J., Raredon, M. S., Le, A., Baevova, P., Yoder, M. C., et al. (2019). Epac Agonist Improves Barrier Function in iPSC-Derived Endothelial colony Forming Cells for Whole Organ Tissue Engineering. *Biomaterials* 200, 25–34. doi:10.1016/j.biomaterials.2019.02.005

Yuan, Y., Khan, S., Stewart, D. J., and Courtman, D. W. (2020). Engineering Blood Outgrowth Endothelial Cells to Optimize Endothelial Nitric Oxide Synthase and Extracellular Matrix Production for Coating of Blood Contacting Surfaces. *Acta Biomater.* 109, 109–120. doi:10.1016/j.actbio.2020.04.016

Zheng, X., Zhang, W., and Hu, X. (2018). Different Concentrations of Lipopolysaccharide Regulate Barrier Function through the PI3K/Akt Signalling Pathway in Human Pulmonary Microvascular Endothelial Cells. *Sci. Rep.* 8, 9963. doi:10.1038/s41598-018-28089-3

Conflict of Interest: LEN is a founder and shareholder in Humacyte, Inc.

The remaining authors declare that the research was conducted in the Q14 absence of any commercial or financial relationships that could be construed as a potential conflict of interest.

Publisher's Note: All claims expressed in this article are solely those of the authors and do not necessarily represent those of their affiliated organizations, or those of the publisher, the editors and the reviewers. Any product that may be evaluated in this article, or claim that may be made by its manufacturer, is not guaranteed or endorsed by the publisher.

Copyright © 2021 Yuan, Leiby, Greaney, Raredon, Qian, Schupp, Engler, Baevova, Adams, Kural, Wang, Obata, Yoder, Kaminski and Niklason. This is an open-access article distributed under the terms of the Creative Commons Attribution License (CC BY). The use, distribution or reproduction in other forums is permitted, provided the original author(s) and the copyright owner(s) are credited and that the original publication in this journal is cited, in accordance with accepted academic practice. No use, distribution or reproduction is permitted which does not comply with these terms.

frontiers in Bioengineering and Biotechnology

BRIEF RESEARCH REPORT
published: 06 January 2022
doi: 10.3389/fbioe.2021.803183

Decellularization Following Fixation of Explanted Aortic Valves as a Strategy for Preserving Native Mechanical Properties and Function

Manisha Singh[1†], *Clara Park*[2†] *and Ellen T. Roche*[1,2*]

[1]*Institute for Medical Engineering and Science, Massachusetts Institute of Technology, Cambridge, MA, United States,*
[2]*Department of Mechanical Engineering, Massachusetts Institute of Technology, Cambridge, MA, United States*

Mechanical or biological aortic valves are incorporated in physical cardiac simulators for surgical training, educational purposes, and device testing. They suffer from limitations including either a lack of anatomical and biomechanical accuracy or a short lifespan, hence limiting the authentic hands-on learning experience. Medical schools utilize hearts from human cadavers for teaching and research, but these formaldehyde-fixed aortic valves contort and stiffen relative to native valves. Here, we compare a panel of different chemical treatment methods on explanted porcine aortic valves and evaluate the microscopic and macroscopic features of each treatment with a primary focus on mechanical function. A surfactant-based decellularization method after formaldehyde fixation is shown to have mechanical properties close to those of the native aortic valve. Valves treated in this method were integrated into a custom-built left heart cardiac simulator to test their hemodynamic performance. This decellularization, post-fixation technique produced aortic valves which have ultimate stress and elastic modulus in the range of the native leaflets. Decellularization of fixed valves reduced the valvular regurgitation by 60% compared to formaldehyde-fixed valves. This fixation method has implications for scenarios where the dynamic function of preserved valves is required, such as in surgical trainers or device test rigs.

Keywords: decellularization, aortic valve, hydrodynamic testing, valvular, mechanical properties, aldehyde fixation

OPEN ACCESS

Edited by:
Kamal Hany Hussein,
Assiut University, Egypt

Reviewed by:
Jiawei Shi,
Huazhong University of Science and Technology, China
Fatemeh Kabirian,
KU Leuven, Belgium
Helen E. Berry,
University of Leeds, United Kingdom

****Correspondence:***
Ellen T. Roche
etr@mit.edu

[†]These authors have contributed equally to this work and share first authorship

Specialty section:
This article was submitted to Biomaterials, a section of the journal Frontiers in Bioengineering and Biotechnology

Received: *27 October 2021*
Accepted: *15 December 2021*
Published: *06 January 2022*

Citation:
Singh M, Park C and Roche ET (2022) Decellularization Following Fixation of Explanted Aortic Valves as a Strategy for Preserving Native Mechanical Properties and Function. Front. Bioeng. Biotechnol. 9:803183. doi: 10.3389/fbioe.2021.803183

INTRODUCTION

Cardiovascular benchtop models with mock circulatory loops are increasingly used for surgical training (Ramphal et al., 2005; Mchale and Frank, 2017; Feins et al., 2017), as educational platforms (Gehron et al., 2019; Villanueva et al., 2020), and for research purposes (Chinchoy et al., 2000; Maglio et al., 2021). These systems are typically composed of a mock circulatory loop connected to a pulsatile pump, but often lack anatomical representations and mechanical properties of the components of the heart (Wu et al., 1996; Timms et al., 2005; Taylor and Miller, 2012). Some cardiac simulators utilize *ex vivo* heart tissue to realistically recapitulate the anatomy and flow response (Vismara et al., 2016; Leopaldi et al., 2012), but the shelf-life of freshly explanted tissue without any chemical preservation or perfusion is limited to approximately 4 h. A new class of *in vitro* cardiac simulators use chemically preserved explanted heart tissue to maintain anatomic fidelity (Park et al., 2020), but competent valves are required for utility as *in vitro* cardiovascular simulators for education and training.

Therefore, we screened methods that would preserve valves, and ultimately surrounding intracardiac tissue, while ensuring their competency to enable physiological biomechanics and hemodynamics. Hence, there is an unmet need for tissue engineering techniques or chemical treatment methods for native tissues in order to; 1) extend their post-explant longevity, 2) enable practical use in mock-circulatory benchtop models, 3) retain biomechanical properties.

Tissue engineering techniques, such as decellularization via surfactants, can successfully produce tissue scaffolds with mechanical properties similar to native valves, but the resulting scaffolds require special storage conditions (e.g., 4°C, or slow cooling medium, etc.) for their long-term usage and may not be suitable for benchtop applications (Maghsoudlou et al., 2013; Urbani et al., 2017; Gupta et al., 2017). Chemically-induced crosslinking (e.g., through aldehydes or carbodiimides) subsequent to surfactant processing has also been reported to enhance the life-span and storage of the decellularized tissues (Liu et al., 2019) at room temperature. Although thin valve leaflets can easily be decellularized and crosslinked with immersion techniques, successful decellularization of a whole heart requires complex perfusion bioreactors (Guyette et al., 2014).

Human cadaveric heart specimens, which are often chemically treated with formaldehyde, are commonly available in medical schools but stiffen due to crosslinking and are rendered immobile, limiting their use to demonstrating gross heart anatomy and preventing them from being reanimated in mock loops. Chemical preservation of valves utilizes aldehyde-based fixatives which alter the mechanical properties of aortic valve leaflets, hence affecting the function of the valves, and thus the biomimicry of any simulator in which they are installed (Christie, 1992). Glutaraldehyde-fixed leaflets have been reported to be about 100 times stiffer than native leaflets (Talman and Boughner, 1995). Therefore, we screened methods that would restore the mechanical properties of previously preserved valves, and ultimately surrounding intracardiac tissue, while ensuring their competency to enable physiological biomechanics and hemodynamics.

In this study, we compare fixation via formaldehyde and decellularization via surfactants. We limit the scope to aortic valve leaflets and specifically examine treatment effects on the multiscale structure and mechanical properties. We hypothesize that a combination of aldehyde-fixation followed by surfactant-based decellularization may preserve the mechanical properties of native aortic leaflets for use in high fidelity mock circulatory loops and cardiac simulators. For this work, formaldehyde crosslinking has been chosen over glutaraldehyde owing to 1) faster crosslinking, 2) availability of formaldehyde-fixed cadaveric hearts in hospitals and medical schools, and 3) fewer concerns of formaldehyde induced toxicity for *in vitro* applications. Many studies have investigated surfactant-based decellularization involving ionic (e.g., sodium dodecyl sulfate, sodium deoxycholate), non-ionic (e.g., Triton X-100), and a combination thereof (Luo et al., 2019; Zhou et al., 2010). For our purposes, we selected a combination of ionic sodium deoxycholate (SD) and a non-ionic surfactant (Triton X-100) to restore the mechanical function of fixed valves due to superior efficiency in cell removal and matrix preservation over other techniques (Kasimir et al., 2003; Luo et al., 2019). Herein, we assess the impact of SD/Triton X-100 decellularization on formaldehyde-fixed valvular leaflets and compare the mechanical properties of the resulting leaflets with their native counterpart. Furthermore, the effects of surfactants on the micromechanics and morphology of fixed valves were evaluated with Fourier transform infrared spectroscopy (FTIR) and scanning electron microscopy (SEM) and compared with native porcine valves. Next, a physiologically relevant left heart cardiac simulator was custom-built to house the chemically treated aortic valves and their hemodynamic performance was compared to native, fixed, and decellularized valves. At present, cardiac hemodynamics and biomechanics are mainly taught using textbooks and computational models (Mittal et al., 2016). Here, we identify a process that may enable realistic recapitulation of valve function on the bench which enables hands-on cardiac biomechanics education. These chemical treatment techniques have the potential to preserve biomimicry and biomechanics of aortic leaflets while extending their shelf-life so they can be installed in cardiac simulators as an educational or research tool.

MATERIALS AND METHODS

Treatment of Porcine Aortic Valves

Fresh porcine hearts with intact ascending aorta were purchased from Sierra for Medical Science Inc., (California, United States). A 3 cm long segment of the aorta with valves attached at the annulus was dissected from the hearts. Before processing, valves were thoroughly washed with 1X phosphate-buffered saline (PBS) of pH 7.4 to remove all blood and blood clots. For aldehyde-based fixation, the explanted aortic valves (n = 3) were submerged in 200 ml of 10% Neutral-buffered Formalin (Sigma Aldrich) over a gentle shaker for 18 h at 25°C and thoroughly washed in 1X PBS thereafter. For decellularization, the explanted valves (n = 3) were treated in a 200 ml mixture of 5% (or 10% for increased surfactant concentration) w/v Sodium Deoxycholate (Sigma Aldrich) and 5% (or 10% for increased surfactant concentration) w/v Triton X-100 (Thermo Fisher Scientific) in 1X PBS over gentle shaking for a total of 48 h at 25°C. The solution was refreshed after 24 h during decellularization. For the combination of fixation and decellularization, the valves were first fixed in formaldehyde followed by the surfactant-based decellularization as mentioned above. The fresh, formaldehyde-treated, decellularized aortic valves, and those that were decellularized after fixation are referred to as "native", "fixed", "decel", and "fixed-decel" respectively throughout the text. Two different concentrations of 5 and 10 w/v% of the surfactants were used and referred to as "fixed-decel 5%" and "fixed-decel 10%", respectively.

Fourier Transform Infrared Spectroscopy

Dried fresh (n = 3) and chemically-treated porcine aortic valves (n = 3) were studied using infrared spectroscopy in Attenuated

Total Reflection mode using a Thermo Fisher FTIR6700 Fourier Transform Infrared Spectrometer. Data were acquired at a resolution of 4 cm^{-1} with 64 scans and a scan range of 4,000–500 cm^{-1}.

Scanning Electron Microscopy

Fresh (n = 3) and chemically treated valves (n = 3) were immersed in 2.5% glutaraldehyde for 1 h, dehydrated with ethanol, and then dried for 12 h before embedding in paraffin wax for cross-sectional evaluation. Prior to imaging with a scanning electron microscope, the samples were sputter-coated (50 nm) with gold. Images were acquired by Zeiss Merlin high-resolution electron microscope at an acceleration voltage of 1 kV and a working distance of 4–6 mm.

Mechanical Performance

The valve leaflets were cut from fresh and chemically treated aortic segments. The leaflets of each type of valve (n = 3) were stretched uniaxially in the radial direction at a rate of 10 mm min^{-1} using an Instron 5944 mechanical tester equipped with a 2-kN load cell. Prior to testing, the thickness and size of each leaflet were measured using a micrometer and vernier caliper respectively to calculate stress and strain from the recorded force vs. displacement data. From literature, it is evident that the strength of an aortic valve leaflet is weaker in the radial direction than circumferential. Testing in the weaker (i.e., radial) direction was performed as it represented the worst case condition for cyclic hydrodynamic testing.

Hydrodynamic Assessment

A mock circulatory loop representing the left heart circulation was built in-house for hydrodynamic evaluation of the aortic valves. A pulsatile pump (Harvard Apparatus, United States) was connected to the loop to create a pulsatile flow at 60 beats per min under physiological conditions at a cardiac output of 3.6 L min^{-1}. The aortic valve was sutured on a sewing ring on a 3D-printed adaptor and mounted onto the circuit. Hydrodynamic parameters were measured in real-time using pressure sensors (PendoTECH) before and after the valve and an ultrasonic flow probe (Transonic) placed after the valve and connected to a T420 multi-channel research console (Transonic). An endoscopic camera (NIDAGE wireless) was used to record real-time valve function and leaflet motion. Sensor output was acquired for approximately 10 beats per sample using PowerLab (ADInstruments). A total of three samples were used for each valve type except for the mechanical valve. Only one specimen was used for mechanical valve due to its high repeatability and robustness.

Statistical Analysis

All data are presented as mean ± Std Dev, with n = 3, unless stated otherwise. The p-values ($^*p < 0.05$) are calculated using one-way ANOVA with Tukey correction in Origin Pro 2019 (64-bit) and ns denotes no statistical difference.

RESULTS

Micromechanics and Surface Characterization of Valve Leaflets

Aortic valves function in a mechanically demanding environment that requires micromechanical remodeling of the leaflet tissue. Explanted valves require chemical treatments to match the inherent mechanical properties of the native valvular tissue. Among various chemical treatments, aldehyde-based fixation is considered the gold standard but causes the aortic valves to stiffen and mechanically deform (**Figure 1A**). Decellularization is an alternative technique but results in a weak scaffold that is prone to material failure. In this study, we have adopted a combination of aldehyde-based fixation and surfactant-based decellularization to yield mechanically strong yet soft leaflets that mimic the native valves closely (**Figure 1A**). The native leaflets are thin, flexible, and mainly comprised of collagen and elastin fibers. The collagen fibers are corrugated and arranged in the circumferential direction whereas elastin fibers are positioned in the radial direction (**Figure 1B**). During diastole, continuous stretching of elastin occurs which causes the initially crimped collagen fibers to uncrimp from a wavy configuration to straight. To detect any conformational and structural alterations in the collagen and elastin fibers due to various chemical treatments, Fourier Transform Infrared Spectroscopy (FTIR) was performed. The overlay of FTIR spectra of treated and control samples showed no new absorption peaks but detected changes in peak intensity and positions (**Figure 1C**). The wide band from 3,500 to 3,200 cm^{-1} corresponds to the symmetric and asymmetric stretching vibrations of -OH and -NH functional groups. The wide peak intensity was reduced by 85% for fixed samples, indicating covalent interactions of amine and hydroxyl groups through aldehyde crosslinking. The asymmetric and symmetric -CH_2 stretching bands from elastin and collagen structures are located at 2,950–2,850 cm^{-1}. The absence of an aldehyde characteristic peak in fixed and fixed-decel samples at 1730 cm^{-1} indicates that no free aldehyde groups are present, and leaflets have been washed thoroughly. The 40% increase in the intensity of amide I (–CO-NH– I) and amide II (–CO-NH– II) peaks at 1,630 cm^{-1} and 1,550 cm^{-1} for fixed-decel samples indicates the conformation and orientation changes in the secondary protein's structure of collagen and elastin as compared to fixed groups.

FTIR surface characterization is also supported by the morphology of the valvular leaflets (**Figure 2**). The crimping of collagen and elastin fibers is observed in the case of fixed samples when imaged under a scanning electron microscope from the surface (**Figure 2B**). No obvious difference in pore size was observed for native, decel, and fixed-decel groups (**Figures 2A,C,D**). The decel group showed thinner fiber structures and loose surface texture when compared to native valves (**Figure 2D**). This is likely due to detergent-mediated solubilization and dissociation of cell membranes. Cross-sectioned morphology exhibits that the fibers in the fixed group are much more tightly packed than the fixed-decel samples (**Figures 2F,G**). The increased porosity in fixed-decel

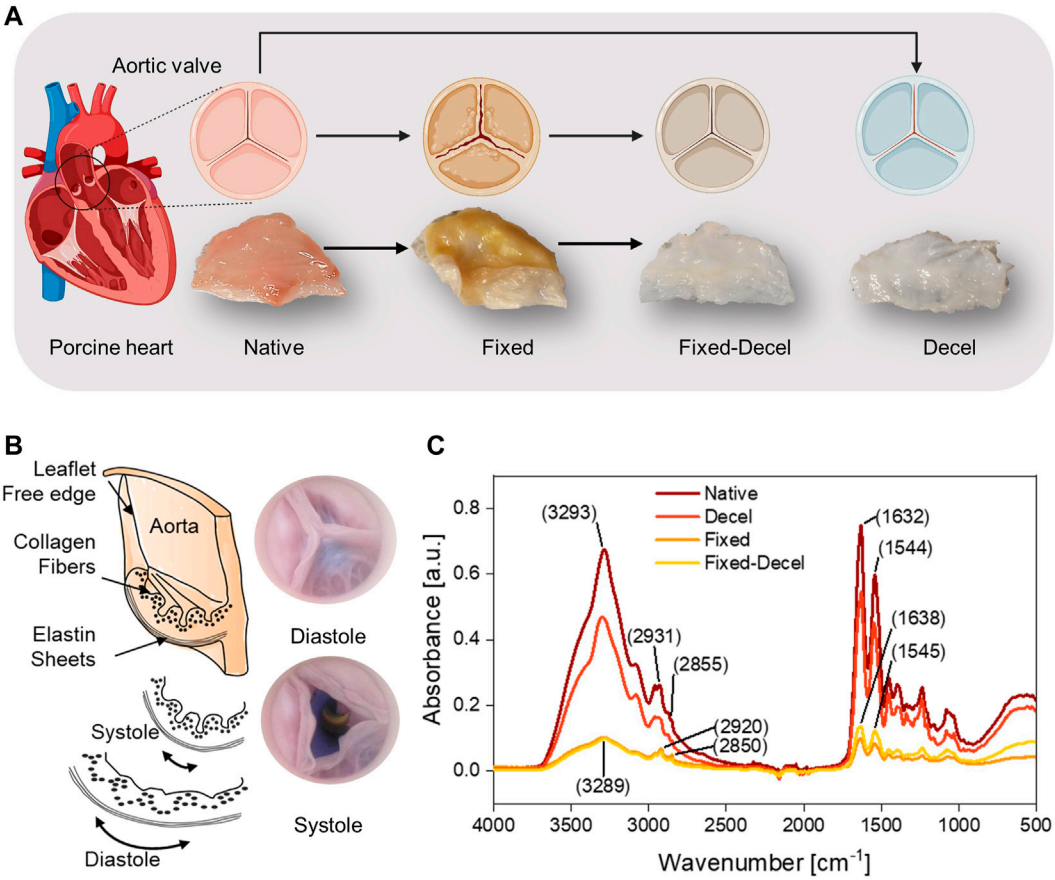

FIGURE 1 | Overall scheme and study design. **(A)** Porcine aortic valves are explanted and either chemically crosslinked with fixative formaldehyde (fixed), or decellularized with surfactants Triton X-100/sodium deoxycholate (decel) or treated with a combination of fixative and surfactants (fixed-decel) to optimize the biomechanical properties. Digital photos of the cut leaflets show that decel and fixed-decel groups were discolored due to the removal of cell and related membrane proteins by the surfactants. Fixed leaflets appear to be distorted in shape relative to the native valve and the original shape was recovered when fixed leaflets were decellularized (fixed-decel). **(B)** Digital pictures and a cross-section schematic of an aortic valve showing composition and orientation of collagen and elastin fibers in different layers during systole and diastole. **(C)** Fourier Transform Infrared Spectroscopy (FTIR) spectra indicate the peak intensity and location of characteristic chemical groups.

samples could be attributed to the solubilization of membrane proteins by surfactants. SEM also confirmed that the cells were removed from the decel group, therefore causing the collagen fibers to loosen to a porous structure (**Figure 2H**).

Combination of Fixation and Decellularization Yields Native Tissue-Mimicking Mechanical Properties

Due to the circumferential orientation of collagen fibers, leaflets are stiffer in the circumferential direction than the radial while exhibiting more extensibility in the radial direction. To compare the mechanical properties of chemically-treated leaflets with native, a uniaxial tensile test was performed in the radial direction (**Figure 3A**). Prior to mounting the samples in a mechanical tester, the thickness of each leaflet was measured with a digital micrometer. The thickness of fixed specimens increased by 67% whereas it decreased by 45% for decellularized samples when compared to native aortic valves (**Figure 3B**). The combination of fixed and decellularization resulted in a thickness comparable to the native tissue. As the weight of surfactants for decellularization was increased from 5 to 10%, a further reduction of 16% was noted in the mean value of thickness for fixed-decel groups, although it is not statistically significant according to one-way ANOVA with Tukey correction. Fixed samples have the highest ultimate stress of 755 ± 17 kPa which is significantly higher than the native porcine aortic valves 677 ± 36 kPa (**Figure 3B**). Combination of fixation and decellularization yielded ultimate stress of 683 ± 44 kPa and 640 ± 54 kPa for 5 and 10% surfactant concentration, respectively. Decellularization alone reduced the maximum stress at the failure to 538 ± 29 kPa, which is significantly weaker than native leaflets. Similar trends were observed in the modulus of elasticity (calculated under 5% strain levels) where fixation alone resulted in significantly stiffer (1.4 ± 0.09 MPa) samples as compared to native tissue (1 ± 0.05 MPa) (**Figure 3C**). Fixed-decel groups yielded an

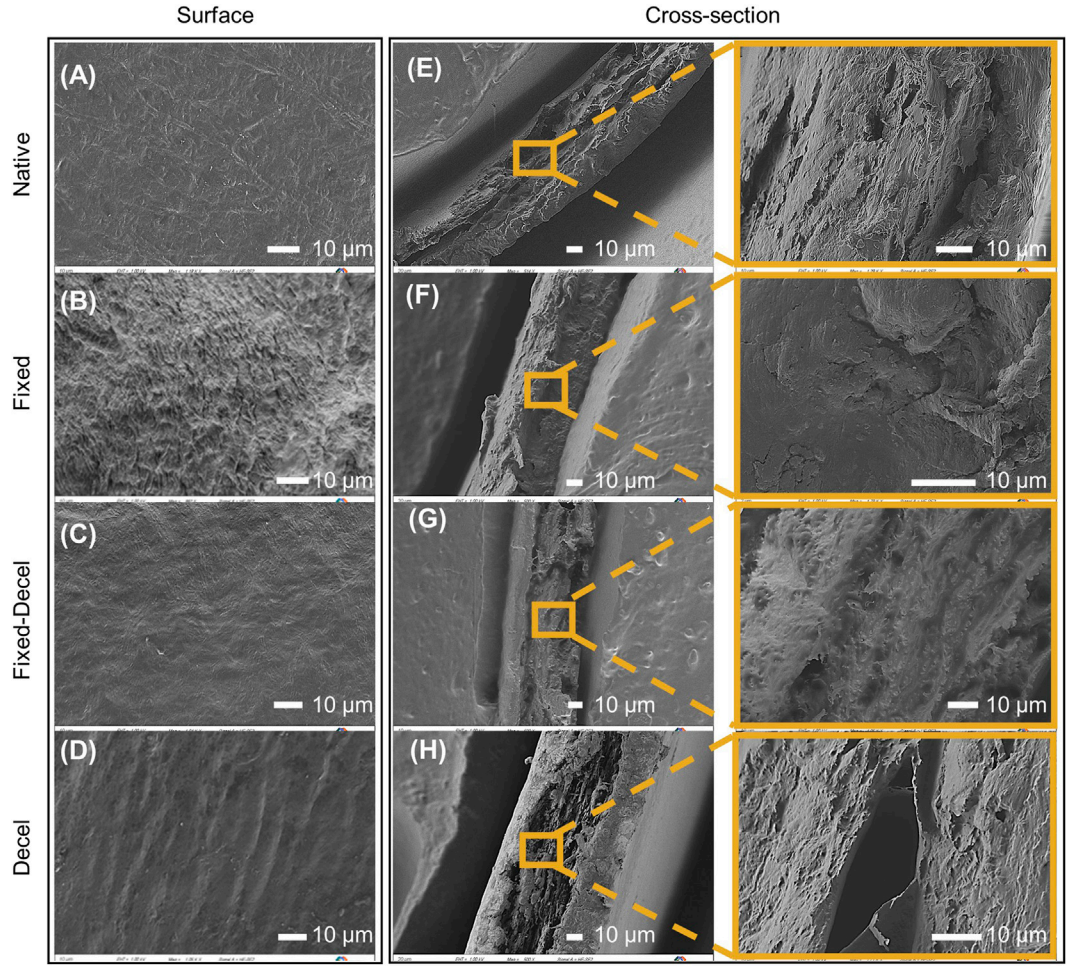

FIGURE 2 | Surface characterization using scanning electron microscopy (SEM). **(A–D)** SEM micrographs showing the morphology of leaflets from the surface. **(E–H)** Micrographs showing cross-sectional morphology of leaflets that have been fixed, decellularized, and a combination thereof including the native control. The scale bar is 10 μm for all.

elastic modulus of 1.2 ± 0.2 MPa and 1 ± 0.08 MPa for 5 and 10% surfactant concentration respectively, both of which matched closely ($p > 0.05$; one-way ANOVA with Tukey correction) with native tissues. Decellularized groups exhibited the lowest modulus of elasticity 0.8 ± 0.02 MPa. There is no statistically significant difference between the ultimate strain of native aortic valves 120 ± 8% to that of fixed-decel 124 ± 6% and 119 ± 7% for 5 and 10%, respectively (**Figure 3C**). Fixed samples exhibited ultimate tensile strains of 94 ± 5%, which is 1.3 times lower than the native group. Ultimate stress and elastic modulus are plotted for a two-dimensional comparison of chemically treated groups with native control (**Figure 3D**). An overlap in the mechanical properties was observed for fixed-decel samples whereas the pristine decel and fixed samples showed a contrasting difference in comparison to native leaflets. From the data above, it can be concluded that the combination of fixation and decellularization techniques matches the mechanical properties of native aortic tissues whereas the controls of fixation and decellularization alone are either too stiff or weak.

Hydrodynamic Assessment of Chemically Treated Aortic Valves

For evaluating the hydrodynamic performance of chemically treated aortic valves, we built a benchtop setup with a pulsatile mock circulatory loop mimicking the left heart circulation (**Figure 4A**). Along with the anatomically accurate aortic valves, our custom-built flow setup houses a reservoir to store the fluid, a compliance chamber to mimic the aortic compliance, and a pulsatile pump to displace fluid at physiologically relevant ventricular stroke volumes (SV) and heart rates. Left ventricular (0–120 mmHg) (LVP) and aortic (60–120 mmHg) pressure (AoP) conditions are simulated by controlling the resistance valves in the flow circuit. Two pressure sensors were placed before and after the valves to acquire the real-time pressures during valve performance testing. A flow probe was placed downstream of the aortic valve to record any changes in the

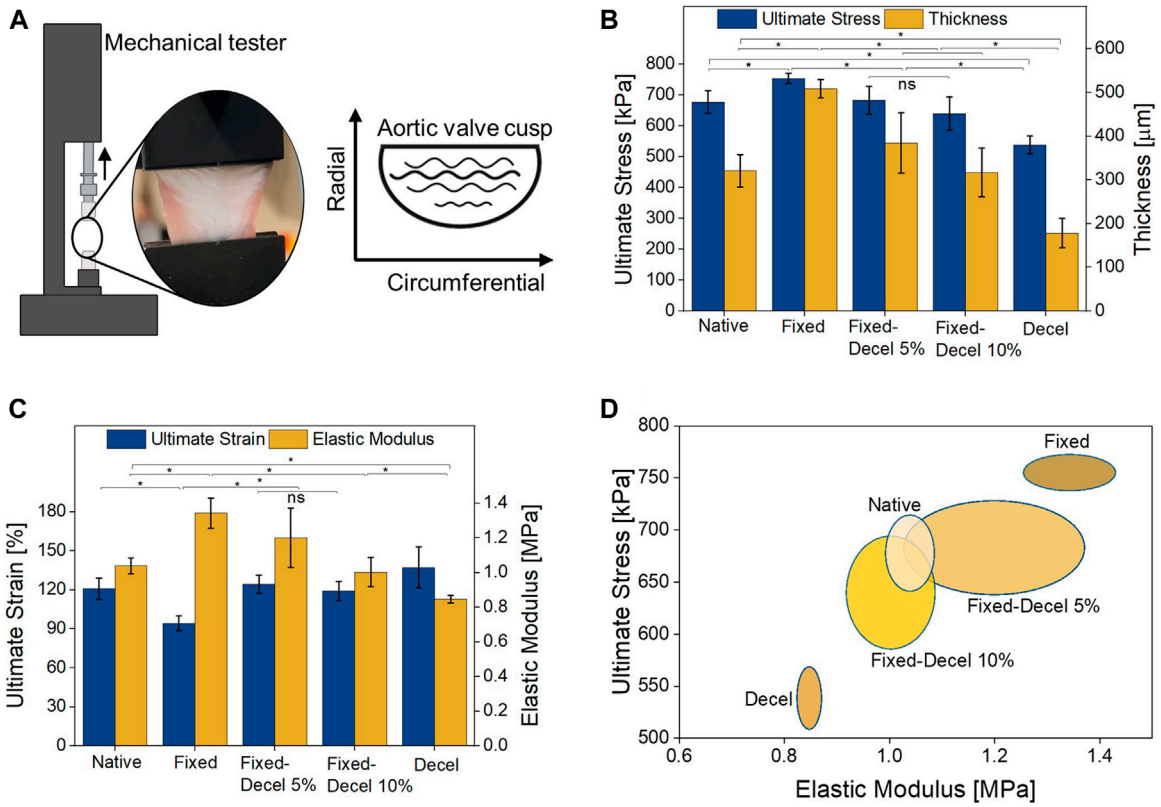

FIGURE 3 | Evaluation of mechanical properties. **(A)** Set up of uniaxial tensile test performed in the radial direction. **(B)** Comparison of leaflet thickness and maximum stress at failure **(C)** Comparison of elastic modulus (i.e., stiffness) and maximum strain at failure. **(D)** two-dimensional comparison (Elastic modulus vs. ultimate stress at break) of mechanical properties among fixed, decellularized, and a combination thereof, including the native control groups. Data presented as mean ± Std. Dev., $n = 3$, p-values are calculated using one-way ANOVA with Tukey correction, $^*p < 0.05$ in Origin Pro 2019 (64-bit); ns denotes no statistical difference).

forward and backward flow. The recorded left ventricle and aortic pressures and flow for native porcine valves at 60 bpm and SV of 60 ml over a few cardiac cycles are shown in **Figures 4B,C**. Based on LVP and AoP readings, the mean transvalvular systolic pressure gradients for native porcine valves were calculated and plotted in **Figure 4D**. Aortic flow data was used to calculate the regurgitation %, which represents the ratio of the regurgitant volume and the stroke volume, expressed in percentage. An endoscopic camera records the real-time leaflet motion during systole and diastole phases (**Figure 4E**, **Supplementary Video S1**). Normalized orifice area determines the ratio of the geometrical opening area of the valves at peak systole and the cross-sectional area of the attached aorta. The geometrical opening area of the valves was calculated using ImageJ (Abràmoff et al., 2004) from the recorded endoscope camera videos. The representative images in **Figure 4E** and **Supplementary Video S1** qualitatively compare the opening (during systole) and closing (during diastole) of chemically treated valves relative to the native/fresh aortic valve and a mechanical St. Jude valve. The aldehyde-based crosslinking continues over time, and treated tissues turn stiffer with age (Sacks and Liao, 2018). In order to account for the stiffening of fixed valves with time, we included an additional control group comprising of one-year-old fixed aortic valves. As seen in **Figure 4E**, the fixed valves turn stiff and do not completely close at diastole. The mechanically deformed area related to the partial closure is highlighted by red dotted circles, which is more apparent in the one-year-old samples. When the fixation was combined with decellularization for the same valves, no gaps were visible between the valve leaflets during diastole (**Figure 4E**). Mean transvalvular pressure gradients (ΔP) also support this observation and ΔP required for complete closure are significantly different in the case of chemically-treated valves relative to the native (**Figure 4F**). The recorded ΔP for fixed and decel groups are 4.6 ± 0.4 and 2.8 ± 0.3 mmHg, respectively which are statistically different ($p < 0.05$; one-way ANOVA with Tukey correction) when compared to native 3.7 ± 0.4 mmHg and fixed-decel 3.9 ± 0.3 mmHg groups. One-year-old (y/o) formaldehyde-fixed groups exhibited an ΔP of 13.0 ± 1.8 mmHg, which was reduced to 8.0 ± 0.6 mmHg when followed by decellularization. Fixation after decellularization clearly reduced the transvalvular pressure gradients relative to fixed groups, but no significant differences ($p > 0.5$) were noted in the normalized orifice area opening at peak systole of fixed vs. fixed-decel groups (**Figure 4G**). However, owing to the synergistic effect of reduced stiffness and ultimate strain (**Figure 3C**) for fixed-decel versus fixed groups, complete closure of fixed-decel groups was observed at peak diastole relative to fixed groups (**Figure 4E**). This observation is also in line with the regurgitant flow calculations (**Figure 4G**). The fixed groups showed the highest regurgitation of 15 ± 2% which was

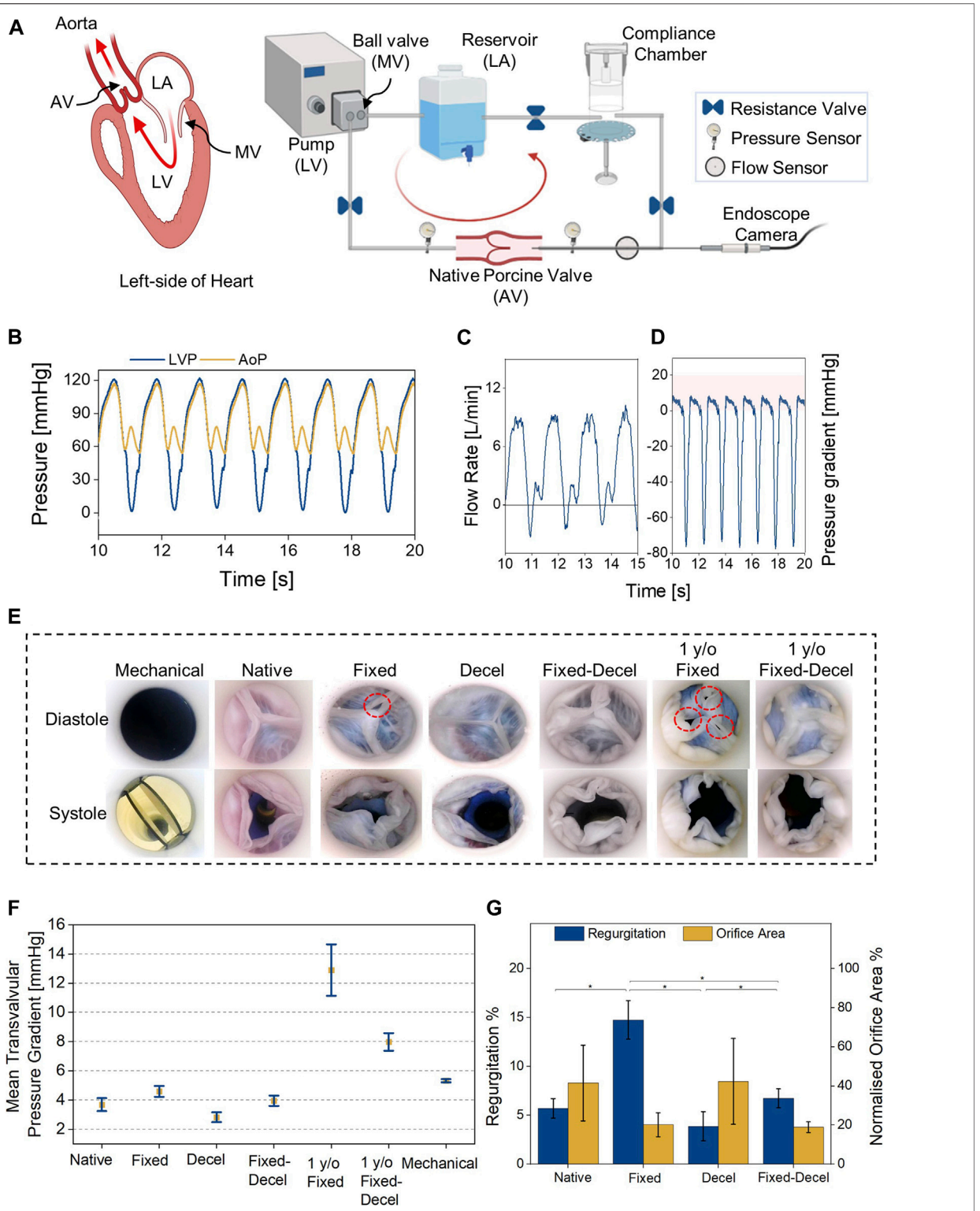

FIGURE 4 | Hydrodynamic assessment. **(A)** Custom-built benchtop setup with a pulsatile mock circulatory loop representing left heart circulation. **(B,C)** Representative pressure and flow waveforms for native aortic valves at 60 bpm and cardiac output of 3.6 L/min. **(D)** Representative transvalvular pressure gradients for native valves over a few cardiac cycles. **(E)** Digital images were captured using an endoscope camera for different groups of aortic valves at peak systole and diastole. **(F)** Comparison of mean transvalvular pressure gradients (ΔP) among fixed, decellularized, and a combination thereof, including the native and commercially available mechanical (St. Jude) control groups. **(G)** Comparison of regurgitant flow and opening orifice area at peak systole. Data presented as mean ± Std Dev, *p*-values are calculated using one-way ANOVA with Tukey correction, $^{*}p < 0.05$ in Origin Pro 2019 (64-bit), ns denotes no statistical difference. LA = left atrium, LV = left ventricle, MV = mitral valve. Decel = decellularized.

lowered to 6 ± 0.9% for fixed-decel groups that match closely with native 5.7 ± 1% groups (**Figure 4G**).

DISCUSSION

In this work, we have demonstrated that hemodynamic function and biomechanical properties of formaldehyde-fixed aortic valve tissues can be improved when treated with a combination of sodium deoxycholate (SD)/Triton X-100 surfactants. We have compared several chemical treatment methods on explanted porcine aortic valves and evaluated microscopic and macroscopic features of each treatment with a primary focus on mechanical function. Our results show that the decellularization process lowers the ultimate strength and elastic modulus of aldehyde-fixed valve leaflets. This reduction in mechanical strength (i.e., ultimate stress and elastic modulus) of the fixed tissues may be attributed to 1) modification of structural components, such as collagen and/or elastin fiber rearrangements (**Figure 2**), 2) solubilization and dissociation of cell membranes by the detergents (**Figure 1C**), or 3) a combination thereof.

The resulting valves with biomimicking mechanical properties can be directly employed in cardiac simulators for educational and training purposes, as shown in our left heart pulsatile flow loop equipped with real-time hydrodynamic readings and intravascular imaging. Using this technique to restore the mechanics of preserved tissues can potentially be extended to high-fidelity physical heart simulators with utility in medical education or procedural planning. For instance, human cadaveric heart specimens, which are commonly used in anatomy labs in medical schools to teach gross anatomy (James et al., 2019), may be restored to have competent valve function and attached to a mock circulatory loop. Further, the preserved hearts can potentially be reanimated using a biohybrid approach (Park et al., 2020) to produce an interactive, beating heart model which would complement the current educational tools with an enhanced learning and training experience. In the future, this technique can potentially be employed for building accurate *in vitro* prototypes to experimentally validate computational models, such as fluid-structure interaction with dynamic function of the aortic valve (Dumont et al., 2004) or for device testing and procedural planning purposes.

Several limitations of the current study should be noted—1) the panel of treatment options did not include decellularization followed by fixation, which is commonly used for bioprosthetic valves made from pericardium for implantation but was excluded from our work as we wish to extend the treatment process to the whole heart, including the vessels and myocardial tissue, ideally without using reperfusion bioreactors for ease of manufacturability; 2) for a proof-of-concept, we selected one protocol for decellularization (i.e., the combination of SD and Triton X-100) and our current study lacks a detailed comparison of the several other alternative decellularization methods described in the literature; 3) since this work focuses on restoring native valve mechanical properties in aldehyde-fixed valves for benchtop applications, the degree of cell removal has not been assessed. Before adaptation of this work for any *in vivo* or tissue engineering application, detailed characterization on cell removal and toxicity is required; 4) preliminary hydrodynamic testing use water which does not mimic the density and viscosity of blood. A monoethylene glycol-based blood-mimicking fluid as described in our previous work (Singh et al., 2021) could improve the hydrodynamic accuracy; 5) since the valves were manually sutured to an adaptor to align them normal to the flow circuit, the natural annulus size and tension applied to the leaflets may have been altered, potentially leading to variability in the normalized orifice area; 6) preliminary hydrodynamic testing does not include the fatigue performance of the valves under pulsatile physiological loading and is part of our future work.

In conclusion, we find that a surfactant-based decellularization technique can restore the native biomechanical properties of aldehyde-fixed aortic valves. The ability to retrospectively decellularize fixed valves and reanimate them in benchtop simulators to recapitulate biomechanics has utility in cardiovascular education, training, and research.

DATA AVAILABILITY STATEMENT

The original contributions presented in the study are included in the article/**Supplementary Material**, further inquiries can be directed to the corresponding author.

AUTHOR CONTRIBUTIONS

MS and CP contributed equally to this study. MS, CP, and ETR designed the study and wrote the manuscript. MS and CP performed the experiments and analyzed the data. All authors contributed to the manuscript, read and approved the submitted version.

FUNDING

This research was funded in part by the Department of Mechanical Engineering at Massachusetts Institute of Technology and in part by a CAREER Award to ETR from the National Science Foundation (1847541).

ACKNOWLEDGMENTS

The authors would like to acknowledge the Materials Science and Engineering Center at the Massachusetts Institute of Technology (MIT), for use of their material analysis and electron microscopy facilities. Figures and digital illustrations are created with Adobe Illustrator and BioRender.com. The data is plotted and evaluated with the software OriginPro 2019.

SUPPLEMENTARY MATERIAL

The Supplementary Material for this article can be found online at: https://www.frontiersin.org/articles/10.3389/fbioe.2021.803183/full#supplementary-material

REFERENCES

Abràmoff, M. D., Magalhães, P. J., and Ram, S. J. (2004). Image Processing with ImageJ. *Biophotonics Int.* 11 (7), 36–42.

Chinchoy, E., Soule, C. L., Houlton, A. J. G., Gallagher, W. J., Hjelle, M. A., Laske, T. G., et al. (2000). Isolated Four-Chamber Working Swine Heart Model. *Ann. Thorac. Surg.* 70 (5), 1607–1614. doi:10.1016/s0003-4975(00)01977-9

Christie, G. (1992). Anatomy of Aortic Heart Valve Leaflets: the Influence of Glutaraldehyde Fixation on Function. *Eur. J. cardio-thoracic Surg.* 6 (Suppl. ment_1), S25–S33. doi:10.1016/1010-7940(92)90018-s

Dumont, K., Stijnen, J. M. A., Vierendeels, J., van de Vosse, F. N., and Verdonck, P. R. (2004). Validation of a Fluid-Structure Interaction Model of a Heart Valve Using the Dynamic Mesh Method in Fluent. *Comput. Methods Biomech. Biomed. Eng.* 7 (3), 139–146. doi:10.1080/10255840410001715222

Feins, R. H., Burkhart, H. M., Conte, J. V., Coore, D. N., Jr, Fann, J. I., Hicks, G. L., et al. (2017). Simulation-based Training in Cardiac Surgery. *Ann. Thorac. Surg.* 103 (1), 312–321. doi:10.1016/j.athoracsur.2016.06.062

Gehron, J., Zirbes, J., Bongert, M., Schäfer, S., Fiebich, M., Krombach, G., et al. (2019). Development and Validation of a Life-Sized Mock Circulatory Loop of the Human Circulation for Fluid-Mechanical Studies. *ASAIO J.* 65 (8), 788–797. doi:10.1097/mat.0000000000000880

Gupta, S. K., Mishra, N. C., and Dhasmana, A. (2017). "Decellularization Methods for Scaffold Fabrication," in *Decellularized Scaffolds and Organogenesis* (Berlin, Germany: Springer), 1–10. doi:10.1007/7651_2017_34

Guyette, J. P., Gilpin, S. E., Charest, J. M., Tapias, L. F., Ren, X., Ott, H. C., et al. (2014). Perfusion Decellularization of Whole Organs. *Nat. Protoc.* 9 (6), 1451–1468. doi:10.1038/nprot.2014.097

James, H. K., Chapman, A. W., Pattison, G. T. R., Griffin, D. R., and Fisher, J. D. (2019). Systematic Review of the Current Status of Cadaveric Simulation for Surgical Training. *Br. J. Surg.* 106 (13), 1726–1734. doi:10.1002/bjs.11325

Kasimir, M.-T., Rieder, E., Seebacher, G., Silberhumer, G., Wolner, E., Weigel, G., et al. (2003). Comparison of Different Decellularization Procedures of Porcine Heart Valves. *Int. J. Artif. Organs* 26 (5), 421–427. doi:10.1177/039139880302600508

Leopaldi, A. M., Vismara, R., Lemma, M., Valerio, L., Cervo, M., Mangini, A., et al. (2012). *In Vitro* hemodynamics and Valve Imaging in Passive Beating Hearts. *J. Biomech.* 45 (7), 1133–1139. doi:10.1016/j.jbiomech.2012.02.007

Liu, J., Jing, H., Qin, Y., Li, B., Sun, Z., Kong, D., et al. (2019). Nonglutaraldehyde Fixation for off the Shelf Decellularized Bovine Pericardium in Anticalcification Cardiac Valve Applications. *ACS Biomater. Sci. Eng.* 5 (3), 1452–1461. doi:10.1021/acsbiomaterials.8b01311

Luo, Y., Lou, D., Ma, L., and Gao, C. (2019). Optimizing Detergent Concentration and Processing Time to Balance the Decellularization Efficiency and Properties of Bioprosthetic Heart Valves. *J. Biomed. Mater. Res.* 107 (10), 2235–2243. doi:10.1002/jbm.a.36732

Maghsoudlou, P., Georgiades, F., Tyraskis, A., Totonelli, G., Loukogeorgakis, S. P., Orlando, G., et al. (2013). Preservation of Micro-architecture and Angiogenic Potential in a Pulmonary Acellular Matrix Obtained Using Intermittent Intra-tracheal Flow of Detergent Enzymatic Treatment. *Biomaterials* 34 (28), 6638–6648. doi:10.1016/j.biomaterials.2013.05.015

Maglio, S., Park, C., Tognarelli, S., Menciassi, A., and Roche, E. T. (2021). High Fidelity Physical Organ Simulators: from Artificial to Bio Hybrid Solutions. *IEEE Trans. Med. Robotics Bionics* 3, 349. doi:10.1109/tmrb.2021.3063808

Mchale, J., and Frank, F. (2017). *Beating Heart Controller and Simulator*. Google Patents.

Mittal, R., SeoSeo, J. H., Vedula, V., ChoiChoi, Y. J., Liu, H., Huang, H. H., et al. (2016). Computational Modeling of Cardiac Hemodynamics: Current Status and Future Outlook. *J. Comput. Phys.* 305, 1065–1082. doi:10.1016/j.jcp.2015.11.022

Park, C., Fan, Y., Hager, G., Yuk, H., Singh, M., Rojas, A., et al. (2020). An Organosynthetic Dynamic Heart Model with Enhanced Biomimicry Guided by Cardiac Diffusion Tensor Imaging. *Sci. Robot* 5 (38), 9106. doi:10.1126/scirobotics.aay9106

Ramphal, P. S., Coore, D. N., Craven, M. P., Forbes, N. F., Newman, S. M., Coye, A. A., et al. (2005). A High Fidelity Tissue-Based Cardiac Surgical Simulator. *Eur. J. Cardio-Thoracic Surg.* 27 (5), 910–916. doi:10.1016/j.ejcts.2004.12.049

Sacks, M. S., and Liao, J. (2018). *Advances in Heart Valve Biomechanics: Valvular Physiology, Mechanobiology, and Bioengineering*. Berlin, Germany: Springer.

Singh, M., Varela, C. E., Whyte, W., Horvath, M. A., Nigel, C. S. T., Ong, C. B., et al. (2021). Minimally Invasive Electroceutical Catheter for Endoluminal Defect Sealing. *Sci. Adv.* 7 (14), eabf6855. doi:10.1126/sciadv.abf6855

Talman, E. A., and Boughner, D. R. (1995). Glutaraldehyde Fixation Alters the Internal Shear Properties of Porcine Aortic Heart Valve Tissue. *Ann. Thorac. Surg.* 60 (2 Suppl. l), S369–S373. doi:10.1016/0003-4975(95)00250-o

Taylor, C. E., and Miller, G. E. (2012). Mock Circulatory Loop Compliance Chamber Employing a Novel Real-Time Control Process. *J. Med. Device* 6 (4), 450031–450038. doi:10.1115/1.4007943

Timms, D., Hayne, M., McNeil, K., and Galbraith, A. (2005). A Complete Mock Circulation Loop for the Evaluation of Left, Right, and Biventricular Assist Devices. *Artif. Organs* 29 (7), 564–572. doi:10.1111/j.1525-1594.2005.29094.x

Urbani, L., Maghsoudlou, P., Milan, A., Menikou, M., Hagen, C. K., Totonelli, G., et al. (2017). Long-term Cryopreservation of Decellularised Oesophagi for Tissue Engineering Clinical Application. *PloS one* 12 (6), e0179341. doi:10.1371/journal.pone.0179341

Villanueva, C., Xiong, J., and Rajput, S. (2020). Simulation-based Surgical Education in Cardiothoracic Training. *ANZ J. Surg.* 90 (6), 978–983. doi:10.1111/ans.15593

Vismara, R., Leopaldi, A. M., Piola, M., Asselta, C., Lemma, M., Antona, C., et al. (2016). *In Vitro* assessment of Mitral Valve Function in Cyclically Pressurized Porcine Hearts. *Med. Eng. Phys.* 38 (4), 346–353. doi:10.1016/j.medengphy.2016.01.007

Wu, Z. J., Gao, B. Z., Slonin, J. H., and Hwang, N. H. C. (1996). Bileaflet Mechanical Heart Valves at Low Cardiac Output. *Asaio J.* 42 (5), M747–M749. doi:10.1097/00002480-199609000-00088

Zhou, J., Fritze, O., Schleicher, M., Wendel, H.-P., Schenke-Layland, K., Harasztosi, C., et al. (2010). Impact of Heart Valve Decellularization on 3-D Ultrastructure, Immunogenicity and Thrombogenicity. *Biomaterials* 31 (9), 2549–2554. doi:10.1016/j.biomaterials.2009.11.088

Conflict of Interest: The authors declare that the research was conducted in the absence of any commercial or financial relationships that could be construed as a potential conflict of interest.

Publisher's Note: All claims expressed in this article are solely those of the authors and do not necessarily represent those of their affiliated organizations, or those of the publisher, the editors and the reviewers. Any product that may be evaluated in this article, or claim that may be made by its manufacturer, is not guaranteed or endorsed by the publisher.

Copyright © 2022 Singh, Park and Roche. This is an open-access article distributed under the terms of the Creative Commons Attribution License (CC BY). The use, distribution or reproduction in other forums is permitted, provided the original author(s) and the copyright owner(s) are credited and that the original publication in this journal is cited, in accordance with accepted academic practice. No use, distribution or reproduction is permitted which does not comply with these terms.

frontiers in Bioengineering and Biotechnology

REVIEW
published: 16 February 2022
doi: 10.3389/fbioe.2022.821852

Decellularized Tissues for Wound Healing: Towards Closing the Gap Between Scaffold Design and Effective Extracellular Matrix Remodeling

Víctor Alfonso Solarte David[1,2], *Viviana Raquel Güiza-Argüello*[3], *Martha L. Arango-Rodríguez*[4], *Claudia L. Sossa*[1,4] *and Silvia M. Becerra-Bayona*[1]*

[1]*Program of Medicine, Faculty of Health Sciences, Universidad Autónoma de Bucaramanga, Bucaramanga, Colombia,* [2]*Program of Biomedical Engineering, Faculty of Engineering, Universidad Autónoma de Bucaramanga, Bucaramanga, Colombia,* [3]*Metallurgical Engineering and Materials Science Department, Faculty of Physicochemical Engineering, Universidad Industrial de Santander, Bucaramanga, Colombia,* [4]*Multi-tissue Bank and Advanced Therapy Center, Fundación Oftalmológica de Santander, Clínica Carlos Ardila Lulle, Floridablanca, Colombia*

OPEN ACCESS

Edited by:
Laura Iop,
University of Padua, Italy

Reviewed by:
Goutam Thakur,
Manipal Institute of Technology, India
Ashley Carson Brown,
North Carolina State University, United States

***Correspondence:**
Silvia M. Becerra-Bayona
sbecerra521@unab.edu.co

Specialty section:
This article was submitted to Biomaterials, a section of the journal Frontiers in Bioengineering and Biotechnology

Received: *24 November 2021*
Accepted: *28 January 2022*
Published: *16 February 2022*

Citation:
Solarte David VA, Güiza-Argüello VR, Arango-Rodríguez ML, Sossa CL and Becerra-Bayona SM (2022) Decellularized Tissues for Wound Healing: Towards Closing the Gap Between Scaffold Design and Effective Extracellular Matrix Remodeling. Front. Bioeng. Biotechnol. 10:821852. doi: 10.3389/fbioe.2022.821852

The absence or damage of a tissue is the main cause of most acute or chronic diseases and are one of the appealing challenges that novel therapeutic alternatives have, in order to recover lost functions through tissue regeneration. Chronic cutaneous lesions are the most frequent cause of wounds, being a massive area of regenerative medicine and tissue engineering to have efforts to develop new bioactive medical products that not only allow an appropriate and rapid healing, but also avoid severe complications such as bacterial infections. In tissue repair and regeneration processes, there are several overlapping stages that involve the synergy of cells, the extracellular matrix (ECM) and biomolecules, which coordinate processes of ECM remodeling as well as cell proliferation and differentiation. Although these three components play a crucial role in the wound healing process, the ECM has the function of acting as a biological platform to permit the correct interaction between them. In particular, ECM is a mixture of crosslinked proteins that contain bioactive domains that cells recognize in order to promote migration, proliferation and differentiation. Currently, tissue engineering has employed several synthetic polymers to design bioactive scaffolds to mimic the native ECM, by combining biopolymers with growth factors including collagen and fibrinogen. Among these, decellularized tissues have been proposed as an alternative for reconstructing cutaneous lesions since they maintain the complex protein conformation, providing the required functional domains for cell differentiation. In this review, we present an in-depth discussion of different natural matrixes recently employed for designing novel therapeutic alternatives for treating cutaneous injuries, and overview some future perspectives in this area.

Keywords: acellular extracellular matrix, wound healing, extracellular matrix proteins, extracellular matrix remodeling, tissue scaffolds, extracellular matrix (ECM)

INTRODUCTION

Tissue engineering involves the use of stem cells, scaffolds and biochemical cues that elicit the cell response required to repair or regenerate specific tissues. Stem cell differentiation is regulated by different biomolecules and mechanical signals that are present in the extracellular microenvironment, known as the extracellular matrix (ECM), including transcription factors and structural proteins produced by cells (Cho et al., 2019). This ECM is being constantly remodeled, depending on the stage of stem cell differentiation: commitment, determination, or maturation. Also, the proteins, glycosaminoglycans and proteoglycans found in the ECM, along with ECM stiffness, activate the intracellular signaling pathways that control cell fate (Hoshiba et al., 2016). Therefore, gaining more insight into the intricate ECM dynamics underlying stem cell behavior may unlock the door to novel and effective strategies to induce specific tissue regeneration.

Human skin is one of the most thoroughly studied organs, due to its vital role as a protective barrier, as well as its unique regenerative properties. In fact, upon injury, distinct and coordinated cell processes start to develop to support skin restoration (Nelson and Bissell, 2006). Particularly, normal wound healing includes four stages: inflammation, re-epithelialization, angiogenesis, and ECM remodeling (Becerra-Bayona et al., 2020). In each of these phases, several types of cells and multiple ECM components and cytokines are essential to properly restore the epidermis and dermis layers (Kim et al., 2018; Tan et al., 2019). For instance, fibroblasts have a relevant role during ECM remodeling by producing collagen and other ECM proteins that allow for dermis maturation (de Mayo et al., 2017). Also, homeostasis and adequate levels of specific proteins are required in each of the wound healing stages to avoid fibrosis and scarring (Dai et al., 2020). When scarring occurs, the conformation of the new skin may differ from that of the native tissue. Similarly, chronic wounds are the consequence of an abnormal healing process in which the healing stages did not take place in the correct order, and one or more stages were not completed. Thus, for cases in which normal skin restoration has been disrupted, several treatment options have been developed to promote and accelerate wound closure (Tracy et al., 2016).

In this sense, several tissue engineering approaches have focused on understanding the effect of scaffold biochemical properties as well as scaffold structure (at the micro and nano levels) on stem cell behavior, towards promoting fast wound closure and, thus, functional skin regeneration (Hoshiba et al., 2016). Specifically, scaffolds provide a microenvironment that resembles that of native tissue (epidermis or dermis), which favors cell migration, angiogenesis, proliferation, differentiation, and ECM production during wound repair (Xu et al., 2021). Nonetheless, advanced alternatives are required when damage to the dermis occurs, since current clinical techniques such as antibiotics, debridement, negative pressure devices, and dressings (de Mayo et al., 2017), fail to provide an effective solution. In this scenario, wound closure is more difficult to achieve, given that the repair process takes place in an asynchronous or discontinuous pattern. This results in ECM instability in the chronic wound, because of the presence of a permanent inflammatory environment and an imbalance between proteolytic enzymes and protease inhibitors, yielding high amounts of matrix metalloproteinases (MMPs) that destroy the regenerated ECM ((Choi et al., 2013). In this context, different skin substitutes for ECM replacement are commercially offered, which are fabricated from autologous, allogenic, and xenogeneic sources (**Table 1**) (Valacchi et al., 2012; Tracy et al., 2016; Goodarzi et al., 2018; Dai et al., 2020). Regarding autografts, their use reduces rejection outcomes, but harvesting is limited and may cause pain and infection in the donor site. For their part, allografts and xenografts can overcome these limitations, but they may lead to immunological rejection and disease transmission (Song et al., 2017)). Consequently, the need to advance existing skin substitutes is compelling, towards developing novel alternatives for engineering biomimetic wound dressings that not only promote skin regeneration through ECM production and cell attachment, but also maintain a moist environment while avoiding inflammatory responses (Kirsner et al., 2015; Kim et al., 2018).

Over the last few decades, decellularized ECM (dECM) obtained from various human and animal tissues has been employed for burn treatment and surgical reconstruction (**Table 1**) (Wainwright, 1995). A growing body of research indicates that dECM guides wound healing progression by coordinating cell phenotype and ECM protein production by, for example, modulating the pro-inflammatory and anti-inflammatory macrophage phenotypes (M1 and M2, respectively), which release cytokines for cell homing and induce tissue remodeling, respectively (Mosser and Edwards, 2008; Rodero and Khosrotehrani, 2010). In this context, Dziki et al. reported that decellularized tissue from small intestinal mucosa, urinary bladder, brain, esophagus, and colon generated M2-macrophage phenotypes, while decellularized dermis promoted M1-macrophage phenotype. On the other hand, the authors showed that ECM derived from skeletal muscle and liver had no remarkable effect on macrophage response (Dziki et al., 2017), demonstrating that dECM effectiveness on acute and chronic wounds depends on its physical, biological, and chemical features, which may differ based on the tissue source and decellularization technique that are used (Milan et al., 2020). Similarly, other authors have reported that dECM influences fibroblast and myofibroblast differentiation by modulating collagen production and induces angiogenesis by promoting endothelial cell migration (Wang et al., 2021a). Therefore, the main goal of this review was to provide a comprehensive analysis of the natural ECM remodeling processes that take place during wound healing, highlighting the importance of the intricate interplay among several ECM elements, without which proper skin regeneration would not be possible. Thus, dECM and dECM-derived scaffolds are discussed as promising tools for the design of skin substitutes that more accurately resemble the biochemical and mechanical complexity of native ECM.

SKIN STRUCTURE AND WOUND HEALING PROCESS

Skin is a vital and complex organ, due to its multifaceted role as a temperature regulator as well as a physical, chemical, and microbiological barrier that protects the host from external

TABLE 1 | Summary of several commercially available treatments for wound regeneration.

Name	Type	Source	Composition	Components relevant to wound healing	References
Epicel	Autograft	Human keratinocytes	Cultured keratinocytes in a fibrin mesh	Not reported	Nathoo et al. (2014)
CellSpray	Autograft	Human keratinocytes	Keratinocytes dispersed in aerosol	Not reported	Nathoo et al. (2014)
Epidex	Autograft	Scalp hair follicles	Cultured keratinocytes on a silicon membrane	Not reported	Dai et al. (2020)
Epifix	Allograft	Human amion and chorion membrane	Basement membrane that contains epithelial cells	Collagen I, collagen III, decorin	Dai et al. (2020)
Alloderm	Allograft	Human cadaveric skin	Decellularized cryopreserved basement membrane	Collagen I, elastin	Nathoo et al. (2014)
dCELL	Allograft	Human cadaveric dermis	Decellularized dermis cryopreserved with glycerol	Collagen I, collagen III, decorin	Elliott et al. (2015)
TransCyte	Allograft	Human newborn fibroblasts	Bilayer graft: 1) nylon mesh coated with porcine dermal collagen, and 2) silicon membrane seeded with fibroblasts	Collagen I, collagen III, collagen V, fibronectin, versican, decorin, tenascin	Noordenbos et al. (1999)
Dermagraft	Allograft	Human living neonatal foreskin fibroblasts	Cultured fibroblasts on a mesh made of polyglycolic acid	Collagen I, collagen III, collagen IV, elastin, decorin	Dai et al. (2020)
StrataGraft	Allograft	Neonatal keratinocytes	Neonatal keratinocytes used to produce a biologically functional stratified epidermis	Collagen I	Schurr et al. (2009)
Apligraft	Allograft	Bovine collagen and neonatal fibroblasts and keratinocytes	Layer of 1) collagen gel with neonatal fibroblast (dermis), and 2) neonatal keratinocytes (epidermis)	Collagen I	Trent and Kirsner, (1998)
OrCel	Allograft	Human neonatal foreskin fibroblasts and keratinocytes	Neonatal foreskin fibroblasts and keratinocytes cultured in bovine collagen sponge	Collagen I	Windsor et al. (2009)
Matriderm	Xenograft	Ligamentum nuchae of cattle	Lyophilized dermis coated with elastin hydrolysate	Collagen I, collagen III, collagen V, elastin	Halim et al. (2010)
Biobrane	Xenograft	Porcine collagen	Bilaminar nylon mesh filled with 1) collagen I, and 2) thin silicone lamina	Collagen I	Alrubaiy and Al-Rubaiy, (2009)
OASIS	Xenograft	Porcine jejunum submucosa	Lyophilized small intestine submucosa	Collagen I, Collagen III, Collagen IV, Collagen VI, fibronectin, elastin, hyaluronan, chondroitin sulfate, decorin	Yeh et al. (2017)
Integra	Xenograft	Bovine collagen and shark chondroitin sulfate	Layer of 1) collagen I from tendon, 2) chondroitine-6-sulfate, and 3) a silicone pseudoepidermis	Collagen I, chondroitin sulfate	Philandrianos et al. (2012)
Nevelia	Xenograft	Bovine collagen	Three-dimensional porous matrix composed of 1) collagen and 2) a semi-permeable silicone membrane	Collagen I	Nicoletti et al. (2018)
Permacol	Xenograft	Porcine dermal tissue matrix	Collagen and elastin crosslinked by diisocyante	Collagen I	Hsu et al. (2009)
Pri-matrix	Xenograft	Fetal bovine dermis	Acellular dermal matrix	Collagen I, collagen III	Sutjarittangtham et al. (2014)

harm (Kanitakis, 2002). In addition, the intricate network of immune cells that resides within this tissue is crucial for host defense and tissue homeostasis (Nguyen and Soulika, 2019). Skin is made up of three layers: epidermis, dermis, and hypodermis (subcutaneous layer). The epidermis is the outermost layer of skin that: 1) prevents microbes, fungi, viruses, toxins, allergens, and irritants from entering the body, 2) absorbs ultraviolet radiation, 3) reduces damage by mechanical forces, and 4) regulates moisture content in the body as well as ion and metabolite loss (Eckhart and Zeeuwen, 2018). Keratinocytes are the most abundant cells in the epidermis (approximately 90%), defining its structure and forming the cornified cell layers that are in direct contact with the environment. The rest of the epidermis is made up of melanocytes, Langerhans cells, and Merkel cells, being the entire cell population distributed throughout several layers, depending on the morphology and biological functions of keratinocytes (Yousef et al., 2021).

The dermis is the mesenchymal component of skin, which is separated from the epidermis by the basement membrane and represents the inner layer of skin between the epidermis and the hypodermis (Rippa et al., 2019). It accounts for approximately 90% of the weight of skin, constituting the foundation of this organ (Nourian Dehkordi et al., 2019). The dermis is a connective tissue composed of ECM, vascular endothelial cells, and fibroblasts, along with adipose glands, sweat glands, hair follicles, blood vessels, and nerve endings. Fibroblasts are the main dermal cell population, and their primary role is to produce collagen and elastin, which confer mechanical strength and elasticity to the skin. Also, the dermis comprises two structurally different layers: the papillary and reticular layers. The papillary layer is located closer to the skin surface and is organized into cords, which are called dermal papillae and contain nerve endings and microvascular vessels that are fundamental for nourishment and innervation. For its part,

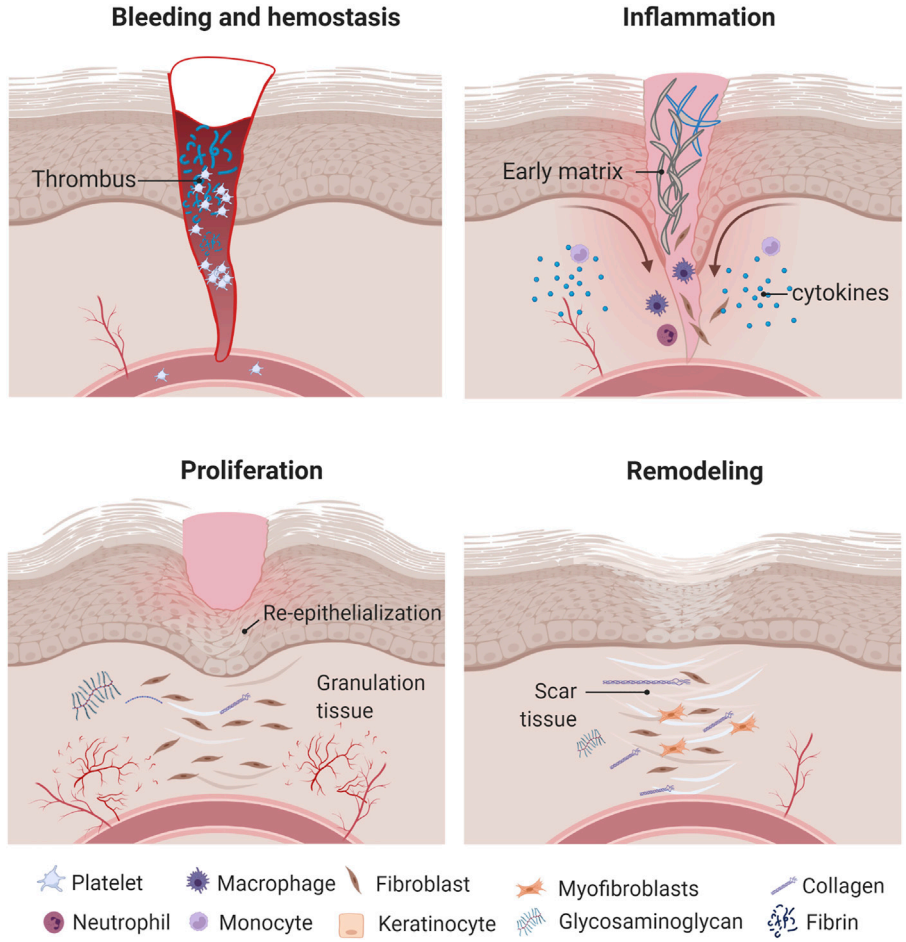

FIGURE 1 | Wound healing process. Once the wound is formed, inflammatory cells produce different cytokines and growth factors that promote cell migration and proliferation as well as ECM formation and remodeling. Created with BioRender.com.

the reticular dermis is separated from the papillary layer by a subpapillary plexus (Rippa et al., 2019). Finally, the hypodermis is the deepest layer of the skin, consisting of loose connective tissue, fat-storing cells, blood vessels, and nerves. This tissue is especially rich in proteoglycans and glycosaminoglycans that support water retention within the tissue (Wong et al., 2016).

Normal Wound Repair Process

Wound healing is a complex and highly regulated biological process that is critical for maintaining the barrier function of skin. It includes four stages that are interrelated and suggest a continuum process: hemostasis, inflammation, proliferation, and remodeling (**Figure 1**). These involve the delivery of different cell types, chemokines, cytokines, growth factors, matrix molecules, and nutrients to the wound site.

Hemostasis Phase

The first response to a skin wound is vasoconstriction of the injured blood vessels to stop the bleeding; this phase lasts 2–3 h. Next, primary and secondary hemostasis occur via two concurrent and mechanistically intertwined pathways (Chaudhry et al., 2021). Primary hemostasis includes platelet adhesion, activation and further aggregation caused by exposure of subendothelial matrix proteins (collagen, von Willebrand factor, and fibronectin), which ultimately results in the formation of a plug at the damaged site. Multiple receptors on the surface of platelets are involved in these adhesive interactions (e.g., GPIb-IX-V, GPVI, and G protein coupled receptors), which are targeted by multiple adhesive proteins (Gale, 2011).

Moreover, secondary hemostasis refers to the activation of the coagulation cascade through which soluble fibrinogen is converted to insoluble strands that make up the fibrin mesh. The platelet plug and the fibrin mesh combine to form the thrombus, which stops the bleeding, release complements and growth factors, and provide a temporary scaffold for cell infiltration during wound healing (Gale, 2011). Secondary hemostasis includes two main coagulation pathways, extrinsic and intrinsic. The extrinsic coagulation pathway occurs when the vascular system is injured and the blood is exposed to extravascular tissues, which are rich in tissue factor (TF), a cofactor for the serine protease factor VIIa (Kirchhofer and Nemerson, 1996). The TF and factor VIIa complex activate

factor X and factor IX. Factor IXa also activates factor X, in the presence of its cofactor, factor VIIIa. Likewise, in the presence of its cofactor, factor Va, factor Xa then activates prothrombin to generate thrombin (Dahlbäck, 2000). Thrombin is the central serine protease in the coagulation cascade, playing a critical role in several reactions (Lane et al., 2005). For instance, thrombin cleaves fibrinogen to generate insoluble fibrin, triggers platelets via cleavage of PAR1 and PAR4 (Kahn et al., 1998), and is also responsible for positive feedback activation of coagulation, which is essential for clot propagation. Furthermore, the intrinsic coagulation pathway takes place when thrombin activates cofactors VIII and V, and factor XI, which then activates factor IX (Lane et al., 2005).

Similar to the coagulation cascade, fibrinolysis is tightly controlled by a series of cofactors, inhibitors and receptors (Collen and Lijnen, 1995). The role of the fibrinolytic system is to dissolve blood clots during wound healing and to prevent blood clot formation in healthy blood vessels (Gale, 2011). The fibrinolytic system is primarily composed of three serine proteases that are present as zymogens in the blood. Plasmin is the primary fibrinolysin and is activated from plasminogen by either of two primary serine proteases: tissue-type plasminogen activator (tPA), or urokinase-type plasminogen activator (uPA) (Chapin and Hajjar, 2015). Whereas tPA is synthesized and released by endothelial cells, uPA is produced by monocytes, macrophages, and urinary epithelium. Both activators have an exceedingly short circulation half-life (4–8 min) due to the presence of high concentrations of specific inhibitors, or serpins, which are also important to prevent excess amounts of unregulated activator (Travis and Salvesen, 1983). The most important serpins in fibrinolysis are plasminogen activator inhibitor-1 (PAI-1), plasminogen activator inhibitor-2 (PAI-2), and α2-antiplasmin (A2AP). When plasmin is bound to fibrin, however, it is protected from A2AP inhibition, allowing for fibrinolysis to proceed (Schneider and Nesheim, 2004). Other non-serpin plasmin inhibitors include α2-macroglobulin, C1-esterase inhibitor, and members of the contact pathway of the coagulation cascade, which also play minor roles in plasmin inhibition. Thrombin-activatable fibrinolysis inhibitor (TAFI) is a non-serpin attenuator that is activated by thrombomodulin-associated thrombin. TAFI is a carboxypeptidase that removes C-terminal lysine and arginine residues on fibrin, thereby decreasing the number of available plasminogen binding sites, slowing plasmin generation, and stabilizing clots (Broze and Higuchi, 1996).

Inflammation Phase

The inflammatory phase mainly involves the activation of the innate immune system so that neutrophils and monocytes rapidly migrate to the injury site. This phase in wound healing starts shortly after hemostasis is achieved and can last from hours to days in acute wounds, while in chronic wounds it can last for weeks or even months, because of the effects of the underlying disease. The primary goal of the inflammatory phase is to clear pathogens as well as foreign material from the wound and to contain the damage to a localized area (Wynn and Barron, 2010). Vascular permeability increases with vasodilation, allowing neutrophils and monocytes to identify the wound site (Han and Ceilley, 2017). A complex interplay of cytokines recruit neutrophils and monocytes to the wound area, culminating in monocyte conversion to macrophages, often thought of as the master regulator of this inflammatory phase of wound healing. Macrophages not only engulf and digest tissue debris and remaining neutrophils, but also secrete growth factors and cytokines that promote tissue proliferation and cell migration (Wallace et al., 2021).

Proliferation Phase

About 3 days after injury has occurred, the proliferative phase centers around fibroblasts and their production of collagen as well as the ground substance that will form the foundation of the tissue scaffold in the wound area. Meanwhile, endothelial cells initiate a rapid growth phase and angiogenesis occurs within the granulation tissue, creating a rich vascular network for the healing zone. The proliferative phase can last several weeks and is characterized by the formation of granulation tissue, re-epithelialization, and neovascularization. During this phase, fibroblasts start to lay down new collagen and glycosaminoglycans, which form the core of the wound and help stabilize it. Then, re-epithelialization starts with the migration of cells from the wound periphery and adjacent edges. Initially, only a thin superficial layer of epithelial cells is laid down, but a thicker and more durable layer of cells will bridge the wound over time (Rodrigues et al., 2019).

On the other hand, endothelial cell and fibroblast proliferation and migration support angiogenesis and new ECM formation, respectively. As the new ECM is reconstructed, the old matrix is degraded by proteases (MMPs). MMPs promote autolytic debridement and cell migration into wounds. The level of MMPs in wounds increases after tissue damage and decreases with remission of inflammation. Epithelial cells migrate from the edge of the wound, initiating epithelialization. Keratinocyte differentiation helps restore the barrier function of the epidermis. Next, neovascularization occurs through angiogenesis and vasculogenesis, which refer to the formation of new blood vessels from existing vessels and endothelial progenitor cells (EPCs), respectively. Once collagen fibers have been laid down on the fibrin framework, the wound starts to mature and contract, being the latter process supported by the continued deposition of fibroblasts and myofibroblasts (Wallace et al., 2021).

Remodeling Phase

The maturation or remodeling phase starts around week 3 and can last up to 12 months. Eventually, an eschar (scab) forms on the surface of the wound (Monavarian et al., 2019). During this phase, the ECM is constantly being reconstructed by myofibroblasts, and wound contraction is induced by the dense network of collagen microfilaments. At the same time, new components are secreted to increase matrix density and stability (Landén et al., 2016). Furthermore, the proportion of different types of collagens begins to change, as type I collagen proportion increases (80–90%), while collagen III proportion decreases (10–20%). The excess collagen degrades, and wound

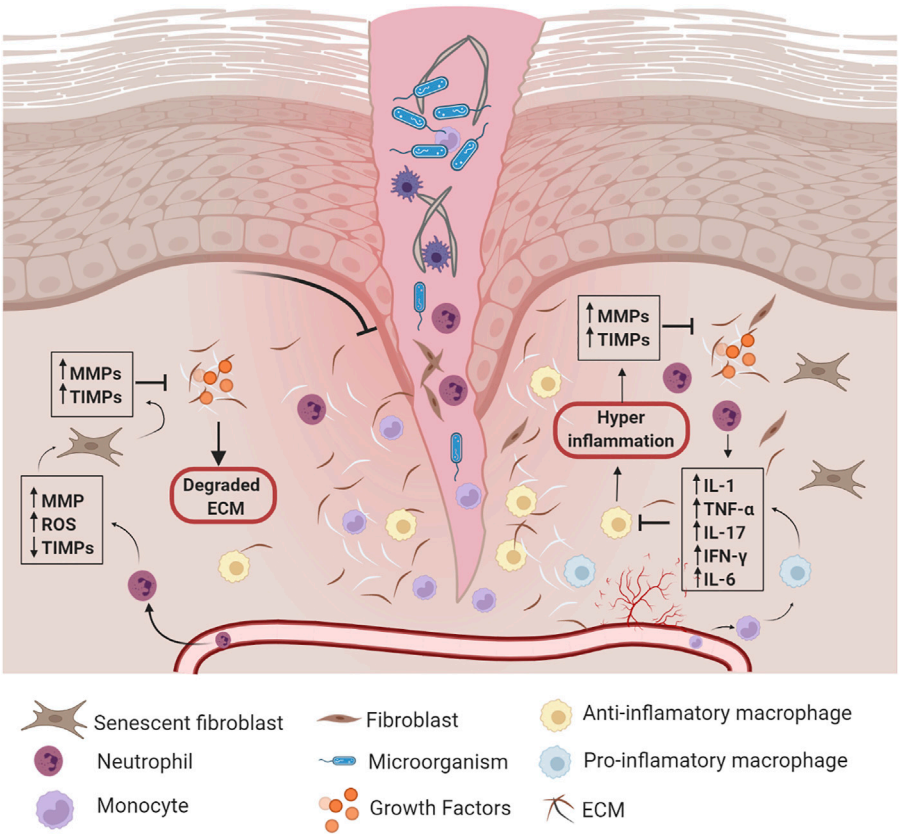

FIGURE 2 | Chronic wound healing. Once the wound is formed, synergy among hemostasis, inflammation, proliferation, and remodeling phases are disrupted by different underlying pathological mechanisms. *Abbreviations: MMPs: Matrix Metalloproteinases, TIMPs: Tissue Inhibitors of Metalloproteinases, ROS: Reactive Oxygen Species, ECM: extracellular matrix, IL-1: Interleukin-1, TNF-α: Tumor Necrosis Factor-Alpha, IL-17: Interleukin-17, IFN-γ: Interferon Gamma, IL-6: Interleukin-6.* Created with BioRender.com.

contraction also begins to peak at around week 3. Finally, after approximately 2–3 weeks, the wound transitions to a remodeling or maturation stage, in which collagen I levels are fully restored and the wound tissue matures, resulting in full cross-linking and restoration of a somewhat normal structure (Xue and Jackson, 2015). In addition to this, apoptosis reduces the density of myofibroblasts, creating room for fibroblasts, which further increases ECM mechanical resistance (Landén et al., 2016). Wound contraction occurs to a much greater extent during secondary healing, relative to the primary healing phase. The maximal tensile strength of the wound area is achieved after about 11–14 weeks, although it never fully reaches its normal, pre-injury mechanical state (only about 80% of the original tissue's tensile strength is recovered) (Bowden et al., 2016).

Chronic Wound Healing

Chronic wounds develop when normal wound healing is delayed or disrupted by different underlying pathological mechanisms, such as continuous inflammation, persistent infections, and necrosis (Raziyeva et al., 2021). Besides, chronic wounds are associated with the impairment of the following processes: growth factor production, angiogenic response, macrophage differentiation, collagen production, epidermal barrier function, granulation tissue formation, keratinocyte and fibroblast migration/proliferation, and bone healing (osteomyelitis has been reported as a predictor of inadequate wound healing and amputation (Burgess et al., 2021)). Compared with normal wound healing, chronic wounds are characterized by changes in the healing phases, as follows: 1) during hemostasis, the hypercoagulability and the decrease in fibrinolysis are altered (Erem et al., 2005); 2) during the inflammatory stage, there is an imbalance of inflammatory cytokines such as interleukin (IL)-1 (IL1), IL6, tumor necrosis factor-alpha (TNF-α), and interferon gamma (IFN-γ), as well as several growth factors, such as platelet derived growth factor (PDGF), epidermal growth factor (EGF), and insulin-like growth factor 1 (IGF-1) (Pradhan et al., 2009); 3) fibroblast and keratinocyte migration and proliferation are diminished; and 4) an imbalance between the accumulation of ECM components and their remodeling by MMPs (Brem and Tomic-Canic, 2007) (**Figure 2**). Decreased cell migration results in deficient re-epithelialization of the chronic wound (Chen et al., 2016), which contributes to defective wound closure and decreased angiogenesis. All of these alterations affect the remodeling phase of wound healing (Santoro and Gaudino, 2005).

THE ROLE OF EXTRACELLULAR MATRIX IN WOUND HEALING

Wound healing begins with a temporary ECM, which is mainly composed of fibrin, plasma fibronectin (FN), vitronectin, and platelets (Chester and Brown, 2017). FN is synthesized as a soluble form by hepatocytes, and it plays an important role in the early phase of wound healing (hemostasis), as it binds to platelets and fibrin, thereby increasing the strength of the fibrin clot (To and Midwood, 2011). As early as 2 days after injury, macrophages increase FN mRNA expression; similarly, granulation tissue fibroblasts begin to express FN proteins at about 7 days after injury (Barker and Engler, 2017). FN is a multidomain glycoprotein with a self-assembled domain that allows FN dimers to interact, producing a three-dimensional (3D) matrix through a process termed fibrillogenesis (Mao and Schwarzbauer, 2005). Given that FN has different binding conditions to different matrix proteins such as heparin, syndecan, and proteoglycans, it facilitates gradual protein and cell assembly within the matrix as healing progresses (Mao and Schwarzbauer, 2005). To mediate cell assembly, FN dimers bind to transmembrane integrin receptors, such as α5β1, while integrins link FN to the actin cytoskeleton through cytoplasmic domain interactions with cytoskeletal proteins (Wu, 1997; Wierzbicka-Patynowski and Schwarzbauer, 2003).

Another important protein in the ECM remodeling is tenascin-C, which is primarily produced by keratinocytes. This matrix protein binds to many extracellular elements, such as soluble factors, matrix proteins, and cells (through interactions with surface receptors) (Midwood et al., 2016). The expression of tenascin is a hallmark of inflammation, and it is present in areas with increased immune cell infiltration during the acute inflammation phase. Along with polymorphonuclear lymphocytes, tenascin is located at the inflamed human dermis, stimulating migration and activation of immune cells (Midwood et al., 2016). Tenascin-C stimulates the production of pro-inflammatory cytokines (TNF-α, IL6, and IL8) in macrophages and fibroblasts by activation of Toll-like receptor 4-mediated signaling pathways (Midwood et al., 2009). Moreover, tenascin-C is also found in new granulation tissue, promoting fibroblast migration and tissue reconstruction; however, its expression decreases at the end of the healing process, indicating that its activity is temporary (Mackie et al., 1988; Midwood et al., 2016).

As wound healing progresses, the role of collagen becomes more important during re-epithelialization, granulation tissue formation, and neovascularization. When granulation tissue formation starts, fibroblasts migrate and produce fibrillar collagen, which ends up replacing most of the temporary fibrin matrix (Bainbridge, 2013). Collagen I can induce keratinocyte migration, which initiates re-epithelialization, as well as keratinocyte secretion of MMPs that allow matrix remodeling (Guo et al., 1990). The appearance of collagen coincides with the early onset of vessel formation, since, for instance, collagens I and III contain von Willebrand factor (vWF) domains that have been shown to regulate bone morphogenetic protein, which promotes blood vessel morphogenesis (Manon-Jensen et al., 2016). Collagen V also has vWF domains, but in this case, this collagen has shown a relevant role in modulating fibroblast migration-proliferation and tissue contraction (Berendsen et al., 2006; Manon-Jensen et al., 2016). During the initial stages of healing, other types of collagens are also found, such as type VI, which has been shown to modulate macrophage adhesion in the healing site (Schnoor et al., 2008), as well as support ECM architecture during ECM deposition (Oono et al., 1993).

On the other hand, collagen VII, plays a role in fibroblast and keratinocyte migration, as its absence has been demonstrated to delay granulation tissue formation and re-epithelialization (Nyström et al., 2013). Collagen VII is the major component of anchoring fibrils at the dermal-epidermal junction, and thus, when it is not present in normal amounts, the skin's resistance to frictional forces is reduced, which can be evidenced as skin blistering (Kiritsi and Nyström, 2018). Moreover, other types of collagens, such as type IV, are the structural foundation for all basement membranes and can be detected in the newly formed tissue after 8–21 days (Cosgrove and Liu, 2017). Collagen IV and laminin self-assemble into two independent supramolecular networks that are linked to nidogen and perlecan to form a morphological discernable basement membrane basal lamina (Mak and Mei, 2017).

Moreover, transmembrane collagen XVII is a highly dynamic modulator of *in vivo* proliferation and motility in activated keratinocytes during epidermal regeneration and is also involved in the anchorage of the epidermis to the underlying basement membrane (Löffek et al., 2014). Collagen XVII is an important part of the hemidesmosomal transmembrane component, modulating integrin-dependent keratinocyte migration via PI3K/Rac1 signaling, through stabilization of the lamellipodia at the leading edge of re-epithelializing wounds (Löffek et al., 2014). Collagen XVII is abundantly secreted in keratinocytes during re-epithelialization of acute wounds and its absence appears to lead to altered cell motility in the wound (Löffek et al., 2014). On the other hand, overexpression of collagen XVIII negatively affects wound healing, since it slows skin repair, inhibits vascularization, as well as decreases myofibroblast density (Seppinen et al., 2008). Thus, collagen regulation is essential for normal wound healing (Rousselle et al., 2019).

Furthermore, as wound healing progresses, other proteins become involved in the process. That is the case of laminin (LM). This matrix protein is a major constituent of the basement membrane separating the epithelium, mesothelium, and endothelium from connective tissue, and although there are 15 different types of LMs, only some have been fully identified during the healing process, such as LM511, LM521 and LM332. At the beginning of the epithelialization process, within hours of injury, LM332 is expressed by epidermal keratinocytes, inducing their migration. It should be noted that LM332 appears to be the first base membrane component laid down onto the wound bed, as its early expression precedes that of all other ECM components (Laplante et al., 2001). A LM322 domain such as LG45 plays a major role in regulating mechanisms underlying keratinocyte and ECM remodeling

during wound repair. LG45 induces expression of the MMP-9 pro-enzyme, which together with MMP-14, exert proteolytic activity within epithelial podosomes, allowing cell scaffolding (Michopoulou et al., 2020). Moreover, LG45-derived peptides have antimicrobial activity and chemotactic activity in mononuclear cells, suggesting that this domain may also participate in host defense (Senyürek et al., 2014). On the other hand, LM511 and LM521 have been found to be related to epidermal regeneration; their expression and deposition on the base membrane increase after re-epithelialization is completed, and they have been suggested to be key factors in promoting keratinocyte differentiation as well (Pouliot et al., 2002; Sugawara et al., 2008).

In addition to this, during late stages of healing, perlecan or heparan sulfate proteoglycan 2 (HSPG2), is an essential protein for basement membrane assembly. It has a connective function, as it aids in creating molecular bridges that fit with cellular interactions (Hohenester and Yurchenco, 2013), orchestrating the binding and signaling of mitogens and morphogens to cells in a temporal and dynamic fashion (Lord et al., 2018). Perlecan acts as a reservoir for heparin-binding growth factors that accelerate keratinocyte migration and skin wound healing (Shirakata et al., 2005). Among other features, the degradation of perlecan during wound healing allows for a rapid introduction of mitogens and trophic factors that modulate the regenerative processes (Lord et al., 2018). Also, perlecan is located along with LM332 at the wound margin of full thickness wounds, which appears to indicate that it is closely related to base membrane remodeling (Yurchenco, 2015); thus, it has been suggested that perlecan plays a role in keratinocyte survival and terminal differentiation (Sher et al., 2006; Whitelock et al., 2008). Nidogens are another family of proteins involved in base membrane restoration, as they work as connecting bridges for other proteins, such as LM, heparan sulfate, proteoglycan and collagen IV (Aumailley et al., 1993), which provide the mechanical reinforcement required to maintain the cytoarchitecture of the skin (Breitkreutz et al., 2009).

On the other hand, structural proteins are abundantly expressed in response to injury. This is the case of thrombospondin (TSP), a protein produced by fibroblasts that can also be found in platelet α-granules (Kyriakides and Maclauchlan, 2009; Rousselle et al., 2019). TSP1 and TSP2 are crucial for developmental angiogenesis; however, while TSP1 is early induced in wound healing and participates in the activation of latent transforming growth factor beta 1 (TGF-β1), TSP2 expression occurs after resolution of the inflammatory phase and during granulation tissue remodeling. Moreover, TSP2 plays a key role in the controlled release of vascular endothelial growth factor (VEGF), as well as MMP-2 and MMP-9 during ECM remodeling (Maclauchlan et al., 2009). Similarly, osteopontin is a structural chemokine-like protein that acts as part of an intracellular signaling complex, taking a role in the formation of fibrous tissue (Icer and Gezmen-Karadag, 2018). It behaves as a cytokine, for example, as fibroblast chemoattractant, and it appears to be essential for fibroblast deposition of ECM components and collagen (Fujisawa et al., 2020), thus, playing a synergistic role with TSP (Rousselle et al., 2019).

For its part, osteonectin, also known as secreted protein acidic and rich in cysteine (SPARC), is a protein secreted by various types of cells, such as fibroblasts, endothelial cells, and platelets (Bradshaw and Sage, 2001), and its expression reaches the highest level during remodeling of the dermal ECM. SPARC participates in the regulation of cell adhesion, proliferation and matrix turnover, modulating the activity of growth factors and ECM, sequestering or releasing these factors according to the dynamic remodeling of the matrix (Motamed, 1999). Also, its mechanism of action is given by interconnection of different matrix proteins, including thrombospondin 1, vitronectin, entactin/nidogen, fibrillar collagens (types I, II, III, and V), and collagen IV, which allow for matrix reticulation (Brekken and Sage, 2000). Specifically, SPARC binds to PDGF and VEGF and decreases their mitogenic potency, due in part by its abrogation of growth factor–receptor interaction (Yan and Sage, 1999). In addition to PDGF, VEGF, and bFGF (basic fibroblast growth factor), SPARC can also modulate the activity of TGF-β, as seen in recent studies with SPARC-null mesangial cells, which allows it to regulate cell migration and differentiation during epithelialization in wound healing (Brekken and Sage, 2000).

Once wound closure is achieved, keratinocytes undergo stratification and differentiation to restore the natural barrier provided by the skin. Nevertheless, successful skin regeneration relies on the coordination of growth factors, cytokines, and chemokines, which must act in synergy with cells to modulate their behavior through specific cell surface receptors or ECM proteins (Davison-Kotler et al., 2019). It is important to note here that, although we have discussed a set of relevant proteins, there are additional proteins that are similarly involved in wound healing regulation.

DECELLULARIZED EXTRACELLULAR MATRIX

Tissue engineering and regenerative medicine involve the use of different synthetic and natural materials, which are frequently combined to produce composite scaffolds. In terms of natural materials, dECM from autologous or allogenic sources appears to be one of the most promising types of scaffolds (Porzionato et al., 2018), which can be used either alone or in combination with other biological components for preclinical and clinical applications. For implantation procedures, tissue decellularization is required to avoid the immune reaction and inflammation response that could be induced by the cells in the source tissue, which otherwise may cause implant rejection (Mendibil et al., 2020). ECM decellularization allows for the obtention of cell-free matrices with low immunogenicity, in which several bioactive components from the natural ECM are preserved, such as structural and specialized proteins, proteoglycans, collagen, elastin, and hyaluronic acid, as well as growth factors (Mendibil et al., 2020).

Decellularized ECM can be sourced from native organs from different species to provide the biological cues needed for cell homing (Badylak et al., 2009). Nevertheless, xenogeneic tissues may carry residual immunogenicity and be contaminated with

TABLE 2 | Summary of several available methods for tissue decellularization.

Method	Main characteristics	Disadvantages	Decellularized tissues	Ref
Chemical Methods				
		(i) Collagen and glycosaminoglycans (GAGs) damage		(Ott et al., 2008)
Acid—base	Cell membrane solubilization	(ii) Insufficient cell removal	Rat heart	(Syed et al., 2014)
Peracetic acid	Disruption of cytoplasmic components and nucleic acids by utilizing charges	(iii) Increased ECM stiffness	Small intestine submucosa	Gilpin and Yang, (2017)
Ethylenediaminetetra-acetic acid (EDTA)		(iv) Decreases salt- and acid-soluble ECM proteins	Urinary bladder	
Reversible alkaline swelling		(v) Alters mechanical properties		
Triton X (100 or 200)	Disruption of lipid–lipid and lipid–protein unions, while leaving protein interactions	(i) Not recommended for ECM when lipids and GAGs are important components		(Wagner et al., 2014); Rieder et al. (2004)
	Very effective in some tissues	(ii) Limited potential by immunogenicity *in vivo*	Normal and emphysematous human lungs	
	Less damaging to tissue structures than ionic surfactants	(iii) Triton X-200 needs to be combined with a zwitterionic detergent to be effective	Porcine heart valves	
		(iv) Triton X-200 damages the matrix similar to SDS		
Sodium dodecyl sulfate (SDS)	Liquefaction of internal and external cell membranes	Tends to denaturalize proteins and induce nuclear and cytoplasmic waste in the remaining matrix (i) Cytotoxic: requires extensive washing steps	Rat forearm	(Yang et al., 2015); (Gilpin and Yang, 2017); Wang et al. (2010)
		(ii) Alters microstructure (i.e., collagen fibers)	Porcine tissues (cornea, myocardium, heart valve, small intestine, kidney) Human vein, lungs and heart	
Witterionic, nondenaturing detergent, 3-[(3-cholamidopropyl) dimethylammonio]-1-propanesulfonate (CHAPS)	Properties of ionic and nonionic detergents	(i) Similar damage as Triton X-100	Human and porcine-derived lung tissues	(Gilpin and Yang, 2017); O'Neill et al. (2013)
	Maintenance of structural ECM proteins and ultrastructure	(ii) Remanent cytoplasmic proteins	Rat lungs	
Tributyl phosphate (TBP)	Destructor of protein structures Disruption of protein–protein interactions	Variable results, leads to collagen degradation but keeping the mechanical properties	Equine flexor tendons, ligaments and articular cartilage	(Deeken et al., 2011); Elder et al. (2009)
Hypertonic and hypotonic solutions	Solutions with a higher/lower solute concentration than that in cells Cell lysis, cell dehydration and cell death because of their osmotic pressure	High amount of cell waste in the remaining matrix	Bovine vessel nerve, small intestinal and submucosa	(Zhang et al., 2022); Kim et al. (2016)
Enzymatic Methods				
Trypsin	Digestion of membrane proteins leading to cell dead Commonly used with EDTA	(i) Can damage the proteins in the ECM, in particular laminin and GAGs (ii) Breaks cell-matrix adhesions	Porcine pulmonary valves and trachea	Giraldo-Gomez et al. (2016)
Pepsin	It targets peptide bonds	Causes high damage in the ECM proteins if left for long periods of time	Porcine lung and liver	(Pouliot et al., 2020); Coronado et al. (2017)
nuclease	Hydrolysis of DNA and RNA	Further cleaning and enzyme removal is required, as they may promote immune response	Bovine osteochondral plugs, human corneal limbus and porcine dermis	(Greco et al., 2015); Fermor et al. (2015)
Physical Methods				
Thermal shock (freeze-thaw cycle)	Disruption of tissue and organ cells	(i) The freeze-thaw cycle causes a small degradation in the structure of the ECM, due to the crystal shape that may damage the scaffold, with little effect on the mechanical properties of ECM	Tendon fragments (large), fibroblast sheets, lumbar vertebrae cells, kidneys, lungs and adipose tissues	(Rabbani et al., 2021); Zhao et al. (2019)

(Continued on following page)

TABLE 2 | (*Continued*) Summary of several available methods for tissue decellularization.

Method	Main characteristics	Disadvantages	Decellularized tissues	Ref
	Frozen water crystals occupy the volume inside the cell and cause the membrane to burst	(ii) The heat shock cycle alone is not capable of removing sensitive cellular components		
Force	Mechanical pressure can be enough to induce cell lysis	(i) Limited to tissues with hard structures, as it can damage the ECM structure (ii) The amount of required force must be precise since both the underlying structure and membrane attachment are vulnerable to any kind of direct mechanical stress	Liver, lung	Gilpin and Yang, (2017)
Immersion and agitation	It is commonly used to facilitate chemical agent infiltration to induce cell lysis The immersion time and intensity of agitation depend on the thickness and density of the tissue	Aggressive processes, such as sonication, can damage the ECM.	Submucosal substrate, laryngeal and intestine tissues	Keane et al. (2015)
Vacuum-assisted decellularization (VAD)	VAD would accelerate and improve the delivery and efficiency of detergents into the deepest parts of the tissue Removal of detergents from a decellularized tissue is the other application of the VAD methodology	It is not a decellularization method but a facilitator	Porcine tracheal specimen and fresh porcine costal cartilage	Alizadeh et al. (2019)
Hydrostatic pressure (water is sprayed with pressure on the target tissue)	Application of high pressure (>600 MPa) to the tissue and induction of cell lysis	(i) Excessive pressure can damage the structure (ii) The formation of ice crystals caused by the presence of water may damage the ECM structure (iii) Increasing the temperature during the process may suppress the creation of the ice crystals, but may increase the entropy and lead to the ECM vulnerability (iv) Residue of DNA fragments (v) Denatures ECM proteins	Porcine retinal specimen, porcine artery, porcine meniscus and rat uterine	Rabbani et al. (2021)
Nonthermal irreversible electroporation	Microsecond electrical pulses are applied throughout a tissue, causing micropores in the cell membrane	The relatively small electrodes that limit the size of the tissue for decellularization	Carotid arteries of rat, liver of porcine and myocardial muscle tissue	Rabbani et al. (2021)
Ultrasonic waves (sonication)	High-power waves are capable of disrupting intermolecular bonds, disrupting the cell membrane, and removing its internal components	The physical phenomenon of cavitation during the process is unavoidable, but uncontrolled cavitation can severely damage the structure and mechanical properties of the tissue	Aortic tissues, small intestine, cartilage tissue and meniscus	Forouzesh et al. (2019)
Pressure gradient	Induction of a pressure gradient can help the enzyme-mediated decellularization method	To be determined	Embryonic veins, tendon, and aortic tissue	Sierad et al. (2015)
Supercritical fluid	Removal of cell debris. It is used in combination with detergents Reduction of the detrimental effect on the ECM mechanical properties	To be determined	Porcine pericardium, aorta and retinal tissues	Guler et al. (2017)
Perfusion	The organ is completely separated from its main blood vessel and the chemical agents are injected into its vascular system after being washed with detergents	(i) The required pressure to drive the agent along the vascular system can cause the capillaries and small vessels to tea (ii) The flow rate control is crucial	Heart muscle, lung, liver, kidney, pancreas, small intestine, skeletal muscle, coronary artery	Tajima et al. (2020)

biological agents. For these reasons, human allogeneic or autologous tissues are the ideal dECM source material, being also suitable for recellularization and implantation (Duda et al., 1999). In addition, human tissues/organs may be obtained from surgery or cadavers, and the resulting dECM may be crosslinked to improve its mechanical properties (Yang et al., 2020; Xu et al., 2021). In fact, the use of dECM from human tissues and organs such as cartilage (hyalin, articular, meniscal, laryngeal, tracheal, and nasoseptal), pericardium, blood vessels, corneas, bone, lung, and nerve have been previously reported (Tao et al., 2021).

In terms of decellularization techniques, a variety of approaches have been studied, which include chemical, physical, and biological treatments, as well as their combinations (Hoshiba et al., 2016; Crapo et al., 2011) (**Table 2**). Specifically, some common decellularization methods are: 1) chemical treatments (i.e., sodium dodecyl sulfate (SDS), sodium lauryl sulfate, ethylenedimine tetraacetic acid (EDTA), Triton X-100, and Tris-HCl); 2) enzymatic treatments, (DNases and RNases), which are frequently used and combined in multistep procedures, although some residual DNA may remain at the end of the treatment; 3) physical methods; 4) osmotic treatments; 5) tissue mechanical fragmentation (or pulverization); and 6) freeze/thaw cycles, which enable pore formation upon ice crystal formation within the tissue (Porzionato et al., 2018). The advantages and limitations of decellularization procedures have been previously discussed (Dussoyer et al., 2020), indicating that the abovementioned techniques can yield decellularized materials that maintain ECM composition levels similar to those of the source tissue, in addition to tissue architecture and 3D organization (Schenke-Layland and Nerem, 2011). In fact, acceptable dECM products can have residual amounts of DNA (up to 50 ng DNA per mg dry weight), preserve around 75% of the collagen component of the native ECM, and maintain natural ECM structure (Hsieh et al., 2020).

Several authors have proposed the use of ECM synthesized during *in vitro* culture of primary cells, known as cell-derived ECMs (CD-ECMs) (Ha et al., 2020; Savitri et al., 2020). Among the advantages of this approach are the maintenance of the ECM architecture and its availability depending on the desired cell-line products, as well as the reduction in immunogenic response and infectious disease transmission. Similarly, some studies have demonstrated the secretion of different cytokines and growth factors by mesenchymal stem cells (MSCs) when cultured *in vitro*, such as bFGF, IGF-1 and VEGF, which are critical proteins for re-epithelialization and angiogenesis induction during wound healing (de Mayo et al., 2017; Becerra-Bayona et al., 2020). Although CD-ECMs may contain specific target biomolecules, they offer limited ability for tuning matrix properties to mimic those of native ECM. In contrast, dECM can be used in varying configurations (dressings, substitutes, powders and fillers), while closely resembling different aspects of natural ECM, such as mechanical properties, microstructure and composition, as evidenced by the content of key molecules: collagens (types I, II, III, IV, V, VI, VII, XIV), proteoglycans, fibrin, FN, vitronectin, versican, tenascin-C and growth factors (Tracy et al., 2016). In the context of diabetic foot ulcer treatments, dECM scaffolds act as a physiological reservoir of growth factors and cytokines that are involved in wound repair, providing signaling molecules that other treatments fail to supply, and improving cell migration and proliferation (Choi et al., 2013; Xu et al., 2021). In particular, decellularization of porcine small intestinal submucosa and urinary bladder matrix are among the most frequently used sources to recover native ECM. Therefore, various studies have reported the potential use of dECM-derived scaffolds as promising therapies for chronic wound healing (**Table 3**).

Decellularized Extracellular Matrix Used as Membranes

Acellular Dermal Matrices

Acellular dermal matrices (ADMs) are considered artificial dermal substitutes that have been clinically utilized for treating chronic wounds, which are acellular full-thickness sections taken from donors, especially human cadavers or bovine/porcine skin, which are assessed for the presence of HIV, hepatitis, and syphilis (Dussoyer et al., 2020), and provide molecules that enhance cell attachment and neovascularization in wound surface repair (Wu et al., 2008). These features are usually enhanced by adding specific biological components to guide distinct cell responses within ADMs. For instance, Hsieh et al. optimized the decellularization of porcine skin with a formic acid treatment, and the resulted ADM was processed with pepsin to obtain hydrogels through pH and temperature control of the gelation process. These hydrogels were mixed with sacchachitin due to its chemotactic effect on inflammatory cells. The composite hydrogels promoted wound healing in full-thickness defects in rats after 14 days by facilitating angiogenesis, granulation tissue formation, and collagen deposition (Hsieh et al., 2020).

Similarly, the inclusion of exogenous hyaluronic acid (HA), which is commonly lost during decellularization, has shown the potential to modulate the production of collagen I and collagen III during ECM remodeling in wound healing (Zhao et al., 2013). In this sense, Zhoe et al. used a rabbit full-thickness wound model to observe the effect of HA-modified ADMs vs ADMs alone, showing that the former not only reduced scar formation and graft contraction because of its greater elasticity and anti-inflammatory properties, but also stimulated the expression of CD44 receptors, leading to a higher number of capillaries, compared to the ADM group. This may explain the therapeutic effects of HA on wound healing (Zhao et al., 2013). These findings are supported by the regulation of mRNA expression of cytokines during the inflammation phase, specifically, the downregulation of IL-1β and TGF-β1 as well as the upregulation of bFGF (Alemzadeh et al., 2020). In fact, overexpression of TGF-β1 may influence myofibroblast differentiation and cause prolonged acute inflammatory response, leading to excessive matrix deposition and exaggerated scar tissue formation (Jackson et al., 2012). That said, adequate coordination and progression of the phases in wound healing may be supported by the introduction of target motifs into ADMs.

Although it has been demonstrated that biologically modified ADMs have a more intensive action in skin repair, they inherently

TABLE 3 | Natural decellularized matrices for wound healing applications.

Decellularized source	Added molecules	Type of scaffold	*In vitro* studies	*In vivo* model	Time of *in vivo* studies	*In vivo* outcomes	Ref
Porcine dermis	HA	Dermal matrix	Not conducted	Rabbit full-thickness wounds	58 days	Contraction rate ↓ Collagen type I and III expression ↑ Vascularization ↑	Zhao et al. (2013)
Sheep dermis	HA and ADSCs	Dermal matrix used as covering dressing	Cell viability	Rat burns	4 weeks	Inflammation ↓ Angiogenesis ↑ Granulation tissue formation ↑ Wound closure ↑	Alemzadeh et al. (2020)
Mouse dermis	Chitosan	Membrane	Biostability Proliferation	Murine full-thickness wounds	28 days	Angiogenesis ↑	Lin et al. (2020)
	MSCs		Cell viability Cell adhesion			Wound closure ↑ MSC retention ↑	
Rat dermis		Hydrogel		Rat full-thickness wounds	21 days	Angiogenesis ↑ Collagen deposition ↓ Wound closure ↑	Bankoti et al. (2020)
	Chitosan Carbon nanodots		Cell migration Antibacterial properties				
	MSCs		Cell viability			Re-epithelialization ↑ Epidermal junction formation ↑	
Porcine skin	Saccha-chitin	Hydrogel	Cell viability	Rat full-thickness wounds	14 days	Hair follicle growth ↑ Sweat gland formation ↑ Wound closure ↑ Collagen deposition ↑ Neovascularization ↑	Hsieh et al. (2020)
Porcine skin	None	Porous crosslinked membrane	Cell viability Cell adhesion	Rabbit full-thickness wounds	15 days	Wound closure ↑ Inflammation ↓ Fibroblast migration ↑ Epidermal layer thickness ↓ Collagen organization ↑	Wang et al. (2021b)
Porcine dermis	None	Crosslinked dermal matrix	Not conducted	Rat full-thickness wounds	90 days	Protease expression ↑ Cellular and vascular infiltration ↓ Time of regeneration ↑	Carlson et al. (2013)
Porcine dermis		Crosslinked dermal matrix	Cell viability Enzymatic degradation	Rat full-thickness wounds	3 weeks	Degradation rate ↓ Antibacterial effect ↑	Chen et al. (2019)
	Chitosan						
	Silver nano-particles		Silver degradation Antibacterial properties			Wound closure ↑	
Porcine dermis	Quercetin	Crosslinked Membrane	Biostability Antibacterial properties	Rat full-thickness wounds	3 weeks	Wound closure ↑	Wang et al. (2020a)
	Tea tree oil		Cell viability			Re-epithelialization ↑	
Porcine tissue		Porous crosslinked membrane	Cell viability Degradation Antibacterial properties	Not conducted	-	-	34,339,783
	Gelatin Chitosan						
Goat small intestine submucosa	Curcumin	Crosslinked membrane	Degradation Free radical scavenging tests Cell viability Hemo-compatibility assays	Not conducted	-	-	Singh et al. (2022)
Porcine urinary bladder		Membrane	Not conducted	Rat burns	28 days	ECM deposition ↑ Granulation tissue formation ↑ Inflammation ↓	Paramasivam et al. (2021)
	pDNA-PDGF						

(Continued on following page)

TABLE 3 | (*Continued*) Natural decellularized matrices for wound healing applications.

Decellularized source	Added molecules	Type of scaffold	*In vitro* studies	*In vivo* model	Time of *in vivo* studies	*In vivo* outcomes	Ref
	rBMSCs					Angiogenesis ↑ Wound closure ↑	
Porcine lung	None	Membrane	Not conducted	Rat-sub-cutaneous implantation	6 weeks	Cell infiltration ↑ Vascularization ↑	Fernandez-Moure et al. (2016)
Porcine adipose tissue	None	Hydrogel	Adipo-genesis Fibroblast migration	Murine full-thickness wounds	14 days	Fibroblast migration ↑ Wound closing ↑ Epithelialization ↑	Tan et al. (2019)
Human Adipose tissue	ADSCs	Hydrogel	Cell Viability Cell proliferation Angiogenic cytokines assay	Murine full-thickness wounds	14 days	Angiogenesis ↑ Wound closure ↑ Angiogenesis ↑ Skin appendages ↑ Dermis thickness ↑	Chen et al. (2021)
Rat heart tissue	PLCL	Nano-fibrous membrane	Cell proliferation Cell adhesion	Rat full-thickness wounds	3 weeks	Angiogenesis ↑ Scarring ↓ Granulation tissue ↑ Macrophage action ↑	Kim et al. (2018)
Equine pericardium	None	Crosslinked matrix	Not conducted	Murine full-thickness wounds	2 weeks	Re-epithelialization ↑ Wound closure ↑ Collagen deposition ↑ Biofilm formation ↓	El Masry et al. (2019)
Human placenta	None	Membrane	Not conducted	Rat Full-thickness wounds	4 weeks	Restoration of epidermis and dermis ↑ Wound closure ↑ Contraction rate ↓ Vascularization ↑	Choi et al. (2013)
Human umbilical cord Wharton's jelly	None	Gelatinous material	Cell migration Cell viability	Murine full-thickness wounds	7 days	Wound length ↓ Cell migration ↑ Cell differentiation ↑	Bakhtyar et al. (2017)
Human placenta, umbilical cord and amniotic membrane	None	Hydrogel	Cell migration Cell proliferation Tube formation assay	Murine full-thickness wounds	14 days	Wound closure ↑ Skin appendage formation ↑ Pro-inflammatory gene expression ↓ Pro-angiogenic gene expression ↑	Wang et al. (2021a)
Human Amnion	PRP	Membrane	Not conducted	Mouse burns	7 days	Epidermis differentiation ↑ Keratinocyte proliferation ↑ Wound contraction ↓ Vascularization ↑	Kshersagar et al. (2018)
Human amniotic membrane	None	Membrane	Not conducted	Rat full-thickness wound	8 months	Wound inflammation ↓ Skin regeneration ↑ Scar formation ↓	Song et al. (2017)
Human amniotic membrane	Silk fibroin	Electro-spun Membrane	Cell viability Cell adhesion	Rabbit full-thickness ear wounds	50 days	Collagen deposition ↑ MMP1 deposition ↓ Scarring ↓	Gholipourmalekabadi et al. (2019)
Human amniotic membrane	None	Membrane	Cell viability	Mouse burns	15 days	Granulation tissue formation ↑ Angiogenesis ↑ Collagen maturation ↑	Milan et al. (2020)
Amniotic membrane	Fibrin HA	Membrane	Cell Adhesion Cell proliferation	Rabbit full-thickness burns	28 days	Epithelialization ↑ Angiogenesis ↑ Skin appendage formation ↑	Ramakrishnan et al. (2020)
Human Amniotic membrane	HWJMSCs	Membrane	Cell Viability	Rat burns	14 days	Re-epithelialization ↑ Granulation tissue formation ↑ Inflammation ↓	Hashemi et al. (2020)

(Continued on following page)

TABLE 3 | (*Continued*) Natural decellularized matrices for wound healing applications.

Decellularized source	Added molecules	Type of scaffold	*In vitro* studies	*In vivo* model	Time of *in vivo* studies	*In vivo* outcomes	Ref
Human amniotic membrane	None	Porous crosslinked membrane	Not conducted	Rat full-thickness wounds	21 days	Density of epidermal basal cells ↑ Length density of blood vessels ↑ Collagen deposition ↑ Gene expression related to regeneration ↑ Wound closure ↑	Nasiry et al. (2021)
Human amniotic membrane	Poly (1,8-octanediolco-citrate)	Membrane	Not conducted	Rat full-thickness muscle and back defects Rat liver injury Rat tibia defect	2 weeks	Foreign body reaction ↓ Inflammation ↓ Fibrosis ↓	Wang et al. (2020b)
Human amniotic membrane	Zinc oxide nano-particles derived from HAM proteins	Crosslinked Membrane	Antibacterial Assays	Not conducted	-	-	Ramasamy et al. (2021)
Bovine amniotic membrane	Chitosan	Sponge-like crosslinked membrane	Cell Adhesion Cell proliferation Blood coagulation test Cell viability	Murine full-thickness wounds	14 days	Wound closure ↑ Granulation tissue formation ↑ Angiogenesis ↑ Fibroblast infiltration ↑ Sebaceous gland and hair follicle formation ↑	Yang et al. (2020)

AbbreviationsHA: hyaluronic acid; PRP: platelet rich plasma; PLCL: poly (L-lactide-co-caprolactone); ADSC: adipose derived stem cells; HWJMSCs: Human Wharton's Jelly Mesenchymal Stem Cells; hSFs: Human Skin Fibroblasts; HAM: human amniotic membrane; PDGF: Platelet-derived Growth Factor; rBMSCs: Transfected Mesenchymal Stem Cells; ECM: extracellular matrix.

lack mechanical properties and have low resistance to enzymatic degradation, which limit their widespread use in the treatment of chronic wounds (Fernandez-Moure et al., 2016; Chen et al., 2019). The most common method to improve ADM mechanical strength is matrix crosslinking (Hu et al., 2013; Wang et al., 2021b; Xu et al., 2021), which may increase the time of tissue reconstruction, but provides longer-term structural integrity, thus, diminishing wound recurrence rate. In this context, Carlson et al. compared the expression of key genes involved in tissue regeneration when non-crosslinked human dermis and crosslinked porcine ADM were utilized to manage full-thickness wounds generated on rats (Carlson et al., 2013). The authors found that the crosslinked ADMs increased the expression of proteolytic enzymes (MMP-9 and CCL12) and lowered the ECM remodeling rate since cellular and vascular infiltration were reduced, relative to non-crosslinked ADMs.

Likewise, Chen at al. worked with naturally derived oxidized chitosan oligosaccharide (OCO), a biocompatible crosslinker, for the fixation of collagen on porcine ADMs through the formation of intra- and intermolecular bonds (Chen et al., 2019). Also, silver nanoparticles were loaded into the matrices to evaluate their antibacterial effect *in vitro,* prior to full-thickness wound studies in rats. The data established that OCO-crosslinked ADMs loaded with silver nanoparticles facilitated a more robust formation of the epidermis and granulation tissue, in comparison to the control, as shown by the higher expression of relevant factors for wound repair (bFGF, VEGF and PDGF). Similarly, other studies have demonstrated the advantage of combining natural antibacterial agents with ADMs, due to their low resistance to infection; besides, some crosslinking substances may reduce ADM biocompatibility and cause cytotoxicity (Zhu et al., 2016). To overcome these limitations, propolis and plant extracts, such as quercetin (QCT) and tea tree oil (TTO), have been proposed as alternative crosslinking agents that also provide antimicrobial properties (Sutjarittangtham et al., 2014). Specifically, TTO extracted from Melaleuca alternifolia is recognized by its antimicrobial activity (Reichling et al., 2006), while QCT has been reported to increase the tensile strength of porcine ADMs about three times, relative to pure ADM (Wang et al., 2020a). Their combined use for treating full-thickness wounds revealed accelerated wound repair due to the increase of re-epithelialization and wound closure rate. Therefore, crosslinking of ADMs may be required to produce wound dressings with superior mechanical strength and stability to ensure desired performance.

Acellular Decellularized Extracellular Matrix From Different Sources

Decellularized ECM-based scaffolds can be fabricated from various tissues and organs. For instance, porcine small intestine (SI) and urinary bladder (UB) are commercially used for skin reconstruction (OASIS, **Table 1**) (Paramasivam et al.,

2021), although novel approaches are being studied to enhance biomolecule diversity within dECMs. The availability of cytokines, pro- and anti-inflammatory molecules as well as pro-angiogenic factors is crucial for properly guiding the four phases of normal skin regeneration. Therefore, among other tissues, heart-derived matrices are attractive since they preserve key molecules for wound healing, such as collagen, elastin, fibrillin, FN, and pro-angiogenic factors (ANG-1, ANG-3, CCN1, FGF-1, FGF-2, leptin, MMP-9, NOV, SDF-1, and VEGF-β) (Seif-Naraghi et al., 2010; Kim et al., 2018). Masry et al. evaluated the role of equine pericardial collagen matrix (PCM) on wound healing progression, using a murine full-thickness model (El Masry et al., 2019). After 2 weeks, wound closure, re-epithelialization and collagen deposition increased compared to the control.

Moreover, PCMs induced and recruited phagocytic cells (macrophages) that lead to fibroblast differentiation into myofibroblasts, which produced collagen I to improve the tensile strength of the repaired skin, indicating an increase in the collagen type I:III ratio that supports formation of vascularized granulation tissue (Hurme et al., 1991; Tomasek et al., 2002). Indeed, the presence of Ang-1 in heart-derived dECM enhances both, blood vessel maturation and M2-macrophage phenotype differentiation, as reported by Kim et al., who assessed the influence of hybrid nanofibrous membranes fabricated by electrospinning of poly (L-lactide-co-caprolactone) (PLCL) and rat heart dECM on rat full-thickness wound healing (Kim et al., 2018). The *in vitro* experiments confirmed the potential of the engineered membrane to produce huvec proliferation and angiogenesis. Also, the authors found denser vessel formation in the rats treated with the hybrid scaffolds, relative to the pure PLCL membranes. The results showed higher number of vessels positive for v-WF and alpha smooth muscle actin (α-SMA) factors, suggesting the capacity of heart-derived dECM to promote vasculogenesis and maturation of new vessels.

Furthermore, other promising sources for dECM production for wound healing applications are lung or adipose tissue-derived matrices (Fernandez-Moure et al., 2016; Tan et al., 2019; Chen et al., 2021). Acellular lung ECM (ALM) contains an association of collagen fibers along with a well-defined vascular architecture, which balance inflammatory response and support cell adhesion (Nichols et al., 2013). Fernandez-Moure et al. compared the ability of ADM vs ALM to stimulate angiogenesis and cellularization (Fernandez-Moure et al., 2016). Towards this, the ADM and ALM were subcutaneously implanted in rats, and after 6 weeks, much higher cell infiltration and vascularization were revealed in the ALM group, relative to the ADM treatment. Particularly, ALM-treated wounds displayed a higher number of infiltrated cells (1,663 ± 228 cells vs. 350 ± 230 cells per 500 μm^2, respectively), as well as vessel ingrowth (57 ± 13 vessels vs. 9 ± 5 vessels per 1 mm^2, respectively), compared to the ADM group. In the case of adipose tissue-derived matrices, adipogenesis is essential for wound healing progression, since adipose stem cells (ADSCs) produce various molecules that act as modulators in skin regeneration (Horsley and Watt, 2017; Plikus et al., 2017).

For instance, fibroblast migration increased when exposed to media obtained from adipocyte cultures, suggesting that adipocyte-secreted molecules may contribute to re-epithelialization and ECM remodeling during wound healing (Tan et al., 2019). Tan et al. examined the repair efficiency of adipose-derived dECM (ADECM) hydrogels with and without ADSCs in a murine full-thickness wound model. They found that both fibroblast migration and wound closing and epithelialization were more pronounced in the ADSC-loaded hydrogels, relative to their ADSC-free counterparts (Tan et al., 2019). Moreover, the data showed *in situ* induction of adipogenesis, which was evidenced by ADSC survival and higher number of adipocytes in the ADSC-loaded hydrogel treated group. Also, the results suggested a positive impact of ADSC-loaded ADCM hydrogels on skin appendage formation, such as hair follicle growth and blood vessel formation, data supported by increased VEGF expression by adipocytes. The paracrine activity of ADSCs was further investigated by Chen et al. by utilizing ADECM-derived hydrogels for delivering human ADSCs on murine full-thickness wounds (Chen et al., 2021). *In vitro* studies of ADSCs cultured on ADECM hydrogels showed significant secretion of angiogenic factors, including HGF (hepatocyte growth factor), VEGF, ANG (angiopoietin) and ANG-2, relative to ADSCs cultured on plastic surfaces. In addition to this, murine wounds had a faster closure rate and enhanced neovascularization when treated with ADSC-loaded ADECM hydrogels, compared to ADSC administration. Cumulatively, the results from using heart and adipose tissue-derived dECM indicate that their inherent architecture and biochemistry provide a favorable microenvironment for skin repair, which may be reinforced by incorporating ADSCs into the matrix.

Moreover, the role of specific pro-angiogenic factors (for example, VEGF, bFGF and PDGF) in the enhancement of the angiogenic response during wound healing has been elucidated. Nonetheless, their use is limited because of their short half-life, low availability, and high cost (Ehrbar et al., 2008). Thus, new engineered matrices modified with recombinant DNA, known as gene-activated matrices (GAMs), have been designed to include specific gene sequences of desirable growth factors to ensure their adequate expression (Pannier and Shea, 2004). In this context, taking advantage of the pro-angiogenic factor content in dECMs along with MSC regenerative properties, some genes have been introduced into dECMs to administer stem cells on impaired wounds, towards attaining an enhanced effect. For instance, Paramasivam et al. fabricated porcine UB with PDGF gene plasmid (Group C) or transfected MSCs with PDGF gene plasmid to embed them into UB dECMs (Group E) (Paramasivam et al., 2021). After 28 days of treating rat burns with the above approaches, acceleration of ECM deposition, granulation tissue formation, as well as angiogenesis and wound closure were observed in Group E, relative to Group C. These results may be explained by the chemo attractant action of PDGF over fibroblast migration and proliferation (Deuel et al., 1991). Similarly, PDGF may induce VEGF expression that leads to increased new vessel formation. Indeed, the authors reported higher VEGF expression and increased fibroblast proliferation in group E relative to Group C, which may have favored ECM

deposition and vessel formation. Altogether, these findings indicate that dECM native features may be enhanced by combining them with stem cells and engineered DNA plasmids that promote relevant growth factor synthesis for controlled wound healing.

Acellular Decellularized Extracellular Matrix From Perinatal-Related Tissues

Perinatal tissues, such as placenta, umbilical cord, chorion, and amniotic membrane are associated with fetal development and discarded after birth. These tissues are appealing for wound healing applications because of their high content of molecules involved in skin regeneration. Notably, the human placenta ECM contains endogenous growth factors that provide a favorable niche for the proliferation and differentiation of cells, modulating injury repair (Choi et al., 2013). Similarly, a few studies have reported the application of Wharton's jelly (WJ) for skin healing. WJ is a gelatinous substance that contains MSCs within a matrix that is mainly composed by collagen and HA, which secrete several molecules that may have an effect in diverse biological processes. In fact, many studies have reported the regeneration potential of both WJ-MSCs and their secretome by accelerating wound closure (Kamolz et al., 2014; Doi et al., 2016). In addition, the amniotic membrane, the inner layer of the placenta membrane that has a thickness between 0.02—5 mm and is composed of three layers (epithelial, basement and connective layers) (Zare-Bidaki et al., 2017; Milan et al., 2020), preserves a number of growth factors that participate in the progression of wound repair (Gholipourmalekabadi et al., 2016; Gholipourmalekabadi et al., 2019).

Acellular Decellularized Extracellular Matrix From Placenta and Wharton's Jelly

The human placenta provides oxygen and nutrients to the fetus during pregnancy and eliminates waste products from its blood system. Decellularized placenta consists of various structural and adhesion proteins such as collagen (I, IV, VII, and XVII), elastin, LM, as well as proteoglycans, which serve as reservoir for many growth factors, including IGF, EGF, PDGF, FGF, VEGF and TGF-β (Choi et al., 2013; Singh et al., 2022). When dECM obtained from human placenta was used to treat rat full-thickness wounds, a well-structured basement membrane was deposited, and an increase in keratinocyte proliferation and differentiation was observed, which led to new epithelial tissue architecture that was very similar to original skin (Choi et al., 2013). Choi et al. produced dECM sheets from human placenta and observed adequate integration with the host's wound tissue, in addition to superior expression of basal and epidermis layer markers (keratin 15 and loricrin), relative to the control (Choi et al., 2013).

Similarly, Wang et al. explored the effect of placenta-derived dECM (PL-dECM) hydrogels vs umbilical cord- and amniotic membrane-derived dECM (UC-dECM and AM-dECM, respectively) hydrogels in murine full-thickness wounds (Wang et al., 2021a). The results revealed different glycosaminoglycan content in each of the perinatal tissues, suggesting a distinct effect of each of the hydrogels on wound healing. In fact, PL-dECM hydrogels displayed a more potent effect on wound closure and skin appendage formation, compared to the other hydrogels. In particular, IL10 and TGF-β expression were upregulated, while IL6 and TNF-α expression were downregulated, which are anti- and pro-inflammatory cytokines, respectively. Also, M1-like macrophage differentiation was induced towards M2-macrophage phenotype by reducing the expression of iNOS and rising the expression of CD206 (M1 and M2 macrophage markers, respectively), relative to the other hydrogel formulations. In addition, PL-dECM hydrogels produced a better pro-angiogenic effect by enhancing expression of VEGF, ANG-1, FGF-2, and PDGF. In another study, Bakhtyar et al. employed WJ-dECM gels to better understand the role of some peptide growth factors that may accumulate in the WJ; for instance, IGF, FGF and TGF-β (Edmondson et al., 2003; Shalitin et al., 2003; Yu et al., 2003). After utilizing these dECM gels for treating murine full-thickness wounds for 7 days, the authors noticed the role of WJ-dECM on myofibroblast differentiation, diminishing wound healing time. Specifically, α-SMA expression (a myofibroblast marker) was higher in WJ-dECM treated groups vs the control, after 5 days of treatment (Bakhtyar et al., 2017), which suggested that WJ induced faster fibroblast differentiation toward myofibroblasts. In this context, components of PL- and WJ-dECMs play a role in inflammation, angiogenesis, and remodeling phases of wound healing, which may be employed to regulate specific responses to enhance restoration of impaired wounds.

Acellular Decellularized Extracellular Matrix From Amniotic Membrane

Due to its intrinsic regenerative properties, amniotic membrane (AM) is a promising tissue source for dECM therapeutic applications. During wound healing, decellularized human AM (dHAM) has been shown to modulate each of the healing stages by reducing inflammation, accelerating epithelialization, and preventing infection (Yuan et al., 2015). The observed restorative action of dHAM may be attributed, among other aspects, to its physical characteristics (e.g., durability, elasticity, permeability) and its ability to appropriately retain several growth factors. There are crucial components of dHAM that produce an anti-inflammatory and pro-angiogenic effect, being the most prominent factors EGF, KGF (keratinocyte growth factor), HGF, NGF (nerve growth factor), bFGF and TGF-β (Koob et al., 2015; Yuan et al., 2015; Milan et al., 2020). In this sense, Song et al. treated rat full-thickness wounds with dHAM and followed up on wound evolution for 8 months, observing a decrease in inflammation and scar formation (Song et al., 2017). These results were supported by the detected alterations of some growth factors; specifically, VEGF and α-SMA secretion were higher in dHAM-covered wounds, while TGF-β1 expression was reduced, in comparison to the control.

Likewise, when dHAM was used to cover mouse burns for 15 days, Milan et al. reported lower number of inflammatory cells as well as higher number of blood vessels, skin appendixes and collagen fibers on the granulation tissue of the dHAM group,

relative to the control (Milan et al., 2020). In addition to applying pure dHAM, other authors have suggested the introduction of cells or other biological molecules to enhance the dHAM healing effect (Kshersagar et al., 2018; Hashemi et al., 2020; Ramakrishnan et al., 2020). For example, Hashemi et al. took advantage of the ability of MSCs to produce paracrine factors that accelerate injury repair (de Mayo et al., 2017) and explored the influence of dHAM combined with MSCs on rat burn repair (Hashemi et al., 2020). After 14 days of treatment, the data revealed significant differences in inflammation, re-epithelialization, and granulation tissue formation between rats treated with MSC-containing dHAM vs the group exposed to dHAM alone. Moreover, in the case of using exogenous factors, Kshersagar et al. proposed loading dHAM with platelet-rich plasma (PRP), since PRP contains several cytokines and growth factors (such as IFN-α, IL1, IL6, IL8, PDGF) that may alleviate inflammation during wound healing (Kshersagar et al., 2018). In a mouse burn model, the authors found that the PRP-loaded dHAM exhibited an enhancing effect on epidermis differentiation, keratinocyte proliferation, as well as wound contraction and vascularization. Collectively, these findings demonstrate the favorable microenvironment induced by dHAM for skin repair, while other studies have also reported dHAM ability to regulate the regeneration of other types of tissue injuries (Wang et al., 2020b).

Despite these promising results, dAM dressings have poor mechanical properties and lack long-term stability, which remains a concern for wound healing applications. Nevertheless, several studies have overcome these disadvantages by creating composite scaffolds (Gholipourmalekabadi et al., 2019; Yang et al., 2020; Nasiry et al., 2021). For instance, Yang et al. designed a bovine dAM-derived composite by utilizing a precursor and a crosslinking agent (chitosan and poly-ethylene glycol diglycidyl ether, respectively) to obtain a sponge-like membrane (CS-BAM) (Yang et al., 2020). The CS-BAM sponge exhibited stronger mechanical properties compared to the control and led to accelerated wound healing by simultaneously decreasing inflammation and increasing collagen deposition and skin appendix formation. Similarly, Gholipourmalekabadi et al. proposed the fabrication of a membrane composed of dHAM and electrospun silk fibroin (SF) to assess its efficacy on rabbit full-thickness ear wounds (Gholipourmalekabadi et al., 2019). They observed that the SF/HAM membrane modulated hypertrophic scar formation by reducing the expression of collagen I and upregulating the production of enzymes that participate in ECM remodeling. These results indicate that the balance between the synthesis of new ECM and ECM remodeling is crucial to avoid hypertrophic scar tissue formation.

In this context, Nasiry et al. suggested the use of a microporous crosslinked dHAM (MC-HAM) towards controlling ECM density during wound healing and avoiding limited cell migration and penetration into the site (Niknejad et al., 2008). The authors reported that healed rat full-thickness wounds improved their mechanical properties relative to the diabetic group; specifically, tensile strength, bending stiffness and energy absorption. In addition, after 21 days of MC-HAM scaffold engrafting, the number of neutrophils and macrophages significantly decreased, while the length density of blood vessels increased, data that was supported by the downregulation of pro-inflammatory factors (TNF-α and IL-1β) and the upregulation of pro-angiogenic genes (TGF-β, bFGF and VEGF). Cumulatively, this indicates that the fabrication of wound dressings derived from dHAM and exogenous cues that favor scaffold biostability and mechanical response, may be beneficial for properly guiding wound healing.

Decellularized Extracellular Matrix Powders for Tissue Specific Regeneration Applications

ECM decellularization techniques are proving increasingly effective for the development of materials that can provide the biological stimuli present in the natural cell microenvironment, without the undesired risks associated with the use of xenogeneic or allogenic tissues. In this sense, the fabrication of tissue-specific scaffolds with biochemical and mechanical properties that more closely resemble the complexity of the native ECM has been one of the main research areas of focus (Storstein, 1989; Morris et al., 2018; Zahiri et al., 2018; Dongen et al., 2019; Ahmed et al., 2020; Hoang Thi et al., 2020; Park et al., 2020; Ventura et al., 2020; Liguori et al., 2021). Moreover, as the need to implement advanced manufacturing approaches such as 3D printing progressively becomes more compelling, enormous research efforts are being made to incorporate dECM into the design of functional bioinks to produce therapeutic alternatives for customized tissue regeneration applications.

Fabrication of Scaffolds for Tissue Regeneration

Recently, in the context of cardiovascular regeneration applications, Aquinas and coworkers explored the use of hydrogels derived from porcine cardiac dECM as material platforms for the controlled delivery of trophic factors produced by human ADSCs (Liguori et al., 2021). ADSCs were cultured for 48 h and the resulting conditioned medium was collected and further concentrated as follows: 20X, 200X, and 2000X. These concentrates were added to pepsin-digested dECM solutions as a 1/20 of the final volume to yield hydrogel precursors loaded with 1X, 10X, and 100X trophic factors, respectively. The release kinetics of seven pro-regenerative factors as well as four pro-inflammatory factors was studied for 5 days, revealing that the fabricated hydrogels provided a sustained release pattern over time. Nonetheless, it was also observed that pro-inflammatory factors were more abundantly released as the concentration of the conditioned medium in the hydrogel increased, which suggested that trophic factor binding kinetics within the hydrogel were affected by the concentration of the ADSC-derived conditioned medium.

In terms of wound healing applications, Van Dongen et al. prepared dECM from the adipose tissue of diabetic and non-diabetic human donors, and upon dECM digestion with pepsin, ADSC-conditioned culture medium was incorporated to create bioactive hydrogels for wound healing (Dongen et al., 2019). Taking advantage of the fact that ADSCs abundantly produce

paracrine factors that influence ECM remodeling, the authors intended to explore the potential of the fabricated hydrogels to absorb and release these factors for the repair of fibroblast monolayers *in vitro*. Results indicated that the proposed hydrogels promoted fibroblast proliferation and migration, in addition to angiogenesis. Moreover, although no significant differences in terms of biological activity were found between the hydrogels from diabetic and non-diabetic origin, the latter exhibited greater mechanical stability and thus, proved to be more appropriate for clinical applications. In this way, the authors demonstrated the potential of ECM-derived hydrogels for the controlled delivery of allogenic paracrine factors and cytokines that provide biochemical support in wound repair processes.

Similarly, Jeon et al. developed a composite hydrogel from recombinant mussel adhesive proteins (MAP) and poly (N-isopropylacrylamide) (PNIPAM) for soft tissue regeneration applications (Jeon et al., 2020). Their goal was to harness the adhesive properties of MAP as well as the thermoresponsive nature of PNIPAM, a polymer that can undergo sol-gel transitions at physiological temperature, to create an injectable tissue-adhesive implant for the delivery of ADSCs and biochemical factors from decellularized adipose tissue (DAT) of human origin. Results from their *in vivo* tests indicated that the incorporation of DAT powder (5 wt%) into the hydrogel precursor significantly increased adipogenesis and vascularization, even in the absence of exogenous induction factors. Moreover, cumulative characterization data of the MAP-PNIPAM hydrogel alone proved its potential to be combined with other types of dECM powders for the delivery of tissue-specific biochemical stimuli.

Furthermore, Kuna and coworkers reported the development of a composite hydrogel system for skin regeneration, based on decellularized pig skin powder from galactose-α1,3-galactose knockout pigs, which was combined with HA ("PSG" sample) (Kuna et al., 2017). An additional formulation was prepared by adding human peripheral blood mononuclear cells (hPBMCs), to evaluate their effect on wound revascularization ("PSG-hPBMCs" sample). These two materials were tested *in vivo* for 25 days, including a pure HA control, using immuno-compromised mice with full-thickness skin wounds. The results indicated that, after 15 days of treatment, full wound closure was achieved in 66% of the mice treated with PSG and in 83% of the mice treated with PSG-hPBMCs, as opposed to the 0% observed for the HA controls. Nonetheless, at the end-point of the experiments (day 25), all mice displayed healed wounds, with some scarring observed in the HA control group. Moreover, enhanced wound healing and revascularization were attained in the PSG-hPBMCs group, as confirmed by CD31 staining. Thus, this composite hydrogel system proved its potential to be used as an autologous scaffold for successful skin tissue regeneration, without the need to incorporate stem cells, which are much harder to harvest in large numbers than PBMCs.

Moreover, regarding lung tissue repair, de Hilster and coworkers studied the fabrication of ECM-derived hydrogels from healthy and diseased human lung tissue (de Hilster et al., 2020). Tissue samples were decellularized following lyophilization and grinding to obtain an ECM powder, which was then enzymatically digested and gelled at 37°C. Stiffness measurements of the prepared hydrogels appeared to be within close range of those of their native tissue counterparts, although the viscoelastic response of the fabricated scaffolds was different from the corresponding tissue samples, since the latter exhibited less stress relaxation. Nonetheless, given that native lung tissue undergoes significant mechanical conditioning, these results revealed the possibility of creating ECM-derived scaffolds that provide biochemical and mechanical stimuli that mimic those naturally found in lung tissue, without the cell material that could trigger undesired immunological responses.

Finally, the development of effective ECM decellularization techniques has also a promising outlook for the advancement of therapeutic approaches in cartilage tissue engineering. For instance, the recent work conducted by Bordbar et al. addressed the evaluation and characterization of dECM hydrogels produced from sheep knee cartilage (Bordbar et al., 2020). Upon dECM digestion with pepsin and further neutralization, rabbit-derived mesenchymal stem cells (MSCs) were either encapsulated or seeded onto the resulting bioactive hydrogels, which were obtained by thermal gelation at 37°C. The experimental data showed that the proposed materials not only supported MSC adhesion and viability in 2D, but also promoted MSC proliferation and differentiation into chondrocytes in a 3D context. Along with this, the rheological properties of the hydrogel precursor indicated that the devised material could be successfully employed as an injectable hydrogel in minimally invasive therapies.

Design of Bio-Inks for Tissue Engineering and Disease Modeling

The use of dECM powder for tissue repair approaches has also extended to the additive manufacturing field, and thus, the development of bio-inks for 3D bioprinting. This technique allows for the fabrication of structures with highly controlled morphological features, which favors the ability to mimic the intricate architecture of native tissue as well as supports the advancement of customized tissue engineering therapies. Although widely used materials such as polyethylene glycol, alginate, and gelatin have been successfully used for the preparation of biocompatible inks (Ouyang et al., 2016; Ying et al., 2018), the incorporation of biochemical cues naturally found in the ECM is essential for guided tissue regeneration. In this sense, the ideal bio-ink should yield scaffolds that provide a 3D environment with biochemical and mechanical properties that resemble those of the target native tissue.

For instance, Kim and coworkers studied the fabrication of a bio-ink in which dECM powder from porcine liver was dispersed as microparticles (<100 μm) into a precursor mixture that contained gelatin, HA and fibrinogen (Kim et al., 2020). Prior to printing, the gelatin component was gelled at low temperatures, and once printing was completed, the bio-ink was further crosslinked by addition of thrombin. The resulting material was compared with a bio-ink counterpart prepared by the traditional method, in which the dECM powder was digested using pepsin, followed by printing and curing at 37°C.

Characterization of all printed constructs revealed that the proposed bio-ink produced structures whose elastic modulus was up to 9.17 times higher than that of the material obtained with the traditional bio-ink, in addition to yielding much more consistent pore size and shape during the printing of 13 layers.

Furthermore, a lot of research efforts have been recently put into gaining a deeper understanding of the influence of several dECM processing variables on the material properties of the final bio-ink. For example, Zhao and coworkers evaluated the effect of dECM digestion time on the mechanical and biological properties of bio-inks prepared in the absence of any additional matrix materials (Zhao et al., 2020). To this end, powdered decellularized porcine tendon was subjected to different digestion times (3, 12, and 72 h) in acidic pepsin solution. At each time point, the pH of the solution was adjusted to 7.4, followed by rheological characterization. Furthermore, printability of the prepared inks was assessed by measuring extrudability, shape fidelity and layer stacking accuracy, using optical microscopy and digital imaging techniques. The authors were able to demonstrate that partially digested dECM (3 h) yielded an ink precursor with desirable viscosity and printability, as well as higher construct reproducibility up to 30 layers, relative to the ink obtained after 72 h of digestion. All of this was achieved while maintaining the viability levels of bone marrow MSCs above 85%. Finally, it was also demonstrated that the bioprinted scaffolds supported significant MSC differentiation towards tendon tissue, as evidenced by COL1A1, EGR1, TNC, and TNMD PCR analysis.

Later, Zhao et al. also studied the impact of the type of dECM digestion solution on the mechanical properties and cytocompatibility of hydrogels produced from tendon dECM derived bio-inks (Zhao et al., 2021). They examined three different acidic solutions for the preparation of pepsin-based digestion solutions: 0.5 M acetic acid, 0.1 M HCl and 0.02 M HCl. Upon neutralization of the dECM solutions, bio-ink precursors were obtained. The osmotic pressure of the bio-ink from the acetic acid solution could not be adjusted to physiological levels, which in turn translated into high cytotoxicity, as evidenced by viability tests conducted on encapsulated bone marrow MSCs, prior to 3D printing. Moreover, the authors found that the mechanical properties of the 3D printed constructs decreased as the acid concentration in the digestion solution increased, being the softer hydrogels more inducing of a tendon-like phenotype.

In line with the abovementioned studies, Jeong and coworkers studied the decellularization efficiency of different types of detergents on porcine liver tissue, as well as their effect on the cytocompatibility, printability, and biochemical and mechanical properties of the resulting dECM derived bio-inks (Jeong et al., 2021). Sodium dodecyl sulfate (SDS), sodium deoxycholate (SDC), Triton X-100 (TX), and Triton X-100 with ammonium hydroxide (TXA) were examined. The authors found that, while SDS appeared to be the most efficient for DNA removal (up to 94% removal in 24 h), about 98% of GAGs and elastin from the native ECM was lost during decellularization with this detergent. On the contrary, TXA dECM samples exhibited adequate preservation of GAGs, collagen, and elastin, in addition to the fastest gelation rate and thus, the best printability. Moreover, TXA treated tissue samples yielded the dECM bio-ink with the most robust mechanical properties, because of its highly organized and packed fibrillar structure, as evidenced by SEM imaging results. This, together with the favorable cytocompatibility observed for the TXA group, demonstrated the suitability of TXA for the fabrication of liver dECM bio-inks.

Moreover, regarding skin dECM bio-inks, Jorgensen et al. examined the effect of the presence of human skin dECM on the bioactivity and mechanical properties of fibrinogen hydrogels for skin bioprinting applications (Jorgensen et al., 2020). Once the corresponding dECM powder was obtained, it was pepsin-solubilized at different concentrations, and these solutions were then combined with the bovine fibrinogen hydrogel precursor at a 1:1 volumetric ratio. Human skin fibroblasts were encapsulated in these hydrogels, following by crosslinking with 20 μL/ml thrombin. After a 2-weeks *in vitro* culture, the fibrinogen hydrogels containing dECM showed enhanced cellularity and almost a 50% increase in cell viability, relative to the pure fibrinogen counterparts. Also, rheological and printability characterization revealed that the proposed hydrogels exhibited favorable shear-thinning properties for the reproducible fabrication of bioprinted constructs.

Similarly, Lee et al. examined the biocompatibility of a bio-ink composed of dECM powder from porcine dermis dissolved in a 2–3% sodium alginate hydrogel, at 10 and 20 mg/ml (Lee et al., 2020). Rheological characterization of the prepared inks showed that ink viscosity could be tuned by varying dECM powder concentration. Moreover, mouse embryonic fibroblasts (NIH3T3) were mixed with the hydrogels at 1×10^6 cells/mL prior to 3D printing, and once the scaffold was printed, it was further crosslinked in 5% $CaCl_2$. After 1 week of culture, live/dead staining and cell metabolic activity tests indicated that cell viability levels within the constructs were maintained at around 75%.

Another remarkable example of skin dECM bio-ink development has been recently shown by Won and coworkers (Won et al., 2019). In their experiments, porcine dermal skin was decellularized to produce collagen, elastin, and GAG-rich dECM powder, which was then pepsin-digested, neutralized, and further combined with a suspension of human dermal fibroblasts. The cell-loaded bio-ink was used for the bioprinting of constructs that were cultured for 7 and 14 days at 37°C. The authors were able to show that the printed 3D dECM constructs maintained their shape, favored cell viability levels of at least 90%, and supported normal fibroblast cell shape during their first week of culture. In addition to this, microarray analyses performed after 1 and 2 weeks of culture revealed that the dECM constructs induced significantly higher upregulation of genes related to dermis and epidermis formation, relative to their corresponding collagen controls.

For their part, Falcones et al. examined the feasibility of using lung dECM bio-inks for enhancing the therapeutic effect of MSCs, in the context of MSC-based therapies for the treatment of respiratory diseases (Falcones et al., 2021).

Specifically, the authors employed porcine lung dECM to produce bio-inks within which lung resident MSCs were embedded. Following this, 3D constructs were bioprinted and cultured *in vitro* for 7 days, with the purpose of pre-conditioning the MSCs. After this, MSCs were released from the constructs through collagenase digestion, recovered, and further used for direct co-culture with human primary small airway epithelial cells (HSAECs) in the presence of lipopolysaccharides (LPS), to create an *in vitro* model of acute respiratory distress syndrome. The authors were able to show that the fabricated lung dECM 3D constructs provided a biochemical and biomechanical environment that promoted desirable MSC morphology and adhesion properties, in addition to improved immunomodulatory potential, as evidenced by the higher expression of CXCR4 and the lower production of IL6, relative to MSCs that were pre-conditioned by standard 2D culture in tissue culture polystyrene.

Moreover, it is noteworthy that dECM derived bio-inks have not only been used for the design of 3D constructs for tissue regeneration, but also for the development of disease models. Specifically, Kort-Mascort et al. recently created a dECM bio-ink that was mechanically reinforced with alginate and gelatin for the reproducible bioprinting of hydrogels that mimic head and neck tumor microenvironments (Kort-Mascort et al., 2021). Towards this end, porcine tongue was selected as the dECM source since this is one of the major sites for head and neck squamous cell carcinoma (HNSCC) development. Prior to bioprinting, human HNSCC cells were encapsulated in these bio-inks. As a result, composite 3D constructs with enhanced printability and mechanical properties that resembled those of native tumors were obtained. After 19 days of *in vitro* culture, cell viability in these hydrogels remained at around 95%, while favorable cell proliferation and tumor formation were evidenced by keratin expression. Finally, the designed tumor model was successfully used for *in vitro* chemotherapy studies using cisplatin and 5-fluorouracil, two drugs clinically employed to treat head and neck cancer.

Finally, Kim and coworkers developed bio-inks from porcine gastric tissue for the creation of *in vitro* 3D gastric cancer models. Prior to bioprinting, human gastric cancer cells (AGS, SNU-1, and KATO3 cell lines) were encapsulated in the bio-ink precursors, and cellulose nanoparticles were incorporated as a mechanical reinforcement agent (Kim et al., 2021). The resulting 3D constructs displayed mechanical properties that were physiologically relevant, and supported the enhanced expression of MMP2, β-catenin, and integrin β1, relative to their collagen and Matrigel controls. These markers are associated with the aggressive and drug-resistant nature of gastric cancer. Cumulatively, the results from the abovementioned studies demonstrate the promising potential of combining additive manufacturing techniques with dECM powders to produce *in vitro* 3D platforms that can closely resemble *in vivo* human microenvironments and, thus, could be used as reliable tools for either tissue regeneration, or drug testing pre-clinical studies in the absence of animal models.

DISCUSSION

Wound healing is a complex multi-step process that involves soluble factors, blood elements, and cells, which interact synergistically in an ECM, through mechanisms of dynamic reciprocity, where wound molecules interact with cell surface receptors and trigger intracellular signal transduction cascades, promoting expression of specific genes and secretion of signal molecules, whose in turn, coordinate the wound healing stages (Bhat and Bissell, 2014; Rousselle et al., 2019). Nevertheless, based on the type of tissue, healing is a process with distinct features. In the case of normal skin, there are three layers that intervene in the process: the epidermis, or the outer layer, which contains the sebaceous glands, sweat glands, and hair follicles; the dermis, which contains a rich ECM that provides strength, nutrients, and immunity; and finally, the hypodermis, which is the subcutaneous adipose tissue that functions as an energy reserve (Gurtner et al., 2008). Despite the differences among these layers, each of their ECM contains structural proteins such as FN, HA, proteoglycans, collagens, glycosaminoglycans, and elastin, in addition to non-structural matricellular proteins, including secreted protein acidic and rich in cysteine (SPARC), tenascin-C, osteopontin, and thrombospondins. The presence and characteristics of these molecules are dynamic during wound healing, and even under non-healing (normal) conditions, they are continuously being regenerated (Takeo et al., 2015; Rousselle et al., 2019).

Even though there is a number of commercially available skin substitutes and tissue-engineered skin products to manage impaired wounds, high manufacturing costs, excessive inflammation, as well as disease transmission have made their massive implementation difficult. To surmount these barriers, the use of dECM obtained from different tissues has emerged as a promising approach since they provide a favorable regeneration microenvironment by preserving cytokines, proteins and growth factors from the natural ECM, which altogether coordinate inflammation, re-epithelialization and ECM remodeling processes (Choi et al., 2013). In fact, as described in previous sections, several studies have elucidated the role of relevant molecules such as TNF-α, TGF-β, PDGF, VEGF, IGF-1, and HGF in wound healing, and have demonstrated their presence in acellular tissues derived from dermis, UB, SI, heart, adipose, and perinatal membranes (**Table 3**). Also, it is well known that different types of cells play a critical role. For instance, fibroblasts produce numerous ECM components, including collagens, FN, and proteoglycans (Tracy et al., 2016) that regulate the balance between degradation and synthesis of new skin. Thus, several researchers have developed dECM-engineered scaffolds that have the ability to modulate the wound healing response to avoid long-term inflammation and hypertrophic scar tissue formation (**Table 3**) (Biernacka et al., 2011).

To gain insight into the role of ECM elements and microenvironment on activation of signaling cascades related to wound healing processes, some studies have examined the individual effect of proteins and growth factors using *in vivo* models (Yang et al., 2015; Castellanos et al., 2017; Pozzi et al., 2017). Regarding cytokines, the literature reports that TGF-β and bFGF are pleiotropic factors that favor multiple wound-related

processes, such as fibroblast and keratinocyte migration, fibroblast differentiation into myofibroblast, M1-like macrophage phenotype towards M2-like phenotype, as well as collagen deposition and remodeling (Castellanos et al., 2017). Similarly, other researchers have suggested the importance of GAG content on dECM because sulfated components may influence the availability of growth factors involved in angiogenesis and vasculogenesis during wound healing (Pozzi et al., 2017). In addition to this, a growing body of evidence indicates the enhanced regenerative effect that may derive from the interaction between the skin and surrounding tissues, such as adipogenic tissue. In particular, adipogenesis plays three key roles: 1) expression of adipogenic genes that trigger skin-related repair; 2) secretion of molecules by adipocytes; and 3) provision of the adipogenic microenvironment that leads to skin appendage formation (Yang et al., 2015). Therefore, natural matrices are promising platforms for the advancement of engineered scaffolds that effectively regulate and promote specific tissue regeneration responses, such as those involved in wound healing processes.

AUTHOR CONTRIBUTIONS

All authors listed have made a substantial, direct, and intellectual contribution to the work. Conceptualization: VS, MA-R, and SB-B. Writing original draft: VS, MA-R, VG-A and SB-B. Editing: VG-A and SB-B. Critical feedback to the final version: VS, MA-R, VG-A and CS. All authors have agreed to be accountable for the content of the work.

FUNDING

This work was supported by Minciencias–Colombia, grant code No. 124777757672.

REFERENCES

Ahmed, E., Saleh, T., Yu, L., Song, S. H., Park, K. M., Kwak, H. H., et al. (2020). Decellularized Extracellular Matrix-rich Hydrogel-Silver Nanoparticle Mixture as a Potential Treatment for Acute Liver Failure Model. *J. Biomed. Mater. Res.* 108, 2351–2367. doi:10.1002/jbm.a.36988

Alemzadeh, E., Oryan, A., and Mohammadi, A. A. (2020). Hyaluronic Acid Hydrogel Loaded by Adipose Stem Cells Enhances Wound Healing by Modulating IL-1β, TGF-β1, and bFGF in Burn Wound Model in Rat. *J. Biomed. Mater. Res.* 108, 555–567. doi:10.1002/jbm.b.34411

Alizadeh, M., Rezakhani, L., Soleimannejad, M., Sharifi, E., Anjomshoa, M., and Alizadeh, A. (2019). Evaluation of Vacuum Washing in the Removal of SDS from Decellularized Bovine Pericardium: Method and Device Description. *Heliyon* 5, e02253. doi:10.1016/j.heliyon.2019.e02253

Alrubaiy, L., and Al-Rubaiy, K. K. (2009). Skin Substitutes: a Brief Review of Types and Clinical Applications. *Oman Med. J.* 24, 4–6. doi:10.5001/omj.2009.2

Aumailley, M., Battaglia, C., Mayer, U., Reinhardt, D., Nischt, R., Timpl, R., et al. (1993). Nidogen Mediates the Formation of Ternary Complexes of Basement Membrane Components. *Kidney Int.* 43, 7–12. doi:10.1038/ki.1993.3

Badylak, S., Freytes, D., and Gilbert, T. (2009). Extracellular Matrix as a Biological Scaffold Material: Structure and Function. *Acta Biomater.* 5, 1–13. doi:10.1016/j.actbio.2008.09.013

Bainbridge, P. (2013). Wound Healing and the Role of Fibroblasts. *J. Wound Care* 22 (407-8), 407–412. doi:10.12968/jowc.2013.22.8.407

Bakhtyar, N., Jeschke, M. G., Mainville, L., Herer, E., and Amini-Nik, S. (2017). Acellular Gelatinous Material of Human Umbilical Cord Enhances Wound Healing: A Candidate Remedy for Deficient Wound Healing. *Front. Physiol.* 8, 200. doi:10.3389/fphys.2017.00200

Bankoti, K., Rameshbabu, A. P., Datta, S., Roy, M., Goswami, P., Roy, S., et al. (2020). Carbon Nanodot Decorated Acellular Dermal Matrix Hydrogel Augments Chronic Wound Closure. *J. Mater. Chem. B* 8, 9277–9294. doi:10.1039/d0tb01574a

Barker, T. H., and Engler, A. J. (2017). The Provisional Matrix: Setting the Stage for Tissue Repair Outcomes. *Matrix Biol.* 60-61, 1–4. doi:10.1016/j.matbio.2017.04.003

Becerra-Bayona, S. M., Solarte-David, V. A., Sossa, C. L., Mateus, L. C., Villamil, M., Pereira, J., et al. (2020). Mesenchymal Stem Cells Derivatives as a Novel and Potential Therapeutic Approach to Treat Diabetic Foot Ulcers. *Endocrinol. Diabetes Metab. Case Rep.* 2020, 19–0164. doi:10.1530/EDM-19-0164

Berendsen, A. D., Bronckers, A. L. J. J., Smit, T. H., Walboomers, X. F., and Everts, V. (2006). Collagen Type V Enhances Matrix Contraction by Human Periodontal Ligament Fibroblasts Seeded in Three-Dimensional Collagen Gels. *Matrix Biol.* 25, 515–522. doi:10.1016/j.matbio.2006.07.006

Bhat, R., and Bissell, M. J. (2014). Of Plasticity and Specificity: Dialectics of the Microenvironment and Macroenvironment and the Organ Phenotype. *Wires Dev. Biol.* 3, 147–163. doi:10.1002/wdev.130

Biernacka, A., Dobaczewski, M., and Frangogiannis, N. G. (2011). TGF-β Signaling in Fibrosis. *Growth Factors* 29, 196–202. doi:10.3109/08977194.2011.595714

Bordbar, S., Lotfi Bakhshaiesh, N., Khanmohammadi, M., Sayahpour, F. A., Alini, M., and Baghaban Eslaminejad, M. (2020). Production and Evaluation of Decellularized Extracellular Matrix Hydrogel for Cartilage Regeneration Derived from Knee Cartilage. *J. Biomed. Mater. Res.* 108, 938–946. doi:10.1002/jbm.a.36871

Bowden, L. G., Byrne, H. M., Maini, P. K., and Moulton, D. E. (2016). A Morphoelastic Model for Dermal Wound Closure. *Biomech. Model. Mechanobiol* 15, 663–681. doi:10.1007/s10237-015-0716-7

Bradshaw, A. D., and Sage, E. H. (2001). SPARC, a Matricellular Protein that Functions in Cellular Differentiation and Tissue Response to Injury. *J. Clin. Invest.* 107, 1049–1054. doi:10.1172/jci12939

Breitkreutz, D., Mirancea, N., and Nischt, R. (2009). Basement Membranes in Skin: Unique Matrix Structures with Diverse Functions? *Histochem. Cel Biol* 132, 1–10. doi:10.1007/s00418-009-0586-0

Brekken, R. A., and Sage, E. H. (2000). SPARC, a Matricellular Protein: at the Crossroads of Cell-Matrix. *Matrix Biol.* 19, 569–580. doi:10.1016/s0945-053x(00)00105-0

Brem, H., and Tomic-Canic, M. (2007). Cellular and Molecular Basis of Wound Healing in Diabetes. *J. Clin. Invest.* 117, 1219–1222. doi:10.1172/jci32169

Broze, G. J., Jr., and Higuchi, D. (1996). Coagulation-dependent Inhibition of Fibrinolysis: Role of Carboxypeptidase-U and the Premature Lysis of Clots from Hemophilic Plasma. *Blood* 88, 3815–3823. doi:10.1182/blood.v88.10.3815.bloodjournal88103815

Burgess, J. L., Wyant, W. A., Abdo Abujamra, B., Kirsner, R. S., and Jozic, I. (2021). Diabetic Wound-Healing Science. *Medicina (Kaunas)* 57. doi:10.3390/medicina57101072

Carlson, T. L., Lee, K. W., and Pierce, L. M. (2013). Effect of Cross-Linked and Non-cross-linked Acellular Dermal Matrices on the Expression of Mediators Involved in Wound Healing and Matrix Remodeling. *Plast. Reconstr. Surg.* 131, 697–705. doi:10.1097/prs.0b013e3182818a3d

Castellanos, G., Bernabé-García, Á., Moraleda, J. M., and Nicolás, F. J. (2017). Amniotic Membrane Application for the Healing of Chronic Wounds and Ulcers. *Placenta* 59, 146–153. doi:10.1016/j.placenta.2017.04.005

Chapin, J. C., and Hajjar, K. A. (2015). Fibrinolysis and the Control of Blood Coagulation. *Blood Rev.* 29, 17–24. doi:10.1016/j.blre.2014.09.003

Chaudhry, R., Usama, S. M., and Babiker, H. M. (2021). *Physiology, Coagulation Pathways, StatPearls, Treasure*. Island (FL).

Chen, D., Hao, H., Fu, X., and Han, W. (2016). Insight into Reepithelialization: How Do Mesenchymal Stem Cells Perform? *Stem Cell Int* 2016, 6120173. doi:10.1155/2016/6120173

Chen, Y., Dan, N., Dan, W., Liu, X., and Cong, L. (2019). A Novel Antibacterial Acellular Porcine Dermal Matrix Cross-Linked with Oxidized Chitosan Oligosaccharide and Modified by *In Situ* Synthesis of Silver Nanoparticles for Wound Healing Applications. *Mater. Sci. Eng. C* 94, 1020–1036. doi:10.1016/j.msec.2018.10.036

Chen, Z., Zhang, B., Shu, J., Wang, H., Han, Y., Zeng, Q., et al. (2021). Human Decellularized Adipose Matrix Derived Hydrogel Assists Mesenchymal Stem Cells Delivery and Accelerates Chronic Wound Healing. *J. Biomed. Mater. Res.* 109, 1418–1428. doi:10.1002/jbm.a.37133

Chester, D., and Brown, A. C. (2017). The Role of Biophysical Properties of Provisional Matrix Proteins in Wound Repair. *Matrix Biol.* 60-61, 124–140. doi:10.1016/j.matbio.2016.08.004

Cho, H., Blatchley, M. R., Duh, E. J., and Gerecht, S. (2019). Acellular and Cellular Approaches to Improve Diabetic Wound Healing. *Adv. Drug Deliv. Rev.* 146, 267–288. doi:10.1016/j.addr.2018.07.019

Choi, J. S., Kim, J. D., Yoon, H. S., and Cho, Y. W. (2013). Full-thickness Skin Wound Healing Using Human Placenta-Derived Extracellular Matrix Containing Bioactive Molecules. *Tissue Eng. A* 19, 329–339. doi:10.1089/ten.tea.2011.0738

Collen, D., and Lijnen, H. R. (1995). Molecular Basis of Fibrinolysis, as Relevant for Thrombolytic Therapy. *Thromb. Haemost.* 74, 167–171. doi:10.1055/s-0038-1642671

Coronado, R. E., Somaraki-Cormier, M., Natesan, S., Christy, R. J., Ong, J. L., and Halff, G. A. (2017). Decellularization and Solubilization of Porcine Liver for Use as a Substrate for Porcine Hepatocyte Culture. *Cel Transpl.* 26, 1840–1854. doi:10.1177/0963689717742157

Cosgrove, D., and Liu, S. (2017). Collagen IV Diseases: A Focus on the Glomerular Basement Membrane in Alport Syndrome. *Matrix Biol.* 57-58, 45–54. doi:10.1016/j.matbio.2016.08.005

Crapo, P. M., Gilbert, T. W., and Badylak, S. F. (2011). An Overview of Tissue and Whole Organ Decellularization Processes. *Biomaterials* 32, 3233–3243. doi:10.1016/j.biomaterials.2011.01.057

Dahlbäck, B. (2000). Blood Coagulation. *The Lancet* 355, 1627–1632. doi:10.1016/s0140-6736(00)02225-x

Dai, C., Shih, S., and Khachemoune, A. (2020). Skin Substitutes for Acute and Chronic Wound Healing: an Updated Review. *J. Dermatol. Treat.* 31, 639–648. doi:10.1080/09546634.2018.1530443

Davison-Kotler, E., Marshall, W. S., and García-Gareta, E. (2019). Sources of Collagen for Biomaterials in Skin Wound Healing. *Bioengineering (Basel)* 6. doi:10.3390/bioengineering6030056

de Hilster, R. H. J., Sharma, P. K., Jonker, M. R., White, E. S., Gercama, E. A., Roobeek, M., et al. (2020). Human Lung Extracellular Matrix Hydrogels Resemble the Stiffness and Viscoelasticity of Native Lung Tissue. *Am. J. Physiology-Lung Cell Mol. Physiol.* 318, L698–L704. doi:10.1152/ajplung.00451.2019

de Mayo, T., Conget, P., Becerra-Bayona, S., Sossa, C. L., Galvis, V., and Arango-Rodríguez, M. L. (2017). The Role of Bone Marrow Mesenchymal Stromal Cell Derivatives in Skin Wound Healing in Diabetic Mice. *PLoS One* 12, e0177533. doi:10.1371/journal.pone.0177533

Deeken, C. R., White, A. K., Bachman, S. L., Ramshaw, B. J., Cleveland, D. S., Loy, T. S., et al. (2011). Method of Preparing a Decellularized Porcine Tendon Using Tributyl Phosphate. *J. Biomed. Mater. Res.* 96B, 199–206. doi:10.1002/jbm.b.31753

Deuel, T. F., Kawahara, R. S., Mustoe, T. A., and Pierce, G. F. (1991). Growth Factors and Wound Healing: Platelet-Derived Growth Factor as a Model Cytokine. *Annu. Rev. Med.* 42, 567–584. doi:10.1146/annurev.me.42.020191.003031

Doi, H., Kitajima, Y., Luo, L., Yan, C., Tateishi, S., Ono, Y., et al. (2016). Potency of Umbilical Cord Blood- and Wharton's Jelly-Derived Mesenchymal Stem Cells for Scarless Wound Healing. *Sci. Rep.* 6, 18844. doi:10.1038/srep18844

Dongen, J. A., Getova, V., Brouwer, L. A., Liguori, G. R., Sharma, P. K., Stevens, H. P., et al. (2019). Adipose Tissue-derived Extracellular Matrix Hydrogels as a Release Platform for Secreted Paracrine Factors. *J. Tissue Eng. Regen. Med.* 13, 973–985. doi:10.1002/term.2843

Duda, S. H., Wiskirchen, J., Erb, M., Schott, U., Khaligi, K., Pereira, P. L., et al. (1999). Suture-mediated Percutaneous Closure of Antegrade Femoral Arterial Access Sites in Patients Who Have Full Anticoagulation Therapy. *Radiology* 210, 47–52. doi:10.1148/radiology.210.1.r99ja3047

Dussoyer, M., Michopoulou, A., and Rousselle, P. (2020). Decellularized Scaffolds for Skin Repair and Regeneration. *Appl. Sci.* 10, 3435. doi:10.3390/app10103435

Dziki, J. L., Wang, D. S., Pineda, C., Sicari, B. M., Rausch, T., and Badylak, S. F. (2017). Solubilized Extracellular Matrix Bioscaffolds Derived from Diverse Source Tissues Differentially Influence Macrophage Phenotype. *J. Biomed. Mater. Res.* 105, 138–147. doi:10.1002/jbm.a.35894

Eckhart, L., and Zeeuwen, P. L. J. M. (2018). The Skin Barrier: Epidermis vs Environment. *Exp. Dermatol.* 27, 805–806. doi:10.1111/exd.13731

Edmondson, S. R., Thumiger, S. P., Werther, G. A., and Wraight, C. J. (2003). Epidermal Homeostasis: the Role of the Growth Hormone and Insulin-like Growth Factor Systems. *Endocr. Rev.* 24, 737–764. doi:10.1210/er.2002-0021

Ehrbar, M., Zeisberger, S. M., Raeber, G. P., Hubbell, J. A., Schnell, C., and Zisch, A. H. (2008). The Role of Actively Released Fibrin-Conjugated VEGF for VEGF Receptor 2 Gene Activation and the Enhancement of Angiogenesis. *Biomaterials* 29, 1720–1729. doi:10.1016/j.biomaterials.2007.12.002

El Masry, M. S., Chaffee, S., Das Ghatak, P., Mathew-Steiner, S. S., Das, A., Higuita-Castro, N., et al. (2019). Stabilized Collagen Matrix Dressing Improves Wound Macrophage Function and Epithelialization. *FASEB j.* 33, 2144–2155. doi:10.1096/fj.201800352r

Elder, B. D., Eleswarapu, S. V., and Athanasiou, K. A. (2009). Extraction Techniques for the Decellularization of Tissue Engineered Articular Cartilage Constructs. *Biomaterials* 30, 3749–3756. doi:10.1016/j.biomaterials.2009.03.050

Elliott, J., Lomas, R., and Chandrasaker, A. (2015). Scalp Reconstruction Using dCELL Human Dermis Allograft: a New and Novel Technique. *Br. J. Oral Maxillofacial Surg.* 53, E128. doi:10.1016/j.bjoms.2015.08.253

Erem, C., Hacıhasanoğlu, A., Çelik, Ş., Ovalı, E., Ersöz, H. Ö., Ukinç, K., et al. (2005). Coagulation and Fibrinolysis Parameters in Type 2 Diabetic Patients with and without Diabetic Vascular Complications. *Med. Princ Pract.* 14, 22–30. doi:10.1159/000081919

Falcones, B., Sanz-Fraile, H., Marhuenda, E., Mendizabal, I., Cabrera-Aguilera, I., Malandain, N., et al. (2021). Bioprintable Lung Extracellular Matrix Hydrogel Scaffolds for 3D Culture of Mesenchymal Stromal Cells. *Polymers (Basel)* 13, 2350. doi:10.3390/polym13142350

Fermor, H. L., Russell, S. L., Williams, S., Fisher, J., and Ingham, E. (2015). Development and Characterisation of a Decellularised Bovine Osteochondral Biomaterial for Cartilage Repair. *J. Mater. Sci. Mater. Med.* 26, 186. doi:10.1007/s10856-015-5517-0

Fernandez-Moure, J. S., Van Eps, J. L., Rhudy, J. R., Cabrera, F. J., Acharya, G. S., Tasciotti, E., et al. (2016). Porcine Acellular Lung Matrix for Wound Healing and Abdominal wall Reconstruction: A Pilot Study. *J. Tissue Eng.* 7, 2041731415626018. doi:10.1177/2041731415626018

Forouzesh, F., Rabbani, M., and Bonakdar, S. (2019). A Comparison between Ultrasonic Bath and Direct Sonicator on Osteochondral Tissue Decellularization. *J. Med. Signals Sens* 9, 227–233. doi:10.4103/jmss.JMSS_64_18

Fujisawa, Y., Matsuda, K., and Uehara, T. (2020). Osteopontin Enhances the Migration of Lung Fibroblasts via Upregulation of Interleukin-6 through the Extracellular Signal-Regulated Kinase (ERK) Pathway. *Biol. Chem.* 401, 1071–1080. doi:10.1515/hsz-2020-0125

Gale, A. J. (2011). Continuing Education Course #2: Current Understanding of Hemostasis. *Toxicol. Pathol.* 39, 273–280. doi:10.1177/0192623310389474

Gholipourmalekabadi, M., Khosravimelal, S., Nokhbedehghan, Z., Sameni, M., Jajarmi, V., Urbanska, A. M., et al. (2019). Modulation of Hypertrophic Scar Formation Using Amniotic Membrane/Electrospun Silk Fibroin Bilayer Membrane in a Rabbit Ear Model. *ACS Biomater. Sci. Eng.* 5, 1487–1496. doi:10.1021/acsbiomaterials.8b01521

Gholipourmalekabadi, M., Sameni, M., Radenkovic, D., Mozafari, M., Mossahebi-Mohammadi, M., and Seifalian, A. (2016). Decellularized Human Amniotic Membrane: How Viable Is it as a Delivery System for Human Adipose Tissue-Derived Stromal Cells? *Cell Prolif.* 49, 115–121. doi:10.1111/cpr.12240

Gilpin, A., and Yang, Y. (2017). Decellularization Strategies for Regenerative Medicine: From Processing Techniques to Applications. *Biomed. Res. Int.* 2017, 9831534. doi:10.1155/2017/9831534

Giraldo-Gomez, D. M., Leon-Mancilla, B., Del Prado-Audelo, M. L., Sotres-Vega, A., Villalba-Caloca, J., Garciadiego-Cazares, D., et al. (2016). Trypsin as Enhancement in Cyclical Tracheal Decellularization: Morphological and

Biophysical Characterization. *Mater. Sci. Eng. C* 59, 930–937. doi:10.1016/j.msec.2015.10.094

Goodarzi, P., Falahzadeh, K., Nematizadeh, M., Farazandeh, P., Payab, M., Larijani, B., et al. (2018). Tissue Engineered Skin Substitutes. *Adv. Exp. Med. Biol.* 1107, 143–188. doi:10.1007/5584_2018_226

Greco, K., Francis, L., Somasundaram, M., Greco, G., English, N. R., Roether, J. A., et al. (2015). Characterisation of Porcine Dermis Scaffolds Decellularised Using a Novel Non-enzymatic Method for Biomedical Applications. *J. Biomater. Appl.* 30, 239–253. doi:10.1177/0885328215578638

Guler, S., Aslan, B., Hosseinian, P., and Aydin, H. M. (2017). Supercritical Carbon Dioxide-Assisted Decellularization of Aorta and Cornea. *Tissue Eng. C: Methods* 23, 540–547. doi:10.1089/ten.tec.2017.0090

Guo, M., Toda, K., and Grinnell, F. (1990). Activation of Human Keratinocyte Migration on Type I Collagen and Fibronectin. *J. Cel Sci* 96 (Pt 2), 197–205. doi:10.1242/jcs.96.2.197

Gurtner, G. C., Werner, S., Barrandon, Y., and Longaker, M. T. (2008). Wound Repair and Regeneration. *Nature* 453, 314–321. doi:10.1038/nature07039

Ha, S. S., Song, E. S., Du, P., Suhaeri, M., Lee, J. H., and Park, K. (2020). Novel ECM Patch Combines Poly(vinyl Alcohol), Human Fibroblast-Derived Matrix, and Mesenchymal Stem Cells for Advanced Wound Healing. *ACS Biomater. Sci. Eng.* 6, 4266–4275. doi:10.1021/acsbiomaterials.0c00657

Halim, A. S., Khoo, T. L., and Yussof, S. J. M. (2010). Biologic and Synthetic Skin Substitutes: An Overview. *Indian J. Plast. Surg.* 43, S23–S28. doi:10.1055/s-0039-1699458

Han, G., and Ceilley, R. (2017). Chronic Wound Healing: A Review of Current Management and Treatments. *Adv. Ther.* 34, 599–610. doi:10.1007/s12325-017-0478-y

Hashemi, S. S., Pourfath, M. R., Derakhshanfar, A., Behzad-Behbahani, A., and Moayedi, J. (2020). The Role of Labeled Cell Therapy with and without Scaffold in Early Excision Burn Wounds in a Rat Animal Model. *Iran J. Basic Med. Sci.* 23, 673–679. doi:10.22038/ijbms.2020.34324.8156

Hoang Thi, T. T., Tran Nguyen, D. H., Nguyen, D. T. D., Nguyen, D. H., and Truong, M. D. (2020). Decellularized Porcine Epiphyseal Plate-Derived Extracellular Matrix Powder: Synthesis and Characterization. *Cells Tissues Organs* 209, 101–109. doi:10.1159/000507552

Hohenester, E., and Yurchenco, P. D. (2013). Laminins in Basement Membrane Assembly. *Cell Adhes. Migration* 7, 56–63. doi:10.4161/cam.21831

Horsley, V., and Watt, F. (2017). Repeal and Replace: Adipocyte Regeneration in Wound Repair. *Cell Stem Cell* 20, 424–426. doi:10.1016/j.stem.2017.03.015

Hoshiba, T., Chen, G., Endo, C., Maruyama, H., Wakui, M., Nemoto, E., et al. (2016). Decellularized Extracellular Matrix as an *In Vitro* Model to Study the Comprehensive Roles of the ECM in Stem Cell Differentiation. *Stem Cell Int* 2016, 6397820. doi:10.1155/2016/6397820

Hsieh, C. M., Wang, W., Chen, Y. H., Wei, P. S., Liu, Y. H., Sheu, M. T., et al. (2020). A Novel Composite Hydrogel Composed of Formic Acid-Decellularized Pepsin-Soluble Extracellular Matrix Hydrogel and Sacchachitin Hydrogel as Wound Dressing to Synergistically Accelerate Diabetic Wound Healing. *Pharmaceutics* 12, 538. doi:10.3390/pharmaceutics12060538

Hsu, P. W., Salgado, C. J., Kent, K., Finnegan, M., Pello, M., Simons, R., et al. (2009). Evaluation of Porcine Dermal Collagen (Permacol) Used in Abdominal wall Reconstruction. *J. Plast. Reconstr. Aesthet. Surg.* 62, 1484–1489. doi:10.1016/j.bjps.2008.04.060

Hu, Y., Liu, L., Dan, W., Dan, N., Gu, Z., and Yu, X. (2013). Synergistic Effect of Carbodiimide and Dehydrothermal Crosslinking on Acellular Dermal Matrix. *Int. J. Biol. Macromolecules* 55, 221–230. doi:10.1016/j.ijbiomac.2013.01.009

Hurme, T., Kalimo, H., Sandberg, M., Lehto, M., and Vuorio, E. (1991). Localization of Type I and III Collagen and Fibronectin Production in Injured Gastrocnemius Muscle. *Lab. Invest.* 64, 76–84.

Icer, M. A., and Gezmen-Karadag, M. (2018). The Multiple Functions and Mechanisms of Osteopontin. *Clin. Biochem.* 59, 17–24. doi:10.1016/j.clinbiochem.2018.07.003

Jackson, W. M., Nesti, L. J., and Tuan, R. S. (2012). Mesenchymal Stem Cell Therapy for Attenuation of Scar Formation during Wound Healing. *Stem Cel Res Ther* 3, 20. doi:10.1186/scrt111

Jeon, E. Y., Joo, K. I., and Cha, H. J. (2020). Body Temperature-Activated Protein-Based Injectable Adhesive Hydrogel Incorporated with Decellularized Adipose Extracellular Matrix for Tissue-specific Regenerative Stem Cell Therapy. *Acta Biomater.* 114, 244–255. doi:10.1016/j.actbio.2020.07.033

Jeong, W., Kim, M. K., and Kang, H. W. (2021). Effect of Detergent Type on the Performance of Liver Decellularized Extracellular Matrix-Based Bio-Inks. *J. Tissue Eng.* 12, 2041731421997091. doi:10.1177/2041731421997091

Jorgensen, A. M., Chou, Z., Gillispie, G., Lee, S. J., Yoo, J. J., Soker, S., et al. (2020). Decellularized Skin Extracellular Matrix (dsECM) Improves the Physical and Biological Properties of Fibrinogen Hydrogel for Skin Bioprinting Applications. *Nanomaterials (Basel)* 10, 1484. doi:10.3390/nano10081484

Kahn, M. L., Zheng, Y.-W., Huang, W., Bigornia, V., Zeng, D., Moff, S., et al. (1998). A Dual Thrombin Receptor System for Platelet Activation. *Nature* 394, 690–694. doi:10.1038/29325

Kamolz, L.-P., Keck, M., and Kasper, C. (2014). Wharton's Jelly Mesenchymal Stem Cells Promote Wound Healing and Tissue Regeneration. *Stem Cel Res Ther* 5, 62. doi:10.1186/scrt451

Kanitakis, J. (2002). Anatomy, Histology and Immunohistochemistry of normal Human Skin. *Eur. J. Dermatol.* 12, 390–391. quiz 400-1.

Keane, T. J., Swinehart, I. T., and Badylak, S. F. (2015). Methods of Tissue Decellularization Used for Preparation of Biologic Scaffolds and *In Vivo* Relevance. *Methods* 84, 25–34. doi:10.1016/j.ymeth.2015.03.005

Kim, J., Jang, J., and Cho, D.-W. (2021). Controlling Cancer Cell Behavior by Improving the Stiffness of Gastric Tissue-Decellularized ECM Bioink with Cellulose Nanoparticles. *Front. Bioeng. Biotechnol.* 9, 605819. doi:10.3389/fbioe.2021.605819

Kim, J. K., Koh, Y.-D., Kim, J. O., and Seo, D. H. (2016). Development of a Decellularization Method to Produce Nerve Allografts Using Less Invasive Detergents and Hyper/hypotonic Solutions. *J. Plast. Reconstr. Aesthet. Surg.* 69, 1690–1696. doi:10.1016/j.bjps.2016.08.016

Kim, M. K., Jeong, W., Lee, S. M., Kim, J. B., Jin, S., and Kang, H.-W. (2020). Decellularized Extracellular Matrix-Based Bio-Ink with Enhanced 3D Printability and Mechanical Properties. *Biofabrication* 12, 025003. doi:10.1088/1758-5090/ab5d80

Kim, T. H., Jung, Y., and Kim, S. H. (2018). Nanofibrous Electrospun Heart Decellularized Extracellular Matrix-Based Hybrid Scaffold as Wound Dressing for Reducing Scarring in Wound Healing. *Tissue Eng. Part A* 24, 830–848. doi:10.1089/ten.tea.2017.0318

Kirchhofer, D., and Nemerson, Y. (1996). Initiation of Blood Coagulation: the Tissue Factor/factor VIIa Complex. *Curr. Opin. Biotechnol.* 7, 386–391. doi:10.1016/s0958-1669(96)80112-1

Kiritsi, D., and Nyström, A. (2018). The Role of TGFβ in Wound Healing Pathologies. *Mech. Ageing Development* 172, 51–58. doi:10.1016/j.mad.2017.11.004

Kirsner, R. S., Bohn, G., Driver, V. R., Mills, J. L., Nanney., Williams, M. L., et al. (2015). Human Acellular Dermal Wound Matrix: Evidence and Experience. *Int. Wound J.* 12, 646–654. doi:10.1111/iwj.12185

Koob, T. J., Lim, J. J., Zabek, N., and Massee, M. (2015). Cytokines in Single Layer Amnion Allografts Compared to Multilayer Amnion/chorion Allografts for Wound Healing. *J. Biomed. Mater. Res.* 103, 1133–1140. doi:10.1002/jbm.b.33265

Kort-Mascort, J., Bao, G., Elkashty, O., Flores-Torres, S., Munguia-Lopez, J. G., Jiang, T., et al. (2021). Decellularized Extracellular Matrix Composite Hydrogel Bioinks for the Development of 3D Bioprinted Head and Neck *In Vitro* Tumor Models. *ACS Biomater. Sci. Eng.* 7, 5288–5300. doi:10.1021/acsbiomaterials.1c00812

Kshersagar, J., Kshirsagar, R., Desai, S., Bohara, R., and Joshi, M. (2018). Decellularized Amnion Scaffold with Activated PRP: a New Paradigm Dressing Material for Burn Wound Healing. *Cell Tissue Bank* 19, 423–436. doi:10.1007/s10561-018-9688-z

Kuna, V. K., Padma, A. M., Håkansson, J., Nygren, J., Sjöback, R., Petronis, S., et al. (2017). Significantly Accelerated Wound Healing of Full-Thickness Skin Using a Novel Composite Gel of Porcine Acellular Dermal Matrix and Human Peripheral Blood Cells. *Cel Transpl.* 26, 293–307. doi:10.3727/096368916x692690

Kyriakides, T. R., and Maclauchlan, S. (2009). The Role of Thrombospondins in Wound Healing, Ischemia, and the Foreign Body Reaction. *J. Cel Commun. Signal.* 3, 215–225. doi:10.1007/s12079-009-0077-z

Landén, N. X., Li, D., and Ståhle, M. (2016). Transition from Inflammation to Proliferation: a Critical Step during Wound Healing. *Cell. Mol. Life Sci.* 73, 3861–3885. doi:10.1007/s00018-016-2268-0

Lane, D. A., Philippou, H., and Huntington, J. A. (2005). Directing Thrombin. *Blood* 106, 2605–2612. doi:10.1182/blood-2005-04-1710

Laplante, A. F., Germain, L., Auger, F. A., and Moulin, V. (2001). Mechanisms of Wound Reepithelialization: Hints from a Tissue-engineered Reconstructed Skin to Long-standing Questions. *FASEB j.* 15, 2377–2389. doi:10.1096/fj.01-0250com

Lee, S. J., Lee, J. H., Park, J., Kim, W. D., and Park, S. A. (2020). Fabrication of 3D Printing Scaffold with Porcine Skin Decellularized Bio-Ink for Soft Tissue Engineering. *Materials (Basel)* 13, 3522. doi:10.3390/ma13163522

Liguori, T. T. A., Liguori, G. R., van Dongen, J. A., Moreira, L. F. P., and Harmsen, M. C. (2021). Bioactive Decellularized Cardiac Extracellular Matrix-Based Hydrogel as a Sustained-Release Platform for Human Adipose Tissue-Derived Stromal Cell-Secreted Factors. *Biomed. Mater.* 16, 025022. doi:10.1088/1748-605x/abcff9

Lin, W., Qi, X., Guo, W., Liang, D., Chen, H., Lin, B., et al. (2020). A Barrier against Reactive Oxygen Species: Chitosan/acellular Dermal Matrix Scaffold Enhances Stem Cell Retention and Improves Cutaneous Wound Healing. *Stem Cel Res Ther* 11, 383. doi:10.1186/s13287-020-01901-6

Löffek, S., Hurskainen, T., Jackow, J., Sigloch, F. C., Schilling, O., Tasanen, K., et al. (2014). Transmembrane Collagen XVII Modulates Integrin Dependent Keratinocyte Migration via PI3K/Rac1 Signaling. *PLoS One* 9, e87263. doi:10.1371/journal.pone.0087263

Lord, M. S., Tang, F., Rnjak-Kovacina, J., Smith, J. G. W., Melrose, J., and Whitelock, J. M. (2018). The Multifaceted Roles of Perlecan in Fibrosis. *Matrix Biol.* 68-69, 150–166. doi:10.1016/j.matbio.2018.02.013

Mackie, E. J., Halfter, W., and Liverani, D. (1988). Induction of Tenascin in Healing Wounds. *J. Cel Biol* 107, 2757–2767. doi:10.1083/jcb.107.6.2757

Maclauchlan, S., Skokos, E. A., Agah, A., Zeng, J., Tian, W., Davidson, J. M., et al. (2009). Enhanced Angiogenesis and Reduced Contraction in Thrombospondin-2-Null Wounds Is Associated with Increased Levels of Matrix Metalloproteinases-2 and −9, and Soluble VEGF. *J. Histochem. Cytochem.* 57, 301–313. doi:10.1369/jhc.2008.952689

Mak, K. M., and Mei, R. (2017). Basement Membrane Type IV Collagen and Laminin: An Overview of Their Biology and Value as Fibrosis Biomarkers of Liver Disease. *Anat. Rec.* 300, 1371–1390. doi:10.1002/ar.23567

Manon-Jensen, T., Kjeld, N. G., and Karsdal, M. A. (2016). Collagen-mediated Hemostasis. *J. Thromb. Haemost.* 14, 438–448. doi:10.1111/jth.13249

Mao, Y., and Schwarzbauer, J. E. (2005). Fibronectin Fibrillogenesis, a Cell-Mediated Matrix Assembly Process. *Matrix Biol.* 24, 389–399. doi:10.1016/j.matbio.2005.06.008

Mendibil, U., Ruiz-Hernandez, R., Retegi-Carrion, S., Garcia-Urquia, N., Olalde-Graells, B., and Abarrategi, A. (2020). Tissue-Specific Decellularization Methods: Rationale and Strategies to Achieve Regenerative Compounds. *Int. J. Mol. Sci.* 21, 5447. doi:10.3390/ijms21155447

Michopoulou, A., Montmasson, M., Garnier, C., Lambert, E., Dayan, G., and Rousselle, P. (2020). A Novel Mechanism in Wound Healing: Laminin 332 Drives MMP9/14 Activity by Recruiting Syndecan-1 and CD44. *Matrix Biol.* 94, 1–17. doi:10.1016/j.matbio.2020.06.004

Midwood, K. S., Chiquet, M., Tucker, R. P., and Orend, G. (2016). Tenascin-C at a Glance. *J. Cel Sci* 129, 4321–4327. doi:10.1242/jcs.190546

Midwood, K., Sacre, S., Piccinini, A. M., Inglis, J., Trebaul, A., Chan, E., et al. (2009). Tenascin-C Is an Endogenous Activator of Toll-like Receptor 4 that Is Essential for Maintaining Inflammation in Arthritic Joint Disease. *Nat. Med.* 15, 774–780. doi:10.1038/nm.1987

Milan, P. B., Amini, N., Joghataei, M. T., Ebrahimi, L., Amoupour, M., Sarveazad, A., et al. (2020). Decellularized Human Amniotic Membrane: From Animal Models to Clinical Trials. *Methods* 171, 11–19. doi:10.1016/j.ymeth.2019.07.018

Monavarian, M., Kader, S., Moeinzadeh, S., and Jabbari, E. (2019). Regenerative Scar-free Skin Wound Healing. *Tissue Eng. B: Rev.* 25, 294–311. doi:10.1089/ten.teb.2018.0350

Morris, A. H., Stamer, D. K., Kunkemoeller, B., Chang, J., Xing, H., and Kyriakides, T. R. (2018). Decellularized Materials Derived from TSP2-KO Mice Promote Enhanced Neovascularization and Integration in Diabetic Wounds. *Biomaterials* 169, 61–71. doi:10.1016/j.biomaterials.2018.03.049

Mosser, D. M., and Edwards, J. P. (2008). Exploring the Full Spectrum of Macrophage Activation. *Nat. Rev. Immunol.* 8, 958–969. doi:10.1038/nri2448

Motamed, K. (1999). SPARC (osteonectin/BM-40). *Int. J. Biochem. Cel Biol* 31, 1363–1366. doi:10.1016/s1357-2725(99)00090-4

Nasiry, D., Khalatbary, A. R., Abdollahifar, M.-A., Amini, A., Bayat, M., Noori, A., et al. (2021). Engraftment of Bioengineered Three-Dimensional Scaffold from Human Amniotic Membrane-Derived Extracellular Matrix Accelerates Ischemic Diabetic Wound Healing. *Arch. Dermatol. Res.* 313, 567–582. doi:10.1007/s00403-020-02137-3

Nathoo, R., Howe, N., and Cohen, G. (2014). Skin Substitutes: an Overview of the Key Players in Wound Management. *J. Clin. Aesthet. Dermatol.* 7, 44–48.

Nelson, C. M., and Bissell, M. J. (2006). Of Extracellular Matrix, Scaffolds, and Signaling: Tissue Architecture Regulates Development, Homeostasis, and Cancer. *Annu. Rev. Cel Dev. Biol.* 22, 287–309. doi:10.1146/annurev.cellbio.22.010305.104315

Nguyen, A. V., and Soulika, A. M. (2019). The Dynamics of the Skin's Immune System. *Int. J. Mol. Sci.* 20. doi:10.3390/ijms20081811

Nichols, J. E., Niles, J., Riddle, M., Vargas, G., Schilagard, T., Ma, L., et al. (2013). Production and Assessment of Decellularized Pig and Human Lung Scaffolds. *Tissue Eng. Part A* 19, 2045–2062. doi:10.1089/ten.tea.2012.0250

Nicoletti, G., Tresoldi, M. M., Malovini, A., Visaggio, M., Faga, A., and Scevola, S. (2018). Versatile Use of Dermal Substitutes: A Retrospective Survey of 127 Consecutive Cases. *Indian J. Plast. Surg.* 51, 46–53. doi:10.4103/ijps.IJPS_217_17

Niknejad, H., Peirovi, H., Peirovi, H., Jorjani, M., Ahmadiani, A., Ghanavi, J., et al. (2008). Properties of the Amniotic Membrane for Potential Use in Tissue Engineering. *eCM* 7, 88–99. doi:10.22203/ecm.v015a07

Noordenbos, J., Doré, C., and Hansbrough, J. F. (1999). Safety and Efficacy of TransCyte* for the Treatment of Partial-Thickness Burns. *J. Burn Care Rehabil.* 20, 275–281. doi:10.1097/00004630-199907000-00002

Nourian Dehkordi, A., Mirahmadi Babaheydari, F., Chehelgerdi, M., and Raeisi Dehkordi, S. (2019). Skin Tissue Engineering: Wound Healing Based on Stem-Cell-Based Therapeutic Strategies. *Stem Cel Res Ther* 10, 111. doi:10.1186/s13287-019-1212-2

Nyström, A., Velati, D., Mittapalli, V. R., Fritsch, A., Kern, J. S., and Bruckner-Tuderman, L. (2013). Collagen VII Plays a Dual Role in Wound Healing. *J. Clin. Invest.* 123, 3498–3509. doi:10.1172/jci68127

O'Neill, J. D., Anfang, R., Anandappa, A., Costa, J., Javidfar, J., Wobma, H. M., et al. (2013). Decellularization of Human and Porcine Lung Tissues for Pulmonary Tissue Engineering. *Ann. Thorac. Surg.* 96, 1046–1056. discussion 1055-6. doi:10.1016/j.athoracsur.2013.04.022

Oono, T., Specks, U., Eckes, B., Majewski, S., Hunzelmann, N., Timpl, R., et al. (1993). Expression of Type VI Collagen mRNA during Wound Healing. *J. Invest. Dermatol.* 100, 329–334. doi:10.1111/1523-1747.ep12470022

Ott, H. C., Matthiesen, T. S., Goh, S.-K., Black, L. D., Kren, S. M., Netoff, T. I., et al. (2008). Perfusion-decellularized Matrix: Using Nature's Platform to Engineer a Bioartificial Heart. *Nat. Med.* 14, 213–221. doi:10.1038/nm1684

Ouyang, L., Yao, R., Zhao, Y., and Sun, W. (2016). Effect of Bioink Properties on Printability and Cell Viability for 3D Bioplotting of Embryonic Stem Cells. *Biofabrication* 8, 035020. doi:10.1088/1758-5090/8/3/035020

Pannier, A. K., and Shea, L. D. (2004). Controlled Release Systems for DNA Delivery. *Mol. Ther.* 10, 19–26. doi:10.1016/j.ymthe.2004.03.020

Paramasivam, T., Maiti, S. K., Palakkara, S., Divy Mohan, R., Manjunthaachar, H. V., et al. (2021). Effect of PDGF-B Gene-Activated Acellular Matrix and Mesenchymal Stem Cell Transplantation on Full Thickness Skin Burn Wound in Rat Model. *Tissue Eng. Regen. Med.* 18, 235–251. doi:10.1007/s13770-020-00302-3

Park, D. Y., Yun, H. W., Lim, S., Truong, M. D., Yin, X. Y., Park, J., et al. (2020). Cross-linked Cartilage Acellular Matrix Film Decreases Postsurgical Peritendinous Adhesions. *Artif. Organs* 44, E136–E149. doi:10.1111/aor.13591

Philandrianos, C., Andrac-Meyer, L., Mordon, S., Feuerstein, J.-M., Sabatier, F., Veran, J., et al. (2012). Comparison of Five Dermal Substitutes in Full-Thickness Skin Wound Healing in a Porcine Model. *Burns* 38, 820–829. doi:10.1016/j.burns.2012.02.008

Plikus, M. V., Guerrero-Juarez, C. F., Ito, M., Li, Y. R., Dedhia, P. H., Zheng, Y., et al. (2017). Regeneration of Fat Cells from Myofibroblasts during Wound Healing. *Science* 355, 748–752. doi:10.1126/science.aai8792

Porzionato, A., Stocco, E., Barbon, S., Grandi, F., Macchi, V., and De Caro, R. (2018). Tissue-Engineered Grafts from Human Decellularized Extracellular Matrices: A Systematic Review and Future Perspectives. *Int. J. Mol. Sci.* 19. doi:10.3390/ijms19124117

Pouliot, N., Saunders, N. A., and Kaur, P. (2002). Laminin 10/11: an Alternative Adhesive Ligand for Epidermal Keratinocytes with a Functional Role in Promoting Proliferation and Migration. *Exp. Dermatol.* 11, 387–397. doi:10.1034/j.1600-0625.2002.110501.x

Pouliot, R. A., Young, B. M., Link, P. A., Park, H. E., Kahn, A. R., Shankar, K., et al. (2020). Porcine Lung-Derived Extracellular Matrix Hydrogel Properties Are Dependent on Pepsin Digestion Time. *Tissue Eng. Part C: Methods* 26, 332–346. doi:10.1089/ten.tec.2020.0042

Pozzi, A., Yurchenco, P. D., and Iozzo, R. V. (2017). The Nature and Biology of Basement Membranes. *Matrix Biol.* 57-58, 1–11. doi:10.1016/j.matbio.2016.12.009

Pradhan, L., Nabzdyk, C., Andersen, N. D., LoGerfo, F. W., and Veves, A. (2009). Inflammation and Neuropeptides: the Connection in Diabetic Wound Healing. *Expert Rev. Mol. Med.* 11, e2. doi:10.1017/s1462399409000945

Rabbani, M., Zakian, N., and Alimoradi, N. (2021). Contribution of Physical Methods in Decellularization of Animal Tissues. *J. Med. Signals Sens* 11, 1–11. doi:10.4103/jmss.jmss_2_20

Ramakrishnan, R., Sreelatha, H. V., Anil, A., Arumugham, S., Varkey, P., Senan, M., et al. (2020). Human-Derived Scaffold Components and Stem Cells Creating Immunocompatible Dermal Tissue Ensuing Regulated Nonfibrotic Cellular Phenotypes. *ACS Biomater. Sci. Eng.* 6, 2740–2756. doi:10.1021/acsbiomaterials.9b01961

Ramasamy, P., Krishnakumar, R., Rekha, R., Vaseeharan, B., Saraswathi, K., Raj, M., et al. (2021). Bio-Fabrication of Human Amniotic Membrane Zinc Oxide Nanoparticles and the Wet/Dry HAM Dressing Membrane for Wound Healing. *Front. Bioeng. Biotechnol.* 9, 695710. doi:10.3389/fbioe.2021.695710

Raziyeva, K., Kim, Y., Zharkinbekov, Z., Kassymbek, K., Jimi, S., and Saparov, A. (2021). Immunology of Acute and Chronic Wound Healing. *Biomolecules* 11. doi:10.3390/biom11050700

Reichling, J., Landvatter, U., Wagner, H., Kostka, K., and Schaefer, U. (2006). *In Vitro* studies on Release and Human Skin Permeation of Australian tea Tree Oil (TTO) from Topical Formulations. *Eur. J. Pharmaceutics Biopharmaceutics* 64, 222–228. doi:10.1016/j.ejpb.2006.05.006

Rieder, E., Kasimir, M.-T., Silberhumer, G., Seebacher, G., Wolner, E., Simon, P., et al. (2004). Decellularization Protocols of Porcine Heart Valves Differ Importantly in Efficiency of Cell Removal and Susceptibility of the Matrix to Recellularization with Human Vascular Cells. *J. Thorac. Cardiovasc. Surg.* 127, 399–405. doi:10.1016/j.jtcvs.2003.06.017

Rippa, A. L., Kalabusheva, E. P., and Vorotelyak, E. A. (2019). Regeneration of Dermis: Scarring and Cells Involved. *Cells* 8, 607. doi:10.3390/cells8060607

Rodero, M. P., and Khosrotehrani, K. (2010). Skin Wound Healing Modulation by Macrophages. *Int. J. Clin. Exp. Pathol.* 3, 643–653.

Rodrigues, M., Kosaric, N., Bonham, C. A., and Gurtner, G. C. (2019). Wound Healing: A Cellular Perspective. *Physiol. Rev.* 99, 665–706. doi:10.1152/physrev.00067.2017

Rousselle, P., Montmasson, M., and Garnier, C. (2019). Extracellular Matrix Contribution to Skin Wound Re-epithelialization. *Matrix Biol.* 75-76, 12–26. doi:10.1016/j.matbio.2018.01.002

Santoro, M., and Gaudino, G. (2005). Cellular and Molecular Facets of Keratinocyte Reepithelization during Wound Healing. *Exp. Cel Res.* 304, 274–286. doi:10.1016/j.yexcr.2004.10.033

Savitri, C., Ha, S. S., Liao, E., Du, P., and Park, K. (2020). Extracellular Matrices Derived from Different Cell Sources and Their Effect on Macrophage Behavior and Wound Healing. *J. Mater. Chem. B* 8, 9744–9755. doi:10.1039/d0tb01885f

Schenke-Layland, K., and Nerem, R. M. (2011). *In Vitro* human Tissue Models - Moving towards Personalized Regenerative Medicine. *Adv. Drug Deliv. Rev.* 63, 195–196. doi:10.1016/j.addr.2011.05.001

Schneider, M., and Nesheim, M. (2004). A Study of the protection of Plasmin from Antiplasmin Inhibition within an Intact Fibrin Clot during the Course of Clot Lysis. *J. Biol. Chem.* 279, 13333–13339. doi:10.1074/jbc.m313164200

Schnoor, M., Cullen, P., Lorkowski, J., Stolle, K., Robenek, H., Troyer, D., et al. (2008). Production of Type VI Collagen by Human Macrophages: a New Dimension in Macrophage Functional Heterogeneity. *J. Immunol.* 180, 5707–5719. doi:10.4049/jimmunol.180.8.5707

Schurr, M. J., Foster, K. N., Centanni, J. M., Comer, A. R., Wicks, A., Gibson, A. L., et al. (2009). Phase I/II Clinical Evaluation of StrataGraft: a Consistent, Pathogen-free Human Skin Substitute. *J. Trauma* 66, 866–874. discussion 873-4. doi:10.1097/ta.0b013e31819849d6

Seif-Naraghi, S. B., Salvatore, M. A., Schup-Magoffin, P. J., Hu, D. P., and Christman, K. L. (2010). Design and Characterization of an Injectable Pericardial Matrix Gel: a Potentially Autologous Scaffold for Cardiac Tissue Engineering. *Tissue Eng. Part A* 16, 2017–2027. doi:10.1089/ten.tea.2009.0768

Senyürek, I., Kempf, W. E., Klein, G., Maurer, A., Kalbacher, H., Schäfer, L., et al. (2014). Processing of Laminin α Chains Generates Peptides Involved in Wound Healing and Host Defense. *J. Innate Immun.* 6, 467–484. doi:10.1159/000357032

Seppinen, L., Sormunen, R., Soini, Y., Elamaa, H., Heljasvaara, R., and Pihlajaniemi, T. (2008). Lack of Collagen XVIII Accelerates Cutaneous Wound Healing, while Overexpression of its Endostatin Domain Leads to Delayed Healing. *Matrix Biol.* 27, 535–546. doi:10.1016/j.matbio.2008.03.003

Shalitin, N., Schlesinger, H., Levy, M. J., Kessler, E., and Kessler-Icekson, G. (2003). Expression of Procollagen C-Proteinase Enhancer in Cultured Rat Heart Fibroblasts: Evidence for Co-regulation with Type I Collagen. *J. Cel. Biochem.* 90, 397–407. doi:10.1002/jcb.10646

Sher, I., Zisman-Rozen, S., Eliahu, L., Whitelock, J. M., Maas-Szabowski, N., Yamada, Y., et al. (2006). Targeting Perlecan in Human Keratinocytes Reveals Novel Roles for Perlecan in Epidermal Formation. *J. Biol. Chem.* 281, 5178–5187. doi:10.1074/jbc.m509500200

Shirakata, Y., Kimura, R., Nanba, D., Iwamoto, R., Tokumaru, S., Morimoto, C., et al. (2005). Heparin-binding EGF-like Growth Factor Accelerates Keratinocyte Migration and Skin Wound Healing. *J. Cel Sci* 118, 2363–2370. doi:10.1242/jcs.02346

Sierad, L. N., Shaw, E. L., Bina, A., Brazile, B., Rierson, N., Patnaik, S. S., et al. (2015). Functional Heart Valve Scaffolds Obtained by Complete Decellularization of Porcine Aortic Roots in a Novel Differential Pressure Gradient Perfusion System. *Tissue Eng. Part C: Methods* 21, 1284–1296. doi:10.1089/ten.tec.2015.0170

Singh, H., Purohit, S. D., Bhaskar, R., Yadav, I., Bhushan, S., Gupta, M. K., et al. (2022). Curcumin in Decellularized Goat Small Intestine Submucosa for Wound Healing and Skin Tissue Engineering. *J. Biomed. Mater. Res.* 110, 210–219. doi:10.1002/jbm.b.34903

Song, M., Wang, W., Ye, Q., Bu, S., Shen, Z., and Zhu, Y. (2017). The Repairing of Full-Thickness Skin Deficiency and its Biological Mechanism Using Decellularized Human Amniotic Membrane as the Wound Dressing. *Mater. Sci. Eng. C* 77, 739–747. doi:10.1016/j.msec.2017.03.232

Storstein, L. (1989). Electrophysiological Alterations in Heart Failure. *Eur. Heart J.* 10 (Suppl. C), 9–12. doi:10.1093/eurheartj/10.suppl_c.9

Sugawara, K., Tsuruta, D., Ishii, M., Jones, J. C. R., and Kobayashi, H. (2008). Laminin-332 and -511 in Skin. *Exp. Dermatol.* 17, 473–480. doi:10.1111/j.1600-0625.2008.00721.x

Sutjarittangtham, K., Sanpa, S., Tunkasiri, T., Chantawannakul, P., Intatha, U., and Eitssayeam, S. (2014). Bactericidal Effects of Propolis/polylactic Acid (PLA) Nanofibres Obtained via Electrospinning. *J. Apicultural Res.* 53, 109–115. doi:10.3896/ibra.1.53.1.11

Syed, O., Walters, N. J., Day, R. M., Kim, H.-W., and Knowles, J. C. (2014). Evaluation of Decellularization Protocols for Production of Tubular Small Intestine Submucosa Scaffolds for Use in Oesophageal Tissue Engineering. *Acta Biomater.* 10, 5043–5054. doi:10.1016/j.actbio.2014.08.024

Tajima, K., Kuroda, K., Otaka, Y., Kinoshita, R., Kita, M., Oyamada, T., et al. (2020). Decellularization of Canine Kidney for Three-Dimensional Organ Regeneration. *Vet. World* 13, 452–457. doi:10.14202/vetworld.2020.452-457

Takeo, M., Lee, W., and Ito, M. (2015). Wound Healing and Skin Regeneration. *Cold Spring Harbor Perspect. Med.* 5, a023267. doi:10.1101/cshperspect.a023267

Tan, Q.-W., Tang, S.-L., Zhang, Y., Yang, J.-Q., Wang, Z.-L., Xie, H.-Q., et al. (2019). Hydrogel from Acellular Porcine Adipose Tissue Accelerates Wound Healing by Inducing Intradermal Adipocyte Regeneration. *J. Invest. Dermatol.* 139, 455–463. doi:10.1016/j.jid.2018.08.013

Tao, M., Ao, T., Mao, X., Yan, X., Javed, R., Hou, W., et al. (2021). Sterilization and Disinfection Methods for Decellularized Matrix Materials: Review, Consideration and Proposal. *Bioactive Mater.* 6, 2927–2945. doi:10.1016/j.bioactmat.2021.02.010

To, W. S., and Midwood, K. S. (2011). Plasma and Cellular Fibronectin: Distinct and Independent Functions during Tissue Repair. *Fibrogenesis Tissue Repair* 4, 21. doi:10.1186/1755-1536-4-21

Tomasek, J. J., Gabbiani, G., Hinz, B., Chaponnier, C., and Brown, R. A. (2002). Myofibroblasts and Mechano-Regulation of Connective Tissue Remodelling. *Nat. Rev. Mol. Cel Biol* 3, 349–363. doi:10.1038/nrm809

Tracy, L. E., Minasian, R. A., and Caterson, E. J. (2016). Extracellular Matrix and Dermal Fibroblast Function in the Healing Wound. *Adv. Wound Care* 5, 119–136. doi:10.1089/wound.2014.0561

Travis, J., and Salvesen, G. S. (1983). Human Plasma Proteinase Inhibitors. *Annu. Rev. Biochem.* 52, 655–709. doi:10.1146/annurev.bi.52.070183.003255

Trent, J. F., and Kirsner, R. S. (1998). Tissue Engineered Skin: Apligraf, a Bi-layered Living Skin Equivalent. *Int. J. Clin. Pract.* 52, 408–413.

Valacchi, G., Zanardi, I., Sticozzi, C., Bocci, V., and Travagli, V. (2012). Emerging Topics in Cutaneous Wound Repair. *Ann. N. Y Acad. Sci.* 1259, 136–144. doi:10.1111/j.1749-6632.2012.06636.x

Ventura, R. D., Padalhin, A. R., Kim, B., Park, M., and Lee, B. T. (2020). Evaluation of Bone Regeneration Potential of Injectable Extracellular Matrix (ECM) from

Porcine Dermis Loaded with Biphasic Calcium Phosphate (BCP) Powder. *Mater. Sci. Eng. C* 110, 110663. doi:10.1016/j.msec.2020.110663

Wagner, D. E., Bonenfant, N. R., Parsons, C. S., Sokocevic, D., Brooks, E. M., Borg, Z. D., et al. (2014). Comparative Decellularization and Recellularization of normal versus Emphysematous Human Lungs. *Biomaterials* 35, 3281–3297. doi:10.1016/j.biomaterials.2013.12.103

Wainwright, D. J. (1995). Use of an Acellular Allograft Dermal Matrix (AlloDerm) in the Management of Full-Thickness burns. *Burns* 21, 243–248. doi:10.1016/0305-4179(95)93866-i

Wallace, H. A., Basehore, B. M., and Zito, P. M. (2021). *Wound Healing Phases*. Treasure Island (FL): StatPearls.

Wang, B., Borazjani, A., Tahai, M., Curry, A. L., Simionescu, D. T., Guan, J., et al. (2010). Fabrication of Cardiac Patch with Decellularized Porcine Myocardial Scaffold and Bone Marrow Mononuclear Cells. *J. Biomed. Mater. Res. A.* 94, 1100–1110. doi:10.1002/jbm.a.32781

Wang, B., Li, W., and Harrison, J. (2020). An Evaluation of Wound Healing Efficacy of a Film Dressing Made from Polymer-Integrated Amnion Membrane. *Organogenesis* 16, 126–136. doi:10.1080/15476278.2020.1844507

Wang, C., Li, G., Cui, K., Chai, Z., Huang, Z., Liu, Y., et al. (2021). Sulfated Glycosaminoglycans in Decellularized Placenta Matrix as Critical Regulators for Cutaneous Wound Healing. *Acta Biomater.* 122, 199–210. doi:10.1016/j.actbio.2020.12.055

Wang, L., Gong, J., Dan, Y., Huang, Y., Dan, N., and Dan, W. (2020). Preparation and Characterization of Antibacterial Porcine Acellular Dermal Matrices with High Performance. *ACS Omega* 5, 20238–20249. doi:10.1021/acsomega.0c01940

Wang, Y., Lu, F., Hu, E., Yu, K., Li, J., Bao, R., et al. (2021). Biogenetic Acellular Dermal Matrix Maintaining Rich Interconnected Microchannels for Accelerated Tissue Amendment. *ACS Appl. Mater. Inter.* 13, 16048–16061. doi:10.1021/acsami.1c00420

Whitelock, J. M., Melrose, J., and Iozzo, R. V. (2008). Diverse Cell Signaling Events Modulated by Perlecan. *Biochemistry* 47, 11174–11183. doi:10.1021/bi8013938

Wierzbicka-Patynowski, I., and Schwarzbauer, J. E. (2003). The Ins and Outs of Fibronectin Matrix Assembly. *J. Cel Sci* 116, 3269–3276. doi:10.1242/jcs.00670

Windsor, M. L., Eisenberg, M., Gordon-Thomson, C., and Moore, G. P. (2009). A Novel Model of Wound Healing in the SCID Mouse Using a Cultured Human Skin Substitute. *Australas. J. Dermatol.* 50, 29–35. doi:10.1111/j.1440-0960.2008.00512.x

Won, J.-Y., Lee, M.-H., Kim, M.-J., Min, K.-H., Ahn, G., Han, J.-S., et al. (2019). A Potential Dermal Substitute Using Decellularized Dermis Extracellular Matrix Derived Bio-Ink. *Artif. Cell Nanomedicine, Biotechnol.* 47, 644–649. doi:10.1080/21691401.2019.1575842

Wong, R., Geyer, S., Weninger, W., Guimberteau, J.-C., and Wong, J. K. (2016). The Dynamic Anatomy and Patterning of Skin. *Exp. Dermatol.* 25, 92–98. doi:10.1111/exd.12832

Wu, C. (1997). Roles of Integrins in Fibronectin Matrix Assembly. *Histol. Histopathol* 12, 233–240.

Wu, X., Kathuria, N., Patrick, C. W., and Reece, G. P. (2008). Quantitative Analysis of the Microvasculature Growing in the Fibrin Interface between a Skin Graft and the Recipient Site. *Microvasc. Res.* 75, 119–129. doi:10.1016/j.mvr.2007.04.012

Wynn, T., and Barron, L. (2010). Macrophages: Master Regulators of Inflammation and Fibrosis. *Semin. Liver Dis.* 30, 245–257. doi:10.1055/s-0030-1255354

Xu, J., Fang, H., Zheng, S., Li, L., Jiao, Z., Wang, H., et al. (2021). A Biological Functional Hybrid Scaffold Based on Decellularized Extracellular Matrix/gelatin/chitosan with High Biocompatibility and Antibacterial Activity for Skin Tissue Engineering. *Int. J. Biol. Macromolecules* 187, 840–849. doi:10.1016/j.ijbiomac.2021.07.162

Xue, M., and Jackson, C. J. (2015). Extracellular Matrix Reorganization during Wound Healing and its Impact on Abnormal Scarring. *Adv. Wound Care* 4, 119–136. doi:10.1089/wound.2013.0485

Yan, Q., and Sage, E. H. (1999). SPARC, a Matricellular Glycoprotein with Important Biological Functions. *J. Histochem. Cytochem.* 47, 1495–1505. doi:10.1177/002215549904701201

Yang, C.-C., Sheu, H.-M., Chung, P.-L., Chang, C.-H., Tsai, Y.-S., Hughes, M. W., et al. (2015). Leptin of Dermal Adipose Tissue Is Differentially Expressed during the Hair Cycle and Contributes to Adipocyte-Mediated Growth Inhibition of Anagen-phase Vibrissa Hair. *Exp. Dermatol.* 24, 57–60. doi:10.1111/exd.12566

Yang, Y., Zhang, Y., Yan, Y., Ji, Q., Dai, Y., Jin, S., et al. (2020). A Sponge-like Double-Layer Wound Dressing with Chitosan and Decellularized Bovine Amniotic Membrane for Promoting Diabetic Wound Healing. *Polymers (Basel)* 12, 535. doi:10.3390/polym12030535

Yeh, D. D., Nazarian, R. M., Demetri, L., Mesar, T., Dijkink, S., Larentzakis, A., et al. (2017). Histopathological Assessment of OASIS Ultra on Critical-Sized Wound Healing: a Pilot Study. *J. Cutan. Pathol.* 44, 523–529. doi:10.1111/cup.12925

Ying, G. L., Jiang, N., Maharjan, S., Yin, Y. X., Chai, R. R., Cao, X., et al. (2018). Aqueous Two-phase Emulsion Bioink-Enabled 3D Bioprinting of Porous Hydrogels. *Adv. Mater.* 30, e1805460. doi:10.1002/adma.201805460

Yousef, H., Alhajj, M., and Sharma, S. (2021). *Anatomy, Skin (Integument), Epidermis, StatPearls*. Treasure Island (FL).

Yu, C., Wang, F., Jin, C., Huang, X., Miller, D. L., Basilico, C., et al. (2003). Role of Fibroblast Growth Factor Type 1 and 2 in Carbon Tetrachloride-Induced Hepatic Injury and Fibrogenesis. *Am. J. Pathol.* 163, 1653–1662. doi:10.1016/s0002-9440(10)63522-5

Yuan, J., Li, W., Huang, J., Guo, X., Li, X., Lu, X., et al. (2015). Transplantation of Human Adipose Stem Cell-Derived Hepatocyte-like Cells with Restricted Localization to Liver Using Acellular Amniotic Membrane. *Stem Cel Res Ther* 6, 217. doi:10.1186/s13287-015-0208-9

Yurchenco, P. D. (2015). Integrating Activities of Laminins that Drive Basement Membrane Assembly and Function. *Curr. Top. Membr.* 76, 1–30. doi:10.1016/bs.ctm.2015.05.001

Zahiri, S., Masaeli, E., Poorazizi, E., and Nasr-Esfahani, M. H. (2018). Chondrogenic Response in Presence of Cartilage Extracellular Matrix Nanoparticles. *J. Biomed. Mater. Res.* 106, 2463–2471. doi:10.1002/jbm.a.36440

Zare-Bidaki, M., Sadrinia, S., Erfani, S., Afkar, E., and Ghanbarzade, N. (2017). Antimicrobial Properties of Amniotic and Chorionic Membranes: A Comparative Study of Two Human Fetal Sacs. *J. Reprod. Infertil* 18, 218–224.

Zhang, X., Chen, X., Hong, H., Hu, R., Liu, J., and Liu, C. (2022). Decellularized Extracellular Matrix Scaffolds: Recent Trends and Emerging Strategies in Tissue Engineering. *Bioactive Mater.* 10, 15–31. doi:10.1016/j.bioactmat.2021.09.014

Zhao, F., Cheng, J., Sun, M., Yu, H., Wu, N., Li, Z., et al. (2020). Digestion Degree Is a Key Factor to Regulate the Printability of Pure Tendon Decellularized Extracellular Matrix Bio-Ink in Extrusion-Based 3D Cell Printing. *Biofabrication* 12, 045011. doi:10.1088/1758-5090/aba411

Zhao, F., Cheng, J., Zhang, J., Yu, H., Dai, W., Yan, W., et al. (2021). Comparison of Three Different Acidic Solutions in Tendon Decellularized Extracellular Matrix Bio-Ink Fabrication for 3D Cell Printing. *Acta Biomater.* 131, 262–275. doi:10.1016/j.actbio.2021.06.026

Zhao, J.-Y., Chai, J.-K., Song, H.-F., Zhang, J., Xu, M.-H., and Liang, Y.-D. (2013). Influence of Hyaluronic Acid on Wound Healing Using Composite Porcine Acellular Dermal Matrix Grafts and Autologous Skin in Rabbits. *Int. Wound J.* 10, 562–572. doi:10.1111/j.1742-481x.2012.01023.x

Zhao, Y., Fan, J., and Bai, S. (2019). Biocompatibility of Injectable Hydrogel from Decellularized Human Adipose Tissue *In Vitro* and *In Vivo*. *J. Biomed. Mater. Res.* 107, 1684–1694. doi:10.1002/jbm.b.34261

Zhu, S., Gu, Z., Hu, Y., Dan, W., and Xiong, S. (2016). Evaluation of Alginate Dialdehyde as a Suitable Crosslinker on Modifying Porcine Acellular Dermal Matrix: The Aggregation of Collagenous Fibers. *J. Appl. Polym. Sci.* 133, 1. doi:10.1002/app.43550

Conflict of Interest: The authors declare that the research was conducted in the absence of any commercial or financial relationships that could be construed as a potential conflict of interest.

Publisher's Note: All claims expressed in this article are solely those of the authors and do not necessarily represent those of their affiliated organizations, or those of the publisher, the editors and the reviewers. Any product that may be evaluated in this article, or claim that may be made by its manufacturer, is not guaranteed or endorsed by the publisher.

Copyright © 2022 Solarte David, Güiza-Argüello, Arango-Rodríguez, Sossa and Becerra-Bayona. This is an open-access article distributed under the terms of the Creative Commons Attribution License (CC BY). The use, distribution or reproduction in other forums is permitted, provided the original author(s) and the copyright owner(s) are credited and that the original publication in this journal is cited, in accordance with accepted academic practice. No use, distribution or reproduction is permitted which does not comply with these terms.

frontiers in Bioengineering and Biotechnology

REVIEW
published: 17 February 2022
doi: 10.3389/fbioe.2022.830899

Can Heart Valve Decellularization Be Standardized? A Review of the Parameters Used for the Quality Control of Decellularization Processes

*F. Naso *† and A. Gandaglia*

Biocompatibility Innovation Srl, Este (PD), Italy

When a tissue or an organ is considered, the attention inevitably falls on the complex and delicate mechanisms regulating the correct interaction of billions of cells that populate it. However, the most critical component for the functionality of specific tissue or organ is not the cell, but the cell-secreted three-dimensional structure known as the extracellular matrix (ECM). Without the presence of an adequate ECM, there would be no optimal support and stimuli for the cellular component to replicate, communicate and interact properly, thus compromising cell dynamics and behaviour and contributing to the loss of tissue-specific cellular phenotype and functions. The limitations of the current bioprosthetic implantable medical devices have led researchers to explore tissue engineering constructs, predominantly using animal tissues as a potentially unlimited source of materials. The high homology of the protein sequences that compose the mammalian ECM, can be exploited to convert a soft animal tissue into a human autologous functional and long-lasting prosthesis ensuring the viability of the cells and maintaining the proper biomechanical function. Decellularization has been shown to be a highly promising technique to generate tissue-specific ECM-derived products for multiple applications, although it might comprise very complex processes that involve the simultaneous use of chemical, biochemical, physical and enzymatic protocols. Several different approaches have been reported in the literature for the treatment of bone, cartilage, adipose, dermal, neural and cardiovascular tissues, as well as skeletal muscle, tendons and gastrointestinal tract matrices. However, most of these reports refer to experimental data. This paper reviews the most common and latest decellularization approaches that have been adopted in cardiovascular tissue engineering. The efficacy of cells removal was specifically reviewed and discussed, together with the parameters that could be used as quality control markers for the evaluation of the effectiveness of decellularization and tissue biocompatibility. The purpose was to provide a panel of parameters that can be shared and taken into consideration by the scientific community to achieve more efficient, comparable, and reliable experimental research results and a faster technology transfer to the market.

Keywords: biocompatibility, heart valve decellularization, protocols standardization, xenoantigens removal, regenerative medicine

OPEN ACCESS

Edited by:
Sotirios Korossis, Loughborough University, United Kingdom

Reviewed by:
Katsuhiro Hosoyama, Iwate Prefectural Central Hospital, Japan
Helen E Berry, University of Leeds, United Kingdom

****Correspondence:***
F. Naso
filippo.naso@biocompatibility.bio

†These authors have contributed equally to this work and share first authorship

Specialty section:
This article was submitted to Biomaterials, a section of the journal Frontiers in Bioengineering and Biotechnology

Received: *07 December 2021*
Accepted: *31 January 2022*
Published: *17 February 2022*

Citation:
Naso F and Gandaglia A (2022) Can Heart Valve Decellularization Be Standardized? A Review of the Parameters Used for the Quality Control of Decellularization Processes. Front. Bioeng. Biotechnol. 10:830899. doi: 10.3389/fbioe.2022.830899

TABLE 1 | Description of the most common components that contribute to forming the ECM.

ECM component	Features and function	
COLLAGEN	Representing the structural proteins that are the most abundant in the ECM. The molecular feature of collagen is the glycine–*X*–*Y* triplet repeat, where *X* frequently represents proline and *Y* represents hydroxyproline. Collagen provides structural strength to the ECM.	**Type I** Fibrillar collagen, primarily found in the ECM of skin and bone. Type I collagen is by far the most abundant type of all collagens. Genetic defects can cause osteogenesis imperfecta. **Type II** Fibrillar collagen, primarily found in the ECM of cartilage. **Type III** Fibrillar collagen, primarily found in the ECM of elastic tissues such as lung and blood vessels. **Type IV** Network-forming collagen, primarily found in the basement membrane. **Type V** Fibrillar collagen found in the ECM of a wide variety of different tissues.
ELASTIN	Mature elastin proteins result in a coiled conformation that allows these proteins to expand and contract in response to tensile stress. Elastin thus endows the ECM with elastic recoil and is abundant in tissues that require frequent expansion and contraction. Predominant tissues requiring this function are the lungs and cardiovascular ones.	
PROTEOGLYCANS	Proteoglycans represent a diverse group of ECM core proteins that are covalently bound to glycosaminoglycans (GAGs). GAGs are unbranched carbohydrates that consist of repeating disaccharide subunits that vary in number, these saccharide elements can undergo modification by epimerization and sulfation resulting in a vast diversity of GAG chains. Through these GAG chains, proteoglycans acquire a high negative charge leading to the attraction of positively charged electrolytes and the movement of water molecules that travel by osmosis to the proteoglycan. The resulting collection of molecules forms a gel that can expand and fulfil important ECM hydration and lubrication effects	**Heparan sulfate** Heparan sulfate (HS) is a linear polysaccharide found in all animal tissues. It occurs as a proteoglycan (PG) in which two or three HS chains are attached near to the cell surface or ECM proteins. It is in this form that HS binds to a variety of protein ligands and regulates a wide variety of biological activities, including developmental processes, angiogenesis, blood coagulation, and tumour metastasis. In the extracellular matrix, especially basement membranes, the multi-domain proteins perlecan, agrin, and collagen XVIII are the main proteins to which heparan sulfate is attached. **Chondroitin sulfate** Chondroitin sulfates (CS) contribute to the tensile strength of cartilage, tendons, ligaments, and walls of the aorta. They have also been known to affect neuroplasticity. **Keratan sulfate** Keratan sulfates (KS) have a variable sulfate content and, unlike many other GAGs, do not contain uronic acid. They are present in the cornea, cartilage, bones, and horns of animals.
HYALURONIC ACID	Non-proteoglycan polysaccharide hyaluronic acid (or "hyaluronan") is a polysaccharide consisting of alternating residues of D-glucuronic acid and N-acetylglucosamine, and unlike other GAGs, is not found as a proteoglycan. Hyaluronic acid in the extracellular space confers upon tissues the ability to resist compression by providing a counteracting turgor (swelling) force by absorbing significant amounts of water. Hyaluronic acid is thus found in abundance in the ECM of load-bearing joints. It is also a chief component of the interstitial gel. Hyaluronic acid is found on the inner surface of the cell membrane and is translocated out of the cell during biosynthesis. Hyaluronic acid acts as an environmental cue that regulates cell behaviour during embryonic development, healing processes, inflammation, and tumour development. It interacts with a specific transmembrane receptor, CD44.	
GLYCOPROTEINS	Glycoproteins greatly contribute to making the ECM a cohesive network of molecules, although they also perform other functions. Glycoproteins are intermediaries that link structural molecules between each other, and also link structural molecules and cells. In each glycoprotein molecule, several domains are binding different molecules that altogether form cross-linked molecular networks. Fibronectins, laminins and tenascins are major glycoproteins of the animal ECM.	**Fibronectin** Fibronectin is a dimer comprised of two similar monomers that have a molecular weight of 220–250 kDa and are covalently linked on the C-terminal ends. Each monomer contains repeating motifs that are organized into distinct functional domains. These domains allow the binding of specific ligands, like integrins and collagens, that participate in signal transduction and contribute to the regulation of cellular activities such as branching morphogenesis. Fibronectins also help at the site of tissue injury by binding to platelets during blood clotting and facilitating cell movement to the affected area during wound healing. **Laminin** Laminins are proteins found in the basal laminae of virtually all animals. Rather than forming collagen-like fibers, laminins form networks of web-like structures that resist tensile forces in the basal lamina. They also assist in cell adhesion. Laminins bind other ECM components such as collagens and nidogens. **Tenascins** The molecular structure shows a modular hexameric organization. Several isoforms of tenascin can be obtained by alternative splicing of the messenger RNA. Tenascin-C is released into the extracellular matrix of tendons, bones and cartilage during embryonary development.

(Continued on following page)

TABLE 1 | (*Continued*) Description of the most common components that contribute to forming the ECM.

ECM component	Features and function
	Tenascin-C is overexpressed as a consequence of tissue damages like a heart attack. Tenascin-R is abundant in the nervous system, both during development and in adults. Tenascin-X is present in the connective tissue and can be abundant in muscles under heavy activity, like in professional athletes. Like other glycoproteins, tenascins change the cohesive state of the ECM by binding integrins, fibronectins, collagens and proteoglycans. In animals, each type of tenascin is expressed in particular locations of the organism, that may change during development. The expression of tenascins is induced in tissues being repaired, or during tumour and pathological processes.

INTRODUCTION

Generally, in biological tissue, the main component in terms of volume is not related to the cells, but rather to the cell-secreted three-dimensional extracellular matrix (ECM; **Table 1**). The ECM provides structural and histoarchitectural integrity and mechanical support in the tissues and organs, working actively in the exchange of ions, nutrients, waters, metabolites, and signals (Gattazzo et al., 2014). The sequencing of the human genome revealed hundreds of proteins that are involved in the constitution of the mature ECM (Naba et al., 2011). The set of these proteins constitutes the matrisome that comprises approximately 1–1.5% of the mammalian proteome (Hynes and Naba, 2011). The ECM acts as a multi-functional environment in which tissue-resident cells attach, communicate and interact, thereby regulating cell dynamics and behaviour and contributing to the maintenance of tissue-specific cell phenotypes and functions. To date, a number of different animal-tissue-derived ECMs have been used to produce bioprosthetic (chemically treated) substitutes for various applications such as for bone, cartilage, muscle, tendon, vascular graft, heart valve, nerve, dermal and gastrointestinal tract tissue repair or replacement (Badylak et al., 2009; Brown and Badylack, 2014; Folli et al., 2018). Many of these biological medical devices have been subjected to treatments that allow preservation of their functionality, but not the viability of their cellular content. Non-viable tissue is not capable of ECM regeneration and remodelling, thus limiting their lifespan and imposing the need for frequent replacement, forcing patients to multiple surgical interventions. To overcome this limitation and develop viable and functional engineered animal-derived ECMs, native tissues have been subjected to controlled removal of their cellular content, generating a decellularized three-dimensional scaffold (Crapo et al., 2011). Reported decellularization protocols have included a combination of physical techniques, detergents, enzymes and chemical compounds that have been shown not to adversely affect the architectural, ultrastructural, mechanical or biological integrity of the ECM (see **Table 2**). Unfortunately, there has been a lack of standardized assessment of tissue-specific decellularization methods, which compromises the effective comparison of the efficiency of different protocols (Bruyneel and Carr, 2017). Post-decellularization tissue characterization has included *in vitro* and *in vivo* studies providing data that are limited to the removal of the endogenous DNA in the ECM scaffolds and the safety of implantable commercial products. However, even when marketed decellularized products have been certified with the ISO standard for biological medical devices, several adverse reactions have been reported when introduced into the clinical setting (Simon et al., 2003; Kasimir et al., 2005; Ruffer et al., 2010; Woo et al., 2016). In particular, clinical application of decellularized porcine pulmonary valves exhibited massive inflammatory reaction associated with necrosis and graft stenosis in adult patients (Breitenbach et al., 2014—; Perri et al., 2012) with a relevant percentage of patients needed reoperation. Similarly, porcine intestinal submucosae (SIS) adopted for heart valve repair and reconstruction exhibited the presence of inflammatory cells, fibrosis and calcification after 4 years from the implant (Padalino et al., 2016—Hofmann et al., 2017—Mosala et al., 2017).

In addition, the literature survey has indicated that many different parameters have not been carefully considered in the assessment of decellularised scaffolds, even though they have been shown to be related to adverse events and/or dramatic side effects that compromised the functionality of the prosthesis in the patient and, ultimately, the patient's health.

HEART VALVE DECELLULARIZATION

Each year, more than 450.000 patients undergo heart valve replacement worldwide, and this number is estimated to reach 1.000.000 by 2050 due to the ageing population and the westernization of the lifestyle in several areas of the world, towards unbalanced diets with fatty foods and, consequently, the increase in cardiovascular disease (Naso and Gandaglia, 2018). Therapies for heart valve disease have most commonly comprised interventional and surgical approaches since pharmacological agents only address symptoms management. Surgical approach to dysfunctional heart valves can be addressed through the use of biological or mechanical prostheses. Bioprosthetic heart valves (BHVs) fabricated from bovine, porcine, or equine pericardium, bovine jugular vein, or porcine heart valve leaflets feature low thrombogenicity with no need for lifelong anti-coagulants (Carpentier et al., 1969). Unfortunately, the longevity of BHVs is limited by structural valve degeneration (SVD), which begins within 5 years after the

TABLE 2 | The most common decellularization approaches.

Decellularization approaches	Type		Rationale	Collateral effects	References
CHEMICALS	Acidic and alkaline solutions	Acetic-, peracetic-, hydrochloric- and sulfuric-acid as well as ammonium hydroxide	Disruption of cell membranes and intracellular organelles	Very aggressive toward the ECM protein such as collagen and to GAGs	Gilbert et al., (2006) Gilbert et al., (2005) Reing et al., (2010) Cornelison et al., (2018)
	Detergents	Non-ionic (Triton X-100), anionic (SDS, SDC), zwitterionic (CHAPS)	Solubilization of cell membranes and lipids	Possibility of denaturing proteins if used for a long time, difficulty of removal, and limited permeability	Korossis et al. (2002) Naso and Gandaglia, (2018) Wilson et al., (1995) Konertz et al., (2005) Erdbrügger et al., (2006) Quint et al. (2011) Mendibil et al. (2020)
	Protease inhibitors	Phenylmethylsulfonylfluoride, aprotinin and leupeptin	Avoidance of ECM damages by endogenous proteases leaked from the lysed cells	Difficulty of removal, residual toxicity for cellular repopulation	Luo et al. (2014) Gallo et al., (2012)
	Antibiotics	Penicillin, streptomycin, or amphotericin B	Prevention of contamination	n.d	Rajab et al., (2020) Gilpin and Yang, (2017) Lin et al., (2004) Leyh et al., (2003)
ENZYMATIC	Nucleases	Endo- or exo-nucleases	Degradation of nucleic acids	n.d	Haupt et al. (2018)
	Proteases	Trypsin, pepsin, protease K	Proteins degradation	Alteration of the ECM structure, degradation of laminin, and removal of GAGs, resulting in severe mechanical weakness of the treated tissue	Naso and Gandaglia, (2018) Rieder et al., (2004) Poon et al. (2013)
	Lipases	Pancreatic, gastric lipase	Lipids hydrolysis and solubilization	n.d	Gilbert, (2012) Schenke-Layland et al. (2003)
	Di-saccharidases	alpha1,3 galactosidase, N-glycolylneuroaminidase	Removal of alpha-Gal and Neu5Gc xenogeneic epitopes	n.d	Gilbert, (2012) Naso et al., (2017)
PHYSICALS	Freeze-thawing	n.d	Mostly combined with shaking or agitation. Cell lysis is caused by the formation of ice crystals following the freezing process	Damaging of the ECM, cellular debris can persist on the ECM	Toumpaniari et al., (2020) Curtil et al., (1997a), Curtil et al., (1997b) Hung et al., (2013) Nonaka et al., (2013) Waletzko et al., (2020)
	Mechanical force	n.d	Facilitating chemical agent infiltration to achieve better cell lysis (shaking, agitation, high hydrostatic pressure, supercritical carbon dioxide)	Avoiding tissues with fragile ECM.	Butler et al., (2017)
	Perfusion (vacuum-assisted)	n.d	Endogenous vascular catheters provide to delivering decellularization solution within tissue even with the high structural organization	It is not always possible to apply, it is susceptible to bacterial infections and air embolization	

implantation and typically necessitates BHV replacement after 10–12 years from the surgery (Shinkawa et al., 2015). In particular, BHVs substitutes are subjected to structural degradation, calcification and immune response (Koziarz et al., 2020) as a consequence of incomplete biocompatibility of the animal tissue (frequently bovine pericardium) adopted for their manufacture (Simionescu et al., 2021). In fact, the treatment with glutaraldehyde (GLU, considered as the standard method to ensure tissue biocompatibility, increased mechanical strength, sterilization and safe storage of BHVs) is not able to reach

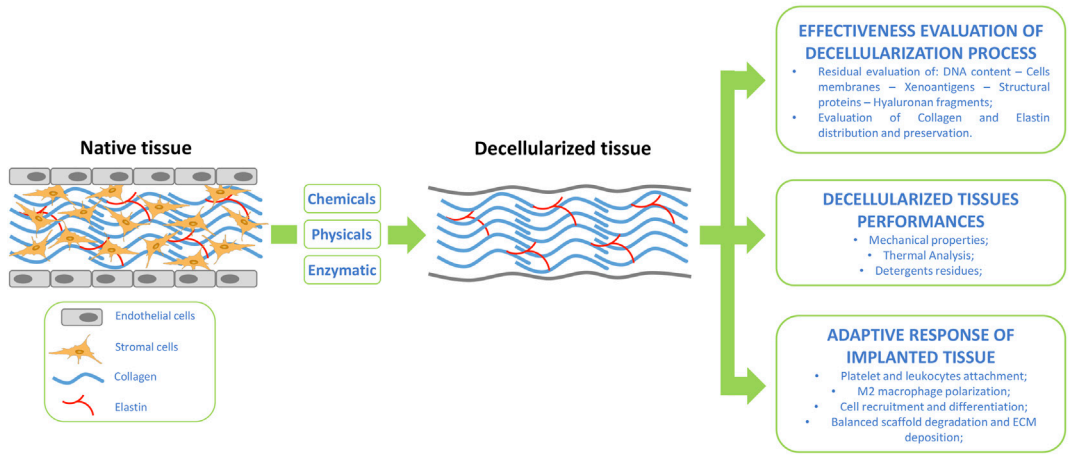

FIGURE 1 | Tissue decellularization flow-scheme supported by suggested assessment for post tissue treatment evaluation and implanted graft integration.

complete masking of the antigenic determinants of animal origin (Naso et al., 2013a). The *in vivo* interaction between such antigens and the patient's circulating antibody was shown to exert a powerful pro-calcific effect. Moreover, GLU is responsible be, by itself, a potential calcium-binding site due to the presence of residual aldehydes, acids and Schiff bases.

Evidence suggests that also homograft (allogeneic valves) suffers from a loss of function due to early donor-specific antibody and T cell-mediated responses to human leukocyte antigens (MHC Class 2 HLA-DR) inducing fever and vascular disfunction (Dignan et al., 2000). In particular, concerns have been expressed about the durability of homograft valves in younger pediatric patients after the failure within 8 months in a small clinical retrospective study, due to T- and B-lymphocytic infiltrates (Rajani et al., 1998).

Mechanical valves (tilting disk or bi-leaflets) are made from metal and/or pyrolytic carbon. The main disadvantage of this type of valve is the formation of thrombotic clots in the stagnation points and/or hemolysis which requires lifelong anticoagulation therapy for the patients (Harris et al., 2015).

Notwithstanding the tremendous technological progress in the field of heart valve therapy, an ideal heart valve replacement has yet to be developed, with current replacement options lowering the quality of life and the life expectancy of heart valve replacement patients when compared to age-matched healthy individuals (Huygens et al., 2016). In addition, heart valve replacements are very costly (circa 15 billion Euros annually in the United States and Europe), mainly due to the postoperative care costs and the need for re-operations (Huygens et al., 2018; Etnel et al., 2019). A clear, unmet clinical need remains for a heart valve substitute that does not degenerate, can adjust to functional and somatic changes, and can be implanted via minimally invasive techniques. To overcome these limitations the xenogeneic decellularised heart valve has been considered as an attractive alternative for the development of a viable biological valve, capable of remodelling and regeneration.

DECELLULARIZATION TECHNIQUES

Chemicals Approaches

A variety of chemicals, including detergents, solvents, acidic and alkaline solutions, and ionic solutions have been used to solubilize cellular membranes along with mechanical agitation or perfusion. Alkaline and acid treatments are very effective in solubilizing the cytoplasmic components; however, they have been rarely used since they are very aggressive towards the ECM proteins. Acetic-, peracetic-, hydrochloric- and sulfuric-acid, as well as ammonium hydroxide, are some examples of chemicals that have been shown to disrupt cellular membranes and intracellular organelles, whilst also dissociating important molecules, such as collagen, protein-protein bonds and GAGs (Gilbert et al., 2005; Gilbert et al., 2006; Reing et al., 2010; Cornelison et al., 2018).

Detergents have been used to solubilize cellular membranes and dissociate the intracellular structure. Nonionic detergents, such as Triton X-100 have been largely used in several decellularization protocols (Malone et al., 1984; Wilson et al., 1995; Bader et al., 1998; Kim et al., 2002; Meyer et al., 2005; Gallo et al., 2012), and has been shown to target the lipid–lipid and lipid-protein chemical bonds, leaving unaltered protein-protein interactions (Cartmell and Dunn, 2000; Woods and Gratzer, 2005). Although Triton X-100 is effective in the decellularization of tissues in which the key ECM component is primarily proteins, it has been generally avoided for the decellularization of tissues particularly rich in glycosaminoglycans (GAGs) (Korossis et al., 2002—; Booth et al., 2002). Moreover, Triton X-100 has often been adopted to remove the remnants of anionic detergents (sodium dodecyl sulfate; SDS) (Naso and Gandaglia, 2018). Anionic detergents including sodium deoxycholate (SDC) and SDS have been also used in many reported studies (Wilson et al., 1995; Korossis et al., 2002; Konertz et al., 2005; Erdbrügger et al., 2006; Gallo et al., 2012). SDS is reported to solubilize

both the external and nuclear membranes, but it has also been recognized to denature proteins, altering the native structure of the ECM (Chen et al., 2004; Elder et al., 2010). Owing to this, short treatments with SDS could be a reasonable choice, aiming at minimizing the possible damage to the ECM proteins and overall structure (Kim et al., 2002 -; Tavassoli et al., 2015). Nevertheless, SDS is considered very proficient in removing nuclear and cytoplasmic waste, even though it is more challenging to be rinsed out of the tissue due to its ionic nature (Rajab et al., 2020—; Syed et al., 2014—; Dettin et al., 2017).

Zwitterionic detergents share features of both nonionic and ionic detergents. They are electrically neutral molecules that have both positive and negative charges. The tendency of these detergents to denature proteins has been demonstrated to be lower than ionic detergents, but higher than nonionic ones. CHAPS {3-[(3-cholamidopropyl)dimethylammonio]-1-propanesulfonate} has been a commonly used zwitterionic detergent (Quint et al., 2011). Noteworthy, zwitterionic detergents have been reported not to be effective permeating agents and, therefore, have been mainly used to decellularize thin tissue (Mendibil et al., 2020).

During decellularization, endogenous proteases have been reported to leak in high amounts from the lysed cells, risking irreversible damage to the ECM (Crapo et al., 2011). Phenylmethylsulfonylfluoride (PMSF), aprotinin and leupeptin are common protease inhibitors that have been adopted to prevent proteolysis (Gallo et al., 2012; Luo et al., 2014). Some decellularization protocols have also included antibiotics, such as penicillin, streptomycin, or amphotericin B, to prevent tissue contamination during treatment (Leyh et al., 2003; Lin et al., 2004; Gilpin and Yang, 2017; Rajab et al., 2020).

Enzymatic Approaches

Biological protocols for tissue decellularization have involved enzymatic reactions, mainly to eliminate cell debris and other undesirable components of the ECM such as nucleic acids residues, fragments of cell membranes and mitochondrial DNA (Londono et al., 2017; Naso and Gandaglia, 2018). The removal of the nucleic acids residues has been of paramount importance in all decellularization processes, due to their tendency to remain stuck to ECM proteins and attract circulating calcium salt. To this end, decellularization protocols have utilized nucleases to catalyze the degradation of nucleic acids. Nucleases have been generally classified into endo- and exo-nucleases that cleave phosphodiester bonds within the nucleic acids and nucleotides from the end of nucleic acids respectively (Haupt et al., 2018).

Proteases have been used to catalyze the degradation of proteins and the effective detachment of the cellular component from its connective support. Among them, trypsin and pepsin have been the most commonly used proteases in decellularization protocols (Naso and Gandaglia, 2018), with the formers targeting the C-side bonds in arginine and lysine, and the latter being a highly aggressive protease commonly found in the stomach and also targeting the bonds between peptides. Noteworthy, the prolonged exposure to proteolytic enzymes has been reported to significantly alter the structure of the ECM, destroying laminin and removing GAGs, thus resulting in severe mechanical weakness of the tissue scaffold (Rieder et al., 2004; Poon et al., 2013; Naso and Gandaglia, 2018).

With a view to removing additional tissue components, different enzymes such as lipase that hydrolyzes lipids and can be useful for fatty tissues, and α-galactosidase that has been shown to be effective in removing the galactose-α-(1,3)-galactose xenoepitope, responsible for xenorejection in humans (Gilbert, 2012) have been used. Due to the aggressiveness of the enzymatic treatments on the ECM proteins, the concentration of the enzymes as well as the duration of the enzymatic treatment, have been shown to be critical parameters for achieving maximal decellularization effectiveness and minimal ECM degradation (Schenke-Layland et al., 2003).

Physical Approaches

Physical techniques alone have been shown inadequate to produce effective tissue decellularization. As such, they have been used in combination with chemical and/or enzymatic processes. Physical methods that have been reported to facilitate the decellularization process are summarized in **Table 2**. Briefly, freezing-thawing, direct pressure, agitation, sonication, vascular perfusion, thermal shock, ultrasonic and manual disruption have been shown to facilitate cell disruption, transportation of the decellularization solution to cells and washing out of the cellular debris from tissues (Toumpaniari et al., 2020).

Programmed Cell Death Approach

Studies have shown that suitable chemical signals can be coordinated for an intentional stimulation of the endogenous cellular apoptotic pathway. This approach has been reported to completely depend on the distribution of the precise ligands (Tumor Necrosis Factor Receptor TNFR1 (DR-1); Fas/CD95 (DR-2); Apoptosis Antigen Apo-3 (DR-3); TNF-related apoptosis inducible ligand-receptor TRAILR (DR-4 and DR-5); Nerve Growth Factor Receptor (NGFR); Ectodysplasin A Receptor (EDAR) that attach their analogous death receptors to the TNF superfamily (TNF alpha; FasL; TL1A; TRAIL; NGF and EDA respectively) and by the expression level of crucial genes elaborated in the extrinsic or intrinsic (perforin/granzyme) apoptotic pathways (Ashkenazi and Dixit, 1998; Wilson et al., 2009). Throughout the progression of apoptosis, the cellular substance has been shown to be retained within the plasma membrane and the apoptotic bodies. As such, the immunogenic cellular components are not secreted into the nearby environment, thus averting an immune-mediated inflammatory response (Bourgine et al., 2013). The lethal-environmental-conditioning method has been utilised by moderating environmental influences, such as temperature and pH, as well as carbon dioxide/oxygen, nitric oxide and hydrogen peroxide content (Somuncu, 2020).

TABLE 3 | Common reference ISO Standard for the production of class III implantable biological medical devices.

ISO Identification number	Subtitle	Topics covered
ISO 13485	Quality Management System (QMS)	The introduction of MDR (EU) 2017/745 provides that the device manufacturer has a Quality Management System (QMS) to improve and increase efficiency organizational processes
ISO 14630	Non-active surgical implants General requirements	The standard specifies the general requirements for performance, design, materials, design evaluation, manufacturing, sterilization, packaging and testing to prove compliance with these requirements
ISO 14971	Medical devices - Application of risk management to medical devices	The preparation of the Risk Analysis document allows the identification of hazards connected with the use of a medical device and in quantifying the risk that the damage occurs
ISO 22442	Medical devices utilizing animal tissues and their derivatives	This type of devices specific requirement is needed, for example for risk management process, contamination by bacteria, virus or anything else that may cause an undesirable pyrogenic, immunologic or toxicologic reaction
ISO 14160	Sterilization of health care products	Liquid chemical sterilizing agents for single-use medical devices utilizing animal tissues and their derivatives
ISO 10993	Biological Evaluation on Medical Devices	The standard provides for the realization of a series of tests for the evaluation of biocompatibility of medical devices, concerning their specific type and application
ISO 11607	Packaging for terminally sterilized medical devices	The standard provides guidance on how to ensure the sterility of the device once it is entered into the distribution cycle. Validation of the packaging guarantees that the packaging has been made properly for the product it contains
ISO 14155	Clinical Investigation of a medical device for human subjects - Good Clinical Practice	The standard provides the technical methodology for designing and carrying out a clinical trial
ISO 5840	Cardiovascular implants -- Cardiac valve prostheses Surgically implanted heart valve substitutes	Such a process involving *in vitro*, preclinical *in vivo*, and clinical evaluations are intended to clarify the required procedures before market release and to enable prompt identification and management of any subsequent problems
IEC 62366	Application of usability engineering to medical devices	Manufacturers to design for high usability of the product, allowing to limit the risks associated with correct use and errors use of the device

ASSESSMENT OF DECELLULARIZATION EFFECTIVENESS

Since 1989, the year in which the pioneer of heart valve surgery Harken DW sanctioned the "ten commandments" for the ideal heart valve substitute (Harken, 1989), none of the developed heart valve replacements has been shown to possess self-repair, adaptively remodelling and growth whilst being resistant to infection and thrombogenicity. However, decellularized porcine tissues (small intestinal submucosa or pulmonary valves) have been utilized for the manufacturing of bioprosthetic heart valves substitutes (Fioretta et al., 2020). The promising results that were reported from preclinical studies did not match those obtained from the clinical application, many of these medical devices, notwithstanding the approval by regulating bodies have been proven to be ineffectively decellularized, eliciting a massive host-specific inflammatory response (Naso et al., 2014). Incidents of leaflets thickening, fibrosis and calcification have been also described. In particular, a strong immunological reaction was reported just a few hours following the implant of the decellularized valve (O'Brien et al., 1999; Dohmen et al., 2003; Leyh et al., 2003; Simon et al., 2003; Dohmen et al., 2005; Ota et al., 2005; Ruiz et al., 2005; Takagi et al., 2006; Iwai et al., 2007; Ruffer et al., 2010; Dohmen et al., 2012; Hopkins et al., 2013; Fallon et al., 2014; Zafar et al., 2015; Hennessy et al., 2017; Mosala et al., 2017; Goecke et al., 2018; Rijswijk et al., 2020).

Preclinical applications of decellularized xenograft valve replacements have been generally issued with the ISO standard for biological medical devices (see **Table 3**). More recently, a specific standard for the evaluation of decellularized products has become available (ASTM International, 2021). Generally, "decellularization" is a recognized complex process that allows the use of animal-derived ECM products in medical treatment "with reduced risk of adverse host immune response and immune rejection" by disrupting and removing cells and/or cell contents while aiming to preserve significant features of the ECM structure and/or composition (F3354-19, 2021). Unfortunately, the ISO guidelines currently in place do not adequately account for the immunological and pro-inflammatory aspects of such decellularized devices. Within the tissue engineering community, DNA quantification and qualitative evaluation of cell removal have represented common practices for the characterization of the decellularization effectiveness. Residual DNA is responsible for triggering a strong inflammatory response against the implanted decellularized xenogeneic tissue, resulting in calcification and structural degeneration (Simon et al., 2003). A threshold of 50 ng/mg (DNA/tissue) has been commonly accepted to be non-immunogenic (Crapo et al., 2011). Despite this, various studies have reported decellularized porcine small

intestine submucosa with up to 6 μg/mg of nucleic acid debris (Naso et al., 2013a; Rijswijk et al., 2020). It is worth noting that often the evaluation of the residual DNA presence after decellularization is only qualitative, limiting the assessment to fluorescence staining based on the use of DAPI (4′,6-diamidino-2-phenylindole, a fluorescent stain that binds strongly to adenine–thymine-rich regions in DNA). Gilbert and colleagues (Gilbert et al., 2009) have proved the existence of DNA fragments in some commercial products even if, when smaller than 300 bp, they do not seem to be enough to stimulate critically the immune system (Soto-Gutierrez et al., 2012).

Although quantification of the residual DNA content represents a reasonable way for assessing the effectiveness of decellularization, this approach is limited and not very representative of the immuno-inflammatory risk that can arise following the implantation of decellularized tissues. Homogenized detergent-decellularised scaffolds have been shown to exhibit a high amount of cytosolic and cytoskeleton proteins, such as glyceraldehyde 3-phosphate dehydrogenase (GAPDH) and smooth muscle actin. Interestedly, about 306 proteins of cytosolic, organelle, nuclear and cell membrane origin have been shown to still be identifiable by mass spectrometry (Böer et al., 2011). In addition to the antigenic molecules derived from cell lysis, it is of particular relevance to consider other aspects, such as the remnants of detergents and the presence of pro-inflammatory structures such as hyaluronan fragments.

Immunocompatibility

Xenograft immunogenicity is directly related to the presence of several antigens including the α-Gal epitope (Naso et al., 2013b), the linked N-glycolyl neuraminic sialic acid (Neu5Gc) (Gao et al., 2017) and the Sd(a) (Byrne et al., 2011). These antigenic molecules are expressed in mammals except for Old World monkeys, apes and humans. Following various stimulation pathways, the human body produces antibodies directed against these molecules. Once a xenogeneic tissue is recognized, the complement cascade is activated, triggering endothelial cell dysfunction, platelet aggregation, and vascular thrombosis (Leventhal et al., 1993; Leventhal et al., 1995; Saadi and Platt, 1995; Hedlund et al., 2008; Pham et al., 2009). In particular, the residual presence of the alpha-Gal xenoantigen significantly increases the human anti-galactose titers specifically directed to the Gala1-3Gal residue, starting from day 10 after BHV implantation and reaching a peak at around 3 months for both IgM and IgG isotypes (Mangold et al., 2009—; Konakci et al., 2005). Such antigenic determinants exposed on the cell surface may persist in membrane residues entrapped between the fibers of the ECM or not properly removed by the action of detergents and may still be capable of reacting despite the elimination of all individual cells (Naso and Gandaglia, 2018).

The treatment most widely used to date to ensure the immunogenic tolerance of animal tissues intended for the manufacture of bioprosthetic heart valves is based on chemical crosslinking with glutaraldehyde (GA). Despite being a benchmark, GA treatment is only partially effective in masking such epitopes (Naso et al., 2013b) resulting susceptible to the development of early BHV degeneration (Hawkins et al., 2016) and immune response following BHV implant (Park et al., 2010—; Schussler et al., 2020). The inability of commercially available treatments capable of effectively inactivating this antigen has recently prompted the U.S. Food and Drug Administration (FDA) to officially approve the production of a genetically modified domestic pig line knocked out for the alpha-Gal in order to provide a source of porcine-based materials for the production of safer and more efficient biomedical devices (U.S. Food and Drug Administration, 2020).

Currently, there are only two technologies that have been reported in the literature to produce complete removal of these xeno-epitopes, including the TriCol decellularization protocol (Gallo et al., 2012) and the FACTA® treatment that has been applied to native and GA-treated animal tissues (Naso et al., 2017).

A correct assessment of the presence of these xeno-epitopes requires an initial *in vitro* evaluation, using suitable antibodies, followed by *in vivo* testing in an animal model. However, current commercially available animal models cannot be considered suitable for this purpose. Wildtype pigs, sheep or rats, like all mammals, do not develop an immunological reaction against these xeno-epitopes, being inefficient in predicting a possible immune-mediated acute or delayed reaction. Owing to this, it is necessary to use animal models that do not express the epitope in question (Old World primates) or humanized animal models, such as genetically modified (knockout) models in which the gene responsible for expression has been inactivated (Smood et al., 2019; Galili and Stone, 2021).

Detergents Remnants

The decellularization procedures reported in the literature have demonstrated several differences, such as detergent type and concentration, treatment duration, and the number of washes. Most of the studies have indirectly evaluated the amount of detergent residuals in the decellularized scaffolds by determining the amount of the detergents in the washing solutions following cell removal and not directly within the scaffold (Erdbrügger et al., 2006; Caamaño et al., 2009). Effective removal of the detergents is important since the interaction of the ECM with anionic ones has been reported to decrease the tensile strength of elastin fibers (the major component of blood vessels) and to increase the susceptibility of insoluble elastin and collagen to enzymatic degradation (Kagan et al., 1972; Jordan et al., 1974; Guantieri et al., 1983). Elastin degradation products, in turn, can promote the myofibroblastic and osteogenic differentiation of fibroblasts and the *in vivo* recruitment of inflammatory cells (Senior et al., 1980; Simionescu et al., 2007).

Bile acids and salts may be considered natural detergents as they emulsify fats and modify the permeability of cellular membranes (Naso and Gandaglia, 2018). They have been reported to exist in several states in biological systems (even conjugated with sodium, potassium, glycine, taurine, etc.), including insoluble gels, micelles or vesicles, and insoluble calcium salts (Hofmann, 1989). Precipitation of bile acids in

the insoluble protonated acid form is mainly controlled by the critical micellization concentration, pH and temperature, Ca^{2+} ion activity, and finally the concentration and structure of the monomeric bile acid anion (Hofmann and Mysels, 1992). Variations of physicochemical conditions may cause the bile salts to transit toward the insoluble gel form, remaining trapped within the ECM fibrillar network determining cell cytotoxicity.

The *in vitro* reseeding of SDS-treated tissues reported controversial results: decellularization of human pericardium and porcine aortic and pulmonary valves using a low concentration of SDS resulted in not cytotoxic drawbacks to *in vitro* cell seeding and cytotoxicity assessment (Mirsadraee et al., 2006—; Vafaee et al., 2018—; Cebotari et al., 2010—; Iop et al., 2014). In a discordant way, Rieder and colleagues reported cytotoxicity of SDS in porcine aortic valves and leaflets treatment (Rieder et al., 2004). In particular, a reduced attachment of human endothelial cells to the matrix was observed (Knight et al., 2005), as well as cytotoxicity of the PBS used for the storage of the decellularized valves, leading to conclude that the residual SDS in the tissue was a cause of cytotoxicity. Noteworthy, even a relatively low residual amount of SDS was correlated with an *in vitro* increased fibroblast activation and *in vivo* foreign body response (Friedrich et al., 2017).

Viability, proliferative capacity and phenotype of human urothelial cells upon urinary bladder matrix scaffolds were maintained on graft treated with Triton X-100, CHAPS and sodium deoxycholate and was similar to cells cultured on the same scaffolds but treated with deionized water (White et al., 2017). SDS treatment resulted in a basement membrane complex with altered ultrastructure and composition, endothelial cells seeded on SDS treated scaffolds reported an atypical morphology, fragmented nuclei and considerably reduced confluence (Faulk et al., 2014).

Reliable information on residual detergents could be used to investigate the relationship, if any, between the actual detergent-based treatment and the observed and/or potential drawbacks in the decellularized scaffold. Additionally, this information could be used for end-product quality control in the manufacturing process of existing decellularised scaffolds currently on the market or under consideration for clinical use. Recently was developed the first cell-based biosensor for residual detergent detection especially in decellularized scaffolds (Ghorbani et al., 2021). This biosensor can be additionally adopted for the evaluation of the cytocompatibility of decellularized tissue giving a comprehensive overview of the general biocompatibility state of the decellularized tissue graft.

Broken Hyaluronic Acid Molecules

Hyaluronic acid also called hyaluronan (HA), is an anionic, non-sulfated glycosaminoglycan distributed widely throughout connective, epithelial, and neural tissues. HA amounts to 18% in porcine aortic leaflets, 25% in porcine pulmonary leaflets, and 15% in the bovine pericardium (Cigliano et al., 2012). It appears usually as a high-molecular-size polymer of up to 2 × 104 kDa, where disaccharides of N-acetyl-glucosamine and glucuronic acid, connected to each other exclusively by β-linkages, are repeated (Prehm, 1984; Lee and Spicer, 2000). The polymer contributes to the maintenance of tissue hydration (Granger et al., 1984), acting also as an anti-apoptotic agent (Forrester and Balazs, 1980; Jing and DeAngelis, 2004). HA has demonstrated excellent anti-inflammatory and immunosuppressive function due to the ability to coat cell membrane thereby preventing access by the ligand to the surface receptors inhibiting phagocytosis by monocytes, macrophages, and polymorphonuclear neutrophils (PMNs) (Forrester and Balazs, 1980).

During the first step of decellularization, cells lysis may release several types of proteases, some of which will be able to degrade HA (either in free forms or being part of proteoglycans PGs). HA fragments, ranging from 500 Da to 1.5 kDa, have shown a marked pro-inflammatory activity able to activate macrophages with the secretion of various pro-inflammatory chemokines (McKee et al., 1996; Horton et al., 1998). Fragments of 1.35 kDa have been reported to result in inducing dendritic cell maturation, which allowed subsequent priming of allogeneic T-cells to initiate the alloimmunity reaction (Termeer et al., 2000). Specifically, when decellularized tissue is implanted in the human host, the functional effects of HA oligomers and their clearance from the jeopardized tissue stimulate the inflammatory response through their interaction with specific host receptors such as CD44, RHAMM and TLR-2,4 (Rayahin et al., 2015). Lysosomes internalize and further degrade such fragments into tetra and hexasaccharides through the intracellular HYAL1 and HYAL2 (Veiseh and Turley, 2011). These small HA pieces, thus obtained, can act as an endogenous danger signal, leading to the activation of both innate and acquired immunity. The separate stimulation of TLR4 and CD44 receptors may prime/amplify the inflammatory response through NF-kB activation (Loniewski et al., 2007—; Hutás et al., 2008).

It is therefore desirable to ensure that no low-molecular-size HA residues will be available in the decellularized scaffold. When HA fragments are entrapped within the insoluble form of bile salt detergent, or not properly washed out from the ECM, they can transform the decellularised graft into a ticking time bomb, ready to trigger acute immune-mediated reaction once perfused with the recipient's blood (Naso and Gandaglia 2018).

NEED FOR THE FUTURE

The in-place guidelines contained in the International Organization for Standardization (especially ISO10993 and ISO 5840, **Table 3**) regulating the manufacturing of decellularized tissue scaffolds appear to need an update. This is evident since the preclinical quantitative assessments of the residual content of xenogeneic reactive molecules, detergents and nucleic acid materials in decellularized scaffolds are insufficient and have led to disastrous results. Decellularized grafts such as the Matrix P prostheses, notwithstanding showed encouraging short-term results, reported unfavourable echocardiographic performances with a relevant dysfunction of the prosthesis in adult patients and a subsequent high rate of reoperation/reintervention for structural pulmonary valve failure (Christ

TABLE 4 | Summary table showing the approaches commonly adopted for evaluating the efficacy of decellularization processes and the methods of investigation for highlighting potentially dangerous tissue changes according to the future performance of the implant.

Common approaches for the effectiveness evaluation of a decellularization process		
	Approach	**Further details**
DNA	Commercial Kit for DNA extraction and quantification	n.d
	Immunofluorescence assessment (qualitative)	Hoechst, Bisbenzimide H, Draq5, Live red dye, Picogreen
	Histological assessment (qualitative)	Feulgen stain
Cells	Immunofluorescence assessment (qualitative)	DAPI (4′,6-diamidino-2-phenylindole)
	Histological assessment (qualitative)	Ematoxylin and Eosin
Xenoantigens	Immunohistochemistry assessment (qualitative)	anti-Neu5Gc, anti alpha-Gal and anti-SDa antibodies
	ELISA test (Quantitative)	n.d
Structural cell proteins	Immunohistochemistry assessment (qualitative)	anti-alpha-smooth muscle actin, beta-actin, vimentin, collagen VI and laminin antibodies
Hyaluronan fragments	Immunofluorescence assessment (qualitative)	Hyaluronan binding protein (HABP) probe biotin-conjugated
Collagen	Quantitative evaluation	Hydroxyproline-based assay, sodium dodecyl sulfate-polyacrylamide gel electrophoresis (SDS–PAGE), High-performance liquid chromatography with fluorescence detection (HPLC-FLD)
	Histological assessment (qualitative)	Masson, Mallory and Van Gieson Trichromic staining, Picro Sirius Red
	Immunofluorescence assessment (qualitative)	anti-collagen I, II and III antibodies
Elastin	Quantitative evaluation	Desmosine-base assay, NaOH extraction
	Histological assessment (qualitative)	Verhoeff, Orcein, Weigert staining kit
	Immunofluorescence assessment (qualitative)	anti-elastin antibodies
POST DECELLULARIZATION ASSESSMENT FOR TISSUES PERFORMANCES		
	Evaluation approach	**Commonly considered parameters**
Mechanical properties	Bi- or uni-axial stress-strain test for patch-shape tissue	Ultimate Tensile Strength (UTS), Elongation, Young's Modulus, Compressive Strength (CS), Suture retention Strength (SRS)
	Pulse duplicator assessment for heart valve	Mean Pressure drop (MPD), Effective Orifice Area (EOA), Peak Pressure drop (PPD), Mean Regurgitation and Mean Energy Losses
Thermal analysis	Thermogravimetric analysis (TGA)	Protein–water interactions and degradation temperatures
	Differential scanning calorimetry (DSC)	Protein thermal transitions (glass transition and denaturation)
Detergent residues	Quantitative chemical evaluation	Dimethylmethylene blue, reverse phase chromatography coupled with UV detection

et al., 2019). Histological examination performed by Breitenbach and colleagues exhibited massive inflammatory reaction and necrosis in the Matrix P Plus prostheses adopted as pulmonary homograft in the Ross procedure in adult patients (Breitenbach et al., 2014). Backhoff and colleagues (Backhoff et al., 2014) reported a massive Matrix P® conduit obstruction after 5 years from the implant in 6 years old patients. Conduit dissection allowing blood flow in the thickness of the conduit wall with the formation of pseudoaneurysms was reported, confirming what was already observed also by Rüffer and colleagues (Rüffer et al., 2010). Histological examination showed massive inflammatory reactions and necrosis. Severe inflammation increased fibrous tissue and foreign-body reaction against valve leaflets and fascial tissue was similarly highlighted even by Vogel in young patients (Voges et al., 2013). The reconstruction of aortic heart valves using a decellularized extracellular matrix (CorMatrix®) in pediatric patients reported severe valve dysfunction occurred suddenly during the first three post-operative months. A migration of inflammatory cells into the graft edge bordering the native tissue was identified inducing a significant thickening of the patch. The inflammatory reaction induced structural and functional changes (Hofmann et al., 2017).

A strict requirement for any biomedical device is standardization. The consistency and reproducibility of the treatments made according to predefined quality criteria can be ensured, also by adopting new standards capable of adapting to technological progress and new scientific knowledge, such as in the case of knockout animal models. Researchers and the scientific community, while always looking for technological improvement, should converge in the definition of acceptance criteria related to ensuring the consistent evaluation and use of decellularization in manufacturing medical products. Such criteria should address the adequacy of cellular disruption and removal of cellular remnants, defining acceptable quality levels for the remaining extracellular matrix components (**Table 4**). It would also be appreciable to define a suitable decellularization reagents list placing selective limits on their persistence on the treated ECM.

Similarly, to what happens for the definition and the quality management of any industrial process, a decellularization protocol should also identify according to the step's objective:

1) the general procedure, 2) materials and equipment utilized, 3) duration or end-point determination, 4) static process parameters, and 5) any variable parameters that may scale with source ECM material characteristics, dimensions, or quantities. Test and inspection procedures should be designed and planned during all the decellularization process, establishing the acceptance criteria in advance. Even if this new standardization approach is unlikely to be applied to products already on the market, it will allow for a more efficient, comparable, and reliable experimental research study to allow a faster technology transfer to the market with an unprecedented level of safety for the patient's health.

AUTHOR CONTRIBUTIONS

FN and AG contributed to the conception and design of the review. FN wrote the first draft of the manuscript. All authors contributed to manuscript revision, read, and approved the submitted version.

REFERENCES

Ashkenazi, A., and Dixit, V. M. (1998). Death Receptors: Signaling and Modulation. *Science* 281, 1305–1308. doi:10.1126/science.281.5381.1305

ASTM International (2021). *F3354-19: Standard Guide for Evaluating Extracellular Matrix Decellularization Processes*. Pennsylvania, USA: ASTM International.

Backhoff, D., Steinmetz, M., Sigler, M., and Schneider, H. (2014). Formation of Multiple Conduit Aneurysms Following Matrix P Conduit Implantation in a Boy with Tetralogy of Fallot and Pulmonary Atresia. *Eur. J. Cardiothorac. Surg.* 46, 500–502. doi:10.1093/ejcts/ezt635

Bader, A., Schilling, T., Teebken, O. E., Brandes, G., Herden, T., Steinhoff, G., et al. (1998). Tissue Engineering of Heart Valves-Hhuman Endothelial Cell Seeding of Detergent Acellularized Porcine Valves. *Eur. J. Cardiothorac. Surg.* 14, 279–284. doi:10.1016/s1010-7940(98)00171-7

Badylak, S., Freytes, D., and Gilbert, T. (2009). Extracellular Matrix as a Biological Scaffold Material: Structure and Function. *Acta Biomater.* 5, 1–13. doi:10.1016/j.actbio.2008.09.013

Böer, U., Lohrenz, A., Klingenberg, M., Pich, A., Haverich, A., and Wilhelmi, M. (2011). The Effect of Detergent-Based Decellularization Procedures on Cellular Proteins and Immunogenicity in Equine Carotid Artery Grafts. *Biomaterials* 32, 9730–9737. doi:10.1016/j.biomaterials.2011.09.015

Booth, C., Korossis, S. A., Wilcox, H. E., Watterson, K. G., Kearney, J. N., Fisher, J., et al. (2002). Tissue Engineering of Cardiac Valve Prostheses I: Development and Histological Characterization of an Acellular Porcine Scaffold. *J. Heart Valve Dis.* 11, 457–462.

Bourgine, P. E., Pippenger, B. E., Todorov, A., Tchang, L., and Martin, I. (2013). Tissue Decellularization by Activation of Programmed Cell Death. *Biomaterials* 34, 6099–6108. doi:10.1016/j.biomaterials.2013.04.058

Breitenbach, I., El-Essawi, A., Pahari, D., Kappenberg, T., Harringer, W., and Anssar, M. (2014). Early Failure of Decellularized Xenogenous Pulmonary Valve Conduit (Matrix-P-Plus) for Reconstruction of the Right Ventricular Outflow Tract in the ross Procedure. *Thorac. Cardiovasc. Surg.* 62, OP123. doi:10.1055/s-0034-1367197

Brown, B. N., and Badylak, S. F. (2014). Extracellular Matrix as an Inductive Scaffold for Functional Tissue Reconstruction. *Translational Res.* 163, 268–285. doi:10.1016/j.trsl.2013.11.003

Bruyneel, A. A. N., and Carr, C. A. (2017). Ambiguity in the Presentation of Decellularized Tissue Composition: The Need for Standardized Approaches. *Artif. Organs* 41, 778–784. doi:10.1111/aor.12838

Butler, C. R., Hynds, R. E., Crowley, C., Gowers, K. H. C., Partington, L., Hamilton, N. J., et al. (2017). Vacuum-assisted Decellularization: an Accelerated Protocol to Generate Tissue-Engineered Human Tracheal Scaffolds. *Biomaterials* 124, 95–105. doi:10.1016/j.biomaterials.2017.02.001

Byrne, G. W., Stalboerger, P. G., Du, Z., Davis, T. R., and McGregor, C. G. A. (2011). Identification of New Carbohydrate and Membrane Protein Antigens in Cardiac Xenotransplantation. *Transplantation* 91, 287–292. doi:10.1097/TP.0b013e318203c27d

Caamaño, S., Shiori, A., Strauss, S. H., and Orton, E. C. (2009). Does Sodium Dodecyl Sulfate Wash Out of Detergent-Treated Bovine Pericardium at Cytotoxic Concentrations?. *J. Heart Valve Dis.* 18, 101–105.

Carpentier, A., Lemaigre, G., Robert, L., Carpentier, S., Dubost, C., and Gerbode, F. (1969). Biological Factors Affecting Long-Term Results of Valvular Heterografts. *J. Thorac. Cardiovasc. Surg.* 58, 467–483. doi:10.1016/s0022-5223(19)42561-0

Cartmell, J. S., and Dunn, M. G. (2000). Effect of Chemical Treatments on Tendon Cellularity and Mechanical Properties. *J. Biomed. Mater. Res.* 49, 134–140. doi:10.1002/(sici)1097-4636(200001)49:1<134:aid-jbm17>3.0.co;2-d

Cebotari, S., Tudorache, I., Jaekel, T., Hilfiker, A., Dorfman, S., Ternes, W., et al. (2010). Detergent Decellularization of Heart Valves for Tissue Engineering: Toxicological Effects of Residual Detergents on Human Endothelial Cells. *Artif. Organs* 34, 206–210. doi:10.1111/j.1525-1594.2009.00796.x

Chen, R.-N., Ho, H.-O., Tsai, Y.-T., and Sheu, M.-T. (2004). Process Development of an Acellular Dermal Matrix (ADM) for Biomedical Applications. *Biomaterials* 25, 2679–2686. doi:10.1016/j.biomaterials.2003.09.070

Christ, T., Paun, A. C., Grubitzsch, H., Holinski, S., Falk, V., and Dushe, S. (2019). Long-term Results after the Ross Procedure with the Decellularized AutoTissue Matrix P Bioprosthesis Used for Pulmonary Valve Replacement. *Eur. J. Cardiothorac. Surg.* 55, 885–892. doi:10.1093/ejcts/ezy377

Cigliano, A., Gandaglia, A., Lepedda, A. J., Zinellu, E., Naso, F., Gastaldello, A., et al. (2012). Fine Structure of Glycosaminoglycans from Fresh and Decellularized Porcine Cardiac Valves and Pericardium. *Biochem. Res. Int.* 2012, 1–10. doi:10.1155/2012/979351

Cornelison, R. C., Wellman, S. M., Park, J. H., Porvasnik, S. L., Song, Y. H., Wachs, R. A., et al. (2018). Development of an Apoptosis-Assisted Decellularization Method for Maximal Preservation of Nerve Tissue Structure. *Acta Biomater.* 77, 116–126. doi:10.1016/j.actbio.2018.07.009

Crapo, P. M., Gilbert, T. W., and Badylak, S. F. (2011). An Overview of Tissue and Whole Organ Decellularization Processes. *Biomaterials* 32, 3233–3243. doi:10.1016/j.biomaterials.2011.01.057

Curtil, A., Pegg, D. E., and Wilson, A. (1997a). Repopulation of Freeze-Dried Porcine Valves with Human Fibroblasts and Endothelial Cells. *J. Heart Valve Dis.* 6, 296–306.

Curtil, A., Pegg, D. E., and Wilson, A. (1997b). Freeze Drying of Cardiac Valves in Preparation for Cellular Repopulation. *Cryobiology* 34, 13–22. doi:10.1006/cryo.1996.1982

Dettin, M., Zamuner, A., Naso, F., Monteleone, A., Spina, M., and Gerosa, G. (2017). Natural Scaffolds for Regenerative Medicine: Direct Determination of Detergents Entrapped in Decellularized Heart Valves. *Biomed. Res. Int.* 2017, 1–9. doi:10.1155/2017/9274135

Dignan, R., O'Brien, M., Hogan, P., Passage, J., Stephens, F., Thornton, A., et al. (2000). Influence of HLA Matching and Associated Factors on Aortic Valve Homograft Function. *J. Heart Valve Dis.* 9, 504–511.

Dohmen, P. M., Ozaki, S., Nitsch, R., Yperman, J., Flameng, W., and Konertz, W. (2003). A Tissue Engineered Heart Valve Implanted in a Juvenile Sheep Model. *Med. Sci. Monit.* 9, BR97–BR104.

Dohmen, P. M., Costa, F. d., Lopes, S. V., Yoshi, S., Souza, F. P. d., Vilani, R., et al. (2005). Results of a Decellularized Porcine Heart Valve Implanted into the Juvenile Sheep Model. *Hsf* 8, 100–104. doi:10.1532/HSF98.20041140

Dohmen, P. M., Costa, F. d., Yoshi, S., Lopes, S. V., Souza, F. P., Vilani, R., et al. (2012). An Experimental Study of Decellularized Xenografts Implanted into the Aortic Position with 4 Months of Follow up. *J. Clin. Exp. Cardiolog* S4. doi:10.4172/2155-9880.S4-004

Elder, B. D., Kim, D. H., and Athanasiou, K. A. (2010). Developing an Articular Cartilage Decellularization Process toward Facet Joint Cartilage Replacement. *Neurosurgery* 66, 722–727. doi:10.1227/01.NEU.0000367616.49291.9F

Erdbrügger, W., Konertz, W., Dohmen, P. M., Posner, S., Ellerbrok, H., Brodde, O.-E., et al. (2006). Decellularized Xenogenic Heart Valves Reveal Remodeling and Growth Potentialin Vivo. *Tissue Eng.* 12, 2059–2068. doi:10.1089/ten.2006.12.2059

Etnel, J. R. G., Huygens, S. A., Grashuis, P., Pekbay, B., Papageorgiou, G., Roos Hesselink, J. W., et al. (2019). Bioprosthetic Aortic Valve Replacement in Nonelderly Adults. *Circ. Cardiovasc. Qual. Outcomes* 12, e005481. doi:10.1161/CIRCOUTCOMES.118.005481

Fallon, A. M., Goodchild, T. T., Cox, J. L., and Matheny, R. G. (2014). *In Vivo* remodeling Potential of a Novel Bioprosthetic Tricuspid Valve in an Ovine Model. *J. Thorac. Cardiovasc. Surg.* 148, 333–340. doi:10.1016/j.jtcvs.2013.10.048

Faulk, D. M., Carruthers, C. A., Warner, H. J., Kramer, C. R., Reing, J. E., Zhang, L., et al. (2014). The Effect of Detergents on the Basement Membrane Complex of a Biologic Scaffold Material. *Acta Biomater.* 10, 183–193. doi:10.1016/j.actbio.2013.09.006

Fioretta, E. S., Motta, S. E., Lintas, V., Loerakker, S., Parker, K. K., Baaijens, F. P. T., et al. (2020). Next-generation Tissue-Engineered Heart Valves with Repair, Remodelling and Regeneration Capacity. *Nat. Rev. Cardiol.* 18, 92–116. doi:10.1038/s41569-020-0422-8

Folli, S., Curcio, A., Melandri, D., Bondioli, E., Rocco, N., Catanuto, G., et al. (2018). A New Human-Derived Acellular Dermal Matrix for Breast Reconstruction Available for the European Market: Preliminary Results. *Aesth Plast. Surg.* 42, 434–441. doi:10.1007/s00266-017-1069-7

Forrester, J. V., and Balazs, E. A. (1980). Inhibition of Phagocytosis by High Molecular Weight Hyaluronate. *Immunology* 40, 435–446.

Friedrich, E. E., Lanier, S. T., Niknam-Bienia, S., Arenas, G. A., Rajendran, D., Wertheim, J. A., et al. (2017). Residual Sodium Dodecyl Sulfate in Decellularized Muscle Matrices Leads to Fibroblast Activation *In Vitro* and Foreign Body Response *In Vivo*. *J. Tissue Eng. Regen. Med.* 12, e1704–e1715. doi:10.1002/term.2604

Galili, U., and Stone, K. R. (2021). *In Situ* "Humanization" of Porcine Bioprostheses: Demonstration of Tendon Bioprostheses Conversion into Human ACL and Possible Implications for Heart Valve Bioprostheses. *Bioengineering* 8, 10. doi:10.3390/bioengineering8010010

Gallo, M., Naso, F., Poser, H., Rossi, A., Franci, P., Bianco, R., et al. (2012). Physiological Performance of a Detergent Decellularized Heart Valve Implanted for 15 Months in Vietnamese Pigs: Surgical Procedure, Follow-Up, and Explant Inspection. *Artif. Organs* 36, E138–E150. doi:10.1111/j.1525-1594.2012.01447.x

Gao, B., Long, C., Lee, W., Zhang, Z., Gao, X., Landsittel, D., et al. (2017). Anti-Neu5Gc and Anti-non-Neu5Gc Antibodies in Healthy Humans. *PLoS One* 12, e0180768. doi:10.1371/journal.pone.0180768

Gattazzo, F., Urciuolo, A., and Bonaldo, P. (2014). Extracellular Matrix: a Dynamic Microenvironment for Stem Cell Niche. *Biochim. Biophys. Acta (Bba) - Gen. Subjects* 1840, 2506–2519. doi:10.1016/j.bbagen.2014.01.010

Ghorbani, F., Abdihaji, M., Roudkenar, M. H., and Ebrahimi, A. (2021). Development of a Cell-Based Biosensor for Residual Detergent Detection in Decellularized Scaffolds. *ACS Synth. Biol.* 10, 2715–2724. doi:10.1021/acssynbio.1c00321

Gilbert, T., Sellaro, T., and Badylak, S. (2006). Decellularization of Tissues and Organs. *Biomaterials* 27, 3675–3683. doi:10.1016/j.biomaterials.2006.02.014

Gilbert, T. W., Freund, J. M., and Badylak, S. F. (2009). Quantification of DNA in Biologic Scaffold Materials. *J. Surg. Res.* 152, 135–139. doi:10.1016/j.jss.2008.02.013

Gilbert, T. W., Stolz, D. B., Biancaniello, F., Simmons-Byrd, A., and Badylak, S. F. (2005). Production and Characterization of ECM Powder: Implications for Tissue Engineering Applications. *Biomaterials* 26, 1431–1435. doi:10.1016/j.biomaterials.2004.04.042

Gilbert, T. W. (2012). Strategies for Tissue and Organ Decellularization. *J. Cel. Biochem.* 113, 2217–2222. doi:10.1002/jcb.24130

Gilpin, A., and Yang, Y. (2017). Decellularization Strategies for Regenerative Medicine: From Processing Techniques to Applications. *Biomed. Res. Int.* 2017, 1–13. doi:10.1155/2017/9831534

Goecke, T., Theodoridis, K., Tudorache, I., Ciubotaru, A., Cebotari, S., Ramm, R., et al. (2018). *In Vivo* performance of Freeze-Dried Decellularized Pulmonary Heart Valve Allo- and Xenografts Orthotopically Implanted into Juvenile Sheep. *Acta Biomater.* 68, 41–52. doi:10.1016/j.actbio.2017.11.041

Granger, H. J., Laine, G. A., Barnes, G. E., and Lewis, R. E. (1984). Dynamics and Control of Transmicrovascular Fluid Exchange. *Edema* 8, 189–224.

Guantieri, V., Tamburro, A. M., and Gordini, D. D. (1983). Interactions of Human and Bovine Elastins with Lipids: Their Proteolysis by Elastase. *Connect. Tissue Res.* 12, 79–83. doi:10.3109/03008208309005614

Harken, D. E. (1989). Heart Valves: Ten Commandments and Still Counting. *Ann. Thorac. Surg.* 48, S18–S19. doi:10.1016/0003-4975(89)90623-1

Harris, C., Croce, B., and Cao, C. (2015). Tissue and Mechanical Heart Valves. *Ann. Cardiothorac. Surg.* 4, 399. doi:10.3978/j.issn.2225-319X.2015.07.01

Haupt, J., Lutter, G., Gorb, S. N., Simionescu, D. T., Frank, D., Seiler, J., et al. (2018). Detergent-based Decellularization Strategy Preserves Macro- and Microstructure of Heart Valves. *Interact. Cardiovasc. Thorac. Surg.* 26, 230–236. doi:10.1093/icvts/ivx316

Hawkins, R. B., Frischtak, H. L., Kron, I. L., and Ghanta, R. K. (2016). Premature Bioprosthetic Aortic Valve Degeneration Associated with Allergy to Galactose-Alpha-1,3-Galactose. *J. Card. Surg.* 31, 446–448. doi:10.1111/jocs.12764

Hedlund, M., Padler-Karavani, V., Varki, N. M., and Varki, A. (2008). Evidence for a Human-specific Mechanism for Diet and Antibody-Mediated Inflammation in Carcinoma Progression. *Proc. Natl. Acad. Sci.* 105, 18936–18941. doi:10.1073/pnas.0803943105

Hennessy, R. S., Go, J. L., Hennessy, R. R., Tefft, B. J., Jana, S., Stoyles, N. J., et al. (2017). Recellularization of a Novel Off-The-Shelf Valve Following Xenogenic Implantation into the Right Ventricular Outflow Tract. *PLoS ONE* 12, e0181614. doi:10.1371/journal.pone.0181614

Hofmann, A. F. (1989). "Enterohepatic Circulation of Bile Acids," in *Handbook of Physiology, the Gastrointestinal System*. Editor S G Schultz (Bethesda, MD: American Physiological Society), 567–596. doi:10.1002/cphy.cp060329

Hofmann, A. F., and Mysels, K. J. (1992). Bile Acid Solubility and Precipitation *In Vitro* and *In Vivo*: the Role of Conjugation, pH, and Ca2+ Ions. *J. Lipid Res.* 33, 617–626. doi:10.1016/s0022-2275(20)41426-9

Hofmann, M., Schmiady, M. O., Burkhardt, B. E., Dave, H. H., Hübler, M., Kretschmar, O., et al. (2017). Congenital Aortic Valve Repair Using CorMatrix : A Histologic Evaluation. *Xenotransplantation* 24, e12341. doi:10.1111/xen.12341

Hopkins, R. A., Bert, A. A., Hilbert, S. L., Quinn, R. W., Brasky, K. M., Drake, W. B., et al. (2013). Bioengineered Human and Allogeneic Pulmonary Valve Conduits Chronically Implanted Orthotopically in Baboons: Hemodynamic Performance and Immunologic Consequences. *J. Thorac. Cardiovasc. Surg.* 145, 1098–1107. doi:10.1016/j.jtcvs.2012.06.024

Horton, M. R., McKee, C. M., Bao, C., Liao, F., Farber, J. M., Hodge-DuFour, J., et al. (1998). Hyaluronan Fragments Synergize with Interferon-γ to Induce the C-X-C Chemokines Mig and Interferon-Inducible Protein-10 in Mouse Macrophages. *J. Biol. Chem.* 273, 35088. doi:10.1074/jbc.273.52.35088

Hung, S.-H., Su, C.-H., Lee, F.-P., and Tseng, H. (2013). Larynx Decellularization: Combining Freeze-Drying and Sonication as an Effective Method. *J. Voice* 27, 289–294. doi:10.1016/j.jvoice.2013.01.018

Hutás, G., Bajnok, É., Gál, I., Finnegan, A., Glant, T. T., and Mikecz, K. (2008). CD44-specific Antibody Treatment and CD44 Deficiency Exert Distinct Effects on Leukocyte Recruitment in Experimental Arthritis. *Blood* 112, 4999–5006. doi:10.1182/blood-2008-04-150383

Huygens, S. A., Goossens, L. M. A., van Erkelens, J. A., Takkenberg, J. J. M., and Rutten-van Mölken, M. P. M. H. (2018). How Much Does a Heart Valve Implantation Cost and what Are the Health Care Costs Afterwards?. *Open Heart* 5, e000672. doi:10.1136/openhrt-2017-000672

Huygens, S. A., Mokhles, M. M., Hanif, M., Bekkers, J. A., Bogers, A. J. J. C., Rutten-van Mölken, M. P. M. H., et al. (2016). Contemporary Outcomes after Surgical Aortic Valve Replacement with Bioprostheses and Allografts: a Systematic Review and Meta-Analysis. *Eur. J. Cardiothorac. Surg.* 50, 605–616. doi:10.1093/ejcts/ezw101

Hynes, R. O., and Naba, A. (2011). Overview of the Matrisome--An Inventory of Extracellular Matrix Constituents and Functions. *Cold Spring Harbor Perspect. Biol.* 4, a004903. doi:10.1101/cshperspect.a004903

Iop, L., Bonetti, A., Naso, F., Rizzo, S., Cagnin, S., Bianco, R., et al. (2014). Decellularized Allogeneic Heart Valves Demonstrate Self-Regeneration Potential after a Long-Term Preclinical Evaluation. *PLoS One* 9, e99593. doi:10.1371/journal.pone.0099593

Iwai, S., Torikai, K., Coppin, C. M., and Sawa, Y. (2007). Minimally Immunogenic Decellularized Porcine Valve Provides *In Situ* Recellularization as a Stentless Bioprosthetic Valve. *J. Artif. Organs* 10, 29–35. doi:10.1007/s10047-006-0360-1

Jing, W., and DeAngelis, P. L. (2004). Synchronized Chemoenzymatic Synthesis of Monodisperse Hyaluronan Polymers. *J. Biol. Chem.* 279, 42345–42349. doi:10.1074/jbc.M402744200

Jordan, R. E., Hewitt, N., Lewis, W., Kagan, H., and Franzblau, C. (1974). Regulation of Elastase-Catalyzed Hydrolysis of Insoluble Elastin by Synthetic and Naturally Occurring Hydrophobic Ligands. *Biochemistry* 13, 3497–3503. doi:10.1021/bi00714a013

Kagan, H. M., Crombie, G. D., Jordan, R. E., Lewis, W., and Franzblau, C. (1972). Proteolysis of Elastin-Ligand Complexes. Stimulation of Elastase Digestion of Insoluble Elastin by Sodium Dodecyl Sulfate. *Biochemistry* 11, 3412–3418. doi:10.1021/bi00768a014

Kasimir, M.-T., Weigel, G., Sharma, J., Rieder, E., Seebacher, G., Wolner, E., et al. (2005). The Decellularized Porcine Heart Valve Matrix in Tissue Engineering. *Thromb. Haemost.* 94, 562–567. doi:10.1160/TH05-01-0025

Kim, W. G., Park, J. K., and Lee, W. Y. (2002). Tissue-engineered Heart Valve Leaflets: an Effective Method of Obtaining Acellularized Valve Xenografts. *Int. J. Artif. Organs* 25, 791–797. doi:10.1177/039139880202500807

Knight, R. L., Booth, C., Wilcox, H. E., Fisher, J., and Ingham, E. (2005). Tissue Engineering of Cardiac Valves: Re-seeding of Acellular Porcine Aortic Valve Matrices with Human Mesenchymal Progenitor Cells. *J. Heart Valve Dis.* 14, 806–813.

Konakci, K., Bohle, B., Blumer, R., Hoetzenecker, W., Roth, G., Moser, B., et al. (2005). Alpha-Gal on Bioprostheses: Xenograft Immune Response in Cardiac Surgery. *Eur. J. Clin. Invest.* 35, 17–23. doi:10.1111/j.1365-2362.2005.01441.x

Konertz, W., Dohmen, P. M., Liu, J., Beholz, S., Dushe, S., Posner, S., et al. (2005). Hemodynamic Characteristics of the Matrix P Decellularized Xenograft for Pulmonary Valve Replacement during the Ross Operation. *J. Heart Valve Dis.* 14, 78–81.

Korossis, S. A., Booth, C., Wilcox, H. E., Watterson, K. G., Kearney, J. N., Fisher, J., et al. (2002). Tissue Engineering of Cardiac Valve Prostheses II: Biomechanical Characterization of Decellularized Porcine Aortic Heart Valves. *J. Heart Valve Dis.* 11, 463–471.

Koziarz, A., Makhdoum, A., Butany, J., Ouzounian, M., and Chung, J. (2020). Modes of Bioprosthetic Valve Failure: a Narrative Review. *Curr. Opin. Cardiol.* 35, 123–132. doi:10.1097/HCO.0000000000000711

Lee, J. Y., and Spicer, A. P. (2000). Hyaluronan: a Multifunctional, megaDalton, Stealth Molecule. *Curr. Opin. Cel Biol.* 12, 581–586. doi:10.1016/s0955-0674(00)00135-6

Leventhal, J. R., John, R., Fryer, J. P., Witson, J. C., Derlich, J. M., Remiszewski, J., et al. (1995). Removal of Baboon and Human Antiporcine IgG and IgM Natural Antibodies by Immunoadsorption. Results of *In Vitro* and *In Vivo* Studies. *Transplantation* 59, 294–300. doi:10.1097/00007890-199501000-00024

Leventhal, J. R., Dalmasso, A. P., Cromwell, J. W., Platt, J. L., Manivel, C. J., Bolman, R. M., et al. (1993). Prolongation of Cardiac Xenograft Survival by Depletion of Complement. *Transplantation* 55, 857–865. doi:10.1097/00007890-199304000-00033

Leyh, R. G., Wilhelmi, M., Walles, T., Kallenbach, K., Rebe, P., Oberbeck, A., et al. (2003). Acellularized Porcine Heart Valve Scaffolds for Heart Valve Tissue Engineering and the Risk of Cross-Species Transmission of Porcine Endogenous Retrovirus. *J. Thorac. Cardiovasc. Surg.* 126, 1000–1004. doi:10.1016/s0022-5223(03)00353-2

Lin, P., Chan, W. C. W., Badylak, S. F., and Bhatia, S. N. (2004). Assessing Porcine Liver-Derived Biomatrix for Hepatic Tissue Engineering. *Tissue Eng.* 10, 1046–1053. doi:10.1089/ten.2004.10.1046

Londono, R., Dziki, J. L., Haljasmaa, E., Turner, N. J., Leifer, C. A., and Badylak, S. F. (2017). The Effect of Cell Debris within Biologic Scaffolds upon the Macrophage Response. *J. Biomed. Mater. Res.* 105, 2109–2118. doi:10.1002/jbm.a.36055

Loniewski, K. J., Patial, S., and Parameswaran, N. (2007). Sensitivity of TLR4- and -7-induced NFκB1 P105-TPL2-ERK Pathway to TNF-Receptor-Associated-Factor-6 Revealed by RNAi in Mouse Macrophages. *Mol. Immunol.* 44, 3715–3723. doi:10.1016/j.molimm.2007.04.002

Luo, J., Korossis, S. A., Wilshaw, S.-P., Jennings, L. M., Fisher, J., and Ingham, E. (2014). Development and Characterization of Acellular Porcine Pulmonary Valve Scaffolds for Tissue Engineering. *Tissue Eng. A* 20, 2963–2974. doi:10.1089/ten.tea.2013.0573

Malone, J. M., Brendel, K., Duhamel, R. C., and Reinert, R. L. (1984). Detergent-extracted Small-Diameter Vascular Prostheses. *J. Vasc. Surg.* 1, 181–191. doi:10.1067/mva.1984.avs0010181

Mangold, A., Szerafin, T., Hoetzenecker, K., Hacker, S., Lichtenauer, M., Niederpold, T., et al. (2009). Alpha-Gal Specific IgG Immune Response after Implantation of Bioprostheses. *Thorac. Cardiovasc. Surg.* 57, 191–195. doi:10.1055/s-0029-1185395

McKee, C. M., Penno, M. B., Cowman, M., Burdick, M. D., Strieter, R. M., Bao, C., et al. (1996). Hyaluronan (HA) Fragments Induce Chemokine Gene Expression in Alveolar Macrophages. The Role of HA Size and CD44. *J. Clin. Invest.* 98, 2403–2413. doi:10.1172/JCI119054

Mendibil, U., Ruiz-Hernandez, R., Retegi-Carrion, S., Garcia-Urquia, N., Olalde-Graells, B., and Abarrategi, A. (2020). Tissue-Specific Decellularization Methods: Rationale and Strategies to Achieve Regenerative Compounds. *Ijms* 21, 5447. doi:10.3390/ijms21155447

Meyer, S. R., Nagendran, J., Desai, L. S., Rayat, G. R., Churchill, T. A., Anderson, C. C., et al. (2005). Decellularization Reduces the Immune Response to Aortic Valve Allografts in the Rat. *J. Thorac. Cardiovasc. Surg.* 130, 469–476. doi:10.1016/j.jtcvs.2005.03.021

Mirsadraee, S., Wilcox, H. E., Korossis, S. A., Kearney, J. N., Watterson, K. G., Fisher, J., et al. (2006). Development and Characterization of an Acellular Human Pericardial Matrix for Tissue Engineering. *Tissue Eng.* 12, 763–773. doi:10.1089/ten.2006.12.763

Naba, A., Clauser, K. R., Hoersch, S., Liu, H., Carr, S. A., and Hynes, R. O. (2011). The Matrisome: In Silico Definition and *In Vivo* Characterization by Proteomics of normal and Tumor Extracellular Matrices. *Mol. Cel. Proteomics* 11, M111014647. doi:10.1074/mcp.M111.014647

Naso, F., Aguiari, P., and Iop, L. (2013a). Biocompatibility Evaluation Criteria for Novel Xenograft Materials: Distribution and Quantification of Remnant Nucleic Acid and Alpha-Gal Epitope. *J. Stem Cel Res. Ther.S6.*. doi:10.4172/2157-7633.S6-009

Naso, F., Gandaglia, A., Bottio, T., Tarzia, V., Nottle, M. B., d'Apice, A. J. F., et al. (2013b). First Quantification of Alpha-Gal Epitope in Current Glutaraldehyde-Fixed Heart Valve Bioprostheses. *Xenotransplantation* 20, 252–261. doi:10.1111/xen.12044

Naso, F., and Gandaglia, A. (2018). Different Approaches to Heart Valve Decellularization: A Comprehensive Overview of the Past 30 Years. *Xenotransplantation* 25, e12354. doi:10.1111/xen.12354

Naso, F., Iop, L., Spina, M., and Gerosa, G. (2014). Are FDA and CE Sacrificing Safety for a Faster Commercialization of Xenogeneic Tissue Devices? Unavoidable Need for Legislation in Decellularized Tissue Manufacturing. *Tissue Antigens* 83, 193–194. doi:10.1111/tan.12275

Naso, F., Stefanelli, U., Buratto, E., Lazzari, G., Perota, A., Galli, C., et al. (2017). Alpha-Gal Inactivated Heart Valve Bioprostheses Exhibit an Anti-calcification Propensity Similar to Knockout Tissues. *Tissue Eng. Part A* 23, 1181–1195. doi:10.1089/ten.tea.2016.0474

Nonaka, P. N., Campillo, N., Uriarte, J. J., Garreta, E., Melo, E., de Oliveira, L. V. F., et al. (2013). Effects of Freezing/thawing on the Mechanical Properties of Decellularized Lungs. *J. Biomed. Mater. Res.* 102, 413–419. doi:10.1002/jbm.a.34708

O'Brien, M. F., Goldstein, S., Walsh, S., Black, K. S., Elkins, R., and Clarke, D. (1999). The SynerGraft Valve: a New Acellular (Nonglutaraldehyde-fixed) Tissue Heart Valve for Autologous Recellularization First Experimental Studies before Clinical Implantation. *Semin. Thorac. Cardiovasc. Surg.* 11, 194–200.

Ota, T., Sawa, Y., Iwai, S., Kitajima, T., Ueda, Y., Coppin, C., et al. (2005). Fibronectin-hepatocyte Growth Factor Enhances Reendothelialization in Tissue-Engineered Heart Valve. *Ann. Thorac. Surg.* 80, 1794–1801. doi:10.1016/j.athoracsur.2005.05.002

Padalino, M. A., Castaldi, B., Fedrigo, M., Gallo, M., Zucchetta, F., Vida, V. L., et al. (2016). Porcine Intestinal Submucosa (CorMatrix) for Semilunar Valve Repair in Children: A Word of Caution after Midterm Results. *Semin. Thorac. Cardiovasc. Surg.* 28, 436–445. doi:10.1053/j.semtcvs.2016.04.015

Park, C. S., Park, S. S., Choi, S. Y., Yoon, S. H., Kim, W. H., and Kim, Y. J. (2010). Anti Alpha-Gal Immune Response Following Porcine Bioprosthesis Implantation in Children. *J. Heart Valve Dis.* 19, 124–130.

Perri, G., Polito, A., Esposito, C., Albanese, S. B., Francalanci, P., Pongiglione, G., et al. (2012). Early and Late Failure of Tissue-Engineered Pulmonary Valve

Conduits Used for Right Ventricular Outflow Tract Reconstruction in Patients with Congenital Heart Disease. *Eur. J. Cardio-Thoracic Surg.* 41, 1320–1325. doi:10.1093/ejcts/ezr221

Pham, T., Gregg, C. J., Karp, F., Chow, R., Padler-Karavani, V., Cao, H., et al. (2009). Evidence for a Novel Human-specific Xeno-Auto-Antibody Response against Vascular Endothelium. *Blood* 114, 5225–5235. doi:10.1182/blood-2009-05-220400

Poncelet, A., Fervaille, C., de Kerchove, L., Gianello, P., and Mosala Nezhad, Z. (2017). Experimental Aortic Valve Cusp Extension with Cormatrix in a Porcine Model. *Thorac. Cardiovasc. Surg.* 65, 206–210. doi:10.1055/s-0036-1586756

Poon, C. J., Pereira E. Cotta, M. V., Sinha, S., Palmer, J. A., Woods, A. A., Morrison, W. A., et al. (2013). Preparation of an Adipogenic Hydrogel from Subcutaneous Adipose Tissue. *Acta Biomater.* 9, 5609–5620. doi:10.1016/j.actbio.2012.11.003

Prehm, P. (1984). Hyaluronate Is Synthesized at Plasma Membranes. *Biochem. J.* 220, 597–600. doi:10.1042/bj2200597

Quint, C., Kondo, Y., Manson, R. J., Lawson, J. H., Dardik, A., and Niklason, L. E. (2011). Decellularized Tissue-Engineered Blood Vessel as an Arterial Conduit. *Proc. Natl. Acad. Sci.* 108, 9214–9219. doi:10.1073/pnas.1019506108

Rajab, T. K., O'Malley, T. J., and Tchantchaleishvili, V. (2020). Decellularized Scaffolds for Tissue Engineering: Current Status and Future Perspective. *Artif. Organs.* 44, 1031–1043. doi:10.1111/aor.13701

Rajani, B., Mee, R. B., and Ratliff, N. B. (1998). Evidence for Rejection of Homograft Cardiac Valves in Infants. *J. Thorac. Cardiovasc. Surg.* 115, 111–117. doi:10.1016/s0022-5223(98)70449-0

Rayahin, J. E., Buhrman, J. S., Zhang, Y., Koh, T. J., and Gemeinhart, R. A. (2015). High and Low Molecular Weight Hyaluronic Acid Differentially Influence Macrophage Activation. *ACS Biomater. Sci. Eng.* 1, 481–493. doi:10.1021/acsbiomaterials.5b00181

Reing, J. E., Brown, B. N., Daly, K. A., Freund, J. M., Gilbert, T. W., Hsiong, S. X., et al. (2010). The Effects of Processing Methods upon Mechanical and Biologic Properties of Porcine Dermal Extracellular Matrix Scaffolds. *Biomaterials* 31, 8626–8633. doi:10.1016/j.biomaterials.2010.07.083

Rieder, E., Kasimir, M.-T., Silberhumer, G., Seebacher, G., Wolner, E., Simon, P., et al. (2004). Decellularization Protocols of Porcine Heart Valves Differ Importantly in Efficiency of Cell Removal and Susceptibility of the Matrix to Recellularization with Human Vascular Cells. *J. Thorac. Cardiovasc. Surg.* 127, 399–405. doi:10.1016/j.jtcvs.2003.06.017

Rüffer, A., Purbojo, A., Cicha, I., Glöckler, M., Potapov, S., Dittrich, S., et al. (2010). Early Failure of Xenogenous De-cellularised Pulmonary Valve Conduits - a Word of Caution!☆. *Eur. J. Cardio-Thoracic Surg.* 38, 78–85. doi:10.1016/j.ejcts.2010.01.044

Ruiz, C. E., Iemura, M., Medie, S., Varga, P., Van Alstine, W. G., Mack, S., et al. (2005). Transcatheter Placement of a Low-Profile Biodegradable Pulmonary Valve Made of Small Intestinal Submucosa: a Long-Term Study in a Swine Model. *J. Thorac. Cardiovasc. Surg.* 130, e1–477. doi:10.1016/j.jtcvs.2005.04.008

Saadi, S., and Platt, J. L. (1995). Transient Perturbation of Endothelial Integrity Induced by Natural Antibodies and Complement. *J. Exp. Med.* 181, 21–31. doi:10.1084/jem.181.1.21

Schenke-Layland, K., Vasilevski, O., Opitz, F., König, K., Riemann, I., Halbhuber, K. J., et al. (2003). Impact of Decellularization of Xenogeneic Tissue on Extracellular Matrix Integrity for Tissue Engineering of Heart Valves. *J. Struct. Biol.* 143, 201–208. doi:10.1016/j.jsb.2003.08.002

Schussler, O., Lila, N., Grau, J., Ruel, M., Lecarpentier, Y., and Carpentier, A. (2020). Possible Link between the ABO Blood Group of Bioprosthesis Recipients and Specific Types of Structural Degeneration. *J. Am. Heart Assoc.* 9, e015909. doi:10.1161/JAHA.119.015909

Senior, R. M., Griffin, G. L., and Mecham, R. P. (1980). Chemotactic Activity of Elastin-Derived Peptides. *J. Clin. Invest.* 66, 859–862. doi:10.1172/JCI109926

Shinkawa, T., Lu, C. K., Chipman, C., Tang, X., Gossett, J. M., and Imamura, M. (2015). The Midterm Outcomes of Bioprosthetic Pulmonary Valve Replacement in Children. *Semin. Thorac. Cardiovasc. Surg.* 27, 310–318. doi:10.1053/j.semtcvs.2015.07.010

Simionescu, A., Simionescu, D. T., and Vyavahare, N. R. (2007). Osteogenic Responses in Fibroblasts Activated by Elastin Degradation Products and Transforming Growth Factor-B1. *Am. J. Pathol.* 171, 116–123. doi:10.2353/ajpath.2007.060930

Simionescu, D., Harpa, M. M., Harpa, M. M., Oprita, C., Movileanu, I., and Simionescu, A. (2021). Tissue Engineering Heart Valves - a Review of More Than Two Decades into Preclinical and Clinical Testing for Obtaining the Next Generation of Heart Valve Substitutes. *Rom. J. Cardio* 31, 501–510. doi:10.47803/rjc.2021.31.3.501

Simon, P., Kasimir, M. T., Seebacher, G., Weigel, G., Ullrich, R., Muhar, U. S., et al. (2003). Early Failure of the Tissue Engineered Porcine Heart Valve SYNERGRAFT in Pediatric Patients. *Eur. J. Cardio-Thoracic Surg.* 23, 1002–1006. doi:10.1016/s1010-7940(03)00094-0

Smood, B., Hara, H., Cleveland, D. C., and Cooper, D. K. C. (2019). In Search of the Ideal Valve: Optimizing Genetic Modifications to Prevent Bioprosthetic Degeneration. *Ann. Thorac. Surg.* 108, 624–635. doi:10.1016/j.athoracsur.2019.01.054

Somuncu, Ö. S. (2019). Decellularization Concept in Regenerative Medicine. *Adv. Exp. Med. Biol.* 1212, 71–85. doi:10.1007/5584_2019_338

Soto-Gutierrez, A., Wertheim, J. A., Ott, H. C., and Gilbert, T. W. (2012). Perspectives on Whole-Organ Assembly: Moving toward Transplantation on Demand. *J. Clin. Invest.* 122, 3817–3823. doi:10.1172/JCI61974

Syed, O., Walters, N. J., Day, R. M., Kim, H.-W., and Knowles, J. C. (2014). Evaluation of Decellularization Protocols for Production of Tubular Small Intestine Submucosa Scaffolds for Use in Oesophageal Tissue Engineering. *Acta Biomater.* 10, 5043–5054. doi:10.1016/j.actbio.2014.08.024

Takagi, K., Fukunaga, S., Nishi, A., Shojima, T., Yoshikawa, K., Hori, H., et al. (2006). *In Vivo* recellularization of plain Decellularized Xenografts with Specific Cell Characterization in the Systemic Circulation: Histological and Immunohistochemical Study. *Artif. Organs* 30, 233–241. doi:10.1111/j.1525-1594.2006.00210.x

Tavassoli, A., Matin, M. M., Niaki, M. A., Mahdavi-Shahri, N., and Shahabipour, F. (2015). Mesenchymal Stem Cells Can Survive on the Extracellular Matrix-Derived Decellularized Bovine Articular Cartilage Scaffold. *Iran J. Basic Med. Sci.* 18, 1221–1227.

Termeer, C. C., Hennies, J., Voith, U., Ahrens, T., M. Weiss, J., Prehm, P., et al. (2000). Oligosaccharides of Hyaluronan Are Potent Activators of Dendritic Cells. *J. Immunol.* 165, 1863–1870. doi:10.4049/jimmunol.165.4.1863

Toumpaniari, S., Hilfiker, A., Haverich, A., and Korossis, S. (2020). *Tissue-Engineered Vascular Grafts*. Springer International Publishing.

U.S. Food & Drug Administration (2020). *FDA Approves First-Of-Its-Kind Intentional Genomic Alteration in Line of Domestic Pigs for Both Human Food, Potential Therapeutic Uses*. Available at: : https://www.fda.gov/news-events/press-announcements/fda-approves-first-its-kind-intentional-genomic-alteration-line-domestic-pigs-both-human-food (Accessed December 14, 2020).

Vafaee, T., Thomas, D., Desai, A., Jennings, L. M., Berry, H., Rooney, P., et al. (2018). Decellularization of Human Donor Aortic and Pulmonary Valved Conduits Using Low Concentration Sodium Dodecyl Sulfate. *J. Tissue Eng. Regen. Med.* 12, e841–e853. doi:10.1002/term.2391

van Rijswijk, J. W., Talacua, H., Mulder, K., van Hout, G. P. J., Bouten, C. V. C., Gründeman, P. F., et al. (2020). Failure of Decellularized Porcine Small Intestinal Submucosa as a Heart Valved Conduit. *J. Thorac. Cardiovasc. Surg.* 160, e201–e215. doi:10.1016/j.jtcvs.2019.09.164

Veiseh, M., and Turley, E. A. (2011). Hyaluronan Metabolism in Remodeling Extracellular Matrix: Probes for Imaging and Therapy of Breast Cancer. *Integr. Biol. (Camb)* 3, 304–315. doi:10.1039/c0ib00096e

Voges, I., Bräsen, J. H., Entenmann, A., Scheid, M., Scheewe, J., Fischer, G., et al. (2013). Adverse Results of a Decellularized Tissue-Engineered Pulmonary Valve in Humans Assessed with Magnetic Resonance Imaging. *Eur. J. Cardiothorac. Surg.* 44, e272–e279. doi:10.1093/ejcts/ezt328

Waletzko, J., Dau, M., Seyfarth, A., Springer, A., Frank, M., Bader, R., et al. (2020). Devitalizing Effect of High Hydrostatic Pressure on Human Cells-Influence on Cell Death in Osteoblasts and Chondrocytes. *Ijms* 21, 3836. doi:10.3390/ijms21113836

White, L. J., Taylor, A. J., Faulk, D. M., Keane, T. J., Saldin, L. T., Reing, J. E., et al. (2017). The Impact of Detergents on the Tissue Decellularization Process: A ToF-SIMS Study. *Acta Biomater.* 50, 207–219. doi:10.1016/j.actbio.2016.12.033

Wilson, G. J., Courtman, D. W., Klement, P., Lee, J. M., and Yeger, H. (1995). Acellular Matrix: a Biomaterials Approach for Coronary Artery Bypass and Heart Valve Replacement. *Ann. Thorac. Surg.* 60, S353–S358. doi:10.1016/0003-4975(95)98967-y

Wilson, N. S., Dixit, V., and Ashkenazi, A. (2009). Death Receptor Signal Transducers: Nodes of Coordination in Immune Signaling Networks. *Nat. Immunol.* 10, 348–355. doi:10.1038/ni.1714

Woo, J. S., Fishbein, M. C., and Reemtsen, B. (2016). Histologic Examination of Decellularized Porcine Intestinal Submucosa Extracellular Matrix (CorMatrix) in Pediatric Congenital Heart Surgery. *Cardiovasc. Pathol.* 25, 12–17. doi:10.1016/j.carpath.2015.08.007

Woods, T., and Gratzer, P. F. (2005). Effectiveness of Three Extraction Techniques in the Development of a Decellularized Bone-Anterior Cruciate Ligament-Bone Graft. *Biomaterials* 26, 7339–7349. doi:10.1016/j.biomaterials.2005.05.066

Zafar, F., Hinton, R. B., Moore, R. A., Baker, R. S., Bryant, R., Narmoneva, D. A., et al. (2015). Physiological Growth, Remodeling Potential, and Preserved Function of a Novel Bioprosthetic Tricuspid Valve. *J. Am. Coll. Cardiol.* 66, 877–888. doi:10.1016/j.jacc.2015.06.1091

Conflict of Interest: FN and AG were employed by Biocompatibility Innovation Srl.

Publisher's Note: All claims expressed in this article are solely those of the authors and do not necessarily represent those of their affiliated organizations, or those of the publisher, the editors, and the reviewers. Any product that may be evaluated in this article, or claim that may be made by its manufacturer, is not guaranteed or endorsed by the publisher.

Copyright © 2022 Naso and Gandaglia. This is an open-access article distributed under the terms of the Creative Commons Attribution License (CC BY). The use, distribution or reproduction in other forums is permitted, provided the original author(s) and the copyright owner(s) are credited and that the original publication in this journal is cited, in accordance with accepted academic practice. No use, distribution or reproduction is permitted which does not comply with these terms.

frontiers in Bioengineering and Biotechnology

MINI REVIEW
published: 21 February 2022
doi: 10.3389/fbioe.2022.802283

Applications of Tissue Decellularization Techniques in Ventricular Myocardial Biofabrication

*Aravind Krishnan, Hanjay Wang and John Ward MacArthur**

Department of Cardiothoracic Surgery, Stanford University School of Medicine, Stanford, CA, United States

Ischemic heart disease is the leading cause of death around the world, and though the advent of coronary revascularization has revolutionized its treatment, many patients who sustain ischemic injury to the heart will go on to develop heart failure. Biofabrication of ventricular myocardium for replacement of irreversibly damaged ischemic myocardium is sought after as a potential therapy for ischemic heart failure, though challenges in reliably producing this biomaterial have limited its clinical application. One method that shows promise for generation of functional myocardium is the use of tissue decellularization to serve as a scaffold for biofabrication. This review outlines the methods, materials, challenges, and prospects of tissue decellularization techniques for ventricular myocardium biofabrication. Decellularization aims to preserve the architecture and composition of the extracellular matrix of the tissue it is applied to, allowing for the subsequent implantation of stem cells of the desired cell type. Decellularization can be achieved with multiple reagents, most of which have detergent properties. A variety of cell types can be implanted in the resulting scaffold, including cardiac progenitor cells, and embryonic or induced pluripotent stem cells to generate a range of tissue, from patches to beating myocardium. The future of this biofabrication method will likely emphasize patient specific tissue engineering to generate complex 3-dimensional constructs that can replace dysfunctional cardiac structures.

Keywords: cardiomyopathy, biofabrication, decellularization, stem cells, transplant surgery

OPEN ACCESS

Edited by:
Laura Iop,
University of Padua, Italy

Reviewed by:
Marie-noelle Giraud,
Université de Fribourg, Switzerland
Camila Hochman-Mendez,
Texas Heart Institute, United States

****Correspondence:***
John Ward MacArthur
Jwm2108@stanford.edu

Specialty section:
This article was submitted to Biomaterials, a section of the journal Frontiers in Bioengineering and Biotechnology

Received: *26 October 2021*
Accepted: *21 January 2022*
Published: *21 February 2022*

Citation:
Krishnan A, Wang H and MacArthur JW (2022) Applications of Tissue Decellularization Techniques in Ventricular Myocardial Biofabrication. Front. Bioeng. Biotechnol. 10:802283. doi: 10.3389/fbioe.2022.802283

INTRODUCTION

Ischemic heart disease remains the number one cause of mortality around the world (Virani et al., 2021). Though coronary revascularization via percutaneous coronary intervention or coronary artery bypass grafting has revolutionized its treatment, myocardial infarction will often progress to heart failure, and a subset of patients will experience end-stage heart failure (Bourassa et al., 1993; Mosterd and Hoes, 2007; King et al., 2010; Briceno et al., 2016; Velazquez et al., 2016; Bahit et al., 2018; Sun et al., 2018; Sun et al., 2020).

While orthotopic heart transplantation is the gold standard treatment for end-stage heart failure, it is challenged by limited donor supply, the lifelong need for immunosuppression, and the need to monitor for rejection (Heidenreich et al., 2020; Bozkurt et al., 2021). Though the use of mechanical circulatory support with left ventricular assist devices or extracorporeal membrane oxygenation, and more aggressive transplantation strategies have increased utilization and improved outcomes in patients awaiting heart transplantation, there is still a huge unmet clinical need for organ replacement (Mehra et al., 2019; Guenthart et al., 2021). Tissue engineered bioscaffolds have

long been proposed as adjunctive therapies that may address heart failure by restoring or replacing the damaged architecture in failing hearts or even the whole heart (Arenas-Herrera et al., 2013; Daley et al., 2018; Tang-Quan et al., 2018).

The two prevailing approaches to generating bioscaffolds for myocardial repair or replacement are "bottom-up" and "top-down" engineering (Arenas-Herrera et al., 2013; Tang-Quan et al., 2018). The "bottom-up" approach focuses on bioprinting scaffolds from native or engineered extracellular matrix components with or without colocalized progenitor cell lines that differentiate into myocardium (Ong et al., 2018). The "top-down" approach produces bioscaffolds from decellularization of tissues or whole organs, leaving acellular extracellular matrix and retained tissue architecture, onto which stem cell lines are then implanted or reperfused, eventually producing functional tissues/organs (Arenas-Herrera et al., 2013; Tang-Quan et al., 2018). The proposed benefit of this latter approach is in the retention of vascular networks through which a recellularized tissue structure could then be perfused (Badylak, 2002; Pla-Palacín et al., 2018; Taylor et al., 2018).

Herein, we will briefly review the history and prevalent methods of decellularization as a method of biofabrication of myocardial tissue, and then focus on its application to replacing ventricular myocardium.

DECELLULARIZATION AND RECELLULARIZATION

History

Tissue decellularization is the process by which chemical, enzymatic, or mechanical stimuli are used to produce an acellular bioscaffold from previously cellularized tissue or whole organs (Wainwright et al., 2010; Gilpin and Yang, 2017; Iop et al., 2017; Rana et al., 2017; Saldin et al., 2017; Daley et al., 2018; Spang and Christman, 2018; Tang-Quan et al., 2018). Prior to 2008, decellularization had mainly been applied to tissues without complex vascular networks; cardiac tissue decellularization had been limited to valve tissue and portions of the aorta (Badylak, 2004; Ketchedjian et al., 2005; Gilbert et al., 2006). In 2008, whole heart decellularization was introduced by the Taylor group whereby cadaveric rat hearts were decellularized through coronary perfusion of a detergent, retaining their coronary vascular networks, and then recellularized via a direct injection method supported by perfusion of cell media through the coronary vasculature (Ott et al., 2008). This method produced hearts that macroscopically contracted, producing stroke work up to 25% of a fetal heart's function (Ott et al., 2008). The subsequent decade produced a convention in determining decellularization in that the decellularized tissue must meet a threshold of <50 ng of double stranded DNA per mg of dry weight and <200 base pairs of DNA fragment length (Nagata et al., 2010). Further improvements in decellularization materials and methods improved the degree of decellularization of whole hearts, and introduced decellularization and reperfusion of porcine hearts (Akhyari et al., 2011; Remlinger et al., 2012; Momtahan et al., 2015). In 2016, the Ott group introduced decellularization and recellularization of human hearts deemed unsuitable for transplantation (Guyette et al., 2016).

Contemporary Methods of Decellularization

Conventional approaches to decellularization of tissue include bathing the tissue in a decellularization agent (Methe et al., 2014) or, in the case of cardiac tissue, intracoronary perfusion of a chemical or enzymatic decellularization agent (Tang-Quan et al., 2018). Chemical decellularization is most commonly achieved with a detergent agent such as sodium dodecyl sulfate (SDS), which can be used in conjunction with other detergents such as Triton X-100 in optimal concentrations to preserve the architecture of the extracellular matrix (Ott et al., 2008; Cebotari et al., 2010; Keane et al., 2015; Gilpin and Yang, 2017).

Enzymatic decellularization involves the use of nucleases such as Dornase or trypsin meant to cleave RNA and DNA or attachments from cells to the ECM, to achieve the standard thresholds of decellularization (Lynch and Ahearne, 2013). This method is most frequently used in conjunction with chemical decellularization but risks inadvertent damage to the extracellular matrix itself (Crapo et al., 2011). Viability of the decellularized scaffold is directly dependent on preservation of the ECM and microvascular architecture (Taylor et al., 2018).

Decellularization can be achieved using physical agitation or alternating cycles of freezing and cooling, or pressurization with supercritical carbon dioxide that lyse the cells (Tang-Quan et al., 2018). Each of these methodologies can be used in combination with other methods, and ultimately a group's protocol for decellularization results from trialing multiple methods to achieve an acceptably low level of remaining DNA.

Recellularization

Decellularized tissues can subsequently be seeded with stem cells via a process called recellularization. The decellularized tissue can be stereotropically repopulated with vascular tissue, muscle, and other functional components of organized myocardium (Tang-Quan et al., 2018). Recellularization with cardiac cell lines can be applied to decellularized ECM (dECM) or bio-scaffolds that are not cardiac in origin (Tan et al., 2009; Francisco et al., 2020). Methods of recellularization are largely based on perfusion of stem cells, direct injection of stem cells, or a combination of the two, into decellularized ECM (Ng et al., 2011; Guyette et al., 2016; Tang-Quan et al., 2018).

Induced pluripotent stem cells (iPSCs) and mesenchymal stem cells (MSCs) are the most commonly used recellularization agents, and differentiate into the appropriate functional unit of the area into which they are seeded due to biomechanical cues from the extracellular matrix (ECM) (Ott et al., 2008; Hynes, 2009; Bowers et al., 2010; Schmuck et al., 2018). Perfusion based recellularization in particular takes advantage of this cross-talk that occurs between the cell line and the ECM by utilizing pauses in perfusion where the perfused cells are able to form physical attachments to the ECM, while simultaneously delivering a critical mass of stem cells to engraft the decellularized tissue (Ott et al., 2008; Hülsmann et al., 2013; Tang-Quan et al., 2018). Direct injection, on the other hand, suffers from poor

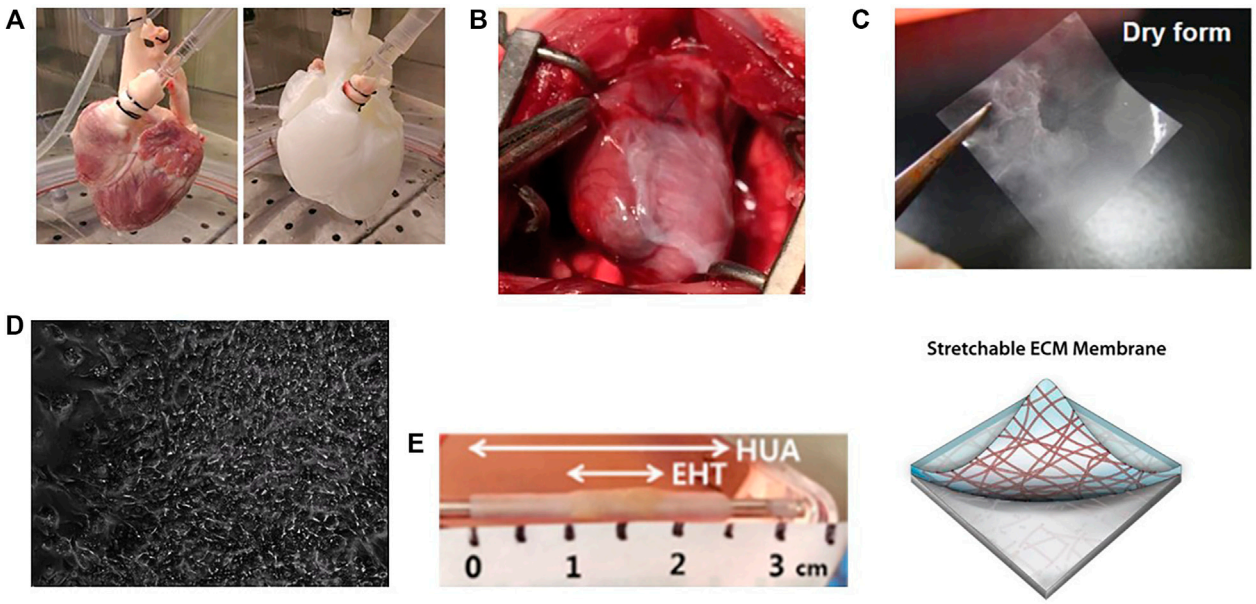

FIGURE 1 | Applications of tissue decellularization for ventricular biofabrication. **(A)** Demonstration of perfusion decellularization of a porcine heart, yielding an acellular extracellular matrix structure retaining the architecture of a heart. Image taken from Tang-Quan et al. (2018). **(B)** Decellularized extracellular matrix can augment ventricular function when applied to damaged myocardium. Image taken from Francisco et al. (2020). **(C)** Decellularized patches can be recellularized and applied to damaged myocardium, not only augmenting function and providing structural support, but also improving angiogenesis and promoting stem cell migration into compromised and damaged ventricular myocardium. Image taken from Kim et al. (2019). **(D)** Decellularized ECM scaffolds recellularized with pluripotent stem cells and programmed to differentiae into ventricular myocardium can display organized contraction. Image taken from Li et al. (2017). **(E)** Beating cardiomyocytes can be seeded onto acellular tubules to generate beating vascular conduits for treatment of congenital ventricular disorders. EHT: Engineered heart tissue (beating cardiomyocytes) seeded onto HUA: decellularized human umbilical artery tissue. Image taken from Kubo et al. (2007).

engraftment, commonly with fewer than 50% of injected cells appropriately seeding the tissue (Iop et al., 2017). The two approaches can be used in tandem to maximize both spatial specificity and diffuse engraftment of recellularized cell populations, as demonstrated by Weymann et al. who utilized perfusion human umbilical cord blood endothelial cells through the coronaries of decellularized porcine hearts, followed by direct injection of rat neonatal cardiomyocytes into the ventricular wall to ultimately generate electrically responsive, viable recellularized porcine hearts (Weymann et al., 2014).

Advances in recellularization have centered on improvements in engraftment as well as specific programming of iPSCs into complex cell lines that form the components of functional myocardium (Iop et al., 2017). A major milestone in successful recellularization is evidence of the formation of gap junctions, allowing for coordinated conductivity, and ultimately, beating myocardium (Tang-Quan et al., 2018). Despite these advances, whole organ recellularization is still limited in efficacy. Attempts at performing heterotopic heart transplantation with decellularized and subsequently recellularized hearts in pigs showed non-viable hearts with non-patent coronary arteries or poorly functional left ventricular myocardium (Kitahara et al., 2016). Despite these limitations, decellularized bioscaffolds presently hold great potential to augment or replace ventricular myocardium.

VENTRICULAR AUGMENTATION AND BIOFABRICATION

Tissue decellularization, with or without recellularization, can be applied to augment or fabricate ventricular myocardium (**Figure 1**). When applied without recellularization, the decellularized extracellular matrix is usually implanted in the form of a patch or a hydrogel into damaged or failing ventricular myocardium to induce regeneration and provide structural support to the myocardium.

Decellularized Extra-Cellular Matrix

Even in the absence of recellularization, purely decellularized ECM can support ventricular myocardium. Wang et al. minced and decellularized neonatal and adult mice hearts using combination of chemical (antibiotic/antimycotic/gentamycin solution), followed by physical (freezing), and finally enzymatic (deoxyribonuclease and ribonuclease) decellularization, producing an ECM powder that was resuspended into a hydrogel (Wang et al., 2019). They demonstrated that in an adult mouse left anterior descending artery ligation model of myocardial infarction that even a single injection of neonatal mouse decellularized ECM into the ventricular myocardium mitigated left ventricular remodeling, improving ejection fraction, and reducing wall stiffening and fibrosis (Wang et al., 2019). In a cell migration experiment, the group showed that human umbilical vein endothelial cells

(HUVECs) demonstrated greater cell activity and migration into neonatal mouse decellularized ECM, postulating that this would lead to downstream angiogenesis (Wang et al., 2019).

Decellularized non-cardiac ECM can be applied in a similar manner to infarcted or damaged ventricular myocardium. Francisco et al. demonstrated that human amniotic membrane could be decellularized via chemical decellularization to produce an ECM bioscaffold patch, impregnated with an anti-inflammatory nanoparticle, and then implanted on the surface of infarcted rat hearts (Francisco et al., 2020). Hearts that received the decellularized amniotic membrane patches, with or without the impregnated nanoparticles, demonstrated greater angiogenesis, decreased scar formation, and greater proliferation of cardiomyocytes, which directly translated into an improved ejection fraction (Francisco et al., 2020).

A limitation to clinical translation of conventional decellularized ECM patches or hydrogels is their physical weakness, ultimately leading to poor long-term engraftment and inability to reliably maintain geometric configurations (Tang-Quan et al., 2018; Kim et al., 2019). Gul Kim et al. offer a potential fix to this issue by stamping decellularized ECM onto polyvinyl alcohol hydrogels, ultimately resulting in a stretchable ECM patch (Kim et al., 2019). When grafted onto infarcted ventricular myocardium, the stretchable decellularized ECM patch not only improved stiffness, ejection fraction, and scar formation, but also improved migration of stem cells into the patched area, with the added three-dimensional structural support that limited priorly described decellularized ECM patches/hydrogels (Kim et al., 2019).

Biofabricating Ventricular Myocardium With Recellularization

Bioscaffolds generated from decellularized ECM and then subsequently recellularized stand to provide the benefits of decellularized ECM patches, namely scar limitation, improved left ventricular remodeling and preservation of ejection fraction, with the added potential of repopulating cardiomyocytes. Kajbafzadeh et al. demonstrate this by decellularizing rabbit pericardium and then recellularizing with autologous adipose-derived mesenchymal stem cells (ADMSCs) (Kajbafzadeh et al., 2017; Kameli et al., 2018). Within the patched portions of the ventricular myocardium, the engrafted ADMSCs demonstrated significantly higher populations of CD34 and desmin-positive cells, suggestive of cardiomyocyte regeneration and angiogenesis (Kajbafzadeh et al., 2017; Kameli et al., 2018). Notably, the mesenchymal stem cells within the bioscaffold engrafted beyond the confines of the patch itself, suggesting that these recellularized patches additionally serve as delivery vehicles for stem cell populations (Kajbafzadeh et al., 2017; Kameli et al., 2018).

Tan et al. demonstrated the added benefit of seeding decellularized tissue with stem cells by showing that decellularized small intestinal submucosa patched onto infarcted rabbit ventricular myocardium in itself could preserve ejection fraction and mitigate adverse remodeling, but patches seeded with mesenchymal stem cells grossly improved capillary formation within the infarcted territory of the rabbit ventricular myocardium (Tan et al., 2009). Demonstration of improved neovascularization is a critical step forward in the use of decellularization to address myocardial disease in given that neovascularization is associated with improved survival after ischemic injury to the heart, as demonstrated in long-term studies of coronary artery bypass grafting and basic science investigations of the role of angiogenesis in treating ischemic heart disease (Shi et al., 2021).

Biofabrication of pure ventricular cardiomyocytes for direct engraftment onto damaged ventricular myocardium has been largely limited by challenges in reliably inducing iPSCs to differentiate into ventricular myocardium when delivered via a decellularized patch. Li et al. addressed this challenge by decellularizing adult rat hearts to produce dECM patches, and subsequently recellularizing them with iPSCs genomically engineered through transcription activator-like effector nucleases (TALEN) to select for cues to differentiate into ventricular cardiomyocytes (Garreta et al., 2016; Li et al., 2017). The result of this decellularization-recellularization method was functional, electrically conductive, beating ventricular myocardium in a petri dish (Li et al., 2017). Though this myocardium has not been grafted onto hearts, reliably converting iPSCs into fully differentiated myocardium represents a major step forward in clinical and therapeutic translation of these methodologies.

Even without directly fabricating ventricular myocardium, decellularization and recellularization can improve currently existing therapies for ventricular disease. For example, congenital defects that result in single ventricle physiology can be treated using surgical techniques such as the Fontan procedure. This procedure utilizes a vascular conduit to redirect central venous blood flow directly into the pulmonary artery in situations where the right ventricle is physiologically or physically absent. A struggle of the procedure is reliably generating forward flow into the pulmonary arterial circuit. Park et al. demonstrate a novel technique to generate a pulsatile vascular conduit that can act like the right ventricle to generate stroke work to push blood flow into the pulmonary artery circuit (Shi et al., 2021). The approach was two-fold: 1) generate a beating sheet of cardiac myocytes, and 2) generate a conduit onto which to wrap the beating cardiomyocytes. The former was produced by chemically decellularizing porcine hearts and recellularizing with a mix of iPSCs with commercially available adult cardiac fibroblasts. The latter was achieved by decellularizing human umbilical cord. The muscle sheets were then engrafted onto the decellularized cord, ultimately producing a pulsatile conduit that could be used for alleviation of congenital single ventricle disease (Park et al., 2020). This approach radically improved on prior attempts at producing pulsatile conduits mainly through its use of decellularization. Prior work has utilized fibrin scaffolds instead of decellularized umbilical cord as the conduit, producing a much smaller amount of stroke work compared to the method developed by Kubo et al. (2007); Park et al. (2020).

Limitations and Future

Ventricular biofabrication represents an area of application of decellularization/recellularization that has not been meaningfully translated into clinical practice, unlike other applications such as bovine pericardial patches or certain decellularized heartvalves (Tang-Quan et al., 2018). Though conventions have been accepted for levels of DNA present in decellularized tissue, the ability to recellularize this tissue and produce functioning myocardium is dependent on preservation of the microarchitecture of the ECM, including appropriate amounts and arrangement of mature, cross-linked collagen, glycosaminoglycans, and growth factors (Kc et al., 2019). The various decellularization strategies described previously may disrupt this microarchitecture, and substantial heterogeneity exists in choosing not only the optimal method, but controlling each of the parameters within each method, be it perfusion, mechanical, or enzymatic decellularization. In addition to removing adequate DNA, while preserving the vital components of the ECM, decellularization must minimize the presence of immunogenic factors such as human leukocyte antigens when using human hearts for decellularization or immunogenic sugars in xenogeneic hearts, an area of active investigation (Galili, 2015; Guyette et al., 2016; Kc et al., 2019). Finally, when decellularizing tissue that has sustained damage whether by decellularization or by the natural history of the heart, there are structural changes in the microvasculature that may hinder recellularization due to disruption of perfusion networks (Guyette et al., 2016).

Preserving the ECM microarchitecture contributes significantly to the major limitation of recellularization: generating enough viable cardiomyocytes from stem cells. Several billion, organized and functioning cardiomyocytes are needed to repopulate a whole decellularized human heart (Guyette et al., 2016). While patches of recellularized dECM have shown potential to augment cardiac function, whole organ or specific ventricular replacement requires highly organized cardiomyocyte electrical, mechanical, and paracrine function. Having enough stem cells to mature and populate a decellularized cardiac graft is incumbent on successful implantation of stem cells, followed by ideal ECM microenvironment conditions to promote appropriate differentiation into the appropriate cell lines (Brizzi et al., 2012; Kc et al., 2019). Current recellularization methods are limited in appropriately distributing multiple stem cell lines to promote not only survival but appropriate differentiation into the organized subunits necessary for complex cardiac function (Vunjak-Novakovic et al., 2010; Kc et al., 2019). However, since 2016 there has been an explosion of meaningful advancements to overcoming the challenges facing ventricular biofabrication. These are namely, the reliable programming of induced pluripotent stem cells into cardiomyocytes, utilizing genomic engineering or optimized cell culture protocols, and clever decellularization of non-cardiac tissue ultimately for cardiac applications. One such advancement in improving stem cell survival and functional maturation is recognition and use of organized mechanical stimuli through biomimetic bioreactors to support recellularization (Hülsmann et al., 2013; Wang et al., 2013; Guyette et al., 2016). Bioreactors are used to simulate contraction of the decellularized cardiac graft while recellularization is ongoing, and the current era of these bioreactors are highly customizable, and have improved the survival and maturation of cardiomyocytes in decellularized human hearts (Guyette et al., 2016).

The clinical utilization of these fabricated sections of ventricular myocardium will likely be incumbent on the reliable generation of microvasculature and generation of a reliable conduction system as well.

CONCLUSION

Biofabrication of ventricular myocardium has been propelled forward, especially in the past 6 years, through the advent of decellularization and recellularization techniques. Though there are competing methodologies to produce functional myocardium or augment dysfunctional myocardium, decellularization based methods uniquely provide organized, three-dimensional structural support, while preserving biophysical cues to instruct native or seeded stem cells to promote angiogenesis and differentiation into fully functional cardiomyocytes. The therapeutic potential of biofabricated myocardium stands to revolutionize the treatment of ischemic cardiomyopathy, and the last decade has introduced unique advancements in these methodologies, bringing the field closer to meaningful clinical translation.

AUTHOR CONTRIBUTIONS

AK, HW, and JM contributed to the drafting, revision, and final approval of the manuscript. All authors take full responsibility for the content shared in this manuscript. JM is the senior author and AK is the first/lead/corresponding author.

FUNDING

This work is institutionally funded.

REFERENCES

Akhyari, P., Aubin, H., Gwanmesia, P., Barth, M., Hoffmann, S., Huelsmann, J., et al. (2011). The Quest for an Optimized Protocol for Whole-Heart Decellularization: A Comparison of Three Popular and a Novel Decellularization Technique and Their Diverse Effects on Crucial Extracellular Matrix Qualities. *Tissue Eng. C: Methods* 17 (9), 915–926. doi:10.1089/ten.tec.2011.0210

Arenas-Herrera, J. E., Ko, I. K., Atala, A., and Yoo, J. J. (2013). Decellularization for Whole Organ Bioengineering. *Biomed. Mater.* 8, 14106–14115. doi:10.1088/1748-6041/8/1/014106

Badylak, S. F. (2004). Xenogeneic Extracellular Matrix as a Scaffold for Tissue Reconstruction. *Transpl. Immunol.* 12 (3-4), 367–377. doi:10.1016/j.trim.2003.12.016

Badylak, S. F. (2002). The Extracellular Matrix as a Scaffold for Tissue Reconstruction. *Semin. Cel Develop. Biol.* 13 (5), 377–383. doi:10.1016/S1084952102000940

Bahit, M. C., Kochar, A., and Granger, C. B. (2018). Post-myocardial Infarction Heart Failure. *JACC Heart Fail.* 6 (3), 179–186. doi:10.1016/j.jchf.2017.09.015

Bourassa, M. G., Gurné, O., Bangdiwala, S. I., Ghali, J. K., Young, J. B., Rousseau, M., et al. (1993). Natural History and Patterns of Current Practice in Heart Failure. The Studies of Left Ventricular Dysfunction (SOLVD) Investigators. *J. Am. Coll. Cardiol.* 22 (4 Suppl. 1), 14A–19A. doi:10.1016/0735-1097(93)90456-B

Bowers, S. L., Banerjee, I., and Baudino, T. A. (2010). The Extracellular Matrix: at the center of it All. *J. Mol. Cel Cardiol* 48 (3), 474–482. doi:10.1016/j.yjmcc.2009.08.024

Bozkurt, B., Bozkurt, B., Hershberger, R. E., Butler, J., Isler, M. L., Grady, K. L., et al. (2021). TEMPORARY NOTICE: 2021 ACC/AHA Key Data Elements and Definitions for Heart Failure: A Report of the American College of Cardiology/American Heart Association Task Force on Clinical Data Standards (Writing Committee to Develop Clinical Data Standards for Heart Failure). *J. Am. Coll. Cardiol.* 77 (16), 2053–2150. doi:10.1016/j.jacc.2020.11.012

Briceno, N., Schuster, A., Lumley, M., and Perera, D. (2016). Ischaemic Cardiomyopathy: Pathophysiology, Assessment and the Role of Revascularisation. *Heart* 102 (5), 397–406. doi:10.1136/HEARTJNL-2015-308037

Brizzi, M. F., Tarone, G., and Defilippi, P. (2012). Extracellular Matrix, Integrins, and Growth Factors as Tailors of the Stem Cell Niche. *Curr. Opin. Cel Biol.* 24 (5), 645–651. doi:10.1016/j.ceb.2012.07.001

Cebotari, S., Tudorache, I., Jaekel, T., Hilfiker, A., Dorfman, S., Ternes, W., et al. (2010). Detergent Decellularization of Heart Valves for Tissue Engineering: Toxicological Effects of Residual Detergents on Human Endothelial Cells. *Artif. Organs* 34 (3), 206–210. doi:10.1111/J.1525-1594.2009.00796.X

Crapo, P. M., Gilbert, T. W., and Badylak, S. F. (2011). An Overview of Tissue and Whole Organ Decellularization Processes. *Biomaterials* 32 (12), 3233–3243. doi:10.1016/j.biomaterials.2011.01.057

Daley, M. C., Fenn, S. L., and Black, L. D. (2018). Applications of Cardiac Extracellular Matrix in Tissue Engineering and Regenerative Medicine. *Adv. Exp. Med. Biol.* 1098, 59–83. doi:10.1007/978-3-319-97421-7_4

E. G. Schmuck, P. Hematti, and A. N. Raval (Editors) (2018). *Cardiac Extracellular Matrix*, 1098. doi:10.1007/978-3-319-97421-7

Francisco, J. C., Uemura, L., Simeoni, R. B., da Cunha, R. C., Mogharbel, B. F., Simeoni, P. R. B., et al. (2020). Acellular Human Amniotic Membrane Scaffold with 15d-PGJ2 Nanoparticles in Postinfarct Rat Model. *Tissue Eng. Part. A.* 26 (21-22), 1128–1137. doi:10.1089/ten.TEA.2019.0340

Galili, U. (2015). *Human Anti-gal and Anti-non-gal Immune Human Anti-gal and Anti-non-gal Immune Response to Porcine Tissue Implants* (Cambridge, MA: Academic Press), 239–267. doi:10.1016/B978-0-12-800196-7.00010-4

Garreta, E., de Oñate, L., Fernández-Santos, M. E., Oria, R., Tarantino, C., Climent, A. M., et al. (2016). Myocardial Commitment from Human Pluripotent Stem Cells: Rapid Production of Human Heart Grafts. *Biomaterials* 98, 64–78. doi:10.1016/j.biomaterials.2016.04.003

Gilbert, T. W., Sellaro, T. L., and Badylak, S. F. (2006). Decellularization of Tissues and Organs. *Biomaterials* 27 (19), 3675–3683. doi:10.1016/j.biomaterials.2006.02.014

Gilpin, A., and Yang, Y. (2017). Decellularization Strategies for Regenerative Medicine: From Processing Techniques to Applications. *Biomed. Res. Int.* 2017, 1–13. doi:10.1155/2017/9831534

Guenthart, B. A., Krishnan, A., Koyano, T., La Francessca, S., Chan, J., Alassar, A., et al. (2021). "Extended Static Hypothermic Preservation in Cardiac Transplantation: A Case Report in Cardiac Transplantation: A Case Report. *Transpl. Proceedings*, 53, 2509–2511. doi:10.1016/j.transproceed.2021.08.021

Guyette, J. P., Charest, J. M., Mills, R. W., Jank, B. J., Moser, P. T., Gilpin, S. E., et al. (2016). Bioengineering Human Myocardium on Native Extracellular Matrix. *Circ. Res.* 118 (1), 56–72. doi:10.1161/CIRCRESAHA.115.306874

Heidenreich, P. A., Fonarow, G. C., Breathett, K., Jurgens, C. Y., Pisani, B. A., Pozehl, B. J., et al. (2020). 2020 ACC/AHA Clinical Performance and Quality Measures for Adults with Heart Failure. *Circ. Cardiovasc. Qual. Outcomes* 13, 919–956. doi:10.1161/HCQ.0000000000000099

Hülsmann, J., Aubin, H., Kranz, A., Godehardt, E., Munakata, H., Kamiya, H., et al. (2013). A Novel Customizable Modular Bioreactor System for Whole-Heart Cultivation under Controlled 3D Biomechanical Stimulation. *J. Artif. Organs* 16 (3), 294–304. doi:10.1007/S10047-013-0705-5

Hynes, R. O. (2009). The Extracellular Matrix: Not Just Pretty Fibrils. *Science* 326 (5957), 1216–1219. doi:10.1126/SCIENCE.1176009

Iop, L., Dal Sasso, E., Menabò, R., Di Lisa, F., and Gerosa, G. (2017). The Rapidly Evolving Concept of Whole Heart Engineering. *Stem Cell Int.* 2017, 1–18. doi:10.1155/2017/8920940

Kajbafzadeh, A.-M., Tafti, S. H. A., Khorramirouz, R., Sabetkish, S., Kameli, S. M., Orangian, S., et al. (2017). Evaluating the Role of Autologous Mesenchymal Stem Cell Seeded on Decellularized Pericardium in the Treatment of Myocardial Infarction: an Animal Study. *Cell Tissue Bank* 18 (4), 527–538. doi:10.1007/S10561-017-9629-2

Kameli, S. M., Khorramirouz, R., Eftekharzadeh, S., Fendereski, K., Daryabari, S. S., Tavangar, S. M., et al. (2018). Application of Tissue-engineered Pericardial Patch in Rat Models of Myocardial Infarction. *J. Biomed. Mater. Res.* 106 (10), 2670–2678. doi:10.1002/jbm.a.36464

Kc, P., Hong, Y., and Zhang, G. (2019). Cardiac Tissue-Derived Extracellular Matrix Scaffolds for Myocardial Repair: Advantages and Challenges. *Regen. Biomater.* 6 (4), 185–199. doi:10.1093/RB/RBZ017

Keane, T. J., Swinehart, I. T., and Badylak, S. F. (2015). Methods of Tissue Decellularization Used for Preparation of Biologic Scaffolds and *In Vivo* Relevance. *Methods* 84, 25–34. doi:10.1016/j.ymeth.2015.03.005

Ketchedjian, A., Jones, A. L., Krueger, P., Robinson, E., Crouch, K., Wolfinbarger, L., Jr, et al. (2005). Recellularization of Decellularized Allograft Scaffolds in Ovine Great Vessel Reconstructions. *Ann. Thorac. Surg.* 79 (3), 888–896. doi:10.1016/j.athoracsur.2004.09.033

Kim, I. G., Hwang, M. P., Park, J. S., Kim, S. H., Kim, J. H., Kang, H. J., et al. (2019). Stretchable ECM Patch Enhances Stem Cell Delivery for Post-MI Cardiovascular Repair. *Adv. Healthc. Mater.* 8 (17), 1900593. doi:10.1002/adhm.201900593

King, S. B., 3rd, Marshall, J. J., and Tummala, P. E. (2010). Revascularization for Coronary Artery Disease: Stents versus Bypass Surgery. *Annu. Rev. Med.* 61, 199–213. doi:10.1146/ANNUREV.MED.032309.063039

Kitahara, H., Yagi, H., Tajima, K., Okamoto, K., Yoshitake, A., Aeba, R., et al. (2016). Heterotopic Transplantation of a Decellularized and Recellularized Whole Porcine Heart. *Interact Cardiovasc. Thorac. Surg.* 22 (5), 571–579. doi:10.1093/ICVTS/IVW022

Kubo, H., Shimizu, T., Yamato, M., Fujimoto, T., and Okano, T. (2007). Creation of Myocardial Tubes Using Cardiomyocyte Sheets and an *In Vitro* Cell Sheet-Wrapping Device. *Biomaterials* 28 (24), 3508–3516. doi:10.1016/j.biomaterials.2007.04.016

Li, B., Yang, H., Wang, X., Zhan, Y., Sheng, W., Cai, H., et al. (2017). Engineering Human Ventricular Heart Muscles Based on a Highly Efficient System for Purification of Human Pluripotent Stem Cell-Derived Ventricular Cardiomyocytes. *Stem Cel Res Ther* 8 (1), 202. doi:10.1186/S13287-017-0651-X

Lynch, A. P., and Ahearne, M. (2013). Strategies for Developing Decellularized Corneal Scaffolds. *Exp. Eye Res.* 108, 42–47. doi:10.1016/j.exer.2012.12.012

Mehra, M. R., Uriel, N., Naka, Y., Cleveland, J. C., Jr, Yuzefpolskaya, M., Salerno, C. T., et al. (2019). A Fully Magnetically Levitated Left Ventricular Assist Device - Final Report. *N. Engl. J. Med.* 380 (17), 1618–1627. doi:10.1056/NEJMOA1900486

Methe, K., Bäckdahl, H., Johansson, B. R., Nayakawde, N., Dellgren, G., and Sumitran-Holgersson, S. (2014). An Alternative Approach to Decellularize Whole Porcine Heart. *BioResearch Open Access* 3 (6), 327–338. doi:10.1089/biores.2014.0046

Momtahan, N., Poornejad, N., Struk, J. A., Castleton, A. A., Herrod, B. J., Vance, B. R., et al. (2015). Automation of Pressure Control Improves Whole Porcine Heart Decellularization. *Tissue Eng. Part. C Methods* 21 (11), 1148–1161. doi:10.1089/ten.TEC.2014.0709

Mosterd, A., and Hoes, A. W. (2007). Clinical Epidemiology of Heart Failure. *Heart* 93 (9), 1137–1146. doi:10.1136/HRT.2003.025270

Nagata, S., Hanayama, R., and Kawane, K. (2010). Autoimmunity and the Clearance of Dead Cells. *Cell* 140 (5), 619–630. doi:10.1016/j.cell.2010.02.014

Ng, S. L. J., Narayanan, K., Gao, S., and Wan, A. C. A. (2011). Lineage Restricted Progenitors for the Repopulation of Decellularized Heart. *Biomaterials* 32 (30), 7571–7580. doi:10.1016/j.biomaterials.2011.06.065

Ong, C. S., Nam, L., Ong, K., Krishnan, A., Huang, C. Y., Fukunishi, T., et al. (2018). 3D and 4D Bioprinting of the Myocardium: Current Approaches, Challenges, and Future Prospects. *Biomed. Res. Int.* 2018, 1–11. doi:10.1155/2018/6497242

Ott, H. C., Matthiesen, T. S., Goh, S.-K., Black, L. D., Kren, S. M., Netoff, T. I., et al. (2008). Perfusion-decellularized Matrix: Using Nature's Platform to Engineer a Bioartificial Heart. *Nat. Med.* 14 (2), 213–221. doi:10.1038/NM1684

Park, J., Anderson, C. W., Sewanan, L. R., Kural, M. H., Huang, Y., Luo, J., et al. (2020). Modular Design of a Tissue Engineered Pulsatile Conduit Using Human Induced Pluripotent Stem Cell-Derived Cardiomyocytes. *Acta Biomater.* 102, 220–230. doi:10.1016/j.actbio.2019.10.019

Pla-Palacín, I., Sainz-Arnal, P., Morini, S., Almeida, M., and Baptista, P. M. (2018). Liver Bioengineering Using Decellularized Whole-Liver Scaffolds. *Methods Mol. Biol.* 1577, 293–305. doi:10.1007/7651_2017_98

Rana, D., Zreiqat, H., Benkirane-Jessel, N., Ramakrishna, S., and Ramalingam, M. (2017). Development of Decellularized Scaffolds for Stem Cell-Driven Tissue Engineering. *J. Tissue Eng. Regen. Med.* 11 (4), 942–965. doi:10.1002/term.2061

Remlinger, N. T., Wearden, P. D., and Gilbert, T. W. (2012). Procedure for Decellularization of Porcine Heart by Retrograde Coronary Perfusion. *JoVE* 70, e50059. doi:10.3791/50059

Saldin, L. T., Cramer, M. C., Velankar, S. S., White, L. J., and Badylak, S. F. (2017). Extracellular Matrix Hydrogels from Decellularized Tissues: Structure and Function. *Acta Biomater.* 49, 1–15. doi:10.1016/j.actbio.2016.11.068

Shi, W., Xin, Q., Yuan, R., Yuan, Y., Cong, W., and Chen, K. (2021). Neovascularization: The Main Mechanism of MSCs in Ischemic Heart Disease Therapy. *Front. Cardiovasc. Med.* 8, 633300. doi:10.3389/fcvm.2021.633300

Spang, M. T., and Christman, K. L. (2018). Extracellular Matrix Hydrogel Therapies: *In Vivo* Applications and Development. *Acta Biomater.* 68, 1–14. doi:10.1016/j.actbio.2017.12.019

Sun, L. Y., Gaudino, M., Chen, R. J., Bader Eddeen, A., and Ruel, M. (2020). Long-term Outcomes in Patients with Severely Reduced Left Ventricular Ejection Fraction Undergoing Percutaneous Coronary Intervention vs Coronary Artery Bypass Grafting. *JAMA Cardiol.* 5 (6), 631–641. doi:10.1001/jamacardio.2020.0239

Sun, L. Y., Tu, J. V., Bader Eddeen, A., and Liu, P. P. (2018). Prevalence and Long-Term Survival after Coronary Artery Bypass Grafting in Women and Men with Heart Failure and Preserved versus Reduced Ejection Fraction. *J. Am. Heart Assoc.* 7 (12), e008902. doi:10.1161/JAHA.118.008902

Tan, M. Y., Zhi, W., Wei, R. Q., Huang, Y. C., Zhou, K. P., Tan, B., et al. (2009). Repair of Infarcted Myocardium Using Mesenchymal Stem Cell Seeded Small Intestinal Submucosa in Rabbits. *Biomaterials* 30 (19), 3234–3240. doi:10.1016/j.biomaterials.2009.02.013

Tang-Quan, K. R., Mehta, N. A., Sampaio, L. C., and Taylor, D. A. (2018). Whole Cardiac Tissue Bioscaffolds. *Adv. Exp. Med. Biol.* 1098, 85–114. doi:10.1007/978-3-319-97421-7_5

Taylor, D. A., Sampaio, L. C., Ferdous, Z., Gobin, A. S., and Taite, L. J. (2018). Decellularized Matrices in Regenerative Medicine. *Acta Biomater.* 74, 74–89. doi:10.1016/j.actbio.2018.04.044

Velazquez, E. J., Lee, K. L., Jones, R. H., Al-Khalidi, H. R., Hill, J. A., Panza, J. A., et al. (2016). Coronary-Artery Bypass Surgery in Patients with Ischemic Cardiomyopathy. *N. Engl. J. Med.* 374 (16), 1511–1520. doi:10.1056/NEJMOA1602001

Virani, S. S., Alonso, A., Aparicio, H. J., Benjamin, E. J., Bittencourt, M. S., Callaway, C. W., et al. (2021). Heart Disease and Stroke Statistics-2021 Update. *Circulation* 143, E254–E743. doi:10.1161/CIR.0000000000000950

Vunjak-Novakovic, G., Tandon, N., Godier, A., Maidhof, R., Marsano, A., Martens, T. P., et al. (2010). Challenges in Cardiac Tissue Engineering. *Tissue Eng. Part. B Rev.* 16 (2), 169–187. doi:10.1089/ten.TEB.2009.0352

Wainwright, J. M., Czajka, C. A., Patel, U. B., Freytes, D. O., Tobita, K., Gilbert, T. W., et al. (2010). Preparation of Cardiac Extracellular Matrix from an Intact Porcine Heart. *Tissue Eng. Part. C Methods* 16 (3), 525–532. doi:10.1089/ten.TEC.2009.0392

Wang, B., Wang, G., To, F., Butler, J. R., Claude, A., McLaughlin, R. M., et al. (2013). Myocardial Scaffold-Based Cardiac Tissue Engineering: Application of Coordinated Mechanical and Electrical Stimulations. *Langmuir* 29 (35), 11109–11117. doi:10.1021/LA401702W

Wang, Z., Long, D. W., Huang, Y., Chen, W. C. W., Kim, K., and Wang, Y. (2019). Decellularized Neonatal Cardiac Extracellular Matrix Prevents Widespread Ventricular Remodeling in Adult Mammals after Myocardial Infarction. *Acta Biomater.* 87, 140–151. doi:10.1016/j.actbio.2019.01.062

Weymann, A., Patil, N. P., Sabashnikov, A., Jungebluth, P., Korkmaz, S., Li, S., et al. (2014). Bioartificial Heart: A Human-Sized Porcine Model - the Way Ahead. *PLoS One* 9 (11), e111591. doi:10.1371/JOURNAL.PONE.0111591

Conflict of Interest: The authors declare that the research was conducted in the absence of any commercial or financial relationships that could be construed as a potential conflict of interest.

Publisher's Note: All claims expressed in this article are solely those of the authors and do not necessarily represent those of their affiliated organizations, or those of the publisher, the editors, and the reviewers. Any product that may be evaluated in this article, or claim that may be made by its manufacturer, is not guaranteed or endorsed by the publisher.

Copyright © 2022 Krishnan, Wang and MacArthur. This is an open-access article distributed under the terms of the Creative Commons Attribution License (CC BY). The use, distribution or reproduction in other forums is permitted, provided the original author(s) and the copyright owner(s) are credited and that the original publication in this journal is cited, in accordance with accepted academic practice. No use, distribution or reproduction is permitted which does not comply with these terms.

frontiers in Bioengineering and Biotechnology

REVIEW
published: 28 February 2022
doi: 10.3389/fbioe.2022.831300

Decellularization Strategies for Regenerating Cardiac and Skeletal Muscle Tissues

Yong How Tan[†], *Haylie R. Helms*[†] *and Karina H. Nakayama* *

Department of Biomedical Engineering, Oregon Health and Science University, Portland, OR, United States

Cardiovascular disease is the leading cause of death worldwide and is associated with approximately 17.9 million deaths each year. Musculoskeletal conditions affect more than 1.71 billion people globally and are the leading cause of disability. These two areas represent a massive global health burden that is perpetuated by a lack of functionally restorative treatment options. The fields of regenerative medicine and tissue engineering offer great promise for the development of therapies to repair damaged or diseased tissues. Decellularized tissues and extracellular matrices are cornerstones of regenerative biomaterials and have been used clinically for decades and many have received FDA approval. In this review, we first discuss and compare methods used to produce decellularized tissues and ECMs from cardiac and skeletal muscle. We take a focused look at how different biophysical properties such as spatial topography, extracellular matrix composition, and mechanical characteristics influence cell behavior and function in the context of regenerative medicine. Lastly, we describe emerging research and forecast the future high impact applications of decellularized cardiac and skeletal muscle that will drive novel and effective regenerative therapies.

Keywords: decellularized muscle, decellularized heart, dECM, decellularized extracellular matrix, skeletal muscle engineering, cardiac engineered tissue, ECM, extracellular matrix

OPEN ACCESS

Edited by:
Laura Iop,
University of Padua, Italy

Reviewed by:
Jangwook P. Jung,
Louisiana State University, United States
Akio Kishida,
Tokyo Medical and Dental University, Japan

***Correspondence:**
Karina H. Nakayama
Nakayaka@ohsu.edu

[†]*These authors have contributed equally to this work*

Specialty section:
This article was submitted to Biomaterials, a section of the journal Frontiers in Bioengineering and Biotechnology

Received: *08 December 2021*
Accepted: *28 January 2022*
Published: *28 February 2022*

Citation:
Tan YH, Helms HR and Nakayama KH (2022) Decellularization Strategies for Regenerating Cardiac and Skeletal Muscle Tissues. Front. Bioeng. Biotechnol. 10:831300. doi: 10.3389/fbioe.2022.831300

1 INTRODUCTION

Cardiovascular disease and musculoskeletal conditions together represent a major global health burden. According to the World Health Organization (WHO), cardiovascular disease is the leading cause of death worldwide and accounts for an estimated 17.9 million deaths annually (World Health Organization, 2021a). Separately, an astonishing 1.71 billion global citizens are affected by musculoskeletal conditions and is the leading cause of disability in 160 countries (World Health Organization, 2021b). Combined, these two health crises are responsible for a global annual economic burden of approximately $1.8 trillion (Bloom et al., 2011; Yelin et al., 2021). These statistics are projected to only worsen by 2030 unless a major shift in treatment options becomes widely available. Regenerative medicine reconceptualizes the approach to this challenge with technologies that potentiate cures over treatments. Through the modulation of the body's response to injury and disease using bioactive materials, the potential for full restoration of function is on the horizon.

Decellularized tissues and extracellular matrices (ECM) are the heavyweights of regenerative biomaterials with decades of clinical use and FDA approvals. These materials possess potent regenerative properties and have the potential to repair and restore function to a wide range of injured and diseased tissues including cardiac and skeletal muscle. In this review, the application of

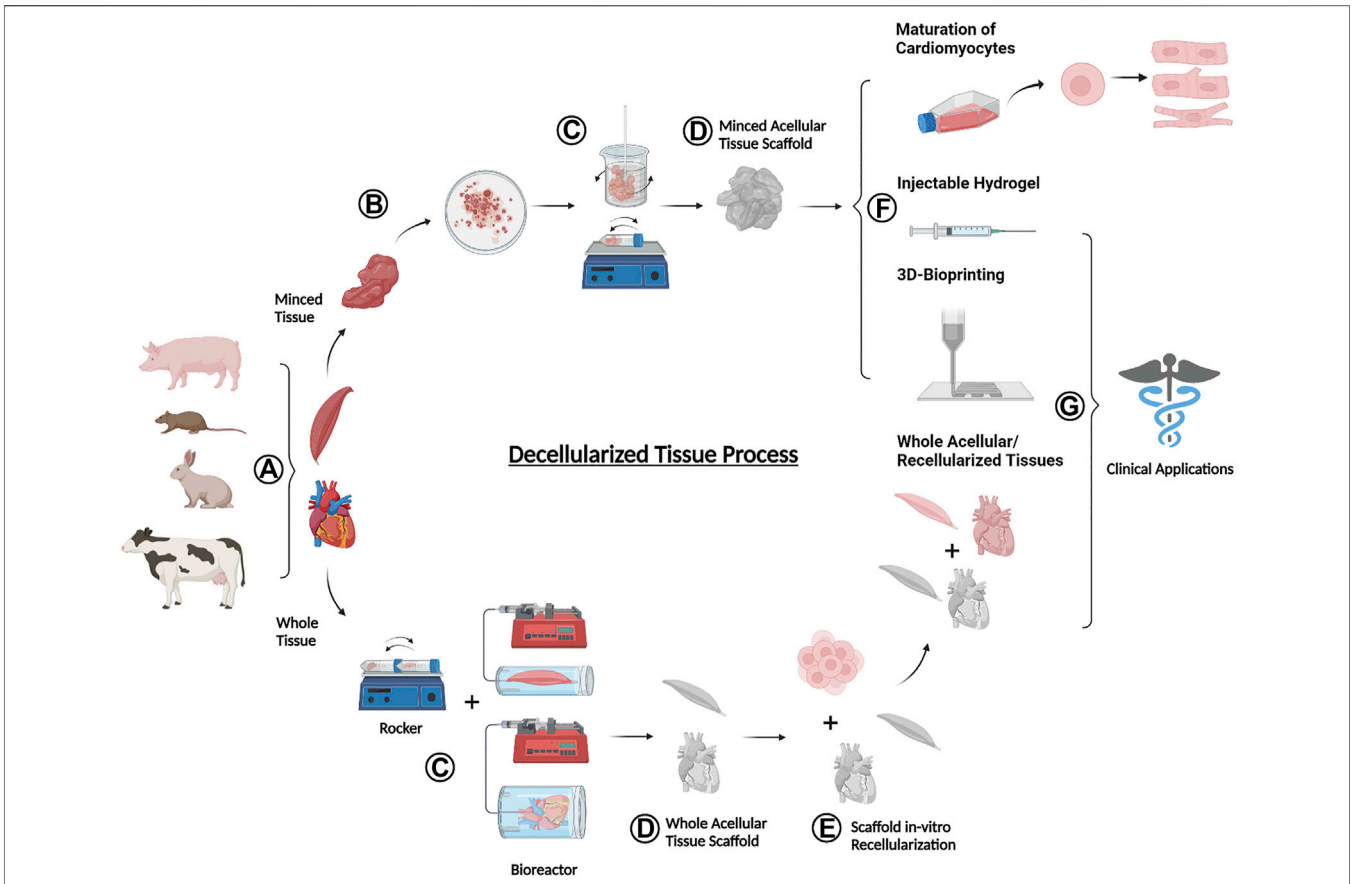

FIGURE 1 | Schematic overview of the donor-to-application lifecycle of decellularized tissues **(A)** Tissues are harvested from an animal donor **(B)** Whole tissues are processed with mechanical agitation to break down into smaller minced tissues **(C)** Whole or minced fresh tissues are exposed to a series of decellularizing agents and procedures to remove cellular materials **(D)** The decellularization end products are acellular tissues containing various ECM components **(E)** Whole acellular tissues may be seeded with cells *in vitro* to test for cell viability **(F)** A variety of dECM forms are used for the maturation of cardiomyocytes, production of injectable hydrogels, and formulation into bioink for 3D bioprinting **(G)** Selected forms of decellularized tissues including injectable hydrogels, 3D bioprinted materials, and whole acellular and recellularized tissues can be used for translational pre-clinical and clinical applications. Figure created using BioRender.com.

decellularized ECM (dECM) in the cellular modulation and regeneration of cardiac and skeletal muscle is described. Specifically, the most widely used decellularization protocols for generating dECM from these two tissues are compared. Herein, we describe how the biophysical properties of composition, topographical and spatial patterning, and biomechanical force transduction are impacted by the decellularization protocol as well as characterize the modulatory role that these properties play in guiding cellular and host interactions *in vitro* and *in vivo*.

2 METHODS OF DECELLULARIZATION

The global process of decellularization involves a series of steps that take the tissue from donor to regenerative application (**Figure 1**). This is done by harvesting tissues from a donor animal (**Figure 1A**), followed by the application of a series of reagent and wash solutions that lyse cells and remove nuclear materials (**Figure 1B,C**) to leave behind a structural matrix made up of ECM proteins (**Figure 1D**). The resulting dECM can then be used as a cell culture tool, solubilized into bioink for 3D printing, or cultured with cells to be transplanted as a regenerative therapeutic into an animal injury model (**Figure 1E–G**).

Historically, tissues have been decellularized primarily via three methods that are based in chemical, physical, and/or enzymatic disruption of the cell-matrix interface. Chemical decellularization utilizes detergents, alcohols, or pH changes to lyse cells by disrupting the cell membrane (Gilpin and Yang, 2017; KC et al., 2019). Methods of physical decellularization include freeze-thaw cycles, agitation, mechanical manipulation, or pressure to forcibly remove cells (Gilpin and Yang, 2017; KC et al., 2019). Lastly, enzymatic decellularization breaks down the protein interactions through the use of nucleases, collagenases, and proteases and/or chelating agents such as ethylenediamine tetraacetic acid (EDTA) or ethylene glycol tetraacetic acid (EGTA) (Gilpin and Yang, 2017; KC et al., 2019). Along with each decellularization approach are associated advantages and disadvantages which must be carefully considered for the end application.

TABLE 1 | Cardiac decellularization protocols.

Application	Species	Tissue form	Decellularization treatments	Study findings	Citation
Decell Methods	Porcine	Whole	Inversion +45°; NaCl; SDS	Improved perfusion efficiency; better DNA clearance, retention of ECM and heart shape	Lee et al. (2017)
Decell Methods	Porcine	Whole	Freeze/thaw; SDC; Triton; PAA	Extensive decellularization while retaining architecture and angiogenic growth factors	Methe et al. (2014)
Decell Methods	Porcine	Whole	1. Freeze/thaw; Trypsin 2. Freeze/thaw; Triton	Multiphoton microscopy and image correlation spectroscopy can predict mechanical properties of dECM	Merna et al. (2013)
Decell Methods	Rat	Whole	Freeze/thaw; Trypsin; SDS; Triton; DCA; PAA + EtOH	Little residual nuclear material; minimizes damage to proteins; retention of heart shape	Ozlu et al., 2019
Decell/Recell Methods	Porcine	Whole	Freeze/thaw; Trypsin; Triton; DCA; PAA + EtOH	Significantly reduced decellularization time to 10 h without damaging the ECM	Wainwright et al. (2010)
Decell/Recell Methods	Rat	Whole	SDS; Triton	Preserved ECM characteristics; promoted hESC-CM attachment, maturation, and electrical activity	Hochman-Mendez et al. (2020)
Decell/Recell Methods	Rat	Whole	Heparin, Adenosine; SDS; Triton	ECM preserved and vasculature perfusable; cardiac and EC recellularization; stimulation produced myocardial contractions	Ott et al. (2008)
Decell/Recell Methods	Mouse	Whole	Freeze/thaw; Trypsin; SDS; Triton; DCA; PAA + EtOH	Cardiac progenitors grown on dECM migrate, proliferate, and differentiate into CMs, SMC, and ECs	Lu et al. (2013)
Recell Methods	Rat	Whole	SDS; Triton	Reendothelialization best with both venous and arterial delivery	Robertson et al. (2014)
Cell Culture Additive	Human	Minced	NaCl; SDS	Atrial dECM in hiPSC-CM differentiation drives atrial cardiomyocyte subtype specification	Mesquita et al. (2021)
Cell Culture Additive	Porcine	Minced	SDS; Triton	Fetal ECM increased neonatal CM attachment and proliferation compared to PLL, adult ECM, or neonatal ECM	Williams et al. (2014)
Cell Culture Additive	Bovine	Minced	Freeze/thaw; SDS; Triton	3D ECM enhances iPSC-CM maturation compared to 2D culture	Fong et al. (2016)
Injectable Therapeutic	Porcine	Minced	SDS; Triton	Injection of solubilized fetal ECM decreased fibrosis and improved cardiac function post MI	Wang, X. et al., 2020
Injectable Therapeutic	Mouse	Minced	Freeze/thaw; RBC lysis; DNase I + RNase	Neonatal ECM decreased fibrosis, promoted angiogenesis, and increased cardiac function post MI; adult ECM did not have the same regenerative effects	Wang, Z. et al., 2019
Hydrogel	Porcine	Minced	SDS; Triton; PAA + EtOH	Developed a hydrogel with tunable mechanical and electrical properties; hydrogel improved hiPSC-CM maturation	Tsui et al. (2021)
Hydrogel	Bovine	Minced	SDS; Triton	Developed an electroactive, *in situ* forming, ECM hydrogel	Mousavi et al. (2021)
Hydrogel/Bioink	Human	Minced	Freeze/Thaw; SDS; Triton	GelMA-MeHA-ECM bioink improved mechanical properties; created an *in vitro* MI model with the bioink	Basara et al. (2021)
Hydrogel/Bioink	Porcine	Minced	SDS	Human cardiac progenitor cells in GelMA-ECM bioink had >75% viability and increased cardiogenic gene expression	Bejleri et al. (2018)

Modern decellularization strategies often involve a balance between effective and efficient removal of cellular debris with the loss of key proteins and matrix components. For example, sodium dodecyl sulfate (SDS) is a chemical decellularization agent that is highly effective in lysing cells but can alter the microstructure of ECM and is cytotoxic if not thoroughly removed (Gilpin and Yang, 2017). Another widely used detergent, Triton X-100, generally preserves the ECM composition and biomechanics but is less effective in the complete clearing of nuclear material (Ott et al., 2008; Merna et al., 2013; Gilpin and Yang, 2017). Similarly, physical decellularization has a high retention and structural preservation of ECM proteins and mechanical properties but is more likely to leave remnant DNA or DNA fragments behind (Gilpin and Yang, 2017). Enzymatic decellularization involves potent digestive enzymes that are efficient at breaking down and removing cellular debris but has been found to decrease glycosaminoglycan (GAG) content and degrade crosslinking proteins leading to altered mechanical properties (Gilpin and Yang, 2017). There is no universal reagent or protocol, but instead the selection of the most appropriate decellularization approach heavily depends on the final application and will dictate the hierarchy of properties to retain. The choice is further complicated by the compositional variations between tissue types, specifically differences in anatomical structure, function, and age. In this section we discuss the range of methods used to decellularize two kinds of muscle tissues, cardiac muscle and skeletal muscle.

2.1 Decellularization Methods for Cardiac Tissue

In 2008, Doris Taylor's group reported the landmark decellularization of a whole heart and simultaneously catapulted an emerging field to the forefront of tissue engineering and regenerative medicine (Ott et al., 2008). Their chemical decellularization approach utilized perfusion of 1% SDS and 1% Triton X-100, with deionized water and 1X PBS washes. This dynamic protocol proved effective in removing native cellular material (residual DNA <4%) while preserving GAG content and fiber composition. The resulting dECM matrix supported the culture of neonatal cardiac cells, without any noted complications from residual reagents. Other whole heart

decellularization protocols have built upon the concepts initially established by Ott et al. (Ott et al., 2008) and even this group has since modified their protocol to incorporate osmotic shock and anatomical inversion during decellularization (Lee et al., 2017) (**Table 1**). Nevertheless, since 2008, this protocol has continued to serve as a foundation for tissue decellularization strategies and a major catalyst for innovation.

Optimization of cardiac decellularization has been guided by the dual goal of ensuring removal of cellular materials and preservation of ECM components. These aims motivated the next generation of decellularization strategies that sought to reduce exposure to harsh reagents through decreased decellularization times. Wainwright et al. was able to significantly reduce total decellularization time to 10 h, compared to the conventional 5–10 days, by using a series of hypertonic, hypotonic, enzymatic, acid, and detergent solutions without damaging the ECM (Wainwright et al., 2010). This time was reduced even further to 2 h and 15 min using a similar mixed method approach (Lu et al., 2013). However, there is no consensus on which component of a decellularization protocol is most critical and method selection is often based on the desired end application properties. In 2011, Akhyari et al. sought to find the best whole heart decellularization protocol in terms of cellular removal, residual DNA, retention of structural proteins, and biocompatibility (Akhyari et al., 2011). Following a comprehensive comparison of four different methods, using a fully automated system, it was concluded that no single approach was superior to the others. While some protocols were more effective at removal of cellular materials, others better preserved the native dECM proteins. Each protocol had a compromise of strengths and limitations and serves as another example to underscore the need to carefully select the appropriate decellularization method based on the final desired ECM properties.

In recent years, the cardiac field has seen a pivot away from using whole tissue matrices for tissue engineered and regenerative therapeutics towards dECM that is ground or solubilized with primary focus on answering *in vitro* biological questions. For these applications, the native heart tissue is minced, thereby increasing surface area, and significantly speeding up the decellularization process. The use of minced tissue also increases research accessibility by eliminating the need for specialized perfusion bioreactors to keep the whole heart intact, and instead utilizes basic tools for decellularization that are available in most research labs (stir bars/orbital shakers). Similar to whole heart decellularization, the minced tissue approach often uses detergents such as 1% SDS and 1% Triton X-100.

The properties linked to tissue origin such as species source and donor age also demonstrate differential responses to different decellularization protocols. An example of the influence of tissue source is evidenced by a study in which a protocol that had been optimized to decellularized fresh porcine hearts was not effective in the complete decellularization of the same sized cadaveric human hearts (Johnson et al., 2014). Cadaveric hearts required much longer SDS treatment in addition to isopropyl alcohol and a DNase/RNase solution containing HCl, MgCl, CaCl, and NaCl at pH 7.4. Even still, there was significant patient-to-patient variability, which increased the difficulty in processing the human tissues. These differences could possibly be explained by the variability in age amongst the cadaveric hearts as well as the difference in age between the human and porcine hearts. Age increases cardiac tissue stiffening through fibrosis and increased ECM cross-linking (Johnson et al., 2014). Similarly, fetal rat and porcine hearts required a more diluted concentration of SDS and Triton X-100 compared to their adult counterparts (Williams et al., 2014; Fong et al., 2016; Wang et al., 2020; Wang et al., 2021). However, there are rare instances in which a protocol has been developed that works reasonably well for tissues of disparate ages. Silva et al. successfully developed a protocol that enabled the parallel decellularization of both fetal and adult rat hearts using freeze-thaw, physical agitation, hypotonic buffer (Tris HCl + EDTA), 0.2% SDS, and DNase (Silva et al., 2016). In summary, there are many variables that influence the effectiveness of a cardiac decellularization protocol that heavily depend on the tissue species, age, and final end application.

2.2 Decellularization Methods for Skeletal Tissue

Over the course of the last decade, an increasing number of different protocols have been developed and modified for skeletal muscle decellularization (**Table 2**). When the field was relatively young, the most common decellularization agent was trypsin, which was often used in combination with detergents such as SDS, Triton X-100, and Sodium Deoxycholate (SDC). The use of trypsin eventually declined when the destructive properties of this enzyme became well-known (Miersch et al., 2018; Sharma et al., 2019). While a harsh decellularization treatment is highly efficient at removing cellular debris and DNA from the tissue, it can also remove essential ECM proteins and proteoglycans. The preservation of the ECM is especially relevant for skeletal muscle, which, based on a proteomic analysis of 21 different organs, has over a 10-fold greater number of unique proteins compared to all other organs (Raffa et al., 2020). The ECM serves as an important driver of cell-fate and tissue regeneration in the healing response of skeletal muscle following injury (Herrera et al., 2018; Csapo et al., 2020; Nicolas et al., 2020). Therefore, like cardiac decellularization protocols, methods for obtaining decellularized skeletal muscle ECM require a balance of removing cellular material while best conserving the biophysical components and integrity of the complex skeletal muscle matrix (Grisales et al., 2021).

There exists a wide variety of approaches for obtaining decellularized skeletal muscle, which range from the more aggressive enzymatic treatments to the use of comparatively mild depolymerizing agents such as Latrunculin B (LatB). Detergent-based methods have historically dominated the field of skeletal muscle decellularization. The most widely used detergents such as SDS, Triton X-100, and SDC are used for their surfactant properties which disrupt the lipid bilayer of cell membranes to facilitate cell lysis (Lichtenberg et al., 2013). More specifically, SDS acts by solubilizing the cytoplasmic and nuclear membranes, while both Triton X-100 and SDC work by targeting

TABLE 2 | Skeletal muscle decellularization protocols.

Application	Species	Tissue Form	Decellularization Treatments	Study Findings	Citation
Comp/ Topo/ Mech	Porcine	Minced	SDS + Triton	dECM bioink improved muscle regeneration when compared to collagen bioink.	Choi et al. (2016)
Comp/ Mech	Rat	Whole	Free/thaw + Trypsin + Triton	*In vivo* transplantation of muscle derived ECM showed a large fibrotic mass production 6 months post-surgery.	Corona et al. (2013)
Comp/ Mech	Rabbit	Whole	LatB + KCl/KI	Xenotransplant scaffold showed low immunogenic response *in vitro* and *in vivo*, suggesting immunosuppressive and anti-inflammatory effects.	Fishman et al. (2013)
Comp/ Topo	Porcine	Minced	SDS Trypsin + Triton + SDC	Exploitation of PDMS elastic property allowed anisotropic reorganization of 3D skeletal muscle dECM; construct supports de novo muscle regeneration.	Jin et al. (2021a)
Comp/ Mech	Rat	Whole	SDS	dECM and minced muscle scaffolds improved recovery in VML injury animal model.	Kasukonis et al. (2016a)
Comp/ Mech	Rat	Whole	SDS	Developed an infusion bioreactor for skeletal muscle decellularization.	Kasukonis et al. (2016b)
Comp/ Mech	Rabbit	Minced	SDS + Triton	Development of cell-free scaffold comprised of decellularized skeletal muscle and IGF-1 promotes tissue regeneration in vivo and in situ.	Lee et al. (2020)
Comp	Human	Minced	LatB + KCl/KI SDC SDS	Harsher SDS treatment shown to decellularize human skeletal muscle better than less harsh LatB + KCl/KI and SDC treatments.	Naik et al. (2020)
Comp/Topo	Bovine	Minced	Freeze-thaw + Triton + NH4OH	Electrospun PCL/dECM scaffold supported myogenesis *in vitro*; scaffold implanted in murine VML *in vivo* model showed increased anti-inflammatory activity and myofiber regeneration.	Patel et al. (2020)
Comp/Mech	Chicken	Whole	LatB + KCl/KI Triton Triton + SDS	LatB + KCl/KI protocol was most efficient for decellularization compared to competing methods, reducing DNA, myosin and actin content significantly.	Reyna et al. (2020)
Comp/ Mech	Bovine	Minced	Freeze/thaw + Triton + NH4OH	In vitro studies of dECM gelloid supported MSC survival, expansion, trophic factor secretion, immunomodulation, and myogenic protein expression.	Talovic et al. (2019)
Comp/ Mech	Rat	Whole	LatB + KCl/KI SDC SDS	Implanted dECM from three different protocols in immune competent model of VML generated functional muscle, vasculature, nervous fibers.	Urciuolo et al. (2018)
Comp	Dog	Whole	Trypsin + SDC + Triton	Comparing decellularized small intestine and skeletal muscle regenerative outcomes shows no difference after prolonged period.	Wolf et al. (2012)
Comp	Porcine	Whole	Trypsin + SDS + Triton	*In vivo* implantation of dECM in partial thickness abdominal wall defects in rats showed neovascularization, myogenesis, and recellularization.	Zhang et al. (2016)
Topo/ Comp/ Mech	Porcine	Minced	SDS + Triton	dECM coating significantly improved myotube and myogenic differentiation compared with collagen/non-coated surfaces.	Choi et al. (2018)
Topo/ Comp/ Mech	Porcine	Minced	SDS + Triton	The 3D printed muscle constructs exhibited high cell viability without hypoxia; enhanced de novo muscle formation in a VML rat model.	Choi et al. (2019)
Topo/ Comp	Porcine	Minced	SDS	Thermally drawn PCL/dECM mix implanted in VML, *a* model showed induced de novo muscle regeneration.	Jin et al. (2021b)
Topo/ Comp/ Mech	Porcine	Minced	SDS + Triton	In vitro cellular responses showed successful recellularization on 3D-printed dECM-based structure.	Kim et al. (2020)
Topo/ Comp/ Mech	Porcine	Minced	SDS + Triton	Photo-crosslinkable, dECM/PVA hydrogel, 3D-printed self-aligned skeletal muscle construct showed rapid restoration of muscle function.	Lee et al. (2021)
Topo/ Comp/ Mech	Bovine	Minced	Freeze-thaw + Triton + NH4OH	Aligned electrospun dECM/PCL scaffolds supported satellite cell growth, myogenic protein expression and myokine production.	Patel et al. (2019)
Topo	Rabbit	Minced	Trypsin + Triton	C2C12 myoblasts recellularization affected by degree of crosslinking (stiffness) and alignment (topography) of electrospun dECM scaffold.	Smoak et al. (2021)

the lipid-protein and lipid-lipid interactions of cells (Reyna et al., 2020). The mechanism of action of these different reagents can dictate the efficiency of cellular removal.

A treatment of 1% SDS has been used in numerous studies as the main decellularization agent for minced muscle and was commonly reported to remove approximately 98% total DNA (Choi et al., 2016; Kim et al., 2020; Lee et al., 2020; Jin et al., 2021a; Jin et al., 2021b). In contrast, groups that used non-SDS agents such as SDC and ammonium hydroxide reported less efficient cellular removal with a range of 50–80% total DNA (Piccoli et al., 2017; Patel et al., 2019; Smoak et al., 2019; Talovic et al., 2019; Jin et al., 2021a). Removal of cellular material and DNA content is critical in the downstream application of decellularized tissues to avoid complications triggered by the host immune response. Several residual components can lead to the activation of an immune response following allo- and xenotransplantation including any remaining DNA fragments, human leukocyte antigens (HLA), and major histocompatibility complex (MHC) molecules (Quake, 2011; Nakamura et al., 2019). However, while detergent-based methods are effective in clearing the tissue of cellular debris, these reagents may also remove key bioactive ECM proteins and proteoglycans (Gilbert et al., 2009; Crapo et al., 2011; Soto-Gutierrez et al., 2011). Therefore, skeletal muscle decellularization protocols must balance the removal of cellular materials with maintaining any essential cell signaling components contained within the ECM.

To mitigate the disruptive properties of detergent-based methods, gentler decellularization approaches have been developed for skeletal

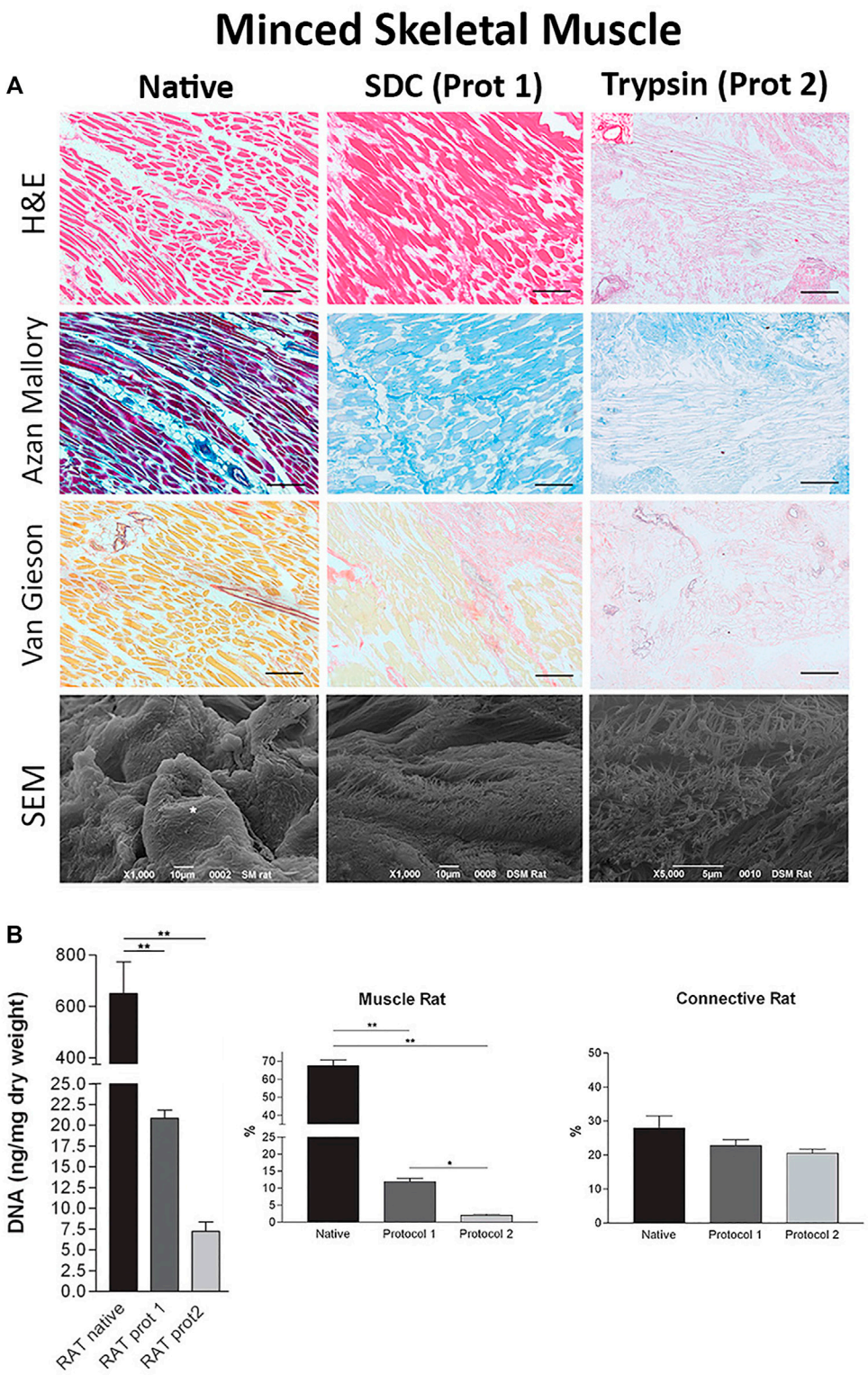

FIGURE 2 | Minced tissue decellularization protocols and outcomes **(A)** Tissue morphology from top to bottom: H&E staining, Azan Mallory stains, Van Gieson stains, and SEM images of minced tissues before (Native, column 1) and after decellularization with SDC (Protocol 1, SDC + DNase I, column 2) and Trypsin (Protocol 2, Trypsin/EDTA + Triton X-NH4OH, column 3) protocols **(B)** DNA, muscle content, and connective tissue content before and after decellularization using protocol one and protocol 2. Figures A,B are adapted from "Decellularized Human Skeletal Muscle as Biologic scaffold for Reconstructive Surgery" by Porzionato et al. (2015) licensed under CC BY 4.0.

muscle. Utilizing a natural toxin produced by aquatic sponges (Spector et al., 1983), Gillies et al. demonstrated a decellularization procedure using LatB together with hyper- and hypotonic salt solutions (Gillies et al., 2011). The LatB treatment depolymerized the actin-myosin filaments of whole skeletal muscle structures in mice, while actively preserving the ECM components including GAGs and collagen (Gillies et al., 2011). Because this protocol is also effective at removing DNA (95% removal, 2.92 ± 0.14 mg/mg dry weight in native muscle to 0.12 ± 0.01 mg/mg dry weight in decellularized muscle), LatB decellularization is increasingly preferred in studies that are highly dependent on preserving dECM bioactivity. However, unlike SDS, it has been suggested that the LatB protocol does not scale well and is less effective at decellularizing larger tissues (Naik et al., 2020). Naik et al. demonstrated that the overall difference in tissue size alters the effectiveness of the decellularization reagents (Naik et al., 2020) and hence, a milder LatB protocol is insufficient in completely eliminating nuclear materials in larger whole human muscles as compared to smaller whole murine muscles.

The decellularization of skeletal muscle is generally approached using either minced or whole tissues, each with their own corresponding advantages and disadvantages. Smaller minced tissues provide a larger surface area for cell lysis compared to larger whole tissues which aides in the effective removal of nuclear material but may sacrifice the spatial context of their original anatomical structures (**Figure 2A,B**). Conversely, decellularized whole tissues preserve the greater structure of the native tissue, but due to diffusion limitations, whole tissue protocols often require a harsher treatment agent, or the use of perfusion techniques to avoid extended decellularization times. However, the end application of the decellularized tissue can help determine which format is most appropriate. Whole tissue decellularization is useful in whole organ transplantation or in the replacement of large sections of injured skeletal muscle, whereas minced tissue decellularization is often used when the macrostructure is not a priority such as in bioink production for 3D printing. Because it is less vital to preserve the ECM spatial architecture for bioink production, these protocols often utilize higher concentrations of SDS (≥1% SDS), compared to whole skeletal muscle decellularization, which is usually performed with perfused 0.25% SDS or LatB (Choi et al., 2016; Kim et al., 2020; Lee et al., 2020; Jin et al., 2021a; Jin et al., 2021b).

In addition to the main decellularizing reagents, many protocols include supplementary chemicals to ensure complete decellularization. For instance, DNase is frequently used after the primary decellularization step to further assist in the removal of residual DNA (Gillies et al., 2011; Zhang et al., 2016; Urciuolo et al., 2018). Likewise, chloroform and isopropyl alcohol are regularly used to extract unwanted lipids from the native tissue before decellularization (Wolf et al., 2012; Ungerleider et al., 2015). In the final stages of the protocol, once a tissue has been decellularized, washes with sterilizing and anti-mycotic agents such as penicillin and streptomycin, (Merritt et al., 2010; Kasukonis B. et al., 2016; Kasukonis B. M. et al., 2016; Jin et al., 2021a; Jin et al., 2021b), peracetic acid, (Wolf et al., 2012; Zhang et al., 2016; Choi et al., 2019), and ethanol (Choi et al., 2019) are used. Lastly, many groups administer EDTA in series or in combination with the first few decellularizing agents to help prevent clot formation as the blood is removed from the tissue vasculature (Gillies et al., 2011; Miranda et al., 2021). Although these supplementary chemicals contribute to a more complete decellularization, they may also impact the ECM retention, myofiber morphology, and overall structural integrity of decellularized tissues. Therefore, the rule of thumb is to use the fewest agents possible and the shortest decellularization times to achieve the targeted dECM properties.

3 BIOPHYSICAL PROPERTIES: ECM COMPOSITION

The ECM is composed of a highly complex network of macromolecules that provide a supportive structural and functional niche for the surrounding cells. While the composition and respective biological functions of ECM are still being investigated, the components of ECM can be broken down into three main groups: glycoproteins, GAGs, and proteoglycans (**Figure 3A**). Glycoproteins, such as collagen, elastin, laminin, and fibronectin, make up the bulk of the ECM and provide the primary structural support and binding sites for cells (Silva et al., 2016) (**Figure 3B,C**). GAGs play a crucial role in modulating biochemical processes such as cell proliferation, migration, and wound repair (Puri et al., 2020). Proteoglycans have GAGs bound to their core and are one of the most complex and multifunctional molecules in cell biology (Walimbe and Panitch, 2020). Some of the reported functions of proteoglycans include growth factor sequestering, control of collagen fibrillogenesis, regulation of angiogenesis, and modulation of cell adhesion, proliferation, and pathway regulation (Walimbe and Panitch, 2020). The ECM is a highly dynamic structure that is constantly changing in response to environmental cues from growth, development, disease, injury, and repair.

3.1 Cardiac dECM Composition

The investigation of cardiac ECM composition was historically challenging due to the low solubility of the tissue's macromolecules and their post-translational modifications (Chang et al., 2016). However, advancements in ECM protein enrichment and technology have enabled a more complete investigation of cardiac ECM (Lindsey et al., 2018). Johnson et al. identified over 200 distinct cardiac ECM proteins in decellularized human hearts, the most prominent being collagen I, collagen IV, fibrillin 1, collagen V, collagen VI, laminin, and perlecan (Johnson et al., 2016).

The composition of cardiac ECM is also dependent on age. Multiple groups have compared the composition of cardiac ECM at varying stages of development and maturation (Williams et al., 2014; Fong et al., 2016; Johnson et al., 2016; Silva et al., 2016). Of the 15 most abundant cardiac proteins detected in rat hearts, adult ECM contained 38% collagen I, 18% fibrillin, 14% laminin, 8% perlecan, while fetal hearts contained 26% fibronectin, 13% fibrillin, 12% perlecan, 11% collagen I (**Figure 3D**) (Williams et al., 2014). Furthermore, fibrillin-2 and emilin-1 were among the top 15 most abundant proteins in fetal cardiac ECM, but not in adult cardiac ECM. These differences in composition provide

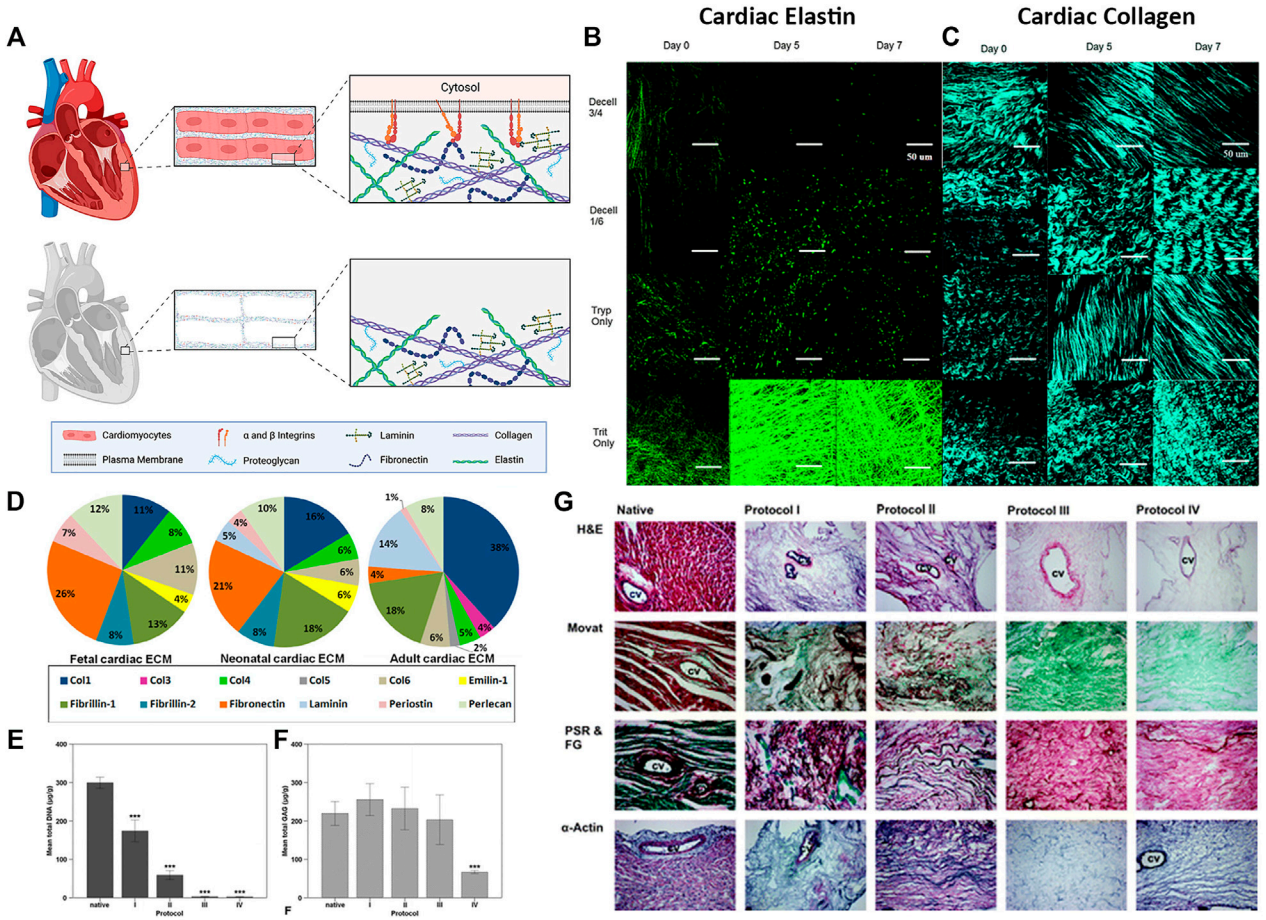

FIGURE 3 | Cardiac extracellular matrix composition **(A)** Schematic of cardiac tissue before and after decellularization **(B–C)** Extracellular matrix microstructure of decellularized whole porcine hearts following four different decellularization protocols. Decell 3/4: Trypsin for 3 days followed by Triton for 4 days. Decell 1/6: Trypsin 1 day, Triton 6 days. Tryp Only: Trypsin 7 days. Trit Only: Triton 7 days. Scale bar 50 μm **(B)** Elastin microstructure. Two photon fluorescence **(C)** Collagen microstructure. Second harmonic generation imaging **(D–F)** Rat myocardial ECM morphology and composition before (native) and after whole heart decellularization using four different decellularization protocols. Briefly, Protocol I: SDS and Triton. Protocol II: Trypsin, EDTA, deoxycholic acid (DCA), and acetic acid. Protocol III: Glycerol, NaN_3, EDTA, NaCl, DCA, SDS, and Triton. Protocol IV: SDS, DCA, NaN_3, Glycerol, EDTA, Saponin, DNase I, and MgCl **(D)** The 15 most abundant proteins in cardiac ECM measured by liquid chromatography–mass spectrometry (LC-MS/MS) at each developmental age **(E)** Mean DNA content and **(F)** mean GAG content of the native whole rat heart before (native) and after decellularization using protocols I - IV **(G)** Rat myocardial ECM morphology from top to bottom: Hematoxylin and Eosin (H&E) staining, Movat Pentachrome (Movat), picrosirius red and fast green (PSR & FG), and alpha-actin of rat hearts before (Native, column 1) and after whole heart decellularization (Protocols I–IV, columns 2—5). CV, coronary vessel. ×100 magnification. Figure A is created using BioRender.com. Figures B, C are adapted with permission from Merna et al. (2013). Figure D is adapted with permission from Williams et al. (2014). Figures E–G are adapted with permission from Akhyari et al. (2011).

insight into the supportive niche of the developing heart and may serve as a blueprint for ideal ECM mixtures to use for modulating regeneration.

3.1.1. How Different Protocols Affect Cardiac dECM Composition

Maintaining cardiac ECM proteins while thoroughly removing native DNA and cellular fragments is crucial for the success of many downstream applications. Most groups validate their decellularization protocol by quantifying the total DNA and GAG content that is left following decellularization. It is widely accepted that a protocol that results in less than 50 ng of double-stranded DNA per mg of tissue dry weight is effective in clearing the tissue of nuclear debris, although it should be noted that many groups measure and report residual DNA content differently (concentration, fragment length, staining) (Gilpin and Yang, 2017). However, reagents that thoroughly remove DNA and cellular debris often also disrupt GAG content. Akhyari et al. used a long duration protocol (5.7 days) with 1% SDS +1% DCA that produced tissues with less than 0.5% residual DNA, but significantly decreased GAGs by almost 70% compared to native content (**Figure 3E–G**) (Akhyari et al., 2011). In contrast, when the same group used a short duration protocol (4.75 h) with 1% SDS and 1% Triton X-100, the resulting tissues showed no decrease in GAGs (255.53 μg/g vs 219.33 μg/g native); however, approximately 13.9% residual DNA was still present.

Fortunately, there are combination protocols that have been shown to strike a balance between GAG retention and DNA removal. Wainwright et al. used a mixture of chemical, physical, and enzymatic decellularization techniques to maintain GAGs while also adequately removing residual DNA (0.66 ng DNA/mg vs 8.48 ng DNA/mg native, a 92% decrease) (Wainwright et al., 2010). A multi-step protocol by Lu et al. used trypsin, triton, cycles of freeze/thaw, SDS, deoxycholic acid, peracetic acid, and ethanol to produce ECM with preserved 3D architecture and filament structure while still achieving ~97% DNA removal (Lu et al., 2013). Alternatively, an adequate retention/removal balance has been achieved with simpler protocols that use classically damaging reagents for a short amount of time, followed by thorough washing to clear the matrix. This includes one of the most published cardiac decellularization approaches which uses 1% SDS and 1% Triton X-100 with several deionized water or PBS rinses (Ott et al., 2008; Robertson et al., 2014; Williams et al., 2014; Hochman-Mendez et al., 2020; Wang et al., 2020; Basara et al., 2021; Mousavi et al., 2021; Tsui et al., 2021). This approach has been demonstrated to have an adequate balance of DNA removal while maintaining ECM composition.

3.1.2 How Cardiac dECM Composition Affects Cell Behavior In Vitro

The ECM is a potent modulator of cell behavior and recent efforts in the field of cardiac dECM have focused on the use of this material to guide cells *in vitro*. Through the sophisticated regulation of soluble factors and cell signaling pathways, the ECM components can guide proliferation, fate specification, and migration. (Mesquita et al., 2021). However, there has been a gradual shift away from classical whole organ decellularization towards protocols that utilize ground or solubilized cardiac ECM. This pivot was thought to have been fueled by growing evidence that the concentration and bioactivity of dECM components played a greater role in guiding recellularization than the overall ultrastructure.

A well-known bottleneck of cardiac tissue engineering has been the limited proliferation potential of cardiomyocytes. However, ground or solubilized cardiac ECM serves as an instructive cell culture additive that can enhance cardiomyocyte proliferation. Williams et al. cultured ventricular cells on solubilized dECM and analyzed attachment, proliferation, and maturation (Williams et al., 2014). They found that fetal cardiac ECM was associated with greater cardiomyocyte adherence and proliferation in comparison to the Poly-L-Lysine (PLL) control and adult ECM. ECM components such as periostin and collagen IV were more abundant in the fetal ECM compared to adult, suggesting that these likely played a decisive role in enhancing myocyte proliferation.

Cardiac ECM has also been shown to improve cardiomyocyte differentiation and maturation (Das et al., 2019; Hochman-Mendez et al., 2020; Mesquita et al., 2021). Hochman-Mendez et al. cultured human embryonic stem cell-derived cardiomyocytes (hESC-CM) with dECM particles (Hochman-Mendez et al., 2020). hESC-CMs attached to the basement membrane and demonstrated enhanced maturation characteristics such electrical coupling, gap junctions, and increased sarcomere lengths. Das et al. showed that neonatal rat cardiomyocytes grown in dECM bioink rather than a single ECM protein of just collagen alone, facilitated a cell-material cross-talk that drove cell morphology and function (Das et al., 2019).

Not only can cardiac ECM improve maturation of stem cell-derived cardiomyocytes, but it can also guide phenotype specificity. Most cardiomyocyte differentiation protocols generate ventricular-like cells, but atrial-like cardiomyocytes are also needed for therapeutics and disease modeling. In order to generate atrial-like cardiomyocytes, high concentrations of retinoic acid are used; however, this agent is unstable in serum-free media, making standardized differentiation protocols difficult. Mesquita et al. demonstrated the use of chamber-specific powdered ECM to drive cardiomyocyte subtype differentiation (Mesquita et al., 2021). When human iPSCs were cultured with human atrial dECM particles, the cells expressed more atrial-like characteristics as verified by proteomics, action potentials, and gene expression. Similarly, human iPSCs cultured with ventricular ECM particles resulted in more mature ventricular CMs, as supported by the electrophysiological characterization, compared to iPSCs differentiated without ECM (Mesquita et al., 2021).

3.1.3 How Cardiac dECM Composition Affects Cell Regeneration In Vivo

Historically, cardiac dECM was viewed as a potential therapeutic in the form of a transplantable whole organ. The idea was to recellularize a full dECM heart with patient-specific cells to provide an autologous organ for transplantation, eliminating the need for lifelong anti-rejection medication. The cell requirements needed to repopulate an entire human heart is a major rate-limiting step and led to the use of dECM segments for use as cardiac patches, which showed promise as a post myocardial infarction (MI) treatment. Shah et al. implanted a 300 μm slice of decellularized porcine myocardium with or without rat adipose stem cells into rats 20 min after coronary artery ligation (Shah et al., 2018). Hearts treated with the dECM patch had increased vascularization and significantly more cells present compared to cells delivered via direct injection after 1 week. While the use of intact dECM is still explored for patches, other forms of dECM are being developed for greater control over the decellularization and recellularization processes.

It is well-understood that the retention of ECM protein composition and integrity are essential for cell adherence, proliferation, and maturation. However, preserving protein bioactivity may come at the expense of residual DNA and cell fragments, which can elicit an immune response, thereby limiting the ECMs regenerative potential (Keane et al., 2012). Fortunately, *in vivo* rat and mouse studies primarily use cardiac dECM in a ground or solubilized form, which enables more efficient removal of cell debris due to optimizing surface area and diffusion distances (Singelyn et al., 2012; Wang et al., 2019; Wang et al., 2020). Without the need to keep the whole heart architecture intact, protocols using minced, ground, or solubilized ECM can more thoroughly remove residual DNA and cell fragments

without inducing significant changes to the overall ECM composition.

dECM injectables have demonstrated translational efficacy in small animal models of cardiac injury (Singelyn et al., 2012). Wang, Z. et al. injected adult or neonatal mouse dECM suspended in saline into the epicardium of mice immediately following induced MI (Wang et al., 2019). Neonatal dECM was shown to improve cardiac function, reduce fibrosis, and promote angiogenesis. Adult dECM did not share the regenerative capabilities of the neonatal dECM, and in many instances, performed no better than the saline control. This study, and similar studies that use injectable dECMs, highlight the functional benefits of solubilized dECM as a material to mitigate the negative remodeling that often follows MI. Moreover, this underscores a paradigm shift away from conventional adult-derived ECM materials and towards a future that looks further into the advantages and understanding of neonatal-derived dECMs.

Another form of solubilized dECM that has been growing in popularity is bioinks that are used to generate cardiac patches. Bejleri et al. bioprinted a GelMA-dECM patch and implanted it onto healthy rat epicardium for 14 days (Bejleri et al., 2018). Histological analysis showed that the patch became vascularized and integrated with the host myocardium. Jang et al. also bioprinted a cardiac patch containing human dECM and polycaprolactone (PCL), with alternating layers of cardiac progenitor cells and mesenchymal stem cells (Jang et al., 2017). The patches were first implanted subcutaneously into the abdomen of the rat for host vascularization. After 28 days, the patch was explanted and then implanted onto the epicardium of rats that had an induced MI 7 days prior. This alternating layered approach led to improved cardiac function, attenuated fibrosis, greater cell migration out from the transplanted patch into the damaged tissue, and enhanced vasculogenesis and myogenesis. These works demonstrate how cardiac dECM can be solubilized and used as a supportive niche to promote a pro-regenerative and mitigate a pro-fibrotic healing response following cardiac injury.

Lastly, the cardiac dECM is rich with cytokines and small molecules that modulate angiogenesis, survival, cell recruitment and the cellular response to inflammation. Decellularized porcine myocardium was found to contain vascular growth factors such as VEGF-A, VEGF-C, and FGF-1, cardiokines including PDGF, HGF, and endoglin, as well as factors involved in the inflammation such as G-CSF and IL-8 (Methe et al., 2014). While these residual factors modulate a range of pro-survival and pro-recruitment functions, they also exhibit batch-to-batch variability and present an ongoing challenge in the standardization of decellularization protocols.

3.2 Skeletal Muscle dECM Composition

The ECM of native skeletal muscle is composed of a combination of proteins and proteoglycans such as collagen, elastin, laminin, fibronectin and GAGs (Csapo et al., 2020). These components serve as modulatory binding sites, structural materials, and gene regulators for the native muscle and if preserved correctly, can serve these same functions as a decellularized material for skeletal muscle regenerative applications (Csapo et al., 2020). However, due to the wide range of decellularization protocols, the resulting dECM composition varies and hence the regenerative capacity of these materials will also vary.

3.2.1 How Different Protocols Affect Skeletal Muscle dECM Composition and Cell Interactions - Trypsin

Trypsin is a serine protease secreted by the pancreas to aid in the digestion of proteins (Miersch et al., 2018). In cell culture, trypsin is commonly used for detaching adherent cells during cell passaging (Sharma et al., 2019) as it disrupts the cell-ECM bonds. For this reason, trypsin is also used as a dissociation agent in skeletal muscle decellularization. However, due to its strong digestive properties, trypsin is also effective in removing essential ECM components like collagen and GAGs which present a challenge for downstream applications that rely on interactions with these components.

Wolf et al. established a decellularization protocol for whole muscles using 0.1% Trypsin, 2% SDC and 1% Triton X-100 (Wolf et al., 2012). ECM characterization using Herovici's and Movat's Pentachrome stains detected the presence of collagen and elastin, while immunostains of the basement membrane showed the preservation of laminin, type IV collagen, and fibronectin. Although the stains showed some ECM presence, the stains also revealed the dysmorphism of the physical structures in decellularized skeletal muscles. Furthermore, only 20% of sulfated GAGs (sGAGs) were retained in decellularized skeletal muscles when compared to native skeletal muscles. When these muscle dECMs were seeded with human perivascular stem cells, NIH 3T3 mouse fibroblasts, and C2C12 mouse myoblasts, cellular proliferation was observed on the surface of the decellularized tissue for all cell types. Additionally, the cultured C2C12s further differentiated into mature myotubes. In contrast, cellular metabolism quantified using Alamar Blue assay indicated higher metabolic activity in the tissue culture flask control compared to cells grown on the decellularized scaffold. *In vivo* implantation of the decellularized scaffold in a rat abdominal wall defect showed dense accumulation of regenerating cells, angiogenesis, and myogenesis around the scaffold surface as shown by histological analyses. Corona et al. used a similar combination of reagents on whole rat tibialis anterior (TA) muscles and showed enhanced cell proliferation of muscle satellite cells *in vitro*, but limited myogenesis when implanted into a volumetric muscle loss (VML) injury (Corona et al., 2013).

In contrast, greater *in vivo* healing outcomes were reported by Zhang et al. who combined 0.02% trypsin with 0.1% SDS and 1% Triton X-100 to perfusion decellularize whole porcine skeletal muscles (Zhang et al., 2016). ECM characterization of the decellularized tissue validated the retention of laminin, type IV collagen, fibronectin, and elastin. Similarly, sGAG quantification of native versus decellularized tissues corresponded to a preservation of roughly 20% sGAGs in the decellularized tissues. The culture and differentiation of C2C12 myoblasts on the dECM scaffold demonstrated improved myogenesis including greater fiber diameter, fusion index, and increased metabolism compared to the tissue culture plastic controls. In a VML injury model involving a rat abdominal wall defect, the transplanted dECM scaffold showed abundant cellular infiltration around the

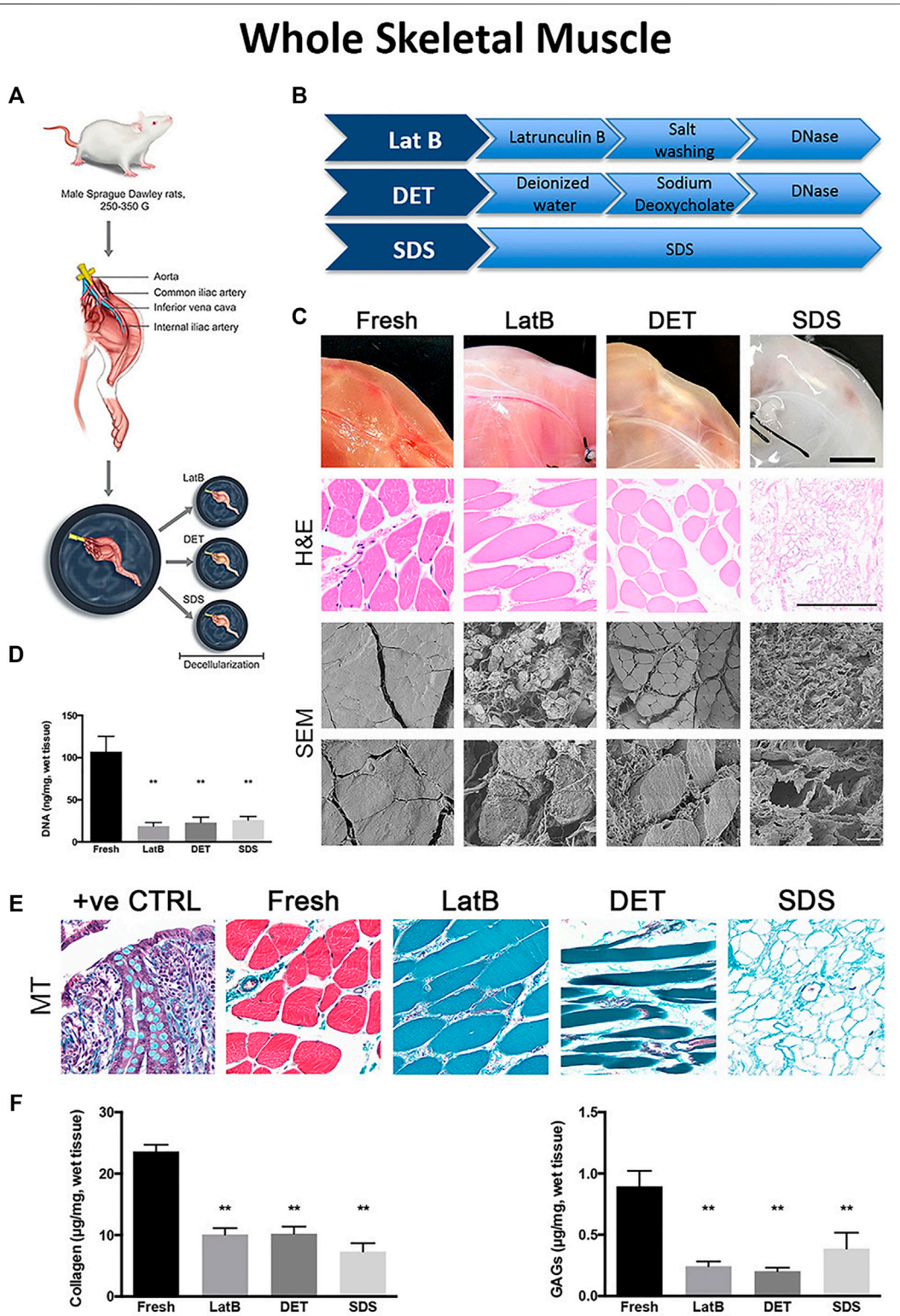

FIGURE 4 | Differences in decellularization protocols determine dECM properties in whole tissues **(A)** Schematic of tissue harvest from a rat hindlimb for whole muscle decellularization **(B)** A breakdown of three example decellularization protocols used in whole tissue decellularization **(C)** Final DNA content after whole tissue decellularization using three different decellularization protocols **(D)** Tissue morphology from top to bottom: Macroscopic tissue images, Hematoxylin and Eosin (H&E) staining, and Scanning Election Microscope (SEM) images of whole tissues before (Fresh, first column) and after decellularization with LatB (second column), DET (third column), and SDS (fourth column) protocols **(E)** Massons Trichrome (MT) staining of whole tissue after decellularization **(F)** ECM content of collagen and GAGs remaining in decellularized whole tissues compared to fresh tissues. Figures A–F are adapted from "Decellularised skeletal muscles allow functional muscle regeneration by promoting host cell migration" by Urciuolo et al. (2018) licensed under CC BY 4.0.

surface of the implant as well as moderate neo-muscle fiber presence up to 5 mm away from the defect. Neovascularization of the skeletal muscle dECM was also greater compared to the controls. Taken together, there is both utility and limitations of using a trypsin-based decellularization agent in which survival and proliferation of cells is supported *in vitro* but structural dysmorphism and loss of GAGs may impact *in vivo* applications.

3.2.2 How Different Protocols Affect Skeletal Muscle dECM Composition and Cell Interaction - SDS

A well strategized SDS treatment can be extremely effective at removing cellular debris, while still retaining ECM components. In an effort to restore normal muscle function following a severe muscle injury, Lee et al. decellularized minced rabbit skeletal muscles using 1% SDS to create a dECM scaffold (Lee et al., 2020). A compositional analysis of the resulting ECM in the decellularized tissue showed the retention of approximately 50% collagen, 74% elastin, and 83% GAGs when compared to native skeletal muscle. When seeded with C2C12 mouse myoblasts, the cellularized constructs maintained a 90% cell viability throughout the 7 days of culture. Alamar Blue assessment of metabolic activity of the cells in the muscle dECM demonstrated an increase in cell proliferation when compared to collagen controls. Additionally, greater *in vitro* myogenesis (myotube formation and maturation) was observed on the dECM scaffolds compared to controls. In a rabbit model of TA VML injury, treatment with the dECM scaffold was associated with a greater number of regenerated muscle fibers when compared to the collagen implant. Therefore, despite the reputation of SDS as a disruptive agent, dECM produced from an SDS protocol has been used for successful *in situ* muscle regeneration.

The decellularization of whole muscle tissues presents additional challenges due to the large volume of tissue that must interface with a decellularization agent to effectively remove cellular components. Protocols that aim to decellularize whole muscles typically include some form of SDS. To decellularize whole rat muscles, Kasukonis et al. employed a 1% SDS perfusion decellularization protocol (Kasukonis B. M. et al., 2016). ECM characterization of the decellularized tissue showed an approximately 90% retention of both collagen and GAGs. *In vitro*, the dECM supported C2C12 proliferation and *in vivo* implantation of the dECM scaffold with and without the addition of minced muscle autografts in a rat VML injury model resulted in reduced fibrosis when compared to the VML only control (Kasukonis B. et al., 2016; Kasukonis B. M. et al., 2016).

To characterize the effects of three different decellularization protocols, Urciuolo et al. employed a perfusion treatment for rat hind limbs using one of three agents: 1) LatB; 2) 4% SDC; or 3) 0.25% SDS (Urciuolo et al., 2018) (**Figure 4A,B**). Compared to native muscles, both H&E and SEM analyses displayed different histological characteristics as a function of decellularization agent (**Figure 4C**). Although the residual DNA content was statically lower than native tissues for all three treatments (**Figure 4D**), marked differences in global tissue morphology and myofiber structure was evident. Tissue architecture was extensively preserved in both the LatB and SDC treatment, whereas myofiber integrity was widely compromised in the SDS treatment (**Figure 4E**). Both the LatB and SDC protocols preserved about 50% of the native collagen content while the SDS protocol retained slightly less collagen at about 40% (**Figure 4F**). However, the same SDS treatment yielded tissues with a better retention of GAGs (~45%), compared to approximately a 25% retention for both the LatB and SDC treatments (**Figure 4F**). Angiogenic cytokine content was also quantified in the three dECMs and revealed a 30 and 25% retention of VEGF using the SDS and SDC protocols respectively, while the LatB protocol showed almost no residual VEGF when compared to native skeletal muscles. Additionally, SDS preserved the greatest amount of IGF-1 (60% retainment) while both LatB and SDC correlated with about 33% compared to native tissues. To further test the regenerative potential of the decellularized tissues, each scaffold was transplanted into a murine extensor digitorum longus (EDL) VML injury model. All sites of implantation showed signs of tissue regeneration with partially restored muscle strength. Despite some differences in dECM composition, *in vivo* application of this material resulted in similar regenerative outcomes.

3.2.3 How Different Protocols Affect Skeletal Muscle dECM Composition and Cell Interaction - LatB

A non-proteolytic, non-detergent based, decellularization method was developed by Gillies et al. for whole skeletal muscle decellularization (Gillies et al., 2011). The protocol consisted of LatB, potassium chloride, potassium iodide, and DNase, applied to whole mice TA muscles. LatB functions by depolymerizing the actin and myosin filaments that are the structural supports of skeletal muscle, making cells more vulnerable to the effects of potassium chloride and potassium iodide salts which are hyper- and hypotonic solutions. Most notably, major ECM components were preserved. Amongst the ECM components, 60% of GAGs and 100% of collagen remained in the decellularized tissue. Moreover, when seeded with C2C12 mouse myoblasts, the skeletal muscle dECM supported cell survival both on the surface and inside the scaffold.

Using this same LatB protocol, Fishman et al. decellularized the cricoarytenoid dorsalis muscles harvested from the larynx of adult rabbits (Fishman et al., 2012). The non-proteolytic, non-detergent protocol actively preserved several major ECM components, which corresponded with the retainment of about 75% collagen, 65% GAGs, preservation of elastin, and low presence of MHC classes I and II antigens. To test the biocompatibility and regenerative properties of the acellular tissue, the skeletal muscle dECM was transplanted into immunocompetent rats with a TA injury (Fishman et al., 2013). Compared to the control PCL scaffolds, the dECM scaffolds produced better cell survival and host integration.

Overall, the LatB decellularization approach pioneered by Gillies et al. is emerging as a viable alternative to the traditional SDS and trypsin treatments. Although a more mild protocol, LatB effectively preserves ECM components and may be an efficient approach for the decellularization of whole skeletal

muscle decellularization without the need for perfusion bioreactors.

4 BIOPHYSICAL PROPERTIES: TOPOGRAPHY

The ECM is an elegant example of form supporting function. The ultrastructure of an ECM niche is dictated by the needs of the cells that it is designed to support. In the case of cardiac and skeletal muscle, this means that the tissue ECM is highly organized and anisotropic to enable fast and uniform transfer of contractile forces across the entire tissue. The topographical features of the ECM are present from the macrostructure down through the sub-cellular organization of fibrillar proteins. The spatial patterning of these structures provides a supportive niche that can direct cell organization, behavior, and function. Topographical patterning using dECM materials is generally performed using two different approaches: 1) use of the intact native matrix with original architecture; 2) use of solubilized matrix that is then printed into specific patterns to guide cell behavior.

4.1 Cardiac dECM Topography

The theme of alignment is pervasive throughout all levels of the cardiac tissue structure from the parallel orientation of the myocardial macrostructure to the sub-micron bands of the sarcomeres (Carson et al., 2016). Much of the structural alignment that is seen in cardiac tissue is primarily dictated by fibronectin and collagen fibers (Batalov et al., 2021), which have diameters ranging from 30 to 120 nm (Carson et al., 2016). Within these fibers are the integrin-binding domains that interact with cells to facilitate attachment and thereby are responsible for guiding cellular alignment. In fibronectin, the most common domain is the arginine-glycine-aspartate peptide (RGD) that facilitates binding through the α5β1 integrin complex (Bellis, 2011). Collagen also has RGD sequences, but these sites are largely inaccessible due to the conformation unless the collagen is cleaved by MMPs or denatured (Bellis, 2011). Other important binding players located on cell membranes are the α1β1 integrin complex, which primarily binds to collagen type IV, and the α2β2 integrin complex, which predominantly binds to collagen type I (Boraschi-Diaz et al., 2017). The accessibility of the integrin-binding domains following decellularization plays a decisive role in guiding cardiac cell binding and cytoskeletal organization. Therefore, the decellularization protocols aimed at generating dECM with specific topographical features, must prioritize the preservation of the ECM components that house these cell-binding domains.

4.1.1 How Different Decellularization Protocols Affect Cardiac dECM Topography

To enable the study of dECM topography, decellularization protocols must avoid disruption of key ECM proteins such as fibronectin and collagen fibers, which contain essential integrin-mediated binding domains. Protocols that remove cells via cell swelling and rupture have been shown to physically disrupt the spatial environment, and repeated freeze-thaw cycles can be severely damaging to fibrillar proteins, leading to inconsistent fiber sizes (Behmer Hansen et al., 2021). Similarly, extended exposure to reagents such as trypsin, SDS, and Triton X-100 can disrupt glycoprotein microstructure which is important for cell adhesion and growth factor regulation (Wilgus, 2012; Gilpin and Yang, 2017). For example, Merna et al. found that hearts decellularized with a combination of trypsin and triton thoroughly removed DNA (<1 ng/mg, ~90% removal), but significantly disrupted the elastin architecture (**Figure 3B**) (Merna et al., 2013). In contrast, a triton-only regimen had less of an effect on elastin content and maintained crimped collagen fibers; however, the protocol resulted in only about 40% decellularization based on residual DNA content.

Fortunately, the most common cardiac decellularization approach of 1% SDS and 1% Triton X-100 is effective in the removal of cells and cellular debris without significant disruption to the ECM. (Ott et al., 2008; Robertson et al., 2014; Williams et al., 2014; Hochman-Mendez et al., 2020; Wang et al., 2020; Basara et al., 2021; Mousavi et al., 2021; Tsui et al., 2021). Using this classic decellularization approach, Hochman-Mendez et al. even confirmed that the wave-like topography of laminin in the cardiomyocyte basement membrane was preserved (Hochman-Mendez et al., 2020). However, the precise level of ECM feature preservation required for adequate cell binding, growth, and patterning still remains to be extensively characterized.

4.1.2 How Cardiac dECM Topography Affects Cell Behavior In Vitro

A significant body of work has been done to study native topography and to characterize the drivers of cardiomyocyte alignment. Micropatterning, nanofiber electrospun scaffolds, flexible posts, and electrical fields are just some of the methods used to guide alignment *in vitro* (Au et al., 2007; Carson et al., 2016; Leonard et al., 2018; Suh et al., 2020; Batalov et al., 2021). While it is well understood that the orientation and elongation of cardiac cells is essential for maturation and proper contractile function, the field has yet to fully elucidate the underlying biophysical, mechanical, and molecular mechanisms that facilitate alignment.

To better understand these complex relationships, Schwan et al. developed an engineered heart tissue (EHT) system from laser cut, decellularized porcine myocardial sheets (Schwan et al., 2016). A major insight from this work was that local matrix cues from the EHT were more influential in guiding cellular alignment than macroscopic cues such as applied load or stiffness, which are historically potent modulators of alignment in isotropic gels (Schwan et al., 2016). When the EHT was recellularized with neonatal rat ventricular myocytes, human embryonic stem cell derived cardiomyocytes, or human induced pluripotent stem cell derived cardiomyocytes (iPSC-CMs), the resulting construct displayed spontaneous beating, cellular alignment, organized sarcomeres, and gap junctions. They found that the mechanical properties, such as peak twitch stress, were dictated by the orientation of the fibers and could be used to recapitulate the contractile anisotropy displayed by native tissues.

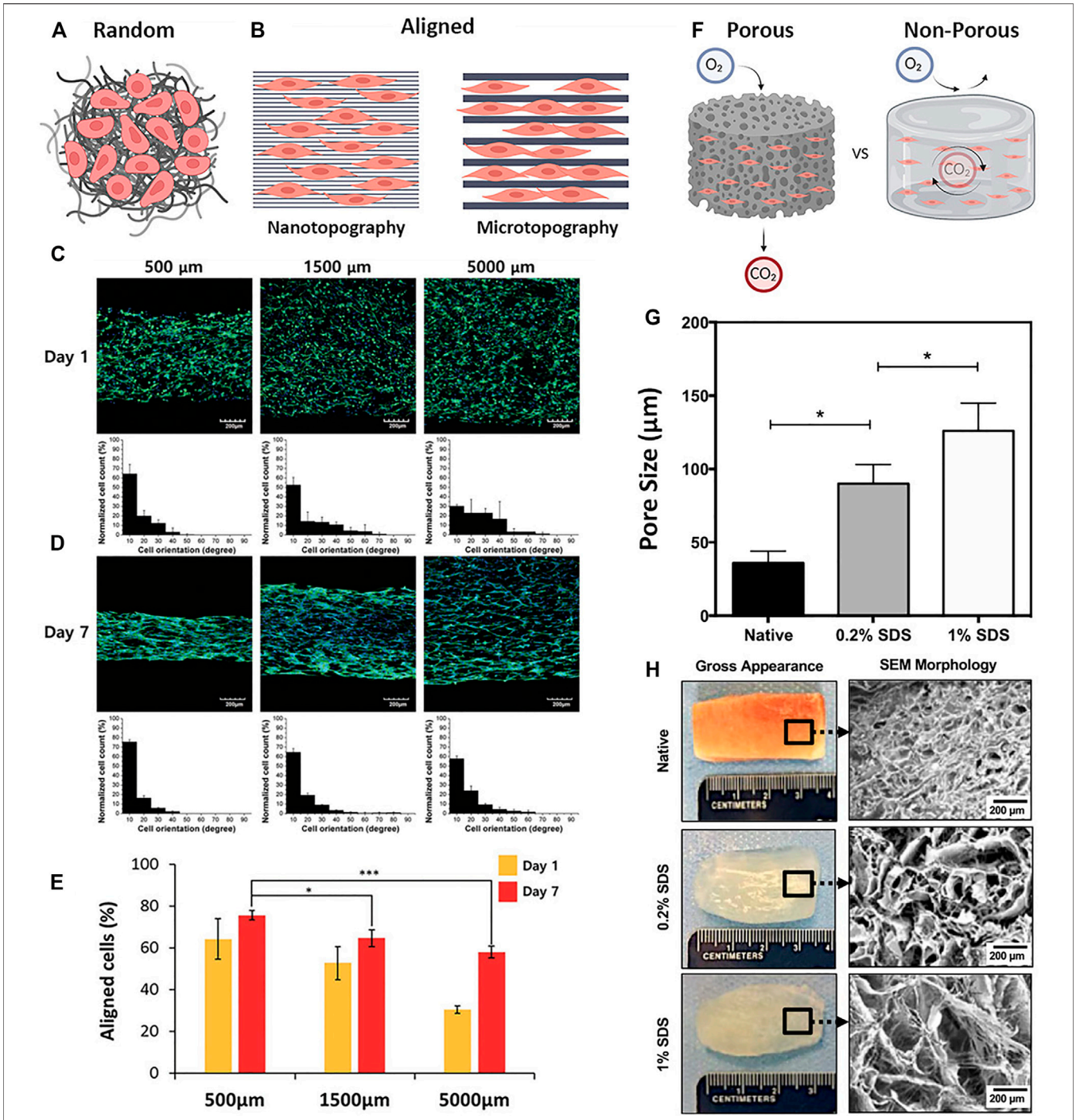

FIGURE 5 | Patterning and topography in dECM biomaterials **(A)** Material topography with a random-orientation of fibers and cells **(B)** Nano- and micropatterned materials with parallel orientation of fibers or channels showing differences in cell guidance and interaction **(C–E)** C2C12 myoblasts cultured on 3D-printed line widths of 500 µm, 1,500 µm, and 5,000 µm on **(C)** day 1 and **(D)** day 7**;** cells were stained green for F-actin (Phalloidin), and blue for nuclei (DAPI) **(E)** Quantification of % aligned cells on the varying line widths at day 1 and 7 **(F)** Porous and Non-Porous properties of bulk materials differentially regulate the diffusion of gases and other soluble factors **(G)** Quantification of average pore sizes in native skeletal muscle tissue and decellularized scaffolds treated with 0.2% SDS and 1% SDS, respectively **(H)** Macroscopic and SEM images of native skeletal muscle and decellularized scaffolds treated with 0.2% SDS and 1% SDS, respectively. Figures A, B, F are created using BioRender.com. Figures C–E are adapted with permission from Choi et al. (2016). Figures G, H are adapted with permission from Shapiro et al. (2019).

Moreover, when they compared the EHT to another anisotropic scaffold, electrospun gelatin, they found that the EHT had a stronger peak stress, suggesting that the dECM possess a diverse multitude of biomechanical factors that similarly patterned synthetic materials cannot recapitulate.

4.1.3 How Cardiac dECM Topography Affects Cell Regeneration In Vivo

The vast majority of *in vivo* studies that use cardiac dECM, do so by using the material in a solubilized form. While topography and patterning of dECM *in vitro* may have provided evidence of guiding cellular and biomechanical outcomes, the story *in vivo* is different. Cardiac dECM injectable therapeutics have had promising results (Singelyn et al., 2012; Wang et al., 2019; Wang et al., 2020). However, there are a few studies that showed the benefit of using dECM with preserved topography as a tool for enhancing cell recruitment or delivery in small animal injury models. Sarig et al. implanted decellularized porcine cardiac patches into rats following induced MI and observed recruitment of native macrophages and cardiomyocyte progenitor cells (CPCs) (Sarig et al., 2016). Recruited CPCs organized into fiber-like clusters with partial striation and positive staining for gap junction marker Connexin43. Sarig et al. concluded that their dECM patch, without recellularization, improved contractility, ejection fraction, and cardiac remodeling following MI (Sarig et al., 2016).

Like Sarig et al., Wang, Q. et al. used intact rat decellularized ECM patches for treatment post MI in a rat model, but also directly compared acellular dECM patches to dECM patches cultured with human iPSC-CMs and $CD90^+$ nonmyocytes (Wang et al., 2016). They found that recellularized patches significantly improved ejection fraction and vascular density, while decreasing infarct size in comparison to acellular dECM patches. However, their recellularization did not produce adequate cellular alignment or cardiomyocyte maturation and they did not study recruitment of host cells. Taken together, *in vivo* application of cardiac dECM is largely driven by modulation of the regenerative niche by the ECM components and, to a much lesser extent, by any specific surface patterning or topographical features.

4.2 Skeletal Muscle dECM Topography

Many studies that look at the topographical contribution of decellularized skeletal muscle aim to utilize and/or mimic the naturally aligned pattern of the ECM to guide myogenic cell differentiation. Similar to cardiac muscle, skeletal muscle is highly oriented along a common axis and is composed of functional myofiber units that are organized in parallel to maximize force contraction. Skeletal muscle is anisotropic and is made up of tightly bundled, aligned structures of densely-packed myofibers (Jana et al., 2016). In the field of skeletal muscle regeneration, differentiation of new myofibers along a uniform direction is a key feature of a successful biomimetic material and supportive niche. Furthermore, it has been widely demonstrated that topographical patterning of cells has a significant impact on morphology, behavior, and function (Nakayama et al., 2018; Nakayama et al., 2019). There are several reoccurring themes in the area of topographical patterning and skeletal muscle dECM that include the contribution of alignment/anisotropy, scale (micro versus nano), and porosity (**Figure 5**).

4.2.1 How Skeletal Muscle dECM Topography Affects Cell Behavior- Alignment

The alignment-mediated cellular response is a key player in myogenesis and the development of functional myotubes and physiologically mimetic myofibers (Ostrovidov et al., 2014). Substrates with either aligned or randomly-patterned topography are often used to assess or enhance contact-driven myogenic fusion (**Figure 5A**). One approach that utilizes skeletal muscle dECM with controlled topographical patterning was demonstrated by Kim et al. using 3D bioprinting methods to produce a cell-laden, dECM-based structure with unique topographical cues (Kim et al., 2020). To test the effect of uniaxial topographical patterning, C2C12 mouse myoblasts were seeded onto either aligned or non-patterned dECM scaffolds and were cultured for 21 days. Significantly greater myoblast alignment, myotube formation, and myogenic gene expression (MyoD1, MYH2, Myog) was observed in the aligned patterned dECM scaffolds when compared with the non-patterned controls. In another alignment-focused study, through the use of elastomeric chips made from polydimethylsiloxane (PDMS), the kinetics of dECM fibrillogenesis was controlled to fabricate both aligned and non-patterned dECM hydrogel scaffolds loaded with induced skeletal muscle progenitor cells (iMPCs) (Jin et al., 2021a). iMPC-loaded aligned dECM hydrogel scaffolds showed increased cell alignment and expression of myogenic markers Mrf5, MyoD1, and Myog at day 10 of *in vitro* cell culture. *In vivo* implantation of both aligned and non-patterned iMPC-loaded 3D constructs in a VML quadriceps femoris mouse model demonstrated a significant reduction of fibrosis as well as greater *de novo* muscle regeneration in the aligned iMPC-loaded hydrogel scaffold compared to the non-patterned control. These combined studies highlight the ability of physical cell alignment to enhance myogenesis *in vitro* and muscle regeneration *in vivo*.

Hybrid dECM bioinks are another approach to guiding alignment-mediated muscle regeneration. Lee et al. created aligned and randomly-oriented bioprinted skeletal muscle constructs using photo-crosslinkable dECM bioink together with poly(vinyl alcohol) (PVA) to modulate topography. The self-aligned printed muscle constructs improved myogenic differentiation *in vitro* evidenced by the expression of mature myogenic markers (MYH4 and MYH2) and exhibited rapid restoration of muscle function *in vivo* in a rat tibialis anterior VML model (Lee et al., 2021). The aligned constructs showed increased myofiber formation, reduced fibrotic tissue area, significant MHC^+ expression, and greater tetanic force production. Together, these studies underscore the modulatory role of dECM alignment in guiding myogenesis.

4.2.2 How Skeletal Muscle dECM Topography Affects Cell Behavior- Scale

Topography can be modulated on the micro- or nano-scale to guide cell behavior and myogenesis; however, it is a highly contested topic as to which topographical scale is most effective at achieving the optimal cell response (Skoog et al.,

2018) (**Figure 5B**). Because of the increasing accessibility of technologies such as 3D bioprinting, electrospinning, soft- and photolithography, patterning using lower resolution microscale topographies are more widely used compared to higher resolution nanoscale topographies (Chia and Wu, 2015). For example, Choi et al. fabricated micro-scale cell-laden dECM muscle constructs using 3D printing of dECM with line widths that ranged between 300 and 1,000 μm. The micropatterned 3D printed constructs demonstrated high cell viability and supported the formation of densely packed aligned-myotubes compared to non-patterned controls. Furthermore, to assess therapeutic efficacy, the 3D micropatterned muscle constructs were implanted into the defect site of a rat tibialis anterior VML injury and displayed *de novo* muscle regeneration and minimal fibrosis when compared to the non-patterned controls (Choi et al., 2019).

Studies have also been done using dECM with different pattern scales to determine the optimal fiber size for myogenesis *in vitro*. Using 3D bioprinting, Choi et al. constructed C2C12-laden scaffolds with fibers that ranged between 500 and 5,000 μm (Choi et al., 2016) (**Figure 5C,D**). It was found that the greatest cellular alignment, elongation, and mechanical strength was seen by cells cultured on scaffolds with the higher resolution range of 500 μm patterning (**Figure 5E**). Evidence that smaller topographies may lead to enhanced myogenesis was demonstrated by this same group using deep X-ray lithography to fabricate sinusoidal microscale patterns of dECM in the range of 20–80 μm (Choi et al., 2018). These wavy dECM surfaces induced myoblast alignment and enhanced myotube formation and differentiation.

Nano-scale ECM topographies have been shown to play a potent role in guiding cell morphology, phenotype, differentiation, and function (Nakayama et al., 2015; Nakayama et al., 2016; Nakayama et al., 2018; Nakayama et al., 2019; Patel et al., 2019; Patel et al., 2020; Jin et al., 2021a). In a study by Patel et al., dECM and polycaprolactone (PCL) were electrospun together to mimic the topographical architecture of native muscle with a fiber diameter range of 500–2000 nm (Patel et al., 2019). The hybrid scaffolds were capable of supporting myogenic cell growth and the secretion of myokine growth factors. The nanofiber scaffold promoted *in vivo* muscle regeneration in a murine model of gastrocnemius-soleus VML with increased myofiber (MHC^+) regeneration and elevated activity of anti-inflammatory M2 macrophage ($arginase^+$) compared to the control groups (Patel et al., 2020). Similarly, nano-scale topographies were used to guide myogenesis using elastomeric PDMS chips together with iMPCs to support mature myotubes *in vitro* and *de novo* muscle regeneration with induced functional restoration of injured quadriceps femoris muscles in a VML mouse model (Jin et al., 2021a).

Both micro- and nano-topographies have been shown to guide myogenesis and functional muscle regeneration *in vitro* and *in vivo* and the optimal topographical scale is dependent on several factors including the desired cellular interactions, type of cells, and substrate properties.

4.2.3 How Skeletal Muscle dECM Topography Affects Cell Behavior- Porosity

The porosity of a biomaterial determines the rate of transportation of gases, removal of waste products, and diffusion of macromolecular proteins from the surrounding environment into the bulk space of the matrix (Choi et al., 2019; Jin et al., 2021a) (**Figure 5F**). Shapiro et al. demonstrated that different concentrations of SDS effect the pore size of the resulting dECM, such that increasing concentrations of SDS produced tissues with greater pore sizes (Shapiro et al., 2019) (**Figures 5G,H**). The larger pore sizes better supported cell infiltration and allowed for the controlled release of IGF-1 to enhance *in situ* muscle regeneration. In a study done by Jin et al., four different types of dECM-PCL substrates were thermally drawn into sheets or fibers following a salt leaching method to incorporate porosity (Jin et al., 2021b). The four types of substrates include non-porous sheets, porous sheets, non-porous fibers, and porous fibers. Culture of iMPCs on the four different substrates resulted greater expression of myogenic genes (MyoD1, Mrf5, Myog, ITGB1, ITGA7, and CDH2) within the porous group when compared to the non-porous group. Others have demonstrated better cell viability when using porous dECM scaffolds compared to non-porous hydrogels (Choi et al., 2019), implicating possible cell hypoxia when scaffolds are not sufficiently porous.

Combinatorial effects of alignment plus porosity have also been associated with improved cellular outcomes. In a comparison of aligned (pore size of 3.39 μm) versus randomly-oriented (pore size of 2.58 μm) muscle constructs, greater cell viability if iMPCs was seen on the aligned scaffolds, which contained the larger pores, compared to the randomly-patterned scaffolds, which contained the comparatively smaller pore size (Jin et al., 2021a). Together, these studies underscore the significance and modulatory role of porosity in the use of skeletal muscle dECM to fabricate regenerative biomaterials; excessively high porosity will lead to lower structural integrity (Jakus et al., 2018) and a lack of porosity will potentiate hypoxia and cell death (Jin et al., 2021a).

5 BIOPHYSICAL PROPERTIES: MECHANICAL PROPERTIES

Cell biomechanics are constantly at play in the regulation of tissue homeostasis and response to injury. In native tissues, cells are naturally exposed to physical forces such as compressive loading, tensile strain, shear, and electrical stimulation (Rando and Ambrosio, 2018). These dynamic mechanical cues transduce signals from the surrounding extracellular environment through the cell membrane and into the cell's nucleus to influence the transcriptional programs that drive morphogenesis. By modulating the process of mechanotransduction, ECM-derived biomaterials can guide cells towards tissue remodeling, regeneration, and ultimately repair following injury.

5.1 Cardiac dECM Mechanical Properties

Disease, injury, and aging cause irreversible remodeling to cardiac ECM leading to fibrosis and a subsequent increase in stiffness, decreased contractility, and eventual heart failure. Due to the dynamic loading and contractile demands of the heart, an effective engineered therapeutic must support and recapitulate these functional mechanical properties. While cardiac dECM has been used to enhance the mechanical integrity of engineered cardiac tissues, the exact contribution of specific dECM biomechanical properties such as architecture, elasticity, and stiffness to the overall outcomes is not well-established (Silva et al., 2016).

5.1.1 How Different Decellularization Protocols Affect Cardiac dECM Mechanical Properties

The exact relationship between specific mechanical properties and the decellularization protocols used to generate these cardiac dECMs is not well-characterized. While there is a consensus that restoration of functional cardiac mechanics is a key benchmark of a successful regenerative technology, there is a marked lack of published studies that characterize the dECM mechanics (Behmer Hansen et al., 2021). However, some broad correlations can be made between some decellularization approaches and the resulting effects on cardiac dECM elasticity and strength. Decellularization protocols that utilize SDS and Triton X-100 for long periods of time risk damaging collagen and elastin fibers by decreasing fiber thickness and losing ultrastructure (Merna et al., 2013; Gilpin and Yang, 2017; Lee et al., 2017; Behmer Hansen et al., 2021). These alterations to ECM glycoproteins can have detrimental effects as they play a role in maintaining cardiac elasticity and tensile strength (Behmer Hansen et al., 2021). Merna et al. measured compressive modulus following various whole heart perfusion decellularization protocols. They found decellularization with triton increased the compressive modulus by 150% in comparison to the native heart while a trypsin plus triton regimen decreased the compressive modulus by <20% (Merna et al., 2013). Careful preservation of dECM mechanical properties and elasticity is especially challenging for perfusion systems which risk overinflating the heart and causing damage to the elastin fibers. Therefore, methods have been developed that optimize perfusion and gravitational forces to minimize mechanical strain during decellularization. Lee et al. found that inverting the heart at a -45° angle, improved perfusion efficiency and also improved retention of ECM proteins and heart shape (Lee et al., 2017).

5.1.2 How Cardiac dECM Mechanical Properties Affect Cell Behavior

Decellularized cardiac ECM provides mechanical cues that have the potential to improve cell attachment, differentiation, and maturation (Lu et al., 2013; Williams et al., 2014; Fong et al., 2016; Sarig et al., 2016; Das et al., 2019; KC et al., 2019; Hochman-Mendez et al., 2020; Mesquita et al., 2021). Specifically, cardiac dECM substrate stiffness can guide cell migration, proliferation, differentiation, and maturation (Merna et al., 2013; Perea-Gil et al., 2018). It has been shown that cardiomyocytes prefer softer substrates; when cultured on poly(ethylene glycol) and fibrinogen (PEGylated fibrinogen) hydrogels, an inverse correlation was found between material stiffness and the magnitude of cardiomyocyte contraction (Shapira-Schweitzer and Seliktar, 2007). As a therapeutic, dECM can provide mechanical support to the injured myocardium and must closely match the native contractile properties. If the dECM does not reflect native stiffness or the recellularized dECM construct contains immature cells, arrhythmias and a cascade of negative immune responses will occur leading to further scarring (Zhang et al., 2018). Therefore, dECM scaffolds must recapitulate the stiffness and mechanical properties of native myocardium as well as support cardiomyocyte contraction and maturation.

5.2 Skeletal Muscle dECM Mechanical Properties

Much like cardiac dECM, the influence of skeletal muscle dECM mechanical properties on myogenesis and muscle regeneration is not well-characterized. The biophysical dECM properties such as biochemical composition and topographical patterning are often the primary targets for modulation of cell behavior and less attention is given to controlling cellular interactions via classical tissue biomechanics. However, replicating the mechanical properties of skeletal muscle are a crucial component in the design of engineered skeletal muscle and regeneration *in vivo* (Lacraz et al., 2015).

The compressive stiffness of skeletal muscle dECM is heavily influenced by the decellularization reagents. In a study by Reyna et al. that compared three different decellularization methods, it was found that the SDS/Triton X and Triton X-only treated tissues had similar stiffnesses to the collagen control, while a LatB treatment produced the least stiff tissue across all groups (Reyna et al., 2020). While this specific study did not examine the downstream effects of stiffness on cellular interactions, two other studies found that the specific dECM that most closely resembled the stiffness of native muscle, promoted the greatest myogenesis *in vitro* and muscle regeneration *in vivo* (Choi et al., 2016; Jin et al., 2021b). To mimic the native structure of muscle, Choi et al. 3D printed muscle scaffolds using dECM bioinks (Choi et al., 2016). The dECM printed muscle scaffold exhibited a stiffness (12 ± 3 kPa) similar to that of native muscle (≈12 kPa) and also supported myoblast proliferation, myotube formation, and myogenic differentiation *in vitro*.

Mechanical variance is unavoidably introduced when dECM is fabricated into scaffolds with varying physical properties, and likely plays a contributing role in guiding subsequent cellular interactions. Jin et al. fabricated two types of muscle constructs by thermal drawing; a porous/fibrous scaffold (12.4 ± 3.5 kPa), and a porous/sheet-like scaffold (29.0 ± 3.8 kPa) (Jin et al., 2021b). The porous/fibrous scaffold had a stiffness that was most similar to native muscle (11.5 ± 1.3 kPa) and outperformed all other groups in myogenesis both *in vitro* and *in vivo*. Similar to cardiac dECM, the regenerative potential of skeletal muscle dECM is optimized when the scaffold's mechanical properties most closely resemble that of the native tissue.

6 EMERGING RESEARCH

The complementary fields of cardiac and skeletal muscle dECM research will continue to evolve and pioneer novel methods and tools for regenerative medicine. There are some very recent studies that stand apart in novelty and provide valuable insights and first steps that have the potential to take the field in a new direction. Herein, select studies are described that approach dECM research from an unexpected direction. While many of these studies were published within the past few years, they describe a dECM application that is a drastic departure from where the majority of the field currently resides.

6.1 Emerging Research in Cardiac dECM

The initial translational goal for cardiac dECM research was to use whole decellularized hearts as a therapeutic alternative for waitlisted organ transplant candidates. While this approach has yet to meet the clinical milestones necessary for a patient-applied treatment, cardiac dECM is nevertheless a versatile and powerful tool used in cardiomyocyte differentiation, maturation, and proliferation (Hochman-Mendez et al., 2020; Mesquita et al., 2021). It has also shown great promise as a therapeutic for the treatment of myocardial infarction, either in the form of a solubilized injectable gel or as an intact cardiac patch. (Sarig et al., 2016; Wang et al., 2016; Wang et al., 2019; Wang et al., 2020). However, despite the many studies demonstrating the utility of dECM for cardiac applications, there remains a gap in knowledge and bottlenecks in clinical translation.

To tackle the ongoing challenge of obtaining a renewable and robust supply of human cardiac dECM, one group has looked towards the use of cardiac organoids as a cultured source for dECM. Chiang et al. used organoids derived from human umbilical cord blood mesenchymal stem cells to lay down a structural protein niche that was then decellularized to provide a dECM scaffold (Chiang et al., 2021). The resulting dECM was shown to possess both essential microarchitecture and functional bioactivity (Chiang et al., 2021). This approach can be easily scaled up to produce large quantities of tissue-specific human ECM under reproducible and controlled laboratory conditions. Through the use of organoid-derived dECM, several major bottlenecks are circumvented by moving away from highly variable animal-derived products towards an approach that could be more easily standardized in a higher throughput setting.

Another approach for dECM cardiac tissue engineering that circumvents the need for healthy cardiac tissue as source material, is the use of other organs such as placenta or small intestine submucosa (SIS) for cardiac applications. Jiang et al. decellularized rat placentas which are highly vascularized, rich in ECM, and more readily available than hearts (Jiang et al., 2021). They recellularized the placenta with hiPSC-CMs and observed spontaneous contraction at a rate of 40—100 bpm. The hiPSC-CMs were also responsive to isoprenaline and had synchronized electromechanical propagation with external electrical stimulation. Additionally, the decellularized placenta significantly upregulated mRNA expression of genes related to cardiomyocyte structure, maturation, and conduction compared to cells culture on Matrigel coated tissue culture plastic. To test the therapeutic efficacy of their bioengineered cardiac patch (BCP), a rat myocardial infarction model was used. BCPs significantly improved left ventricular function, decreased infarct size, and increased cell retention compared to decellularized placenta or hiPSC-CMs alone after 4 weeks (Jiang et al., 2021).

The general concept of repurposing non-cardiac dECM for cardiac applications has also garnered significant interest and excitement with the emerging field of plant decellularization. Although decellularized vegetal scaffolds do not contain identical ECM components to decellularized cardiac tissues, their use has increased in popularity in recent years due to their innate networks for fluid transportation that resembles the human tissue vasculature. Additionally, plant tissue possesses similar mechanical properties, are highly accessible at a low cost, and non-immunogenic in nature (Harris et al., 2021). Plant tissue is primarily composed of cellulose, a well-studied, biodegradable compound that is widely used in a variety of clinical applications including wound dressing and drug delivery (Harris et al., 2021). Decellularized vegetal scaffolds are often coated with fibronectin, collagen, or poly-L-lysine (PLL) to promote cellular attachment and tune mechanical properties (Robbins et al., 2020; Harris et al., 2021). For cardiac tissue engineering, decellularized spinach (*spinacia oleracea*) and tomato (*solanum lycopersicum*) leaves have been identified as the ideal source material because their mechanical properties are in the range of human cardiac tissue (Gershlak et al., 2017; Robbins et al., 2020; Harris et al., 2021). Gershlak et al. decellularized spinach leaves, coated with fibronectin, and recellularized the vascular component with human umbilical vein endothelial cells (HUVECs) and the surface of the leaves with a combination of human mesenchymal stem cells (hMSCs) and hiPSC-CMs. The vasculature remained patent and perfusable and all cell types adhered and matured over the course of the 21 days study. The hiPSC-CMs began to spontaneously contact 5 days after seeding, exhibiting a 1% contractile strain and a contractile rate of 0.8 Hz (Gershlak et al., 2017). More recently, the same group recorded 3.94 ± 1.20% contractile strain which they hypothesized was due to their updated decellularization protocol which uses 1% SDS instead of 10% SDS (Robbins et al., 2020). While these results are promising, the contractile strain is still much smaller than the of adult myocardium (15.9–22.1%) (Yingchoncharoen et al., 2013). Therefore, significant work is still needed to meet the clinical milestones necessary for this cardiac patch to become a patient-applied treatment. Nonetheless, the use of plant-derived dECM for regenerative cardiac applications is an exciting new direction and may catalyze a paradigm shift and permenant new direction for cardiac decellularization.

6.2 Emerging Research in Skeletal Muscle dECM

The gold standard technology in skeletal muscle decellularization is experiencing a gradual shift away from the use of whole acellular tissue scaffolds towards more controlled 3D bioprinted approaches. Skeletal muscle dECM is now often solubilized into a bioink for extrusion printing, which allows

for the construction of complex geometries and patterns that can be printed in multiple layers to support different cell types and deep vascular networks. A major advantage of muscle dECM printing is the ability to mass produce large quantities of bioactive materials, which has the potential to increase accessibility and thereby pave a smoother road towards clinical adoption as a therapeutic for muscle regeneration. However, despite these many advancements in skeletal muscle dECM 3D-printing, the ability to commercialize dECM using strictly bio-printing technology has yet to be fully realized (Dzobo et al., 2019). Many of the same bottlenecks originally associated with whole tissue decellularization, such as the yield of dECM, tissue supply, and cost, are carried over into 3D bioprinting approaches. These factors all still need to be evaluated before large-scale commercialization is possible. Therefore, similar to cardiac tissues, alternative sources of dECM materials have been a recent focus for skeletal muscle regeneration.

As an alternative to animal-derived proteins, some select plants are emerging as materials for engineering aligned muscle fibers. Monocotyledon plants, such as green onions, have a highly structured parallel architecture made up of cellulose. Decellularized monocotyledon plants possess anisotopy similar to striated human muscle tissue and were show to guide myogenesis through these topographical cues (Cheng et al., 2020). A wide variety of plants were decellularized using a basic protocol of 1% SDS for a 3 weeks duration. Out of the fruits and vegetables that were decellularized in the study, the monocotyledon plants such as asparagus, green onions, leeks, and celery all exhibited good anisotropic and aligned scaffold structures. This unidirectional structure in green onion plants, comprised of grooves that are about 20 μm wide and 10 μm deep, served as natural topographical templates for myogenesis (Cheng et al., 2020). Specifically, decellularized plants scaffolds seeded with human skeletal muscle cells (hMSCs) and C2C12 myoblasts induced a higher level of anisotropic organization of both cell types when compared to glass coverslip controls. Furthermore, the plant scaffolds demonstrated greater myogenesis in the form of myotube formation compared to controls. In the cardiac study by Gershlak et al., which also utilized dicotyledon plants (decellularized spinach leaves), it was shown that a wide range of cell types including endothelial cells and mesenchymal stem cells, are supported by these decellularized plant materials (Gershlak et al., 2017). Given the diverse assortment of decellularizable plant structures, this approach reduces the potential production cost, impact on the environment, and offers a vegan-friendly foundation for bringing this technology to mass production.

Engineering plant-based solutions could also solve a major problem in the meat production industry. About 60% of global greenhouse gas emissions can be traced back to the production of animal-based foods (Xu et al., 2021). Bioartificial lab-grown meat is an emerging area in the biotechnology sector and has the potential to provide edible meat alternatives to large sectors of the global population. There are currently over 70 cultured meat startup companies and who collectively raised $366 million last year (Byrne and Murray, 2021). These companies produce cell-based meat that mimics beef, poultry, pork, and seafood and many base their products on derivatives of dECM. In a specific study by Jones et al., decellularized spinach leaves were used as a matrix for culturing bovine satellite cells as they were developed into edible "meat" (Jones et al., 2021). The decellularization of spinach leaves utilized a 1% SDS protocol, and resulted in a dECM structure filled with a deep hollow vascular network suitable for cellular infiltration. Approximately 25% of the bovine satellite cells stained positive for myosin heavy-chain expression and showed good cytoskeletal alignment (average kappa value of 0.71 ± 0.1) supportive of anisotropic myogenesis. While the field of cultured meats is still relatively young, if successful, this industry has the potential to make a massive impact on the supply chain of food worldwide.

7 COMMENTARY ON FUTURE DIRECTIONS FOR CARDIAC AND SKELETAL MUSCLE dECM

Although the use of dECM in tissue engineering has led to many paradigm-shifting insights, there is still much work to be done before it can become standard clinical practice. There needs to be better methods for standardization of decellularization protocols and dECM characterization following decellularization. Many of the published protocols do not specify durations and often assess decellularization visually based on non-quantitative color-based metrics. To overcome batch-to-batch variations, decellularization protocols should be followed by characterization of both the biochemical and mechanical properties of the dECM using such tools as liquid chromatography-mass spectrometry, atomic force microscopy, and electron microscopy. It is crucial to retain the structure and bioactive components of the dECM and it has been shown that overexposure to many of the decellularization agents cause irreversible damage. Conversely, incomplete decellularization results in unwanted immune responses and limits recellularization. To date, there is no universal decellularization protocol as there are many complex factors that influence how a tissue will decellularize. Oftentimes, the selected protocol is a true compromise built on the sacrifice of some biophysical properties in favor of others. As our understanding of the underlying mechanisms driving cell-dECM interactions are uncovered, the fields of cardiac and skeletal muscle decellularization will evolve and refine to increase in translational relevance and expand in impact on human health.

AUTHOR CONTRIBUTIONS

KN, YT, and HH. designed, wrote, and edited the manuscript. YT and HH contributed equally.

FUNDING

This work was supported by grants to KN through the National Institutes of Health (National Heart, Lung and Blood Institute R00HL136701); Alliance for Regenerative Rehabilitation Research and Training (CNVA00048860); the Oregon Health and Science University Foundation (Collins Medical Trust); and

MTF Biologics. This work was also supported by fellowships to HH through the Oregon Health and Science University Strain Fellowship; the National Institutes of Health (National Institute of Dental and Craniofacial Research T90DE030859); and the Achievement Rewards for College Scientists (ARCS) Foundation.

REFERENCES

Akhyari, P., Aubin, H., Gwanmesia, P., Barth, M., Hoffmann, S., Huelsmann, J., et al. (2011). The Quest for an Optimized Protocol for Whole-Heart Decellularization: a Comparison of Three Popular and a Novel Decellularization Technique and Their Diverse Effects on Crucial Extracellular Matrix Qualities. *Tissue Eng. C: Methods* 17 (9), 915–926. doi:10.1089/ten.TEC.2011.0210

Au, H. T. H., Cheng, I., Chowdhury, M. F., and Radisic, M. (2007). Interactive Effects of Surface Topography and Pulsatile Electrical Field Stimulation on Orientation and Elongation of Fibroblasts and Cardiomyocytes. *Biomaterials* 28 (29), 4277–4293. doi:10.1016/j.biomaterials.2007.06.001

Basara, G., Ozcebe, S. G., Ellis, B. W., and Zorlutuna, P. (2021). Tunable Human Myocardium Derived Decellularized Extracellular Matrix for 3D Bioprinting and Cardiac Tissue Engineering. *Gels* 7 (2), 70. doi:10.3390/gels7020070

Batalov, I., Jallerat, Q., Kim, S., Bliley, J., and Feinberg, A. W. (2021). Engineering Aligned Human Cardiac Muscle Using Developmentally Inspired Fibronectin Micropatterns. *Sci. Rep.* 11 (1), 11502. doi:10.1038/s41598-021-87550-y

Behmer Hansen, R. A., Wang, X., Kaw, G., Pierre, V., and Senyo, S. E. (2021). Accounting for Material Changes in Decellularized Tissue with Underutilized Methodologies. *Biomed. Res. Int.* 2021, 1–15. doi:10.1155/2021/6696295

Bejleri, D., Streeter, B. W., Nachlas, A. L. Y., Brown, M. E., Gaetani, R., Christman, K. L., et al. (2018). A Bioprinted Cardiac Patch Composed of Cardiac-Specific Extracellular Matrix and Progenitor Cells for Heart Repair. *Adv. Healthc. Mater.* 7 (23), 1800672. doi:10.1002/adhm.201800672

Bellis, S. L. (2011). Advantages of RGD Peptides for Directing Cell Association with Biomaterials. *Biomaterials* 32 (18), 4205–4210. doi:10.1016/j.biomaterials.2011.02.029

Bloom, D. E., Cafiero, E. T., Jané-Llopis, E., Abrahams-Gessel, S., Bloom, L. R., Fathima, S., et al. (2011). *The Global Economic Burden of Noncommunicable Diseases*. Geneva: World Economic Forum.

Boraschi-Diaz, I., Wang, J., Mort, J. S., and Komarova, S. V. (2017). Collagen Type I as a Ligand for Receptor-Mediated Signaling. *Front. Phys.* 5 (12). doi:10.3389/fphy.2017.00012

Byrne, B., and Murray, S. (2021). *2020 State of the Industry Report: Cultivated Meat*. Washington, DC: Good Food Institute.

Carson, D., Hnilova, M., Yang, X., Nemeth, C. L., Tsui, J. H., Smith, A. S. T., et al. (2016). Nanotopography-Induced Structural Anisotropy and Sarcomere Development in Human Cardiomyocytes Derived from Induced Pluripotent Stem Cells. *ACS Appl. Mater. Inter.* 8 (34), 21923–21932. doi:10.1021/acsami.5b11671

Chang, C. W., Dalgliesh, A. J., López, J. E., and Griffiths, L. G. (2016). Cardiac Extracellular Matrix Proteomics: Challenges, Techniques, and Clinical Implications. *Prot. Clin. Appl.* 10 (1), 39–50. doi:10.1002/prca.201500030

Cheng, Y.-W., Shiwarski, D. J., Ball, R. L., Whitehead, K. A., and Feinberg, A. W. (2020). Engineering Aligned Skeletal Muscle Tissue Using Decellularized Plant-Derived Scaffolds. *ACS Biomater. Sci. Eng.* 6 (5), 3046–3054. doi:10.1021/acsbiomaterials.0c00058

Chia, H. N., and Wu, B. M. (2015). Recent Advances in 3D Printing of Biomaterials. *J. Biol. Eng.* 9 (1), 4. doi:10.1186/s13036-015-0001-4

Chiang, C. E., Fang, Y. Q., Ho, C. T., Assunção, M., Lin, S. J., Wang, Y. C., et al. (2021). Bioactive Decellularized Extracellular Matrix Derived from 3D Stem Cell Spheroids under Macromolecular Crowding Serves as a Scaffold for Tissue Engineering. *Adv. Healthc. Mater.* 10 (11), 2100024. doi:10.1002/adhm.202100024

Choi, Y.-J., Jun, Y.-J., Kim, D. Y., Yi, H.-G., Chae, S.-H., Kang, J., et al. (2019). A 3D Cell Printed Muscle Construct with Tissue-Derived Bioink for the Treatment of Volumetric Muscle Loss. *Biomaterials* 206, 160–169. doi:10.1016/j.biomaterials.2019.03.036

Choi, Y.-J., Kim, T. G., Jeong, J., Yi, H.-G., Park, J. W., Hwang, W., et al. (2016). 3D Cell Printing of Functional Skeletal Muscle Constructs Using Skeletal Muscle-Derived Bioink. *Adv. Healthc. Mater.* 5 (20), 2636–2645. doi:10.1002/adhm.201600483

Choi, Y.-J., Park, S. J., Yi, H.-G., Lee, H., Kim, D. S., and Cho, D.-W. (2018). Muscle-derived Extracellular Matrix on Sinusoidal Wavy Surfaces Synergistically Promotes Myogenic Differentiation and Maturation. *J. Mater. Chem. B* 6 (35), 5530–5539. doi:10.1039/c8tb01475b

Corona, B. T., Wu, X., Ward, C. L., McDaniel, J. S., Rathbone, C. R., and Walters, T. J. (2013). The Promotion of a Functional Fibrosis in Skeletal Muscle with Volumetric Muscle Loss Injury Following the Transplantation of Muscle-ECM. *Biomaterials* 34 (13), 3324–3335. doi:10.1016/j.biomaterials.2013.01.061

Crapo, P. M., Gilbert, T. W., and Badylak, S. F. (2011). An Overview of Tissue and Whole Organ Decellularization Processes. *Biomaterials* 32 (12), 3233–3243. doi:10.1016/j.biomaterials.2011.01.057

Csapo, R., Gumpenberger, M., and Wessner, B. (2020). Skeletal Muscle Extracellular Matrix - what Do We Know about its Composition, Regulation, and Physiological Roles? A Narrative Review. *Front. Physiol.* 11 (253), 253. doi:10.3389/fphys.2020.00253

Das, S., Kim, S.-W., Choi, Y.-J., Lee, S., Lee, S.-H., Kong, J.-S., et al. (2019). Decellularized Extracellular Matrix Bioinks and the External Stimuli to Enhance Cardiac Tissue Development *In Vitro*. *Acta Biomater.* 95, 188–200. doi:10.1016/j.actbio.2019.04.026

Dzobo, K., Motaung, K. S. C. M., and Adesida, A. (2019). Recent Trends in Decellularized Extracellular Matrix Bioinks for 3D Printing: An Updated Review. *Ijms* 20 (18), 4628. doi:10.3390/ijms20184628

Fishman, J. M., Ansari, T., Sibbons, P., De Coppi, P., and Birchall, M. A. (2012). Decellularized Rabbit Cricoarytenoid Dorsalis Muscle for Laryngeal Regeneration. *Ann. Otol. Rhinol. Laryngol.* 121 (2), 129–138. doi:10.1177/000348941212100210

Fishman, J. M., Lowdell, M. W., Urbani, L., Ansari, T., Burns, A. J., Turmaine, M., et al. (2013). Immunomodulatory Effect of a Decellularized Skeletal Muscle Scaffold in a Discordant Xenotransplantation Model. *Proc. Natl. Acad. Sci.* 110 (35), 14360–14365. doi:10.1073/pnas.1213228110

Fong, A. H., Romero-López, M., Heylman, C. M., Keating, M., Tran, D., Sobrino, A., et al. (2016). Three-Dimensional Adult Cardiac Extracellular Matrix Promotes Maturation of Human Induced Pluripotent Stem Cell-Derived Cardiomyocytes. *Tissue Eng. A* 22 (15-16), 1016–1025. doi:10.1089/ten.tea.2016.0027

Gershlak, J. R., Hernandez, S., Fontana, G., Perreault, L. R., Hansen, K. J., Larson, S. A., et al. (2017). Crossing Kingdoms: Using Decellularized Plants as Perfusable Tissue Engineering Scaffolds. *Biomaterials* 125, 13–22. doi:10.1016/j.biomaterials.2017.02.011

Gilbert, T. W., Freund, J. M., and Badylak, S. F. (2009). Quantification of DNA in Biologic Scaffold Materials. *J. Surg. Res.* 152 (1), 135–139. doi:10.1016/j.jss.2008.02.013

Gillies, A. R., Smith, L. R., Lieber, R. L., and Varghese, S. (2011). Method for Decellularizing Skeletal Muscle without Detergents or Proteolytic Enzymes. *Tissue Eng. Part C: Methods* 17 (4), 383–389. doi:10.1089/ten.tec.2010.0438

Gilpin, A., and Yang, Y. (2017). Decellularization Strategies for Regenerative Medicine: From Processing Techniques to Applications. *Biomed. Res. Int.* 2017, 1–13. doi:10.1155/2017/9831534

Grisales, P. A., Aziz, J. M., Muir, S. M., Marino, D. I., La Pointe, C., Asthana, A., et al. (2021). "How the Transplant Landscape Is Changing in the Regenerative Medicine Era," in *Organ Repair and Regeneration*. Editors G. Orlando and S. Keshavjee (Academic Press), 273–284. doi:10.1016/b978-0-12-819451-5.00009-3

Harris, A. F., Lacombe, J., and Zenhausern, F. (2021). The Emerging Role of Decellularized Plant-Based Scaffolds as a New Biomaterial. *Ijms* 22 (22), 12347. doi:10.3390/ijms222212347

Herrera, J., Henke, C. A., and Bitterman, P. B. (2018). Extracellular Matrix as a Driver of Progressive Fibrosis. *J. Clin. Invest.* 128 (1), 45–53. doi:10.1172/jci93557

Hochman-Mendez, C., Pereira De Campos, D. B., Pinto, R. S., Mendes, B. J. d. S., Rocha, G. M., Monnerat, G., et al. (2020). Tissue-engineered Human Embryonic Stem Cell-Containing Cardiac Patches: Evaluating Recellularization of Decellularized Matrix. *J. Tissue Eng.* 11, 204173142092148. doi:10.1177/2041731420921482

Jakus, A. E., Geisendorfer, N. R., Lewis, P. L., and Shah, R. N. (2018). 3D-printing Porosity: A New Approach to Creating Elevated Porosity Materials and Structures. *Acta Biomater.* 72, 94–109. doi:10.1016/j.actbio.2018.03.039

Jana, S., Levengood, S. K. L., and Zhang, M. (2016). Anisotropic Materials for Skeletal-Muscle-Tissue Engineering. *Adv. Mater.* 28 (48), 10588–10612. doi:10.1002/adma.201600240

Jang, J., Park, H.-J., Kim, S.-W., Kim, H., Park, J. Y., Na, S. J., et al. (2017). 3D Printed Complex Tissue Construct Using Stem Cell-Laden Decellularized Extracellular Matrix Bioinks for Cardiac Repair. *Biomaterials* 112, 264–274. doi:10.1016/j.biomaterials.2016.10.026

Jiang, Y., Sun, S.-J., Zhen, Z., Wei, R., Zhang, N., Liao, S.-Y., et al. (2021). Myocardial Repair of Bioengineered Cardiac Patches with Decellularized Placental Scaffold and Human-Induced Pluripotent Stem Cells in a Rat Model of Myocardial Infarction. *Stem Cel. Res. Ther.* 12 (1), 13. doi:10.1186/s13287-020-02066-y

Jin, Y., Jeon, E. J., Jeong, S., Min, S., Choi, Y. S., Kim, S. H., et al. (2021a). Reconstruction of Muscle Fascicle-Like Tissues by Anisotropic 3D Patterning. *Adv. Funct. Mater.* 31 (25), 2006227. doi:10.1002/adfm.202006227

Jin, Y., Shahriari, D., Jeon, E. J., Park, S., Choi, Y. S., Back, J., et al. (2021b). Functional Skeletal Muscle Regeneration with Thermally Drawn Porous Fibers and Reprogrammed Muscle Progenitors for Volumetric Muscle Injury. *Adv. Mater.* 33 (14), 2007946. doi:10.1002/adma.202007946

Johnson, T. D., Dequach, J. A., Gaetani, R., Ungerleider, J., Elhag, D., Nigam, V., et al. (2014). Human versus Porcine Tissue Sourcing for an Injectable Myocardial Matrix Hydrogel. *Biomater. Sci.* 2 (5), 735–744. doi:10.1039/c3bm60283d

Johnson, T. D., Hill, R. C., Dzieciatkowska, M., Nigam, V., Behfar, A., Christman, K. L., et al. (2016). Quantification of Decellularized Human Myocardial Matrix: A Comparison of Six Patients. *Prot. Clin. Appl.* 10 (1), 75–83. doi:10.1002/prca.201500048

Jones, J. D., Rebello, A. S., and Gaudette, G. R. (2021). Decellularized Spinach: An Edible Scaffold for Laboratory-Grown Meat. *Food Biosci.* 41, 100986. doi:10.1016/j.fbio.2021.100986

Kasukonis, B., Kim, J., Brown, L., Jones, J., Ahmadi, S., Washington, T., et al. (2016a). Codelivery of Infusion Decellularized Skeletal Muscle with Minced Muscle Autografts Improved Recovery from Volumetric Muscle Loss Injury in a Rat Model. *Tissue Eng. Part A* 22 (19-20), 1151–1163. doi:10.1089/ten.tea.2016.0134

Kasukonis, B. M., Kim, J. T., Washington, T. A., and Wolchok, J. C. (2016b). Development of an Infusion Bioreactor for the Accelerated Preparation of Decellularized Skeletal Muscle Scaffolds. *Biotechnol. Prog.* 32 (3), 745–755. doi:10.1002/btpr.2257

Kc, P., Hong, Y., and Zhang, G. (2019). Cardiac Tissue-Derived Extracellular Matrix Scaffolds for Myocardial Repair: Advantages and Challenges. *Regenerative Biomater.* 6 (4), 185–199. doi:10.1093/rb/rbz017

Keane, T. J., Londono, R., Turner, N. J., and Badylak, S. F. (2012). Consequences of Ineffective Decellularization of Biologic Scaffolds on the Host Response. *Biomaterials* 33 (6), 1771–1781. doi:10.1016/j.biomaterials.2011.10.054

Kim, W., Lee, H., Lee, J., Atala, A., Yoo, J. J., Lee, S. J., et al. (2020). Efficient Myotube Formation in 3D Bioprinted Tissue Construct by Biochemical and Topographical Cues. *Biomaterials* 230, 119632. doi:10.1016/j.biomaterials.2019.119632

Lacraz, G., Rouleau, A.-J., Couture, V., Söllrald, T., Drouin, G., Veillette, N., et al. (2015). Increased Stiffness in Aged Skeletal Muscle Impairs Muscle Progenitor Cell Proliferative Activity. *PLOS ONE* 10 (8), e0136217. doi:10.1371/journal.pone.0136217

Lee, H., Ju, Y. M., Kim, I., Elsangeedy, E., Lee, J. H., Yoo, J. J., et al. (2020). A Novel Decellularized Skeletal Muscle-Derived ECM Scaffolding System for *In Situ* Muscle Regeneration. *Methods* 171, 77–85. doi:10.1016/j.ymeth.2019.06.027

Lee, H., Kim, W., Lee, J., Park, K. S., Yoo, J. J., Atala, A., et al. (2021). Self-aligned Myofibers in 3D Bioprinted Extracellular Matrix-Based Construct Accelerate Skeletal Muscle Function Restoration. *Appl. Phys. Rev.* 8 (2), 021405. doi:10.1063/5.0039639

Lee, P.-F., Chau, E., Cabello, R., Yeh, A. T., Sampaio, L. C., Gobin, A. S., et al. (2017). Inverted Orientation Improves Decellularization of Whole Porcine Hearts. *Acta Biomater.* 49, 181–191. doi:10.1016/j.actbio.2016.11.047

Leonard, A., Bertero, A., Powers, J. D., Beussman, K. M., Bhandari, S., Regnier, M., et al. (2018). Afterload Promotes Maturation of Human Induced Pluripotent Stem Cell Derived Cardiomyocytes in Engineered Heart Tissues. *J. Mol. Cell Cardiol.* 118, 147–158. doi:10.1016/j.yjmcc.2018.03.016

Lichtenberg, D., Ahyayauch, H., and Goñi, F. M. (2013). The Mechanism of Detergent Solubilization of Lipid Bilayers. *Biophysical J.* 105 (2), 289–299. doi:10.1016/j.bpj.2013.06.007

Lindsey, M. L., Jung, M., Hall, M. E., and Deleon-Pennell, K. Y. (2018). Proteomic Analysis of the Cardiac Extracellular Matrix: Clinical Research Applications. *Expert Rev. Proteomics* 15 (2), 105–112. doi:10.1080/14789450.2018.1421947

Lu, T.-Y., Lin, B., Kim, J., Sullivan, M., Tobita, K., Salama, G., et al. (2013). Repopulation of Decellularized Mouse Heart with Human Induced Pluripotent Stem Cell-Derived Cardiovascular Progenitor Cells. *Nat. Commun.* 4 (1), 1. doi:10.1038/ncomms3307

Merna, N., Robertson, C., La, A., and George, S. C. (2013). Optical Imaging Predicts Mechanical Properties during Decellularization of Cardiac Tissue. *Tissue Eng. Part C: Methods* 19 (10), 802–809. doi:10.1089/ten.tec.2012.0720

Merritt, E. K., Hammers, D. W., Tierney, M., Suggs, L. J., Walters, T. J., and Farrar, R. P. (2010). Functional Assessment of Skeletal Muscle Regeneration Utilizing Homologous Extracellular Matrix as Scaffolding. *Tissue Eng. Part. A.* 16 (4), 1395–1405. doi:10.1089/ten.TEA.2009.0226

Mesquita, F. C. P., Morrissey, J., Lee, P.-F., Monnerat, G., Xi, Y., Andersson, H., et al. (2021). Cues from Human Atrial Extracellular Matrix Enrich the Atrial Differentiation of Human Induced Pluripotent Stem Cell-Derived Cardiomyocytes. *Biomater. Sci.* 9 (10), 3737–3749. doi:10.1039/d0bm01686a

Methe, K., Bäckdahl, H., Johansson, B. R., Nayakawde, N., Dellgren, G., and Sumitran-Holgersson, S. (2014). An Alternative Approach to Decellularize Whole Porcine Heart. *BioResearch Open Access* 3 (6), 327–338. doi:10.1089/biores.2014.0046

Miersch, C., Stange, K., and Röntgen, M. (2018). Effects of Trypsinization and of a Combined Trypsin, Collagenase, and DNase Digestion on Liberation and *In Vitro* Function of Satellite Cells Isolated from Juvenile Porcine Muscles. In Vitro *Cell.Dev.Biol.-Animal* 54 (6), 406–412. doi:10.1007/s11626-018-0263-5

Miranda, C. M. F. C., Leonel, L. C. P. C., Cañada, R. R., Maria, D. A., Miglino, M. A., Del Sol, M., et al. (2021). Effects of Chemical and Physical Methods on Decellularization of Murine Skeletal Muscles. *Acad. Bras. Ciênc.* 93 (2). doi:10.1590/0001-3765202120190942

Mousavi, A., Mashayekhan, S., Baheiraei, N., and Pourjavadi, A. (2021). Biohybrid Oxidized Alginate/myocardial Extracellular Matrix Injectable Hydrogels with Improved Electromechanical Properties for Cardiac Tissue Engineering. *Int. J. Biol. Macromolecules* 180, 692–708. doi:10.1016/j.ijbiomac.2021.03.097

Naik, A., Griffin, M., Szarko, M., and Butler, P. E. (2020). Optimizing the Decellularization Process of an Upper Limb Skeletal Muscle; Implications for Muscle Tissue Engineering. *Artif. Organs* 44 (2), 178–183. doi:10.1111/aor.13575

Nakamura, T., Shirouzu, T., Nakata, K., Yoshimura, N., and Ushigome, H. (2019). The Role of Major Histocompatibility Complex in Organ Transplantation-Donor Specific Anti-major Histocompatibility Complex Antibodies Analysis Goes to the Next Stage -. *Ijms* 20 (18), 4544. doi:10.3390/ijms20184544

Nakayama, K. H., Alcazar, C., Yang, G., Quarta, M., Paine, P., Doan, L., et al. (2018). Rehabilitative Exercise and Spatially Patterned Nanofibrillar Scaffolds Enhance Vascularization and Innervation Following Volumetric Muscle Loss. *Npj Regen. Med.* 3 (1), 1. doi:10.1038/s41536-018-0054-3

Nakayama, K. H., Joshi, P. A., Lai, E. S., Gujar, P., Joubert, L.-M., Chen, B., et al. (2015). Bilayered Vascular Graft Derived from Human Induced Pluripotent Stem Cells with Biomimetic Structure and Function. *Regenerative Med.* 10 (6), 745–755. doi:10.2217/rme.15.45

Nakayama, K. H., Quarta, M., Paine, P., Alcazar, C., Karakikes, I., Garcia, V., et al. (2019). Treatment of Volumetric Muscle Loss in Mice Using Nanofibrillar Scaffolds Enhances Vascular Organization and Integration. *Commun. Biol.* 2 (1), 170. doi:10.1038/s42003-019-0416-4

Nakayama, K. H., Surya, V. N., Gole, M., Walker, T. W., Yang, W., Lai, E. S., et al. (2016). Nanoscale Patterning of Extracellular Matrix Alters Endothelial Function under Shear Stress. *Nano Lett.* 16 (1), 410–419. doi:10.1021/acs.nanolett.5b04028

Nicolas, J., Magli, S., Rabbachin, L., Sampaolesi, S., Nicotra, F., and Russo, L. (2020). 3D Extracellular Matrix Mimics: Fundamental Concepts and Role of

Materials Chemistry to Influence Stem Cell Fate. *Biomacromolecules* 21 (6), 1968–1994. doi:10.1021/acs.biomac.0c00045

Ostrovidov, S., Hosseini, V., Ahadian, S., Fujie, T., Parthiban, S. P., Ramalingam, M., et al. (2014). Skeletal Muscle Tissue Engineering: Methods to Form Skeletal Myotubes and Their Applications. *Tissue Eng. B: Rev.* 20 (5), 403–436. doi:10.1089/ten.teb.2013.0534

Ott, H. C., Matthiesen, T. S., Goh, S.-K., Black, L. D., Kren, S. M., Netoff, T. I., et al. (2008). Perfusion-decellularized Matrix: Using Nature's Platform to Engineer a Bioartificial Heart. *Nat. Med.* 14 (2), 213–221. doi:10.1038/nm1684

Ozlu, B., Ergin, M., Budak, S., Tunali, S., Yildirim, N., and Erisken, C. (2019). A Bioartificial Rat Heart Tissue: Perfusion Decellularization and Characterization. *Int. J. Artif. Organs* 42 (12), 757–764. doi:10.1177/0391398819863434

Patel, K. H., Dunn, A. J., Talovic, M., Haas, G. J., Marcinczyk, M., Elmashhady, H., et al. (2019). Aligned Nanofibers of Decellularized Muscle ECM Support Myogenic Activity in Primary Satellite Cells *In Vitro*. *Biomed. Mater.* 14 (3), 035010. doi:10.1088/1748-605X/ab0b06

Patel, K. H., Talovic, M., Dunn, A. J., Patel, A., Vendrell, S., Schwartz, M., et al. (2020). Aligned Nanofibers of Decellularized Muscle Extracellular Matrix for Volumetric Muscle Loss. *J. Biomed. Mater. Res.* 108 (6), 2528–2537. doi:10.1002/jbm.b.34584

Perea-Gil, I., Gálvez-Montón, C., Prat-Vidal, C., Jorba, I., Segú-Vergés, C., Roura, S., et al. (2018). Head-to-head Comparison of Two Engineered Cardiac Grafts for Myocardial Repair: From Scaffold Characterization to Pre-clinical Testing. *Sci. Rep.* 8 (1), 1. doi:10.1038/s41598-018-25115-2

Piccoli, M., Trevisan, C., Maghin, E., Franzin, C., and Pozzobon, M. (2017). *Mouse Skeletal Muscle Decellularization*. New York: Springer, 87–93. doi:10.1007/7651_2017_28

Porzionato, A., Sfriso, M., Pontini, A., Macchi, V., Petrelli, L., Pavan, P., et al. (2015). Decellularized Human Skeletal Muscle as Biologic Scaffold for Reconstructive Surgery. *Ijms* 16 (12), 14808–14831. doi:10.3390/ijms160714808

Puri, S., Coulson-Thomas, Y. M., Gesteira, T. F., and Coulson-Thomas, V. J. (2020). Distribution and Function of Glycosaminoglycans and Proteoglycans in the Development, Homeostasis and Pathology of the Ocular Surface. *Front. Cel. Dev. Biol.* 8, 731. doi:10.3389/fcell.2020.00731

Quake, S. (2011). DNA Mismatch Reveals Organ Rejection [Online]. *Nature* doi:10.1038/news.2011.189

Raffa, P., Scattolini, V., Gerli, M. F. M., Perin, S., Cui, M., De Coppi, P., et al. (2020). Decellularized Skeletal Muscles Display Neurotrophic Effects in Three-Dimensional Organotypic Cultures. *STEM CELLS Translational Med.* 9 (10), 1233–1243. doi:10.1002/sctm.20-0090

Rando, T. A., and Ambrosio, F. (2018). Regenerative Rehabilitation: Applied Biophysics Meets Stem Cell Therapeutics. *Cell Stem Cell* 22 (3), 306–309. doi:10.1016/j.stem.2018.02.003

Reyna, W. E., Pichika, R., Ludvig, D., and Perreault, E. J. (2020). Efficiency of Skeletal Muscle Decellularization Methods and Their Effects on the Extracellular Matrix. *J. Biomech.* 110, 109961. doi:10.1016/j.jbiomech.2020.109961

Robbins, E. R., Pins, G. D., Laflamme, M. A., and Gaudette, G. R. (2020). Creation of a Contractile Biomaterial from a Decellularized Spinach Leaf without ECM Protein Coating: An *In Vitro* Study. *J. Biomed. Mater. Res.* 108 (10), 2123–2132. doi:10.1002/jbm.a.36971

Robertson, M. J., Dries-Devlin, J. L., Kren, S. M., Burchfield, J. S., and Taylor, D. A. (2014). Optimizing Recellularization of Whole Decellularized Heart Extracellular Matrix. *PLoS ONE* 9 (2), e90406. doi:10.1371/journal.pone.0090406

Sarig, U., Sarig, H., de-Berardinis, E., Chaw, S.-Y., Nguyen, E. B. V., Ramanujam, V. S., et al. (2016). Natural Myocardial ECM Patch Drives Cardiac Progenitor Based Restoration Even after Scarring. *Acta Biomater.* 44, 209–220. doi:10.1016/j.actbio.2016.08.031

Schwan, J., Kwaczala, A. T., Ryan, T. J., Bartulos, O., Ren, Y., Sewanan, L. R., et al. (2016). Anisotropic Engineered Heart Tissue Made from Laser-Cut Decellularized Myocardium. *Sci. Rep.* 6 (1), 32068. doi:10.1038/srep32068

Shah, M., Kc, P., Copeland, K. M., Liao, J., and Zhang, G. (2018). A Thin Layer of Decellularized Porcine Myocardium for Cell Delivery. *Sci. Rep.* 8 (1), 1. doi:10.1038/s41598-018-33946-2

Shapira-Schweitzer, K., and Seliktar, D. (2007). Matrix Stiffness Affects Spontaneous Contraction of Cardiomyocytes Cultured within a PEGylated Fibrinogen Biomaterial. *Acta Biomater.* 3 (1), 33–41. doi:10.1016/j.actbio.2006.09.003

Shapiro, L., Elsangeedy, E., Lee, H., Atala, A., Yoo, J. J., Lee, S. J., et al. (2019). *In Vitro* evaluation of Functionalized Decellularized Muscle Scaffold for *In Situ* Skeletal Muscle Regeneration. *Biomed. Mater.* 14 (4), 045015. doi:10.1088/1748-605x/ab229d

Sharma, M., Kumar, R., Sharma, S., Thomas, B., Kapatia, G., Singh, G., et al. (2019). *Sustained Exposure to Trypsin Causes Cells to Transition into a State of Reversible Stemness that Is Amenable to Transdifferentiation*. Cold Spring Harbor, NY: Cold Spring Harbor Laboratory.

Silva, A. C., Rodrigues, S. C., Caldeira, J., Nunes, A. M., Sampaio-Pinto, V., Resende, T. P., et al. (2016). Three-dimensional Scaffolds of Fetal Decellularized Hearts Exhibit Enhanced Potential to Support Cardiac Cells in Comparison to the Adult. *Biomaterials* 104, 52–64. doi:10.1016/j.biomaterials.2016.06.062

Singelyn, J. M., Sundaramurthy, P., Johnson, T. D., Schup-Magoffin, P. J., Hu, D. P., Faulk, D. M., et al. (2012). Catheter-deliverable Hydrogel Derived from Decellularized Ventricular Extracellular Matrix Increases Endogenous Cardiomyocytes and Preserves Cardiac Function post-myocardial Infarction. *J. Am. Coll. Cardiol.* 59 (8), 751–763. doi:10.1016/j.jacc.2011.10.888

Skoog, S. A., Kumar, G., Narayan, R. J., and Goering, P. L. (2018). Biological Responses to Immobilized Microscale and Nanoscale Surface Topographies. *Pharmacol. Ther.* 182, 33–55. doi:10.1016/j.pharmthera.2017.07.009

Smoak, M. M., Han, A., Watson, E., Kishan, A., Grande-Allen, K. J., Cosgriff-Hernandez, E., et al. (2019). Fabrication and Characterization of Electrospun Decellularized Muscle-Derived Scaffolds. *Tissue Eng. Part C: Methods* 25 (5), 276–287. doi:10.1089/ten.tec.2018.0339

Soto-Gutierrez, A., Zhang, L., Medberry, C., Fukumitsu, K., Faulk, D., Jiang, H., et al. (2011). A Whole-Organ Regenerative Medicine Approach for Liver Replacement. *Tissue Eng. Part C: Methods* 17 (6), 677–686. doi:10.1089/ten.tec.2010.0698

Spector, I., Shochet, N. R., Kashman, Y., and Groweiss, A. (1983). Latrunculins: Novel Marine Toxins that Disrupt Microfilament Organization in Cultured Cells. *Science* 219 (4584), 493–495. doi:10.1126/science.6681676

Suh, T. C., Amanah, A. Y., and Gluck, J. M. (2020). Electrospun Scaffolds and Induced Pluripotent Stem Cell-Derived Cardiomyocytes for Cardiac Tissue Engineering Applications. *Bioengineering* 7 (3), 105. doi:10.3390/bioengineering7030105

Talovic, M., Patel, K., Schwartz, M., Madsen, J., and Garg, K. (2019). Decellularized Extracellular Matrix Gelloids Support Mesenchymal Stem Cell Growth and Function *In Vitro*. *J. Tissue Eng. Regen. Med.* 13 (10), 1830–1842. doi:10.1002/term.2933

Tsui, J. H., Leonard, A., Camp, N. D., Long, J. T., Nawas, Z. Y., Chavanachat, R., et al. (2021). Tunable Electroconductive Decellularized Extracellular Matrix Hydrogels for Engineering Human Cardiac Microphysiological Systems. *Biomaterials* 272, 120764. doi:10.1016/j.biomaterials.2021.120764

Ungerleider, J. L., Johnson, T. D., Rao, N., and Christman, K. L. (2015). Fabrication and Characterization of Injectable Hydrogels Derived from Decellularized Skeletal and Cardiac Muscle. *Methods* 84, 53–59. doi:10.1016/j.ymeth.2015.03.024

Urciuolo, A., Urbani, L., Perin, S., Maghsoudlou, P., Scottoni, F., Gjinovci, A., et al. (2018). Decellularised Skeletal Muscles Allow Functional Muscle Regeneration by Promoting Host Cell Migration. *Sci. Rep.* 8 (1), 8398. doi:10.1038/s41598-018-26371-y

Wainwright, J. M., Czajka, C. A., Patel, U. B., Freytes, D. O., Tobita, K., Gilbert, T. W., et al. (2010). Preparation of Cardiac Extracellular Matrix from an Intact Porcine Heart. *Tissue Eng. Part C: Methods* 16 (3), 525–532. doi:10.1089/ten.tec.2009.0392

Walimbe, T., and Panitch, A. (2020). Proteoglycans in Biomedicine: Resurgence of an Underexploited Class of ECM Molecules. *Front. Pharmacol.* 10 (1661), 1661. doi:10.3389/fphar.2019.01661

Wang, Q., Yang, H., Bai, A., Jiang, W., Li, X., Wang, X., et al. (2016). Functional Engineered Human Cardiac Patches Prepared from Nature's Platform Improve Heart Function after Acute Myocardial Infarction. *Biomaterials* 105, 52–65. doi:10.1016/j.biomaterials.2016.07.035

Wang, X., Pierre, V., Liu, C., Senapati, S., Park, P. S.-H., and Senyo, S. E. (2021). Exogenous Extracellular Matrix Proteins Decrease Cardiac Fibroblast Activation in Stiffening Microenvironment through CAPG. *J. Mol. Cell Cardiol.* 159, 105–119. doi:10.1016/j.yjmcc.2021.06.001

Wang, X., Senapati, S., Akinbote, A., Gnanasambandam, B., Park, P. S.-H., and Senyo, S. E. (2020). Microenvironment Stiffness Requires Decellularized Cardiac Extracellular Matrix to Promote Heart Regeneration in the Neonatal Mouse Heart. *Acta Biomater.* 113, 380–392. doi:10.1016/j.actbio.2020.06.032

Wang, Z., Long, D. W., Huang, Y., Chen, W. C. W., Kim, K., and Wang, Y. (2019). Decellularized Neonatal Cardiac Extracellular Matrix Prevents Widespread Ventricular Remodeling in Adult Mammals after Myocardial Infarction. *Acta Biomater.* 87, 140–151. doi:10.1016/j.actbio.2019.01.062

Wilgus, T. A. (2012). Growth Factor-Extracellular Matrix Interactions Regulate Wound Repair. *Adv. Wound Care* 1 (6), 249–254. doi:10.1089/wound.2011.0344

Williams, C., Quinn, K. P., Georgakoudi, I., and Black, L. D. (2014). Young Developmental Age Cardiac Extracellular Matrix Promotes the Expansion of Neonatal Cardiomyocytes *In Vitro*. *Acta Biomater.* 10 (1), 194–204. doi:10.1016/j.actbio.2013.08.037

Wolf, M. T., Daly, K. A., Reing, J. E., and Badylak, S. F. (2012). Biologic Scaffold Composed of Skeletal Muscle Extracellular Matrix. *Biomaterials* 33 (10), 2916–2925. doi:10.1016/j.biomaterials.2011.12.055

World Health Organization, WHO (2021a). *Cardiovascular Diseases (CVDs) [Online]*. Available at: https://www.who.int/news-room/fact-sheets/detail/cardiovascular-diseases-(cvds (Accessed December 3, 2021).

World Health Organization, WHO (2021b). *Musculoskeletal Conditions [Online]*. Available at: https://www.who.int/news-room/fact-sheets/detail/musculoskeletal-conditions (Accessed December 3, 2021).

Xu, X., Sharma, P., Shu, S., Lin, T.-S., Ciais, P., Tubiello, F. N., et al. (2021). Global Greenhouse Gas Emissions from Animal-Based Foods Are Twice Those of Plant-Based Foods. *Nat. Food* 2 (9), 724–732. doi:10.1038/s43016-021-00358-x

Yelin, E. H., Cisternas, M., and Watkins-Castillo, S. I. (2021). *The Burden of Muskuloskeletal Diseases in the United States [Online]*. Available at: https://www.boneandjointburden.org/fourth-edition/if1/direct-costs (Accessed December 3, 2021).

Yingchoncharoen, T., Agarwal, S., Popović, Z. B., and Marwick, T. H. (2013). Normal Ranges of Left Ventricular Strain: a Meta-Analysis. *J. Am. Soc. Echocardiography* 26 (2), 185–191. doi:10.1016/j.echo.2012.10.008

Zhang, J., Hu, Z. Q., Turner, N. J., Teng, S. F., Cheng, W. Y., Zhou, H. Y., et al. (2016). Perfusion-decellularized Skeletal Muscle as a Three-Dimensional Scaffold with a Vascular Network Template. *Biomaterials* 89, 114–126. doi:10.1016/j.biomaterials.2016.02.040

Zhang, J., Zhu, W., Radisic, M., and Vunjak-Novakovic, G. (2018). Can We Engineer a Human Cardiac Patch for Therapy? *Circ. Res.* 123 (2), 244–265. doi:10.1161/circresaha.118.311213

Conflict of Interest: The authors declare that the research was conducted in the absence of any commercial or financial relationships that could be construed as a potential conflict of interest.

Publisher's Note: All claims expressed in this article are solely those of the authors and do not necessarily represent those of their affiliated organizations, or those of the publisher, the editors and the reviewers. Any product that may be evaluated in this article, or claim that may be made by its manufacturer, is not guaranteed or endorsed by the publisher.

Copyright © 2022 Tan, Helms and Nakayama. This is an open-access article distributed under the terms of the Creative Commons Attribution License (CC BY). The use, distribution or reproduction in other forums is permitted, provided the original author(s) and the copyright owner(s) are credited and that the original publication in this journal is cited, in accordance with accepted academic practice. No use, distribution or reproduction is permitted which does not comply with these terms.

frontiers in Bioengineering and Biotechnology

ORIGINAL RESEARCH
published: 09 March 2022
doi: 10.3389/fbioe.2022.832178

Novel Decellularization Method for Tissue Slices

Maria Narciso[1,2], *Anna Ulldemolins*[1], *Constança Júnior*[1,2], *Jorge Otero*[1,2,3], *Daniel Navajas*[1,2,3], *Ramon Farré*[1,3,4], *Núria Gavara*[1,2] *and Isaac Almendros*[1,3,4]*

[1]*Unitat de Biofísica i Bioenginyeria, Facultat de Medicina i Ciències de la Salut, Universitat de Barcelona, Barcelona, Spain,* [2]*The Institute for Bioengineering of Catalonia (IBEC), The Barcelona Institute of Science and Technology, Barcelona, Spain,* [3]*CIBER de Enfermedades Respiratorias, Madrid, Spain,* [4]*Institut d'Investigacions Biomèdiques August Pi i Sunyer, Barcelona, Spain*

Decellularization procedures have been developed and optimized for the entire organ or tissue blocks, by either perfusion of decellularizing agents through the tissue's vasculature or submerging large sections in decellularizing solutions. However, some research aims require the analysis of native as well as decellularized tissue slices side by side, but an optimal protocol has not yet been established to address this need. Thus, the main goal of this work was to develop a fast and efficient decellularization method for tissue slices—with an emphasis on lung—while attached to a glass slide. To this end, different decellularizing agents were compared for their effectiveness in cellular removal while preserving the extracellular matrix. The intensity of DNA staining was taken as an indicator of remaining cells and compared to untreated sections. The presence of collagen, elastin and laminin were quantified using immunostaining and signal quantification. Scaffolds resulting from the optimized protocol were mechanically characterized using atomic force microscopy. Lung scaffolds were recellularized with mesenchymal stromal cells to assess their biocompatibility. Some decellularization agents (CHAPS, triton, and ammonia hydroxide) did not achieve sufficient cell removal. Sodium dodecyl sulfate (SDS) was effective in cell removal (1% remaining DNA signal), but its sharp reduction of elastin signal (only 6% remained) plus lower attachment ratio (32%) singled out sodium deoxycholate (SD) as the optimal treatment for this application (6.5% remaining DNA signal), due to its higher elastin retention (34%) and higher attachment ratio (60%). Laminin and collagen were fully preserved in all treatments. The SD decellularization protocol was also successful for porcine and murine (mice and rat) lungs as well as for other tissues such as the heart, kidney, and bladder. No significant mechanical differences were found before and after sample decellularization. The resulting acellular lung scaffolds were shown to be biocompatible (98% cell survival after 72 h of culture). This novel method to decellularize tissue slices opens up new methodological possibilities to better understand the role of the extracellular matrix in the context of several diseases as well as tissue engineering research and can be easily adapted for scarce samples like clinical biopsies.

Keywords: decellularization, bioscaffold recellularization, biocompatibility, extracellular matrix, tissue slices, lung

OPEN ACCESS

Edited by:
Kamal Hany Hussein, Assiut University, Egypt

Reviewed by:
Anna Guller, Macquarie University, Australia
Bruce Alan Bunnell, University of North Texas Health Science Center, United States

***Correspondence:**
Isaac Almendros
isaac.almendros@ub.edu

Specialty section:
This article was submitted to Biomaterials, a section of the journal Frontiers in Bioengineering and Biotechnology

Received: *09 December 2021*
Accepted: *09 February 2022*
Published: *09 March 2022*

Citation:
Narciso M, Ulldemolins A, Júnior C, Otero J, Navajas D, Farré R, Gavara N and Almendros I (2022) Novel Decellularization Method for Tissue Slices. Front. Bioeng. Biotechnol. 10:832178. doi: 10.3389/fbioe.2022.832178

1 INTRODUCTION

The extracellular matrix (ECM) plays an important role by regulating cell behavior through structural and biochemical stimulation. The ECM is composed of more than 300 core structural components (Burgstaller et al., 2017) that provide physical and chemical cues that regulate essential cellular mechanisms (Gattazzo et al., 2014), including proliferation, migration and differentiation. Overall, the ECM is divided into two major compartments: the interstitial ECM and the basement membrane. The interstitial ECM is in the intercellular spaces and is composed mostly of fibrous proteins and polysaccharides, most predominantly collagen type I and III, elastin, and fibronectin. The basement membrane is made up of sheets of deposition of ECM components—mainly collagen type IV and laminins—that are located under epithelial and endothelial cells (Pompili et al., 2021). These two layers make up the "core matrisome." However, the ECM has other components such as ECM-affiliated proteins and secreted factors that are typically removed during decellularization and thus less frequently characterized (Hynes and Naba 2012). The study of the ECM and its characteristics yields an important understanding of the complex interactions between cells and their microenvironment, which plays a pivotal role in various diseases including cancer and fibrosis (Rendin et al., 2019; Wishart et al., 2020; Júnior et al., 2021). Accordingly, decellularized ECM scaffolds have great potential for tissue engineering and regenerative medicine. In fact, decellularized tissues can be used for the generation of ECM hydrogels (Falcones et al., 2021), for the recellularization of whole acellular organs (Ohata and Ott 2020), as well as applications in tissue regeneration (Zhu et al., 2019). Thus, it is unsurprising the growing interest to work on physiomimetic tissue scaffolds by decellularizing different types of tissues (Mendibil et al., 2020).

To remove cells from their ECM, several strategies can be employed (Mendibil et al., 2020) by using physical, chemical, enzymatic or a combination of approaches. Physical strategies include freeze/thawing cycles, which induce crystals in the matrix disrupting the cell membrane, as well as agitation, which is commonly used in conjunction with another/s decellularizing agent/s facilitating cell lysis. Chemical strategies include detergents, such as Sodium Dodecyl Sulfate (SDS) or Sodium Deoxycholate (SD), that solubilize the cell membrane and hypertonic or hypotonic solutions, that will cause cell disruption by osmotic shock. Finally, enzymatic approaches can target the adhesion of cells to the ECM, such as the combination of trypsin with EDTA (ethylenediaminetetraacetic acid) or target the nuclear material of the cell, such as with deoxyribonuclease (DNAse). In this context, each decellularizing agent can affect differently each specific ECM components. In fact, to assess the quality of the resulting scaffold it is required to analyze the effects of the decellularizing agent on the ECM components. At times, only components of the interstitial ECM are analyzed, like collagen type I and elastin (O'Neill et al., 2013a; Balestrini et al., 2015; Alshaikh et al., 2020). However, the evaluation of the basement membrane is of paramount importance especially for tissue engineering and cell culture applications since these components heavily influence cell adhesion and differentiation (Rasmussen and Karsdal 2016). The most analyzed basement membrane components include collagen type IV and laminins (Maghsoudlou et al., 2013; Zhang et al., 2016).

The available decellularization protocols have important limitations. Most of them require prolonged periods, taking from 6–7 h (Rosmark et al., 2018) to several days (Wishart et al., 2020; Wüthrich et al., 2020). Additionally, most of the available methods fail in the preservation of some ECM components. For instance, significant decreases in elastin (Maghsoudlou et al., 2013; Alshaikh et al., 2020), collagen (Hill et al., 2015; Alshaikh et al., 2020), glycosaminoglycans (Mendoza-Novelo et al., 2011; Lü et al., 2014), laminins (Hill et al., 2015; Wüthrich et al., 2020) and proteoglycans (Hill et al., 2015; Calle et al., 2016) have been described. In addition to these limitations, the current protocols are still not particularly flexible or accessible. Most decellularization procedures are suited for

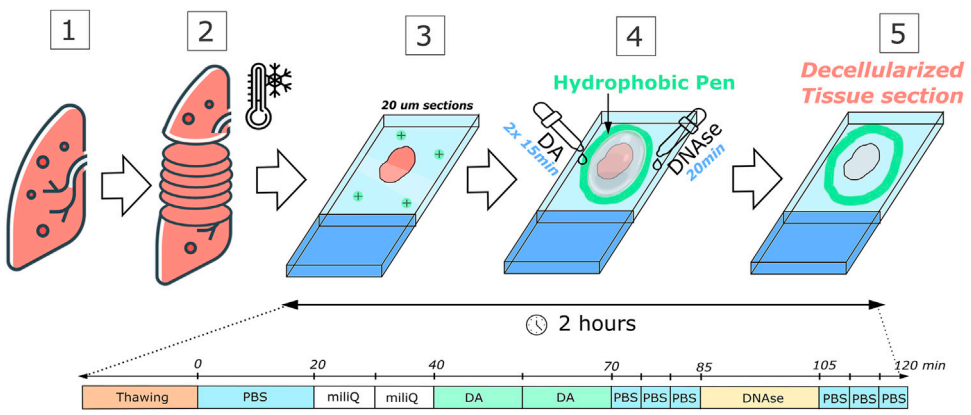

FIGURE 1 | Schematic of the novel decellularization method for a lung sample. (1) Organs are harvested and stored at −80°C and embedded in OCT; (2) then they are cryosectioned into 20 µm sections and (3) deposited onto positively charged glass slides; (4) Decellularization is performed through a series of washes and rinses, including the decellularizing agent (DA) and a Deoxyribonuclease I (DNAse) incubation. After carefully removing the reagents with PBS, a fully decellularized section is produced in 2 h (5). MilliQ is a form of ultrapurified water.

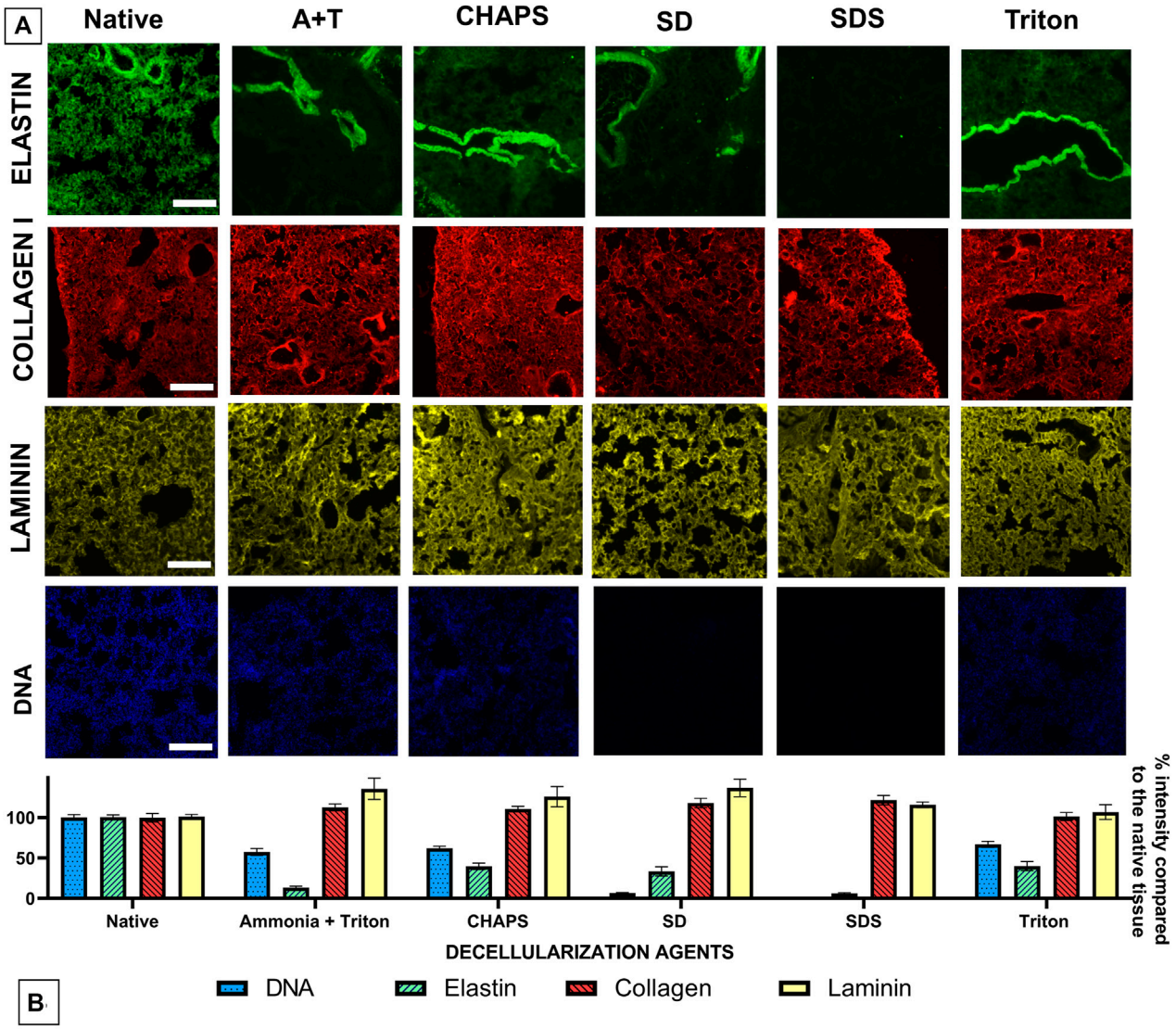

Decellularizing agent	Sample attachment, %	Native DNA signal, %
(None—native)	100±0	100±24
Ammonia + Triton	100±0	57±31
CHAPS	82±12	62±22
SD	60±23	6.5±5.8
SDS	32±22	1±0.5
Triton	100±0	67±28
Trypsin	0±0	-

Decellularizing agent	Tissue	Sample attachment, %
SD	Bladder	100±0
	Kidney	100±0
	Heart	100±0
	Lungs	60±23

FIGURE 2 | (A) Staining and signal quantification of 20 µm lung sections from mice for nuclei, elastin, type I collagen, and laminin. Lung sections had been previously subjected to five different decellularization treatments (Ammonia + Triton, CHAPS, SD, SDS, and Triton). Laminin and elastin fluorescent images were changed from the original red color to yellow and green respectively for easier image readability. Native tissue's signal was normalized to 100% Scale bar = 200 µm. **(B)** Table describing the attachment ratio of tissue slices from the glass slide for each decellularization treatment (left) and Table describing the attachment ratio of different tissues treated with SD (right). Data are mean ± SEM.

decellularizing a whole organ or thick sections of an organ (or blocks). However, this type of protocol would not be useful for many experimental conditions as is the case for small clinical biopsies. Indeed, this type of sample is scarce and cannot be decellularized by accessing the tissue's vasculature. Furthermore, the full biopsy cannot often be decellularized since it is also required for later histopathological testing. Other experimental setups might require consecutive native and acellular sections of the same individual. This is the case for studies on cancer samples where the tumor location and inner structures must be identified

prior to decellularization. For early-stage tumors especially, this is of paramount importance as the cancer cells are removed during decellularization and its location could not be pinpointed. As no current methods have explored the decellularization of glass-attached thin tissue sections (under 100 μm), a novel protocol that allows for the study of the exact location before and after decellularization is needed to fill this gap.

In this study, we set out to develop a novel decellularization method where a thin tissue section is kept attached to a glass slide allowing for "*in situ*" decellularization without removing the sample from a microscopic stage. This method is significantly faster and less wasteful than other available methods while maintaining the mechanical properties of the sample and being suited for cell culture applications. Our findings show that this method is highly versatile and applicable to tissues of different animal origins and from different organs, such as the bladder, heart, and kidney. Additionally, it provides the option to study the same tissue section before and after decellularization, which is invaluable for studies of certain pathologies and of scarce or valuable clinical samples.

2 MATERIALS AND METHODS

2.1 Organ Procurement and Sample Preparation

This work was approved by the Institutional Committee of Universitat de Barcelona and the Animal Experimentation Committee of regional authorities (Generalitat de Catalunya, OB 168/19 and 10972). The lungs were obtained from male C57BL/6J mice (10 weeks old; Charles River Laboratories, Saint Germain sur L'arbresle, France) and male Sprague-Dawley rats (body weight ~ 300 g Charles River Laboratories, Saint Germain sur L'arbresle, France). Bladders, hearts, and kidneys were harvested from the adult mice and embedded in Optimum Cutting Temperature compound, OCT (Tissue-Tek, Sakura, Torrance, CA, United States) and immediately stored at −80°C. Porcine lungs were obtained from the local butcher and a small portion was embedded in OCT. Mice lung samples were sectioned at 20 and 100 μm using a cryostat, with a working temperature of −24°C. All other samples were sectioned only at 20 μm thickness. Slices were deposited onto a positively charged glass slide (Superfrost Plus; Thermo Fischer Scientific) and air-dried for 15 min before being stored at −80°C until further use. Before decellularization, 20 μm thick sections were thawed are room temperature for 20 min and 100 μm thick sections were thawed for 40 min. It is important to thaw the sample completely for increased attachment. The freeze-thaw cycle already functions as an initial step of decellularization (Gilpin and Yang 2017).

2.2 Decellularization Protocol and Methods Comparison

Before decellularization, the area surrounding each sample was traced with a liquid repellent slide marker pen (or hydrophobic pen) to better control and reduce the volume of reagents needed (**Figure 1**). Acellular sections were produced by consecutive washes and rinses of the sliced section with different solutions while still firmly attached to the glass slide.

All decellularizing protocols studied in this work followed the same schedule. For 20 μm sections, an initial 20-min PBS wash to remove the OCT from the sample. To cause an osmotic shock and disrupt the cellular membrane, the next step was to apply two consecutive 10-min washes with ultrapure water. Subsequently, the decellularizing agent was incubated twice for 15 min intervals to dissolve the cellular membrane and detach the cells from the matrix. The following step was to remove the decellularizing agent with three 5-min washes of PBS. A 20-min incubation with DNAse I solution (0.3 mg/ml, 5 mM $MgCl_2$, 5 mM $CaCl_2$ in 1 mM Tris-HCl) was carried out to remove DNA fragments. Finally, 5-min washes (x3) of PBS were performed to remove the DNAse I solution. For 100 μm sections, DNAse I solution was incubated for 40 min at 37°C, for optimal enzymatic activity.

Six decellularizing agents (DAs) were tested and compared. The DAs and their concentrations were adapted from existing decellularization protocols, and were as follows:

Method 1: Ammonium Hydroxide 0.5% + Triton 0.1%, based on (Ng et al., 2019);
Method 2: CHAPS 0.5%, based on (Rosmark et al., 2018);
Method 3: Sodium Deoxycholate (SD) 2%, based on (Xiong et al., 2015);
Method 4: Sodium Dodecyl Sulfate (SDS) 1%, based on (Jorba et al., 2019);
Method 5: Triton X-100 1%, based on (Mendoza-Novelo et al., 2011);
Method 6: Trypsin 0.05% + EDTA 0.02%, based on (Schenke-Layland et al., 2003);

Detailed information about the existing decellularization protocols can be found in **Supplementary Table S1**.

2.3 Attachment to the Glass Slide

For this decellularization method, one key factor is the attachment of the sample to the glass slide throughout the decellularization protocol. Thus, we calculated the percentage of sample attachment (number of samples that remained attached after the treatment/total number of samples tested) × 100%. It is a visual observation as the sample is clearly detached and removed from the glass slide during decellularization. Five decellularization experiments were conducted and samples were counted before and after decellularization. For each experiment, 5, 6 sections were used per treatment.

2.4 Immunofluorescence, DNA and Histological Staining

Both cellular and acellular mice lung sections from Methods 1–5 were stained for laminin, type I collagen, elastin, and DNA to determine the effects of the decellularization protocol on the matrix proteins as well as the cellular material and DNA. These proteins were specifically chosen because they are three major components of the ECM: collagen and elastin can provide information on the interstitial ECM and laminin on the basement membrane. For native sections

where the decellularization protocol was not followed, immunofluorescent staining was performed after consecutive washes of PBS to remove the OCT. For decellularized sections, the staining protocol was performed immediately after the decellularization procedure described above. The tissue was fixed using 4% paraformaldehyde (PFA) for 10 min at room temperature (RT). Samples were then blocked using a buffer composed of 10% fetal bovine serum (FBS) and supplemented with 3% bovine serum albumin (BSA) for 1 h at RT. Primary antibodies against elastin (rabbit anti elastin, BioNova, 1:100), type I collagen (rabbit anti-collagen type I, Abcam, 1:100), and laminin (rabbit anti laminin, Thermo Fisher Scientific, Waltham, MA, 1:100) were incubated in the same formulation of the blocking buffer overnight at 4°C and constant agitation (80 rpm). Sections were then rinsed three times with the blocking buffer. The secondary antibody (goat anti-rabbit Cy3, Thermo Fischer, 1:200) was incubated at a 1:200 dilution in the blocking buffer for 2 h, at 37°C and constant agitation (80 rpm). Three 15 min rinses with PBS were performed to eliminate the unbound secondary antibodies. DNA of cellular and acellular samples was stained by incubation with Hoechst 33342 (Thermo Fisher Scientific)—for 20 min at 80 rpm in an orbital shaker followed by three 5-min PBS washes to remove excess staining with the same agitation settings. The Hoechst staining concentration was carried out following the manufacturer's instructions. Finally, samples were mounted in Fluoromount mounting media (Thermo Fisher Scientific) and stored at 4°C. For each experiment, laminin, type I collagen, and elastin staining was performed in consecutive lung sections. The color of the laminin and elastin fluorescent images was changed after image acquisition from red to yellow and green respectively, for easier figure readability. Brightness and contrast were improved for the same purpose. Both cellular and acellular mice lung sections from Methods 1–5 were stained using Picro-Sirius Red Stain Kit (ScyTek Laboratories, US) for collagen type I and III presence and Hematoxylin and Eosin (PanReac Applichem) to assess the presence of the nuclei.

2.5 Mechanical Testing by Atomic Force Microscopy

To assess mechanical changes in the tissue before and after decellularization, an Atomic Force Microscope (AFM) was used to measure the stiffness, viscosity and force adhesion of the samples. In a custom-built AFM system, the cantilever was displaced in 3D with nanometer resolution employing piezo actuators coupled to strain gauge sensors (Physik Instrumente, Germany) to measure the vertical displacement of the cantilever. The deflection of the cantilever was measured with a quadrant photodiode (S4349, Hamamatsu, Japan). The cantilevers employed had a nominal spring constant value of 0.03 N/m and a silicon oxide bead with a 4.5 μm diameter attached to its end (Novascan Technologies, IA).

The lung ECM was probed while submersed in PBS at RT. Three lung sections from different mice were measured using AFM before and after decellularization using the SD-based protocol. Before the measurements, a small region in the lung parenchyma was selected and marked with a pen. With the visual assistance of the optical microscope, the tip was positioned macroscopically over the region of interest of the lung sample. Up to 20 randomly selected locations were indented within the delineated region before decellularization and the same was performed after decellularization within the same region. Only alveolar structures were considered by excluding airways, blood vessels and the pleural region.

The deflection and displacement of the cantilever were recorded as the cantilever descended and contacted the sample surface at constant speed up to a maximum loading force, with a ramp amplitude of 15 μm and frequency of 1 Hz. To calculate the model's parameters, each curve was fitted through a custom MATLAB code (MATLAB, The MathWorks Inc. MA, United States). The Young's modulus fitting was performed using the approaching curve and fitting the appropriate tip-sample contact model to the force-indentation curve (Jorba et al., 2017). Viscosity measurements were computed by following the model described in (Rebelo et al., 2013) and force adhesion was obtained by computing the minimum of the retracting curves. All mechanical values were obtained by computing the mean values of the five curves recorded consecutively at each point.

2.6 Cell Culture

Primary human Bone Marrow-Derived Mesenchymal Stromal Cells (hBM-MSCs) (PCS-500-012, ATCC) were cultured in Mesenchymal Stromal Cell Basal Medium (PCS-500-030, ATCC) following manufacturer's instructions at 37°C in air with 5% CO_2 and 95% relative humidity. Cells from passages 3–6 were used for experiments.

2.7 Biocompatibility Assay

After decellularization, the 20 μm-thick and 100 μm-thick scaffolds were incubated for 2 h with a peracetic acid solution (269336, Sigma-Aldrich) 0, 1% (v/v) in 4% ethanol for sterilization. Subsequently, they were washed with PBS (11593377, Gibco) and $5{\cdot}10^4$ cells/cm^2 hBM-MSCs were seeded on top of the lung scaffolds. Control cultures were seeded on conventional culture plastic flasks and maintained in parallel with the same conditions. After 24, 48, and 72 h of recellularization, samples were stained using the LIVE/DEAD Viability/Cytotoxicity kit (L-3224, Invitrogen). Calcein-AM was used to indicate live cells (green), and ethidium homodimer-1 was used to indicate dead cells (red) as previously described (Bonenfant et al., 2013; O'Neill et al., 2013b; Syed et al., 2014). After 72 h, F-Actin was stained in the 100 μm scaffolds (phalloidin, Thermo Scientific, Waltham, MA, United States) and visualized by a confocal microscope. The results were obtained by counting the number of live cells from five independent biocompatibility assays.

2.8 Imaging and Decellularization Quantification

Epifluorescent images of the tissue sections were acquired with a Leica SP5 inverted microscope equipped with a CCD camera (C9100, Hamamatsu Photonics K.K. Hamamatsu, Japan) and using a ×10 and ×20 Plan Fluor objective (Nikon). For 3D images

of the 100 μm scaffolds and cellular distribution, a Nikon D-Eclipse Ci confocal microscope was used in conjunction with a ×20 Plan Apo immersion oil objective (Nikon). For the imaging of the cytoskeleton of the cells ×20, ×60, and ×100 immersion oil objectives were used (Nikon). For the histological stains, a ×20 and a ×40 objective was used with an Olympus BX41TF upright microscope.

Decellularization quantification was performed as previously described (Narciso et al., 2021). Briefly, images belonging to a given treatment (decellularized slices) and corresponding control condition (native slices belonging to the same organ and animal) were acquired in a single imaging session. Exposure times for the phase contrast (PC) and the fluorescent channels were set based on the control (native) sections corresponding to each experiment. At least ten locations per condition were imaged except when less than ten locations were needed to cover the complete tissue area. Images were taken 1 mm apart from each other starting from the edge of a sample until covering the entirety of the sample length. The DNA signal intensity of the images from decellularized sections was compared to the DNA signal intensity of the corresponding native sections. The same method was used to quantify collagen, elastin, and laminin signals resulting from immunofluorescent staining. The signal corresponding to the ECM proteins of the untreated native sections was normalized to 100%.

2.9 Versatility of the Method for Different Species and Organs

To assess whether the SD decellularization method can be used for other types of tissues, 20 μm-thick sections of mice bladder, heart and kidney were subjected to the same decellularization protocol previously described in **Section 2.2**. Three independent decellularization experiments of each organ were performed. Additionally, three independent decellularization experiments were conducted using lung slices from pigs and rats, since these species are commonly used in animal models of respiratory diseases.

2.10 Statistical Analysis

For experiments with two groups (native and decellularized), statistical comparisons were performed by an unpaired two-tailed *t*-test. Unless mentioned, all data are mean ± SD. Differences were considered statistically significant for $p < 0.05$. Statistical analysis was performed using GraphPad Prism (GraphPad software 9.1.0, Inc. San Diego, CA, United States).

3 RESULTS

3.1 SD and SDS are the Most Effective Treatments for Cellular Removal

Even though trypsin + EDTA has been previously used in decellularization protocols, this method detached all tested samples and thus it is not suited for decellularization protocols on a glass slide. For that reason, no results on DNA staining and ECM proteins are presented here for trypsin decellularization, since no samples could be stained. All other decellularization methods resulted in scaffolds suited for further staining.

In **Figure 2**, representative UV images of Hoechst staining clearly show the removal of cell nuclei and DNA from all different methods studied. Cell nuclei are clearly present in native sections and noticeably absent (or reduced) after each decellularization treatment. To quantify the different decellularization levels resulting from different treatments, pixels corresponding to tissue were separated from background pixels, quantified, and compared to native tissue pixel intensities as previously described (Narciso et al., 2021). The DNA signal from native sections was normalized to 100% for easier comparison. All methods resulted in a significant reduction in DNA staining ($p < 0.05$) when compared to untreated native sections, as evidenced in **Figure 2**. SD and SDS treatments resulted in a marked DNA signal decrease (6.5 ± 5.8% and 1 ± 0.5% of native DNA signal, respectively) indicating that most cells and residual DNA was removed. On the other hand, CHAPS, Triton, and Ammonia/Triton mixture showed 62 ± 22%, 67 ± 28%, and 57 ± 31% of the native DNA signal, respectively, not reaching an acceptable decellularization level. A qualitative analysis of nuclei of lung sections stained with the hematoxylin and eosin (**Supplementary Figure S1**) validates the results obtained from the UV images of Hoechst33342-stained nuclei: only SDS and SD seemed to have efficiently removed cell nuclei from the sample, while the other methods did not reach sufficient cell removal rates.

3.2 All Treatments Preserved the ECM Proteins

As shown in **Figure 2**, all treatments resulted in a reduction of the elastin signal. SDS and the Ammonia and triton mixture in particular, showed a marked degradation of elastin signal where 6 ± 3% and 13 ± 8% of the native elastin signal remained, respectively. SD, CHAPS, and Triton, on the other hand, showed higher rates of elastin preservation, accounting for 34 ± 25%, 40 ± 19%, and 40 ± 24% of the pre-treatment elastin signal. This decrease is especially visible in the lung parenchyma, while blood vessels and airways seem to maintain elastin signal levels (**Figure 2**). Regarding laminin and collagen, none of the treatments used showed a decrease in laminin or collagen signal when compared to the corresponding native section. A quantitative analysis of samples stained with Picro-Sirius red (**Supplementary Figure S2**) showed a clear reduction in collagen type I and III stain in the SDS treated samples (81 ± 3%) when compared to the native samples (100% signal). Samples treated with the other decellularizing agents showed no marked differences when compared visually to the native sections: Ammonia + Triton, CHAPS, SD and Triton treatments showed 100 ± 4%, 108 ± 4%, 98 ± 3%, and 108 ± 3% when compared to the native image, respectively.

3.3 Samples Remained Attached to the Glass Slide

As observed in **Figure 2B**, treatments with higher rates of cellular removal were more likely to detach the sample from the glass

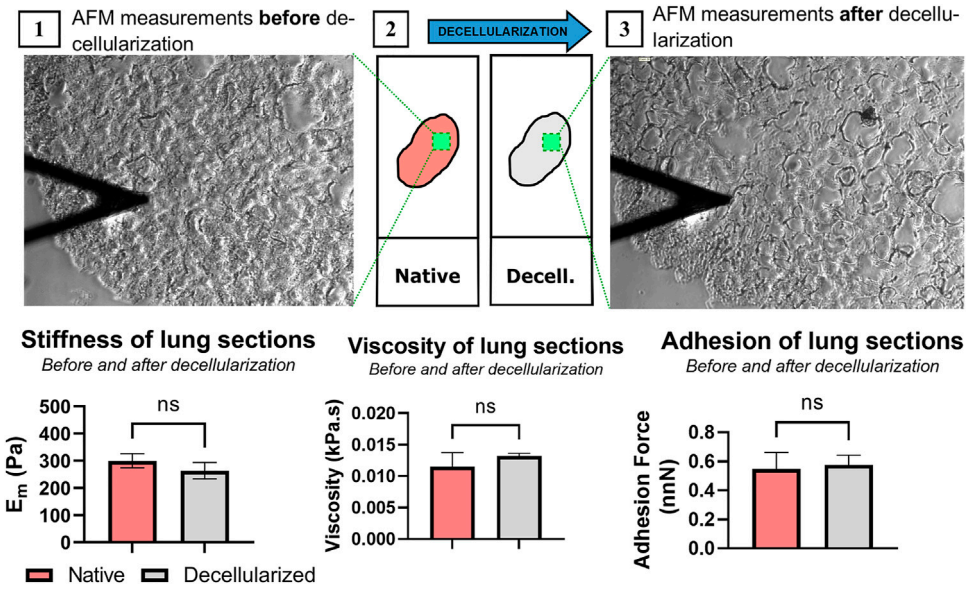

FIGURE 3 | Effect of the SD decellularization protocol on the mechanical properties of the lung scaffold. **(A)** Representative image of AFM measurements of the same tissue slice before (1) and after (3) decellularization ($n = 3$). Results of stiffness, viscosity, and adhesion force of the same sample before and after decellularization. Significance was $p < 0.05$.

slide; Ammonia + Triton, CHAPS and Triton treatments did not affect the attachment of the sample to the glass slide, for the most part, achieving 100 ± 00%, 82 ± 12%, and 100 ± 00% of sample attachment, respectively. For treatments that achieved higher cell removal—SDS and SD -, 32 ± 22% and 60 ± 23% of samples remained attached after decellularization treatments, respectively. By comparing all types of tissues, 60% of the lung sections remained attached while bladder, heart, and kidney sections never detached, achieving a sample attachment ratio of 100 ± 00% after using SD as the decellularizing agent. Taking into account the effectiveness in the removal of cellular material described in 3.1, the preservation of collagen, elastin, and laminin, and previous accounts of SDS's effects on the matrix, SD was considered to be the best treatment for on-slide decellularization. Thus, biomechanical, biocompatibility, and versatility analysis were performed on scaffolds resulting from the SD decellularization method.

3.4 SD Treatment did not Significantly Change the ECM Stiffness, Viscosity or Adhesion

The mean Young's modulus, viscosity, and force adhesion from each sample were computed from the same indentations and are shown in **Figure 3**. As expected, there was a slight, but not significant, decrease in the sample stiffness after decellularization. E_m for the native untreated samples was 299.6 ± 26.1 Pa while the E_m for the same sections but after decellularization was of 263.0 ± 29.9 Pa. Viscosity and force adhesion measurements were similar before and after decellularization (0.012 ± 0.002 vs. 0.013 ± 0.001 kPa·s and 0.48 ± 0.13 vs. 0.51 ± 0.01 nN, respectively). These results indicate that the decellularization protocol does not significantly change the mechanical properties of the lung sections.

3.5 SD Derived ECM Scaffolds are Biocompatible

The results of the biocompatibility assay were quantified and are detailed in **Figure 4.1**. Overall, cells survived similarly on both the 20 and 100 μm ECM scaffold thickness for 24, 48, and 72 h. More specifically, the viable cell ratio did not significantly differ after 24 h: at 72 h the cell viability ratio was 98.5 ± 2.0% and 97.9 ± 0.8% for 20 and 100 μm, respectively. After 72 h, the cell viability was similar to the cell count on the conventional culture flask (99.1 ± 0.8%). Accordingly, the distribution of the cells through the scaffold was assessed with a three-dimensional live/dead image and Z-distribution of the cells within the decellularized ECM structure can be seen in **Figure 4.2**. Alive cells were attached to the different parts of the matrix at different heights, which is an indicator of cell mobility and distribution within the lung scaffold. Previous topographical data indicates that lung scaffolds have gradual changes in height at the cellular level (around more or less 10 μm of variation), which is far below the variation in cell distribution seen in **Figure 4**. The cytoskeleton of the cells seeded on the matrix (**Figure 4.3**) shows a spread morphology indicative of their healthy attachment to the new scaffold.

3.6 The SD Method is Successful in Decellularizing Tissues From Different Animals and Organs

The quantification of the decellularization level of the mice's bladder, heart, and kidney is displayed in **Figure 5**, showing that

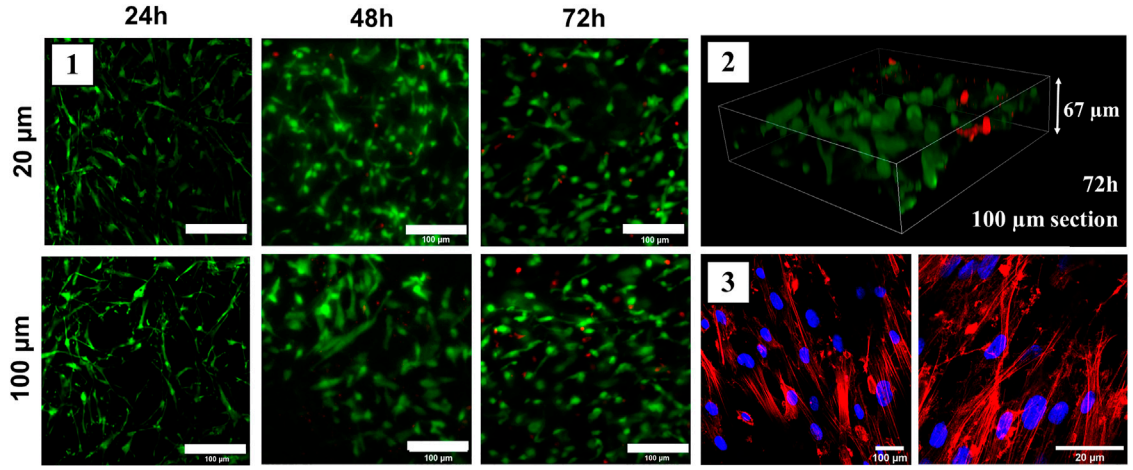

FIGURE 4 | Biocompatibility of the lung scaffold. Representative images of biocompatibility assay of 20 and 100 µm scaffolds for 24, 48, and 72 h. Live cells are seen in green while dead cells are red (1); 3D image of a 100 µm scaffold seeded with MSCs after 72 h. Stack showed covers 67 µm of the scaffold (2); Phalloidin staining of actin fibers (red) of cells seeded in 100 µm lung scaffold after 72 h (3). Samples decellularized with SD.

all organs were successfully decellularized. The decellularization level of the sections was quantified as described previously. Bladder decellularized sections had a mean value of 4% ± 1% of the native DNA signal intensity; kidney and heart decellularized sections both resulted in the same DNA intensity value of 1 ± 1% of the native DNA signal intensity value. It is important to note that, unlike lung samples, heart, kidney, and bladder samples remained attached for 100% of the decellularization trials. Porcine, rat, and mice lungs were decellularized and evaluated using the same protocol described previously. Lungs from the three different species were successfully decellularized (**Figure 5**). As expected, the decellularization of porcine and rat lung sections resulted in similar results to mice lung sections. Porcine lung sections averaged 5 ± 2% of the native DNA signal intensity while rat lung sections averaged 6 ± 2%. Mice lung decellularization with SD treatment was already described in **Figure 1**.

4 DISCUSSION

In this work, we present an easy, reliable, and versatile method to decellularize tissue sections attached to a glass slide with the main advantage that it allows for the identification and comparison of biophysical and biochemical conditions before and after decellularization from small samples. A summary of the comparison between the different decellularization treatments can be found in **Table 1**. After comparing common strategies for tissue decellularization, SD resulted in the most efficient treatment to remove cells and maintain the ECM components. This method has been successfully tested for other tissues including the heart, bladder, and kidneys, and in different species such as porcine, murine (mice and rat) lung samples. The resulting scaffolds showed no mechanical differences to the corresponding native sections, and could be repopulated with MSCs with high viability rates for at least 72 h. Therefore, this novel decellularization method provides a reliable alternative to current decellularization protocols due to its simplicity, lower sample mass requirements, and most importantly, it opens up new research opportunities to understand the role of the ECM in some physiologic and pathological conditions as well as for tissue repair and engineering.

Most of the available protocols for tissue decellularization are designed to decellularize whole organs or individual pieces of tissues not attached to a surface (da Palma et al., 2015; Urbano et al., 2017). Also, these protocols have been optimized for each organ and tissue type considering their structure and composition. To obtain a novel method capable to decellularize tissue samples attached to a glass slide, we compared and simplified the most common available protocols involving different techniques including perfusion, orbital agitation, and tissue immersion. The concentration employed for each decellularizing agent was the one previously optimized for lung tissues (see **Section 2.2** and **Supplementary Materials**). From all decellularizing agents included in this study, only SD and SDS were able to remove efficiently the cells. Although SDS is the most effective treatment (1 ± 0.5% remaining native DNA), it was also very aggressive resulting in a marked ECM degradation, particularly in elastin. In contrast to SDS, treatment with SD preserved much better the ECM structure and composition maintaining a high level of cell removal (6.5 ± 5.8% of native DNA). In addition, collagen I and III staining using Picro-Sirius red indicated a reduction in these proteins in samples treated with SDS (81%) but not with other treatments. Since immunostaining of collagen type I did not show such decrease, this reduction suggests a removal of collagen type III specifically in SDS treatment. Furthermore, samples treated with SDS remained attached to the glass slide only 32 ± 22% compared to the 60 ± 23% of sample attachment after SD treatment. Thus, the selected decellularization process achieved an optimal balance between cell removal, ECM integrity and sample attachment.

The degradation/preservation of each ECM component depends on the decellularizing strategy employed. The more aggressive behavior of SDS shown here is in agreement with

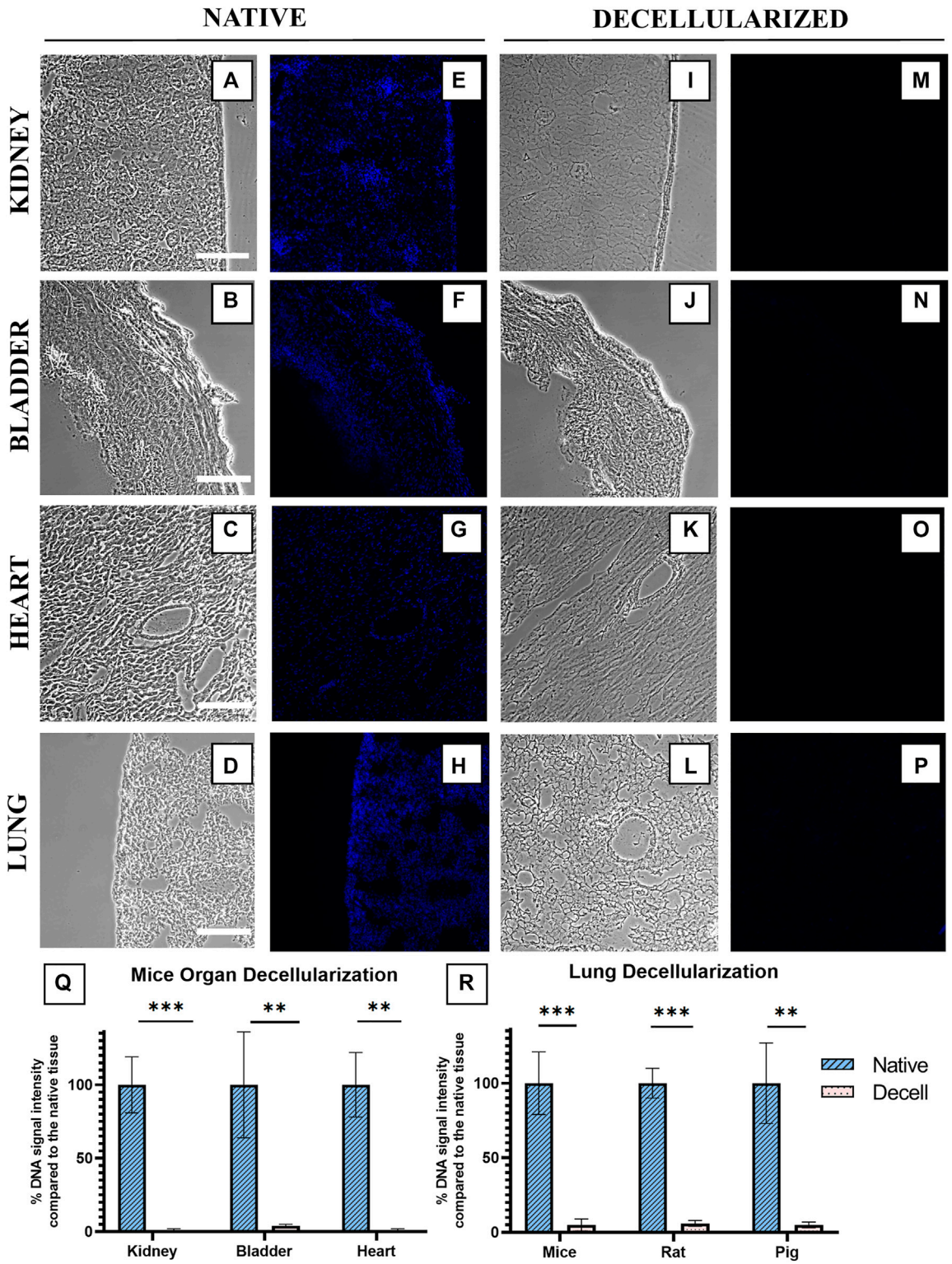

FIGURE 5 | Effect of the decellularization treatment with SD on the DNA signal of tissues of different animal origins and organs. Phase contrast **(A–D,I–L)** and Hoechst 33342 nuclei stained images **(E–H,M–P)** of native **(A–H)** and decellularized **(I–P)** sections of kidney, bladder, heart, and lung. Quantification of different organ DNA content percentage (%) **(Q)** and different animal lung tissue DNA content percentage (%) **(R)** after decellularization treatment with SD. Native tissue's DNA signal is normalized to 100%.

TABLE 1 | Summary of results (%DNA retention, % sample attachment, %collagen, elastin and laminin retention) for the different decellularization methods.

Decellularization method	DNA retention, %	Sample attachment, %	Elastin retention, %	Collagen I retention, %	Laminin retention, %
Ammonium hydroxide 0.5% + Triton 0.1%	57.4	100.0	13.2	112.5	135.5
CHAPS 0.5%	61.8	82.1	39.7	110.6	125.8
Sodium Deoxycholate (SD) 2%	6.5	60.0	33.4	118.0	136.6
Sodium Dodecyl Sulfate (SDS) 1%	0.95	32.1	6.2	121.5	115.8
Triton X-100 1%	66.8	100.0	40.0	101.3	106.8
Trypsin 0.05% + EDTA 0.02%	—	0	—	—	—

previous works. For instance, SDS promotes the denaturalization of the triple-helical collagen molecule while CHAPS and SD do not (Hwang et al., 2017) and reduce drastically the content of glycosaminoglycans (GAGs) (Ren et al., 2013). Additionally, White et al. found that SDS treatments lead to atypical phenotype, lower viability, and a reduced confluence of urothelial cells on decellularized scaffolds in contrast to SDS, Triton, and CHAPS treatments (White et al., 2017). Regarding ECM composition, none of the protocols tested in this work decreased the among of type I collagen or laminin. Elastin, which is known to be sensitive to the decellularization process (Maghsoudlou et al., 2013; O'Neill et al., 2013b; Alshaikh et al., 2020), was reduced for all decellularization methods tested. SDS and Ammonia + Triton, reduced the native elastin signal to 6%–13% while the other methods were able to preserve it better (30–40%). The sharp reduction in elastin signal was not hand in hand with levels of cellular removal; SDS was able to remove virtually all cellular material while the Ammonia + Triton mixture did not achieve sufficient decellularization levels (67 ± 28% of native DNA remained). This evidence suggests that the elastin decrease is influenced by the specific chemical interactions between decellularizing agents and the ECM network and not simply by the decellularization procedure. Additionally, by comparing the effect of the procedure on different organs, the elastin of bladder samples was highly preserved using the same SD based protocol, where 95 ± 36% of the native elastin signal was measured after decellularization (**Supplementary Figure S3**). Thus, elastin degradation seems to be organ-dependent and implicitly depend on the structure and organization of the ECM. Considering all these observations, although SDS is also extremely efficient in the removal of cellular material, we selected SD as the best option in terms of ECM preservation.

When comparing the effects of the decellularization procedure on the interstitial and basement membrane of the ECM, only a component of the interstitial ECM was significantly affected throughout procedures (elastin) while the component analyzed from the basement membrane (laminin) was not reduced in any of the treatments. This difference might be explained by the different locations of these layers: the interstitial ECM surrounds the cells and provides structural support to the tissue while the basement membrane is more compact (Cox and Erler 2011). This denser feature of the basement membrane might protect it from being removed during decellularization, while components from the interstitial ECM that are intertwined with the cells might be more vulnerable and disrupted when these are removed. Additionally, more components from both components of the ECM, like collagen type IV and fibronectin, could be analyzed for a more in-depth study on the effect of the decellularization procedure on the different layers of the ECM.

The key point in this novel method is to maintain the sample attached to the glass slide while applying the different decellularization solutions. Among all tissues employed, lungs have some unique features that could complicate their attachment. Specifically, lung scaffolds have large areas of empty spaces corresponding to the multiple alveoli and airways. These structures reduce the effective contact area between the scaffold and the glass slide in comparison to other more homogeneous tissues. While the lungs are being decellularized, the contact area with the glass slide can be further reduced by cellular removal leading to sample detachment during the different washes. For this reason, we selected lungs as the most difficult sample type to optimize the protocol. In fact, among all four organs tested in this work, the lungs were the only tissue where some samples would detach (40% for SD treatment) from the glass slide. Bladder, heart, and kidney samples remained attached to the glass slide for 100% of all experiments whilst reaching the same decellularization success using the same SD treatment. On the other hand, when testing solely lung samples, different detergents had dissimilar effects on the attachment of the slides. This could be explained by the effective contact area hypothesis just mentioned above, where the higher amount of cells removed, the smaller the contact area remaining with the glass slide and thus a higher chance of detachment. This is consistent with the results of this work, since the most effective decellularizing agents (SD and SDS) were less likely to preserve attachment when compared to less effective treatments, like triton and CHAPS. However, it is also worthy of note that ionic surfactants (SD and SDS) caused lower attachment levels when compared to non-ionic and zwitterionic surfactants (triton and CHAPS, respectively). Although the nature of this disruption is unclear, it is possible that the ionic nature of these reagents reacts with the ionic coating of the glass slides, disrupting it. We hypothesize that if this coating is replaced by a non-ionic treatment, attachment rates for treatments with SD and SDS might significantly improve.

Since this method maintains the sample attached to the glass slide, we were able to measure the mechanical properties of the same lung section before and after lung decellularization, unlike other protocols where mechanical properties are measured in different samples (Mendoza-Novelo et al., 2011; Maghsoudlou et al., 2013). In fact, it is possible to perform the decellularization *in situ* on the AFM stage, substantially reducing sources of variability. It is of the utmost importance that the scaffold

maintains the mechanical properties of the native tissue, especially for cell culture and tissue engineering applications. As expected, tissue stiffness, viscosity and adhesion were maintained after decellularization in agreement with previous works that indicate that elastin does not play a significant role in the mechanics of the static lung (Guimarães et al., 2020).

One of the potential limitations of this method is the diffusion of the decellularizing agents through thicker samples as well as the increased chance of detachment, since with increased thickness the electrostatic bonds that secure the sample to the glass slide are not strong enough to retain the increased sample mass. To demonstrate the effectiveness in thicker sections, we tested the same protocol in 100 µm sections reaching similar decellularization levels by employing a longer incubation period of DNAse of 40 min at 37°C. It should be noted however, that incubation at higher temperatures may result in increased sample detachment (Eckhard et al., 2019). Thus, we would advise the use of additional adhesion treatments that form stronger bonds between the sample and the glass slide, such as transglutaminase or cellTAK. Both these compounds have been used in the past to secure tissues to surfaces for AFM measurements (Sahai et al., 2016). Notwithstanding the potential applications of this method to thicker tissue sections, one of the main advantages of the method described here is the fact that the decellularization of tissue slice by slice requires a minimal amount of tissue and effort. One of the main problems with the decellularization of organs from humans and large animals like the pig is the complex procedure to decellularize the whole organ that can weight more than 1 kg. This process usually requires organ-specific decellularizing reagents which also are applied by different approaches (vascular/airways perfusion, site injections, among others) (Balestrini et al., 2015; Pouliot et al., 2016). Here, we tested the decellularization method for lung slices with samples from mice, rats, and pigs obtaining similar results. Thus, this will open the opportunity to decellularize tissue slices from small clinical biopsies where the whole or a large section of an organ is not available.

In conclusion, the decellularization method presented here will provide a useful tool for many research aims, but mainly in 1) studies that require the identification of anatomical structures which can only be detected in native samples. For instance, the location of small metastasis in decellularized tissue samples may present a challenge since cancer cells have been removed. Since this novel approach provides access to the sample before and after decellularization in the same or consecutive slices, the native structure can be located before decellularization. The low mass requirements make this protocol an important tool for 2) studies of scarce and valuable samples, since sections as low as 10 µm could be decellularized with this protocol, unlike full organ or tissue submergence decellularization protocols. This is the case for clinical biopsies or smaller structures like the cornea. And 3) to use the decellularized ECM as a cell culture substrate. To this end, the biocompatibility of the scaffolds was also assessed after 72 h. The decellularized lung scaffolds showed the capability of supporting cell attachment and growth similar to the conventional culture conditions, as further evidenced by actin staining showing the spread morphology of the cells within the scaffold. In addition, we observed that cells seeded on this lung scaffold did not form a monolayer in the surface but reached different depths within the decellularized ECM opening new options for tissue repair and engineering.

DATA AVAILABILITY STATEMENT

The raw data supporting the conclusion of this article will be made available by the authors, without undue reservation.

ETHICS STATEMENT

This work was approved by the Institutional Committee of Universitat de Barcelona and the Animal Experimentation Committee of regional authorities (Generalitat de Catalunya, OB 168/19 and 10972).

AUTHOR CONTRIBUTIONS

MN and IA participated in the conceptual framework of the project, analysed data, and drafted components of the manuscript. MN, AU, and CJ performed experiments. JO, RF, DN, and NG provided critical insights and participated in the drafting of the manuscript. MN and IA drafted the previous versions of the manuscript. IA, RF, and DN are responsible for the financial support of the project. All authors have reviewed and approved the final version of the manuscript.

FUNDING

IA is funded by Ministerio de Ciencia e Innovación (PID2019-108958RB-I00) and SEPAR (900-2019). MN and CJ were funded by the H2020 European Research and Innovation Programme under the Marie Skłodowska-Curie grant agreement "Phys2BioMed" contract no. 812772. RF, JO, and NG were funded by the Spanish Ministry of Sciences, Innovation and Universities, PID2020-113910RB-I00-AEI/10.13039/501100011033, PGC2018-097323-A-I00, and PID2020-116808RB-I00 AEI-Retos, respectively.

ACKNOWLEDGMENTS

The authors wish to thank Miguel Ángel Rodríguez from the Unit of Biophysics and Bioengineering (University of Barcelona) for his technical assistance.

SUPPLEMENTARY MATERIAL

The Supplementary Material for this article can be found online at: https://www.frontiersin.org/articles/10.3389/fbioe.2022.832178/full#supplementary-material

REFERENCES

Alshaikh, A. B., Padma, A. M., Dehlin, M., Akouri, R., Song, M. J., Brännström, M., et al. (2020). Decellularization and Recellularization of the Ovary for Bioengineering Applications; Studies in the Mouse. *Reprod. Biol. Endocrinol.* 18 (1), 75. doi:10.1186/s12958-020-00630-y

Balestrini, J. L., Gard, A. L., Liu, A., Leiby, K. L., Schwan, J., Kunkemoeller, B., et al. (2015). Production of Decellularized Porcine Lung Scaffolds for Use in Tissue Engineering. *Integr. Biol.* 7 (12), 1598–1610. doi:10.1039/c5ib00063g

Bonenfant, N. R., Sokocevic, D., Wagner, D. E., Borg, Z. D., Lathrop, M. J., Lam, Y. W., et al. (2013). The Effects of Storage and Sterilization on De-cellularized and Re-cellularized Whole Lung. *Biomaterials* 34 (13), 3231–3245. doi:10.1016/j.biomaterials.2013.01.031

Burgstaller, G., Oehrle, B., Gerckens, M., White, E. S., Schiller, H. B., and Eickelberg, O. (2017). The Instructive Extracellular Matrix of the Lung: Basic Composition and Alterations in Chronic Lung Disease. *Eur. Respir. J.* 50 (1), 1601805. doi:10.1183/13993003.01805-2016

Calle, E. A., Hill, R. C., Leiby, K. L., Le, A. V., Gard, A. L., Madri, J. A., et al. (2016). Targeted Proteomics Effectively Quantifies Differences between Native Lung and Detergent-Decellularized Lung Extracellular Matrices. *Acta Biomater.* 46 (December), 91–100. doi:10.1016/j.actbio.2016.09.043

Cox, T. R., and Erler, J. T. (2011). Remodeling and Homeostasis of the Extracellular Matrix: Implications for Fibrotic Diseases and Cancer. *Dis. Models Mech.* 4 (2), 165–178. doi:10.1242/dmm.004077

da Palma, R. K., Campillo, N., Uriarte, J. J., Oliveira, L. V. F., Navajas, D., and Farré, R. (2015). Pressure- and Flow-Controlled Media Perfusion Differently Modify Vascular Mechanics in Lung Decellularization. *J. Mech. Behav. Biomed. Mater.* 49 (September), 69–79. doi:10.1016/j.jmbbm.2015.04.024

Eckhard, A. H., O'Malley, J. T., Nadol, J. B., and Adams, J. C. (2019). Mechanical Compression of Coverslipped Tissue Sections during Heat-Induced Antigen Retrieval Prevents Section Detachment and Preserves Tissue Morphology. *J. Histochem. Cytochem.* 67 (6), 441–452. doi:10.1369/0022155419826940

Falcones, B., Sanz-Fraile, H., Marhuenda, E., Mendizábal, I., Cabrera-Aguilera, I., Malandain, N., et al. (2021). Bioprintable Lung Extracellular Matrix Hydrogel Scaffolds for 3D Culture of Mesenchymal Stromal Cells. *Polymers* 13 (14), 2350. doi:10.3390/polym13142350

Gattazzo, F., Urciuolo, A., and Bonaldo, P. (2014). Extracellular Matrix: A Dynamic Microenvironment for Stem Cell Niche. *Biochim. Biophys. Acta (Bba) - Gen. Subjects* 1840 (8), 2506–2519. doi:10.1016/j.bbagen.2014.01.010

Gilpin, A., and Yang, Y. (20172017). Decellularization Strategies for Regenerative Medicine: From Processing Techniques to Applications. *Biomed. Res. Int.* 2017, 1–13. doi:10.1155/2017/9831534

Guimarães, C. F., Gasperini, L., Marques, A. P., and Reis, R. L. (2020). The Stiffness of Living Tissues and its Implications for Tissue Engineering. *Nat. Rev. Mater.* 5 (5), 351–370. doi:10.1038/s41578-019-0169-1

Hill, R. C., Calle, E. A., Dzieciatkowska, M., Niklason, L. E., and Hansen, K. C. (2015). Quantification of Extracellular Matrix Proteins from a Rat Lung Scaffold to Provide a Molecular Readout for Tissue Engineering. *Mol. Cell Proteomics* 14 (4), 961–973. doi:10.1074/mcp.M114.045260

Hwang, J., Boi Hoa, S., Neill, J. T., Lisa, J. W., Denver, M. F., Stephen, F., et al. (2017). Molecular Assessment of Collagen Denaturation in Decellularized Tissues Using a Collagen Hybridizing Peptide. *Acta Biomat.* 53 (April), 268–278. doi:10.1016/j.actbio.2017.01.079

Hynes, R. O., and Naba, A. (2012). Overview of the Matrisome--An Inventory of Extracellular Matrix Constituents and Functions. *Cold Spring Harbor Perspect. Biol.* 4 (1), a004903. doi:10.1101/cshperspect.a004903

Jorba, I., Beltrán, G., Falcones, B., Suki, B., Farré, R., García-Aznar, J. M., et al. (2019). Nonlinear Elasticity of the Lung Extracellular Microenvironment Is Regulated by Macroscale Tissue Strain. *Acta Biomater.* 92 (July), 265–276. doi:10.1016/j.actbio.2019.05.023

Jorba, I., Uriarte, J. J., Campillo, N., Farré, R., and Navajas, D. (2017). Probing Micromechanical Properties of the Extracellular Matrix of Soft Tissues by Atomic Force Microscopy. *J. Cel. Physiol* 232 (1), 19–26. doi:10.1002/jcp.25420

Júnior, C., Narciso, M., Marhuenda, E., Almendros, I., Farré, R., Navajas, D., et al. (2021). Baseline Stiffness Modulates the Non-linear Response to Stretch of the Extracellular Matrix in Pulmonary Fibrosis. *Ijms* 22 (23), 12928. doi:10.3390/ijms222312928

Lü, W.-D., Zhang, L., Wu, C.-L., Liu, Z.-G., Lei, G.-Y., Liu, J., et al. (2014). "Development of an Acellular Tumor Extracellular Matrix as a Three-Dimensional Scaffold for Tumor Engineering, *PLoS ONE* 9 (7), e103672. doi:10.1371/journal.pone.0103672

Maghsoudlou, P., Georgiades, F., Tyraskis, A., Totonelli, G., Loukogeorgakis, S. P., Orlando, G., et al. (2013). Preservation of Micro-architecture and Angiogenic Potential in a Pulmonary Acellular Matrix Obtained Using Intermittent Intratracheal Flow of Detergent Enzymatic Treatment. *Biomaterials* 34 (28), 6638–6648. doi:10.1016/j.biomaterials.2013.05.015

Mendibil, U., Ruiz-Hernandez, R., Retegi-Carrion, S., Garcia-Urquia, N., Olalde-Graells, B., and Abarrategi, A. (2020). Tissue-Specific Decellularization Methods: Rationale and Strategies to Achieve Regenerative Compounds. *Ijms* 21 (15), 5447. doi:10.3390/ijms21155447

Mendoza-Novelo, B., Avila, E. E., Cauich-Rodríguez, J. V., Jorge-Herrero, E., Rojo, F. J., Guinea, G. V., et al. (2011). Decellularization of Pericardial Tissue and its Impact on Tensile Viscoelasticity and Glycosaminoglycan Content. *Acta Biomater.* 7 (3), 1241–1248. doi:10.1016/j.actbio.2010.11.017

Narciso, M., Otero, J., Navajas, D., Farré, R., Almendros, I., and Gavara, N. (2021). Image-Based Method to Quantify Decellularization of Tissue Sections. *Ijms* 22 (16), 8399. doi:10.3390/ijms22168399

Ng, W. H., Ramasamy, R., Yong, Y. K., Ngalim, S. H., Lim, V., Shaharuddin, B., et al. (2019). Extracellular Matrix from Decellularized Mesenchymal Stem Cells Improves Cardiac Gene Expressions and Oxidative Resistance in Cardiac C-Kit Cells. *Regenerative Ther.* 11 (December), 8–16. doi:10.1016/j.reth.2019.03.006

O'Neill, J. D., Anfang, R., Anandappa, A., Costa, J., Javidfar, J., Wobma, H. M., et al. (2013a). Decellularization of Human and Porcine Lung Tissues for Pulmonary Tissue Engineering. *Bone* 96 (3), 1046–1056. doi:10.1016/j.athoracsur.2013.04.022.Decellularization

O'Neill, J. D., Anfang, R., Anandappa, A., Costa, J., Javidfar, J., Wobma, H. M., et al. (2013b). Decellularization of Human and Porcine Lung Tissues for Pulmonary Tissue Engineering. *Ann. Thorac. Surg.* 96 (3), 1046–1056. doi:10.1016/j.athoracsur.2013.04.022

Ohata, K., and Ott, H. C. (2020). Human-Scale Lung Regeneration Based on Decellularized Matrix Scaffolds as a Biologic Platform. *Surg. Today* 50 (7), 633–643. doi:10.1007/s00595-020-02000-y

Pompili, S., Latella, G., Gaudio, E., Sferra, R., and Vetuschi, A. (2021). The Charming World of the Extracellular Matrix: A Dynamic and Protective Network of the Intestinal Wall. *Front. Med.* 8 (April), 610189. doi:10.3389/fmed.2021.610189

Pouliot, R. A., Link, P. A., Mikhaiel, N. S., Schneck, M. B., Valentine, M. S., Kamga Gninzeko, F. J., et al. (2016). Development and Characterization of a Naturally Derived Lung Extracellular Matrix Hydrogel. *J. Biomed. Mater. Res.* 104 (8), 1922–1935. doi:10.1002/jbm.a.35726

Rasmussen, D. G. K., and Karsdal, M. A. (2016). "Laminins," in *Biochemistry of Collagens, Laminins and Elastin* (Amsterdam, Netherlands: Elsevier), 163–196. doi:10.1016/B978-0-12-809847-9.00029-5

Rebelo, L. M., de Sousa, J. S., Mendes Filho, J., and Radmacher, M. (2013). Comparison of the Viscoelastic Properties of Cells from Different Kidney Cancer Phenotypes Measured with Atomic Force Microscopy. *Nanotechnology* 24 (5), 055102. doi:10.1088/0957-4484/24/5/055102

Rendin, L. E., LöfdahlLöfdahl, A., Åhrman, E., Müller, C., Notermans, T., Michaliková, B., et al. (2019). Matrisome Properties of Scaffolds Direct Fibroblasts in Idiopathic Pulmonary Fibrosis. *Ijms* 20 (16), 4013. doi:10.3390/ijms20164013

Ren, H., Xiaolei, S., Liang, T., Jiangqiang, X., Bing, H., Yue, Z., et al. (2013). Evaluation of Two Decellularization Methods in the Development of a Whole-Organ Decellularized Rat Liver Scaffold. *Liver Int.* 33 (3), 448–458. doi:10.1111/liv.12088

Rosmark, O., Åhrman, E., Müller, C., Rendin, L. E., Eriksson, L., Malmström, A., et al. (2018). Quantifying Extracellular Matrix Turnover in Human Lung Scaffold Cultures. *Sci. Rep.* 8 (1), 5409. doi:10.1038/s41598-018-23702-x

Sahai, S., Marysuna, W., Ana Maria, Z., Scott, D. O., Charles, S. C., and Fabio, T. (2016). A Cost-Effective Method to Immobilize Hydrated Soft-Tissue Samples for Atomic Force Microscopy. *BioTechniques* 61 (4), 206–209. doi:10.2144/000114461

Schenke-Layland, K., Vasilevski, O., Opitz, F., König, K., Riemann, I., Halbhuber, K. J., et al. (2003). Impact of Decellularization of Xenogeneic Tissue on

Extracellular Matrix Integrity for Tissue Engineering of Heart Valves. *J. Struct. Biol.* 143 (3), 201–208. doi:10.1016/j.jsb.2003.08.002

Syed, O., Walters, N. J., Day, R. M., Kim, H.-W., and Knowles, J. C. (2014). Evaluation of Decellularization Protocols for Production of Tubular Small Intestine Submucosa Scaffolds for Use in Oesophageal Tissue Engineering. *Acta Biomater.* 10 (12), 5043–5054. doi:10.1016/j.actbio.2014.08.024

Urbano, J. J., da Palma, R. K., de Lima, F. M., Fratini, P., Guimaraes, L. L., Uriarte, J. J., et al. (2017). Effects of Two Different Decellularization Routes on the Mechanical Properties of Decellularized Lungs. *PLOS ONE* 12 (6), e0178696. doi:10.1371/journal.pone.0178696

White, L. J., Adam, J. T., Denver, M. F., Timothy, J. K., Lindsey, T. S., Janet, E. R., et al. (2017). The Impact of Detergents on the Tissue Decellularization Process: A ToF-SIMS Study. *Acta Biomat.* 50 (March), 207–219. doi:10.1016/j.actbio.2016.12.033

Wishart, A. L., Conner, S. J., Guarin, J. R., Fatherree, J. P., Peng, Y., McGinn, R. A., et al. (2020). Decellularized Extracellular Matrix Scaffolds Identify Full-Length Collagen VI as a Driver of Breast Cancer Cell Invasion in Obesity and Metastasis. *Sci. Adv.* 6 (43), eabc3175. doi:10.1126/sciadv.abc3175

Wüthrich, T., Lese, I., Haberthür, D., Zubler, C., Hlushchuk, R., Hewer, E., et al. (2020). Development of Vascularized Nerve Scaffold Using Perfusion-Decellularization and Recellularization. *Mater. Sci. Eng. C* 117 (December), 111311. doi:10.1016/j.msec.2020.111311

Xiong, G., Flynn, T. J., Chen, J., Trinkle, C., and Xu, R. (2015). Development of Anex Vivobreast Cancer Lung Colonization Model Utilizing a Decellularized Lung Matrix. *Integr. Biol.* 7 (12), 1518–1525. doi:10.1039/c5ib00157a

Zhang, J., Hu, Z. Q., Turner, N. J., Teng, S. F., Cheng, W. Y., Zhou, H. Y., et al. (2016). Perfusion-Decellularized Skeletal Muscle as a Three-Dimensional Scaffold with a Vascular Network Template. *Biomaterials* 89 (May), 114–126. doi:10.1016/j.biomaterials.2016.02.040

Zhu, M., Li, W., Dong, X., Yuan, X., Midgley, A. C., Chang, H., et al. (2019). *In Vivo* Engineered Extracellular Matrix Scaffolds with Instructive Niches for Oriented Tissue Regeneration. *Nat. Commun.* 10 (1), 4620. doi:10.1038/s41467-019-12545-3

Conflict of Interest: The authors declare that the research was conducted in the absence of any commercial or financial relationships that could be construed as a potential conflict of interest.

Publisher's Note: All claims expressed in this article are solely those of the authors and do not necessarily represent those of their affiliated organizations, or those of the publisher, the editors and the reviewers. Any product that may be evaluated in this article, or claim that may be made by its manufacturer, is not guaranteed or endorsed by the publisher.

Copyright © 2022 Narciso, Ulldemolins, Júnior, Otero, Navajas, Farré, Gavara and Almendros. This is an open-access article distributed under the terms of the Creative Commons Attribution License (CC BY). The use, distribution or reproduction in other forums is permitted, provided the original author(s) and the copyright owner(s) are credited and that the original publication in this journal is cited, in accordance with accepted academic practice. No use, distribution or reproduction is permitted which does not comply with these terms.

frontiers in Bioengineering and Biotechnology

ORIGINAL RESEARCH
published: 10 March 2022
doi: 10.3389/fbioe.2022.855186

Bioprinting of Decellularized Porcine Cardiac Tissue for Large-Scale Aortic Models

Beu P. Oropeza[1], *Jason R. Adams*[2], *Michael E. Furth*[1], *Jack Chessa*[2] *and Thomas Boland*[1]*

[1]*Biomedical Device, Delivery and Diagnostic Laboratory, Metallurgical, Materials and Biomedical Engineering Department, The University of Texas at El Paso, El Paso, TX, United States,* [2]*Aerospace and Mechanical Engineering, The University of Texas at El Paso, El Paso, TX, United States*

Bioprinting is an emerging technique used to layer extrudable materials and cells into simple constructs to engineer tissue or arrive at *in vitro* organ models. Although many examples of bioprinted tissues exist, many lack the biochemical complexity found in the native extracellular matrix. Therefore, the resulting tissues may be less competent than native tissues—this can be especially problematic for tissues that need strong mechanical properties, such as cardiac or those found in the great vessels. Decellularization of native tissues combined with processing for bioprinting may improve the cellular environment for proliferation, biochemical signaling, and improved mechanical characteristics for better outcomes. Whole porcine hearts were decellularized using a series of detergents, followed by lyophilization and mechanical grinding in order to produce a fine powder. Temperature-controlled enzymatic digestion was done to allow for the resuspension of the decellularized extracellular matrix into a pre-gel solution. Using a commercial extrusion bioprinter with a temperature-controlled printhead, a 1:1 scale model of a human ascending aorta and dog bone shaped structures were printed into a reservoir of alginate and xanthium gum then allowed to crosslink at 37C. The bioengineered aortic construct was monitored for cell adhesion, survival, and proliferation through fluorescent microscopy. The dog bone structure was subjected to tensile mechanical testing in order to determine structural and mechanical patterns for comparison to native tissue structures. The stability of the engineered structure was maintained throughout the printing process, allowing for a final structure that upheld the dimensions of the original Computer-Aided Design model. The decellularized ECM ($\bar{E}$ = 920 kPa) exhibited almost three times greater elasticity than the porcine cardiac tissue ($\bar{E}$ = 330 kPa). Similarly, the porcine cardiac tissue displayed two times the deformation than that of the printed decellularized ECM. Cell proliferation and attachment were observed during the *in vitro* cell survivability assessment of human aortic smooth muscle cells within the extracellular matrix, along with no morphological abnormalities to the cell structure. These observations allow us to report the ability to bioprint mechanically stable, cell-laden structures that serve as a bridge in the current knowledge gap, which could lead to future work involving complex, large-scale tissue models.

Keywords: decellularization, tissue engineering and regenerative medicine, bioprinting, biomechanics, biomaterials, extracellular matrix

OPEN ACCESS

Edited by:
Laura Iop,
University of Padua, Italy

Reviewed by:
Alonzo Cook,
InviRx, United States
Jun Negishi,
Shinshu University, Japan

****Correspondence:***
Thomas Boland
tboland@utep.edu

Specialty section:
This article was submitted to Biomaterials, a section of the journal Frontiers in Bioengineering and Biotechnology

Received: *14 January 2022*
Accepted: *23 February 2022*
Published: *10 March 2022*

Citation:
Oropeza BP, Adams JR, Furth ME, Chessa J and Boland T (2022) Bioprinting of Decellularized Porcine Cardiac Tissue for Large-Scale Aortic Models. Front. Bioeng. Biotechnol. 10:855186. doi: 10.3389/fbioe.2022.855186

INTRODUCTION

In the United States alone, 40,000 children are born with a congenital heart problem each year (Jenkins et al., 2007). The current procedures used to treat aortic defects involve synthetic materials, usually textiles, as grafts that replace aortic sections or stents that give additional support to the aortic wall (Kleigman, 2011). Each of these options results in numerous surgical interventions throughout a child's developing years, leading to extended hospital stays, and potential trauma (Fawzy et al., 2004; Walhout et al., 2004; Carr et al., 2005). Additionally, it has been found that children who suffer from congenital heart defects can be subject to developmental and language delays (Limperopoulos et al., 2002; Easson et al., 2019; Fourdain et al., 2019). Bioprinting, an emerging technique in the biomedical engineering field, has the potential to solve the problems that arise from repetitive surgical intervention. Bioengineers are able to extrusion print using materials specifically characterized for the engineered tissue. The layered biomaterials and cells form precise structures modeled from native biological tissues that can grow along with the child (Murphy and Atala, 2014; Zhang et al., 2016; Rider et al., 2018).

Although many tissues have been engineered using bioprinting, maintaining the biochemical complexity and structural integrity necessary to retain native function has posed a problem in the past. The decellularization of native tissues in order to acquire the extracellular matrix (ECM) as a whole or as components has allowed researchers to bridge the gap in biochemical mimicry. It has been found that ECM helps control tissue-specific functions using interactions with the surrounding cells through a dynamic bidirectional system extending past the cell membrane to the level of gene expression (Bissell et al., 1982; Bornstein et al., 1982; Nelson and Bissell, 2006). This relationship between the cell and its

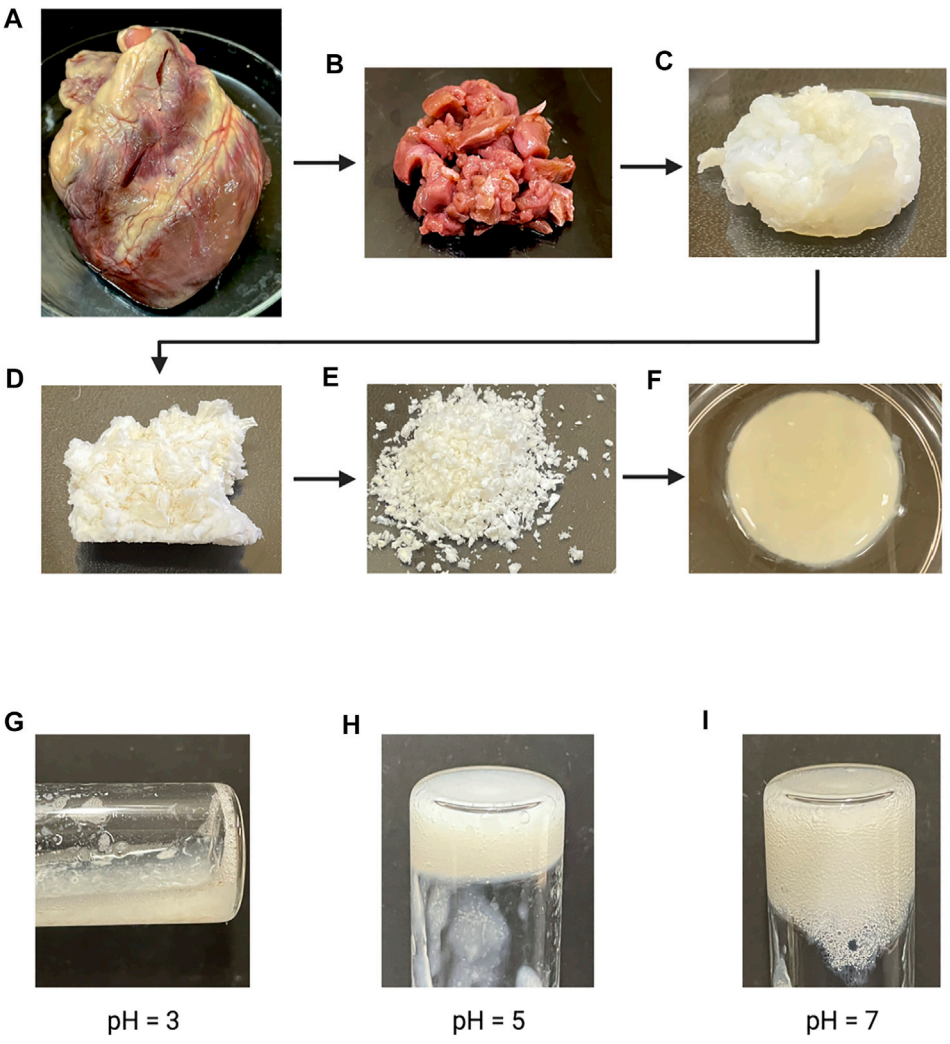

FIGURE 1 | (A) Fresh whole porcine heart. **(B)** Cut sections of porcine cardiac tissue prior to decellularization. **(C)** Cut sections of cardiac tissue post chemical decellularization. **(D)** Lyophilized decellularized ECM. **(E)** Powdered decellularized ECM. **(F)** Final gelled form of the enzymatically digested decellularized ECM. **(G–I)** Enzymatically digested decellularized ECM at different pH after a 1 h incubation at 37°C.

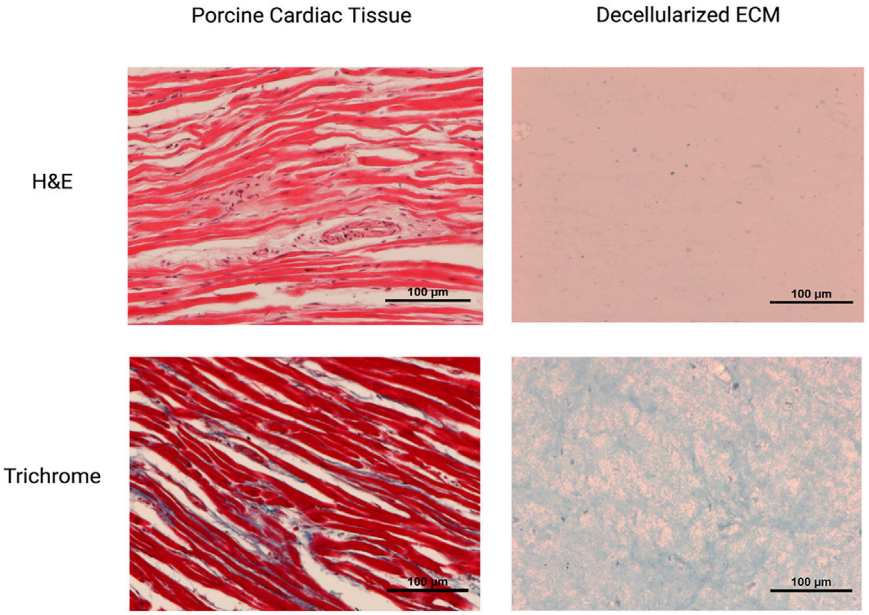

FIGURE 2 | Histological staining of the tissues pre and post decellularization.

surroundings stimulates proliferation, cell growth and, through the presence of laminin and fibrin, increases cell adhesion properties (Ott et al., 2008; Badylak et al., 2009; Park and Woo, 2012; Wolf et al., 2012).

Equal importance must be given to the mechanical properties of the engineered tissues. As with all living things, these structures are meant to exist in a dynamic environment, oftentimes with relatively large forces acting upon them (Fung, 1933). Removing the tissue from its native environment and processing it for decellularization leads to alterations in the ECM's physical, structural, and mechanical characteristics (Gilbert et al., 2006). This study places particular interest in defining the ECM's characteristics prior to decellularization as well as after the bioprinting process is complete. Using samples of porcine cardiac tissue as a control, we compare it to printed dECM and assess the physiological and biochemical makeup, surface topography, and mechanical characteristics.

MATERIALS AND METHODS

Decellularization of Porcine Hearts

Fresh whole porcine hearts were acquired from Nebraska Scientific (Omaha, NE) and cut down to sections not exceeding 2 mm^3. The tissues were then placed in 2.5 L of a 1% SDS solution for 48 h, stirred continuously. The solution was replaced at 24 h, and it was ensured no agglomerations had formed. The cardiac tissue was then treated with 1% Triton X-100 for 30 min followed by 3 days of PBS washes, where the buffer was replaced every day, and the tissues are stirred continuously. To sterilize the decellularized tissue, it was treated with 1% peracetic acid for 4 h and washed five times with sterile PBS and sterile distilled water. All decellularization steps were done at room temperature. The strained tissue was then frozen at -80°C overnight and lyophilized. All decellularization techniques followed were taken from Pati *et al.* with minimal modification (Pati et al., 2014).

Cell Culture

Human Aortic Smooth Muscle Cells were grown in vascular growth media (ATCC PCS-100-030) plus smooth muscle kit (ATCC PCS-100-042) under normal environmental culture conditions at 37°C with 5% CO_2 in a fully aseptic environment. Before printing, cell membranes were stained using PKH26 red fluorescent live cell membrane stain (Sigma MINI26-1KT).

Bioprinting

The lyophilized dECM was digested and re-suspended in order to form a printable gel material. Lyophilized dECM was mechanically pulverized using burr grinding methods, then 3 g of dECM were digested with 30 mg of pepsin from porcine gastric mucosa (Sigma P7125-100G, ≥3,200 units/mg protein) in 100 ml of 0.5 M acetic acid for 48 h at room temperature with continuous stirring (Pati et al., 2014). Centrifugation at 500 x *g* for 10 min prior to pH adjustment was done to allow separation of any particles that were not solubilized; this allowed for a homogenous texture when printing. Ice cold 10M NaOH was used to adjust the pH of the dECM solution to the physiological range; while the dECM was kept below 10°C to avoid premature crosslinking of the solution. A Bio X bioprinter (Cellink, Boston, MA) equipped with a cooling printhead and an 18-gauge blunt needle was used for all printed samples. Printhead temperature was maintained at 14°C to avoid premature crosslinking of the bioink, print bed

temperature was kept at 30°C to help begin the crosslinking process prior to the 1-hour incubation period to achieve full gelation. A print stabilizing solution of 1% Xanthium Gum was used to ensure the stability of the print prior to gelation, a modification of the technique described in Noor et al. (2019). For the cell-laden bio printed structure a cell suspension of 1×10 (Limperopoulos et al., 2002) cells/mL was mixed with the solubilized, pH-adjusted dECM immediately prior to bioprinting. Printhead and print bed temperatures were maintained at 14 and 30°C, respectively.

Autodesk Fusion 360 was used for Computer-Aided Design (CAD). The tensile testing shape was drawn to ASTM D412- Die A for thermoplastic elastomers, with minor modifications due to the biological nature of the samples. Dimensions for the aorta construct were taken from previous literature (Walther et al., 1985; Jarvisalo et al., 2001; Skilton et al., 2005; Taketazu et al., 2017).

Histological Staining

The tissue samples were processed using a Thermo Scientific Spin Tissue Processor Microm STP-120. Tissues were fixed using 4% formalin at 4°C overnight, followed by dehydration. Samples were dehydrated in increasing ethanol concentrations (starting with 70, 95, and 100%), followed by immersion in xylene two times and paraffin infiltration. Paraffin-embedded tissues were sectioned at 4–6 µm using a Shandon Finesse ® E/ME microtome. All samples were deparaffinized in three xylene washes then rehydrated in decreasing ethanol concentrations (100, 95, 70, and 50%), with each wash lasting 3 min. Hematoxylin and eosin (H&E) staining was done post-deparaffinization. Following rehydration, the samples were exposed to hematoxylin solution for 2 min, then rinsed with running water for 1-minute, distilled water for 30 s, and 95% alcohol for an additional 30 s. Immediately after, the samples were exposed to eosin solution for 1 min, then washed with increasing amounts of alcohol (95% x2, 100% x2) for 2 min each, then two xylene washes each for 2 min. Trichrome staining was done using Masson's Trichrome Staining Kit; all kit procedures were precisely followed. All samples were mounted using Cytoseal™60 (Thermo Scientific REF#8310-4).

Microscopy

For scanning electron microscopy imaging, samples were fixed using 4% formalin and dehydrated in increasing ethanol concentrations prior to lyophilization. All samples were sputter-coated for 20 s and viewed using a Hitachi S-4800-II SEM. A Nikon AZ100 inverted light microscope was used for histological imaging.

Mechanical Testing

Uniaxial tensile testing was done at room temperature in order to determine the mechanical properties of native tissue and decellularized printed tissue. One group of samples was taken from a fresh whole porcine heart; rectangles were cut vertically along the sagittal plane. Each sample's thickness was determined by measurements using a digital caliper. The second sample group consisted of printed decellularized ECM made to ASTM standard D638—Type I and also measured using a digital caliper. All specimens were patted dry, fixed to grips, and placed in the uniaxial electromechanical tensile testing machine (MTESTQuattro), where they were subjected to a strain rate of $5\ \text{mm min}^{-1}$ at room temperature until rupture. Forces were measured by a 200 lb. load cell and elongation by the internal sensor as well as by displacement of the reference grid.

Tensile Data Analysis

The stress-strain relationships for the samples tested were obtained using the Mooney-Rivlin Model for incompressible hyperelastic materials (Peattie et al., 1996; Rubin and Krempl, 2010; Ruiz de Galarreta et al., 2016). Where:

$$Tensile\ stress\ \sigma = \frac{F}{A_o} \tag{1}$$

$$Stretch\ ratio\ \lambda = \frac{\Delta L}{L_0} - 1 \tag{2}$$

Because the mechanical testing conducted was a uniaxial tensile test:

$$\sigma_{1\,1} - \sigma_{3\,3} = 2C_1\left(\lambda^2 - \frac{1}{\lambda}\right) - 2C_2\left(\frac{1}{\lambda^2} - \lambda\right) \tag{3}$$

And:

$$\sigma_{2\,2} - \sigma_{3\,3} = 0 \tag{4}$$

In this case, the model can be further simplified under the assumption of simple tension making:

$$\sigma_{2\,2} = \sigma_{3\,3} = 0 \tag{5}$$

Therefore:

$$\sigma_{1\,1} = \left(2C_1 + \frac{2C_2}{\lambda}\right)\left(\lambda^2 - \frac{1}{\lambda}\right) \tag{6}$$

This data was then plotted to find the predicted stress-stretch ratio diagrams. Young's modulus was derived from the slope at the linear region of the graph. Poisson's ratio was determined by taking the transversal elongation and dividing by axial compression.

RESULTS

Decellularization of Porcine Hearts

Chemical decellularization of the cardiac tissue resulted in visual, physical changes to the structure and state of the tissue sections (**Figures 1A–F**). When subjected to temperatures of 37°C post enzymatic digestion the decellularized ECM showed three different stages of crosslinking. At a pH of 3 it was a low viscosity fluid, transitioned to being highly viscous at a pH of 5, and finally crosslinked successfully at a pH of 7 (**Figures 1G–I**). Hematoxylin and eosin staining of the cardiac tissue pre-decellularization confirmed normal morphology of the cellular structures, no nuclear irregularity or clumping of the chromatin to indicate cancerous areas. Staining with Masson's Trichrome showed collagenous areas throughout the section; a normal

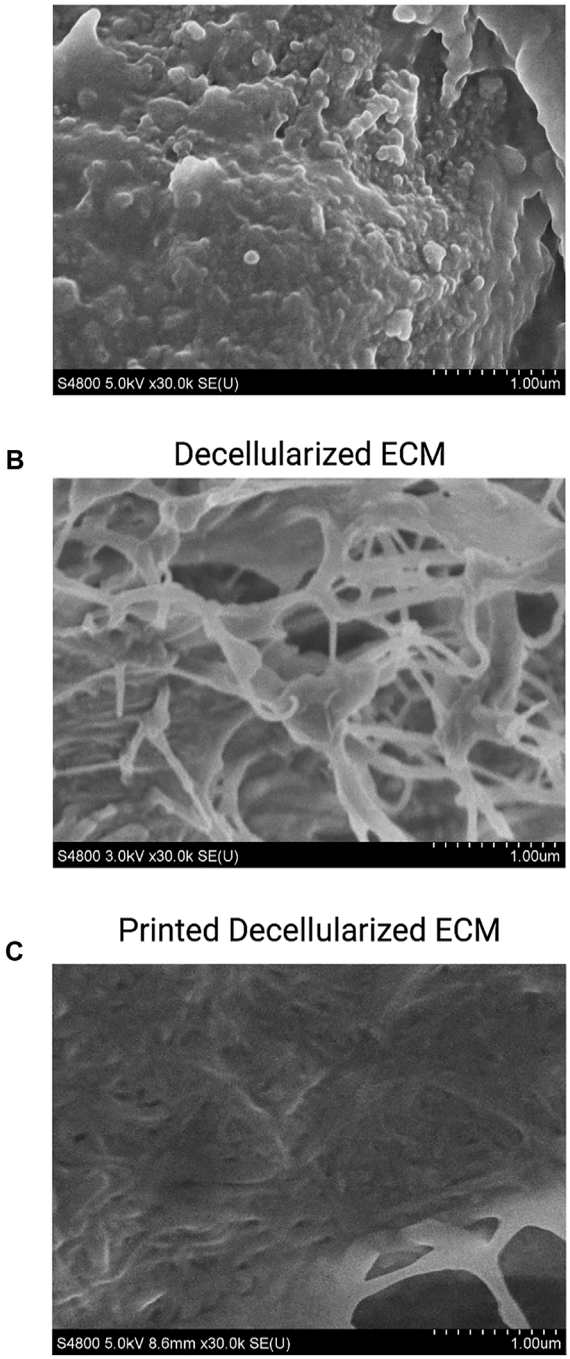

FIGURE 3 | SEM of porcine cardiac tissue **(A)**, decellularized extracellular matrix **(B)**, and printed decellularized matrix **(C)**.

extracellular matrix was visible and necessary for future experiments' success. Once chemical decellularization, enzymatic digestion, and gelation of the decellularized ECM was completed, the stains were repeated to determine the presence of cellular matter and collagen. Staining showed a lack of cellular structures and nuclear matter; collagen fibrils are uniformly seen throughout the decellularized sample (see **Figure 2**). Randomly oriented collagen fibrils can be seen in the decellularized ECM's dense network, whereas the printed decellularized ECM's topography was similar to that of the porcine cardiac tissue (see **Figure 3**).

Mechanical Characteristics

Video stills of the tensile testing allowed for precise comparison of the change in length (ΔL) and change in width (ΔH) (**Figure 4**) in addition to the information gathered for the stress-strain ratio curves. Due to the samples' large deformations when undergoing forces, a Mooney-Rivlin model was used to find the samples' effective stresses (**Figure 5**). The response of the cardiac tissue (**Figures 5A, C**) indicates an overall higher tensile strength and greater plasticity than that of the printed decellularized ECM (**Figures 5B, D**). Young's Modulus and Poisson's Ratio for the individual samples are shown in **Table 1**. The printed decellularized ECM ($\bar{E}$ = 920 kPa) exhibited 2.7 times greater elasticity than the porcine cardiac tissue ($\bar{E}$ = 330 kPa). Similarly, the porcine cardiac tissue displayed 1.8 times the deformation ($\bar{\nu}$ = 3.93) prior to failure than the printed decellularized ECM ($\bar{\nu}$ = 2.13). Neither value showed a significant ($p < 0.05$) difference between the two sample types.

Bioprinting

Due to the highly viscous nature of the bioink used a larger gauge needle was selected for bioprinting. The dog bone and cylindrical structures were printed without deformation issues or bleeding of the bioink into the support bath (**Figure 6**). The printed aortic structures maintained their original shape and dimensions post crosslinking, as did the tensile testing samples. Confocal imaging of the bioprinted HASMC indicates normal cell attachment and morphology 24 h post-print, with no necrotic areas as seen in **Figure 6D**.

DISCUSSION

The study examined mechanical characteristics and cellular compatibility of bioprinted decellularized ECM. Successful decellularization is an essential first step in the process; cellular remnants in the bioink cause necrotic pockets, which lead to contamination and complete failure of the construct. Additionally, as the project's end goal is implantation into a body, rejection is a considerable concern; complete decellularization ensures the possibility of rejection is lowered. Hematoxylin and Eosin staining of the tissues pre-decellularization show normal physiology with clear musculature orientation; once the tissue has undergone decellularization, a drastic change to the physiological properties occurs, with little to no cells present in the sample. Trichrome staining exhibited large quantities of collagen in both samples. Once decellularized, the fibers are no longer uniformly oriented; instead, they are found disbursed throughout the sample, seemingly at random. This can also be seen in the SEM images. Fibrillar collagen and additional elastic fibers comprise approximately 50% of the aorta's dry weight, making it the primary defining element in the mechanical properties of

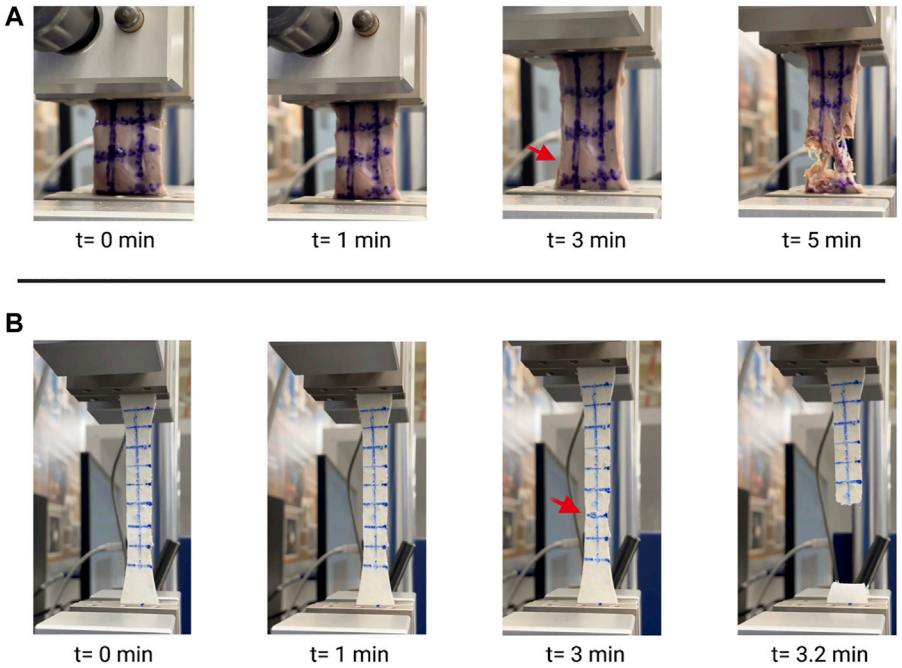

FIGURE 4 | Video stills of porcine cardiac tissue **(A)** and decellularized ECM **(B)** undergoing tensile testing. Red arrows indicate initial failure point.

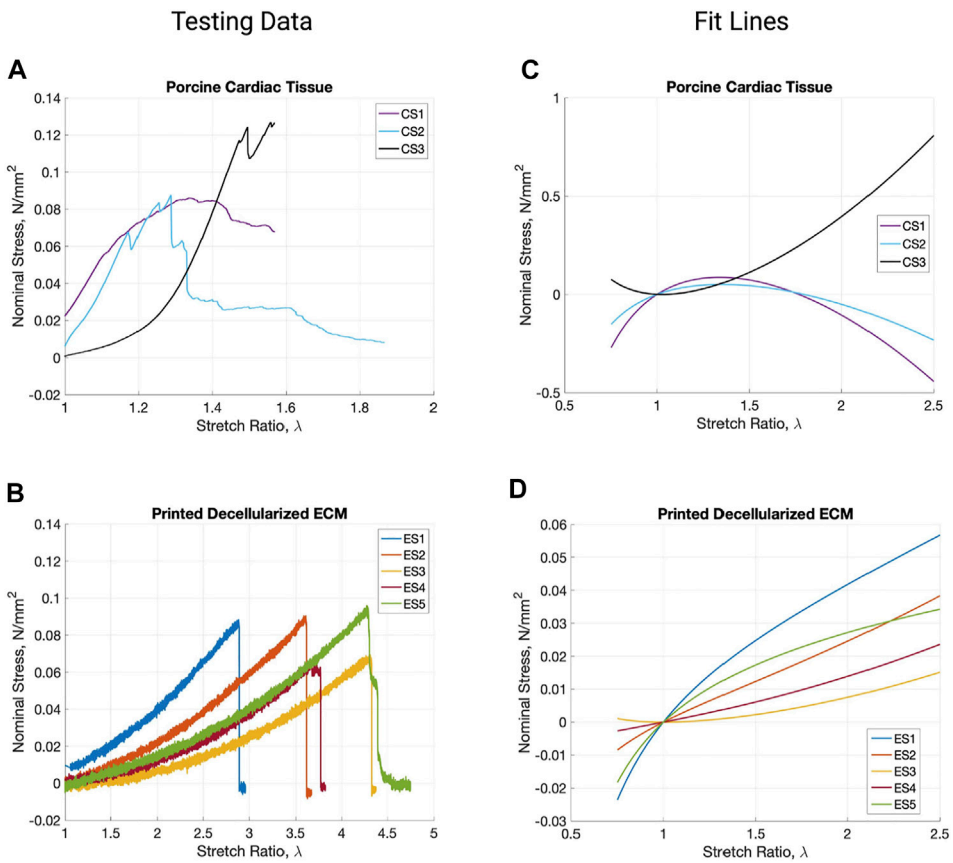

FIGURE 5 | Stress *vs.* stretch ratio graphs of the raw testing data from porcine cardiac tissue **(A)** and printed decellularized ECM **(B)**. Mooney-Revilin fit lines for the testing data curves of cardiac tissue **(C)** and the printed decellularized ECM **(D)**.

TABLE 1 | Mechanical Characteristics.

Sample	Young's modulus (E) kPa	Poisson's ratio (*v*)
CS1	233	3.17
CS2	288	6.93
CS3	470	1.69
ES1	1,284	1.61
ES2	1,134	0.74
ES3	831	3.00
ES4	576	3.83
ES5	770	1.46

CS1–3 refers to the porcine cardiac tissue samples 1–3. ES1–5 refers to the printed decellularized extracellular matrix samples 1–5.

the large vessel (Harkness et al., 1955; Borst et al., 1983; Jana et al., 2019). Fiber orientation is responsible for the strength of the vessel wall; therefore, the non-uniform orientation of the fibers diminishes the tensile strength of the tissue (Wagenseil and Mecham, 2009).

Similarly, the digestion of the dECM must be carefully monitored. Enzymatic activity is temperature, pH, and concentration sensitive, as is protein structural stability; the lower pH of 3 and 5 lack the environmental factors necessary to promote the electrostatic and hydrophobic interactions between the collagen molecules that facilitate proper thermal crosslinking (Theocharis et al., 2019). At physiological pH (7), not only are the crosslinking capabilities optimized, but the environment for cellular adhesion, proliferation, and signaling is ideal.

Currently, SDS treatment for decellularization, such as what was used, is considered the preferred method for preserving the structural components of elastin and collagen (Grauss et al., 2003; Liao et al., 2007). These previous studies have been done on whole tissue sections and found minor, non-significant differences in the tangent modulus (Zou and Zhang, 2012). Alternatively, bioprinting of the matrix requires more aggressive treatments to the tissue, leading to significant structural and chemical alterations to the matrix. Fresh cardiac tissue samples were compared to the bioprinted samples for uniaxial tensile testing. Though both exhibited hyperplastic properties, the printed dECM samples saw a heightened elasticity, 2.7X that of the cardiac tissue. This elasticity of 920 kPa is 1.8X that of a native infant ascending aorta at normal physiological pressure (60 mmHg) and closer to the elasticity seen under the high stress conditions of higher blood pressure (967.45 kPa) (Ligere et al., 2012).

A lack of stiffness in a vessel is usually associated with structural immaturity, which is remedied by progressive blood pressure increases during fetal development, or aging of the vessel (Dobrin, 1978; Lang et al., 1994; Akira and Yoshiyuki, 2006). In this case, the tested samples contained no cells, thus lacking the

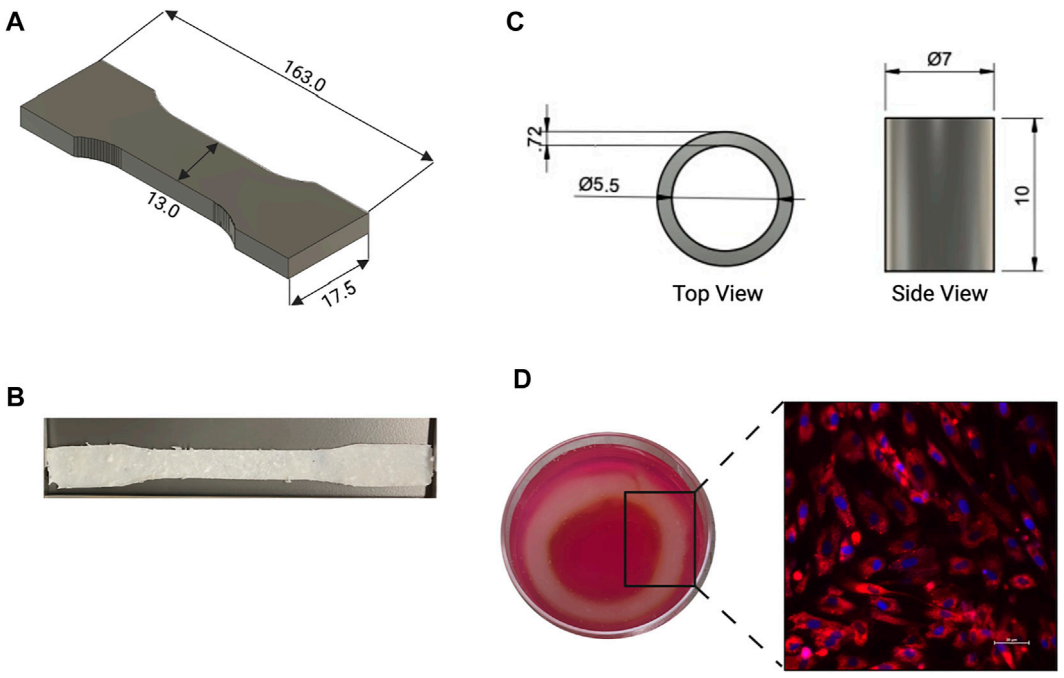

FIGURE 6 | (A) CAD and **(B)** image of dog bone shape used for tensile testing of the printed dECM. **(C)** Top and side viewpoint of CAD used to print aortic construct. **(D)** Printed aortic construct in media and confocal image of Human Aortic Smooth Muscle Cells (HASMC) that were grown for 24 h after bioprinting, red represents the membrane (PKH26 general membrane stain), blue represents the nuclear region of the cells (DAPI).

additional stability given by the smooth muscle fibers and the biomechanical morphological changes that come from the environmental and biochemical stimuli the cells receive.

Additionally, elasticity of the aortic tissue is greatly affected by surgical interventions. Depending on the type of anastomosis that the physician chooses, the moduli can range from 683.29–1,232.79 kPa for an extended end-to-end anastomosis or 902.39–1,261.35 kPa for an end-to-end anastomosis (Ligere et al., 2012). As the elastic moduli of the dECM falls within the parameters that are seen for post-operative aortic tissues, we anticipate the addition of cells to the construct will bring the overall elasticity down to levels near those of the native aorta.

In a step towards making full aortic constructs, we incorporated human cells by co-printing and culturing ASMC in the dECM. This allowed us to determine cellular viability and adhesion capabilities of the cells within the matrix. 24 h post-printing, the ASMC exhibited normal morphology, and no necrotic areas were visible. The biocompatibility of the dECM post-printing is promising, pointing to the ability of the cells to grow within the matrix for extended periods of time. Overall, the study found an increase in hyperelasticity of the dECM and an ability for ASMC to thrive *in vitro* post-printing, indicating our ability to bioengineer an immature large-scale aortic model, furthering the capabilities of vascular engineering.

DATA AVAILABILITY STATEMENT

The raw data supporting the conclusion of this article will be made available by the authors, without undue reservation.

AUTHOR CONTRIBUTIONS

BO—design of experiments, bioprinting, data analysis, drafting of manuscript. JA—data analysis. MF—imaging. JC—conceptual design, mechanical testing design, mechanical data interpretation. TB—conceptual design, experimental design, editing of manuscript.

FUNDING

This material is based upon work supported by the National Science Foundation (NSF) Graduate Research Fellowship under Grant No. 1744621. This research and BO was also funded by the National Institute of General Medical Sciences (NIGMS) of the National Institutes of Health (NIH) under linked Award Numbers RL5GM118969, TL4GM118971, and UL1GM118970. The content of this study is solely the responsibility of the authors and does not necessarily represent the official views of the NIH, NSF, and UTEP.

REFERENCES

Akira, M., and Yoshiyuki, S. (2006). Placental Circulation, Fetal Growth, and Stiffness of the Abdominal Aorta in Newborn Infants. *J. Pediatr.* 148, 49–53. doi:10.1016/j.jpeds.2005.06.044

Badylak, S. F., Freytes, D. O., and Gilbert, T. W. (2009). Extracellular Matrix as a Biological Scaffold Material: Structure and Function. *Acta Biomater.* 5, 1–13. doi:10.1016/j.actbio.2008.09.013

Bissell, M. J., Hall, H. G., and Parry, G. (1982). How Does the Extracellular Matrix Direct Gene Expression? *J. Theor. Biol.* 99, 31–68. doi:10.1016/0022-5193(82)90388-5

Bornstein, P., McPherson, J., and Sage, H. (1982). "Synthesis and Secretion of Structural Macromolecules by Endothelial Cells in Culture," in *Pathobiology of the Endothelial Cell, P and S Biomedical Sciences Symposia*. Editors H. L. Nossel and H. J. Vogel (Amsterdam, Netherlands: Elsevier), 6, 215–228. doi:10.1016/b978-0-12-521980-8.50020-1

Borst, H., Walterbusch, G., and Schaps, D. (1983). Extensive Aortic Replacement Using "Elephant Trunk" Prosthesis. *Thorac. Cardiovasc. Surg.* 31, 37–40. doi:10.1055/s-2007-1020290

Carr, J. A., Amato, J. J., and Higgins, R. S. D. (2005). Long-Term Results of Surgical Coarctectomy in the Adolescent and Young Adult with 18-Year Follow-Up. *Ann. Thorac. Surg.* 79, 1950–1956. doi:10.1016/j.athoracsur.2005.01.004

Dobrin, P. (1978). Mechanical Properties of Arteries. *Physiol. Rev.* 58, 397–460. doi:10.1152/physrev.1978.58.2.397

Easson, K., Dahan-Oliel, N., Rohlicek, C., Sahakian, S., Brossard-Racine, M., Mazer, B., et al. (2019). A Comparison of Developmental Outcomes of Adolescent Neonatal Intensive Care Unit Survivors Born with a Congenital Heart Defect or Born Preterm. *J. Pediatr.* 207, 34–41. e2. doi:10.1016/j.jpeds.2018.11.002

Fawzy, M. E., Awad, M., Hassan, W., Al Kadhi, Y., Shoukri, M., and Fadley, F. (2004). Long-term Outcome (Up to 15 years) of Balloon Angioplasty of Discrete Native Coarctation of the Aorta in Adolescents and Adults. *J. Am. Coll. Cardiol.* 43, 1062–1067. doi:10.1016/j.jacc.2003.10.040

Fourdain, S., St-Denis, A., Harvey, J., Birca, A., Carmant, L., Gallaghera, A., et al. (2019). Language Development in Children with Congenital Heart Disease Aged 12–24 Months. *Eur. J. Paediatr. Neurol.* 23, 491–499. doi:10.1016/j.ejpn.2019.03.002

Fung, Y. (1933). *Mechanical Properties of Living Tissues*, 24. Berlin/Heidelberg, Germany: Springer.

Gilbert, T. W., Sellaro, T. L., and Badylak, S. F. (2006). Decellularization of Tissues and Organs. *Biomaterials* 27, 3675–3683. doi:10.1016/j.biomaterials.2006.02.014

Grauss, R. W., Hazekamp, M. G., Van Vliet, S., Gittenberger-De Groot, A. C., and DeRuiter, M. C. (2003). Decellularization of Rat Aortic Valve Allografts Reduces Leaflet Destruction and Extracellular Matrix Remodeling. *J. Thorac. Cardiovasc. Surg.* 126, 2003–2010. doi:10.1016/s0022-5223(03)00956-5

Harkness, M., Harkness, R., and McDonald, D. (1955). The Collagen and Elastin Content of the Arterial wall. *J. Physiol.* 127, 33–4p.

Jana, S., Hu, M., Shen, M., and Kassiri, Z. (2019). Extracellular Matrix, Regional Heterogeneity of the Aorta, and Aortic Aneurysm. *Exp. Mol. Med.* 51. doi:10.1038/s12276-019-0286-3

Jarvisalo, M., Jartti, L., Nanto-Salonen, K., Irjala, K., Rönnemaa, T., Hartiala, J. J., et al. (2001). Increased Aortic Intima-media Thickness: a Marker of Preclinical Atherosclerosis in High-Risk Children. *Circulation* 104, 2943–2947. doi:10.1161/hc4901.100522

Jenkins, K. J., Correa, A., Feinstein, J. A., Botto, L., Britt, A. E., Daniels, S. R., et al. (2007). Noninherited Risk Factors and Congenital Cardiovascular Defects: Current Knowledge - A Scientific Statement from the American Heart Association Council on Cardiovascular Disease in the Young. *Circulation* 115, 2995–3014. doi:10.1161/circulationaha.106.183216

Kleigman, R. M. (2011). *Nelson Textbook of Padetricians*. Amsterdam, Netherlands: Elsevier.

Lang, R. M., Cholley, B. P., Korcarz, C., Marcus, R. H., and Shroff, S. G. (1994). Measurement of Regional Elastic Properties of the Human Aorta: A New Application of Transesophageal Echocardiography with Automated Border Detection and Calibrated Subclavian Pulse Tracings. *Circulation* 90, 1875–1882. doi:10.1161/01.cir.90.4.1875

Liao, J., Yang, L., Grashow, J., and Sacks, M. S. (2007). The Relation between Collagen Fibril Kinematics and Mechanical Properties in the Mitral Valve Anterior Leaflet. *J. Biomech. Eng.* 129, 78–87. doi:10.1115/1.2401186

Ligere, E., Kasyanov, V., Sikora, N., and Lacis, A. (2012). "Biomechanical Properties of the Aorta in Neonates and Infants," in *Analysis and Design of Biological Materials and Structures*. Editors A. Ochsner, L. F. M. da Silva, and H. Altenbach (Berlin; Heidelberg: Springer-Verlag), 6, 125–132. doi:10.1007/978-3-642-22131-6_10

Limperopoulos, C., Majnemer, A., Shevell, M. I., Rohlicek, C., Rosenblatt, B., Tchervenkov, C., et al. (2002). Predictors of Developmental Disabilities after Open Heart Surgery in Young Children with Congenital Heart Defects. *J. Pediatr.* 141, 51–58. doi:10.1067/mpd.2002.125227

Murphy, S. V., and Atala, A. (2014). 3D Bioprinting of Tissues and Organs. *Nat. Biotechnol.* 32, 773–785. doi:10.1038/nbt.2958

Nelson, C. M., and Bissell, M. J. (2006). Of Extracellular Matrix, Scaffolds, and Signaling: Tissue Architecture Regulates Development, Homeostasis, and Cancer. *Annu. Rev. Cel Dev. Biol.* 22, 287–309. doi:10.1146/annurev.cellbio.22.010305.104315

Noor, N., Shapira, A., Edri, R., Gal, I., Wertheim, L., and Dvir, T. (2019). 3D Printing of Personalized Thick and Perfusable Cardiac Patches and Hearts. *Adv. Sci.* 6, 1900344. doi:10.1002/advs.201900344

Ott, H. C., Matthiesen, T. S., Goh, S.-K., Black, L. D., Kren, S. M., Netoff, T. I., et al. (2008). Perfusion-decellularized Matrix: Using Nature's Platform to Engineer a Bioartificial Heart. *Nat. Med.* 14, 213–221. doi:10.1038/nm1684

Park, K. M., and Woo, H. M. (2012). Porcine Bioengineered Scaffolds as New Frontiers in Regenerative Medicine. *Transpl. Proc.* 44, 1146–1150. doi:10.1016/j.transproceed.2012.03.043

Pati, F., Jang, J., Ha, D.-H., Kim, S. W., Rhie, J.-W., Shim, J.-H., et al. (2014). Printing Three-Dimensional Tissue Analogues with Decellularized Extracellular Matrix Bioink. *Nat. Commun.* 5, 1–11. doi:10.1038/ncomms4935

Peattie, R. A., Asbury, C. L., Bluth, E. I., and Riehle, T. J. (1996). Steady Flow in Models of Abdominal Aortic Aneurysms. Part II: Wall Stresses and Their Implication for *In Vivo* Thrombosis and Rupture. *J. Ultrasound Med.* 15, 689–696. doi:10.7863/jum.1996.15.10.689

Rider, P., Kačarević, Ž. P., Alkildani, S., Retnasingh, S., and Barbeck, M. (2018). Bioprinting of Tissue Engineering Scaffolds. *J. Tissue Eng.* 9, 2041731418802090. doi:10.1177/2041731418802090

Rubin, D., and Krempl, E. (2010). *Introduction to Continuum Mechanics. Introduction to Continuum Mechanics*. Amsterdam, Netherlands: Elsevier. doi:10.1016/B978-0-7506-8560-3.X0001-1

Ruiz de Galarreta, S., Cazón, A., Antón, R., and Finol, E. A. (2016). A Methodology for Verifying Abdominal Aortic Aneurysm Wall Stress. *J. Biomech. Eng.* 139, 011006. doi:10.1115/1.4034710

Skilton, M. R., Evans, N., Griffiths, K. A., Harmer, J. A., and Celermajer, D. S. (2005). Aortic wall Thickness in Newborns with Intrauterine Growth Restriction. *Lancet* 365, 1484–1486. doi:10.1016/s0140-6736(05)66419-7

Taketazu, M., Sugimoto, M., Saiki, H., Ishido, H., Masutani, S., and Senzaki, H. (2017). Developmental Changes in Aortic Mechanical Properties in Normal Fetuses and Fetuses with Cardiovascular Disease. *Pediatr. Neonatol.* 58, 245–250. doi:10.1016/j.pedneo.2016.05.004

Theocharis, A. D., Manou, D., and Karamanos, N. K. (2019). The Extracellular Matrix as a Multitasking Player in Disease. *FEBS J.* 286, 2830–2869. doi:10.1111/febs.14818

Wagenseil, J. E., and Mecham, R. P. (2009). Vascular Extracellular Matrix and Arterial Mechanics. *Physiol. Rev.* 89, 957–989. doi:10.1152/physrev.00041.2008

Walhout, R. J., Lekkerkerker, J. C., Oron, G. H., Bennink, G. B. W., and Meijboom, E. J. (2004). Comparison of Surgical Repair with Balloon Angioplasty for Native Coarctation in Patients from 3 Months to 16 Years of Age. *Eur. J. Cardiothoracic Surg.* 25, 722–727. doi:10.1016/j.ejcts.2004.04.008

Walther, F. J., Siassi, B., King, J., and Wu, P. Y. K. (1985). Normal Values of Aortic Root Measurements in Neonates. *Pediatr. Cardiol.* 6, 61–63. doi:10.1007/bf02282739

Wolf, M. T., Daly, K. A., Brennan-Pierce, E. P., Johnson, S. A., Carruthers, C. A., D'Amore, A., et al. (2012). A Hydrogel Derived from Decellularized Dermal Extracellular Matrix. *Biomaterials* 33, 7028–7038. doi:10.1016/j.biomaterials.2012.06.051

Zhang, Y. S., Arneri, A., Bersini, S., Shin, S.-R., Zhu, K., Goli-Malekabadi, Z., et al. (2016). Bioprinting 3D Microfibrous Scaffolds for Engineering Endothelialized Myocardium and Heart-On-A-Chip. *Biomaterials* 110, 45–59. doi:10.1016/j.biomaterials.2016.09.003

Zou, Y., and Zhang, Y. (2012). Mechanical Evaluation of Decellularized Porcine Thoracic Aorta. *J. Surg. Res.* 175, 359–368. doi:10.1016/j.jss.2011.03.070

Conflict of Interest: The authors declare that the research was conducted in the absence of any commercial or financial relationships that could be construed as a potential conflict of interest.

Publisher's Note: All claims expressed in this article are solely those of the authors and do not necessarily represent those of their affiliated organizations, or those of the publisher, the editors and the reviewers. Any product that may be evaluated in this article, or claim that may be made by its manufacturer, is not guaranteed or endorsed by the publisher.

Copyright © 2022 Oropeza, Adams, Furth, Chessa and Boland. This is an open-access article distributed under the terms of the Creative Commons Attribution License (CC BY). The use, distribution or reproduction in other forums is permitted, provided the original author(s) and the copyright owner(s) are credited and that the original publication in this journal is cited, in accordance with accepted academic practice. No use, distribution or reproduction is permitted which does not comply with these terms.

frontiers in Bioengineering and Biotechnology

REVIEW
published: 10 March 2022
doi: 10.3389/fbioe.2022.833163

Re-Endothelialization of Decellularized Liver Scaffolds: A Step for Bioengineered Liver Transplantation

Kewei Li[1,2†], *Mohammad Tharwat*[1,3†], *Ellen L. Larson*[1], *Philipp Felgendreff*[1,4], *Seyed M. Hosseiniasl*[1], *Anan Abu Rmilah*[1], *Khaled Safwat*[3], *Jeffrey J. Ross*[5] *and Scott L. Nyberg*[1,6*]

[1]Department of Surgery, Mayo Clinic, Rochester, MN, United States, [2]Department of Pediatric Surgery, West China Hospital of Sichuan University, Chengdu, China, [3]General Surgery Department, Faculty of Medicine, Zagazig University, Zagazig, Egypt, [4]Department for General, Visceral and Vascular Surgery, University Hospital Jena, Jena, Germany, [5]Miromatrix Medical Inc, Eden Prairie, MN, United States, [6]William J. von Liebig Center for Transplantation and Clinical Regeneration, Mayo Clinic, Rochester, MN, United States

Bioengineered livers (BELs) are an attractive therapeutic alternative to address the donor organ shortage for liver transplantation. The goal of BELs technology aims at replacement or regeneration of the native human liver. A variety of approaches have been proposed for tissue engineering of transplantable livers; the current review will highlight the decellularization-recellularization approach to BELs. For example, vascular patency and appropriate cell distribution and expansion are critical components in the production of successful BELs. Proper solutions to these components of BELs have challenged its development. Several strategies, such as heparin immobilization, heparin-gelatin, REDV peptide, and anti-CD31 aptamer have been developed to extend the vascular patency of revascularized bioengineered livers (rBELs). Other novel methods have been developed to enhance cell seeding of parenchymal cells and to increase graft functionality during both bench and *in vivo* perfusion. These enhanced methods have been associated with up to 15 days of survival in large animal (porcine) models of heterotopic transplantation but have not yet permitted extended survival after implantation of BELs in the orthotopic position. This review will highlight both the remaining challenges and the potential for clinical application of functional bioengineered grafts.

Keywords: bioengineered livers (BELs), liver transplantation, decellularization, scaffolds, heterotopic transplantation, orthotopic transplantation

OPEN ACCESS

Edited by:
Kamal Hany Hussein, Assiut University, Egypt

Reviewed by:
Ji Bao, Sichuan University, China
Basak E. Uygun, Massachusetts General Hospital and Harvard Medical School, United States
Kazuki Tajima, Kitasato University School of Veterinary Medicine, Japan

***Correspondence:**
Scott L. Nyberg
Nyberg.Scott@mayo.edu

[†]These authors have contributed equally to this work and share first authorship

Specialty section:
This article was submitted to Biomaterials, a section of the journal Frontiers in Bioengineering and Biotechnology

Received: *10 December 2021*
Accepted: *11 February 2022*
Published: *10 March 2022*

Citation:
Li K, Tharwat M, Larson EL, Felgendreff P, Hosseiniasl SM, Rmilah AA, Safwat K, Ross JJ and Nyberg SL (2022) Re-Endothelialization of Decellularized Liver Scaffolds: A Step for Bioengineered Liver Transplantation. Front. Bioeng. Biotechnol. 10:833163. doi: 10.3389/fbioe.2022.833163

Abbreviations: BELs, Bioengineered livers; rBELs, revascularized bioengineered livers; HCC, Hepatocellular carcinoma; NAFLD, Non-alcoholic fatty liver disease; ALD, Acute liver disease; ESLD, End stage liver disease; ECM, Extracellular matrix; ECs, Endothelial cells; PV, Portal vein; SHIVC, Suprahepatic inferior vena cava; HUVECs, Human umbilical vein endothelial cells; HG, Heparin-gelatin mixture; GFP, Green fluorescent protein; MSCs, Mesenchymal stem cells; TAA, Thioacetamide; iPSCs, Induced pluripotent stem cells; AFP, Alpha-fetoprotein; ALB, Albumin; GCR, Glucose consumption rate; IHIVC, Infrahepatic inferior vena cava; IVC, Inferior vena cava.

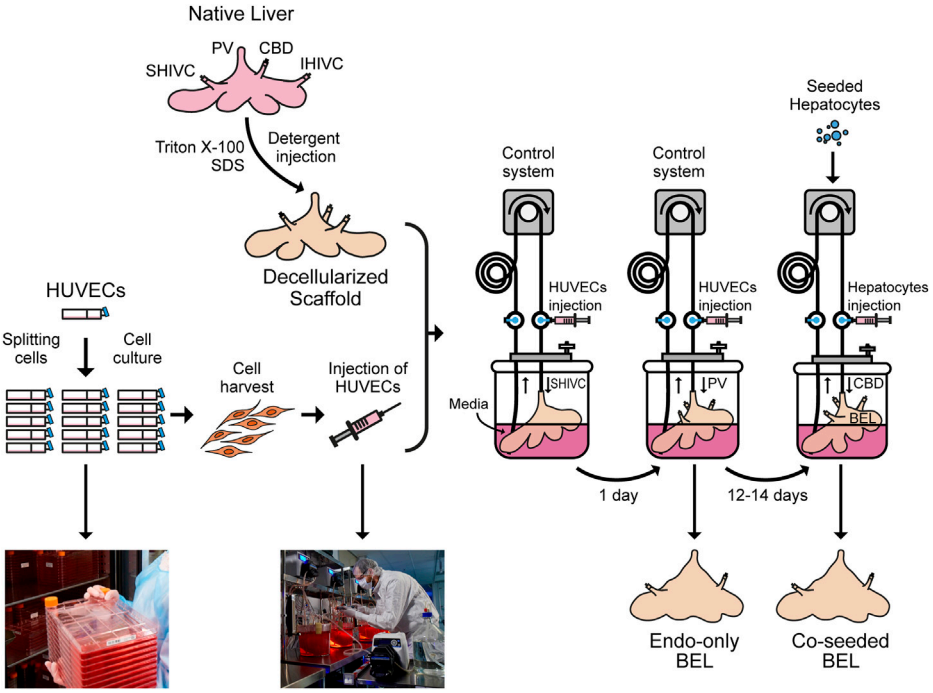

GRAPHICAL ABSTRACT | Native porcine livers are cannulated on the PV, IVC and SVC and perfused with Triton X-100 and SDS solutions to get a decellularized liver. Meanwhile, HUVECs are cultured in 2D tissue culture flasks, harvested and injected through the SHIVC of the decellularized liver, followed by the PV 24 h later to get endo-only BEL. After 12–14 days in media the seeded hepatocytes can be injected through the CBD to get co-seeded BEL.

INTRODUCTION

Chronic liver disease is a major global health challenge, responsible for approximately two million deaths each year (Melaram, 2021). As a result, liver disease accounts for 3.5% of all deaths worldwide. This evolution can be attributed to the rising prevalence of liver cirrhosis and hepatocellular carcinoma (Asrani et al., 2019). Despite the fact that the cause of this disease varies from country to country. Hepatitis B and C viruses are primarily responsible for the pathogenesis of cirrhosis and HCC in Asian countries, whereas toxic factors are mostly responsible for chronic liver disease in Western industrialized nations (Wang et al., 2014). Also, NAFLD and ALD are on the rise, notwithstanding the efforts to eradicate and control viral hepatitis through programs such as WHO 2030. Patients with liver disease are becoming an increasingly difficult medical and socioeconomic challenge, as this trend is unlikely to be reversed in the foreseeable future. Furthermore, we need to improve and expand our therapeutic options to ensure that patients are provided the opportunity for treatment (Paik et al., 2020).

Currently, only a limited number of treatment options are available for patients with end-stage liver disease (ESLD). Most of these options aim to save the liver quality and stabilize the disease with a palliative intent. The only curative treatment for patients with ESLD is liver transplantation. This invasive procedure offers the opportunity not only to replace the entire affected organ, including the local tumor, but also to prevent additional metastases (Jimenez-Romero et al., 2019; Yang et al., 2019; Mazzaferro et al., 2020). The key proof for the clinical effectiveness of curative liver transplantation is the patients' postoperative survival. As a result, the 1- and 5-years survival rates of ESLD patients following transplantation were generally 70–90% and 60–80%, respectively (Haydon and Neuberger, 2000). To optimize the likelihood of success of liver transplantation, it is critical to identify appropriate recipients and make transplantable donor organs readily available. One of the most significant obstacles to modern transplantation surgery is the scarcity of donor organs acceptable for transplantation, as well as the related higher mortality of patients on the waiting list (Arulraj and Neuberger, 2011).

Xenogenic liver transplantation offers an infinite supply of donor organ material. However, numerous significant translational difficulties, such as immunological incompatibility, basic variations in basal metabolism between humans and other animals, and coagulopathy, stand in the way of this solution (Mazza et al., 2018; Suchy et al., 2018). Alternatively, as a result of low cell engraftment effectiveness and loss of cell function over time, isolated hepatocyte transplantation as an alternative to whole liver transplantation may only be considered as interim metabolic treatment of inherited liver disease or a bridge therapy in acute liver failure as it does not correct the sequelae of portal hypertension created by a cirrhotic liver (Nicolas et al., 2016). Consequently, it is essential to find new and innovative sources for usable organs as long as others substitutes such as xenogenic liver transplantation and isolated hepatocyte transplantation failed to compensate the need for

transplantable organs. One experimental approach that has been advanced by many transplantation experts is the development of bioengineered livers as an alternative and potentially inexhaustible organ source (Pla-Palacin et al., 2018; Mirdamadi et al., 2020).

BEL is a promising therapeutic alternative to liver transplantation, aiming to replace or regenerate the human liver. It is emerging as one of the most significant scientific advances in the field of tissue engineering (Gilpin and Yang, 2017; Li et al., 2017; Agarwal et al., 2019; Kakabadze et al., 2019; Naeem et al., 2019). Moreover, this technique may potentially offer an endless source of patient-specific livers as it could eliminate the need for immunosuppression of recipients (Croce et al., 2019).

PRINCIPALS FOR BIOENGINEERED LIVERS

In order to develop a completely competent transplantable organ utilizing BEL, the two stages of decellularization and recellularization are necessary (Badylak et al., 2011; Baptista et al., 2011). Decellularization seeks to create a biocompatible decellularized scaffold that preserves the three-dimensional architecture and biochemical content of the original tissue while removing the cellular material to decrease the immunological reactivity (Uygun et al., 2010; Debnath et al., 2020; Hou et al., 2020; Moulisova et al., 2020). Enzymes and chemicals, along with mechanical agitation, freezing/thawing, and sonication, are various strategies for decellularization by disturbing cells and liberating their substance. In any case, the utilization of substances such as nonionic Triton X-100 and ionic sodium dodecyl sulfate (SDS), thought to be limited at whatever point conceivable to stay away from harm to the microarchitecture of the original ECM (Badylak et al., 2011). Decellularization may result in the loss of ECM components as well as permanent damage to the microarchitecture of the ECM. The success of decellularization is better evaluated by a multi-scale quantitative method based on measuring the remaining DNA and on histological evaluation of the preserved liver-specific microarchitecture (Moulisova et al., 2020).

ECM-based scaffold components and functions are assumed to be relatively conserved across species, and thus the scaffolds are thought to be less or nonimmunogenic, even when obtained from xenogeneic sources (Wang et al., 2011; Badylak, 2014; Struecker et al., 2015). The creation of a biological scaffold is closely tied to the success of liver regeneration, in addition to providing structural stability of the organ. The scaffold is critical as a substrate for cell adhesion, differentiation, and proliferation, as well as for facilitating vascularization for nutrition, oxygenation, and the physiological discharge of waste cell-derived metabolites (Ohashi et al., 2007; Haycock, 2011; Park et al., 2016; Naeem et al., 2019). Put another way, the ECM-based scaffold is no longer just considered as a lifeless or barren environment such as 2D cultures on Petri dishes, but rather a platform that actively participates in the dynamic control of the biological activity of the liver *in vivo* through creating a similar environment to the native one. This environment encourages cell growth and proliferation, preserves the complex structure of the vascular tree and facilitates cell-cell interaction (Ansari et al., 2020).

Two primary processes are regarded to ensure a proper recellularization of a decellularized graft: cell seeding followed by perfusion culture, which is commonly used to prepare cells for *in vivo* activity. The objective of cell seeding is to distribute cells with the graft matrix using a physiological composition and an appropriate number of cells similar to that in the native liver. For example, the adult human liver contains around 2.8×10^{11} hepatocytes (Baptista et al., 2011). Furthermore, the arrangement of cells into niches inside the scaffold is essential to closely approximate their normal distribution. Whether parenchymatous cells, such as hepatocytes which are responsible for function, or non-parenchymatous cells, such as endothelial cells which serve as an antithrombotic barrier, the distribution of these cells will determine the functionality of the new engineered liver graft. These cells are introduced into the scaffold by a variety of techniques, including injection and perfusion (Badylak et al., 2011; Baptista et al., 2011).

Significant progress has been made in the fabrication of tissue-engineered structures such as blood vessels, urinary bladder, and trachea. The transplantation of these structures requires the anastomosis of smaller vessels to the recipient circulation. However, a larger and more complex vascular supply will be necessary to maintain patency and perfusion of the network of vessels required for functionality of a totally tissue-engineered solid organ such as the heart, lung, and liver (Badylak et al., 2011; Baptista et al., 2011; Bao et al., 2015).

The liver is a particularly active metabolic organ, which presents prospective obstacles for the development of clinical-scale, implantable organs with significant perfusion and vascularization requirements (Zheng and Roberts, 2016). For example, normal function of hepatocytes requires a complex hierarchical vascular network that includes multiple enormous branches at the organ size as well as complex microvessels at the sinusoidal level (Shirakigawa et al., 2013; Watanabe et al., 2019). Furthermore, hepatocytes are rich in mitochondria and consume 10-fold more oxygen than most other cells of the body. Due to the high oxygen requirement of hepatocytes, the liver's normal vascular anatomy provides transport of oxygen and nutrients to approximately 200 μm or less. Similar requirements are necessary to avoid ischemic injury in BELs after transplantation (Cho et al., 2007; Uygun et al., 2010).

EARLY STAGES OF DECELLULARIZATION AND REVASCULARIZED SCAFFOLDS

One of the first studies of a tissue engineered organ was reported by Ott and colleagues in 2007, after they had developed a decellularization technique on rat hearts by coronary perfusion with detergents including SDS and Triton-X100. These methods succeeded in disrupting cells and nuclei and eliminating DNA without significant damage to the extracellular matrix scaffold. After recellularization, the new construct successfully maintained contractile function and drug responsiveness after 8 days in culture (Ott et al., 2008). These results represented a significant breakthrough for the application of this technique to other organs. Namely, an efficient and reproducible method

yielding a natural acellular three-dimensional framework void of cells from any organ (Croce et al., 2019).

This technique was subsequently optimized for liver decellularization, then preliminarily expanded with the development of methods for re-establishing a vascularized network within the decellularized graft using endothelial cells (ECs). Thus, the keystone for successful BEL is the presence of an intact vascular tree for optimal reperfusion (Uygun et al., 2010; Baptista et al., 2011; Struecker et al., 2015). That's why Baptista and colleagues designed their decellularized rat liver grafts to ensure getting an intact capillary bed with indefinite leakage *in vitro*. Also, they transplanted the grafts into the abdominal cavity of rats. In heparinized host animals, these grafts maintained normal blood flow for up to 1 hour (Baptista et al., 2011).

Uygun and colleagues demonstrated an approach to generate decellularized and recellularized liver grafts which could support liver-specific function, including albumin secretion, urea synthesis, and cytochrome P450 expression. This method introduced primary rat hepatocytes *via* the portal vein of a decellularized scaffold. After auxiliary liver grafts were transplanted into rats and kept for 8 h, the TUNEL staining of those harvested grafts revealed minimal ischemic damage. Preliminary revascularization with ECs also showed attachment and viability within the graft *in vitro* (Uygun et al., 2010). Also, Baptista and colleagues populated their scaffolds with human fetal liver and endothelial cells, resulting in a liver-like tissue *in vitro*. Endothelial cells were implanted throughout the whole circle of a vascular channel by using the vena cava and portal pathways, and the cells displayed preserved cell-cell connections. They also discovered that the adherence and presence of platelets were significantly reduced in endothelialized scaffolds (Baptista et al., 2011). This finding that coverage of the vascular tree by endothelial cells was significant for preventing platelet adherence and maintaining vascular patency suggested that synthetic grafts could be implanted without drug anticoagulation (Ko et al., 2015). However, until a method of complete endothelial seeding of perfused grafts was optimized, blood clotting of grafts remained problematic and handicapped the progress of BELs (Orlando et al., 2012; Kojima et al., 2018).

PASSIVATION METHODS AND ANTICOAGULANTS FOR REVASCULARIZED BIOENGINEERED LIVERS (RBELS)

Other considerations are important to maintain graft patency. For example, collagenous fibers from the vascular basement membrane that are exposed to blood flow activate the clotting cascade during extracorporeal blood perfusion or after *in vivo* transplantation (Kipshidze et al., 2004; Caralt et al., 2014; Wang et al., 2020). The surface charge of graft materials is a pivotal reason why grafts are prone to thrombosis. Heparin has a large negative charge density and repels albumin and fibrinogen, preventing them from sticking to the graft due to static repulsion between heparin and these proteins. The issue is that heparin release patterns are frequently characterized by a substantial initial burst of heparin. After which very little or nothing remains on the scaffold, so strategies to limit and control heparin release have been developed "Heparin immobilization" (Matsuzaki et al., 2021). Therefore, to get better hemocompatibility after *in vivo* perfusion of decellularized scaffolds of swine liver, heparin immobilization technique was used by Bao et al. (2015) before auxiliary transplantation. In their trial, they used the swine median lobe scaffolds where the PV of the graft was anastomosed to the host left renal vein as an inflow and the SHIVC of the graft was anastomosed to the host splenic vein as an outflow. It is found that heparin immobilized on the scaffolds can release slowly, therefore achieving improved anticoagulation. The heparinized scaffolds showed convenient blood flow for 60 min, compared to no blood flow throughout the control scaffolds after 20 min of perfusion. *In vitro* studies indicated the heparinized scaffolds could support rat primary hepatocytes and human umbilical vein endothelial cells (HUVECs) adhesion and growth (Bao et al., 2015).

Hussein et al. (2016) found that a heparin-gelatin mixture (HG) improved ECs' ability to migrate and adhere to vessel discs, which could efficiently cover the vascular network lumen and maintain function and proliferate. Gelatin contains many integrin binding sites for EC adhesion, migration, and differentiation, similar to the binding sites that are detected in natural collagen and other extracellular matrix proteins (Hajiali et al., 2011; Hussein et al., 2016). The addition of heparin to gelatin increases cell recruitment and migration, which is due to its highly negative charge density and electrostatic interaction with positively charged proteins in the ECM (Trindade et al., 2008; Camci-Unal et al., 2013; Hussein et al., 2016). The authors manufactured bioengineered scaffolds based on the decellularized right lateral lobes of swine livers, which were co-cultured by hepatocellular carcinoma cells (HepG2) and ECs (EA.hy926 cells) and then heterotopically transplanted into pigs. Some of these scaffolds were HG-coated before ECs perfusion. After 1 h of *in vivo* implantation, the scaffolds were retrieved, canulated for portography, and tissue specimens were taken to assess HepG2 cells function. Vascular patency was demonstrated in HG-precoated scaffolds, and their HepG2 cells exhibited greater metabolic and synthetic function than those of uncoated scaffolds. Moreover, the HG-precoated re-endothelialized grafts revealed no thrombosis after 24 h of *ex vivo* whole-blood perfusion (Hussein et al., 2016).

While heparin immobilization scaffolds were promising as engineered liver grafts, this process was only temporary and replenishment of the immobilized heparin was not possible *in vivo* (Baptista et al., 2016; Meng et al., 2019). Accordingly, reendothelialization appeared to be necessary to provide bioengineered livers with persistent anti-thrombotic capability (Meng et al., 2019). Meng et al. (2019) reported that gelatin hydrogel-based perfusion significantly increased the number of immortalized endothelial cells that were retained in the decellularized rat liver scaffolds, within which active blood flow could be observed 8 days post-transplantation (Meng et al., 2019).

Substances such as polyethylene glycol, zwitterionic polymers, heparin or thrombomodulin are used to coat the ECM in order to

achieve surface modification of it. While this surface modification efficiently reinforced hemocompatibility in the liver scaffolds, these modified surfaces appeared too hydrophilic to facilitate ECs adhesion to the vessel walls. Devalliere et al. (2018) presented an efficient approach for improving revascularization of acellular liver scaffolds by conjugating the REDV cell-binding domain *in vitro*. REDV-ELP peptide conjugation facilitates cell-specific binding of ECs, leading to the formation of a uniform and well-spread EC monolayer, significantly reducing activation and adhesion of platelets to the vasculature without functionality change or toxicity in hepatocytes. As opposed to surface coating techniques, REVD-ELP peptide provides an additional cell adhesion signal to the ECM of the liver scaffolds that improves ECs attachment (higher level of VE-cadherin) and proliferation (higher level of VEGF), as well as maintains the structural and mechanical integrity of ECM (Devalliere et al., 2018).

In general, passivation methods and anticoagulants such as heparin immobilization, heparin-gelatin and REDV peptide have been attempted to increase the vascular patency of BELs and increase the survival of the graft by keeping them well perfused without ischemic damage. However, reported survival of liver grafts prepared by passivation methods has not exceeded 8 days (Bao et al., 2015; Hussein et al., 2016; Park et al., 2016; Saleh et al., 2020; Kim et al., 2021).

ANTI-ENDOTHELIAL CELL ANTIBODIES AND APTAMER FOR REVASCULARIZED LIVER SCAFFOLDS

Ko and colleagues demonstrated the generation of clinically relevant-sized ECM scaffolds with an intact vascular network extending to the capillary bed in a porcine model. To enhance the attachment of vascular endothelial cells expressing GFP protein (MS1) under physiologic blood flow, they developed an effective method by conjugating anti-endothelial cell antibodies (rat anti-mouse CD31 antibody). They heterotopically transplanted the revascularized liver scaffolds with inflow from the renal artery and outflow to the renal vein; the transplants were able to withstand physiologic blood pressure and maintain blood flow for 24 h (Ko et al., 2015).

Although the anti-CD31 antibody ensures better attachment of endothelial cells, in regard of the limitations of mass-producing ability and immunogenicity, Kim and colleagues adopted an anti-CD31 single-stranded DNA aptamer as a coating agent in the context of re-endothelization scaffolds. Compared to antibodies, aptamers have lower immunogenicity and stronger binding affinity for particular proteins (Song et al., 2012; Toh et al., 2015; Zhou and Rossi, 2017; Kim et al., 2021). Next, the aptamer-coated scaffolds were repopulated with HepG2 cells, LX2 cells, HUVECs, and MSCs (Kim et al., 2021). Quantitatively, Kim and colleagues achieved higher endothelial coverage (95.53 ± 3.1%) and more re-endothelialized vessels per field (87.37 ± 1.59%) in the aptamer group compared to constructs without aptamer coating. They perfused the scaffolds through the rat renal circulatory system for 2 h. After perfusion with whole blood, the aptamer-coated constructs had low levels of integrin aIIb-positive platelets (a marker expressed by activated platelets) by immunostaining analysis, whereas a number of integrin aIIb-positive platelets accumulated around the vascular network in the anti-CD31 antibody-coated scaffolds. Furthermore, they also showed that aptamer-coated scaffolds, when implanted into the interlobular space of the cirrhotic liver, could ameliorate hepatic cirrhosis and restore liver function in the TAA-induced hepatic fibrosis rat models (Kim et al., 2021).

IPSCS-DERIVED CELLS IN BIOENGINEERED LIVERS

Even with advancements in immunosuppressive regimens for transplant patients, the requirement for long-term medication with systemic adverse effects, as well as being an immunocompromised patient, remain significant hurdles for organ transplantation. One of the long-term aims of BEL transplantation is to eliminate the need for immunosuppressor drugs by producing donor-matched grafts that do not trigger the immune system, resulting in graft rejection (Wadström et al., 2017). Induced pluripotent stem cells (iPSCs) from humans are a readily available source of reprogrammed adult somatic cells which would participate in producing donor-matched grafts. Many experiments were conducted in order to create hepatocyte-like cells obtained from iPSCs (Bizzaro et al., 2019). Park and colleagues reported the first attempt to repopulate decellularized rat liver scaffolds with functional iPSC-Heps. When the recellularized liver scaffolds were heterotopically transplanted into rats for up to 2 h, the grafts expressed hepatocyte markers (AFP and ALB) and did not rupture. However, coagulation occurred in all grafts after about one to 2 h of *in vivo* blood perfusion (Park et al., 2016). Also, it was suggested that iPSCs-derived endothelial cells might be a potential substitute for reconstructing the vascular network in bioengineered organs as they could be recipient-specific and reduce or even remove the need for immunosuppression after transplantation (Clayton et al., 2015; Jiang et al., 2015; Park et al., 2016). However, it is found that iPSCs are immunogenic cells which can activate NK cells and trigger T cell-dependent immune response. This immunogenicity can be attributed to epigenetic abnormalities, coding mutations, or genes translocation which lead to generating immunogenic antigens or decreased expression of self-antigens. So, the immunogenicity of these cells should be examined before their clinical application (Zhao et al., 2011; Liu et al., 2017; Otsuka et al., 2020).

IMPROVED REVASCULARIZED BIOENGINEERED LIVERS SURVIVAL IN HETEROTOPIC PORCINE TRANSPLANTATION MODEL

Our team has shown that complete re-seeding of decellularized whole porcine livers with human umbilical vein endothelial cells (HUVECs) and implantation heterotopically into immunosuppressed pigs could sustain perfusion for up to

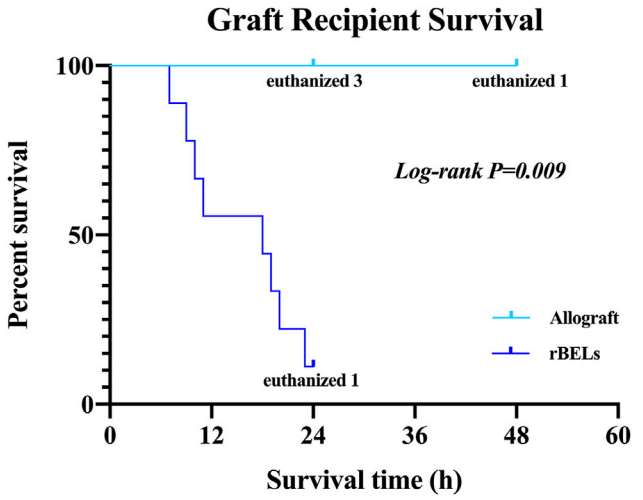

FIGURE 1 | Kaplan-Meier analysis of survival of the allograft group and the rBELs group. Survival rate at 24 h was significantly higher in the allograft group compared to rBELs group (4 of 4, 100% vs. 1 of 9, 11.1%, $p = 0.01$). The study endpoint was death or the presence of a death equivalent endpoint. Death equivalent endpoints were: absent graft blood flow, grade IV hepatic encephalopathy, and uncontrolled bleeding, and animals were euthanized.

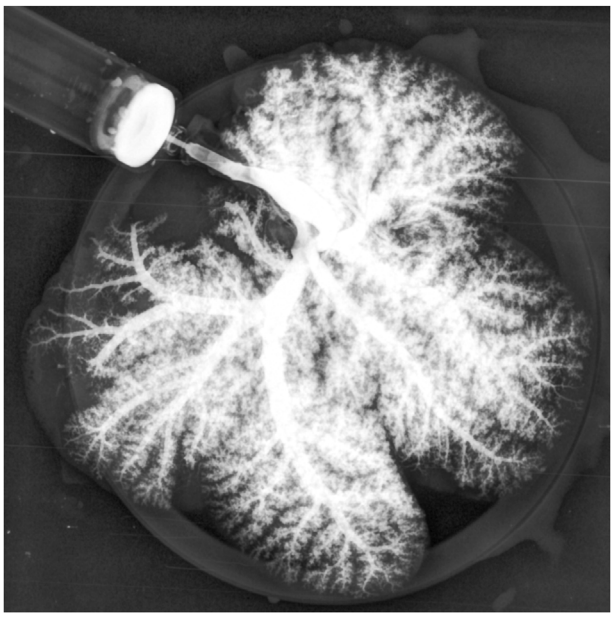

FIGURE 2 | Portal venogram of Decell-recell liver graft demonstrating patency of vasculature and no evidence of thrombosis after 1-h *in vivo* perfusion.

15 days. We identified glucose consumption rate (GCR) as a reliable metric for non-destructively monitoring cell proliferation and ultimately predicting graft patency following blood perfusion (Shaheen et al., 2020).

More recently, we studied the co-seeded BELs, produced by adding primary porcine hepatocytes after HUVEC reendothelialization, to evaluate the function of the grafts in heterotopic position. Graft viability was stable before and after the transplant. A portosystemic shunt was employed to limit portal hypertension due to the limited space and smaller graft size in this heterotopic transplantation model. These studies followed our stepwise approach to using larger grafts with greater functionality in an orthotopic model (Anderson et al., 2021).

UPDATED ORTHOTOPIC LIVER TRANSPLANTATION DATA FOR REVASCULARIZED BIOENGINEERED LIVERS

Heterotopic liver transplantation can be challenging in clinical practice due to a variety of factors, including suboptimal venous outflow, limitation of space for the graft, and poor long-term outcomes. Thus, heterotopic liver transplantation has remained a rare approach clinically compared to orthotopic liver transplantation (Anderson et al., 2021; Rammohan et al., 2021). Nyberg and colleagues have created an orthotopic liver transplantation model with rBELs. We performed the liver transplant by caval interposition technique as previously reported by Calne et al. (1968) rather than the piggy-back technique as there is no plane of dissection between the liver and IVC in pigs. In our preliminary functionality studies only anastomosis to the SHIVC, IHIVC, and PV were performed. The hepatic artery and common bile duct were not utilized. SHIVC was sewn by traditional end-to-end technique. However, end-to-end anastomoses to IHIVC and PV were performed over a silicone tube insertion method to minimize the anhepatic phase and the ischemic time of rBELs implantation.

As expected, the survival rate at 24 h was significantly higher in the pig allograft group compared to the rBELs group (4 of 4, 100% vs. 1 of 9, 11.1%, $p = 0.01$); the median survival time in the rBELs group was 18 h (range, 7–24 h) as illustrated in **Figure 1**. However, our rBELs showed patent vasculature with good graft reperfusion *in vitro* portal venogram and *in vivo* on declamping the PV, as shown in the **Supplementary Videos**. We also assessed the patency of the vasculature by portal venogram after 1 hour of *in vivo* perfusion with an intact vascular tree and no evidence of thrombosis (see **Figure 2**).

The rBEL grafts shown in **Figure 1** and **Figure 2** were "endo-only grafts" seeded with HUVEC cells; they lacked hepatocytes and did not possess an intact biliary system required for clinical use. Liver grafts co-seeded with both HUVECs and primary hepatocytes have been studied on the bench and in heterotopic position, and soon may be ready for orthotopic transplantation studies. The co-seeded grafts showed an intact lobular structure after reseeding on H & E staining with mitotically active cells on staining with Ki-67 (see **Figure 3**). These data suggest steady progress of rBELs towards eventual clinical practice.

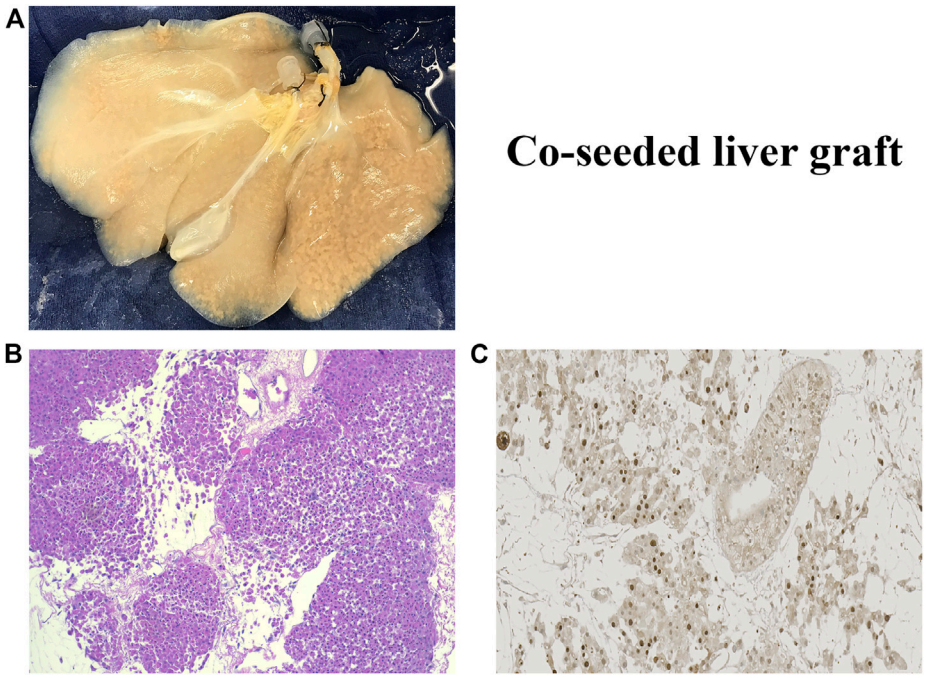

FIGURE 3 | (A). Decell-recell liver graft co-seeded with HUVEC endothelial cells and primary hepatocytes. **(B)**. Light microscopy of co-seeded graft showing lobular structure after reseeding (H&E staining). **(C)**. IHC microscopy of co-cultured graft showing mitotically active cells after reseeding (Ki67 staining).

CLINICAL RELEVANCE OF REVASCULARIZED BIOENGINEERED LIVERS DATA

The survival data shown in **Figure 1** after transplantation of endo-only rBEL grafts may have clinical relevance to human surgeries. In particular, in some regions, it is standard to perform *ex vivo* liver resection and autotransplantation for end-stage hepatic alveolar echinococcosis. In the anhepatic phase of this human operation, the native liver is completely removed from the abdominal cavity for treatment, an artificial vascular graft is applied to temporarily reconstruct the IVC, and a portocaval shunt is established (Yang et al., 2018). The reported anhepatic phase in alveolar echinococcosis ranges from 104 to 879 min (Aji et al., 2018; Yang et al., 2018; Yang et al., 2020). According to the anhepatic phase of human reality viewpoint and comparing it with the survival data of our study, our rBELs would be efficient for sustaining physical perfusion phase in the absence of visible clots if they are used for this purpose in the future.

CONCLUSION

The increasing need for liver transplantation as the only curative treatment for liver failure makes BEL a glimmer of hope for the future. Many obstacles stand in the way of achieving functional transplantable BELs, such as finding a suitable platform for the cells with proper dispersion and getting a patent vasculature. The use of scaffolds and the development of decell-recell techniques coupled with the availability of different cell lines and sources made a quantum leap in the development of BELs. The decellularized scaffolds became a platform that is not only a cell container but also a participant in their activity and functionality. Many trials were conducted to overcome the problem of blood clotting and failed reperfusion. Re-endothelialization is considered a cornerstone for a successful reperfusion phase. Not only by applying endothelial cells but also with proper attachment and extension throughout the vascular tree. Also, the use of anticoagulants, such as heparin immobilization, heparin-gelatin, and REDV peptide, has also been employed to improve BEL vascular patency. However, to the best of our knowledge, the grafts' survival during *in vivo* perfusion did not surpass 8 days by any method. Shaheen et al. (2020) showed that sustained perfusion of our revascularized bioengineered livers heterotopically transplanted into immunosuppressed pigs survived for up to 15 days, which is considered a step in creating a more stable bioengineered graft. In our unpublished new study, we created an orthotopic BEL model that could survive for up to 24 h. However, as our rBELs are still preclinical trials, they are considered promising results as the 24-h graft survival can be useful in cases such as *ex-vivo* liver resection and autologous liver transplantation for end-stage hepatic alveolar echinococcosis. Till now, these results can't be applied as a substitute for traditional liver transplantation. So, the next step is to utilize the new model for the transplantation of fully recellularized BELs. That's why we developed our co-seeded grafts as a step toward the next tri-seeded grafts by adding cholangiocytes and then transplanting them in the orthotopic position, as we established in our latest model.

AUTHOR CONTRIBUTIONS

SN, KL and MT conceptualized the manuscript. SN and KL performed experiments. KL, MT, EL, PF, SH, AR and SN wrote the manuscript. KS and JR critically reviewed the manuscript.

FUNDING

This study received funding from R01 DK106667, West China Hospital, Mayo Foundation, Egyptian Ministry of Higher Education, Walter-Benjamin Program of the German Research Foundation, and Miromatrix Medical Inc. Miromatrix Medical Inc. provided funding for some of the transplantation experiments discussed in this review article.

SUPPLEMENTARY MATERIAL

The Supplementary Material for this article can be found online at: https://www.frontiersin.org/articles/10.3389/fbioe.2022.833163/full#supplementary-material

REFERENCES

Agarwal, T., Maiti, T. K., and Ghosh, S. K. (2019). Decellularized Caprine Liver-Derived Biomimetic and Pro-angiogenic Scaffolds for Liver Tissue Engineering. *Mater. Sci. Eng. C* 98, 939–948. doi:10.1016/j.msec.2019.01.037

Aji, T., Dong, J.-H., Shao, Y.-M., Zhao, J.-M., Li, T., Tuxun, T., et al. (2018). *Ex Vivo* liver Resection and Autotransplantation as Alternative to Allotransplantation for End-Stage Hepatic Alveolar Echinococcosis. *J. Hepatol.* 69 (5), 1037–1046. doi:10.1016/j.jhep.2018.07.006

Anderson, B. D., Nelson, E. D., Joo, D., Amiot, B. P., Katane, A. A., Mendenhall, A., et al. (2021). Functional Characterization of a Bioengineered Liver after Heterotopic Implantation in Pigs. *Commun. Biol.* 4 (1), 1157. doi:10.1038/s42003-021-02665-2

Ansari, T., Southgate, A., Obiri-Yeboa, I., Jones, L. G., Greco, K., Olayanju, A., et al. (2020). Development and Characterization of a Porcine Liver Scaffold. *Stem Cell Dev.* 29 (5), 314–326. doi:10.1089/scd.2019.0069

Arulraj, R., and Neuberger, J. (2011). Liver Transplantation: Filling the Gapbetween Supply and Demand. *Clin. Med.* 11 (2), 194–198. doi:10.7861/clinmedicine.11-2-194

Asrani, S. K., Devarbhavi, H., Eaton, J., and Kamath, P. S. (2019). Burden of Liver Diseases in the World. *J. Hepatol.* 70 (1), 151–171. doi:10.1016/j.jhep.2018.09.014

Badylak, S. F. (2014). Decellularized Allogeneic and Xenogeneic Tissue as a Bioscaffold for Regenerative Medicine: Factors that Influence the Host Response. *Ann. Biomed. Eng.* 42 (7), 1517–1527. doi:10.1007/s10439-013-0963-7

Badylak, S. F., Taylor, D., and Uygun, K. (2011). Whole-organ Tissue Engineering: Decellularization and Recellularization of Three-Dimensional Matrix Scaffolds. *Annu. Rev. Biomed. Eng.* 13, 27–53. doi:10.1146/annurev-bioeng-071910-124743

Bao, J., Wu, Q., Sun, J., Zhou, Y., Wang, Y., Jiang, X., et al. (2015). Hemocompatibility Improvement of Perfusion-Decellularized Clinical-Scale Liver Scaffold through Heparin Immobilization. *Sci. Rep.* 5, 10756. doi:10.1038/srep10756

Baptista, P. M., Moran, E. C., Vyas, D., Ribeiro, M. H., Atala, A., Sparks, J. L., et al. (2016). Fluid Flow Regulation of Revascularization and Cellular Organization in a Bioengineered Liver Platform. *Tissue Eng. C: Methods* 22 (3), 199–207. doi:10.1089/ten.TEC.2015.0334

Baptista, P. M., Siddiqui, M. M., Lozier, G., Rodriguez, S. R., Atala, A., and Soker, S. (2011). The Use of Whole Organ Decellularization for the Generation of a Vascularized Liver Organoid. *Hepatology* 53 (2), 604–617. doi:10.1002/hep.24067

Bizzaro, D., Russo, F. P., and Burra, P. (2019). New Perspectives in Liver Transplantation: From Regeneration to Bioengineering. *Bioengineering* 6 (3), 81. doi:10.3390/bioengineering6030081

Calne, R. Y., Yoffa, D. E., White, H. J., and Maginn, R. R. (1968). A Technique of Orthotopic Liver Translantation in the Pig. *Br. J. Surg.* 55 (3), 203–206. doi:10.1002/bjs.1800550310

Camci-Unal, G., Nichol, J. W., Bae, H., Tekin, H., Bischoff, J., and Khademhosseini, A. (2013). Hydrogel Surfaces to Promote Attachment and Spreading of Endothelial Progenitor Cells. *J. Tissue Eng. Regen. Med.* 7 (5), 337–347. doi:10.1002/term.517

Caralt, M., Velasco, E., Lanas, A., and Baptista, P. M. (2014). Liver Bioengineering. *Organogenesis* 10 (2), 250–259. doi:10.4161/org.29892

Cho, C. H., Park, J., Nagrath, D., Tilles, A. W., Berthiaume, F., Toner, M., et al. (2007). Oxygen Uptake Rates and Liver-specific Functions of Hepatocyte and 3T3 Fibroblast Co-cultures. *Biotechnol. Bioeng.* 97 (1), 188–199. doi:10.1002/bit.21225

Clayton, Z. E., Sadeghipour, S., and Patel, S. (2015). Generating Induced Pluripotent Stem Cell Derived Endothelial Cells and Induced Endothelial Cells for Cardiovascular Disease Modelling and Therapeutic Angiogenesis. *Int. J. Cardiol.* 197, 116–122. doi:10.1016/j.ijcard.2015.06.038

Croce, S., Peloso, A., Zoro, T., Avanzini, M. A., and Cobianchi, L. (2019). A Hepatic Scaffold from Decellularized Liver Tissue: Food for Thought. *Biomolecules* 9 (12), 813. doi:10.3390/biom9120813

Debnath, T., Mallarpu, C. S., and Chelluri, L. K. (2020). Development of Bioengineered Organ Using Biological Acellular Rat Liver Scaffold and Hepatocytes. *Organogenesis* 16 (2), 61–72. doi:10.1080/15476278.2020.1742534

Devalliere, J., Chen, Y., Dooley, K., Yarmush, M. L., and Uygun, B. E. (2018). Improving Functional Re-endothelialization of Acellular Liver Scaffold Using REDV Cell-Binding Domain. *Acta Biomater.* 78, 151–164. doi:10.1016/j.actbio.2018.07.046

Gilpin, A., and Yang, Y. (2017). Decellularization Strategies for Regenerative Medicine: From Processing Techniques to Applications. *Biomed. Res. Int.* 2017, 1–13. doi:10.1155/2017/9831534

Hajiali, H., Shahgasempour, S., Naimi-Jamal, M. R., and Peirovi, H. (2011). Electrospun PGA/gelatin Nanofibrous Scaffolds and Their Potential Application in Vascular Tissue Engineering. *Ijn* 6, 2133–2141. doi:10.2147/IJN.S24312

Haycock, J. W. (2011). 3D Cell Culture: a Review of Current Approaches and Techniques. *Methods Mol. Biol.* 695, 1–15. doi:10.1007/978-1-60761-984-0_1

Haydon, G. H., and Neuberger, J. (2000). Liver Transplantation of Patients in End-Stage Cirrhosis. *Best Pract. Res. Clin. Gastroenterol.* 14 (6), 1049–1073. doi:10.1053/bega.2000.0146

Hou, Y. t., Hsu, S. h., and Lee, K. M. (2020). Decellularized Liver Matrix as Substrates for rescue of Acute Hepatocytes Toxicity. *J. Biomed. Mater. Res.* 108 (4), 1592–1602. doi:10.1002/jbm.b.34506

Hussein, K. H., Park, K.-M., Kang, K.-S., and Woo, H.-M. (2016). Heparin-gelatin Mixture Improves Vascular Reconstruction Efficiency and Hepatic Function in Bioengineered Livers. *Acta Biomater.* 38, 82–93. doi:10.1016/j.actbio.2016.04.042

Jiang, B., Jen, M., Perrin, L., Wertheim, J. A., and Ameer, G. A. (2015). SIRT1 Overexpression Maintains Cell Phenotype and Function of Endothelial Cells Derived from Induced Pluripotent Stem Cells. *Stem Cell Dev.* 24 (23), 2740–2745. doi:10.1089/scd.2015.0191

Jiménez-Romero, C., Manrique, A., Calvo, J., Caso, Ó., Marcacuzco, A., García-Sesma, Á., et al. (2019). Liver Transplantation Using Uncontrolled Donors after Circulatory Death: A 10-year Single-center Experience. *Transplantation* 103 (12), 2497–2505. doi:10.1097/Tp.0000000000002780

Kakabadze, Z., Karalashvili, L., Chakhunashvili, D., Havlioglu, N., Janelidze, M., Kakabadze, A., et al. (2019). Decellularized Bovine Placentome for Portacavally-Interposed Heterotopic Liver Transplantation in Rats. *Mater. Sci. Eng. C* 97, 293–301. doi:10.1016/j.msec.2018.12.025

Kim, D.-H., Ahn, J., Kang, H. K., Kim, M.-S., Kim, N.-G., Kook, M. G., et al. (2021). Development of Highly Functional Bioengineered Human Liver with

Perfusable Vasculature. *Biomaterials* 265, 120417. doi:10.1016/j.biomaterials.2020.120417

Kipshidze, N., Dangas, G., Tsapenko, M., Moses, J., Leon, M., Kutryk, M., et al. (2004). Role of the Endothelium in Modulating Neointimal formationVasculoprotective Approaches to Attenuate Restenosis after Percutaneous Coronary Interventions. *J. Am. Coll. Cardiol.* 44 (4), 733–739. doi:10.1016/j.jacc.2004.04.04810.1016/s0735-1097(04)01083-6

Ko, I. K., Peng, L., Peloso, A., Smith, C. J., Dhal, A., Deegan, D. B., et al. (2015). Bioengineered Transplantable Porcine Livers with Re-endothelialized Vasculature. *Biomaterials* 40, 72–79. doi:10.1016/j.biomaterials.2014.11.027

Kojima, H., Yasuchika, K., Fukumitsu, K., Ishii, T., Ogiso, S., Miyauchi, Y., et al. (2018). Establishment of Practical Recellularized Liver Graft for Blood Perfusion Using Primary Rat Hepatocytes and Liver Sinusoidal Endothelial Cells. *Am. J. Transpl.* 18 (6), 1351–1359. doi:10.1111/ajt.14666

Li, Y., Wu, Q., Wang, Y., Li, L., Chen, F., Shi, Y., et al. (2017). Construction of Bioengineered Hepatic Tissue Derived from Human Umbilical Cord Mesenchymal Stem Cells via Aggregation Culture in Porcine Decellularized Liver Scaffolds. *Xenotransplantation* 24 (1), e12285. doi:10.1111/xen.12285

Liu, X., Li, W., Fu, X., and Xu, Y. (2017). The Immunogenicity and Immune Tolerance of Pluripotent Stem Cell Derivatives. *Front. Immunol.* 8, 645. doi:10.3389/fimmu.2017.00645

Matsuzaki, Y., Ulziibayar, A., Shoji, T., and Shinoka, T. (2021). Heparin-Eluting Tissue-Engineered Bioabsorbable Vascular Grafts. *Appl. Sci.* 11 (10), 4563. doi:10.3390/app11104563

Mazza, G., Al-Akkad, W., Rombouts, K., and Pinzani, M. (2018). Liver Tissue Engineering: From Implantable Tissue to Whole Organ Engineering. *Hepatol. Commun.* 2 (2), 131–141. doi:10.1002/hep4.1136

Mazzaferro, V., Citterio, D., Bhoori, S., Bongini, M., Miceli, R., De Carlis, L., et al. (2020). Liver Transplantation in Hepatocellular Carcinoma after Tumour Downstaging (XXL): a Randomised, Controlled, Phase 2b/3 Trial. *Lancet Oncol.* 21 (7), 947–956. doi:10.1016/S1470-2045(20)30224-2

Melaram, R. (2021). Environmental Risk Factors Implicated in Liver Disease: A Mini-Review. *Front. Public Health* 9, 738. doi:10.3389/fpubh.2021.683719

Meng, F., Almohanna, F., Altuhami, A., Assiri, A. M., and Broering, D. (2019). Vasculature Reconstruction of Decellularized Liver Scaffolds via Gelatin-Based Re-endothelialization. *J. Biomed. Mater. Res.* 107 (2), 392–402. doi:10.1002/jbm.a.36551

Mirdamadi, E. S., Kalhori, D., Zakeri, N., Azarpira, N., and Solati-Hashjin, M. (2020). Liver Tissue Engineering as an Emerging Alternative for Liver Disease Treatment. *Tissue Eng. B: Rev.* 26 (2), 145–163. doi:10.1089/ten.TEB.2019.0233

Moulisová, V., Jiřík, M., Schindler, C., Červenková, L., Pálek, R., Rosendorf, J., et al. (2020). Novel Morphological Multi-Scale Evaluation System for Quality Assessment of Decellularized Liver Scaffolds. *J. Tissue Eng.* 11, 204173142092112. doi:10.1177/2041731420921121

Naeem, E. M., Sajad, D., Talaei-Khozani, T., Khajeh, S., Azarpira, N., Alaei, S., et al. (2019). Decellularized Liver Transplant Could Be Recellularized in Rat Partial Hepatectomy Model. *J. Biomed. Mater. Res.* 107 (11), 2576–2588. doi:10.1002/jbm.a.36763

Nicolas, C. T., Wang, Y., and Nyberg, S. L. (2016). Cell Therapy in Chronic Liver Disease. *Curr. Opin. Gastroenterol.* 32 (3), 1–194. doi:10.1097/MOG.0000000000000262

Ohashi, K., Yokoyama, T., Yamato, M., Kuge, H., Kanehiro, H., Tsutsumi, M., et al. (2007). Engineering Functional Two- and Three-Dimensional Liver Systems *In Vivo* Using Hepatic Tissue Sheets. *Nat. Med.* 13 (7), 880–885. doi:10.1038/nm1576

Orlando, G., Farney, A. C., Iskandar, S. S., Mirmalek-Sani, S.-H., Sullivan, D. C., Moran, E., et al. (2012). Production and Implantation of Renal Extracellular Matrix Scaffolds from Porcine Kidneys as a Platform for Renal Bioengineering Investigations. *Ann. Surg.* 256 (2), 363–370. doi:10.1097/SLA.0b013e31825a02ab

Otsuka, R., Wada, H., Murata, T., and Seino, K. I. (2020). Immune Reaction and Regulation in Transplantation Based on Pluripotent Stem Cell Technology. *Inflamm. Regen.* 40 (1), 12–19. doi:10.1186/s41232-020-00125-8

Ott, H. C., Matthiesen, T. S., Goh, S.-K., Black, L. D., Kren, S. M., Netoff, T. I., et al. (2008). Perfusion-decellularized Matrix: Using Nature's Platform to Engineer a Bioartificial Heart. *Nat. Med.* 14 (2), 213–221. doi:10.1038/nm1684

Paik, J. M., Golabi, P., Younossi, Y., Mishra, A., and Younossi, Z. M. (2020). Changes in the Global Burden of Chronic Liver Diseases from 2012 to 2017: The Growing Impact of NAFLD. *Hepatology* 72 (5), 1605–1616. doi:10.1002/hep.31173

Park, K.-M., Hussein, K. H., Hong, S.-H., Ahn, C., Yang, S.-R., Park, S.-M., et al. (2016). Decellularized Liver Extracellular Matrix as Promising Tools for Transplantable Bioengineered Liver Promotes Hepatic Lineage Commitments of Induced Pluripotent Stem Cells. *Tissue Eng. A* 22 (5-6), 449–460. doi:10.1089/ten.TEA.2015.0313

Pla-Palacín, I., Sainz-Arnal, P., Morini, S., Almeida, M., and Baptista, P. M. (2017). Liver Bioengineering Using Decellularized Whole-Liver Scaffolds. *Methods Mol. Biol.* 1577, 293–305. doi:10.1007/7651_2017_98

Rammohan, A., Reddy, M. S., Line, P. D., and Rela, M. (2021). Heterotopic Liver Transplantation: Temporary Solution, Permanent Problem. *Am. J. Transpl.* 21 (2), 903–904. doi:10.1111/ajt.16271

Saleh, T., Ahmed, E., Yu, L., Song, S. H., Park, K. M., Kwak, H. H., et al. (2020). Conjugating Homogenized Liver-extracellular Matrix into Decellularized Hepatic Scaffold for Liver Tissue Engineering. *J. Biomed. Mater. Res.* 108 (10), 1991–2004. doi:10.1002/jbm.a.36920

Shaheen, M. F., Joo, D. J., Ross, J. J., Anderson, B. D., Chen, H. S., Huebert, R. C., et al. (2020). Sustained Perfusion of Revascularized Bioengineered Livers Heterotopically Transplanted into Immunosuppressed Pigs. *Nat. Biomed. Eng.* 4 (4), 437–445. doi:10.1038/s41551-019-0460-x

Shirakigawa, N., Takei, T., and Ijima, H. (2013). Base Structure Consisting of an Endothelialized Vascular-Tree Network and Hepatocytes for Whole Liver Engineering. *J. Biosci. Bioeng.* 116 (6), 740–745. doi:10.1016/j.jbiosc.2013.05.020

Song, K.-M., Lee, S., and Ban, C. (2012). Aptamers and Their Biological Applications. *Sensors* 12 (1), 612–631. doi:10.3390/s120100612

Struecker, B., Hillebrandt, K. H., Voitl, R., Butter, A., Schmuck, R. B., Reutzel-Selke, A., et al. (2015). Porcine Liver Decellularization under Oscillating Pressure Conditions: a Technical Refinement to Improve the Homogeneity of the Decellularization Process. *Tissue Eng. Part C: Methods* 21 (3), 303–313. doi:10.1089/ten.TEC.2014.0321

Suchy, F., Yamaguchi, T., and Nakauchi, H. (2018). iPSC-Derived Organs *In Vivo*: Challenges and Promise. *Cell Stem Cell* 22 (1), 21–24. doi:10.1016/j.stem.2017.12.003

Toh, S. Y., Citartan, M., Gopinath, S. C. B., and Tang, T.-H. (2015). Aptamers as a Replacement for Antibodies in Enzyme-Linked Immunosorbent Assay. *Biosens. Bioelectron.* 64, 392–403. doi:10.1016/j.bios.2014.09.026

Trindade, E. S., Oliver, C., Jamur, M. C., Rocha, H. A. O., Franco, C. R. C., Bouças, R. I., et al. (2008). The Binding of Heparin to the Extracellular Matrix of Endothelial Cells Up-Regulates the Synthesis of an Antithrombotic Heparan Sulfate Proteoglycan. *J. Cel. Physiol.* 217 (2), 328–337. doi:10.1002/jcp.21504

Uygun, B. E., Soto-Gutierrez, A., Yagi, H., Izamis, M.-L., Guzzardi, M. A., Shulman, C., et al. (2010). Organ Reengineering through Development of a Transplantable Recellularized Liver Graft Using Decellularized Liver Matrix. *Nat. Med.* 16 (7), 814–820. doi:10.1038/nm.2170

Wadström, J., Ericzon, B.-G., Halloran, P. F., Bechstein, W. O., Opelz, G., Serón, D., et al. (2017). Advancing Transplantation. *Transplantation* 101 (2), S1–S42. doi:10.1097/tp.0000000000001563

Wang, A., Kuriata, O., Xu, F., Nietzsche, S., Gremse, F., Dirsch, O., et al. (2020). A Survival Model of *In Vivo* Partial Liver Lobe Decellularization towards *In Vivo* Liver Engineering. *Tissue Eng. Part C: Methods* 26 (8), 402–417. doi:10.1089/ten.TEC.2019.0194

Wang, F. S., Fan, J. G., Zhang, Z., Gao, B., and Wang, H. Y. (2014). The Global burden of Liver Disease: the Major Impact of China. *Hepatology* 60 (6), 2099–2108. doi:10.1002/hep.27406

Wang, Y., Cui, C.-B., Yamauchi, M., Miguez, P., Roach, M., Malavarca, R., et al. (2011). Lineage Restriction of Human Hepatic Stem Cells to Mature Fates Is Made Efficient by Tissue-specific Biomatrix Scaffolds. *Hepatology* 53 (1), 293–305. doi:10.1002/hep.24012

Watanabe, M., Yano, K., Okawa, K., Yamashita, T., Tajima, K., Sawada, K., et al. (2019). Construction of Sinusoid-Scale Microvessels in Perfusion Culture of a Decellularized Liver. *Acta Biomater.* 95, 307–318. doi:10.1016/j.actbio.2018.12.042

Yang, C., Yang, H.-J., Deng, S.-P., and Zhang, Y. (2020). Current Status of *Ex-Vivo* Liver Resection and Autologous Liver Transplantation for End-Stage Hepatic

Alveolar Echinococcosis. *Ann. Palliat. Med.* 9 (4), 2271–2278. doi:10.21037/apm-20-184

Yang, J. D., Hainaut, P., Gores, G. J., Amadou, A., Plymoth, A., and Roberts, L. R. (2019). A Global View of Hepatocellular Carcinoma: Trends, Risk, Prevention and Management. *Nat. Rev. Gastroenterol. Hepatol.* 16 (10), 589–604. doi:10.1038/s41575-019-0186-y

Yang, X., Qiu, Y., Huang, B., Wang, W., Shen, S., Feng, X., et al. (2018). Novel Techniques and Preliminary Results of *Ex Vivo* Liver Resection and Autotransplantation for End-Stage Hepatic Alveolar Echinococcosis: A Study of 31 Cases. *Am. J. Transpl.* 18 (7), 1668–1679. doi:10.1111/ajt.14621

Zhao, T., Zhang, Z.-N., Rong, Z., and Xu, Y. (2011). Immunogenicity of Induced Pluripotent Stem Cells. *Nature* 474 (7350), 212–215. doi:10.1038/nature10135

Zheng, Y., and Roberts, M. A. (2016). Scalable Vascularized Implants. *Nat. Mater* 15 (6), 597–599. doi:10.1038/nmat4637

Zhou, J., and Rossi, J. (2017). Aptamers as Targeted Therapeutics: Current Potential and Challenges. *Nat. Rev. Drug Discov.* 16 (3), 181–202. doi:10.1038/nrd.2016.199

Conflict of Interest: JR was employed by Miromatrix Medical Inc.

The remaining authors declare that the research was conducted in the absence of any commercial or financial relationships that could be construed as a potential conflict of interest.

The reviewer JB declared a shared affiliation, with no collaboration, with one of the authors KL to the handling editor at the time of the review.

Publisher's Note: All claims expressed in this article are solely those of the authors and do not necessarily represent those of their affiliated organizations, or those of the publisher, the editors and the reviewers. Any product that may be evaluated in this article, or claim that may be made by its manufacturer, is not guaranteed or endorsed by the publisher.

Copyright © 2022 Li, Tharwat, Larson, Felgendreff, Hosseiniasl, Rmilah, Safwat, Ross and Nyberg. This is an open-access article distributed under the terms of the Creative Commons Attribution License (CC BY). The use, distribution or reproduction in other forums is permitted, provided the original author(s) and the copyright owner(s) are credited and that the original publication in this journal is cited, in accordance with accepted academic practice. No use, distribution or reproduction is permitted which does not comply with these terms.

frontiers in Bioengineering and Biotechnology

ORIGINAL RESEARCH
published: 24 March 2022
doi: 10.3389/fbioe.2022.816513

Photooxidation and Pentagalloyl Glucose Cross-Linking Improves the Performance of Decellularized Small-Diameter Vascular Xenograft *In Vivo*

Yuhong Liu[1†], Chunyang Chen[1†], Xinlong Xie[1], Haoyong Yuan[1], Zhenjie Tang[1], Tao Qian[1], Yalin Liu[1], Mingzhe Song[1], Sixi Liu[1], Ting Lu[1] and Zhongshi Wu[1,2]**

[1]Department of Cardiovascular Surgery, The Second Xiangya Hospital of Central South University, Changsha, China, [2]NHC Key Laboratory of Birth Defect for Research and Prevention, Hunan Provincial Maternal and Child Health Care Hospital, Changsha, China

Small-diameter vascular grafts have a significant need in peripheral vascular surgery and procedures of coronary artery bypass graft (CABG); however, autografts are not always available, synthetic grafts perform poorly, and allografts and xenografts dilate, calcify, and induce inflammation after implantation. We hypothesized that cross-linking of decellularized xenogeneic vascular grafts would improve the mechanical properties and biocompatibility and reduce inflammation, degradation, and calcification *in vivo*. To test this hypothesis, the bovine internal mammary artery (BIMA) was decellularized by detergents and ribozymes with sonication and perfusion. Photooxidation and pentagalloyl glucose (PGG) were used to cross-link the collagen and elastin fibers of decellularized xenografts. Modified grafts' characteristics and biocompatibility were studied *in vitro* and *in vivo*; the grafts were implanted as transposition grafts in the subcutaneous of rats and the abdominal aorta of rabbits. The decellularized grafts were cross-linked by photooxidation and PGG, which improved the grafts' biomechanical properties and biocompatibility, prevented elastic fibers from early degradation, and reduced inflammation and calcification *in vivo*. Short-term aortic implants in the rabbits showed collagen regeneration and differentiation of host smooth muscle cells. No occlusion and stenosis occurred due to remodeling and stabilization of the neointima. A good patency rate (100%) was maintained. Notably, implantation of non-treated grafts exhibited marked thrombosis, an inflammatory response, calcification, and elastin degeneration. Thus, photooxidation and PGG cross-linking are potential tools for improving grafts' biological performance within decellularized small-diameter vascular xenografts.

Keywords: small-diameter vascular graft, bovine internal mammary artery, decellularization, cross-linking, neointima, tissue engineering vascular graft

OPEN ACCESS

Edited by:
Laura Iop,
University of Padua, Italy

Reviewed by:
Qiao Zhang,
Duke University, United States
Anton G. Kutikhin,
Research Institute for Complex Issues of Cardiovascular Diseases (RAS), Russia

****Correspondence:***
Ting Lu
luna295@csu.edu.cn
Zhongshi Wu
owenzswu@csu.edu.cn

[†]These authors have contributed equally to this work and share first authorship

Specialty section:
This article was submitted to Biomaterials, a section of the journal Frontiers in Bioengineering and Biotechnology

Received: *16 November 2021*
Accepted: *04 March 2022*
Published: *24 March 2022*

Citation:
Liu Y, Chen C, Xie X, Yuan H, Tang Z, Qian T, Liu Y, Song M, Liu S, Lu T and Wu Z (2022) Photooxidation and Pentagalloyl Glucose Cross-Linking Improves the Performance of Decellularized Small-Diameter Vascular Xenograft In Vivo. Front. Bioeng. Biotechnol. 10:816513. doi: 10.3389/fbioe.2022.816513

INTRODUCTION

Cardiovascular disease (CVD) is a serious disease that threatens human health. According to the World Health Organization, more than 17 million people die of CVD every year (Organization, 2013). Nearly 400,000 procedures of coronary artery bypass grafts (CABGs) are performed in the Unites States, and 50,000 procedures are performed in China each year, and there are still many patients waiting for surgery (Writing Group et al., 2016; Ma et al., 2020). The use of the grate saphenous vein, internal mammary artery, and radial artery is the most suitable choice for CABG procedures and peripheral vascular surgery, but some patients have insufficient access to suitable autologous blood vessels due to trauma, varices, infection reoperation, etc. (Wang et al., 2007; Desai et al., 2011).

With the development of tissue engineering vascular grafts, a variety of biodegradable and non-biodegradable synthetic polymers are widely used in reconstructive operations. Polymers, such as expanded polytetrafluoroethylene (ePTFE, Gore-Tex) and polyethylene terephthalate (PET, Dacron), are widely used for large diameter applications (> 6 mm) (Klinkert et al., 2004). However, no synthetic small-diameter vascular grafts (<6 mm) have been approved for clinical applications (Pektok et al., 2008; de Valence et al., 2012). Decellularized biological vascular grafts from xenogenic or allogenic tissues have shown great potential to serve as a new generation of tissue engineering vascular grafts (TEVG) which are composed of an extracellular matrix (ECM), sufficient collagen, elastin, and glycosaminoglycan (GAG). They can provide a friendly microenvironment due to their abundant cell signaling factors that are conducive to cell adhesion, proliferation, migration, and differentiation (Schmidt and Baier, 2000). Furthermore, the decellularized grafts can successfully match size, length, and compliance between donor and recipient vessels. However, the decellularized biological vascular grafts may have incomplete removal of cellular components or alterations in the structure of the ECM and exposure of collagen fibers. Several reasons of failure including thrombosis, immune rejection, aneurysm, intimal hyperplasia, and calcification are still challenges before the clinical application of xenogeneic small-diameter vascular grafts (Lin et al., 2018).

There are a few decellularized products on the market, such as the bovine carotid artery (Artegraft®), bovine mesenteric vein (ProCol®), and bovine ureter (SynerGraft®), which are used for clinical applications (Sharp et al., 2004; Das et al., 2011; Pashneh-Tala et al., 2016; Lin et al., 2018). The bovine internal mammary artery (BIMA) is used as a substitute for heterogeneous small-caliber blood vessels, but it has not undergone decellularization and properly cross-linking treatment, resulting in certain limitations in clinical application (Mitchell et al., 1993; Craig and Walker, 1994; Esposito et al., 1994). However, the BIMA also has a desired length (15–20 cm) and its diameter uniformly changes from 5 to 3 mm from the proximal to the distal end, which is conducive to clinical requirements, such as the replacement of peripheral blood vessels, the implantation of coronary artery bypass grafts, and the hemodialysis of the fistula (Catto et al., 2014; Mahara et al., 2015). Therefore, the BIMA is a suitable candidate material for the construction of small-diameter vascular grafts in tissue engineering.

The combination of different protocols, such as detergent, physical shake, and biological enzyme, was the most commonly used decellularized method (Crapo et al., 2011). Based on our previously described multistep detergent and enzymatic decellularization procedure (Lü et al., 2009), we modified a new decellularization strategy that combines sonication and perfusion, which can be used to reduce the concentration of detergent and exposure time and preserve the three-dimensional structure of the extracellular matrix. Previous studies have shown that alterations in the ECM structure, which depends greatly on the decellularization process, also lead to changes in the mechanical properties. In addition, the decellularization process can reduce the antigenicity of xenogeneic biomaterials (Böer et al., 2011), but there is still more inflammatory cell infiltration after *in vivo* implantation, and cross-linking can inhibit immune inflammatory cell infiltration and tissue degradation (Courtman et al., 2001). The physical and chemical cross-linking method can improve biomechanical properties and biocompatibility performance and reduce an inflammatory response by inhibiting the penetration of inflammatory cells or blocking part of the antigenic sites exposed by the denaturation of protein of ECM secondary conformation (Stock and Schenke-Layland, 2006). Chemically, glutaraldehyde, carbodiimide, and polyglycidyl ethers are common cross-linkers as well as physical cross-linking methods that include photooxidation and dehydrothermal methods. All of these methods mediate the formation of covalent bonds between amine groups and carboxyl groups on the collagen fibers of the bioscaffold. Although chemical cross-linkers, such as glutaraldehyde, can achieve better cross-linking effects, their residual toxicity or excessive cross-linking can cause calcification or less cellular infiltration, leading to failure (Schmidt and Baier, 2000; Parenteau-Bareil et al., 2010).

Photooxidation cross-linking has the advantages of non-toxicity, less calcification, and mild inflammation, but it does not cross-link in elastic fibers, which is also responsible for failure of vascular implantation, such as early degradation of elastic fibers, aneurysmal dilatation, and impaired vascular mechanical properties (Moore and Adams, 2001; Meuris et al., 2003). Our previous studies have shown that photooxidation cross-linking of decellularized bovine jugular vein can prevent ECM degradation and promote the regeneration of collagen, GAGs, and cell infiltration, but the elastic fibers are gradually degraded, which may lead to binding of elastin molecules' peptide chain backbone to calcium ions, resulting in calcification. Elastic fibers are richer in the arterial walls; therefore, elastic fibers need to be further processed (Lü et al., 2010). PGG is a polyphenol antioxidant and cross-linker of elastic protein and has the function of stabilizing elastic fiber, reducing the degradation and calcification of ECM, and attenuating excess reactive oxygen species (ROS) and anti-inflammatory effects in the regulation of an inflammatory response (Fraga et al., 2010; Leopoldini et al., 2011).

Overcoming early acute thrombosis, an acute inflammation, degradation, and calcification in a decellularized small-diameter vascular xenograft is challenging. We hypothesized that a

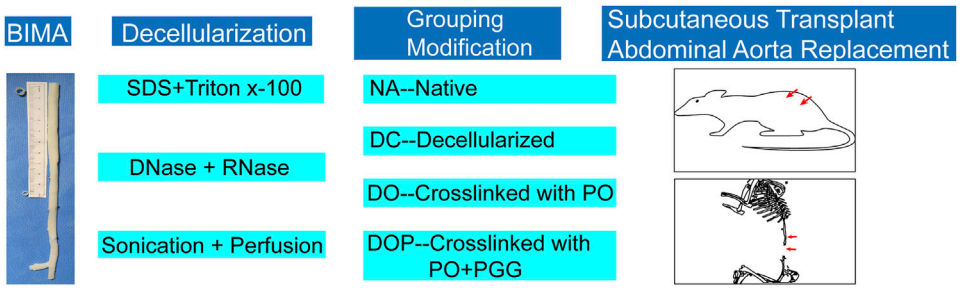

FIGURE 1 | Experimental setup. After decellularization by ultrasound and perfusion, the vascular grafts were grouped, modified by cross-linking, and implanted in the animal models. PO, photooxidation; PGG, pentagalloyl glucose.

modified decellularization protocol with photooxidation and PGG cross-linking could improve the properties of biomechanical and biocompatibility; reduce inflammatory responses, degradation of elastin, calcification; and promote neointimal stabilization and remodeling. To test this hypothesis, we used BIMA as a tissue engineering vascular graft, which is based on a modified decellularization strategy that combines sonication, perfusion, and cross-linking with photooxidation and PGG in this study. In addition to quantification of DNA and ECM proteins, characterization of surface topography, biomechanical strength, fixation index, susceptibility to elastinase, cell biocompatibility *in vitro*, short-term subcutaneous transplants in rat, and abdominal aorta replacement in rabbit were performed to assess graft performance, cell migration, remodeling, and mass spectrum of neointima *in vivo*.

MATERIALS AND METHODS

Fresh BIMA was received from a local slaughterhouse, cleaned from adherent tissues as well as residual fat, and consecutively rinsed using phosphate-buffered saline (PBS). In addition, 10-cm segments were cut from the BIMA, and the segments (n = 80) were stored at 4°C in PBS supplemented with 1% streptomycin/penicillin. The blood vessels in our laboratory are generally stored for 2 weeks in PBS containing 1% streptomycin/penicillin at 4°C. After gamma radiation sterilization at a dose of 25 KGy, the grafts can be stored in 60% alcohol for 1 year. Thereafter, the BIMA was further processed as indicated in our flow scheme (**Figure 1**).

Decellularization Procedure

The decellularization procedure was based on a combination of physical, chemical, and biological methods and a system which consisted of an ultrasonic cell breaker and a peristaltic pump. The steps were as follows: first, we used a peristaltic pump (80–100 ml/min) to perfuse BIMA with 0.5% sodium dodecyl sulfate (SDS, Sigma, L3771, United States) and 0.5% Triton X-100 (Sigma, X-100, United States) for 24 h and combined with sonication treatment (20 kHz, 200w) for 12 h. Second, after sonication treatment, samples were washed with PBS solution by using the peristaltic pump for 30 min and DNAse (40 U/ml, Servicebio, G5043, China) and RNAse (0.3 mg/ml, Servicebio, G3413, China) was added in the decellularized container at 37°C water bath for 24 h. Third, after ribozyme treatment, samples were washed in the perfusion system with PBS for 48 h. Finally, the decellularized BIMAs (DC) (n = 60) were stored in sterile PBS at 4°C before further use.

Photooxidation and PGG Cross-Linking

Decellularized BIMAs were cross-linked by using a dye-mediated photooxidation technique, according to the method of Moore et al. (1994). The experimental process refers to our previous research (Lü et al., 2010). In brief, the grafts were immersed in a chilled PBS containing glucose (pH 7.6, Osm: 680 osm) for 4 h, followed by a 2-step cross-linking process. First, the grafts were incubated in a cross-linking solution, a chilled PBS containing glucose (pH 7.6, Osm: 320 osm) that comprised 0.1% methylene blue (Sigma, M9140, United States) for 4 h at 4–20 °C in the dark. In the second step, the cross-linking solution and DC graft reacted with a 500-W broad wavelength light source and worked for 48 h at 0–15 °C with 10 ml/min air sparged through the stirred reaction solution. The inner and outer walls of the grafts were treated by photooxidation for 24 h, and the reaction solution was changed every 24 h. After cross-linking, the DC with photooxidation cross-linking grafts (DO, n = 20) was washed in sterile PBS and stored in sterilized PBS at 4°C for further study.

The DO grafts were cross-linked with different concentrations (0.1%/0.25%/0.5%) of sterile PGG (Biopurify, 14937-32-7, China) in 50 mM phosphate buffer of pH 5.5 containing 20% isopropanol for 24 h (Pennel et al., 2014), and then the PGG-treated DO-BIMA (DOP, n = 20) was washed three times with PBS. All the grafts were sterilized by 25 KGy gamma irradiations and stored in 60% alcohol at 4°C for further use.

DNA Quantification and Electrophoresis

The total DNA amount of native BIMA (NA) or DC-BIMA grafts was quantified by using a DNA detection kit (TIANamp Genomic DNA kit) for grafts. We then prepared an agarose gel, followed by making an electrophoresis gel membrane, and finally added a marker and DNA samples, respectively. The electrophoresis parameters were 100 V of current for a duration between 30 and 45 min. Then the electrophoresis

gel membrane was exposed under UV light and scanned the picture.

Histological Analysis

The samples were fixed in 4% formaldehyde solution for 24 h, followed by gradient dehydration in alcohol. Then paraffin infiltration and embedding were performed, and slides of 5 μm each were cut out. Then the slides were stained by hematoxylin and eosin (H/E, Servicebio, G1005, China) stain for general morphology and cell nuclei, Masson's trichrome (Servicebio, G1006, China) stain for collagen demonstration, elastic van Gieson (EVG, Servicebio, GP1035, China) stain for elastin demonstration, and immunohistochemistry (IHC) stain for identification of the α-gal antigen.

Mechanical Testing

The four groups of NA/DC/DO/DOP-BIMA were cut into short conduits with a diameter of 4 mm and a length of 10 mm (n = 6). The grafts were used to measure the radial mechanical properties, burst pressure, and suture tension. An INSTRON instrument, which measures radial mechanical properties, was used. In addition, 2-cm length of graft (n = 6) was used for a suture retention test, performed by placing a 6-0 prolene suture 2 mm from the end of the graft and pulled to failure on an INSTRON tensile testing system. The burst pressure was measured by delivering PBS from a 50-ml syringe *via* a control valve. The diametrical compliance (C) was calculated by using equations published by Hamilton's group (Tai et al., 1999). In brief, the diameters were recorded between pressure of 120 and 80 mm Hg by slowly injecting PBS into each group of vascular grafts (n = 6).

Fixation Index Determination

The ninhydrin (NHN) assay can be used to reflect the degree of tissue cross-linking by the fixation index (FI). The FI was calculated by using equations published by Hsu's group (Sung et al., 1996). In brief, after being fixed, all samples were lyophilized and weighted. Then tissues were put into NHN solution (Aladdin, N105629, China) and heated to boil for 20 min. Optical absorbance of the solution was detected by a microplate absorbance reader at 570 nm.

Scanning Electron Microscopy

For scanning electron microscopy (SEM), the NA/DC/DO/DOP-BIMA samples were fixed and dried by a graded ethanol series and then freeze-dried for dehydration. Dried samples were sputter coated with 20 nm of gold and analyzed using a FEI Nova NanoSEM (FEI Electron Optics B.V, Czech). The number of pores, ratio of the pore area, and diameter of a fiber were calculated by Image-Pro Plus 6.0 analysis software.

Elastin Degradation Experiments

To test the elastin degradation ability of NA/DC/DO/DOP-BIMA, different grafts were freeze-dried and weighed. Elastase (20 IU/ml, Biomatik, A4126, China) was added and the grafts were incubated at 37°C for 24 h; then the grafts were freeze-dried and weighed. Finally, the degradation rate of each group's materials was calculated.

Cell Biocompatibility

Cytotoxicity Assessment

The human umbilical vein endothelial cell line (EAhy926) was cultured in a high glucose Dulbecco's modified Eagle mediumwith 10% fetal bovine serum (DMEM/10%FBS, Servicebio, G4510, G8001, China). A sample size of 1 × 1 cm^2 was cut from BIMA grafts and cultured in DMEM/10%FBS at 37°C for 24 h at a density of 2.5 ml/cm^2. The culture media (leach liquor) were collected and preserved. The media were replaced with leach liquor from the scaffold cultures diluted with DMEM/10%FBS at a ratio of 1:2. The cells were cultured for a further 1, 3, and 5 days at 37°C. A negative control was prepared using DMEM/10%FBS alone. The mitochondrial metabolic (MTT, Servicebio, G4104, China) assay was applied in assessing the cell growth on the scaffold. The optical density at 570 nm was determined using a microplate reader. The cytotoxicity of each protocol was evaluated by calculating the relative growth rate (RGR) to determine the proliferation index (Xu et al., 2017). RGR = (mean OD for each group)/(mean OD of the negative control) × 100%.

Cell Viability Assay

Samples of the four groups were cut into 5 × 5 mm pieces, washed with sterile PBS for 20 min, soaked in DMEM/10%FBS for 24 h, and then placed in a 48-well plate. A total of 5 × 10^3 cells were seeded on each sample. After 30 min, 500 μl of DMEM/10%FBS was added to each well and cultured for 7 days. The culture medium was changed every 2 days. The pieces of vascular grafts were transferred to clean wells and washed with a PBS solution, and 100 μl of 10 μmol/ml 6-CDCFDA (carboxy-2′,7′-dichlorofluorescein diacetate, Yuhengbio, C4096, China) live cell fluorescent dye was added to each well and incubated for 30 min in incubators. Cells were visualized by using an inverted fluorescence microscope. Then the pieces were fixed and prepared for SEM. In addition, we used immunofluorescence staining of F-actin to show the morphology of cells with phalloidin (Servicebio, G1028, China) and acquired images using a laser scanning confocal microscope (LSCM, LSM780, Zeiss, Germany).

In Vivo Subcutaneous Implantation in Rat and Abdominal Aorta Replacement in Rabbit

Subcutaneous Implantation

All animal experiments were approved by the Animal Research and Ethics Committee of The Second Xiangya Hospital of Central South University (CSU) and performed by the Department of Cardiac Surgery of The Second Xiangya Hospital. Host cell infiltration and immune inflammation responses against the different groups of NA/DC/DO/DOP BIMA (n = 4) were evaluated in rat subcutaneous implantation models. In this regard, about 4-week-old Sprague–Dawley rats (SD) with mean weight of 140 g were selected and anesthetized by sodium pentobarbital (30 mg/kg), and the vascular grafts with the size of 1 × 1 cm^2 were implanted on each side of the subject rats. A 2-0 Mersilk suture was used to suture the skin of rats.

Finally, the samples were removed to undergo histological examination after 28 days by using H/E staining. IHC staining was performed using anti-mouse CD3 (1:400, Servicebio, GB11014, China) and CD68 (1:200, Servicebio, GB11067,China) primary antibodies.

Abdominal Aorta Replacement

Grafts of three groups (DC/DO/DOP, n = 5) were evaluated in a total of 15 rabbits. The length of the grafts was 2 cm, and the diameter was 3.5 mm. Animals were anesthetized and sedated with 30 mg/kg sodium pentobarbital. Following a left paraspinal incision, the aorta was dissected free of surrounding tissues and the inferior vena cava. Intravenous heparin (1 mg/kg) was administered before implantation and grafts were implanted into infrarenal aorta by end-to-end anastomoses using 7-0 prolene sutures. All grafts were implanted for 4 weeks to compare the progression of remodeling of neointima, inflammation degradation of elastin, and calcification. Prior to the animals being euthanized, abdominal computed tomography angiography (CTA) was performed at 4th week, and the graft diameters were measured to evaluate the presence or absence of stenosis. After 4 weeks, grafts were then excised and washed with saline. The samples were analyzed histologically using the HE staining, Masson's trichrome staining, and von Kossa (Servicebio, G1043,China). The EVG staining for elastin and quantification of elastin's relative content from the histological images was performed by Image-Pro Plus 6.0 analysis software. The content of elastin in implanted grafts was compared with that in pre-implanted grafts to calculate the preservation ratio of elastin. The identification of different types of collagen fibers and content ratios in the neointima was determined by Picro-Sirius Red staining (Abcam, ab246832, United Kingdom). Studies have used the differences between the appearances of different collagen fibers under polarized light to differentiate between different types of collagen fibers. The color of type I collagen fibers is yellow/orange birefringence and type III collagen fibers is green birefringence. Using Image-Pro Plus 6.0 analysis software, the pixel area of type I collagen and the pixel area of type III collagen in the neointimal area of each group was measured uniformly with the pixel area as the standard unit; the type I and type III collagen pixel area ratios were calculated. IHC or immunofluorescence (IF) identification of endothelial cells was performed with antibodies to CD31 (1:200, Abcam, ab9498, United Kingdom), CD68 for macrophages (1:200, Servicebio, GB14043, China), CD206 for M2 macrophages (1:1,000, Abcam, ab254471, United Kingdom), alpha-smooth muscle cell actin (1:200, Gene Tex, GTX18147, United States) for fibroblast, calponin (1:500, Abcam, ab700, United Kingdom) for smooth muscle cell, and vimentin (1:200, Abcam, Ab8978, United Kingdom) for mesenchymal cell. The exact protocol is described in the **Supplementary Material**.

Mass Spectrum

The sample was rinsed and wiped dry using a dust-free paper. In total, 8 M urea +100 mM Tris-HCl (pH 7.2) lysate (with protease inhibitor) was added to solubilize protein. The protein concentration was determined by using the BCA method. A total of 500 μg protein was extracted from each group of samples; then mass spectroscopy-grade trypsin was added with at a ratio of 1:50 and digested overnight at 37°C. The peptide-containing solution was freeze-dried, and the peptide was dissolved for a mass spectrometry analysis. The Nono LC. LTQ Oribtrap MS was used for the mass spectrometry analysis. An electrospray ion source using a positive ion mode detection with a spray voltage of 2.4 kV at an ion source temperature of 350°C was used. The first-level FT scan was at the resolution of 60000 FWHM; the second-level IT scan was within the range of 280–1,500, in the TOP 20 mode, at the resolution of 7500 FWHM with a collision energy at 35%. The software Protome Discovery 2.0 (Thermo Fisher) was used to search the MS RAW files in the Uniprot TrEMBL database. Search database parameter settings are as follows: the species is rabbit; the cleavage enzyme is trypsin; the maximum number of missed cleavages is 1; the error of primary precursor ion is 10 ppm; and the error of secondary daughter ion is 0.5 Da. A false discovery rate of 0.01 was used and two biological replicates were analyzed. Proteins were stated identified if at least three unique peptides were detected.

Statistical Analysis

The results of quantitative studies were expressed as the median and the interquartile range. For analysis of two groups with unpaired samples, the Mann–Whitney *U* test was used. For analysis of three or more groups, the Kruskal–Wallis test with Tukey's post hoc test was used and analyzed using a statistical analysis software IMB SPSS Statistics 22.0 (IBM, United States), and graphs were generated using GraphPad Prism 8 (GraphPad, United States). p-values ≤ 0.05 were considered to be statistically significant.

RESULTS

Decellularized BIMA Preparation and Characterization

The decellularized BIMA with a diameter of 3–6 mm and a length of 10–15 cm were obtained. The acelluar BIMA showed optimal three-dimensional structure of the extracellular matrix by HE, Masson, and EVG staining (**Figure 2**). The comparison of expression levels of α-gal (IHC scores) in NA and DC groups showed that α-gal antigen were significantly reduced in decellularized grafts (**Figure 2L**). DNA electrophoresis (**Figure 2I**) showed no macromolecular bands, and the DNA content (**Figure 2J**) was significantly reduced in decellularized grafts (**Figure 2**). The content of collagen and elastin was not significantly different between the NA and DC groups (**Figure 2K**). The BIMA showed a complete internal elastin lamina membrane, thin media, which contained collagen and elastic fibers, and a relatively loose adventitia.

Mechanical Properties of Cross-Linked BIMA

To test the effect of cross-linking on the biomechanical properties of vascular scaffolds, the ninhydrin experiment,

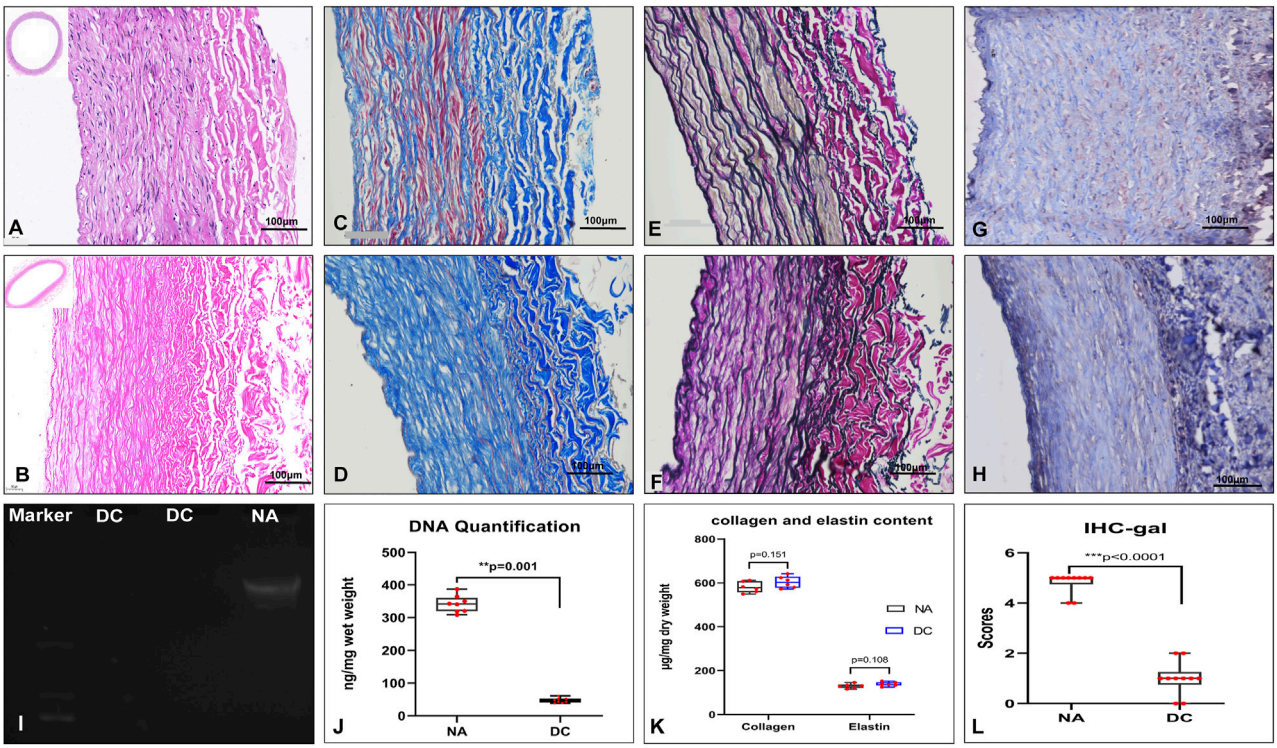

FIGURE 2 | Characteristics of the bovine internal mammary artery (BIMA) before **(A,C,E,G)** and after **(B,D,F,H)** acellularization. H&E staining **(A,B)**, Masson's trichrome staining **(C,D)**, van Gieson staining **(E,F)**, and immunohistochemistry of α-gal **(G,H)**. **(I)** DNA electrophoresis showed no macromolecular bands of the decellularized bovine internal mammary artery (BIMA). **(J)** DNA quantification of native and decellularized BIMA (Mann–Whitney *U* test). **(K)** Content of collagen and elastin was insignificant between the NA and DC groups (Mann–Whitney *U* test). **(L)** Comparison of α-gal antigen content (IHC scores) of native and decellularized BIMA (Mann–Whitney *U* test). NA, native BIMA; DC, decellularized BIMA.

the compliance, and the resistance to elastase were assayed. The aforementioned three experiments were tested in the DOP groups (0.1%, 0.25%, and 0.5%), and the results indicated that moderate cross-linking of PGG improved the fixation index and resistance to elastase, but excessive cross-linking also led to reduced vascular compliance. Therefore, 0.25% PGG was chosen as our cross-linked concentrations. (The comparison data of different concentrations of DOP group are shown in the **Supplementary Material**.) The ninhydrin experiment results showed that the cross-linking degree of the DO and DOP groups was approximately 20% and 40%, respectively (**Figure 3A**). The compliance was approximately 24%, 14%, 15%, and 17% in the NA, DC, DO, and DOP groups, respectively (**Figure 3B**). The compliance of the DOP group was lower than that of the NA group but significantly higher than that of DC and DO groups. The elastin degradation test showed that the DOP group had the lowest weight compared with the other three groups (**Figure 3C**).

After comparing the NA, DC, DO, and DOP groups' radial mechanical properties, we found that there was no significant difference in Young's modulus, maximum tensile stress, and burst pressure among the four groups ($p > 0.05$, as shown in **Figure 3D** and **Figure 3E**), but in the suture retention strength, the DOP group was significantly higher than NA and DC, and there was an insignificant difference from the DO group (**Figure 3F**).

SEM and Staining

To observe the structure and morphology of blood vessels after cross-linking, HE/MASSON/EVG staining were performed in DO and DOP groups (**Figure 4**). From the SEM results, the NA group showed a tight fiber connection without obvious pores. The SEM images of the same area of DC/DO/DOP groups were selected, and then the number of pores per unit area and ratio of pore area were counted and analyzed which demonstrated that there were significant differences among the groups. The DOP group showed that the number of pores and the ratio of pore areas were less than that of other groups (**Figure 5**).

Cell Biocompatibility

The cytotoxicity of the four groups' scaffolds was determined by using the MTT assay. As shown in **Figure 6**, the relative growth ratios (RGRs) of HUVECs were grown in the presence of leach liquor from the scaffolds at concentrations after 1, 3, and 5 days of culture were evaluated. On Day 1, no apparent differences were observed in the RGRs between the four groups; on Day 3 and Day 5, the RGRs in the four groups reached level 1 and showed an

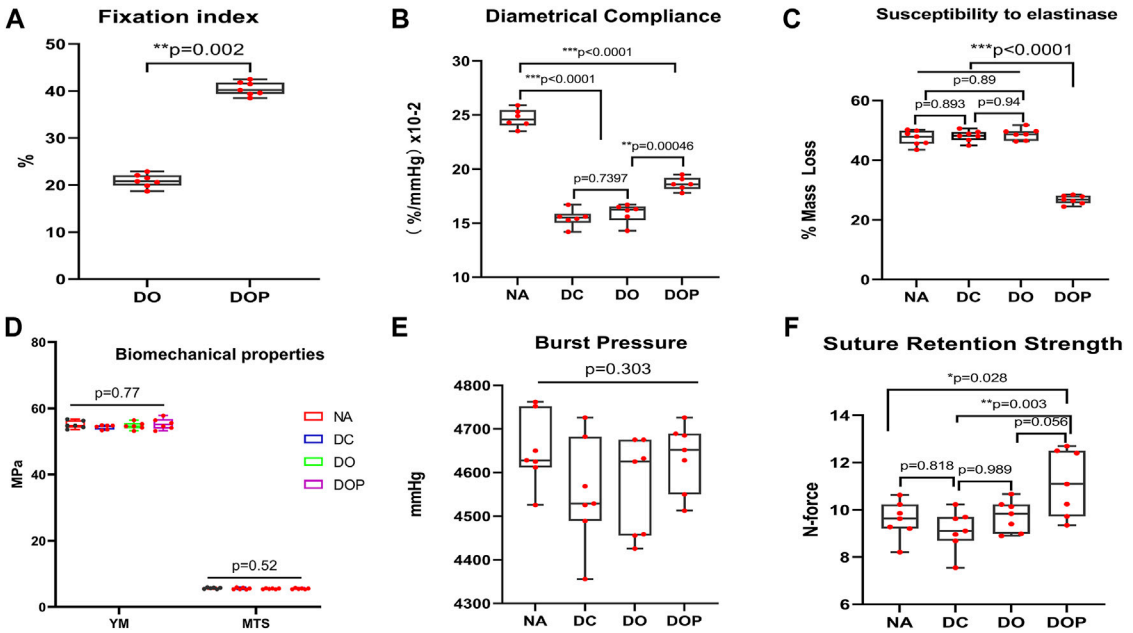

FIGURE 3 | Bovine internal mammary artery's (BIMA) property before and after cross-linking. **(A)** Fixation index of the DOP group was significantly increased compared to the DO group (Mann–Whitney *U* test). **(B)** Diametrical compliance significantly decreased in the DC, DO, and DOP groups, but it was significantly increased in DOP groups compared with the DC and DO groups. **(C)** Resistance to elastinase in DOP groups was significantly higher than that in the NA, DC, and DO groups. **(D,E)** Difference of the four groups' burst pressure and radial mechanical was insignificant. **(F)** Suture retention strength of the DOP group significantly increased compared to the NA and DC groups. For B, C, D, E, and F, box and whiskers, minimum to maximum, shows all points. The Kruskal–Wallis test with Tukey's post hoc test. NA, native BIMA, DC, decellularized BIMA; DO, photooxidation cross-linked BIMA; DOP, photooxidation and PGG cross-linked BIMA; YM, Young's modulus; MTS, maximum tensile stress.

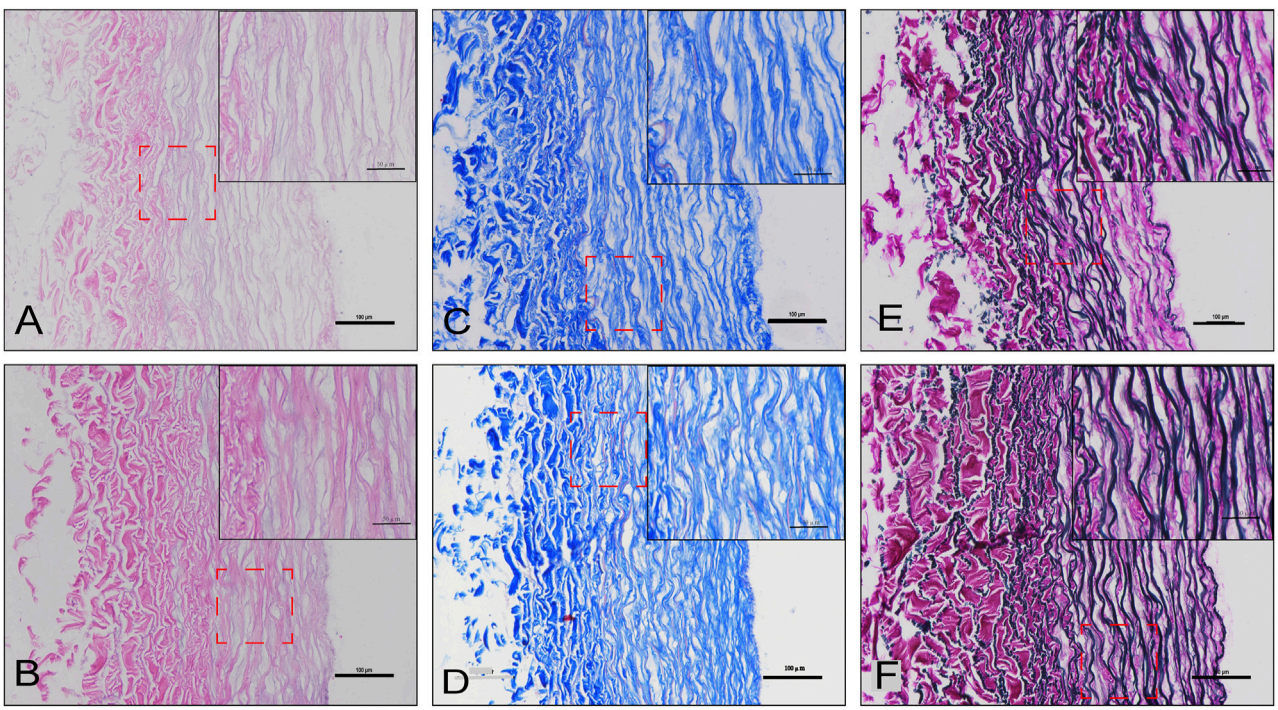

FIGURE 4 | Histological staining of the DO and DOP groups. H&E staining **(A,B)**, Masson's trichrome staining **(C,D)**, and van Gieson staining **(E,F)** of the DO **(A,C,E)** and DOP **(B,D,F)** groups.

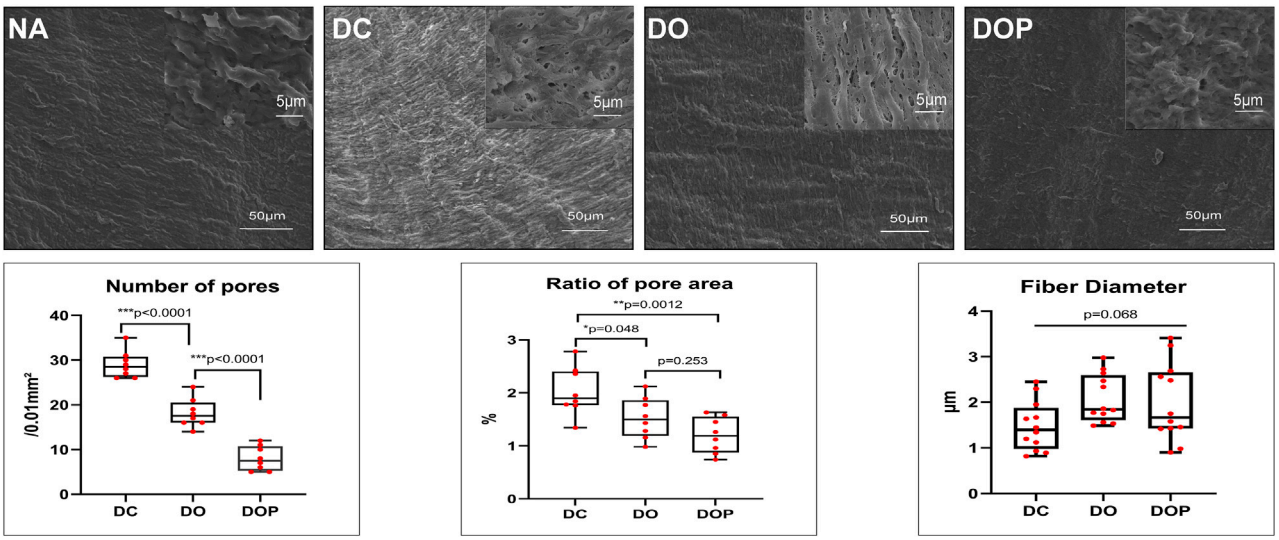

FIGURE 5 | Morphology assessed by SEM and semi-quantitative results of pore number, area, and mean fiber diameter in the groups. The number of pores and the ratio of the pore area in the DOP group were significantly less than those in the DO and DOP groups. The difference of fiber diameter was insignificant in the groups. Box and whiskers, min to max, show all points; The Kruskal–Wallis test with Tukey's post hoc test. NA, native BIMA; DC, decellularized BIMA; DO, photooxidation cross-linked BIMA; DOP, photooxidation and PGG cross-linked BIMA.

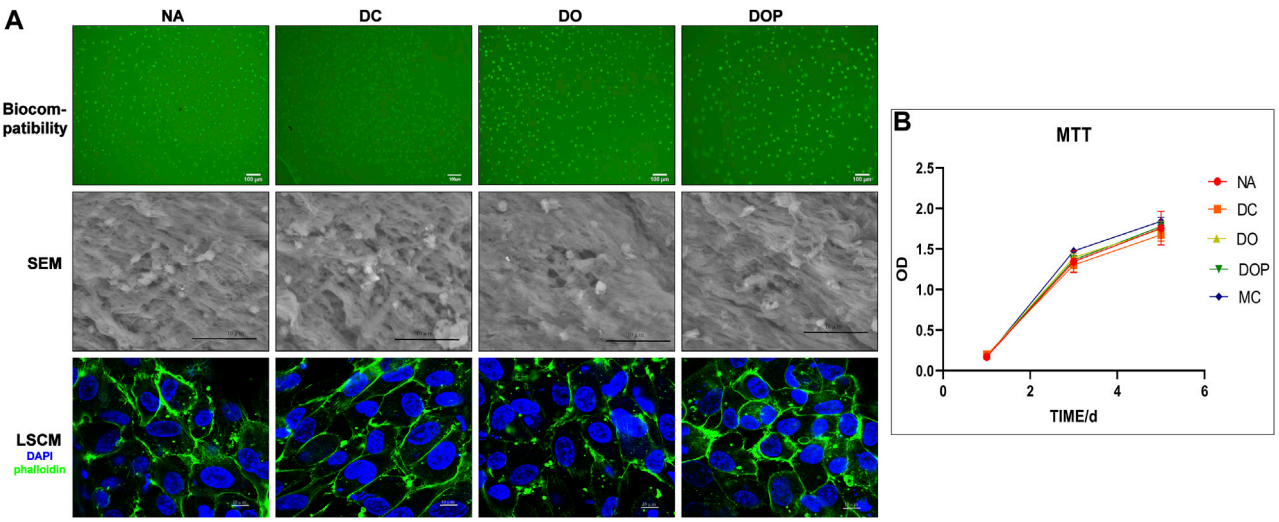

FIGURE 6 | Cell biocompatibility of the NA, DC, DO, and DOP groups are shown. **(A)** Human umbilical vein endothelial cells adhered and spread on the materials after 7 days, and cell adhesion and morphology was assessed by 6-CDCFDA live cell fluorescent staining, scanning electron microscopy (SEM), and the immunofluorescence staining of F-actins for the cell shape (DAPI: blue; phalloidin: green). **(B)** Cytotoxicities were determined by the MTT assay and showed no significance in the relative growth ratio between the experiment groups and control groups (Kruskal–Wallis test with Tukey's post hoc test, $p > 0.05$). NA, native BIMA; DC, decellularized BIMA; DO, photooxidation cross-linked BIMA; DOP, photooxidation and PGG cross-linked BIMA.

insignificant difference between different groups. For the cell viability assay of the DC, DO, and DOP groups, the cells adhered and spread on the materials. The live cell 6-CDCFDA fluorescent staining and results of SEM and IHC-CD31 confirmed the reseeded cells' viability, and there were no significant difference in the four groups. The F-actins' immunofluorescence staining of phalloidin showed that the cells adhered to the luminal surface of the vessels in a cobblestone shape. (The results of IHC show in the **Supplementary Material**.)

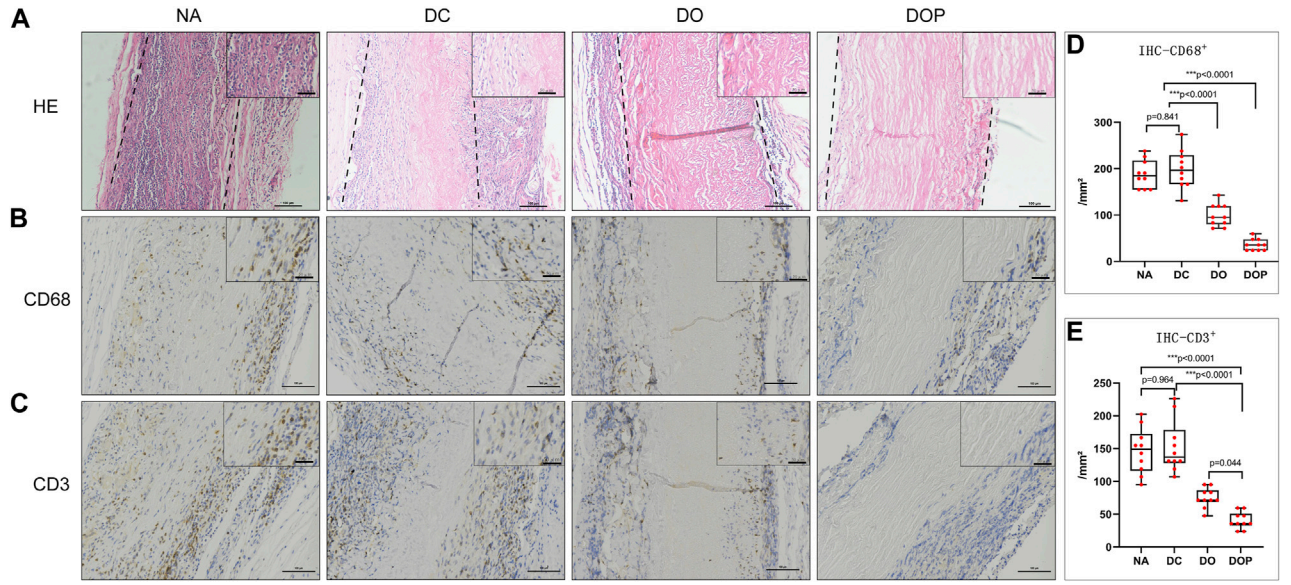

FIGURE 7 | Histological staining of four groups' grafts implanted into the subcutaneous transplants of rats for 4 weeks. **(A)** Histological staining (H&E). The dotted line depicts the edge of the implanted graft; **(B)** immunohistochemical (IHC) staining for macrophages (CD68); **(C)** IHC staining for T lymphocyte (CD3); **(D,E)** quantitative analysis of the number of $CD68^+$ and $CD3^+$ cells in the four groups. The number of positive cells in the NA group and DC group was significantly higher than the DO and DOP groups, and the number of positive cells in the DOP group is significantly reduced (box and whiskers, min to max, show all points; Kruskal–Wallis test with Tukey's post hoc test). NA, native BIMA; DC, decellularized BIMA; DO, photooxidation cross-linked BIMA; DOP, photooxidation and PGG cross-linked BIMA.

Host Cell Infiltration and Inflammation of the Grafts *In Vivo*

Before the end of the study, the rats did not receive any drugs and antibiotics. After 28 days, no reactions, including local and systemic infections as well as infections of the implanted scaffolds in animal models at the surgical sites, were observed. The four groups' HE stain examination showed that in the NA group, many cells were infiltrated in the graft and parts of the internal and adventitia membranes were degraded (**Figure 7**). In the DC group, many cells were infiltrated in the graft, and the internal and adventitia membranes were partially degraded. In the DO group, a small cell amount in the graft was infiltrated; the blood vessel was not degraded. In the DOP group, there was almost no cell infiltration in the graft, and the structure of the graft was basically intact. The IHC results showed the presence of more $CD68^+$ and $CD3^+$ cells in the NA and DC groups ($p < 0.01$), distributed in the vascular wall and the fibrous capsule. Compared with the DOP group, there were more $CD68^+$ and $CD3^+$ cells in the DO group that infiltrated in the superficial vascular wall and the fibrous capsule, while the positive cells in the DOP group only existed in the fibrous capsule (**Figure 7**).

In Vivo Performance of Abdominal Aortic Implantation

New Zealand white rabbits were used for abdominal aorta transplantation. All rabbits survived surgery without complications, such as paraplegia and infections. CTA results showed that the patency in the DC group was 60% at 4w and that in the DO and DOP groups were 100%. In the DC group, there were two cases of occlusion due to thrombosis. In the DO group, there were two cases with stenosis in the middle of the graft or anastomotic site (stenosis degree >30%) and two cases in the DC group (**Table 1**). Grossly, connective tissue adhered to the grafts' abluminal surface explanted on the fourth week and the grafts' luminal surface appeared glossy in the DO and DOP groups (**Figure 8**). The results of HE, Masson trichrome, EVG, and Picro-Sirius Red staining showed that there were a large number of cell infiltrations in the adventitia and deposition of new collagen fibers in the neointima in the three groups. In the DOP group, the new collagen fibers were arranged orderly, and the structure was similar to that of natural blood vessels; the preservation rate of elastic fibers of vascular wall in the DOP group was higher than that in the other two groups. (The comparison data of preservation rates of elastin are in the **Supplementary Material**.) von Kossa staining showed local calcium deposition in both the DC and DO groups but no calcium deposition in the DOP group (**Figure 9**).

TABLE 1 | Summary for abdominal aorta replacement in rabbit.

	4W	Occlude	Stenosis	Patency (%)	Survival at 4W (%)
DC	5	2	2	60	100
DO	5	0	2	100	100
DOP	5	0	0	100	100

Results of the IHC and IF showed that α-SMA^+ cells and $vimentin^+$ cells were distributed in the neointima of all the groups. In the DOP group, there were no CD68 + cells in the

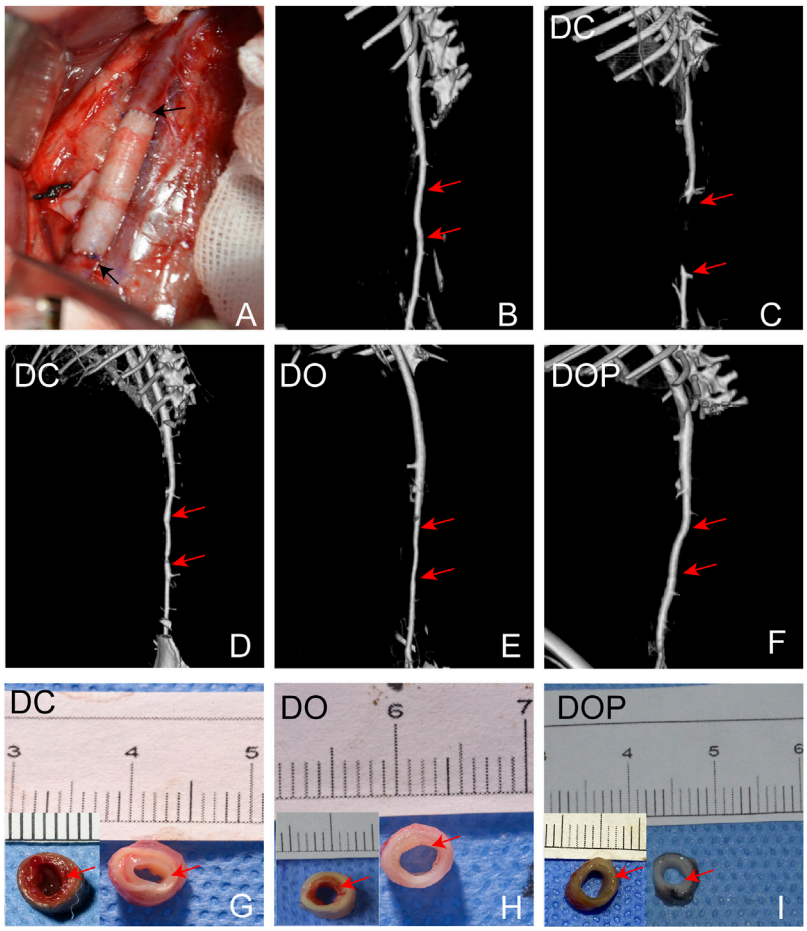

FIGURE 8 | (A) Macroscopic images of the rabbit infrarenal abdominal aortic transplantation model. **(B)** CTA results on the first day after operation. **(C,D)** CTA results of occlusion and stenosis after 1 month of vascular implantation in the DC group. **(E)** CTA results of stenosis after 1 month of vascular implantation in the DO group. **(F)** CTA results of DOP group after 1 month of vascular implantation. Red arrows depict the anastomoses; the mid-section gross images of grafts implanted for 1 month in the DC **(G)**, DO **(H)**, and DOP **(I)** groups. Red arrows depict the neointima. DC, decellularized BIMA; DO, photooxidation cross-linked BIMA; DOP, photooxidation and PGG cross-linked BIMA.

vascular grafts, which could be detected in the DC and DO groups. (The comparison data of $CD68^+$ cells are in the **Supplementary Material**.) The $CD206^+$ cells and calponin+/α-SMA + double positive cells were detected in the neointima of the DO and DOP groups. However, there was no CD31 positive cell adhesion in the three groups (**Figure 10**).

Mass Spectrum of Neointima

To identify the composition of the neointima, the different groups' samples were digested using trypsin and analyzed by Orbitrap mass spectroscopy using a label-free quantification method. The possible components of neointima in each group were analyzed. The principal component analysis showed the relative distance between the experimental groups (**Figure 11A**). The results of the mass spectrometry analysis showed that the major categories whose protein abundance accounted for the top 70% of samples in the three groups were plasma protein components (albumin, hemoglobin, fibrinogen, immunoglobulin, transferrin, etc.), cytoskeletal protein components (actin–aortic smooth muscle, actin–alpha skeletal muscle, tropomyosin alpha-1 chain, etc.), glycoproteins, and secreted factors (glyceraldehyde-3-phosphate dehydrogenase, protein S100-A12, vitamin D-binding protein, etc.) (**Figure 11B**). We analyzed differential expression among the three groups, but no statistically significant differential proteins were found (FDR-adjusted $p < 0.05$). The heatmap and Venn diagram demonstrated the proteins with the top 20 differential fold change among the three groups (**Figures 11C, D**). The heatmap demonstrated differential proteins with $p < 0.05$ in the three groups (**Figures 11E**). GO annotations were not analyzed due to the low number of identifications of differential proteins, and FDR-adjusted $p > 0.05$. (The data of proteins/peptides are shown in the **Supplementary Material**.)

DISCUSSION

Although the artificial vascular graft of synthetic materials research and its clinical application have been in use for a

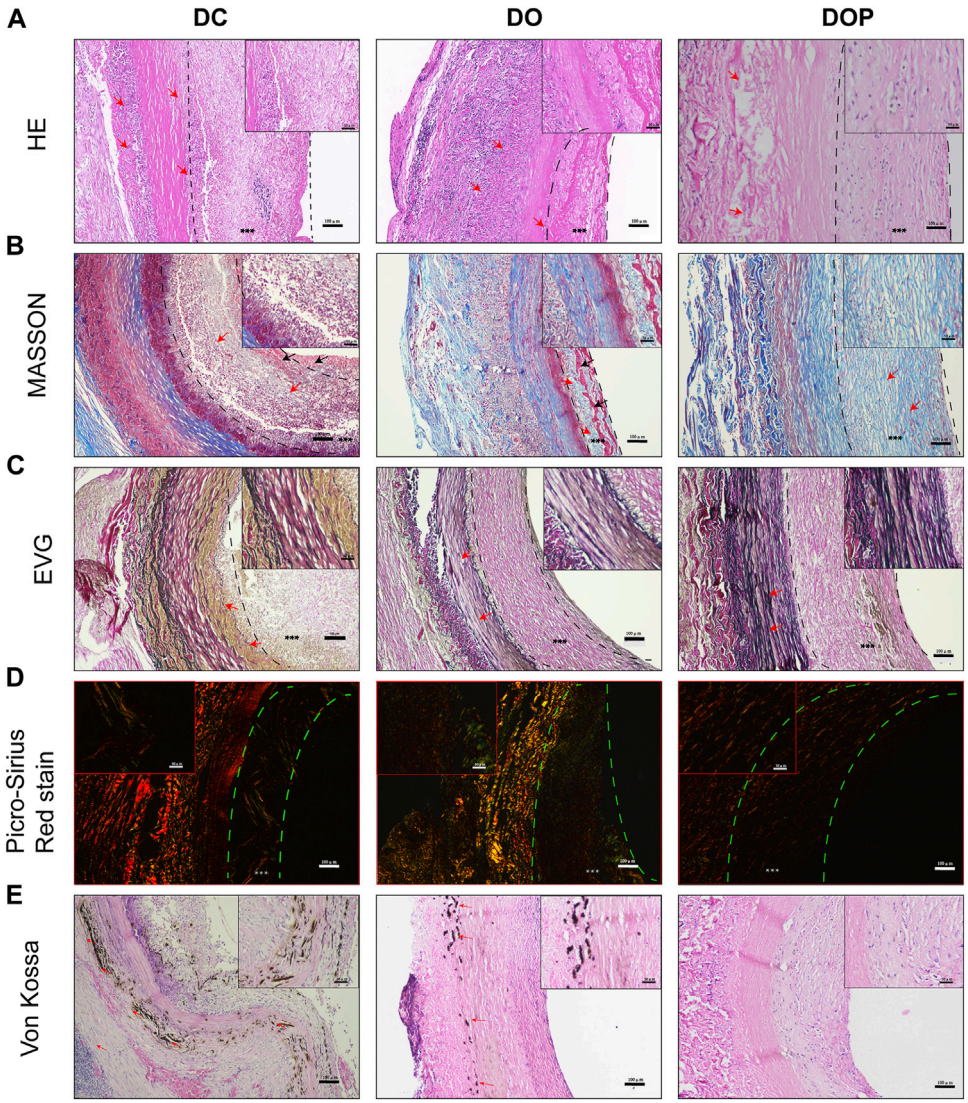

FIGURE 9 | Histological staining of three groups' grafts implanted into the abdominal aorta of rabbits for 1 month. **(A)** Histological staining. The red arrows depict cell infiltration in the basement membrane and adventitia of grafts in the DC and DO groups. In DOP group, a few cells infiltrated the adventitia of graft. **(B)** Masson's trichrome staining. The red arrows depict the regenerated collagen fibers and structural morphology of neointima in each group. In DC and DO groups, the black arrows depict the fibrin of neointima. **(C)** Elastin van Gieson staining. The red arrows depict the structural morphology of elastin in each group of scaffolds. Elastin appeared fragmented and degraded in the DC and DO groups. **(D)** Picro-Sirius Red staining. The color of type I collagen fibers is yellow/orange birefringence and that of type III collagen fibers is green birefringence. **(E)** von Kossa staining: the red arrows depict the calcification. There was no calcium deposition in the DOP group. Scale bars are 100 μm. The left dotted line indicates location of basement membrane and the right dotted line indicates location of vascular graft luminal surface. *** depict the neointima. DC, decellularized BIMA; DO, photooxidation cross-linked BIMA; DOP, photooxidation and PGG cross-linked BIMA.

long time, its complications, such as intimal hyperplasia, thrombosis, chronic inflammation, and slow tissue regeneration, are still the main reasons that limit its application in the field of small-diameter vascular grafts (Schneider et al., 2018; Schneider et al., 2020).

We described for the first time the use of decellularized BIMA in a rabbit abdominal aortic replacement model. BIMA has optimal biomechanical properties. In our study, its burst pressure was as high as 4,700 mmHg, and the suture retention reached approximately 9.0 N, which fully met the needs of human arterial blood pressure and had good durability. The results showed that the decellularization procedure combined with physical, chemical, and biological enzymes can remove cellular components and antigens of α-gal and retain the three-dimensional structure of the ECM. In our research, the decellularization results proved that the physical method of ultrasound combined with perfusion can efficiently remove cell components, and the reaction time and concentration of SDS and Triton X-100 can be reduced. The decellularization procedure was shortened to 3–4 days, which minimized the damage of detergent to ECM structure's integrity. The DNA was almost completely removed, and electrophoresis of DNA showed no

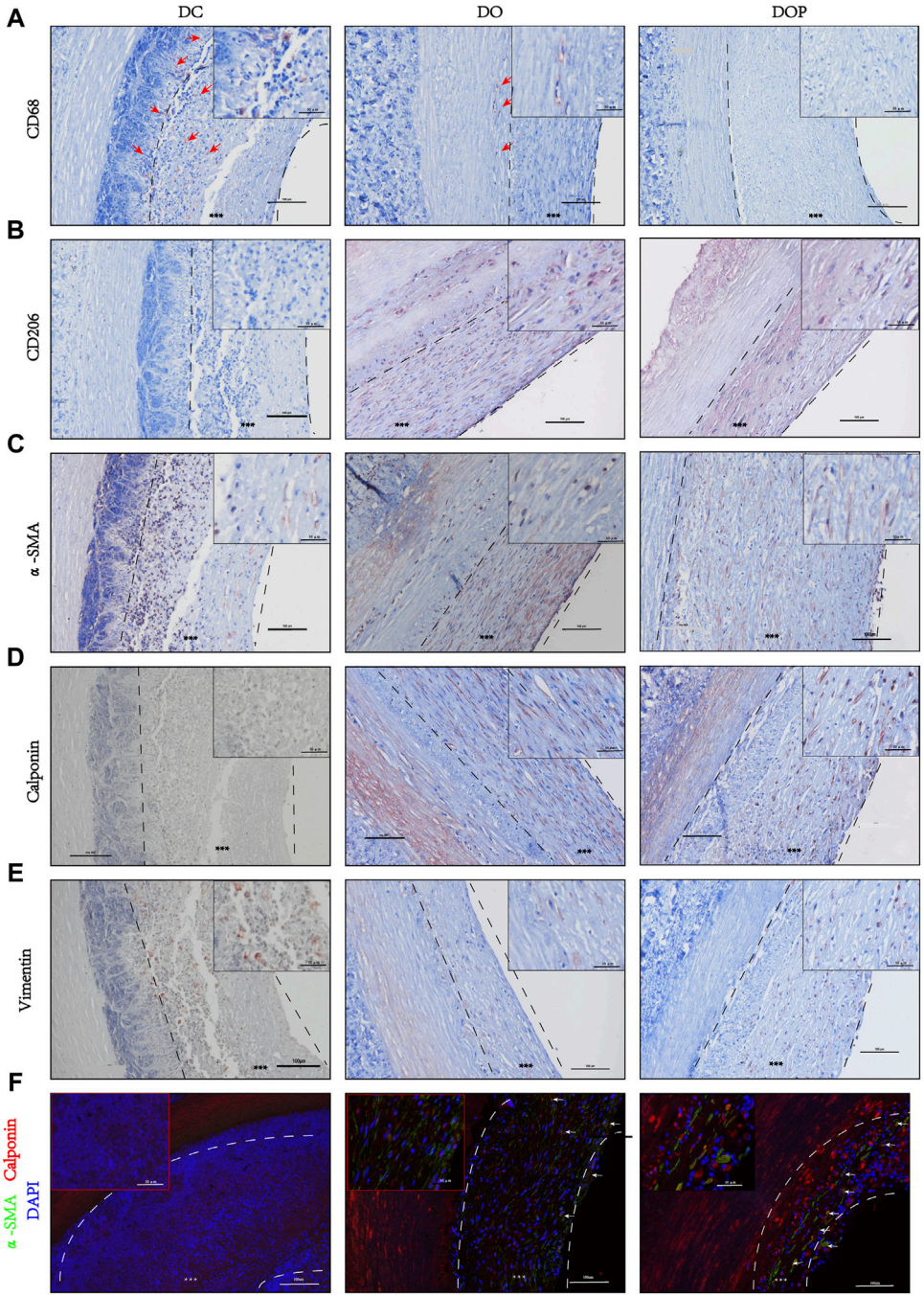

FIGURE 10 | Cell histological staining of three groups' grafts implanted into the abdominal aorta of rabbits for 1 month. **(A)** Immunohistochemical (IHC) staining for macrophages (CD68). Red arrows depict the positive cells. **(B)** IHC staining for M2 Macrophages (CD206). **(C)** IHC staining for fibroblast (α-SMA). **(D)** IHC staining for smooth muscle cell (calponin). **(E)** IHC staining for mesenchymal cell (vimentin). **(F)** Double immunofluorescence staining, α-SMA (green), calponin (red), and DAPI (blue). White arrows depict the double positive cells. Scale bars are 100 μm. The left dotted line indicates location of the basement membrane, and the right dotted line indicates location of vascular graft luminal surface. *** depict the neointima. DC, decellularized BIMA; DO, photooxidation cross-linked BIMA; DOP, photooxidation and PGG cross-linked BIMA. α-SMA, alpha-smooth muscle actin. DAPI, 4′,6-diamidino-2-phenylindole.

large molecular bands. The histological HE staining also indicated the cellular components' removal. Additionally, the grafts were removed of most of the α-gal antigen and reduced of the acute natural anti-gal antibodies that mediated rejection of the xenografts (Kasimir et al., 2005; Daly et al., 2009). The Masson and EVG staining showed that the decellularized BIMA had optimal extracellular matrix morphology and a fiber structure with no obvious breakage of collagen and

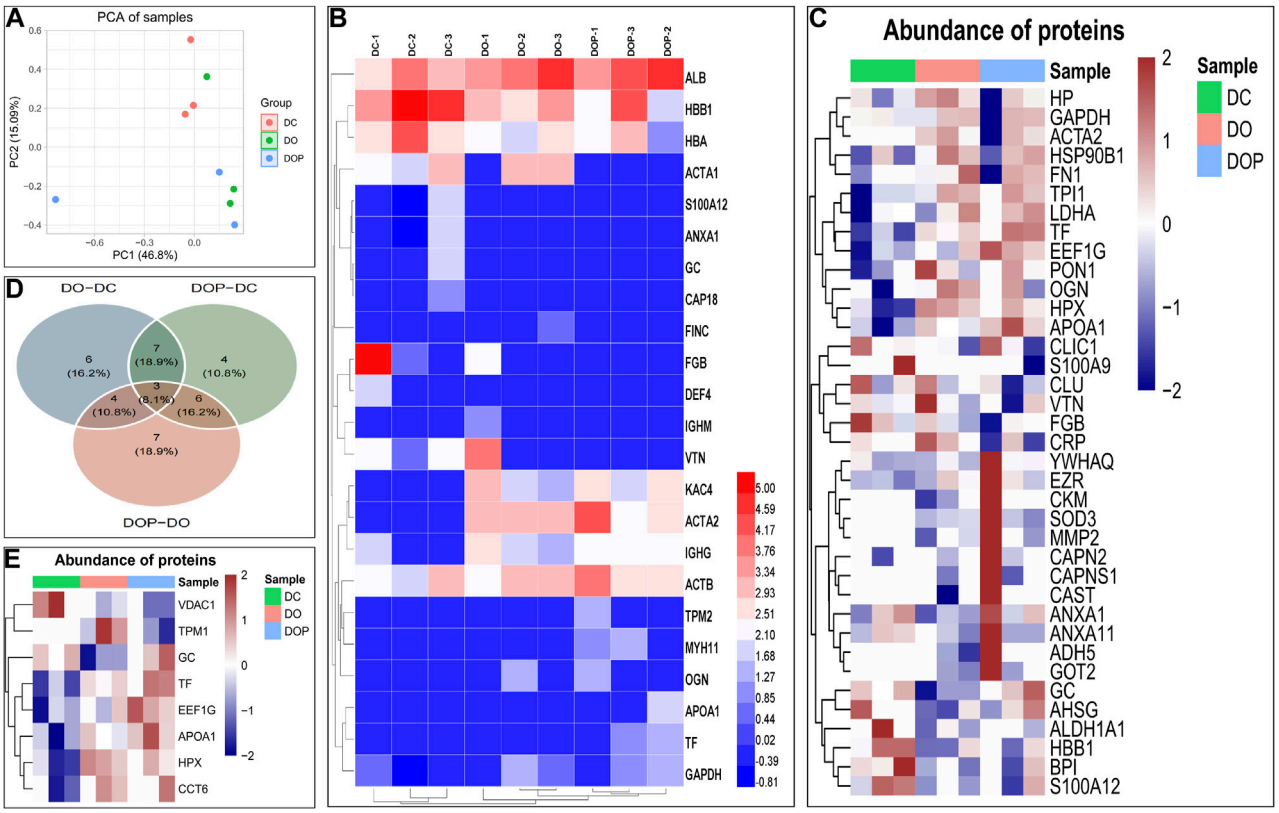

FIGURE 11 | To identify the composition of the neointima, the different groups' samples by an Orbitrap mass spectrometer using a label-free quantification method. The principal component analysis shows the relative distance between the experimental groups **(A)**. Heatmap showed that the major proteins/peptides whose abundance accounted for the top 70% of samples in the three groups **(B)**. Heatmap and Venn diagram demonstrated the proteins with the top 20 differential fold change among the three groups. The Limma package in the R language was used for difference analysis. **(C,D)** Heatmap demonstrated differential proteins with $p < 0.05$ in the three groups **(E)**. DC, decellularized BIMA; DO, photooxidation cross-linked BIMA; DOP, photooxidation and PGG cross-linked BIMA.

elastic fibers. The decellularization procedure's short-term and effectivity could be attributed to the sonication cavitation effects and perfusion, which could break the cells and facilitate the detergent penetration through the tissue (Azhim et al., 2014; Schneider et al., 2016).

The decellularization process will cause a damage to the ECM and expose the laminin of the basement membrane and collagen structure, leading to the degradation of mechanical properties and the exposure of procoagulant and antigenic sites on the fiber, which can cause early acute thrombosis, degradation of fibers, and inflammation (Lopera Higuita and Griffiths, 2020). Photooxidation cross-linked the graft's collagen fibers to cover parts of the exposed antigen sites, which reduced the immune response and the foreign body reaction and prevented rapid cell infiltration and early degradation of the ECM to form an aneurysm or rupture (Lü et al., 2010). However, the degree of the vascular graft's cross-linking by photooxidation treatment was not sufficient. Our previous studies have also shown that after photooxidation cross-linking of decellularized bovine veins, elastic fiber were degraded, which may reduce its biomechanical properties *in vivo*. The results indicated that moderate cross-linking of photooxidation and PGG can improve the biomechanical properties of vascular scaffolds, but excessive cross-linking can also lead to reduced vascular compliance. Appropriately cross-linked elastin fibers improved the vascular grafts' compliance, which has been proven to be related to the intimal hyperplasia *in vivo* and can reduce the failure rate of vascular graft (Cocciolone et al., 2018; Thrivikraman et al., 2020). As a commonly used cross-linking agent, PGG cross-links and stabilizes elastin fiber in vascular graft and also possesses anti-inflammatory, antioxidant, and immunomodulatory effects (Fraga et al., 2010; Leopoldini et al., 2011).

In our study, the photooxidation and PGG cross-linking improved the graft's biomechanical properties, biocompatibility, and stability. The biomechanical results showed that the DOP groups' compliance, suture retention strength, and resistance to elastase degradation were improved. The residual biomechanical properties, which reflected the stress state in the vascular tissue were important for the vascular wall's regeneration, reconstruction, and the smooth muscle cell functions' regulation (Cocciolone et al., 2018). Additionally, the degree of cross-linking and SEM showed that the cross-linking strengthened the fiber connections, reduced the decellularized material's pore structure, and covered the coagulation and antigen sites caused by the decellularization

process. However, excessive cross-linking will cause the vascular graft fibers to be tightly connected and stiff, and the luminal surface's pore structure will be significantly reduced, which may inhibit cell infiltration and remodeling (Liang et al., 2004). The results of cell adhesion experiments and the cytotoxic MTT test showed that there was no difference between the four groups, indicating that the decellularization process and cross-linking did not increase the vascular graft's toxicity. The strategy of cross-linking for collagen and elastic fibers improved the performance of decellularized vascular grafts.

The implantation of heterogeneous tissue materials in the body will cause a series of inflammation in the body. Studies have shown that immunogenic heterogeneous tissues can cause a continuous immune rejection in the body and eventually decline (Lopera Higuita and Griffiths, 2020). Hsing Wen Sung's groups showed that un-cross-linked acellular tissue can cause an inflammatory reaction *in vivo* and can be infiltrated and degraded by inflammatory cells (Liang et al., 2004). Additionally, un-cross-linked and excessive cross-linking of acellular tissues can lead to tissue regeneration failure *in vivo* due to excessive degradation or inhibition of cell infiltration, respectively. However, the process of decellularization will also cause the collagen fibers' antigen sites to be exposed, causing the infiltration of inflammatory immune cells. An appropriate cross-linking treatment may cover part of the antigenic sites and inhibit the excessive inflammatory response at the early stage *in vivo* while permitting the infiltration of cells to promote the tissue regeneration at the late stage. The HE results showed that the vascular wall was infiltrated by cells in the NA and DC groups, while the cell infiltration in the DOP group was mild, only infiltrating the outer layer's superficial part and the basement membrane's surface layer. The IHC results of our rat subcutaneous embedding experiments showed that there were more $CD68^+$ macrophage cells and $CD3^+$ cells in the NA and DC groups at 4w, indicating that the inflammatory immune response persisted after implantation because the existence of natural BIMA cells and antigen components caused the host's response. However, the $CD68^+$ macrophage cells and $CD3^+$ cells were significantly decreased in the DO and DOP groups. This may be due to the photooxidation and PGG cross-linking, which strengthened DC-BIMA's biomechanical properties and inhibited inflammation *in vivo*. When modifying decellularized materials' properties, an appropriate cross-linking treatment can effectively improve vascular grafts' performance *in vivo*. When tissue-engineered blood vessels are implanted in the body, the best reconstruction process is the balance of the degradation rate and regeneration of ECM *in vivo*. Degradation that occurs too quickly can lead to loss of the vascular graft's biomechanical properties and the formation of aneurysm, especially in the arterial system, which may rupture.

To evaluate the function of the BIMA *in vivo*, the vascular grafts were implanted into the replacement model of the rabbit abdominal aorta. In the DC group, there were two cases of occlusion due to thrombus and two cases of stenosis. There were also two cases of stenosis in the DO group. The results of morphology showed that a large number of cells infiltrated in the adventitia and neointima of the vessel wall, the elastic fibers were fractured and degraded, the structure of the neointima was disorganized, and the regenerated collagen fibers were irregularly arranged in the DC and DO groups. In addition, the exposed basement membrane and fibers might promote the adsorption and activation of fibrinogen, which further activated platelets, resulting in an acute thrombus. However, in the DOP group, there was little cellular infiltration in the adventitia of vascular grafts. The elastic fiber structure was almost intact and elastin preservation was significantly higher in the DC and DO groups. Furthermore, the regenerated collagen fiber structure in the neointima was regular with uniform distribution of cells, which may avoid thrombus and stenosis, resulting to the high patency rate. Photooxidation treatment as well as the PGG cross-linked collagen and elastin fiber and the combination of the two was effective in maintaining matrix integrity, pointing to stabilized arterial scaffolds as viable small-diameter vascular grafts.

In vivo calcification of xenogeneic tissue materials was also the cause of vascular transplantation failure. Acellular materials exposed the calcification sites of collagen or elastic fibers *in vivo*, which combined with calcium ions *in vivo*, resulted in calcium deposition (Basalyga et al., 2004; Pai et al., 2011). Additionally, the degradation and fracture of elastic fiber *in vivo* can further expose the calcification sites and aggravate the calcium deposition *in vivo*. Previous studies have shown that PGG cross-linking of biomaterials can prevent early degradation of elastic fibers and inhibit calcification (Pennel et al., 2014; Jiang et al., 2017). In our study, calcium deposition occurred in both the DC and DO groups at 4 weeks. EVG results also showed that the elastic fibers of BIMA in the DOP group were almost similar to those before implantation, while the elastic fibers in the DO and DC groups were broken and degraded. The results showed that PGG treatment prevented the early degradation of elastic fibers and may be contributed to inhibit calcification *in vivo*. Thus, to hinder calcification, it was necessary to treat acellular vessels with decalcification and prevent the fiber degradation.

In the current research, the inflammatory response of biomaterial was closely related to tissue regeneration *in vivo*. An excessive inflammatory response can lead to a foreign body reaction and degradation of biomaterials (Umashankar et al., 2013; Aamodt and Grainger, 2016). The study demonstrated that photooxidation and PGG cross-linking inhibited the infiltration of $CD68^+$ macrophage cells in the graft, promoted the regeneration of host SMC, and remodeled neointima. Similar to the results of subcutaneous implantation in rats, in the DC and DO groups, the $CD68^+$ macrophages were present in the neointima and grafts, suggesting that partial degradation occurs in the early stage of vascular grafts, exposing part of the antigenic sites and promoting inflammatory cell infiltration, which may lead to vascular calcification, expansion, or rupture in the later stage of implantation. The appearance of $calponin^+$ and $\alpha\text{-}SMA^+$ cells in the neointima, accompanied by the infiltration of

vimentin$^+$ cells, suggested that host cells infiltrated and differentiated into vascular smooth muscle cells and fibroblasts within the vascular scaffold, leading to early remodeling of the grafts. In the DOP group, there were no CD68$^+$ cells in the neointima, less cell infiltration in the vascular wall and less elastin degradation, indicating that the photooxidation and PGG cross-linking might prevent the early degradation of vascular scaffolds and inhibit the inflammatory response. The CD206$^+$ M2 macrophages cells and calponin$^+$/α- SMA$^+$ double positive cells were found in the neointima, suggesting that functional type smooth muscle cells appeared in the grafts might initiate the vascular invasion early phase of remodeling and regeneration. It may be that PGG has an anti-inflammatory effect, which enhanced the effect of anti-inflammatory cells and accelerated the resolution of inflammation. Previous studies have shown that an increase in type I collagen fibers can cause intimal hyperplasia with a corresponding decrease in the content of type I collagen fibers (Purushothaman et al., 2011). In our study, the ratio of relative content of type I/III collagen fibers in the DOP group was significantly higher than that in the DO and DC groups, which indicated that the regenerated collagen fibers in the neointima were accelerated into type I fibers and improved the patency. Although there was a monolayer of cell coverage on the luminal surface of blood vessels in the groups, there was no CD31 positive cell adhesion, suggesting that vascular grafts had no regeneration of endothelial cell at 4w.

Previous studies have shown that xenogeneic biomaterials can form neointima after implantation *in vivo*, but its composition are still unknown (Pennel et al., 2013; Pennel et al., 2014). Our study was the first to analyze the neointima by mass spectrometry to further understand the composition and mechanism of decellularized small-diameter vascular xenograft remodeling in a rabbit abdominal aortic replacement model at 4w. The mass spectrometry analysis showed that neointima contained similar protein species in the three groups. The protein components are mainly plasma-related proteins, cytoskeleton proteins, glycoproteins, and secreted factors. Due to the species of experimental animals, we only identified a small number of proteins and failed to find statistically significant difference proteins. In the groups, the composition of the neointima was mainly fibrinogen, hemoglobin, albumin, vitronectin, and IgG from blood components, maybe due to the fact that the decellularization treatment exposed the basement membrane and a significant number of collagen fibers, leading to multiple protein adsorption in plasma, cell recruitment, and platelet activation, which caused excessive inflammatory response, thrombosis, and failure to resolve in time at the early stage. Although no statistically significant differential proteins were found among the three groups, the results of IHC, Sirius Red, and Masson stains showed that the neointima quickly achieved a stable structure in the DOP group, which indicated that modification of the grafts may alter the remodeling of the neointima. Interestingly, we preliminarily analyzed that in the neointima, plasma proteins constitute the major component, which may be related to the process of protein adsorption, with large amounts of albumin, platelets, fibrinogen, hemoglobin, and immunoglobulins adsorbed on the luminal surface of small-diameter vascular grafts at the early stage (Othman et al., 2018). Protein adsorption on the biomaterial surface is one of the very first events in the interaction between materials and blood, which is a determinant for the subsequent processes of cell growth, differentiation, and extracellular matrix formation (Yang et al., 20142014; Swartzlander et al., 2015). Further observations and studies are essential to the relationship between protein adsorption and the neointimal regeneration and remodeling of decellularized vascular grafts. This will help in understanding the regeneration mechanism of small-diameter vascular xenografts *in vivo* and provide new strategies for designing better tissue engineering vascular grafts.

Finally, we recommend that a more effective decellularization process should be used to completely remove cellular and most of antigen components to preserve a good three-dimensional structure and to obtain a potentially homogenous or heterogeneous decellularized small-caliber vascular graft for clinical use. Due to the decellularization process tend to alter the structure of ECM and expose the basement membrane, fibers and antigen sites, the decellularized grafts require an appropriate cross-linking, which can improve biomechanical properties and biocompatibility.

Limitations of the Study

The study's main limitation was that the implantation time of the rabbit abdominal aorta model was too short, and the long-term patency rate and the remodeling situation still need further research. Additionally, no further modifications were made in the graft to promote the regeneration of endothelial cells. Before clinical application, small-caliber acellular material vascular grafts still need to be studied and observed in a large animal model.

CONCLUSION

The procedure of decellularization by sonication treatment and perfusion can effectively remove the cellular components and α-gal antigen of BIMA and can preserve a good three-dimensional structure. The decellularized BIMA cross-linked by photooxidation and PGG improved the biomechanical properties and biocompatibility of the grafts, including the reduction of inflammatory response, the protection of elastic fibers, the remodeling of the neointima, and the inhibition of calcification, thereby resulted in high patency. Modified BIMA is a promising candidate for constructing tissue engineering vascular graft.

DATA AVAILABILITY STATEMENT

The raw data supporting the conclusion of this article will be made available by the authors, without undue reservation.

ETHICS STATEMENT

The animal study was reviewed and approved by the Institutional Animal Care and Use Committee (IACUC), The Second Xiangya Hospital, Central South University, China.

AUTHOR CONTRIBUTIONS

All authors listed have made a substantial, direct, and intellectual contribution to the work and approved it for publication.

FUNDING

This work was supported by the National Natural Science Foundation of China (Grant/Award Number: 81771991), the Natural Science Foundation of Hunan Province, China (Grant/Award Number: 2020JJ5834), and the Natural Science Foundation of Hunan Province, China (Grant/Award Number: 2020JJ5819).

ACKNOWLEDGMENTS

The authors thank all members of High-Resolution Mass Spectrometry Lab of Advanced Research Center, CSU, for the LC-MS experiments.

SUPPLEMENTARY MATERIAL

The Supplementary Material for this article can be found online at: https://www.frontiersin.org/articles/10.3389/fbioe.2022.816513/full#supplementary-material

REFERENCES

Aamodt, J. M., and Grainger, D. W. (2016). Extracellular Matrix-Based Biomaterial Scaffolds and the Host Response. *Biomaterials* 86, 68–82. doi:10.1016/j.biomaterials.2016.02.003

Azhim, A., Syazwani, N., Morimoto, Y., Furukawa, K., and Ushida, T. (2014). The Use of Sonication Treatment to Decellularize Aortic Tissues for Preparation of Bioscaffolds. *J. Biomater. Appl.* 29 (1), 130–141. doi:10.1177/0885328213517579

Basalyga, D. M., Simionescu, D. T., Xiong, W., Baxter, B. T., Starcher, B. C., and Vyavahare, N. R. (2004). Elastin Degradation and Calcification in an Abdominal Aorta Injury Model. *Circulation* 110 (22), 3480–3487. doi:10.1161/01.CIR.0000148367.08413.E9

Böer, U., Lohrenz, A., Klingenberg, M., Pich, A., Haverich, A., and Wilhelmi, M. (2011). The Effect of Detergent-Based Decellularization Procedures on Cellular Proteins and Immunogenicity in Equine Carotid Artery Grafts. *Biomaterials* 32 (36), 9730–9737. doi:10.1016/j.biomaterials.2011.09.015

Catto, V., Farè, S., Freddi, G., and Tanzi, M. C. (2014). Vascular Tissue Engineering: Recent Advances in Small Diameter Blood Vessel Regeneration. *ISRN Vasc. Med.* 2014, 1–27. doi:10.1155/2014/923030

Cocciolone, A. J., Hawes, J. Z., Staiculescu, M. C., Johnson, E. O., Murshed, M., and Wagenseil, J. E. (2018). Elastin, Arterial Mechanics, and Cardiovascular Disease. *Am. J. Physiology-Heart Circulatory Physiol.* 315 (2), H189–H205. doi:10.1152/ajpheart.00087.2018

Courtman, D. W., Errett, B. F., and Wilson, G. J. (2001). The Role of Crosslinking in Modification of the Immune Response Elicited against Xenogenic Vascular Acellular Matrices. *J. Biomed. Mater. Res.* 55 (4), 576–586. doi:10.1002/1097-4636(20010615)55:4<576::aid-jbm1051>3.0.co;2-9

Craig, S., and Walker, W. (1994). The Use of Bovine Internal Mammary Artery (Bioflow) Grafts in Coronary Artery Surgery. *Eur. J. Cardio-Thoracic Surg.* 8 (1), 43–45. doi:10.1016/1010-7940(94)90132-5

Crapo, P. M., Gilbert, T. W., and Badylak, S. F. (2011). An Overview of Tissue and Whole Organ Decellularization Processes. *Biomaterials* 32 (12), 3233–3243. doi:10.1016/j.biomaterials.2011.01.057

Daly, K. A., Stewart-Akers, A. M., Hara, H., Ezzelarab, M., Long, C., Cordero, K., et al. (2009). Effect of the αGal Epitope on the Response to Small Intestinal Submucosa Extracellular Matrix in a Nonhuman Primate Model. *Tissue Eng. A* 15 (12), 3877–3888. doi:10.1089/ten.TEA.2009.0089

Das, N., Bratby, M. J., Shrivastava, V., Cornall, A. J., Darby, C. R., Boardman, P., et al. (2011). Results of a Seven-Year, Single-centre Experience of the Long-Term Outcomes of Bovine Ureter Grafts Used as Novel Conduits for Haemodialysis Fistulas. *Cardiovasc. Intervent Radiol.* 34 (5), 958–963. doi:10.1007/s00270-011-0096-z

de Valence, S., Tille, J.-C., Mugnai, D., Mrowczynski, W., Gurny, R., Möller, M., et al. (2012). Long Term Performance of Polycaprolactone Vascular Grafts in a Rat Abdominal Aorta Replacement Model. *Biomaterials* 33 (1), 38–47. doi:10.1016/j.biomaterials.2011.09.024

Desai, M., Seifalian, A. M., and Hamilton, G. (2011). Role of Prosthetic Conduits in Coronary Artery Bypass Grafting. *Eur. J. Cardio-Thoracic Surg.* 40 (2), 394–398. doi:10.1016/j.ejcts.2010.11.050

Esposito, F., Vitale, N., Crescenzi, B., Scardone, M., de Luca, L., and Cotrufo, M. (1994). Short-term Results of Bovine Internal Mammary Artery Use in Cardiovascular Surgery. *Tex. Heart Inst. J.* 21 (3), 193–197.

Fraga, C. G., Galleano, M., Verstraeten, S. V., and Oteiza, P. I. (2010). Basic Biochemical Mechanisms behind the Health Benefits of Polyphenols. *Mol. Aspects Med.* 31 (6), 435–445. doi:10.1016/j.mam.2010.09.006

Jiang, B., Suen, R., Wang, J.-J., Zhang, Z. J., Wertheim, J. A., and Ameer, G. A. (2017). Vascular Scaffolds with Enhanced Antioxidant Activity Inhibit Graft Calcification. *Biomaterials* 144, 166–175. doi:10.1016/j.biomaterials.2017.08.014

Kasimir, M.-T., Rieder, E., Seebacher, G., Wolner, E., Weigel, G., and Simon, P. (2005). Presence and Elimination of the Xenoantigen Gal (α1, 3) Gal in Tissue-Engineered Heart Valves. *Tissue Eng.* 11 (7-8), 1274–1280. doi:10.1089/ten.2005.11.1274

Klinkert, P., Post, P. N., Breslau, P. J., and van Bockel, J. H. (2004). Saphenous Vein versus PTFE for Above-Knee Femoropopliteal Bypass. A Review of the Literature. *Eur. J. Vasc. Endovascular Surg.* 27 (4), 357–362. doi:10.1016/j.ejvs.2003.12.027

Leopoldini, M., Russo, N., and Toscano, M. (2011). The Molecular Basis of Working Mechanism of Natural Polyphenolic Antioxidants. *Food Chem.* 1252, 288–306. doi:10.1016/j.foodchem.2010.08.012

Liang, H.-C., Chang, Y., Hsu, C.-K., Lee, M.-H., and Sung, H.-W. (2004). Effects of Crosslinking Degree of an Acellular Biological Tissue on its Tissue Regeneration Pattern. *Biomaterials* 25 (17), 3541–3552. doi:10.1016/j.biomaterials.2003.09.109

Lin, C.-H., Hsia, K., Ma, H., Lee, H., and Lu, J.-H. (2018). *In Vivo* Performance of Decellularized Vascular Grafts: A Review Article. *Ijms* 19 (7), 2101. doi:10.3390/ijms19072101

Lopera Higuita, M., and Griffiths, L. G. (2020). Small Diameter Xenogeneic Extracellular Matrix Scaffolds for Vascular Applications. *Tissue Eng. B: Rev.* 26 (1), 26–45. doi:10.1089/ten.TEB.2019.0229

Lü, W.-D., Zhang, M., Wu, Z.-S., and Hu, T.-H. (2009). Decellularized and Photooxidatively Crosslinked Bovine Jugular Veins as Potential Tissue Engineering Scaffolds☆. *Interact Cardiovasc. Thorac. Surg.* 8 (3), 301–305. doi:10.1510/icvts.2008.194076

Lü, W.-D., Zhang, M., Wu, Z.-S., Hu, T.-H., Xu, Z.-J., Liu, W., et al. (2010). The Performance of Photooxidatively Crosslinked Acellular Bovine Jugular Vein Conduits in the Reconstruction of Connections between Pulmonary Arteries and Right Ventricles. *Biomaterials* 31 (10), 2934–2943. doi:10.1016/j.biomaterials.2009.12.046

Ma, L. Y., Chen, W. W., Gao, R. L., Liu, L. S., Zhu, M. L., Wang, Y. J., et al. (2020). China Cardiovascular Diseases Report 2018: an Updated Summary. *J. Geriatr. Cardiol.* 17 (1), 1–8. doi:10.11909/j.issn.1671-5411.2020.01.001

Mahara, A., Somekawa, S., Kobayashi, N., Hirano, Y., Kimura, Y., Fujisato, T., et al. (2015). Tissue-engineered Acellular Small Diameter Long-Bypass Grafts with Neointima-Inducing Activity. *Biomaterials* 58, 54–62. doi:10.1016/j.biomaterials.2015.04.031

Meuris, B., Phillips, R., Moore, M. A., and Flameng, W. (2003). Porcine Stentless Bioprostheses: Prevention of Aortic wall Calcification by Dye-Mediated Photo-Oxidation. *Artif. Organs* 27 (6), 537–543. doi:10.1046/j.1525-1594.2003.07108.x

Mitchell, I. M., Essop, A. R., Scott, P. J., Martin, P. G., Gupta, N. K., Saunders, N. R., et al. (1993). Bovine Internal Mammary Artery as a Conduit for Coronary Revascularization: Long-Term Results. *Ann. Thorac. Surg.* 55 (1), 120–122. doi:10.1016/0003-4975(93)90485-z

Moore, M. A., and Adams, A. K. (2001). Calcification Resistance, Biostability, and Low Immunogenic Potential of Porcine Heart Valves Modified by Dye-Mediated Photooxidation. *J. Biomed. Mater. Res.* 56 (1), 24–30. doi:10.1002/1097-4636(200107)56:1<24::aid-jbm1064>3.0.co;2-q

Moore, M. A., Bohachevsky, I. K., Cheung, D. T., Boyan, B. D., Chen, W.-M., Bickers, R. R., et al. (1994). Stabilization of Pericardial Tissue by Dye-Mediated Photooxidation. *J. Biomed. Mater. Res.* 28 (5), 611–618. doi:10.1002/jbm.820280511

Organization, W. H. J. W. H. O. (2013). *A Global Brief on Hypertension : Silent Killer, Global Public Health Crisis: World Health Day 2013*. World Health Organization.

Othman, Z., Cillero Pastor, B., van Rijt, S., and Habibovic, P. (2018). Understanding Interactions between Biomaterials and Biological Systems Using Proteomics. *Biomaterials* 167, 191–204. doi:10.1016/j.biomaterials.2018.03.020

Pai, A., Leaf, E. M., El-Abbadi, M., and Giachelli, C. M. (2011). Elastin Degradation and Vascular Smooth Muscle Cell Phenotype Change Precede Cell Loss and Arterial Medial Calcification in a Uremic Mouse Model of Chronic Kidney Disease. *Am. J. Pathol.* 178 (2), 764–773. doi:10.1016/j.ajpath.2010.10.006

Parenteau-Bareil, R., Gauvin, R., and Berthod, F. (2010). Collagen-Based Biomaterials for Tissue Engineering Applications. *Materials* 3 (3), 1863–1887. doi:10.3390/ma3031863

Pashneh-Tala, S., MacNeil, S., and Claeyssens, F. (2016). The Tissue-Engineered Vascular Graft-Past, Present, and Future. *Tissue Eng. Part B: Rev.* 22 (1), 68–100. doi:10.1089/ten.teb.2015.0100

Pektok, E., Nottelet, B., Tille, J.-C., Gurny, R., Kalangos, A., Moeller, M., et al. (2008). Degradation and Healing Characteristics of Small-Diameter Poly(ε-Caprolactone) Vascular Grafts in the Rat Systemic Arterial Circulation. *Circulation* 118 (24), 2563–2570. doi:10.1161/CIRCULATIONAHA.108.795732

Pennel, T., Fercana, G., Bezuidenhout, D., Simionescu, A., Chuang, T.-H., Zilla, P., et al. (2014). The Performance of Cross-Linked Acellular Arterial Scaffolds as Vascular Grafts; Pre-clinical Testing in Direct and Isolation Loop Circulatory Models. *Biomaterials* 35 (24), 6311–6322. doi:10.1016/j.biomaterials.2014.04.062

Pennel, T., Zilla, P., and Bezuidenhout, D. (2013). Differentiating Transmural from Transanastomotic Prosthetic Graft Endothelialization through an Isolation Loop-Graft Model. *J. Vasc. Surg.* 58 (4), 1053–1061. doi:10.1016/j.jvs.2012.11.093

Purushothaman, K.-R., Purushothaman, M., Muntner, P., Lento, P. A., O'Connor, W. N., Sharma, S. K., et al. (2011). Inflammation, Neovascularization and Intraplaque Hemorrhage Are Associated with Increased Reparative Collagen Content: Implication for Plaque Progression in Diabetic Atherosclerosis. *Vasc. Med.* 16 (2), 103–108. doi:10.1177/1358863X11402249

Schmidt, C. E., and Baier, J. M. (2000). Acellular Vascular Tissues: Natural Biomaterials for Tissue Repair and Tissue Engineering. *Biomaterials* 21 (22), 2215–2231. doi:10.1016/s0142-9612(00)00148-4

Schneider, K. H., Aigner, P., Holnthoner, W., Monforte, X., Nürnberger, S., Rünzler, D., et al. (2016). Decellularized Human Placenta Chorion Matrix as a Favorable Source of Small-Diameter Vascular Grafts. *Acta Biomater.* 29, 125–134. doi:10.1016/j.actbio.2015.09.038

Schneider, K. H., Enayati, M., Grasl, C., Walter, I., Budinsky, L., Zebic, G., et al. (2018). Acellular Vascular Matrix Grafts from Human Placenta Chorion: Impact of ECM Preservation on Graft Characteristics, Protein Composition and *In Vivo* Performance. *Biomaterials* 177, 14–26. doi:10.1016/j.biomaterials.2018.05.045

Schneider, K. H., Rohringer, S., Kapeller, B., Grasl, C., Kiss, H., Heber, S., et al. (2020). Riboflavin-mediated Photooxidation to Improve the Characteristics of Decellularized Human Arterial Small Diameter Vascular Grafts. *Acta Biomater.* 116, 246–258. doi:10.1016/j.actbio.2020.08.037

Sharp, M. A., Phillips, D., Roberts, I., and Hands, L. (2004). A Cautionary Case: the SynerGraft Vascular Prosthesis. *Eur. J. Vasc. Endovascular Surg.* 27 (1), 42–44. doi:10.1016/j.ejvs.2003.09.015

Stock, U. A., and Schenke-Layland, K. (2006). Performance of Decellularized Xenogeneic Tissue in Heart Valve Replacement. *Biomaterials* 27 (1), 1–2. doi:10.1016/j.biomaterials.2005.05.100

Sung, H.-W., Shih, J.-S., and Hsu, C.-S. (1996). Crosslinking Characteristics of Porcine Tendons: Effects of Fixation with Glutaraldehyde or Epoxy. *J. Biomed. Mater. Res.* 30 (3), 361–367. doi:10.1002/(sici)1097-4636(199603)30:3<361::aid-jbm10>3.0.co;2-n

Swartzlander, M. D., Barnes, C. A., Blakney, A. K., Kaar, J. L., Kyriakides, T. R., and Bryant, S. J. (2015). Linking the Foreign Body Response and Protein Adsorption to PEG-Based Hydrogels Using Proteomics. *Biomaterials* 41, 26–36. doi:10.1016/j.biomaterials.2014.11.026

Tai, N. R. M., Giudiceandrea, A., Salacinski, H. J., Seifalian, A. M., and Hamilton, G. (1999). *In Vivo* femoropopliteal Arterial wall Compliance in Subjects with and without Lower Limb Vascular Disease. *J. Vasc. Surg.* 30 (5), 936–945. doi:10.1016/s0741-5214(99)70020-0

Thrivikraman, G., Johnson, S. L., Syedain, Z. H., Hill, R. C., Hansen, K. C., Lee, H. S., et al. (2020). Biologically-engineered Mechanical Model of a Calcified Artery. *Acta Biomater.* 110, 164–174. doi:10.1016/j.actbio.2020.04.018

Umashankar, P. R., Arun, T., and Kumary, T. V. (2013). Effect of Chronic Inflammation and Immune Response on Regeneration Induced by Decellularized Bovine Pericardium. *J. Biomed. Mater. Res.* 101A (8), 2202–2209. doi:10.1002/jbm.a.34535

Wang, X., Lin, P., Yao, Q., and Chen, C. (2007). Development of Small-Diameter Vascular Grafts. *World J. Surg.* 31 (4), 682–689. doi:10.1007/s00268-006-0731-z

Writing Group, M., Mozaffarian, D., Benjamin, E. J., Go, A. S., Arnett, D. K., Blaha, M. J., et al. (2016). Heart Disease and Stroke Statistics-2016 Update: A Report from the American Heart Association. *Circulation* 133 (4), e38–360. doi:10.1161/CIR.0000000000000350

Xu, S., Lu, F., Cheng, L., Li, C., Zhou, X., Wu, Y., et al. (2017). Preparation and Characterization of Small-Diameter Decellularized Scaffolds for Vascular Tissue Engineering in an Animal Model. *Biomed. Eng. Online* 16 (1), 55. doi:10.1186/s12938-017-0344-9

Yang, M.-H., Yuan, S.-S., Chung, T.-W., Jong, S.-B., Lu, C.-Y., Tsai, W.-C., et al. (20142014). Characterization of Silk Fibroin Modified Surface: a Proteomic View of Cellular Response Proteins Induced by Biomaterials. *Biomed. Res. Int.* 2014, 1–13. doi:10.1155/2014/209469

Conflict of Interest: The authors declare that the research was conducted in the absence of any commercial or financial relationships that could be construed as a potential conflict of interest.

Publisher's Note: All claims expressed in this article are solely those of the authors and do not necessarily represent those of their affiliated organizations, or those of the publisher, the editors, and the reviewers. Any product that may be evaluated in this article, or claim that may be made by its manufacturer, is not guaranteed or endorsed by the publisher.

Copyright © 2022 Liu, Chen, Xie, Yuan, Tang, Qian, Liu, Song, Liu, Lu and Wu. This is an open-access article distributed under the terms of the Creative Commons Attribution License (CC BY). The use, distribution or reproduction in other forums is permitted, provided the original author(s) and the copyright owner(s) are credited and that the original publication in this journal is cited, in accordance with accepted academic practice. No use, distribution or reproduction is permitted which does not comply with these terms.

frontiers | Frontiers in Bioengineering and Biotechnology

REVIEW
published: 25 April 2022
doi: 10.3389/fbioe.2022.805299

Decellularization in Tissue Engineering and Regenerative Medicine: Evaluation, Modification, and Application Methods

Afarin Neishabouri[1†], *Alireza Soltani Khaboushan*[1,2†], *Faezeh Daghigh*[3], *Abdol-Mohammad Kajbafzadeh*[1*] and *Masoumeh Majidi Zolbin*[1*]

[1]Pediatric Urology and Regenerative Medicine Research Center, Children's Medical Center, Pediatric Center of Excellence, Tehran University of Medical Science, Tehran, Iran, [2]Students' Scientific Research Center, Tehran University of Medical Sciences, Tehran, Iran, [3]Department of Physiology, Faculty of Medicine, Tabriz Medical Sciences, Islamic Azad University, Tabriz, Iran

OPEN ACCESS

Edited by:
Kamal Hany Hussein,
Assiut University, Egypt

Reviewed by:
Renata Kelly Da Palma,
Universidad Francisco de Vitoria, Spain
Chiara Magliaro,
University of Pisa, Italy
Xiaojun Yu,
Stevens Institute of Technology, United States

***Correspondence:**
Masoumeh Majidi Zolbin
Masoumeh.majidizolbin@gmail.com
Abdol-Mohammad Kajbafzadeh
kajbafzd@tums.ac.ir

[†]These authors share first authorship

Specialty section:
This article was submitted to Biomaterials, a section of the journal Frontiers in Bioengineering and Biotechnology

Received: 30 October 2021
Accepted: 04 April 2022
Published: 25 April 2022

Citation:
Neishabouri A, Soltani Khaboushan A, Daghigh F, Kajbafzadeh A-M and Majidi Zolbin M (2022) Decellularization in Tissue Engineering and Regenerative Medicine: Evaluation, Modification, and Application Methods. Front. Bioeng. Biotechnol. 10:805299. doi: 10.3389/fbioe.2022.805299

Reproduction of different tissues using scaffolds and materials is a major element in regenerative medicine. The regeneration of whole organs with decellularized extracellular matrix (dECM) has remained a goal despite the use of these materials for different purposes. Recently, decellularization techniques have been widely used in producing scaffolds that are appropriate for regenerating damaged organs and may be able to overcome the shortage of donor organs. Decellularized ECM offers several advantages over synthetic compounds, including the preserved natural microenvironment features. Different decellularization methods have been developed, each of which is appropriate for removing cells from specific tissues under certain conditions. A variety of methods have been advanced for evaluating the decellularization process in terms of cell removal efficiency, tissue ultrastructure preservation, toxicity, biocompatibility, biodegradability, and mechanical resistance in order to enhance the efficacy of decellularization methods. Modification techniques improve the characteristics of decellularized scaffolds, making them available for the regeneration of damaged tissues. Moreover, modification of scaffolds makes them appropriate options for drug delivery, disease modeling, and improving stem cells growth and proliferation. However, considering different challenges in the way of decellularization methods and application of decellularized scaffolds, this field is constantly developing and progressively moving forward. This review has outlined recent decellularization and sterilization strategies, evaluation tests for efficient decellularization, materials processing, application, and challenges and future outlooks of decellularization in regenerative medicine and tissue engineering.

Keywords: extracellular matrix, recellularization, regenerative medicine, decellularizalion, tissue engineering

1 INTRODUCTION

Tissue engineering, as a division of regenerative medicine, combines engineering and biological science in order to reproduce tissues and organs that can help to overcome the lack of enough donor organs (Shafiee and Atala, 2017). Tissue engineering applies cells into desirable biological structures in a defined framework to restore the normal function of tissues. This process includes three cornerstones, namely scaffolds, cells, and signaling factors. As a critical component in tissue

engineering, scaffolds provide mechanical stability and structural support for exogenous cell attachment and proliferation and facilitate the delivery of required growth factors for tissue regeneration (Vacanti and Langer, 1999; Soltani Khaboushan et al., 2021).

Scaffolds could be made up of natural tissues harvested from animal or human sources or being constructed using synthetic biomaterials. Natural scaffolds represent biological characteristics that better fit the regular tissue microenvironment, promoting appropriate cellular interactions, biocompatibility, and degradability. Decellularization is the process of eliminating cells and their components (especially DNA and RNA) from the extracellular matrix (ECM) to yield a natural matrix with saved mechanical integrity. It has been demonstrated that decellularized extracellular matrix (dECM) is a suitable type of natural scaffold for tissue engineering since the ECM plays a crucial role in tissue development (Gilbert et al., 2006).

ECM is mainly composed of water, proteins (mainly collagen), and polysaccharides (Frantz et al., 2010). The composition and arrangement of ECM components and microenvironmental conditions (e.g., mechanical properties, pH, CO_2 concentration) of the matrix differ from one tissue to another based on the tissue function and its residing cells that secrete ECM components (Kawecki et al., 2018). Fibroblasts, adipocytes, and chondrocytes are among the cells involved in the formation of ECM components (including growth factors and structural proteins such as fibronectin). Physical, chemical, and biological methods have been utilized to produce acellular scaffolds, either by perfusion- or immersion/agitation-based systems, or even a combination of methods (Crapo et al., 2011).

So far, a wide variety of decellularization methods have been studied and developed (Crapo et al., 2011; Fu et al., 2014; Keane et al., 2015; Choudhury et al., 2020). Since acellular scaffolds have low immunogenicity and are biologically recognizable, they are beneficial for cell adhesion, proliferation, and survival. Because of these properties, decellularized materials have the potential to regenerate injured tissues or organs (Damodaran and Vermette, 2018). After decellularization, dECM should be sterilized, and several tests should assess the efficacy of decellularization. These tests are carried out to ensure the removal of cellular contents and preservation of biochemical and mechanical properties and include macroscopic and microscopic assessments, staining for evaluation of remaining components, and mechanical analyzes (Crapo et al., 2011). Moreover, these acellular scaffolds can be processed before application to acquire desired characteristics of the ECM for further use. Modifying and refining the dECM, recellularizing the scaffold, and providing a suitable biochemical and physical environment via bioreactors, could improve its characteristics and boost its regeneration ability in host tissues (Garreta et al., 2017).

The application of dECM as wound healing products and surgical mesh devices has been reported (Damodaran and Vermette, 2018; Daryabari et al., 2019; Uday Chandrika et al., 2021). In addition to therapeutic applications, dECM could be used for modeling various diseases, such as tumors, which helps to understand the pathophysiology and progression process of the disease (Liu et al., 2019; Pina et al., 2019). Despite the recent progress, tissue engineering is still in its early stages, and multiple studies are being conducted to develop functional organs. Up to the present, research was mainly directed towards discovering the ideal decellularization methods; and translational studies were performed to achieve functioning materials. This review aims to provide an overview of decellularization techniques, evaluation tests, dECM modification, practical approaches, clinical application, current insufficiencies, and future prospects in tissue decellularization.

2 DECELLULARIZATION AGENTS AND METHODS

Several decellularization techniques have been developed to date to reconstruct different types of living organs. The main principle in all methods is removing cellular material and leaving the ECM ultrastructure unchanged in the tissue. Decellularization techniques differ in terms of applied materials (reagent combinations) and the routes used to deliver the main reagent, namely vascular, airway, or both (Uygun et al., 2010; Badylak et al., 2011; Crapo et al., 2011; Daryabari et al., 2019).

Generally, tissue decellularization methods are classified into three main groups: chemical methods, such as alkaline/acid, detergents, and alcohols; physical methods, such as electroporation, pressurization, freeze/thaw; biological methods, such as enzymes (**Table 1**) (Badylak et al., 2011; Gilpin and Yang, 2017). Several characteristics could sway the quality of the tissue decellularization process, including cell density, matrix thickness, and tissue morphology. These characteristics are different in various tissues; Thus, it is crucial to determine which method is the most suitable one for a specific tissue (Crapo et al., 2011; Heath, 2019).

2.1 Chemical Agents

2.1.1 Ionic Detergents

Ionic detergents act by solubilizing DNA and cell membrane and tend to denature the proteins, thus decreasing collagen integrity. Ionic detergents are powerful in removing glycosaminoglycans (GAGs) and growth factors, therefore destroying ECM rigidity and function. Sodium dodecyl sulfate (SDS), sodium deoxycholate (SD), and Triton X-200 are ionic detergents that have been used in decellularization (Hudson et al., 2004; Gilbert et al., 2006; Lumpkins et al., 2008; Montoya and McFetridge, 2009; Zhou et al., 2010). Alshaikh et al. (Alshaikh et al., 2019) have examined SDS and SD in ovary decellularization. They have suggested a better ECM preservation in SD than SDS but lower donor DNA content in SDS. Due to polarity, ionic detergents such as SDS are hard to remove from ECM, and extensive wash with non-ionic detergents such as Triton X-100 is usually needed to take away the remnant ionic detergents from tissue (Gilpin and Yang, 2017).

2.1.2 Non-Ionic Detergents

Non-ionic detergents, such as Triton X-100, can strongly break lipid-lipid and lipid-protein bonds, but they are less effective on protein-protein interaction. Although they maintain the

TABLE 1 | Decellularization methods and agents.

Method	Category	Agent	Properties	References
Chemical	Organic Solvents	Alcohols (e.g., ethanol) Acetone	Cell lysis by dehydrating the tissue May disrupt ECM ultrastructure	Wollmann et al. (2019), Walawalkar and Almelkar, (2019)
		TnBP	Disrupts protein-protein connections May enhance collagen crosslinking	Deeken et al. (2011), Duarte et al. (2021)
	Chelators	EDTA EGTA	Disrupts cell adhesions Usually combined with other agents such as trypsin due to low efficacy in cell removal	Rieder et al. (2004), Cheng et al. (2019), Caralt et al. (2015), Huh et al. (2018)
	Toxins	Latrunculin B	Acts through actin rearrangement Mostly used for decellularizing skeletal muscle	Reyna et al. (2020), Assmann et al. (2017)
	Ionic detergents	SDS SD Triton X-200	High efficacy in cell removal by solubilizing cell membrane May disrupt ECM ultrastructure	Hudson et al. (2004), Alshaikh et al. (2019), O'Neill et al. (2013)
	Non-ionic detergents	Triton X-100	Gentle cell removal by disrupting lipid-lipid and lipid-protein connections Gentle disruption of the ECM structure	Fu et al. (2010), Huh et al. (2018), Liao et al. (2008)
	Zwitterionic detergents	CHAPS SB-10 SB-16	Properties of ionic and non-ionic detergents May disrupt basement membrane	Tsuchiya et al. (2014), Gupta et al. (2017), Song et al. (2021)
	Hypotonic and hypertonic solutions	Sodium chloride solution	Osmotic shock induction Low efficacy in remnant removal Minimal ECM disruption	Kim et al. (2016), Goktas et al. (2014)
	Acid and Alkaline	PAA and EDTA Sodium hydroxide	Solubilizing cytoplasmic cell components and nucleic acid disruption Can disrupt ECM components	Wollmann et al. (2019), Poornejad et al. (2016), Mimler et al. (2019)
Biological	Esterase	Phospholipase A2	Cleaving ester bonds in the cell membrane May disrupt ECM components	Isidan et al. (2019), Huang et al. (2011)
	Protease	Trypsin Pepsin Dispase	Cleaving peptide bonds May disrupt ECM components over prolonged exposure	Prasertsung et al. (2008), Rahman et al. (2018), Pouliot et al. (2020)
	Nuclease	DNase RNase	Cleaving nucleotide bonds	Simsa et al. (2018), McCrary et al. (2020b), Philips et al. (2018b)
Physical	Freeze-thaw cycles		Cell death due to crystallization of intracellular water Extracellular crystallization can disrupt ECM	Roth et al. (2017), Fernández-Pérez and Ahearne, (2019b)
	Agitation		Cell death directly or by assisting in chemical exposure and remnant/toxic removal	Starnecker et al. (2018), Simsa et al. (2019), Yusof et al. (2019)
	Pressure		Cell Membrane destruction May damage biomechanical properties of ECM	Funamoto et al. (2010), Watanabe et al. (2019)
	Supercritical fluids		Assisting in chemical exposure and remnant/toxic removal	Chou et al. (2020), Duarte et al. (2021)

Abbreviations: TnBP, Tri(n-butyl) phosphate; EDTA, Ethylene diamine tetraacetic acid; EGTA, Ethylene glycol tetraacetic acid; SDS, Sodium dodecyl sulfate; SD, Sodium deoxycholate; CHAPS, 3-[(3-cholamidopropyl)dimethylammonio]-1-propanesulfonate; SB, Sulfobetaine; PAA, Peracetic acid; DNase, Deoxyribonuclease; RNase, Ribonuclease.

ultrastructure of the decellularized tissue and preserve the growth factors, they are less effective in removing cellular materials than SDS. The Triton X-100 is not appropriate for tissues where GAGs and lipids are important parts. Accordingly, the effectiveness of non-ionic detergents depends on the tissue undergoing the decellularization process (Gilbert et al., 2006; Lumpkins et al., 2008; Fu et al., 2010; Crapo et al., 2011; Gupta et al., 2018).

2.1.3 Zwitterionic Detergents

Zwitterionic detergents have the properties of both ionic and non-ionic detergents. They have shown better cell removal than non-ionic detergents and improved preservation of the ECM ultrastructure than ionic detergents (Hudson et al., 2004; Gupta et al., 2018; Heath, 2019). Zwitterionic detergents, include sulfobetaine-10 (SB-10), SB-16, Tri (n-butyl) phosphate (TnBP), and 3-[(3-cholamidopropyl) dimethylammonio]-1-propanesulfonate (CHAPS). CHAPS is a common zwitterionic agent that has been widely used in tissue decellularization (Tsuchiya et al., 2016; Gupta et al., 2018). TnBP is an organic solvent that dissociates protein-protein Interactions. TnBP was reported to match SDS in cell removal in tendon and ligament tissues (Deeken et al., 2011). Kuna et al. (Kuna et al., 2018) have reported that decellularization of the human saphenous vein using Triton X-100, TnBP, and deoxyribonuclease (DNase) resulted in properly removing the cells.

2.1.4 Chelators and Toxins

Ethylene glycol tetraacetic acid (EGTA) and ethylenediaminetetraacetic acid (EDTA) are used as chelating agents in organ decellularization through binding to divalent metal cations at the cell adhesion site of ECM. This binding was found to dissociate the cell from the remaining ECM. Due to their

ability to damage cells, Cytotoxic agents could be used in the decellularization process (Crapo et al., 2011). Reyna et al. (Reyna et al., 2020) have shown the high efficiency of latrunculin, a toxin, in removing skeletal muscle cells by disrupting actin and myosin, thus damaging the cell and reducing DNA content to less than 10% compared to controls have shown the high efficiency of latrunculin, a toxin, in removing skeletal muscle cells by reducing DNA content to less than 10% compared to controls. They stated that this toxin is more effective in decellularizing skeletal muscle than ionic and non-ionic agent treatments.

2.1.5 Bases

Solutions with extreme pH were indicated to be effective in the decellularization process. Alkaline substances including sodium sulfide, ammonium hydroxide, calcium hydroxide, and sodium hydroxide were suggested as commonly used in organ decellularization processes. It has been shown that increasing the PH of CHAPS during decellularization increases the effectiveness of cell and protein removal. Bases could eliminate growth factors and disrupt the mechanical structure of the scaffold (Komai and Ushiki, 1991; Prasertsung et al., 2008; Choi et al., 2010; Reing et al., 2010; Sheridan et al., 2012; Tsuchiya et al., 2014; Gupta et al., 2018).

2.1.6 Acids

Acids were found to dissociate nuclear DNA from ECM by disrupting nucleic acids and solubilizing cytoplasmic components. Moreover, acids could facilitate the denaturation of the biomolecules. Acetic acid, hydrochloric acid, and sulfuric acid can disrupt cell membranes and be used in decellularization (Gilbert et al., 2006; Gupta et al., 2018). Lin et al. used and compared formic acid, acetic acid, and citric acid for porcine cornea decellularization (Lin et al., 2019). They showed that formic acid treatment had the optimal decellularizing effect and preserved *in vitro* and *in vivo* recellularization. Peracetic acid (PAA) can also be used as a decellularizing agent; however, it is mostly used as a sterilizing agent and has an unsuitable impact on decellularization. Kao and colleagues (Kao et al., 2020) have reported that the use of PAA in bladder decellularization was not successful because the levels of remaining DNA were similar to the native tissue.

2.1.7 Alcohols

Alcohols play their role in the decellularization process via dehydration; they diffuse into the cells, replace the intracellular water, disrupt the cells, and decrease their genetic materials. Alcohols such as methanol and ethanol are effective in lipid solubilization. Due to their role in tissue fixation and protein deposition, ethanol and methanol may affect the ultrastructure of the tissues. Lumpkin et al. have demonstrated that the use of acetone/ethanol in the decellularization of the temporomandibular joint disc came up with a stiffer tissue compared to Triton X-100 and SDS, and the mechanical characteristics of the decellularized tissue were not appropriately preserved (Lumpkins et al., 2008; Jamur and Oliver, 2010; Crapo et al., 2011).

2.1.8 Hypertonic and Hypotonic Solutions

Hypotonic and hypertonic solutions can lead to cell lysis and disruption of the DNA. Although they do not remove the cellular debris, they could improve decellularization in combination with other chemical reagents since they do not disturb ECM composition (Woods and Gratzer, 2005; Gupta et al., 2018).

2.2 Biological Enzymes

Enzymatic agents include phospholipase A2, proteases (e.g., trypsin, dispase), and nucleases (e.g., DNase, ribonuclease (RNase) are used in the decellularization process. Trypsin breaks peptides containing Lys and Arg, and in extended exposure, it may damage the ECM structure (Stenn et al., 1989; Gilbert et al., 2006; Rahman et al., 2018). Dispase chiefly cleaves fibronectin and collagen IV. It has been used in the decellularization of the porcine cornea and skin (Wilson et al., 2016; Joszko et al., 2019). Nucleases are mainly used in combination with other detergents to expedite the removal of DNAs and RNAs from the scaffold (Grauss et al., 2005; Heath, 2019). The application of phospholipase A2 in decellularization helps maintain collagen and proteoglycans in the tissue. It has been demonstrated that phospholipase A2, along with SD, was influential in producing the acellular porcine corneal stroma (Wu et al., 2009; Rahman et al., 2018).

2.3 Physical Methods

2.3.1 Freeze-Thaw Cycles

The freeze-thaw cycle is being done by fluctuation between freezing temperature (−80c°) and biological temperature. The freeze-thaw cycle disrupts the cell membranes and cell lysis via the formation of intracellular crystals. It has been demonstrated that this method considerably keeps the structure of the ECM but does not effectively remove the remnant cellular debris; thus, further detergents are needed after the freeze-thaw cycle. Multiple freeze-thaw cycles can be used in the decellularization process, whereas they could deteriorate the ECM structure (Pulver et al., 2014; Xing et al., 2015; Rahman et al., 2018).

2.3.2 Agitation Immersion and Pressure

The agitation in conjunction with immersion leads to cell lysis, but it is mostly used with chemical reagents to enhance the exposure of the ECM to the detergents and to augment the decellularization process. Agitation could be applied in the decellularization of the thin tissues, including the small intestine and bladder. In addition, the use of agitation and immersion in the decellularization of the tracheal tissue has been reported. The time of the protocol and intensity of agitation depends on the thickness of the tissue. Agitation may cause cell lysis before exposure to the detergents; thus, deteriorating the structure of the ECM. Furthermore, pressure could promote accessibility of the detergents to the ECM, hence decreasing the time of the decellularization process. Also, it can improve the removal of cellular remnant materials. The pressure leads to minimal changes in ECM structure, even less than agitation (Crapo et al., 2011; Heath, 2019; Rabbani et al., 2021). Sonication is another physical method and can be

considered a subtype of agitation. It has been demonstrated that direct or indirect sonication increases agent penetration to the scaffold, therefore enhancing chemical decellularization while causing less damage to the ECM structural content (Forouzesh et al., 2019).

2.3.3 Supercritical Fluids

The supercritical fluids are over their critical pressure and temperature where it is not distinctly gas or liquid. Due to high permeability, these fluids could easily be removed from the tissue without the need for further washing. They can remove remnant cellular particles from the scaffold and decrease harmful changes in the ECM. Supercritical carbon dioxide has recently attracted attention in tissue decellularization because its critical temperature is appropriate for ECM processing. Recently, different studies reported complete effective removal of porcine skin via supercritical CO_2 (Crapo et al., 2011; Chou et al., 2020; Rabbani et al., 2021). Supercritical CO_2 not only decellularizes different tissues with better ECM structure preservation compared to conventional detergent-based techniques but also is used for sterilization of the dECM. Efficient cell removal and preserved ECM integrity were achieved by applying different supercritical CO_2-based protocols on the optic nerve, myocardium, and cornea (Topuz et al., 2020).

3 STERILIZATION

Decontamination of the dECM via sterilization and disinfection process is necessary before further evaluations and *in vitro* or *in vivo* application. Sterilization kills all microorganisms, but the disinfection process only removes vegetative microorganisms and does not affect the bacterial spores. There are different sterilization methods that can be used for dECM methods. Appropriate sterilization and disinfection method should be selected considering various properties of the decellularized scaffold, including chemical and physical characteristics. Moreover, the needed time, availability, and target of application are important factors in choosing the proper method for sterilization (Kajbafzadeh et al., 2013; Fidalgo et al., 2018; Moradi et al., 2020a; Tao et al., 2021). Irradiation is a physical sterilization strategy that directly destroys nucleic acids and proteins from microorganisms. Gamma irradiation is extensively used for the sterilization of various tissues. Gamma irradiation can effectively sterilize corneal xenografts while preserving their structure and integrity. The irradiation has strong penetrance to the tissue without toxicity. Ultraviolet (UV) rays as a convenient physical disinfectant for the environment and surfaces are used for disinfecting thin decellularized scaffolds with a large surface. Large tissues such as decellularized kidneys cannot entirely be sterilized by UV, and it may interfere with further cell seeding on dECM (Islam et al., 2019; Moradi et al., 2020a; Gosztyla et al., 2020; Tao et al., 2021).

Ethylene oxide sterilizes the tissues by disrupting the function of the nucleic acids and proteins of the microorganisms. With its strong penetration, ethylene oxide can be used for sterilizing various decellularized scaffolds without causing toxicity. Peroxides are widely used as a disinfectant, which can also cause sterilization in specific conditions. They do not produce any toxic product after decomposition (Hennessy et al., 2017; Moradi et al., 2020a; Tao et al., 2021). According to a study, it has been demonstrated that PAA, as a peroxide, has the ability to decontaminate acellular rabbit kidney completely, whereas γ-irradiation destructed the structure tissue and UV failed to eliminate microorganisms (Moradi et al., 2020a). Alcohols are disinfectants that destroy the proteins within microorganisms, but they do not remove spores (Tao et al., 2021). They have minimal effects on the tissue structure; thus, they have been widely used to disinfect dECM derived from various tissues. Supercritical CO_2, in addition to its effects on decellularization process, can lead to disinfection and sterilization of the decellularized scaffolds (Hennessy et al., 2017; Antons et al., 2018; Tao et al., 2021). CO_2 laser, although less commonly used, has a great potential to be used for the sterilization process. CO_2 laser bursts effectively removed bacteria inoculated on pig skin in an experiment. A sterile environment is a prerequisite of regenerative endodontic treatment, which could be effectively achieved with the assistance of a CO_2 laser (Mullarky et al., 1985; Nammour and Majerus, 1991; Divya et al., 2021). Low-level laser with 660 nm wavelength and 100 mW power has been used for sterilization of the decellularized lung tissues (Lopes Guimarães et al., 2020). Laser is an appropriate option for effectively disinfecting tissues, and its potential for disinfecting the dECM should be further explored (Mullarky et al., 1985; Nammour and Majerus, 1991; Divya et al., 2021).

These methods may impact the structural and biochemical characteristics of the matrices. The γ-irradiation mainly affects the ultrastructure and mechanical properties of the scaffold, while ethanol and peracetic acid increase the ECM crosslinking (Hennessy et al., 2017; Johnson et al., 2017; Islam et al., 2019). In order to assess the efficacy of the sterilization method and its effects on the scaffold, several evaluations, including histological evaluations, 3-(4, 5-dimethylthiazol-2-yl)-2, 5-diphenyltetrazolium bromide (MTT) assay, mechanical tests, and bacterial and fungal cultures may be applied (Moradi et al., 2020b).

4 EVALUATION OF DECELLULARIZED EXTRACELLULAR MATRIX

Although decellularization techniques cannot remove 100% of cell material, quantitative analysis of cell components such as mitochondria, double-stranded DNA (dsDNA), and membrane-associated molecules (e.g., phospholipids) is a crucial way to ensure the effectiveness of the decellularization model. On the other hand, the ideal decellularization method should conserve biochemical and mechanical properties with the lowest toxicity rate for the subsequent recellularizing phase to occur. Various evaluation tests and assessments have been introduced to appraise the different characteristics of the dECM (**Figure 1**).

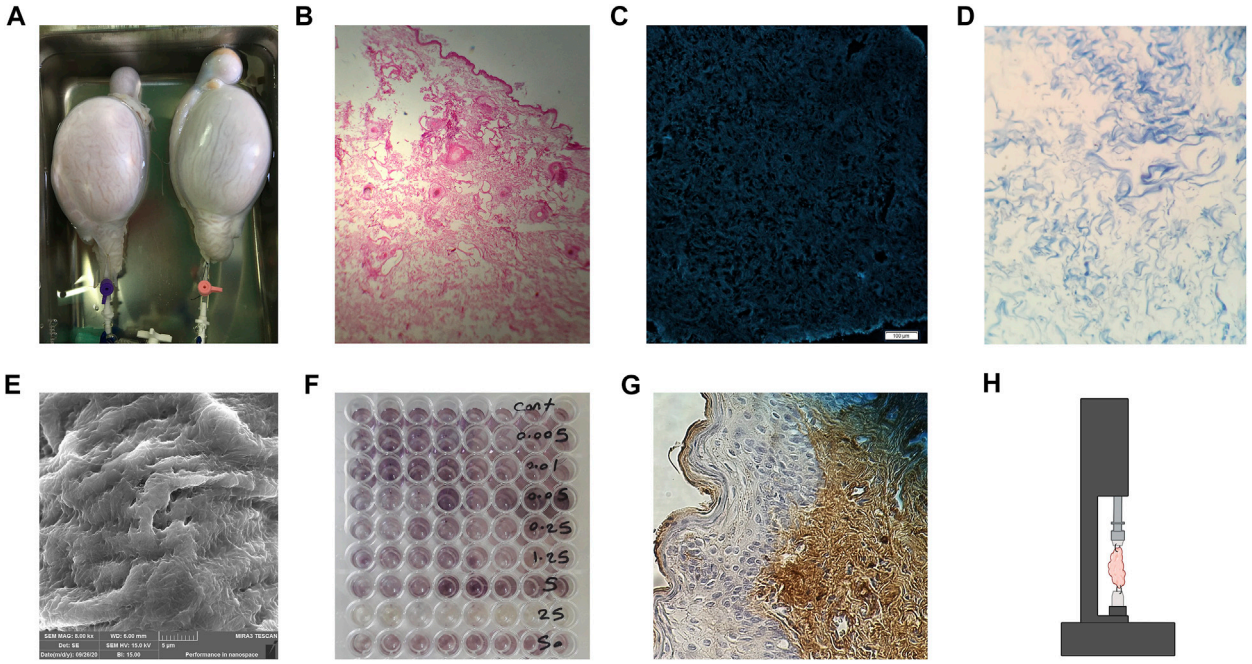

FIGURE 1 | Evaluating the dECM. **(A)** Gross inspection of the decellularized ovine whole testes. **(B)** Hematoxylin and Eosin H&E staining of decellularized human breast skin, no nucleus can be observed. **(C)** 4',6-diamidino-2-phenylindole (DAPI) staining of decellularized human skin with no stained DNA. **(D)** Masson's Trichome staining of the human ovary, showing preserved collagen fibers while no nucleus is seen. **(E)** SEM imaging of decellularized ovine ovary tissue. **(F)** 3-(4, 5-dimethylthiazol-2-yl)-2, 5-diphenyltetrazolium bromide (MTT) assay, showing cellular viability and activity where the purple dye is observed. **(G)** Immunohistochemistry (IHC) staining using antibodies against collagen I in human skin after recellularization. **(H)** Schematic imaging of the tensile test, tissue is placed in the middle of the apparatus and dragged in opposite directions to evaluate the mechanical strength of the dECM.

4.1 Macroscopic Evaluation

Despite the fact that gross inspection alone is not an entirely reliable evaluation method, it is the first step in the evaluation of the decellularized scaffold, which should be followed by more accurate assessments. Different studies use macroscopic imaging analysis as one of the first assessment steps to determine the level of transparency of dECM compared to native tissue (Philips et al., 2018a). Moreover, light transmittance is essential in several organ reconstructions, such as cornea (Oliveira et al., 2013). Transparency is measured by placing samples on a patterned surface. Then, the intensity is calculated by assessing the transmitted light by processing images with software (Oliveira et al., 2013; Philips et al., 2018a; Fernández-Pérez and Ahearne, 2019a).

4.2 Cell Removal Efficacy and Immunogenicity

Various tests assay the effectiveness of the decellularization method. Complete removal of antigens and nucleic acids, along with other cellular components, ensures the biocompatibility of the scaffold. The dECM must be implanted without host immune response activation and graft rejection or the formation of vascular thrombosis. Besides, transgenic transmission has been reported by retained DNA in genetically engineered tissue implantation (Hussein et al., 2016). Crapo et al. have suggested criteria for decellularization satisfaction with cut-off amounts for dsDNA per mg ECM dry weight and DNA fragment length, 50ng and 20bp, respectively, and lack of visible nuclear content in microscopic evaluation (Crapo et al., 2011). Also, extended agent exposure has been used to reduce DNA content by approximately 93% (Tenreiro et al., 2021). Histological analysis of the tissue allows evaluation of general morphology of dECM, as well as cell content and structural integrity (Philips et al., 2018a). Hematoxylin and Eosin (H&E) is mainly used in assessing tissue morphology and cell nuclei, while fluorescent staining with 4',6-diamidino-2-phenylindole (DAPI) are used in the detection of remaining nuclear structures (Crapo et al., 2011; Su et al., 2018). Other histological staining such as Safrin O, Movat's pentachrome, Masson's Trichome, and Hoescht can also be used to evaluate the existence of remnant DNA or cytoplasmic and extracellular molecules in decellularized tissue (Garreta et al., 2017; Gaetani et al., 2018).

DNA quantification using immunofluorescence, electrophoresis, or polymerase chain reaction is also of great use (Pors et al., 2019; Naik et al., 2020; Hussein et al., 2018; da Mata Martins et al., 2020). Of note, electron microscopic assessment can be but is not commonly used to evaluate the existence of nuclear material or cytoplasmic debris due to the cost and the technical complexity (Gilbert et al., 2006).

4.3 Ultrastructure Evaluation

Preservation of 3 dimensional (3D) architecture and structure of the scaffold can be evaluated using different assessments, such as electron microscope (Giraldo-Gomez et al., 2019). A scanning

electron microscope (SEM) is used to reveal surface topography, while transmission electron microscopy (TEM) is used for the detailed orientation of materials and cellular organelles (Márquez et al., 2009). These assessments are utilized to indicate the efficacy of decellularization treatment in conserving the native structure of ECM. In addition, they can show the debris and remaining cell components in the decellularized tissue (Philips et al., 2018a). In a study by Forouzesh et al., SEM images showed sonication-induced micropores with 0.5–5 μm diameter on the surface of decellularized cartilage tissue. Compared to the ultrasound-induced ones, these smaller micropores resulted in increased surface roughness, and suitable cell adhesion was imaged by SEM (Forouzesh et al., 2019).

4.4 Cytocompatibility

Prior to *in vivo* use, it is crucial to investigate the cellular interaction of cells with the decellularized scaffold. In other words, the damaging effects of the decellularization method or agent on the scaffolds should be assessed *ex vivo* to guarantee the clinical efficacy of the dECM. In this regard, the initial step is to quantify the remaining chemicals after washing and sterilizing. Decellularizing and sterilizing agents are cytotoxic and prevent efficient recellularization. The threshold for chemicals cytotoxic concentration, such as SDS has been investigated (Zvarova et al., 2016). The most valued biocompatibility test is *in vitro* cell culture, either indirect or direct (Hussein et al., 2016). In indirect contact assay, cellular proliferation (e.g., live/dead assay or DNA quantification) and metabolic activity (e.g., MTT assay) will be evaluated when cultured in samples extraction, while in direct contact assay, cells will be directly cultured on the decellularized samples and investigated.

4.5 Biochemical Analysis

Following decellularization, it is necessary to determine the remaining desirable ECM components such as GAGs, elastic fibers, collagens, and adhesion proteins like fibronectin and laminin in the decellularized tissue (Gilbert et al., 2006). An adequate amount of these molecules in ECM contributes to the tissue's normal function, structure, and mechanical characteristics. Various stains, kits, and immunohistochemistry (IHC) markers can be used for the detection of these materials (Garreta et al., 2017; Kajbafzadeh et al., 2019). For instance, Masson's trichrome is used for collagen fiber staining, and laminin can be detected by IHC antibodies (Kajbafzadeh et al., 2019).

4.6 Mechanical Tests

Following verification of complete cell removal, the impact of decellularization on the mechanical characteristics of ECM is also important. The ECM is composed of a network of molecules that confer a proper mechanical architecture in the tissue required to grow the desired cell population in tissue remodeling. It has been demonstrated that ECM elasticity plays a role in determining stem cell lineage specification, as matrices with elasticity similar to the brain, muscle, or collagenous bone induced neurogenic, myogenic, and osteogenic differentiation of mesenchymal stem cells (MSCs) (Engler et al., 2006). Atomic force microscopy (AFM), and single or bi-axial mechanical tests are vastly used to measure and compare the mechanical strength of the decellularized and native tissue. In AFM, samples are subjected to a probe, and indentation stress curves are obtained. Then these curves are analyzed, and AFC is measured and compared to native tissue (Peng et al., 2019). Moreover, mechanical testing, namely the burst pressure test, can provide insight into the existence, distribution, and integrity of collagen and elastin fibers within dECM (Bielli et al., 2018; Cai et al., 2019).

4.7 Additional Tests

Based on the purpose of the study and future function of the grafted dECM, researchers evaluate various components and characteristics of their acellular scaffold. Proteomic analysis of the dECM can precisely show and compare the proteome of the ECM before and after decellularization treatment. Proteomic evaluation can be exerted by different techniques, such as nano liquid chromatography and tandem mass spectrometry, and is used to assess the complete protein profile of the ECM, including remaining enzymes and growth factors (Nakayama et al., 2013). Computed tomography angiography is a technique to demonstrate remained vasculature of tissue after decellularization (Daryabari et al., 2019). In addition, during the process of hydrogel production, the ability of dECM to form gel could be analyzed by gelation assay of dECM to form a gel by gelation assay (Gaetani et al., 2018).

5 PRE-APPLICATION PROCESSING

Before being applied, an acellular tissue may undergo a series of *in vitro* procedures, including cell seeding. Processing the scaffolds enhance their ability in successful grafting and function (García-Gareta et al., 2020; Mendibil et al., 2020) (**Figure 2**).

5.1 Modification and Refinement

5.1.1 Vascularization

Oxygen delivery to the tissues is one of the hindrances against applying the decellularized scaffolds, and tissue thickness is an important index for this matter. Preserving the ECM components and vascular structure of the tissue yields better perfusion post-implantation, facilitating further angiogenesis. For instance, laminin and fibronectin in the basement membrane and lamina propria play an essential role in the revascularization of the tissue. Hence, evaluation of the scaffold components and structure after the decellularization process can help us estimate the extent of blood supply (Partington et al., 2013; García-Gareta et al., 2020). Vascularization can be induced by adding angiogenic factors to the matrix or prevascularization of the matrix (Amirsadeghi et al., 2020). Various growth factors were introduced to enhance angiogenesis. Drew et al. observed neovascularization in the presence of exogenous Vascular Endothelial Growth Factor (VEGF) (Dew et al., 2016). However, another study revealed that in bladder tissue regeneration, poly (octamethylene citrate) (POC) composites

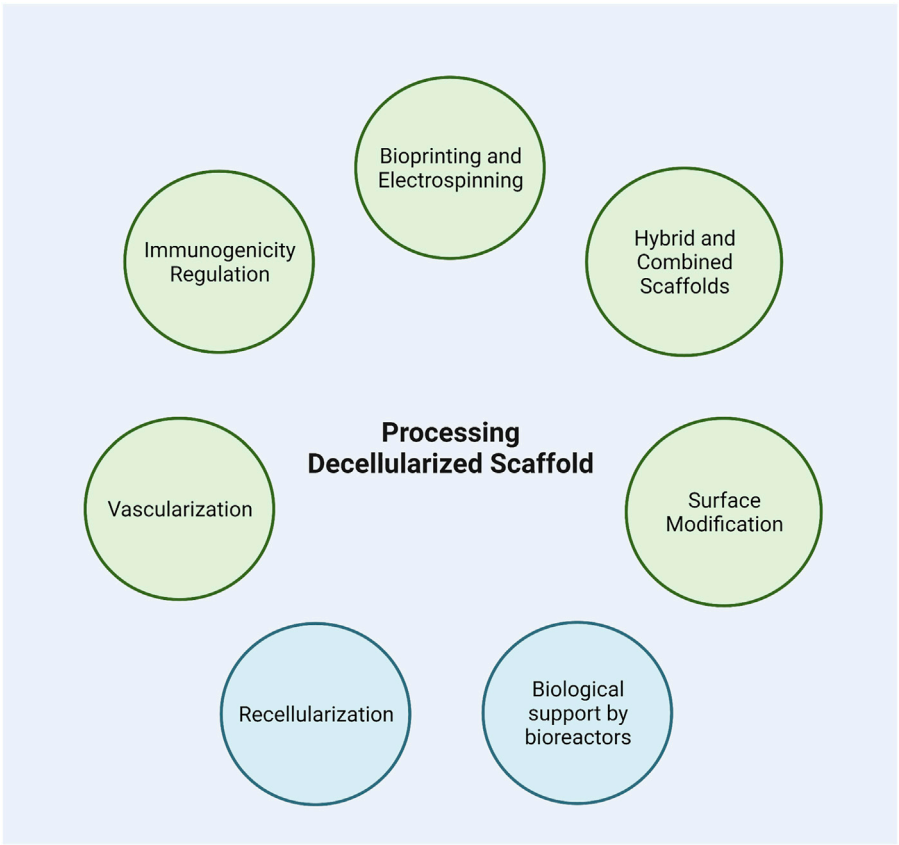

FIGURE 2 | Pre-application processing of decellularized scaffolds. Modifying the decellularized scaffolds improves their capacity to regenerate damaged tissues without causing adverse events. In addition, processing scaffolds with stem cells and bioreactors helps improve their regeneration capacity.

outperformed small intestinal submucosa (SIS) scaffolds in tissue vascularization, while POC scaffolds lack any exogenous growth factor (Bury et al., 2021). Stem cells are considered beneficial in angiogenesis induction, as they can differentiate into endothelial cells or secrete various growth factors. Adipose-derived stem cells (ADSCs) were reported to significantly enhance vascular network formation in decellularized adipose tissue scaffolds (Han et al., 2015). Prevascularization is a technique of creating microvasculature inside the synthetic scaffold; a decellularized tissue is already prevascularized. Whole organ matrices maintain the internal vasculature of the scaffold, bypassing the perfusion limits regardless of thickness and density (Wang et al., 2019). Hence, it is crucial to produce acellular organs with optimally preserved vessels and ECM composition for repopulating a capable scaffold and restoring blood circulation after implantation.

5.1.2 Immunogenicity Regulation

Non-autologous materials or cells on an engineered organ may trigger the immune response. Activation of the host immune system against synthetic, biological, and decellularized xenogeneic and allogeneic grafts has been reported as a hurdle in the transplantation of engineered tissues and organs (Wiles et al., 2016). Studies have proposed various approaches to overcome immune reaction against engineered tissue, including modulatory coatings on the scaffold surface, immune cloaking, modification of Damage Associated Molecular Pattern (DAMP) proteins which may remain after decellularization, and recellularization with autologous cells to suppress the immune response to materials (Wiles et al., 2016). Moreover, genetically engineered hypoimmunogenic stem cells are alternative to autologous cells to evade immune rejection (Deuse et al., 2019). One of the limitations concerning tissue decellularization is that most studies have examined these scaffolds on animal models, and limited human studies have been conducted so far. Consequently, translation of animal findings on the immune response to humans can be challenging. Human-like animals, such as nonhuman primates and humanized mouse models, with immune systems similar to humans, are being investigated to improve our understanding of the immunogenic components of the acellular scaffold (Bhattacharya et al., 2019; Bilodeau et al., 2020).

5.1.3 Bioprinting and Electrospinning

Bioprinting is a process through which bioinks are used to produce a 3D construct resembling human tissue that can be used to regenerate injured tissues and treat various diseases. Although bioprinting is progressively used in regenerative

medicine to develop novel and effective treatments for various diseases, the lack of suitable bioinks hinders its widespread application in medicine (Ferreira et al., 2020; De Santis et al., 2021). Bioinks should be both cytocompatible and appropriate for structuring 3D tissues. 3D bioengineering of tissues using dECM bioink helps provide scaffolds for modeling diseases and developing efficient treatments for them. However, dECM needs augmentation to mechanically resemble the natural ECM (Ferreira et al., 2020; De Santis et al., 2021). Hydrogels could be made through solubilizing dECM followed by reformation of scaffold controlled by temperature and pH. Formation of dECM hydrogels is highly dependent on the collagen content of dECM. Hydrogel bioink derived from dECM can help deliver biomolecules and provide an appropriate surface for cells to migrate and grow (Saldin et al., 2017; Ferreira et al., 2020; De Santis et al., 2021). The biochemical, structural, and viscoelastic properties of dECM are tunable via combination with other biomaterials and crosslinking to provide maximum cytocompatibility along with structural support for tissues and cells. Alginate/dECM compositions as bioink demonstrated beneficial impacts on blood vessel formation after transplantation and prevention of foreign body reactions (Saldin et al., 2017; Ferreira et al., 2020; De Santis et al., 2021). Alginate reinforced with methacrylate-dECM demonstrated augmented bioactivity of hydrogel bioprinted scaffold and osteogenic differentiation of ADSCs (Lee et al., 2020).

Electrospinning has recently become increasingly popular for modifying the dECMs. Electrospinning may help design nanofibrous scaffolds from dECM with similar characteristics to the native tissue, including ultrastructure, porosity, and mechanical characteristics. Electrospun scaffolds demonstrated superior functionality and histocompatibility compared to scaffolds that are combined with other methods. Reinforcing rat decellularized vessels with Polycaprolactone (PCL) using the electrospinning method resulted in increased biomechanical endurance. Electrospinning provides an efficient method to combine natural and synthetic materials to achieve hybrid scaffolds that resemble native tissue with biomimetic architecture and enhanced biomechanical properties (Schenke-Layland et al., 2009; Kai et al., 2013; Gong et al., 2016).

5.1.4 Hybrid and Combined Scaffolds

Combining the decellularized scaffolds with other molecules, including biomaterials, drugs, and growth factors may help modify the characteristics of the decellularized scaffolds. The methods for designing combined scaffolds include solvent casting and particulate leaching, lyophilization (freeze-drying), thermal-induced phase separation (TIPS), gas foaming, rapid prototyping, stereolithography, fused deposition modeling, selective laser sintering, 3D printing, bioprinting, cross-linking, and electrospinning (Eltom et al., 2019; Wasyłeczko et al., 2020).

It was demonstrated that decellularized omentum scaffolds coated with gold (Au) nanoparticles (NP) could provide proper electrical conductivity and characteristics. Hence after seeding cardiac cells, the AuNP-decellularized scaffold can cause higher contraction force, decrease the excitability threshold, and increase the calcium channels currents. Also, silver (Ag) NPs show proangiogenic properties and enhance the biocompatibility of the scaffolds (Shevach et al., 2014; Saleh et al., 2019). When modified with the methoxy polyethylene glycol, an acellular adipose matrix decreases the immunogenicity and increases the adipogenicity of the scaffold (Liu et al., 2021a). Furthermore, polypropylene mesh coated with the ECM inhibits the M1 macrophages and increases the M1/M2 ratio (Wolf et al., 2014). Electrospun PCL blended with collagen in combination with decellularized rabbit aorta was found to provide biocompatibility and rigidity (Ghorbani et al., 2017). Scaffolds fabricated from dECM mixed with PCL have suitable properties for the growth and migration of stem cells. In addition, PCL/Poly Lactic-co-Glycolic Acid (PLGA) electrospun scaffold can support the cell-derived ECM to produce a dECM with desirable mechanical properties and biocompatibility (Schenke-Layland et al., 2009; Bracaglia and Fisher, 2015). Sugar-induced modification of the decellularized kidneys increases mechanical strength and resistance to deformation (Sant et al., 2021). Recently multilayered decellularized scaffolds demonstrated promising bioactivity and should be further studied to be widely used (Smith et al., 2022). Moreover, growth factors and drugs could be loaded on the dECMs, making them more potent. The addition of neurotrophic factors to dECM as well as removing chondroitin sulfate proteoglycans from dECM promote neurite outgrowth (Boyer et al., 2015; Qiu et al., 2020). Heparinized decellularized scaffolds have been examined for promoting angiogenesis and preventing clot formation (Wu et al., 2016). Layer-by-layer coating of the decellularized porcine aortic valve with basic fibroblast growth factor (bFGF) and heparin preserve a sustained release of these factors leading to improved biological activity (De Cock et al., 2010). Another study loaded fibroblast-derived ECM with VEGF and heparin to boost angiogenesis. Application of heparin/VEGF ECM encapsulated with alginate resulted in a prolonged release of these factors as well as enhanced bioactivity (Du et al., 2014). The dECMs are promising options for drug delivery; meanwhile, further studies are needed to increase their effectiveness.

5.1.5 Surface Modification

In order to achieve improved cytocompatibility, mechanical properties, and biological function of decellularized scaffolds without inflammatory reactions, the surface modification could be done via various methods and biomaterials (Ozasa et al., 2013; Liu et al., 2021b). It is demonstrated that immersion of decellularized tendons with carbodiimide-derivatized hyaluronic acid and gelatin could alleviate the tendon's gliding resistance by augmenting its surface's smoothness (Ozasa et al., 2013). Moreover, riboflavin-mediated UV crosslinking may repair the damages caused by the decellularization process and increase the smoothness and mechanical strength of the dECM; therefore, it could be used as the luminal surface in the vascular prosthesis (Schneider et al., 2020). Laser micro-ablation is another method that can produce microporosity in the scaffold's surface (Matuska and McFetridge, 2018). In addition, coating the surface of the scaffolds using heparin reduces the thrombogenicity and makes their surface

appropriate to be used as vascular grafts (Wu et al., 2016). Decellularized aorta covalently linked with heparin through "click" coating inhibited platelet adhesion and thrombogenicity. Also, Proper adhesion and proliferation of the endothelial cells were observed (Dimitrievska et al., 2015). Immobilization of VEGF on the surface of dECM through "click" reactions improves angiogenic properties of scaffolds (Wang et al., 2014). Accordingly, surface modification can optimize dECMs for various applications.

5.2 Recellularization

Acellular scaffolds have the capacity of *in vitro* or *in vivo* cell seeding. *In situ* tissue regeneration takes advantage of the recipient's body's regenerative capabilities and biological supply. Therefore, cell seeding of the scaffold prior to transplantation is not always necessary, but adding the bioactive molecules would reinforce the regeneration process (Yang et al., 2020). Thrombogenic and immunogenic factors on decellularized matrices may trigger thrombogenesis or the host immune response. These factors can be hidden, degraded, or modified by cells. Robertson et al. have shown that reendothelialization of whole heart ECM reduced the scaffold thrombogenicity (Robertson et al., 2014).

During the recellularization process, whole organ repopulation is difficult due to the complexity of the scaffold, the challenges of introducing cells to different parts of the scaffold, the need for the presence of different cell types, and uncertainty about the viability and functionality of cells after organ grafting (Bilodeau et al., 2020). However, advances in cell seeding techniques have provided solutions. Several strategies for the recellularization of a whole organ have been advocated, including slicing, perfusion, and injections (Figliuzzi et al., 2017). For instance, studies reported that the perfusion-based method is fruitful for the recellularization of acellular lungs and kidneys through the trachea and ureter, respectively (Song et al., 2013; Kuevda et al., 2016). Daryabari et al. implanted patches of the decellularized ovine whole uterus into uterine horns of female rats. They demonstrated regeneration of endometrium and myometrium layers, and vascularization was apparent (Daryabari et al., 2019). Whole organ recellularization through the vascular system on the liver, heart, pancreas, kidney, and lung with preservation of original architecture has been widely investigated (Gilpin et al., 2014a; Sabetkish et al., 2015; Scarrit et al., 2015; Ferng et al., 2017). Also, innovative techniques such as the exertion of negative trans-renal pressure gradient and magnetic guidance to direct cells have been proposed for repopulating complex tissues (Song et al., 2013; Ghodsizad et al., 2014).

Moreover, as an alternative method, intraparenchymal injection of the renal cell into the acellular porcine kidneys resulted in satisfactory repopulation and function (Abolbashari et al., 2016). Despite the progress in reseeding methods, slicing the organ demolishes its native 3D structure, the introduction of non-epithelial cells via perfusion is ineffective, and numerous cell injections may cause injuries to the scaffold (Figliuzzi et al., 2017). Therefore, multiple recellularization techniques might be employed to achieve optimal results in the meantime.

Although recellularization is considered a beneficial stage in the regeneration process, *in vitro* cell reseeding could be associated with some constraints. The recellularization process is time-consuming, especially when using induced pluripotent stem cells (iPSCs) derived from the patient's somatic cells. One of the most important things to keep in mind is to utilize an adequate amount of the appropriate cell type. This factor varies in different tissues and organs and should be considered to reduce the risk of teratoma formation or immune response induction (Badylak et al., 2011; Kim et al., 2020). Multiple types of cells have been investigated for the recellularization of the scaffolds. Limited differentiation and expansion capacity of specialized cells restrains their effectiveness in recellularizing whole organ scaffolds. Stem cells have higher proliferation capacity and are mainly classified into adult stem cells, embryonic stem cells (ESCs), fetal stem cells, iPSCs, and other engineered cells (Denstedt and Atala, 2009; Bacakova et al., 2018). Mesenchymal stem cells (MSCs) and hematopoietic stem cells (HSCs) are the most common stem cells that have been used in the recellularization process. ESCs are pluripotent, but supply issues and ethical concerns restrain their application potential. The iPSCs are produced by the genetic reprogramming of adult somatic cells (Moser and Ott, 2014). Although iPSCs ensure histocompatibility and avoid ethical conflicts, tumor formation remains unresolved. Recently, iPSCs have been shown to produce self-organizing organoids with different cell types through genetic reprogramming or exposure to environmental signaling factors (Ebrahimkhani and Levin, 2021). Gilpin et al. evaluated the recellularization of decellularized lung scaffold with lung endothelial and epithelial progenitor cells derived from human iPSCs. They found decellularized lung scaffold could provide an appropriate environment for iPSC-derived progenitor cells (Gilpin et al., 2014b). Therefore, iPSCs seem promising in providing various functional cells for repopulating whole organs. MSCs are multipotent stem cells and can be easily harvested from various tissues such as bone marrow and adipose tissue. They can differentiate into several cell lineages and have demonstrated encouraging results in recellularizing different tissues. Thus, these cells have been used as a source for reseeding diverse tissues, such as cartilage (Zheng et al., 2011), respiratory tract (Hou et al., 2011; Mendez et al., 2014), urinary tract (Huang et al., 2007; Coutu et al., 2014), and cardiovascular system (Zhao et al., 2010).

It is preferred to use autologous cells for recellularizing acellular scaffolds since these cells would not trigger the host immune system reactions and rejection after transplantation. It has been demonstrated that reseeding acellular diaphragm and lung matrices with stromal cells from homogenized rat lung and diaphragm tissues had lower inflammation and fibrosis formation compared to reseeding with mesenchymal stem cells (Kuevda et al., 2019). In another study by Hellström and colleagues, primary uterine cells and bone marrow-derived mesenchymal stem cells (BM-MSCs) were seeded on rat decellularized uterine scaffolds (Hellström et al., 2016). They observed that these matrices were able to bear pregnancy and normal fetus development. The co-culture of parenchymal cells with non-parenchymal cells could enhance tissue development.

Combining tissue-derived cells with endothelial cells or fibroblasts has been reported to improve ECM remodeling, cellular function, and cell organization (Badylak et al., 2011; Gilpin and Yang, 2017). Shen and colleagues have shown that endothelial cells are a critical component for neurogenesis of neural stem cells (Shen et al., 2004). Endothelial cells work as a barrier to prevent thrombosis and organ loss due to immunogenicity of the matrix after transplantation, especially in vascular and valvular grafts (Lichtenberg et al., 2006; Robertson et al., 2014). Furthermore, reendothelialization of whole decellularized heart vascular structures with rat aortic endothelial cells enhanced the contractility of left ventricular constructs (Robertson et al., 2014).

5.3 Bioreactors

Intercellular interactions and signaling play a major role in tissue development and function. Bioreactors provide a refreshing environment regarding factors, nutrients, and mechanical force that together enhance cell seeding (Martin et al., 2004). Mostly, bioreactors are perfusion-based systems involving a simple flow. Enhancement in the systems includes gravity involvement or providing a rotatory environment, optimization in oxygenation, or regulation of mechanical stimuli to mimic a natural microenvironment, such as compression and shear stress (Selden and Fuller, 2018). Spinning flasks, rotating cylindrical devices, perfusion bioreactors, and microfluidic systems are among the most used types of bioreactors (Ahmed et al., 2019). Unlike static culture conditions, bioreactors are able to monitor and control the environmental factors precisely. The incorporation of sensors into these devices allows detection of any changes, namely pH or concentration of factors (Simmons et al., 2017). The automation of these systems not only eliminates the need for manual and invasive balancing of the ECM and cellular interactions but also decreases manufacturing costs and enables inclusive clinical application (Martin et al., 2004).

6 APPLICATION OF DECELLULARIZED SCAFFOLDS IN REGENERATIVE MEDICINE

6.1 *In Vitro* Application

Decellularized scaffolds are being used for modeling the diseases to investigate their pathophysiology. Cell-cell communication, intracellular signaling, stem cell secretions, and therapeutics approaches could be studied in a 3D *ex vivo* scaffold to evaluate the role of the microenvironment in the progression of diseases, such as tumors and inflammatory conditions (García-Gareta et al., 2020). It has been shown that breast cancer cells had improved growth profiles when seeded on decellularized human adipose tissue compared to two-dimensional and Matrigel three-dimensional cultures (Dunne et al., 2014). In a recent study by Wishart and colleagues, the involvement of collagen-IV in breast cancer cell invasion was demonstrated (Wishart et al., 2020). Moreover, using decellularized human colorectal cancer matrices, Pinto et al. advocated that tumoral ECM macrophages enhanced cancer cell invasion *via* cytokine signaling (Pinto et al., 2017).

The underlying mechanism of the diseases and the effectiveness of the drugs could be assessed by modeling the diseases using decellularized scaffolds (McCrary et al., 2020a). For instance, acellular human intestine ECM was cultured with intestinal myofibroblasts to assess intestine fibrosis subsequent to inflammatory bowel disease (Giuffrida et al., 2019). Altered sensitivity of breast cancer cells to doxorubicin and lapatinib was also demonstrated in human adipose tissue-derived ECM scaffolds compared with 2D-cultured cells (Dunne et al., 2014). In another research, higher resistance to drug administration in cancer cells was reported in 3D cultures rather than 2D (Ganjibakhsh et al., 2019). Such studies support the beneficial aspects of *in vitro* application of decellularized tissue from normal or diseased tissues.

6.2 *In Vivo* Application

Since decellularized materials are biocompatible and stable compared to synthetic matrices, these cell-free scaffolds are being widely used (Kawecki et al., 2018). However, the attraction of desired stem cells to the site of the scaffold transplantation still remained challenging. Growth factors and chemoattractant substances could help overcome this pitfall (Yang et al., 2020). Sabetkish et al. used decellularized human testicles from patients with testicular feminization syndrome and implanted them between the thigh muscles of mice. Spermatogonial stem-like cells were observed during follow-up (Sabetkish et al., 2021).

Decellularized tissues, either cell-free or recellularized, primarily aim to function as implantable matrices for lost or injured organ regeneration (**Figure 3**). Multiple tissues have been introduced as candidates for tissue engineering, including the gastrointestinal tract, respiratory system, vascular, and neural tissues (Mendibil et al., 2020). Gilpin et al. have classified the applicable acellular scaffolds into cell sheets, tissues, and whole organs (Gilpin and Yang, 2017). Cell sheets are simple constructs mainly derived from a single cell type and may heal minor lesions or more complex structures when different sheets are combined. Cell-derived matrices are state-of-the-art ECM that can be used as an alternative to native tissue-derived matrices since human cells are accessible and limitless, and matrix properties can be controlled (Fitzpatrick and McDevitt, 2015).

It is evidenced that genetic modification may improve the characteristics of ECM and the efficacy of the decellularization process. Effective decellularization process could be reached via apoptosis of death-inducible stem cells. Also, genetic modification of the stem cells may help tune the ECM composition, such as modifying VEGF expression by stem cells (Papadimitropoulos et al., 2015; Bourgine et al., 2017; Morris et al., 2018). Acellular ECM derived from BM-MSC sheets was used to treat osteochondral defects in rabbits (Wang et al., 2020). These matrices promoted regeneration of articular cartilage and subchondral bone with some degrees of vascularization. Reconstruction of blood vessels, combination of various decellularized cartilage sheets to produce two-dimensional cartilage assembly, and recellularization of periodontal ligament cell sheets were also reported (Fitzpatrick et al., 2008; Gilpin and Yang, 2017).

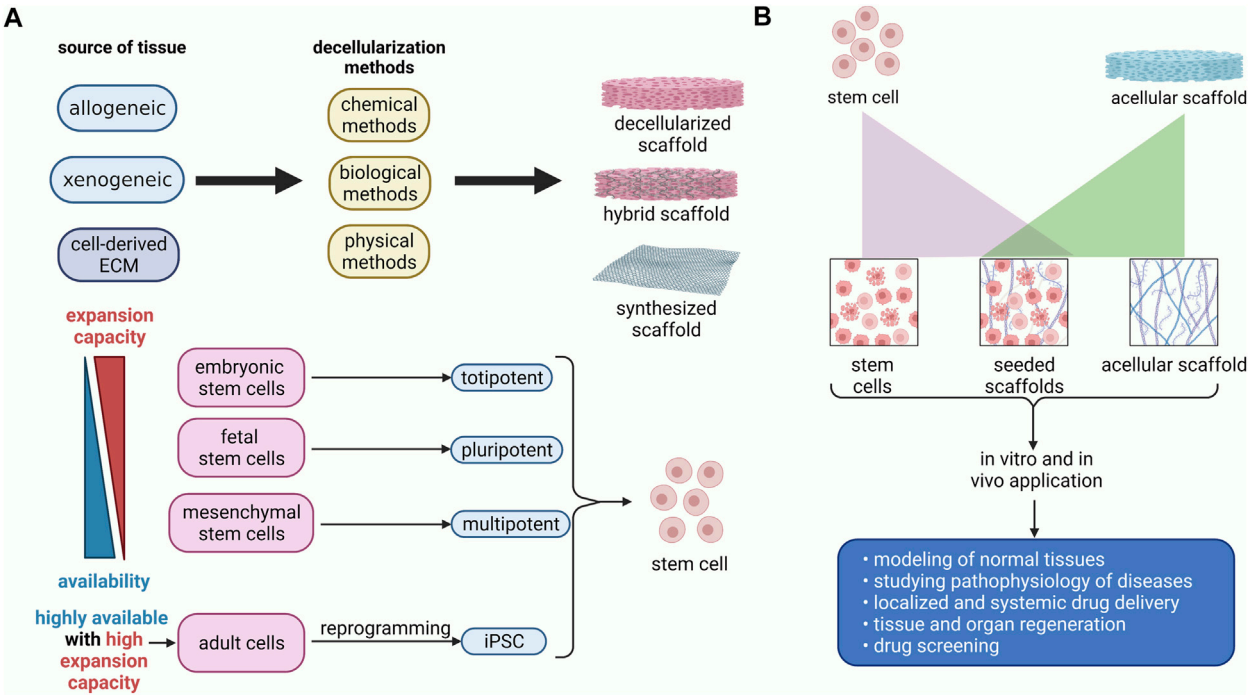

FIGURE 3 | Schematic diagram of preparation and application of the recellularized scaffolds. **(A)** The decellularized scaffolds could be obtained via chemical, biological, and physical approaches from human or animal sources. It has been demonstrated that stem cells from embryonic sources have a higher expansion capacity, albeit they are not easily accessible. Conversely, stem cells from adult sources, including mesenchymal stem cells, are highly available, whereas they do not have proliferation and differentiation capability as much as embryonic stem cells. Nevertheless, mesenchymal stem cells are multipotent stem cells that can differentiate into various cell lineages. The iPSC can be obtained via genetic modification of mature cells. Thus, they are highly expansible and readily available. **(B)** decellularized scaffolds can be used as cell-free grafts, or they can be seeded with stem cells. Decellularized scaffolds with or without stem cells could be transplanted for regeneration of the damaged tissues. Moreover, they are used in drug delivery, drug screening, disease modeling, and studying the pathophysiology of diseases.

Acellular ECM hydrogels can also provide a scaffold for transplantation and injection (Young et al., 2011; Wolf et al., 2012). In addition, transplantation of recellularized acellular scaffolds has been approached by many researchers. In a study, regenerated rat lungs were orthotopically transplanted to investigate the function of reendothelialized pulmonary vasculature (Tsuchiya et al., 2017). They showed blood perfusion in the transplanted lung as well as leak-free ventilation. Transplantation of reseeded decellularized diaphragm into rats resulted in improved spirometry parameters (Gubareva et al., 2016).

Currently, decellularized tissues are widely being studied for organ regeneration. Kajbafzadeh and colleagues have implanted acellular rat colon-derived scaffolds into the mesenteric tissue as a graft with an end-to-end anastomosis to the colon of host rats that resulted in recellularization of the scaffold (Kajbafzadeh et al., 2020). The trachea, heart valve, and urethra are examples that have been clinically regenerated with decellularized scaffolds (Versteegden et al., 2017; Porzionato et al., 2018).

6.3 Human Studies

Human application of different acellular organs is probably the ultimate goal of tissue engineering and regenerative medicine. Due to the shortcoming of living organs donation, decellularization and tissue engineering methods could pave the way for regenerating tissues and organs to treat diseases in a less invasive procedure.

Variability in human tissues and their immunogenicity makes it inconceivable to propose a standardized decellularization method, thus precluding acellular whole-organ transplantation (Tenreiro et al., 2021; Mattei et al., 2017). Other hindrances include ideal vascularization, innervation, or recellularization of acellular scaffolds (Choudhury et al., 2018). Application of cell-free grafts is a relatively new area of the clinical setting to use acellular matrices. Many commercial companies have been producing dECM, namely Biohorizon and Axogen, which produce acellular skin graft and dECM nerve scaffolds. In addition, many human organ-derived dECM-bioprinted hydrogels have been used in drug screening and delivery (Choudhury et al., 2020; Lopresti et al., 2015; Cui et al., 2019). Also, AlloDerm (derived from the allogenic human cadaveric dermis), Strattice (derived from porcine dermis), and OaSIS (derived from porcine SIS) are commercial cell-free products that have been used in recent decades mainly for covering the skin flaps donor sites, breast reconstruction, and managing ulcers and wounds, respectively (Cui et al., 2019). In a clinical trial, human

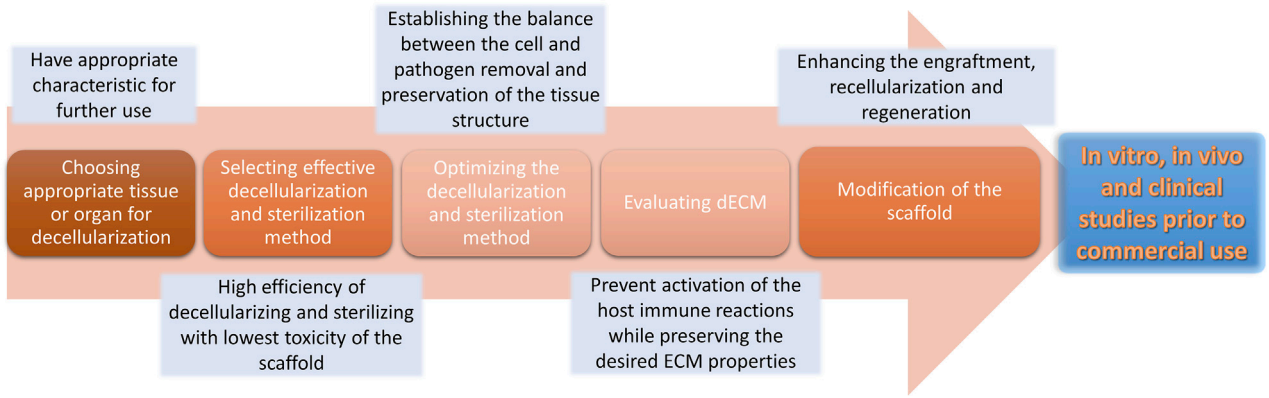

FIGURE 4 | Challenges and hurdles regarding the decellularization process. The decellularization process encounters different challenges that may affect the resulting scaffold.

acellular vessels showed safety and functionality in providing access for hemodialysis in end-stage renal disease patients (Lawson et al., 2016). Different decellularized tissues and their application status is reviewed by Liao et al. (Liao et al., 2020). Currently, several clinical trials in different phases are investigating the application of decellularized tissue in the regeneration of injured or lost organs. An active phase II study is being conducted at the Department of Biomedical Engineering, Johns Hopkins University, investigating acellular adipose tissue for soft tissue reconstruction (identifier: NCT03544632, clinicaltrials.gov). Various decellularized scaffolds from animal and human sources have been used clinically, mainly for wound healing and surgical mesh devices, albeit their application is still limited, and further studies are needed to make decellularized scaffolds commercially available treatment of disease (Damodaran and Vermette, 2018).

7 DISCUSSION: CHALLENGES AND FUTURE DIRECTIONS

Despite favorable characteristics of the decellularized scaffolds for implementation in clinical practice, there are some constraints and challenges in their application. Determining the suitable tissue, decellularization and sterilization method selection, optimizing the efficacy of these techniques, dECM quality assessment, modification of acellular scaffolds *in vitro* and *in vivo* study, and transplantation problems (e.g., the timing of biomaterial transplantation) are among the unsolved challenges regarding the clinical translation of the decellularized scaffolds (**Figure 4**) (Zhang et al., 2021).

The decellularization method is selected based on the type of tissue and its characteristics. Developing cell removal techniques with lower toxic agents or productions, in addition to enhancing sterilizing techniques, would be beneficial. Apart from that, unlike most synthetic scaffolds (Han et al., 2015), purified ECM provides a natural microenvironment for the cells that is challenging to preserve its properties during the decellularization process (Frantz et al., 2010; Crapo et al., 2011). Ongoing research is aspiring to develop new techniques to better preserve the ECM architecture and components, such as vacuum-assisted and apoptosis-assisted decellularization (Zhang et al., 2021). Removing cells from ECM can become more efficient if an innate cellular process or an exogenous stimulus, such as a drug, promotes cell death, thereby eliminating possible ECM structural damage. Cartilage ECM was yielded by culturing human mesenchymal stromal cells with death-inducible genetic systems. This method resulted in more productive bone tissue engineering compared to cartilage ECM obtained from freeze-thaw cycles (Bourgine et al., 2014). Also, camptothecin-treated nerve tissue resulted in cellular apoptosis and clearance, which was immunogenically tolerable *in vivo* (Cornelison et al., 2018).

Various evaluation tests have already been established to ensure that cellular compounds have been cleared from the dECM during the decellularization treatment, while the chemical and biomechanical properties remain intact and the residual detergent is removed from the decellularized tissue, as the remaining detergents may cause cell toxicity in the scaffold (Zhang et al., 2021). Each tissue has unique characteristics that make it proper for a research plan and further clinical use. Additional novel analyzing tests should be developed for each tissue and its future point of function, letting researchers assess the acellular scaffold specifically and exclusively.

Application of naturally-derived ECM is restricted owing to limited animal sources that are free of by-products and contaminants, while synthetic scaffolds are available in ample amounts (Frantz et al., 2010). Polymerization of biodegradable materials is becoming increasingly popular since manufacturing techniques such as electrospinning can help create a large number of scaffolds with controllable indexes, including shapes, porosities, and fiber arrangements (Nam et al., 2007; Langer

and Vacanti, 2016; Asghari et al., 2017). In order to overcome the damages caused by the decellularization process and take advantage of engineered materials, many researchers have attempted to modify decellularized scaffolds, print 3D scaffolds using bio-inks, or design ECM-derived hydrogels (García-Gareta et al., 2020). In terms of regenerative medicine, 3D printing is a valuable tissue fabrication technology since it is capable of reproducing the structure of the desired organ; however, clinical application of these 3D bioprinted constructs depends on further regulations and improvements (Ji and Guvendiren, 2017; Bilodeau et al., 2020).

Although the aforementioned strategies have been effective to a large extent in the decellularization process, there are still many hindrances in the endless road of dECM engineering. Despite all progress in this field, further investigations are needed to overcome challenges regarding the clinical application of decellularized biomaterials and the ultimate goal of whole organ transplantation.

AUTHOR CONTRIBUTIONS

AN conceptualized the title, prepared the first draft, revised the manuscript, and designed the table and figures. ASK conceptualized the title, prepared the first draft, revised the manuscript, and designed the figures. FD conceptualized the title and prepared the first draft. MMZ conceptualized the title, critically revised the manuscript, edited and finalized the draft, supervised the project. A-MK conceptualized the title, critically revised the manuscript, edited and finalized the draft, and supervised the project. All the authors have read and approved the final draft of the manuscript.

ACKNOWLEDGMENTS

Figure 1F, **Figure 2**, and **Figure 3** have been created with BioRender.com.

REFERENCES

Abolbashari, M., Agcaoili, S. M., Lee, M.-K., Ko, I. K., Aboushwareb, T., Jackson, J. D., et al. (2016). Repopulation of Porcine Kidney Scaffold Using Porcine Primary Renal Cells. *Acta Biomater.* 29, 52–61. doi:10.1016/j.actbio.2015.11.026

Ahmed, S., Chauhan, V. M., Ghaemmaghami, A. M., and Aylott, J. W. (2019). New Generation of Bioreactors that advance Extracellular Matrix Modelling and Tissue Engineering. *Biotechnol. Lett.* 41 (1), 1–25. doi:10.1007/s10529-018-2611-7

Alshaikh, A. B., Padma, A. M., Dehlin, M., Akouri, R., Song, M. J., Brännström, M., et al. (2019). Decellularization of the Mouse Ovary: Comparison of Different Scaffold Generation Protocols for Future Ovarian Bioengineering. *J. Ovarian Res.* 12 (1), 58–59. doi:10.1186/s13048-019-0531-3

Amirsadeghi, A., Jafari, A., Eggermont, L. J., Hashemi, S.-S., Bencherif, S. A., and Khorram, M. (2020). Vascularization Strategies for Skin Tissue Engineering. *Biomater. Sci.* 8 (15), 4073–4094. doi:10.1039/d0bm00266f

Antons, J., Marascio, M. G., Marascio, M., Aeberhard, P., Weissenberger, G., Hirt-Burri, N., et al. (2018). Decellularised Tissues Obtained by a CO2-philic Detergent and Supercritical CO2. *eCM* 36, 81–95. doi:10.22203/ecm.v036a07

Asghari, F., Samiei, M., Adibkia, K., Akbarzadeh, A., and Davaran, S. (2017). Biodegradable and Biocompatible Polymers for Tissue Engineering Application: a Review. *Artif. Cell nanomedicine, Biotechnol.* 45 (2), 185–192. doi:10.3109/21691401.2016.1146731

Assmann, A., Struß, M., Schiffer, F., Heidelberg, F., Munakata, H., Timchenko, E. V., et al. (2017). Improvement of the *In Vivo* Cellular Repopulation of Decellularized Cardiovascular Tissues by a Detergent-free, Non-proteolytic, Actin-Disassembling Regimen. *J. Tissue Eng. Regen. Med.* 11 (12), 3530–3543. doi:10.1002/term.2271

Bacakova, L., Zarubova, J., Travnickova, M., Musilkova, J., Pajorova, J., Slepicka, P., et al. (2018). Stem Cells: Their Source, Potency and Use in Regenerative Therapies with Focus on Adipose-Derived Stem Cells - a Review. *Biotechnol. Adv.* 36 (4), 1111–1126. doi:10.1016/j.biotechadv.2018.03.011

Badylak, S. F., Taylor, D., and Uygun, K. (2011). Whole-organ Tissue Engineering: Decellularization and Recellularization of Three-Dimensional Matrix Scaffolds. *Annu. Rev. Biomed. Eng.* 13, 27–53. doi:10.1146/annurev-bioeng-071910-124743

Bhattacharya, R., Das, P., Joardar, S. N., Biswas, B. K., Batabyal, S., Das, P. K., et al. (2019). Novel Decellularized Animal Conchal Cartilage Graft for Application in Human Patient. *J. Tissue Eng. Regen. Med.* 13 (1), 46–57. doi:10.1002/term.2767

Bielli, A., Bernardini, R., Varvaras, D., Rossi, P., Di Blasi, G., Petrella, G., et al. (2018). Characterization of a New Decellularized Bovine Pericardial Biological Mesh: Structural and Mechanical Properties. *J. Mech. Behav. Biomed. Mater.* 78, 420–426. doi:10.1016/j.jmbbm.2017.12.003

Bilodeau, C., Goltsis, O., Rogers, I. M., and Post, M. (2020). Limitations of Recellularized Biological Scaffolds for Human Transplantation. *J. Tissue Eng. Regen. Med.* 14 (3), 521–538. doi:10.1002/term.3004

Bourgine, P. E., Scotti, C., Pigeot, S., Tchang, L. A., Todorov, A., and Martin, I. (2014). Osteoinductivity of Engineered Cartilaginous Templates Devitalized by Inducible Apoptosis. *Proc. Natl. Acad. Sci. U.S.A.* 111 (49), 17426–17431. doi:10.1073/pnas.1411975111

Bourgine, P. E., Gaudiello, E., Pippenger, B., Jaquiery, C., Klein, T., Pigeot, S., et al. (2017). Engineered Extracellular Matrices as Biomaterials of Tunable Composition and Function. *Adv. Funct. Mater.* 27 (7), 1605486. doi:10.1002/adfm.201605486

Boyer, R. B., Sexton, K. W., Rodriguez-Feo, C. L., Nookala, R., Pollins, A. C., Cardwell, N. L., et al. (2015). Adjuvant Neurotrophic Factors in Peripheral Nerve Repair with Chondroitin Sulfate Proteoglycan-Reduced Acellular Nerve Allografts. *J. Surg. Res.* 193 (2), 969–977. doi:10.1016/j.jss.2014.09.023

Bracaglia, L. G., and Fisher, J. P. (2015). Extracellular Matrix-Based Biohybrid Materials for Engineering Compliant, Matrix-Dense Tissues. *Adv. Healthc. Mater.* 4 (16), 2475–2487. doi:10.1002/adhm.201500236

Bury, M. I., Fuller, N. J., Sturm, R. M., Rabizadeh, R. R., Nolan, B. G., Barac, M., et al. (2021). The Effects of Bone Marrow Stem and Progenitor Cell Seeding on Urinary Bladder Tissue Regeneration. *Sci. Rep.* 11 (1), 1–12. doi:10.1038/s41598-021-81939-5

Cai, Z., Gu, Y., Cheng, J., Li, J., Xu, Z., Xing, Y., et al. (2019). Decellularization, Cross-Linking and Heparin Immobilization of Porcine Carotid Arteries for Tissue Engineering Vascular Grafts. *Cell Tissue Bank* 20 (4), 569–578. doi:10.1007/s10561-019-09792-5

Caralt, M., Uzarski, J. S., Iacob, S., Obergfell, K. P., Berg, N., Bijonowski, B. M., et al. (2015). Optimization and Critical Evaluation of Decellularization Strategies to Develop Renal Extracellular Matrix Scaffolds as Biological Templates for Organ Engineering and Transplantation. *Am. J. Transplant.* 15 (1), 64–75. doi:10.1111/ajt.12999

Cheng, J., Wang, C., and Gu, Y. (2019). Combination of Freeze-Thaw with Detergents: A Promising Approach to the Decellularization of Porcine Carotid Arteries. *Bme* 30 (2), 191–205. doi:10.3233/bme-191044

Choi, J. S., Williams, J. K., Greven, M., Walter, K. A., Laber, P. W., Khang, G., et al. (2010). Bioengineering Endothelialized Neo-Corneas Using Donor-Derived Corneal Endothelial Cells and Decellularized Corneal Stroma. *Biomaterials* 31 (26), 6738–6745. doi:10.1016/j.biomaterials.2010.05.020

Chou, P.-R., Lin, Y.-N., Wu, S.-H., Lin, S.-D., Srinivasan, P., Hsieh, D.-J., et al. (2020). Supercritical Carbon Dioxide-Decellularized Porcine Acellular Dermal Matrix Combined with Autologous Adipose-Derived Stem Cells: its Role in Accelerated Diabetic Wound Healing. *Int. J. Med. Sci.* 17 (3), 354–367. doi:10.7150/ijms.41155

Choudhury, D., Anand, S., and Naing, M. W. (2018). The Arrival of Commercial Bioprinters - towards 3D Bioprinting Revolution! *Int. J. Bioprint* 4 (2), 139. doi:10.18063/IJB.v4i2.139

Choudhury, D., Yee, M., Sheng, Z. L. J., Amirul, A., and Naing, M. W. (2020). Decellularization Systems and Devices: State-Of-The-Art Review. *Acta Biomater.* 115, 51–59. doi:10.1016/j.actbio.2020.07.060

Cornelison, R. C., Wellman, S. M., Park, J. H., Porvasnik, S. L., Song, Y. H., Wachs, R. A., et al. (2018). Development of an Apoptosis-Assisted Decellularization Method for Maximal Preservation of Nerve Tissue Structure. *Acta Biomater.* 77, 116–126. doi:10.1016/j.actbio.2018.07.009

Coutu, D. L., Mahfouz, W., Loutochin, O., Galipeau, J., and Corcos, J. (2014). Tissue Engineering of Rat Bladder Using Marrow-Derived Mesenchymal Stem Cells and Bladder Acellular Matrix. *PLoS One* 9 (12), e111966. doi:10.1371/journal.pone.0111966

Crapo, P. M., Gilbert, T. W., and Badylak, S. F. (2011). An Overview of Tissue and Whole Organ Decellularization Processes. *Biomaterials* 32 (12), 3233–3243. doi:10.1016/j.biomaterials.2011.01.057

Cui, H., Chai, Y., and Yu, Y. (2019). Progress in Developing Decellularized Bioscaffolds for Enhancing Skin Construction. *J. Biomed. Mater. Res. A.* 107 (8), 1849–1859. doi:10.1002/jbm.a.36688

da Mata Martins, T. M., da Silva Cunha, P., Rodrigues, M. A., de Carvalho, J. L., de Souza, J. E., de Carvalho Oliveira, J. A., et al. (2020). Epithelial Basement Membrane of Human Decellularized Cornea as a Suitable Substrate for Differentiation of Embryonic Stem Cells into Corneal Epithelial-like Cells. *Mater. Sci. Eng. C* 116, 111215. doi:10.1016/j.msec.2020.111215

Damodaran, R., and Vermette, P. (2018). Tissue and Organ Decellularization in Regenerative Medicine. *Biotechnol. Prog.* 34 (6), 1494–1505. doi:10.1002/btpr.2699

Daryabari, S. S., Kajbafzadeh, A.-M., Fendereski, K., Ghorbani, F., Dehnavi, M., Rostami, M., et al. (2019). Development of an Efficient Perfusion-Based Protocol for Whole-Organ Decellularization of the Ovine Uterus as a Human-Sized Model and *In Vivo* Application of the Bioscaffolds. *J. Assist. Reprod. Genet.* 36 (6), 1211–1223. doi:10.1007/s10815-019-01463-4

De Cock, L. J., De Koker, S., De Vos, F., Vervaet, C., Remon, J.-P., and De Geest, B. G. (2010). Layer-by-layer Incorporation of Growth Factors in Decellularized Aortic Heart Valve Leaflets. *Biomacromolecules* 11 (4), 1002–1008. doi:10.1021/bm9014649

De Santis, M. M., Alsafadi, H. N., Tas, S., Bölükbas, D. A., Prithiviraj, S., Da Silva, I. A. N., et al. (2021). Extracellular-Matrix-Reinforced Bioinks for 3D Bioprinting Human Tissue. *Adv. Mater.* 33 (3), e2005476. doi:10.1002/adma.202005476

Deeken, C. R., White, A. K., Bachman, S. L., Ramshaw, B. J., Cleveland, D. S., Loy, T. S., et al. (2011). Method of Preparing a Decellularized Porcine Tendon Using Tributyl Phosphate. *J. Biomed. Mater. Res.* 96B (2), 199–206. doi:10.1002/jbm.b.31753

Denstedt, J., and Atala, A. (2009). *Biomaterials and Tissue Engineering in Urology*. Amsterdam, Netherlands: Elsevier.

Deuse, T., Hu, X., Gravina, A., Wang, D., Tediashvili, G., De, C., et al. (2019). Hypoimmunogenic Derivatives of Induced Pluripotent Stem Cells Evade Immune Rejection in Fully Immunocompetent Allogeneic Recipients. *Nat. Biotechnol.* 37 (3), 252–258. doi:10.1038/s41587-019-0016-3

Dew, L., English, W. R., Chong, C. K., and MacNeil, S. (2016). Investigating Neovascularization in Rat Decellularized Intestine: an *In Vitro* Platform for Studying Angiogenesis. *Tissue Eng. Part. A.* 22 (23-24), 1317–1326. doi:10.1089/ten.TEA.2016.0131

Dimitrievska, S., Cai, C., Weyers, A., Balestrini, J. L., Lin, T., Sundaram, S., et al. (2015). Click-coated, Heparinized, Decellularized Vascular Grafts. *Acta Biomater.* 13, 177–187. doi:10.1016/j.actbio.2014.11.015

Divya, D., Naik, S., Raju, O., Shivani, B., Basappa, N., and Betur, A. (2021). Conceptual Combination of Disinfection in Regenerative Endodontics: Conventional versus Laser-Assisted Disinfection. *J. Conserv Dent* 24 (3), 252–259. doi:10.4103/jcd.jcd_96_21

Du, P., Hwang, M. P., Noh, Y. K., Subbiah, R., Kim, I. G., Bae, S. E., et al. (2014). Fibroblast-derived Matrix (FDM) as a Novel Vascular Endothelial Growth Factor Delivery Platform. *J. Controlled Release* 194, 122–129. doi:10.1016/j.jconrel.2014.08.026

Duarte, M. M., Ribeiro, N., Silva, I. V., Dias, J. R., Alves, N. M., and Oliveira, A. L. (2021). Fast Decellularization Process Using Supercritical Carbon Dioxide for Trabecular Bone. *J. Supercrit. Fluids* 172, 105194. doi:10.1016/j.supflu.2021.105194

Dunne, L. W., Huang, Z., Meng, W., Fan, X., Zhang, N., Zhang, Q., et al. (2014). Human Decellularized Adipose Tissue Scaffold as a Model for Breast Cancer Cell Growth and Drug Treatments. *Biomaterials* 35 (18), 4940–4949. doi:10.1016/j.biomaterials.2014.03.003

Ebrahimkhani, M. R., and Levin, M. (2021). Synthetic Living Machines: A New Window on Life. *Iscience* 24, 102505. doi:10.1016/j.isci.2021.102505

Eltom, A., Zhong, G., and Muhammad, A. (2019). Scaffold Techniques and Designs in Tissue Engineering Functions and Purposes: A Review. *Adv. Mater. Sci. Eng.* 2019, 3429527. doi:10.1155/2019/3429527

Engler, A. J., Sen, S., Sweeney, H. L., and Discher, D. E. (2006). Matrix Elasticity Directs Stem Cell Lineage Specification. *Cell* 126 (4), 677–689. doi:10.1016/j.cell.2006.06.044

Fernández-Pérez, J., and Ahearne, M. (2019). The Impact of Decellularization Methods on Extracellular Matrix Derived Hydrogels. *Sci. Rep.* 9 (1), 14933. doi:10.1038/s41598-019-49575-2

Fernández-Pérez, J., and Ahearne, M. (2019). The Impact of Decellularization Methods on Extracellular Matrix Derived Hydrogels. *Scientific Rep.* 9 (1), 1–12.

Ferng, A. S., Connell, A. M., Marsh, K. M., Qu, N., Medina, A. O., Bajaj, N., et al. (2017). Acellular Porcine Heart Matrices: Whole Organ Decellularization with 3D-Bioscaffold & Vascular Preservation. *J. Clin. Transl Res.* 3 (2), 260–270.

Ferreira, L. P., Gaspar, V. M., and Mano, J. F. (2020). Decellularized Extracellular Matrix for Bioengineering Physiomimetic 3D *In Vitro* Tumor Models. *Trends Biotechnol.* 38 (12), 1397–1414. doi:10.1016/j.tibtech.2020.04.006

Fidalgo, C., Iop, L., Sciro, M., Harder, M., Mavrilas, D., Korossis, S., et al. (2018). A Sterilization Method for Decellularized Xenogeneic Cardiovascular Scaffolds. *Acta Biomater.* 67, 282–294. doi:10.1016/j.actbio.2017.11.035

Figliuzzi, M., Bonandrini, B., and Remuzzi, A. (2017). Decellularized Kidney Matrix as Functional Material for Whole Organ Tissue Engineering. *J. Appl. Biomater. Funct. Mater.* 15 (4), e326–e333. doi:10.5301/jabfm.5000393

Fitzpatrick, L. E., and McDevitt, T. C. (2015). Cell-derived Matrices for Tissue Engineering and Regenerative Medicine Applications. *Biomater. Sci.* 3 (1), 12–24. doi:10.1039/c4bm00246f

Fitzpatrick, J. C., Clark, P. M., and Capaldi, F. M. (2008). Effect of Decellularization Protocol on the Mechanical Behavior of Porcine Descending Aorta. *Int. J. Biomater.* 2010, 620503. doi:10.1155/2010/620503

Forouzesh, F., Rabbani, M., and Bonakdar, S. (2019). A Comparison between Ultrasonic bath and Direct Sonicator on Osteochondral Tissue Decellularization. *J. Med. Signals Sens* 9 (4), 227–233. doi:10.4103/jmss.JMSS_64_18

Frantz, C., Stewart, K. M., and Weaver, V. M. (2010). The Extracellular Matrix at a Glance. *J. Cel. Sci.* 123 (24), 4195–4200. doi:10.1242/jcs.023820

Fu, Y., Fan, X., Chen, P., Shao, C., and Lu, W. (2010). Reconstruction of a Tissue-Engineered Cornea with Porcine Corneal Acellular Matrix as the Scaffold. *Cells Tissues Organs* 191 (3), 193–202. doi:10.1159/000235680

Fu, R. H., Wang, Y. C., Liu, S. P., Shih, T. R., Lin, H. L., Chen, Y. M., et al. (2014). Decellularization and Recellularization Technologies in Tissue Engineering. *Cel Transpl.* 23 (4-5), 621–630. doi:10.3727/096368914X678382

Funamoto, S., Nam, K., Kimura, T., Murakoshi, A., Hashimoto, Y., Niwaya, K., et al. (2010). The Use of High-Hydrostatic Pressure Treatment to Decellularize Blood Vessels. *Biomaterials* 31 (13), 3590–3595. doi:10.1016/j.biomaterials.2010.01.073

Gaetani, R., Aude, S., DeMaddalena, L. L., Strassle, H., Dzieciatkowska, M., Wortham, M., et al. (2018). Evaluation of Different Decellularization Protocols on the Generation of Pancreas-Derived Hydrogels. *Tissue Eng. C: Methods* 24 (12), 697–708. doi:10.1089/ten.tec.2018.0180

Ganjibakhsh, M., Mehraein, F., Koruji, M., Aflatoonian, R., and Farzaneh, P. (2019). Three-dimensional Decellularized Amnion Membrane Scaffold as a Novel Tool for Cancer Research; Cell Behavior, Drug Resistance and Cancer Stem Cell Content. *Mater. Sci. Eng. C* 100, 330–340. doi:10.1016/j.msec.2019.02.090

García-Gareta, E., Abduldaiem, Y., Sawadkar, P., Kyriakidis, C., Lali, F., and Greco, K. V. (2020). Decellularised Scaffolds: Just a Framework? Current Knowledge and Future Directions. *J. Tissue Eng.* 11, 2041731420942903. doi:10.1177/2041731420942903

Garreta, E., Oria, R., Tarantino, C., Pla-Roca, M., Prado, P., Fernández-Avilés, F., et al. (2017). Tissue Engineering by Decellularization and 3D Bioprinting. *Mater. Today* 20 (4), 166–178. doi:10.1016/j.mattod.2016.12.005

Ghodsizad, A., Bordel, V., Wiedensohler, H., Elbanayosy, A., Koerner, M. M., Gonzalez Berjon, J. M., et al. (2014). Magnetically Guided Recellularization of Decellularized Stented Porcine Pericardium-Derived Aortic Valve for TAVI. *ASAIO J.* 60 (5), 582–586. doi:10.1097/mat.0000000000000110

Ghorbani, F., Moradi, L., Shadmehr, M. B., Bonakdar, S., Droodinia, A., and Safshekan, F. (2017). In-vivo Characterization of a 3D Hybrid Scaffold Based on PCL/decellularized Aorta for Tracheal Tissue Engineering. *Mater. Sci. Eng. C* 81, 74–83. doi:10.1016/j.msec.2017.04.150

Gilbert, T. W., Sellaro, T. L., and Badylak, S. F. (2006). Decellularization of Tissues and Organs. *Biomaterials* 27 (19), 3675–3683. doi:10.1016/j.biomaterials.2006.02.014

Gilpin, A., and Yang, Y. (2017). Decellularization Strategies for Regenerative Medicine: from Processing Techniques to Applications. *Biomed. Res. Int.* 2017, 9831534. doi:10.1155/2017/9831534

Gilpin, S. E., Guyette, J. P., Gonzalez, G., Ren, X., Asara, J. M., Mathisen, D. J., et al. (2014). Perfusion Decellularization of Human and Porcine Lungs: Bringing the Matrix to Clinical Scale. *J. Heart Lung Transplant.* 33 (3), 298–308. doi:10.1016/j.healun.2013.10.030

Gilpin, S. E., Ren, X., Okamoto, T., Guyette, J. P., Mou, H., Rajagopal, J., et al. (2014). Enhanced Lung Epithelial Specification of Human Induced Pluripotent Stem Cells on Decellularized Lung Matrix. *Ann. Thorac. Surg.* 98 (5), 1721–1729. doi:10.1016/j.athoracsur.2014.05.080

Giraldo-Gomez, D. M., García-López, S. J., Tamay-de-Dios, L., Sánchez-Sánchez, R., Villalba-Caloca, J., Sotres-Vega, A., et al. (2019). Fast Cyclical-Decellularized Trachea as a Natural 3D Scaffold for Organ Engineering. *Mater. Sci. Eng. C.* 105, 110142. doi:10.1016/j.msec.2019.110142

Giuffrida, P., Curti, M., Al-Akkad, W., Biel, C., Crowley, C., Frenguelli, L., et al. (2019). Decellularized Human Gut as a Natural 3D Platform for Research in Intestinal Fibrosis. *Inflamm. Bowel Dis.* 25 (11), 1740–1750. doi:10.1093/ibd/izz115

Goktas, S., Matuska, A. M., Pierre, N., Gibson, T. M., Dmytryk, J. J., and McFetridge, P. S. (2014). Decellularization Method Influences Early Remodeling of an Allogenic Tissue Scaffold. *J. Biomed. Mater. Res.* 102 (1), 8–16. The Japanese Society for Biomaterials, and The Australian Society for Biomaterials and the Korean Society for Biomaterials. doi:10.1002/jbm.a.34692

Gong, W., Lei, D., Li, S., Huang, P., Qi, Q., Sun, Y., et al. (2016). Hybrid Small-Diameter Vascular Grafts: Anti-expansion Effect of Electrospun Poly ε-caprolactone on Heparin-Coated Decellularized Matrices. *Biomaterials* 76, 359–370. doi:10.1016/j.biomaterials.2015.10.066

Gosztyla, C., Ladd, M. R., Werts, A., Fulton, W., Johnson, B., Sodhi, C., et al. (2020). A Comparison of Sterilization Techniques for Production of Decellularized Intestine in Mice. *Tissue Eng. Part C: Methods* 26 (2), 67–79. doi:10.1089/ten.tec.2019.0219

Grauss, R., Hazekamp, M., Oppenhuizen, F., Vanmunsteren, C., Gittenbergerdegroot, A., and DeRuiter, M. (2005). Histological Evaluation of Decellularised Porcine Aortic Valves: Matrix Changes Due to Different Decellularisation Methods. *Eur. J. Cardio-Thoracic Surg.* 27 (4), 566–571. doi:10.1016/j.ejcts.2004.12.052

Gubareva, E. A., Sjöqvist, S., Gilevich, I. V., Sotnichenko, A. S., Kuevda, E. V., Lim, M. L., et al. (2016). Orthotopic Transplantation of a Tissue Engineered Diaphragm in Rats. *Biomaterials* 77, 320–335. doi:10.1016/j.biomaterials.2015.11.020

Gupta, S. K., Mishra, N. C., and Dhasmana, A. (2017). Decellularization Methods for Scaffold Fabrication. Decellularized Scaffolds and Organogenesis. *Methods Mol. Biol.* 1577, 1–10. doi:10.1007/7651_2017_34

Gupta, S. K., Mishra, N. C., and Dhasmana, A. (2018). "Decellularization Methods for Scaffold Fabrication," in *Decellularized Scaffolds and Organogenesis: Methods and Protocols*. Editor K. Turksen (New York, NY: Springer New York), 1–10.

Han, T. T. Y., Toutounji, S., Amsden, B. G., and Flynn, L. E. (2015). Adipose-derived Stromal Cells Mediate *In Vivo* Adipogenesis, Angiogenesis and Inflammation in Decellularized Adipose Tissue Bioscaffolds. *Biomaterials* 72, 125–137. doi:10.1016/j.biomaterials.2015.08.053

Heath, D. E. (2019). A Review of Decellularized Extracellular Matrix Biomaterials for Regenerative Engineering Applications. *Regen. Eng. Transl. Med.* 5 (2), 155–166. doi:10.1007/s40883-018-0080-0

Hellström, M., Moreno-Moya, J. M., Bandstein, S., Bom, E., Akouri, R. R., Miyazaki, K., et al. (2016). Bioengineered Uterine Tissue Supports Pregnancy in a Rat Model. *Fertil. Steril* 106 (2), 487–e1. doi:10.1016/j.fertnstert.2016.03.048

Hennessy, R. S., Jana, S., Tefft, B. J., Helder, M. R., Young, M. D., Hennessy, R. R., et al. (2017). Supercritical Carbon Dioxide-Based Sterilization of Decellularized Heart Valves. *JACC: Basic Translational Sci.* 2 (1), 71–84. doi:10.1016/j.jacbts.2016.08.009

Hou, N., Cui, P., Luo, J., Ma, R., and Zhu, L. (2011). Tissue-engineered Larynx Using Perfusion-Decellularized Technique and Mesenchymal Stem Cells in a Rabbit Model. *Acta oto-laryngologica* 131 (6), 645–652. doi:10.3109/00016489.2010.547517

Huang, H., Zhang, J., and Chu, H. (2007). Feasibility of Constructing Tissue-Engineered Corpus Cavernous Urethra with Rabbit Bone Marrow Mesenchymal Stem Cells. *Zhongguo Zuzhi Gongcheng Yanjiu Yu Linchuang Kangfu* 11, 2665–2668. doi:10.1016/j.biomaterials.2014.03.003

Huang, M., Li, N., Wu, Z., Wan, P., Liang, X., Zhang, W., et al. (2011). Using Acellular Porcine Limbal Stroma for Rabbit Limbal Stem Cell Microenvironment Reconstruction. *Biomaterials* 32 (31), 7812–7821. doi:10.1016/j.biomaterials.2011.07.012

Hudson, T. W., Liu, S. Y., and Schmidt, C. E. (2004). Engineering an Improved Acellular Nerve Graft via Optimized Chemical Processing. *Tissue Eng.* 10 (9-10), 1346–1358. doi:10.1089/ten.2004.10.1641

Huh, M. I., Lee, K. P., Kim, J., Yi, S., Park, B. U., and Kim, H. K. (2018). Generation of Femtosecond Laser-Cut Decellularized Corneal Lenticule Using Hypotonic Trypsin-EDTA Solution for Corneal Tissue Engineering. *J. Ophthalmol.* 2018, 2590536. doi:10.1155/2018/2590536

Hussein, K. H., Park, K.-M., Kang, K.-S., and Woo, H.-M. (2016). Biocompatibility Evaluation of Tissue-Engineered Decellularized Scaffolds for Biomedical Application. *Mater. Sci. Eng. C* 67, 766–778. doi:10.1016/j.msec.2016.05.068

Hussein, K. H., Saleh, T., Ahmed, E., Kwak, H.-H., Park, K.-M., Yang, S.-R., et al. (2018). Biocompatibility and Hemocompatibility of Efficiently Decellularized Whole Porcine Kidney for Tissue Engineering. *J. Biomed. Mater. Res.* 106 (7), 2034–2047. doi:10.1002/jbm.a.36407

Isidan, A., Liu, S., Li, P., Lashmet, M., Smith, L. J., Hara, H., et al. (2019). Decellularization Methods for Developing Porcine Corneal Xenografts and Future Perspectives. *Xenotransplantation* 26 (6), e12564. doi:10.1111/xen.12564

Islam, M. M., Sharifi, R., Mamodaly, S., Islam, R., Nahra, D., Abusamra, D. B., et al. (2019). Effects of Gamma Radiation Sterilization on the Structural and Biological Properties of Decellularized Corneal Xenografts. *Acta Biomater.* 96, 330–344. doi:10.1016/j.actbio.2019.07.002

Jamur, M. C., and Oliver, C. (2010). Cell Fixatives for Immunostaining. *Methods Mol. Biol.* 588, 55–61. doi:10.1007/978-1-59745-324-0_8

Ji, S., and Guvendiren, M. (2017). Recent Advances in Bioink Design for 3D Bioprinting of Tissues and Organs. *Front. Bioeng. Biotechnol.* 5, 23. doi:10.3389/fbioe.2017.00023

Johnson, C. M., Guo, D., Ryals, S., Postma, G. N., and Weinberger, P. M. (2017). The Feasibility of Gamma Radiation Sterilization for Decellularized Tracheal Grafts. *The Laryngoscope* 127 (8), E258–E264. doi:10.1002/lary.26367

Joszko, K., Gzik-Zroska, B., Kawlewska, E., Klama-Baryła, A., Suchoń, S., Burkacki, M., et al. (2019). Evaluation of the Impact of Decellularization and Sterilization on Tensile Strength Transgenic Porcinedermal Dressings. *Acta Bioeng. Biomech.* 21 (3), 87–97.

Kai, D., Jin, G., Prabhakaran, M. P., and Ramakrishna, S. (2013). Electrospun Synthetic and Natural Nanofibers for Regenerative Medicine and Stem Cells. *Biotechnol. J.* 8 (1), 59–72. doi:10.1002/biot.201200249

Kajbafzadeh, A.-M., Javan-Farazmand, N., Monajemzadeh, M., and Baghayee, A. (2013). Determining the Optimal Decellularization and Sterilization Protocol for Preparing a Tissue Scaffold of a Human-Sized Liver Tissue. *Tissue Eng. Part C: Methods* 19 (8), 642–651. doi:10.1089/ten.tec.2012.0334

Kajbafzadeh, A.-M., Khorramirouz, R., Nabavizadeh, B., Ladi Seyedian, S.-S., Akbarzadeh, A., Heidari, R., et al. (2019). Whole Organ Sheep Kidney Tissue Engineering and *In Vivo* Transplantation: Effects of Perfusion-Based Decellularization on Vascular Integrity. *Mater. Sci. Eng. C* 98, 392–400. doi:10.1016/j.msec.2019.01.018

Kajbafzadeh, A. M., Fendereski, K., Khorramirouz, R., Daryabari, S. S., Masoomi, A., Moosavi, S., et al. (2020). *In Vivo* application of Decellularized Rat colon and Evaluation of the Engineered Scaffolds Following 9 Months of Follow-up. *Cell Biol Int* 44 (11), 2253–2262. doi:10.1002/cbin.11433

Kao, C.-Y., Nguyen, H.-Q. -D., and Weng, Y.-C. (2020). Characterization of Porcine Urinary Bladder Matrix Hydrogels from Sodium Dodecyl Sulfate Decellularization Method. *Polymers* 12 (12), 3007. doi:10.3390/polym12123007

Kawecki, M., Łabuś, W., Klama-Baryla, A., Kitala, D., Kraut, M., Glik, J., et al. (2018). A Review of Decellurization Methods Caused by an Urgent Need for Quality Control of Cell-free Extracellular Matrix' Scaffolds and Their Role in Regenerative Medicine. *J. Biomed. Mater. Res.* 106 (2), 909–923. doi:10.1002/jbm.b.33865

Keane, T. J., Swinehart, I. T., and Badylak, S. F. (2015). Methods of Tissue Decellularization Used for Preparation of Biologic Scaffolds and *In Vivo* Relevance. *Methods* 84, 25–34. doi:10.1016/j.ymeth.2015.03.005

Kim, J. K., Koh, Y.-D., Kim, J. O., and Seo, D. H. (2016). Development of a Decellularization Method to Produce Nerve Allografts Using Less Invasive Detergents and Hyper/hypotonic Solutions. *J. Plast. Reconstr. Aesthet. Surg.* 69 (12), 1690–1696. doi:10.1016/j.bjps.2016.08.016

Kim, J., Koo, B.-K., and Knoblich, J. A. (2020). Human Organoids: Model Systems for Human Biology and Medicine. *Nat. Rev. Mol. Cel Biol* 21 (10), 571–584. doi:10.1038/s41580-020-0259-3

Komai, Y., and Ushiki, T. (1991). The Three-Dimensional Organization of Collagen Fibrils in the Human Cornea and Sclera. *Invest. Ophthalmol. Vis. Sci.* 32 (8), 2244–2258.

Kuevda, E. V., Gubareva, E. A., Sotnichenko, A. S., Gumenyuk, I. S., Gilevich, I. V., Polyakov, I. S., et al. (2016). Experience of Perfusion Recellularization of Biological Lung Scaffold in Rats. *Rjtao* 18 (1), 38–44. doi:10.15825/1995-1191-2016-1-38-44

Kuevda, E. V., Gubareva, E. A., Nakokhov, R. Z., Verevkin, A. A., and Puzanov, D. P. (2019). Obtaining and Characterization of Cells from Native Lung and Diaphragm Rat Tissues for Recellularization of Tissue Engineered Constructs. *Cell Tiss. Biol.* 13 (2), 136–143. doi:10.1134/s1990519x19020056

Kumar Kuna, V., Xu, B., and Sumitran-Holgersson, S. (2018). Decellularization and Recellularization Methodology for Human Saphenous Veins. *J. visualized experiments: JoVE.* (137), e57803. doi:10.3791/57803

Langer, R., and Vacanti, J. (2016). Advances in Tissue Engineering. *J. Pediatr. Surg.* 51 (1), 8–12. doi:10.1016/j.jpedsurg.2015.10.022

Lawson, J. H., Glickman, M. H., Ilzecki, M., Jakimowicz, T., Jaroszynski, A., Peden, E. K., et al. (2016). Bioengineered Human Acellular Vessels for Dialysis Access in Patients with End-Stage Renal Disease: Two Phase 2 Single-Arm Trials. *The Lancet* 387 (10032), 2026–2034. doi:10.1016/s0140-6736(16)00557-2

Lee, J., Hong, J., Kim, W., and Kim, G. H. (2020). Bone-derived dECM/alginate Bioink for Fabricating a 3D Cell-Laden Mesh Structure for Bone Tissue Engineering. *Carbohydr. Polym.* 250, 116914. doi:10.1016/j.carbpol.2020.116914

Liao, J., Joyce, E. M., and Sacks, M. S. (2008). Effects of Decellularization on the Mechanical and Structural Properties of the Porcine Aortic Valve Leaflet. *Biomaterials* 29 (8), 1065–1074. doi:10.1016/j.biomaterials.2007.11.007

Liao, J., Xu, B., Zhang, R., Fan, Y., Xie, H., and Li, X. (2020). Applications of Decellularized Materials in Tissue Engineering: Advantages, Drawbacks and Current Improvements, and Future Perspectives. *J. Mater. Chem. B* 8 (44), 10023–10049. doi:10.1039/d0tb01534b

Lichtenberg, A., Tudorache, I., Cebotari, S., Ringes-Lichtenberg, S., Sturz, G., Hoeffler, K., et al. (2006). *In Vitro* re-endothelialization of Detergent Decellularized Heart Valves under Simulated Physiological Dynamic Conditions. *Biomaterials* 27 (23), 4221–4229. doi:10.1016/j.biomaterials.2006.03.047

Lin, H. J., Wang, T. J., Li, T. W., Chang, Y. Y., Sheu, M. T., Huang, Y. Y., et al. (2019). Development of Decellularized Cornea by Organic Acid Treatment for Corneal Regeneration. *Tissue Eng. Part. A.* 25 (7-8), 652–662. doi:10.1089/ten.TEA.2018.0162

Liu, G., Wang, B., Li, S., Jin, Q., and Dai, Y. (2019). Human Breast Cancer Decellularized Scaffolds Promote Epithelial-to-mesenchymal Transitions and Stemness of Breast Cancer Cells *In Vitro*. *J. Cell Physiol.* 234 (6), 9447–9456. doi:10.1002/jcp.27630

Liu, K., He, Y., Yao, Y., Zhang, Y., Cai, Z., Ru, J., et al. (2021). Methoxy Polyethylene Glycol Modification Promotes Adipogenesis by Inducing the Production of Regulatory T Cells in Xenogeneic Acellular Adipose Matrix. *Mater. Today Bio* 12, 100161. doi:10.1016/j.mtbio.2021.100161

Liu, X., Yu, K., Cheng, S., Ren, T., Maitusong, M., Liu, F., et al. (2021). Ulvan Mediated VE Cadherin Antibody and REDV Peptide Co-modification to Improve Endothelialization Potential of Bioprosthetic Heart Valves. *Mater. Sci. Eng. C* 128, 112337. doi:10.1016/j.msec.2021.112337

Lopes Guimarães, L., Aparecida De Brito, A., Gonçalves Santos, T., Daronco Cereta, A., De Oliveira, L. V., Ligeiro De Oliveira, A. P., et al. (2020). Low-level Laser Boosts Extracellular Matrix Cues and Enhances Acellular Lung Scaffold Recellularization. *Eur. Respir. J.* 56 (Suppl. 64), 561. doi:10.1183/13993003.congress-2020.561

Lopresti, S. T., and Brown, B. N. (2015). "Host Response to Naturally Derived Biomaterials," in *Host Response to Biomaterials*. Editor F. Badylak (Cambridge, Massachusetts, United States: Academic Press), 53–79. doi:10.1016/b978-0-12-800196-7.00004-9

Lumpkins, S. B., Pierre, N., and McFetridge, P. S. (2008). A Mechanical Evaluation of Three Decellularization Methods in the Design of a Xenogeneic Scaffold for Tissue Engineering the Temporomandibular Joint Disc. *Acta Biomater.* 4 (4), 808–816. doi:10.1016/j.actbio.2008.01.016

Márquez, S. P., Martínez, V. S., Ambrose, W. M., Wang, J., Gantxegui, N. G., Schein, O., et al. (2009). Decellularization of Bovine Corneas for Tissue Engineering Applications. *Acta Biomater.* 5 (6), 1839–1847. doi:10.1016/j.actbio.2009.02.011

Martin, I., Wendt, D., and Heberer, M. (2004). The Role of Bioreactors in Tissue Engineering. *Trends. Biotechnol.* 22 (2), 80–86. doi:10.1016/j.tibtech.2003.12.001

Mattei, G., Magliaro, C., Pirone, A., and Ahluwalia, A. (2017). Decellularized Human Liver Is Too Heterogeneous for Designing a Generic Extracellular Matrix Mimic Hepatic Scaffold. *Artif. organs* 41 (12), E347–E355. doi:10.1111/aor.12925

Matuska, A. M., and McFetridge, P. S. (2018). Laser Micro-ablation of Fibrocartilage Tissue: Effects of Tissue Processing on Porosity Modification and Mechanics. *J. Biomed. Mater. Res.* 106 (5), 1858–1868. doi:10.1002/jbm.b.33997

McCrary, M. W., Bousalis, D., Mobini, S., Song, Y. H., and Schmidt, C. E. (2020). Decellularized Tissues as Platforms for *In Vitro* Modeling of Healthy and Diseased Tissues. *Acta Biomater.* 111, 1–19. doi:10.1016/j.actbio.2020.05.031

McCrary, M. W., Vaughn, N. E., Hlavac, N., Song, Y. H., Wachs, R. A., and Schmidt, C. E. (2020). Novel Sodium Deoxycholate-Based Chemical Decellularization Method for Peripheral Nerve. *Tissue Eng. Part C: Methods* 26 (1), 23–36. doi:10.1089/ten.tec.2019.0135

Mendez, J. J., Ghaedi, M., Steinbacher, D., and Niklason, L. E. (2014). Epithelial Cell Differentiation of Human Mesenchymal Stromal Cells in Decellularized Lung Scaffolds. *Tissue Eng. Part. A.* 20 (11-12), 1735–1746. doi:10.1089/ten.TEA.2013.0647

Mendibil, U., Ruiz-Hernandez, R., Retegi-Carrion, S., Garcia-Urquia, N., Olalde-Graells, B., and Abarrategi, A. (2020). Tissue-specific Decellularization Methods: Rationale and Strategies to Achieve Regenerative Compounds. *Ijms* 21 (15), 5447. doi:10.3390/ijms21155447

Mimler, T., Nebert, C., Eichmair, E., Winter, B., Aschacher, T., Stelzmueller, M.-E., et al. (2019). Extracellular Matrix in Ascending Aortic Aneurysms and Dissections - what We Learn from Decellularization and Scanning Electron Microscopy. *PLoS ONE* 14 (3), e0213794. doi:10.1371/journal.pone.0213794

Montoya, C. V., and McFetridge, P. S. (2009). Preparation of Ex Vivo-Based Biomaterials Using Convective Flow Decellularization. *Tissue Eng. Part C: Methods* 15 (2), 191–200. doi:10.1089/ten.tec.2008.0372

Moradi, L., Mohammadi Jobania, B., Jafarnezhad-Ansariha, F., Ghorbani, F., Esmaeil-Pour, R., Majidi Zolbina, M., et al. (2020). Evaluation of Different Sterilization Methods for Decellularized Kidney Tissue. *Tissue and Cell* 66, 101396. doi:10.1016/j.tice.2020.101396

Moradi, L., Mohammadi Jobania, B., Jafarnezhad-Ansariha, F., Ghorbani, F., Esmaeil-Pour, R., Majidi Zolbina, M., et al. (2020). Evaluation of Different Sterilization Methods for Decellularized Kidney Tissue. *Tissue and Cell* 66, 101396. doi:10.1016/j.tice.2020.101396

Morris, A. H., Lee, H., Xing, H., Stamer, D. K., Tan, M., and Kyriakides, T. R. (2018). Tunable Hydrogels Derived from Genetically Engineered Extracellular Matrix Accelerate Diabetic Wound Healing. *ACS Appl. Mater. Inter.* 10 (49), 41892–41901. doi:10.1021/acsami.8b08920

Moser, P. T., and Ott, H. C. (2014). Recellularization of Organs. *Curr. Opin. Organ Transplant.* 19 (6), 603–609. doi:10.1097/mot.0000000000000131

Mullarky, M. B., Norris, C. W., and Goldberg, I. D. (1985). The Efficacy of the Co2 Laser in the Sterilization of Skin Seeded with Bacteria. *The Laryngoscope* 95 (2), 186–187. doi:10.1288/00005537-198502000-00011

Naik, A., Griffin, M., Szarko, M., and Butler, P. E. (2020). Optimizing the Decellularization Process of an Upper Limb Skeletal Muscle; Implications for Muscle Tissue Engineering. *Artif. Organs* 44 (2), 178–183. doi:10.1111/aor.13575

Nakayama, K. H., Lee, C. C. I., Batchelder, C. A., and Tarantal, A. F. (2013). Tissue Specificity of Decellularized Rhesus Monkey Kidney and Lung Scaffolds. *PLoS ONE* 8 (5), e64134. doi:10.1371/journal.pone.0064134

Nam, J., Huang, Y., Agarwal, S., and Lannutti, J. (2007). Improved Cellular Infiltration in Electrospun Fiber via Engineered Porosity. *Tissue Eng.* 13 (9), 2249–2257. doi:10.1089/ten.2006.0306

Nammour, S., and Majerus, P. (1991). Sterilization Potential of the CO2 Laser. *Acta Stomatol Belg.* 88 (4), 183–186.

Oliveira, A. C., Garzón, I., Ionescu, A. M., Carriel, V., Cardona, J. d. l. C., González-Andrades, M., et al. (2013). Evaluation of Small Intestine Grafts Decellularization Methods for Corneal Tissue Engineering. *PLoS ONE* 8 (6), e66538. doi:10.1371/journal.pone.0066538

O'Neill, J. D., Anfang, R., Anandappa, A., Costa, J., Javidfar, J., Wobma, H. M., et al. (2013). Decellularization of Human and Porcine Lung Tissues for Pulmonary Tissue Engineering. *Ann. Thorac. Surg.* 96 (3), 1046–1056. doi:10.1016/j.athoracsur.2013.04.022

Ozasa, Y., Amadio, P. C., Thoreson, A. R., An, K.-N., and Zhao, C. (2013). The Effect of Surface Modification on Gliding Ability of Decellularized Flexor Tendon in a Canine Model *In Vitro*. *J. Hand Surg.* 38 (9), 1698–1704. doi:10.1016/j.jhsa.2013.05.023

Papadimitropoulos, A., Scotti, C., Bourgine, P., Scherberich, A., and Martin, I. (2015). Engineered Decellularized Matrices to Instruct Bone Regeneration Processes. *Bone* 70, 66–72. doi:10.1016/j.bone.2014.09.007

Partington, L., Mordan, N. J., Mason, C., Knowles, J. C., Kim, H.-W., Lowdell, M. W., et al. (2013). Biochemical Changes Caused by Decellularization May Compromise Mechanical Integrity of Tracheal Scaffolds. *Acta Biomater.* 9 (2), 5251–5261. doi:10.1016/j.actbio.2012.10.004

Peng, X., Kristi, N., Gafur, A., Wang, J., Wang, G., and Ye, Z. (2019). Micromechanical Property Analyses of Decellularized Vessels by Atomic Force Microscopy. *J. Phys. D: Appl. Phys.* 52 (42), 425401. doi:10.1088/1361-6463/ab33ce

Philips, C., Campos, F., Roosens, A., Sánchez-Quevedo, M. d. C., Declercq, H., and Carriel, V. (2018). Qualitative and Quantitative Evaluation of a Novel Detergent-Based Method for Decellularization of Peripheral Nerves. *Ann. Biomed. Eng.* 46 (11), 1921–1937. doi:10.1007/s10439-018-2082-y

Philips, C., Campos, F., Roosens, A., Sánchez-Quevedo, M. d. C., Declercq, H., and Carriel, V. (2018). Qualitative and Quantitative Evaluation of a Novel Detergent-Based Method for Decellularization of Peripheral Nerves. *Ann. Biomed. Eng.* 46 (11), 1921–1937. doi:10.1007/s10439-018-2082-y

Pina, S., Ribeiro, V. P., Marques, C. F., Maia, F. R., Silva, T. H., Reis, R. L., et al. (2019). Scaffolding Strategies for Tissue Engineering and Regenerative Medicine Applications. *Materials (Basel)* 12 (11), 1824. doi:10.3390/ma12111824

Pinto, M. L., Rios, E., Silva, A. C., Neves, S. C., Caires, H. R., Pinto, A. T., et al. (2017). Decellularized Human Colorectal Cancer Matrices Polarize Macrophages towards an Anti-inflammatory Phenotype Promoting Cancer Cell Invasion via CCL18. *Biomaterials* 124, 211–224. doi:10.1016/j.biomaterials.2017.02.004

Poornejad, N., Schaumann, L. B., Buckmiller, E. M., Momtahan, N., Gassman, J. R., Ma, H. H., et al. (2016). The Impact of Decellularization Agents on Renal Tissue Extracellular Matrix. *J. Biomater. Appl.* 31 (4), 521–533. doi:10.1177/0885328216656099

Pors, S. E., Ramløse, M., Nikiforov, D., Lundsgaard, K., Cheng, J., Andersen, C. Y., et al. (2019). Initial Steps in Reconstruction of the Human Ovary: Survival of Pre-antral Stage Follicles in a Decellularized Human Ovarian Scaffold. *Hum. Reprod.* 34 (8), 1523–1535. doi:10.1093/humrep/dez077

Porzionato, A., Stocco, E., Barbon, S., Grandi, F., Macchi, V., and De Caro, R. (2018). Tissue-engineered Grafts from Human Decellularized Extracellular Matrices: a Systematic Review and Future Perspectives. *Ijms* 19 (12), 4117. doi:10.3390/ijms19124117

Pouliot, R. A., Young, B. M., Link, P. A., Park, H. E., Kahn, A. R., Shankar, K., et al. (2020). Porcine Lung-Derived Extracellular Matrix Hydrogel Properties Are Dependent on Pepsin Digestion Time. *Tissue Eng. Part C: Methods* 26 (6), 332–346. doi:10.1089/ten.tec.2020.0042

Prasertsung, I., Kanokpanont, S., Bunaprasert, T., Thanakit, V., and Damrongsakkul, S. (2008). Development of Acellular Dermis from Porcine Skin Using Periodic Pressurized Technique. *J. Biomed. Mater. Res.* 85B (1), 210–219. The Japanese Society for Biomaterials, and The Australian Society for Biomaterials and the Korean Society for Biomaterials. doi:10.1002/jbm.b.30938

Pulver, S. A., Leybovich, B., Artyuhov, I., Maleev, Y., and Peregudov, A. (2014). Production of Organ Extracellular Matrix Using a Freeze-Thaw Cycle Employing Extracellular Cryoprotectants. *Cryo Lett.* 35 (5), 400–406.

Qiu, S., Rao, Z., He, F., Wang, T., Xu, Y., Du, Z., et al. (2020). Decellularized Nerve Matrix Hydrogel and Glial-derived Neurotrophic Factor Modifications Assisted Nerve Repair with Decellularized Nerve Matrix Scaffolds. *J. Tissue Eng. Regen. Med.* 14 (7), 931–943. doi:10.1002/term.3050

Rabbani, M., Zakian, N., and Alimoradi, N. (2021). Contribution of Physical Methods in Decellularization of Animal Tissues. *J. Med. Signals Sens* 11 (1), 1–11. doi:10.4103/jmss.jmss_2_20

Rahman, S., Griffin, M., Naik, A., Szarko, M., and Butler, P. E. (2018). Optimising the Decellularization of Human Elastic Cartilage with Trypsin for Future Use in Ear Reconstruction. *Sci. Rep.* 8 (1), 1–11. doi:10.1038/s41598-018-20592-x

Reing, J. E., Brown, B. N., Daly, K. A., Freund, J. M., Gilbert, T. W., Hsiong, S. X., et al. (2010). The Effects of Processing Methods upon Mechanical and Biologic Properties of Porcine Dermal Extracellular Matrix Scaffolds. *Biomaterials* 31 (33), 8626–8633. doi:10.1016/j.biomaterials.2010.07.083

Reyna, W. E., Pichika, R., Ludvig, D., and Perreault, E. J. (2020). Efficiency of Skeletal Muscle Decellularization Methods and Their Effects on the Extracellular Matrix. *J. Biomech.* 110, 109961. doi:10.1016/j.jbiomech.2020.109961

Rieder, E., Kasimir, M.-T., Silberhumer, G., Seebacher, G., Wolner, E., Simon, P., et al. (2004). Decellularization Protocols of Porcine Heart Valves Differ Importantly in Efficiency of Cell Removal and Susceptibility of the Matrix to Recellularization with Human Vascular Cells. *J. Thorac. Cardiovasc. Surg.* 127 (2), 399–405. doi:10.1016/j.jtcvs.2003.06.017

Robertson, M. J., Dries-Devlin, J. L., Kren, S. M., Burchfield, J. S., and Taylor, D. A. (2014). Optimizing Recellularization of Whole Decellularized Heart Extracellular Matrix. *PloS one* 9 (2), e90406. doi:10.1371/journal.pone.0090406

Roth, S. P., Glauche, S. M., Plenge, A., Erbe, I., Heller, S., and Burk, J. (2017). Automated Freeze-Thaw Cycles for Decellularization of Tendon Tissue - a Pilot Study. *BMC Biotechnol.* 17 (1), 13–10. doi:10.1186/s12896-017-0329-6

Sabetkish, S., Kajbafzadeh, A.-M., Sabetkish, N., Khorramirouz, R., Akbarzadeh, A., Seyedian, S. L., et al. (2015). Whole-organ Tissue Engineering: Decellularization and Recellularization of Three-Dimensional Matrix Liver Scaffolds. *J. Biomed. Mater. Res.* 103 (4), 1498–1508. doi:10.1002/jbm.a.35291

Sabetkish, S., Kajbafzadeh, A.-M., and Sabetkish, N. (2021). Recellularization of Testicular Feminization Testis in C57bl6 as a Natural Bioreactor for Creation of Cellularized Seminiferous Tubules: an Experimental Study. *Cell Tissue Bank* 22 (2), 287–295. doi:10.1007/s10561-020-09877-6

Saldin, L. T., Cramer, M. C., Velankar, S. S., White, L. J., and Badylak, S. F. (2017). Extracellular Matrix Hydrogels from Decellularized Tissues: Structure and Function. *Acta Biomater.* 49, 1–15. doi:10.1016/j.actbio.2016.11.068

Saleh, T., Ahmed, E., Yu, L., Kwak, H.-H., Kang, B.-J., Park, K.-M., et al. (2019). Characterization of Silver Nanoparticle-Modified Decellularized Rat Esophagus for Esophageal Tissue Engineering: Structural Properties and Biocompatibility. *J. Biosci. Bioeng.* 128 (5), 613–621. doi:10.1016/j.jbiosc.2019.04.017

Sant, S., Wang, D., Abidi, M., Walker, G., and Ferrell, N. (2021). Mechanical Characterization of Native and Sugar-Modified Decellularized Kidneys. *J. Mech. Behav. Biomed. Mater.* 114, 104220. doi:10.1016/j.jmbbm.2020.104220

Scarrit, M. E., Pashos, N. C., and Bunnell, B. A. (2015). A Review of Cellularization Strategies for Tissue Engineering of Whole Organs. *Front. Bioeng. Biotechnol.* 3, 43. doi:10.3389/fbioe.2015.00043

Schenke-Layland, K., Rofail, F., Heydarkhan, S., Gluck, J. M., Ingle, N. P., Angelis, E., et al. (2009). The Use of Three-Dimensional Nanostructures to Instruct Cells to Produce Extracellular Matrix for Regenerative Medicine Strategies. *Biomaterials* 30 (27), 4665–4675. doi:10.1016/j.biomaterials.2009.05.033

Schneider, K. H., Rohringer, S., Kapeller, B., Grasl, C., Kiss, H., Heber, S., et al. (2020). Riboflavin-mediated Photooxidation to Improve the Characteristics of Decellularized Human Arterial Small Diameter Vascular Grafts. *Acta Biomater.* 116, 246–258. doi:10.1016/j.actbio.2020.08.037

Selden, C., and Fuller, B. (2018). Role of Bioreactor Technology in Tissue Engineering for Clinical Use and Therapeutic Target Design. *Bioengineering* 5 (2), 32. doi:10.3390/bioengineering5020032

Shafiee, A., and Atala, A. (2017). Tissue Engineering: toward a new era of Medicine. *Annu. Rev. Med.* 68, 29–40. doi:10.1146/annurev-med-102715-092331

Shen, Q., Goderie, S. K., Jin, L., Karanth, N., Sun, Y., Abramova, N., et al. (2004). Endothelial Cells Stimulate Self-Renewal and Expand Neurogenesis of Neural Stem Cells. *science* 304 (5675), 1338–1340. doi:10.1126/science.1095505

Sheridan, W. S., Duffy, G. P., and Murphy, B. P. (2012). Mechanical Characterization of a Customized Decellularized Scaffold for Vascular Tissue Engineering. *J. Mech. Behav. Biomed. Mater.* 8, 58–70. doi:10.1016/j.jmbbm.2011.12.003

Shevach, M., Fleischer, S., Shapira, A., and Dvir, T. (2014). Gold Nanoparticle-Decellularized Matrix Hybrids for Cardiac Tissue Engineering. *Nano Lett.* 14 (10), 5792–5796. doi:10.1021/nl502673m

Simmons, A. D., Williams, C., III, Degoix, A., and Sikavitsas, V. I. (2017). Sensing Metabolites for the Monitoring of Tissue Engineered Construct Cellularity in Perfusion Bioreactors. *Biosens. Bioelectron.* 90, 443–449. doi:10.1016/j.bios.2016.09.094

Simsa, R., Padma, A. M., Heher, P., Hellström, M., Teuschl, A., Jenndahl, L., et al. (2018). Systematic *In Vitro* Comparison of Decellularization Protocols for Blood Vessels. *PLoS One* 13 (12), e0209269. doi:10.1371/journal.pone.0209269

Simsa, R., Vila, X. M., Salzer, E., Teuschl, A., Jenndahl, L., Bergh, N., et al. (2019). Effect of Fluid Dynamics on Decellularization Efficacy and Mechanical Properties of Blood Vessels. *PLoS ONE* 14 (8), e0220743. doi:10.1371/journal.pone.0220743

Smith, M. J., Dempsey, S. G., Veale, R. W., Duston-Fursman, C. G., Rayner, C. A. F., Javanapong, C., et al. (2022). Further Structural Characterization of Ovine Forestomach Matrix and Multi-Layered Extracellular Matrix Composites for Soft Tissue Repair. *J. Biomater. Appl.* 36 (6), 996–1010. doi:10.1177/08853282211045770

Soltani Khaboushan, A., Shakibaei, M., Kajbafzadeh, A-M., and Majidi Zolbin, M. (2021). Prenatal Neural Tube Anomalies: A Decade of Intrauterine Stem Cell Transplantation Using Advanced Tissue Engineering Methods. *Stem Cel Rev. Rep.* 18, 1–16. doi:10.1007/s12015-021-10150-w

Song, J. J., Guyette, J. P., Gilpin, S. E., Gonzalez, G., Vacanti, J. P., and Ott, H. C. (2013). Regeneration and Experimental Orthotopic Transplantation of a Bioengineered Kidney. *Nat. Med.* 19 (5), 646–651. doi:10.1038/nm.3154

Song, Y. H., Maynes, M. A., Hlavac, N., Visosevic, D., Daramola, K. O., Porvasnik, S. L., et al. (2021). Development of Novel Apoptosis-Assisted Lung Tissue Decellularization Methods. *Biomater. Sci.* 9 (9), 3485–3498. doi:10.1039/d1bm00032b

Starnecker, F., König, F., Hagl, C., and Thierfelder, N. (2018). Tissue-engineering Acellular Scaffolds-The Significant Influence of Physical and Procedural Decellularization Factors. *J. Biomed. Mater. Res.* 106 (1), 153–162. doi:10.1002/jbm.b.33816

Stenn, K. S., Link, R., Moellmann, G., Madri, J., and Kuklinska, E. (1989). Dispase, a Neutral Protease from Bacillus Polymyxa, Is a Powerful Fibronectinase and Type IV Collagenase. *J. Invest. Dermatol.* 93 (2), 287–290. doi:10.1111/1523-1747.ep12277593

Su, J., Satchell, S. C., Shah, R. N., and Wertheim, J. A. (2018). Kidney Decellularized Extracellular Matrix Hydrogels: Rheological Characterization and Human Glomerular Endothelial Cell Response to Encapsulation. *J. Biomed. Mater. Res.* 106 (9), 2448–2462. doi:10.1002/jbm.a.36439

Tao, M., Ao, T., Mao, X., Yan, X., Javed, R., Hou, W., et al. (2021). Sterilization and Disinfection Methods for Decellularized Matrix Materials: Review, Consideration and Proposal. *Bioactive Mater.* 6 (9), 2927–2945. doi:10.1016/j.bioactmat.2021.02.010

Tenreiro, M. F., Almeida, H. V., Calmeiro, T., Fortunato, E., Ferreira, L., Alves, P. M., et al. (2021). Interindividual Heterogeneity Affects the Outcome of Human Cardiac Tissue Decellularization. *Sci. Rep.* 11 (1), 1–11. doi:10.1038/s41598-021-00226-5

Topuz, B., Günal, G., Guler, S., and Aydin, H. M. (2020). Use of Supercritical CO2 in Soft Tissue Decellularization. *Methods Cel. Biol.* 157, 49–79. doi:10.1016/bs.mcb.2019.10.012

Tsuchiya, T., Balestrini, J. L., Mendez, J., Calle, E. A., Zhao, L., and Niklason, L. E. (2014). Influence of pH on Extracellular Matrix Preservation during Lung Decellularization. *Tissue Eng. Part C: Methods* 20 (12), 1028–1036. doi:10.1089/ten.tec.2013.0492

Tsuchiya, T., Mendez, J., Calle, E. A., Hatachi, G., Doi, R., Zhao, L., et al. (2016). Ventilation-based Decellularization System of the Lung. *BioResearch open access* 5 (1), 118–126. doi:10.1089/biores.2016.0012

Tsuchiya, T., Mitsutake, N., Nishimura, S., Matsuu-Matsuyama, M., Nakazawa, Y., Ogi, T., et al. (2017). Transplantation of Bioengineered Rat Lungs Recellularized with Endothelial and Adipose-Derived Stromal Cells. *Sci. Rep.* 7 (1), 1–5. doi:10.1038/s41598-017-09115-2

Uday Chandrika, K., Tripathi, R., Kameshwari, Y., Rangaraj, N., Mahesh Kumar, J., and Singh, S. (2021). Refunctionalization of Decellularized Organ Scaffold of Pancreas by Recellularization: Whole Organ Regeneration into Functional Pancreas. *Tissue Eng. Regen. Med.* 18 (1), 99–112. doi:10.1007/s13770-020-00296-y

Uygun, B. E., Soto-Gutierrez, A., Yagi, H., Izamis, M.-L., Guzzardi, M. A., Shulman, C., et al. (2010). Organ Reengineering through Development of a Transplantable Recellularized Liver Graft Using Decellularized Liver Matrix. *Nat. Med.* 16 (7), 814–820. doi:10.1038/nm.2170

Vacanti, J. P., and Langer, R. (1999). Tissue Engineering: the Design and Fabrication of Living Replacement Devices for Surgical Reconstruction and Transplantation. *The lancet* 354, S32–S34. doi:10.1016/s0140-6736(99)90247-7

Versteegden, L. R. M., de Jonge, P. K. J. D., IntHout, J., van Kuppevelt, T. H., Oosterwijk, E., Feitz, W. F. J., et al. (2017). Tissue Engineering of the Urethra: a Systematic Review and Meta-Analysis of Preclinical and Clinical Studies. *Eur. Urol.* 72 (4), 594–606. doi:10.1016/j.eururo.2017.03.026

Walawalkar, S., and Almelkar, S. (2019). Fabrication of Aortic Bioprosthesis by Decellularization, Fibrin Glue Coating and Re-endothelization: a Cell Scaffold Approach. *Prog. Biomater.* 8 (3), 197–210. doi:10.1007/s40204-019-00122-2

Wang, L., Zhao, M., Li, S., Erasquin, U. J., Wang, H., Ren, L., et al. (2014). "Click" Immobilization of a VEGF-Mimetic Peptide on Decellularized Endothelial Extracellular Matrix to Enhance Angiogenesis. *ACS Appl. Mater. Inter.* 6 (11), 8401–8406. doi:10.1021/am501309d

Wang, Z., Mithieux, S. M., and Weiss, A. S. (2019). Fabrication Techniques for Vascular and Vascularized Tissue Engineering. *Adv. Healthc. Mater.* 8 (19), 1900742. doi:10.1002/adhm.201900742

Wang, Z., Han, L., Sun, T., Ma, J., Sun, S., Ma, L., et al. (2020). Extracellular Matrix Derived from Allogenic Decellularized Bone Marrow Mesenchymal Stem Cell Sheets for the Reconstruction of Osteochondral Defects in Rabbits. *Acta Biomater.* 118, 54–68. doi:10.1016/j.actbio.2020.10.022

Wasyłeczko, M., Sikorska, W., and Chwojnowski, A. (2020). Review of Synthetic and Hybrid Scaffolds in Cartilage Tissue Engineering. *Membranes (Basel)* 10 (11), 348. doi:10.3390/membranes10110348

Watanabe, N., Mizuno, M., Matsuda, J., Nakamura, N., Otabe, K., Katano, H., et al. (2019). Comparison of High-Hydrostatic-Pressure Decellularized versus Freeze-Thawed Porcine Menisci. *J. Orthop. Res.* 37 (11), 2466–2475. doi:10.1002/jor.24350

Wiles, K., Fishman, J. M., De Coppi, P., and Birchall, M. A. (2016). The Host Immune Response to Tissue-Engineered Organs: Current Problems and Future Directions. *Tissue Eng. B: Rev.* 22 (3), 208–219. doi:10.1089/ten.teb.2015.0376

Wilson, S. L., Sidney, L. E., Dunphy, S. E., Dua, H. S., and Hopkinson, A. (2016). Corneal Decellularization: A Method of Recycling Unsuitable Donor Tissue for Clinical Translation? *Curr. Eye Res.* 41 (6), 769–782. doi:10.3109/02713683.2015.1062114

Wishart, A. L., Conner, S. J., Guarin, J. R., Fatherree, J. P., Peng, Y., McGinn, R. A., et al. (2020). Decellularized Extracellular Matrix Scaffolds Identify Full-Length Collagen VI as a Driver of Breast Cancer Cell Invasion in Obesity and Metastasis. *Sci. Adv.* 6 (43), eabc3175. doi:10.1126/sciadv.abc3175

Wolf, M. T., Daly, K. A., Brennan-Pierce, E. P., Johnson, S. A., Carruthers, C. A., D'Amore, A., et al. (2012). A Hydrogel Derived from Decellularized Dermal Extracellular Matrix. *Biomaterials* 33 (29), 7028–7038. doi:10.1016/j.biomaterials.2012.06.051

Wolf, M. T., Dearth, C. L., Ranallo, C. A., LoPresti, S. T., Carey, L. E., Daly, K. A., et al. (2014). Macrophage Polarization in Response to ECM Coated Polypropylene Mesh. *Biomaterials* 35 (25), 6838–6849. doi:10.1016/j.biomaterials.2014.04.115

Wollmann, L., Suss, P., Mendonça, J., Luzia, C., Schittini, A., Rosa, G. W. X. D., et al. (2019). Characterization of Decellularized Human Pericardium for Tissue

Engineering and Regenerative Medicine Applications. *Arq Bras Cardiol.* 113, 11–17. doi:10.5935/abc.20190094

Woods, T., and Gratzer, P. F. (2005). Effectiveness of Three Extraction Techniques in the Development of a Decellularized Bone-Anterior Cruciate Ligament-Bone Graft. *Biomaterials* 26 (35), 7339–7349. doi:10.1016/j.biomaterials.2005.05.066

Wu, Z., Zhou, Y., Li, N., Huang, M., Duan, H., Ge, J., et al. (2009). The Use of Phospholipase A2 to Prepare Acellular Porcine Corneal Stroma as a Tissue Engineering Scaffold. *Biomaterials* 30 (21), 3513–3522. doi:10.1016/j.biomaterials.2009.03.003

Wu, Q., Li, Y., Wang, Y., Li, L., Jiang, X., Tang, J., et al. (2016). The Effect of Heparinized Decellularized Scaffolds on Angiogenic Capability. *J. Biomed. Mater. Res.* 104 (12), 3021–3030. doi:10.1002/jbm.a.35843

Xing, Q., Yates, K., Tahtinen, M., Shearier, E., Qian, Z., and Zhao, F. (2015). Decellularization of Fibroblast Cell Sheets for Natural Extracellular Matrix Scaffold Preparation. *Tissue Eng. Part C: Methods* 21 (1), 77–87. doi:10.1089/ten.tec.2013.0666

Yang, H., Atala, A., and Yoo, J. J. (2020). Kidney Regeneration Approaches for Translation. *World J. Urol.* 38 (9), 2075–2079. doi:10.1007/s00345-019-02999-x

Young, D. A., Ibrahim, D. O., Hu, D., and Christman, K. L. (2011). Injectable Hydrogel Scaffold from Decellularized Human Lipoaspirate. *Acta Biomater.* 7 (3), 1040–1049. doi:10.1016/j.actbio.2010.09.035

Yusof, F., Sha'ban, M., and Azhim, A. (2019). Development of Decellularized Meniscus Using Closed Sonication Treatment System: Potential Scaffolds for Orthopedics Tissue Engineering Applications. *Ijn* Vol. 14, 5491–5502. doi:10.2147/ijn.s207270

Zhang, X., Chen, X., Hong, H., Hu, R., Liu, J., and Liu, C. (2021). Decellularized Extracellular Matrix Scaffolds: Recent Trends and Emerging Strategies in Tissue Engineering. *Bioactive Mater.* 10, 15–31. doi:10.1016/j.bioactmat.2021.09.014

Zhao, Y., Zhang, S., Zhou, J., Wang, J., Zhen, M., Liu, Y., et al. (2010). The Development of a Tissue-Engineered Artery Using Decellularized Scaffold and Autologous Ovine Mesenchymal Stem Cells. *Biomaterials* 31 (2), 296–307. doi:10.1016/j.biomaterials.2009.09.049

Zheng, X.-F., Lu, S.-B., Zhang, W.-G., Liu, S.-Y., Huang, J.-X., and Guo, Q.-Y. (2011). Mesenchymal Stem Cells on a Decellularized Cartilage Matrix for Cartilage Tissue Engineering. *Biotechnol. Bioproc. E* 16 (3), 593–602. doi:10.1007/s12257-010-0348-9

Zhou, J., Fritze, O., Schleicher, M., Wendel, H.-P., Schenke-Layland, K., Harasztosi, C., et al. (2010). Impact of Heart Valve Decellularization on 3-D Ultrastructure, Immunogenicity and Thrombogenicity. *Biomaterials* 31 (9), 2549–2554. doi:10.1016/j.biomaterials.2009.11.088

Zvarova, B., Uhl, F. E., Uriarte, J. J., Borg, Z. D., Coffey, A. L., Bonenfant, N. R., et al. (2016). Residual Detergent Detection Method for Nondestructive Cytocompatibility Evaluation of Decellularized Whole Lung Scaffolds. *Tissue Eng. Part C: Methods* 22 (5), 418–428. doi:10.1089/ten.tec.2015.0439

Conflict of Interest: The authors declare that the research was conducted in the absence of any commercial or financial relationships that could be construed as a potential conflict of interest.

Publisher's Note: All claims expressed in this article are solely those of the authors and do not necessarily represent those of their affiliated organizations, or those of the publisher, the editors and the reviewers. Any product that may be evaluated in this article, or claim that may be made by its manufacturer, is not guaranteed or endorsed by the publisher.

Copyright © 2022 Neishabouri, Soltani Khaboushan, Daghigh, Kajbafzadeh and Majidi Zolbin. This is an open-access article distributed under the terms of the Creative Commons Attribution License (CC BY). The use, distribution or reproduction in other forums is permitted, provided the original author(s) and the copyright owner(s) are credited and that the original publication in this journal is cited, in accordance with accepted academic practice. No use, distribution or reproduction is permitted which does not comply with these terms.

GLOSSARY

ECM extracellular matrix
dECM decellularized extracellular matrix
3D three-dimensional
GAG glycosaminoglycans
SDS sodium dodecyl sulfate
SD sodium deoxycholate
SB sulfobetaine
TnBP tri (n-butyl) phosphate
CHAPS 3-[(3-cholamidopropyl)dimethylammonio]-1-propanesulfonate
DNase deoxyribonuclease
EGTA ethylene glycol tetraacetic acid
EDTA ethylenediaminetetraacetic acid
PAA peracetic acid
RNase ribonuclease
UV ultraviolet
MTT 3-(4, 5-dimethylthiazol-2-yl)-2, 5-diphenyltetrazolium bromide
dsDNA double-stranded DNA
H&E hematoxylin and eosin
DAPI 4',6-diamidino-2-phenylindole
SEM scanning electron microscope
TEM transmission electron microscopy
IHC immunohistochemistry
MSCs mesenchymal stem cells
AFM atomic force microscopy
VEGF vascular endothelial growth factor
POC poly(octamethylene citrate)
SIS small intestinal submucosa
ADSCs adipose-derived stem cells
DAMP damage associated molecular pattern
TIPS thermal-induced phase separation
Au gold
NP nanoparticle
Ag silver
PLGA poly lactic-co-glycolic acid
bFGF basic fibroblast growth factor
iPSCs induced pluripotent stem cells
ESCs embryonic stem cells
HSCs hematopoietic stem cells
BM-MSCs bone marrow-derived mesenchymal stem cells

frontiers | Frontiers in Bioengineering and Biotechnology

ORIGINAL RESEARCH
published: 16 May 2022
doi: 10.3389/fbioe.2022.833244

Decellularization of Porcine Carotid Arteries: From the Vessel to the High-Quality Scaffold in Five Hours

*Maria Stefania Massaro[1], Petra Kochová[2], Richard Pálek[1,3], Jáchym Rosendorf[1,3], Lenka Červenková[1], Uta Dahmen[4], Václav Liška[1,3] and Vladimíra Moulisová[1]**

[1]Biomedical Center, Faculty of Medicine in Pilsen, Charles University, Pilsen, Czechia, [2]New Technologies for Information Society-NTIS, University of West Bohemia, Pilsen, Czechia, [3]Department of Surgery, Faculty of Medicine in Pilsen, Charles University, Pilsen, Czechia, [4]Experimental Transplantation Surgery, Department of General, Visceral and Vascular Surgery, University Hospital Jena, Jena, Germany

The use of biologically derived vessels as small-diameter vascular grafts in vascular diseases is currently intensely studied. Vessel decellularization provides a biocompatible scaffold with very low immunogenicity that avoids immunosuppression after transplantation. Good scaffold preservation is important as it facilitates successful cell repopulation. In addition, mechanical characteristics have to be carefully evaluated when the graft is intended to be used as an artery due to the high pressures the vessel is subjected to. Here, we present a new and fast decellularization protocol for porcine carotid arteries, followed by investigation of the quality of obtained vessel scaffolds in terms of maintenance of important extracellular matrix components, mechanical resistance, and compatibility with human endothelial cells. Our results evidence that our decellularization protocol minimally alters both the presence of scaffold proteins and their mechanical behavior and human endothelial cells could adhere to the scaffold *in vitro*. We conclude that if a suitable protocol is used, a high-quality decellularized arterial scaffold of non-human origin can be promptly obtained, having a great potential to be recellularized and used as an arterial graft in transplantation medicine.

Keywords: porcine carotid artery, optimized decellularization, scaffold quality, ECM proteins, endothelial cell adhesion, mechanical properties

OPEN ACCESS

Edited by:
Sotirios Korossis, Loughborough University, United Kingdom

Reviewed by:
Helen E. Berry, University of Leeds, United Kingdom
Martin L. Tomov, Emory University, United States

****Correspondence:***
Vladimíra Moulisová
vladimira.moulisova@lfp.cuni.cz

Specialty section:
This article was submitted to Biomaterials, a section of the journal Frontiers in Bioengineering and Biotechnology

Received: *10 December 2021*
Accepted: *06 April 2022*
Published: *16 May 2022*

Citation:
Massaro MS, Kochová P, Pálek R, Rosendorf J, Červenková L, Dahmen U, Liška V and Moulisová V (2022) Decellularization of Porcine Carotid Arteries: From the Vessel to the High-Quality Scaffold in Five Hours. Front. Bioeng. Biotechnol. 10:833244. doi: 10.3389/fbioe.2022.833244

1 INTRODUCTION

Significant progress has been made in the last 20 years on the development of treatments to resolve small-diameter vascular diseases. Nevertheless, there is still lack of standardized procedures (Conklin et al., 2002; Chandra and Anthony, 2019; Seiffert et al., 2021). Autologous vessels, the currently most used solution, are difficult to harvest and can cause problems at the harvesting site that are not really desirable for the patient (Nagaoka et al., 2014). The use of artificial grafts, which are made of polytetrafluoroethylene (PTFE) or polyethylene terephthalate (such as Dacron), causes infection risks (Carrabba and Madeddu 2018). Furthermore, artificial grafts in the small caliber scale are more likely to develop thrombosis because the material is not completely compatible with blood circulation. Smaller diameters increase the occlusion possibilities derived from surface-mediated platelet activation. The ideal solution would be a small-caliber biological matrix that enhances endothelial cell adhesion and growth, with the decellularized vessel being a very promising candidate.

Decellularized tissues have already been approved and are currently used for clinical applications (Parmaksiz et al., 2016). The advantage of decellularized scaffolds lies in the removal of immunogenic cellular components that allows limiting or even avoiding immunosuppression (Massaro et al., 2021a). Moreover, well-decellularized tissues retain the major proteins and extracellular matrix components. These proteins are a real gain in biologically derived scaffolds because they enhance cell adhesion and growth, fundamental characteristics in tissue regeneration and healing (Schmidt and Baier 2000). Decellularized small-diameter blood vessels are still under development in terms of xenogeneic species of origin, decellularization protocols, and cell seeding. The selection of a suitable donor species and a vessel type has to be carefully considered in terms of dimensions and availability of the graft. Previous studies have focused on the use of porcine (Sheridan et al., 2014; Gu et al., 2018; Cheng et al., 2019; Cai et al., 2020), ovine (Li et al., 2016; Ilanlou et al., 2019), and canine (Cai et al., 2009; Zhou et al., 2009) carotid arteries with an inner diameter around 5 mm or smaller. The research has already led to a commercial product from decellularized bovine carotid arteries called Artegraft (North Brunswick, NJ), with very promising results from a 5-year follow-up study (Lindsey et al., 2018).

Despite this, there are still issues linked to the use of such material related to the immunologic reaction caused by inefficient decellularization (Chemla and Morsy 2009) and the lack of standardized decellularization procedures to obtain a good scaffold quality in reasonable time.

All available decellularization protocols require procedures lasting way more than 24 h, mostly even days (Dahl et al., 2003; Roy et al., 2005; Dahan et al., 2012; Sheridan et al., 2012; López-Ruiz et al., 2017; Wang et al., 2017; Gu et al., 2018; Cai et al., 2019; Cheng et al., 2019; Cai et al., 2020). Ideally, the decellularization protocol should be as fast as possible, while keeping the ultrastructure intact. Successful recellularization depends on good preservation of the individual scaffold components and their protein conformation (Gilpin and Yang 2017), which is, in turn, pivotal in the active functionalization of the tissue in terms of fast recreation of the endothelial cell layer, lowering the risk of thrombosis in the graft.

Considering our ongoing work on the decellularization of porcine liver (Moulisová et al., 2020) and porcine caval veins (Massaro et al., 2021b), our aim was to address these issues by developing a faster decellularization protocol for porcine carotid arteries with higher flexibility in obtaining the tissue scaffold and resulting in an ECM scaffold of high quality at the same time.

2 MATERIALS AND METHODS

2.1 Experimental Design

The initial prerequisite for preparing a good-quality vessel scaffold through decellularization is to prevent any damage to the source tissue that would decrease the preservation of the ECM. Thus, all porcine carotid arteries were harvested from anesthetized animals at our surgical facility to obtain fresh tissues (**Figures 1A and B**). The vessels were either subjected to decellularization within 24 h, or mechanical testing within 3 h, or cryopreservation for long-term storage and later processing. Characterization of scaffolds after decellularization was performed by testing mechanical properties, by assessing the level of decellularization, and by identification of important ECM proteins by histological and immunofluorescence techniques. Finally, the cytocompatibility of the scaffolds was analyzed by seeding endothelial cells and by visualizing cells by H&E staining and immunofluorescence.

2.2 Tissue Harvesting and Storage

The left and right carotid arteries (n = 46) were extracted from healthy Prestice black-spotted pigs (n = 23) aged 2–3 months and weighing 30–40 kg. The animals were premedicated by intramuscular administration of 10 mg/kg ketamine (Spofa, a.s., Czech Republic), 5 mg/kg azaperon (Janssen Pharmaceutica NV, Belgium), and 1 mg atropine (Hoechst Biotika, Slovak Republic). Propofol (1% mixture 5–10 mg/kg/h) was used for general anesthesia (Fresenius Kabi Norges as, Norway) and fentanyl (1–2 μg/kg/h) (Chiesi CZ s.r.o., Czech Republic) for analgesia. The animals were intubated and mechanically ventilated. Carotid explantation was initiated by making two longitudinal incisions on both sides of the neck of the pig parallel to the sternomastoid muscles. Common carotid arteries were gently dissected from the level of the brachiocephalic trunk until the branching into internal and external carotid arteries (**Figure 1A**). The arteries were then resected in the whole length (**Figure 1B**) and used either as fresh (fresh native – FN, fresh decellularized – FD) or cryopreserved (cryopreserved native – CN, cryopreserved decellularized – CD) and stored at −80°C for at least 2 months.

Native vessels (FN) were kept in saline on wet ice and tested for mechanical properties for up to 3 h. The vessels to be decellularized (FD) were stored in sterile saline at 4°C overnight (up to 16 h), prior to decellularization. The vessels to be decellularized after the freezing step (CD) were stored in Dulbecco's modified Eagle medium (DMEM, Biosera Europe, France), supplemented with 10% fetal bovine serum (Biosera Europe, France), and 10% dimethyl sulfoxide (DMSO, Serva, Germany). Carotids tested as native after freezing (CN) were stored in saline supplemented with cryoprotective 10% DMSO. The samples to be cryopreserved were kept in Mr. Frosty™ Freezing Container (TermoFisher Scientific, MA, United States) at −80°C overnight, ensuring gradual cooling down (1°C/min), and then stored at −80°C for 2 months. The animals were euthanized under deep anesthesia with cardioplegic solution. All the procedures were performed under the approval MSMT-15629/2020-4 granted by the Ministry of Education, Youth and Sports of the Czech Republic, compliant with EU legislation. These animals were part of an approval for training of medical students in surgical techniques, and the carotid extraction took place immediately before euthanasia to maximize the use of animals in research in accordance with the 3Rs principle.

2.3 Decellularization Protocol

Freshly explanted vessels were stored in saline at 4°C and decellularized within 16 h, while cryopreserved vessels were

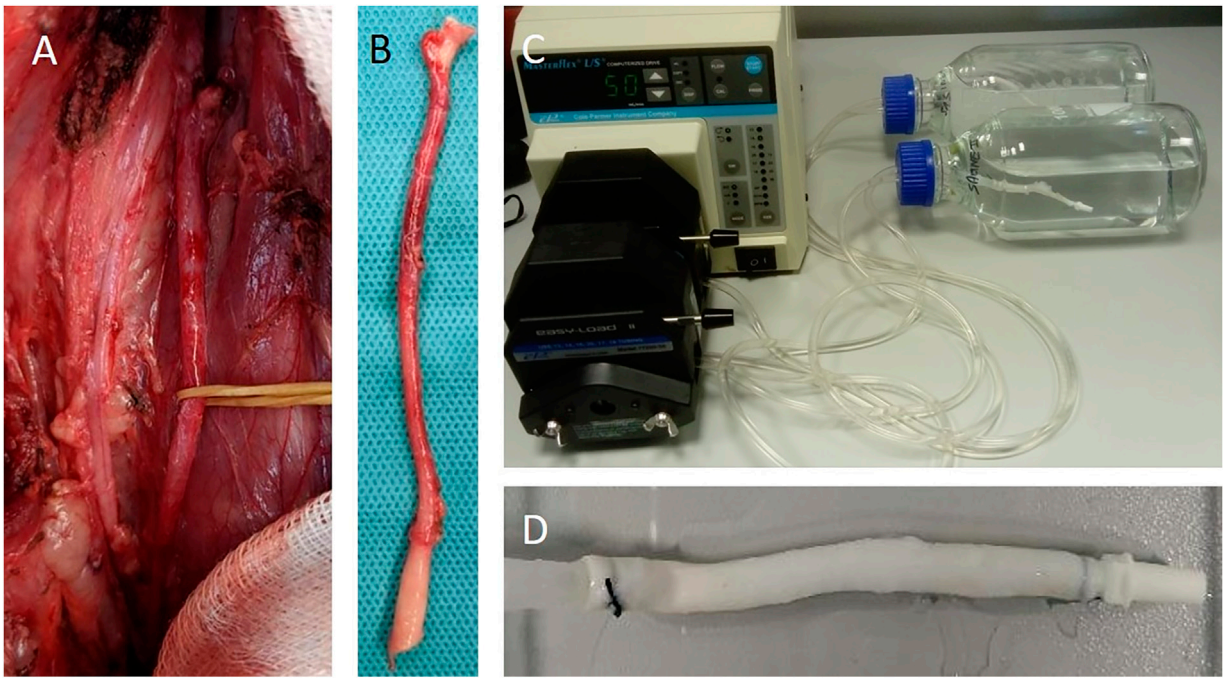

FIGURE 1 | Explant and decellularization of carotid arteries: **(A)** carotid artery identified in the animal before the explant, **(B)** explanted carotid artery – the proximal side is at the bottom of the picture, and it is identifiable by its higher diameter if compared to the distal part that has the branches for the internal and external carotid arteries. The decellularization setup is shown in **(C)**; the masterflex pump speed is set to 50, but its corresponding value depends on the tube type and dimensions; and in our case, it corresponds to 250 ml/min. The decellularized artery scaffold is shown in **(D)**. The arteries are explanted from the animals and then rather decellularized within 24 h or stored for the long term at –80°C in a cryoprotective solution.

stored for at least 2 months. At the time of decellularization, the vessels were thawed for 1 h at room temperature before starting the procedure. A 5-mm ring of the native artery from the proximal region was cut and fixed in 4% formaldehyde (Bamed s.r.o., Czech Republic) for histological comparison with the decellularized sample. The artery was then ligated at both ends to Luer connectors with a 3–0 Mersilk ligature (Ethicon Inc., NJ, United States) and connected to the decellularization setup consisting of flexible plastic tubing (Tygon S3, Saint Gobain, France). The two ends of the tubes were immersed in a glass bottle with a modified cap to allow the passage of the tubing. The tubing was inserted in a recirculating perfusion system driven by a peristaltic pump (Masterflex, Cole Parmer, IL, United States). The vessels were inserted while respecting the natural blood flow in the arteries from the proximal part toward the distal using a flow rate of 250 ml/min. The perfusion system is shown in **Figure 1C**, and the running saline cycle is documented in **Supplementary Video 1**. The first perfusion step was a saline wash for 10 min to clear the vessel of eventual blood clots and of the residues of cryoprotective solution in case of cryopreserved samples. Then, two successive perfusion cycles with 1% Triton X-100 solution for 1 h were applied, followed by two cycles of 1 h of 1% sodium dodecyl sulfate (SDS) solution. Both the detergent solutions were prepared by dissolving Triton X-100 (Carl Roth, Germany) and SDS pellets (Carl Roth, Germany) in sterile ultrapure deionized water (resulting pH for Triton X-100 and SDS solutions was 6 and 7, resp.). Finally, four consecutive washing steps lasting 15 min using saline were used to remove residual SDS from the scaffold. At the end of the procedure, the decellularized vessel was removed from the system, a 5-mm segment was harvested from the proximal region for histological evaluation, and the vessel was kept in a storing solution (PBS complemented with 1% penicillin/streptomycin and 0.2% amphotericin B (Cat. Nos. 15140122 and 15290018, respectively, Gibco, Paisley, United Kingdom)) at 4°C until further use. All the procedures were conducted under sterile conditions. For the *in vitro* assays, additional washing steps were applied to the scaffolds: The scaffold was added in a container with 100 ml of new solution used for storage and agitated for 24 h at room temperature. Then, the solution was changed, and the same wash was repeated to obtain a 2-day washed scaffold. By repeating this washing, a 4-day washed scaffold was prepared.

2.4 Histology and Immunofluorescence

Proximal parts of the arteries were fixed in neutral-buffered formalin (Bamed, Czech Republic), dehydrated in ethanol, and embedded in paraffin blocks. The tissue was cut to obtain 5-µm sections using a microtome (Leica RM2255, Germany). The sections were deparaffinized, rehydrated, and stained using six histological methods and four immunofluorescence (IF) stainings as described hereafter.

Hematoxylin and eosin (H&E) staining was used to assess the efficiency of decellularization in terms of the remaining nuclei in scaffolds decellularized from fresh tissue (freshly decellularized,

FD, n = 12) or after cryopreservation (cryopreserved decellularized, CD, n = 17). The number of samples differs between the two groups because while fresh samples were used only in mechanical testing, the cryopreserved arteries were used for both mechanical testing and endothelial cell seeding. A scoring system from 0 to 3 was introduced to quantify the decellularization efficacy; score 0 refers to complete decellularization, while score 3 means that less than 50% of the section area was decellularized (details in **Supplementary Table 1**). Whole slide images were processed in this analysis, and scans were generated on Zeiss Axioscan.

Verhoeff's hematoxylin with green trichrome staining (Kocová 1970) and *orcein staining* (Tanzer's orcein, Bowley Biochemical Inc., Danvers, MA, United States) were used to stain elastic fibers. *Picrosirius red staining* (Direct Red 80, Sigma-Aldrich, Germany) was used for visualization of collagen fibers in polarized light (Lattouf et al., 2014). *Standard Alcian blue staining* (pH 2.5) combined with periodic acid–Schiff (PAS) was used for the detection of both neutral mucins and acidic glycosaminoglycans (GAGs).

Immunofluorescence staining of paraffin sections was used to further characterize the completely decellularized matrix. Primary antibodies for *collagen I* (1:400, MA1-26771, Invitrogen, MA, United States), *elastin* (1:100; ab21610, Abcam, United Kingdom), *fibronectin* (1:200, ab6328, Abcam, United Kingdom), and *laminin* (1:30, L9393, Sigma-Aldrich, Germany) were selected. Goat anti-mouse AF 568 (1:200, A11004, Invitrogen, MA, United States) was used as a secondary antibody for collagen I and fibronectin, while chicken anti-rabbit AF 647 (1:200, A21443, Invitrogen, MA, United States) was used as a secondary antibody for elastin and laminin. For IF staining of samples from *in vitro* experiments, the whole formaldehyde-fixed vessel pieces were used (see **Section 2.7**). Cellular actin was detected using CruzFluor 488 phalloidin (1:1,000, Santa Cruz Biotechnologies, TX, United States), the cell nuclei were stained with 1 μM DAPI solution (Sigma-Aldrich, Germany), and the scaffold was visualized by staining with collagen I antibody in the same dilution as for the sections mentioned earlier. For imaging the sample surface with cells, the vessels were flattened on the microscopic slide using a coverslip. All IF images were obtained using a fluorescence microscope Olympus IX80 either at 10x or 20x magnification.

2.5 Mechanical Testing

To evaluate the effect of the decellularization procedure on the mechanical strength of the scaffold, the native non-decellularized vessels were compared with the decellularized arteries. To further characterize the scaffold, both fresh and cryopreserved tissues were tested. Four different groups of arteries were used: freshly explanted (fresh native, FN, n = 10), frozen native (cryopreserved native, CN, n = 8), decellularized from fresh tissue (fresh decellularized, FD, n = 8), and decellularized from frozen tissue (cryopreserved decellularized, CD, n = 6); the storage conditions are detailed in **Section 2.1**. The number of samples in each group was different due to processing and decellularization scores (only scaffolds with scores 0 and 1 were used). The FN samples were kept at 4°C for storage/transport and used within 3 h from the explant. The CN specimens were thawed in a water bath at 37°C for 10 min to reduce the damage due to potential recrystallization inside the cells (Amini et al., 2020). The arteries were allowed to assimilate to room temperature for 20 min before starting the mechanical measurement. Each vessel (total length was about 100 mm) was divided into three sections: distal, middle, and proximal. A detailed photo-documentation (Olympus camera) and measurement of the size and shape of the whole artery, artery segments, diameters, and rings were carried out. Larger specimens were pictured next to the ruler (**Supplementary Figure 1A**), whereas smaller artery segments and arterial rings were placed on graph paper (**Supplementary Figure 1B**). Pictures of arterial rings from the edges were used to directly assess the initial cross-sectional area of the artery using Ellipse software (ViDiTo Inc., Slovak Republic). Briefly, the picture was calibrated according to the graph paper (a square is equivalent to 1 × 1 mm), then the outer and inner diameters were manually annotated, followed by the calculation of circular areas (**Supplementary Figure 1C**). Finally, the initial artery cross-sectional area was calculated as the average of the difference between the area of the outer and inner circle of artery edges.

2.5.1 Determination of Opening Angle

After measuring the cross-sectional area, the rings were opened, and the opening angle was measured after 15 min incubation in saline. The opening angle was defined as the angle formed between two lines starting from the middle point of the inner layer and passing from the middle part of the wall in the opened region, as shown in the scheme in **Figure 6C**.

2.5.2 Determination of the Uniaxial Tensile Properties

For uniaxial mechanical tension tests, each sample was clamped with the jaws of the mechanical measurement device (574LE2, TestResources Inc., MN, United States). Ten cycles of stretching to 15% of the initial length were performed to precondition the arteries before the actual measurement was started. The test consisted of pulling on both ends. The initial length of the sample inside the jaws was 10 mm. Then, the samples were loaded with a linear increasing elongation until the tissue ruptured at 6 mm/min, which corresponds to 1% per second. The initial cross-sectional area for each individual segment and initial length was used to estimate the stress and strain of the samples. The stress (σ) was simply calculated as the ratio between the force detected by the load cell on the sample (F) and the initial cross-sectional area (A_0). The strain (ε) was the actual elongation (l) divided by the initial length value (l_0). Young's modulus (E) was calculated as the ratio between the stress and strain.

$$\sigma = \frac{F}{A_0}\,[MPa] \qquad \varepsilon = \frac{l - l_0}{l_0} \qquad E = \frac{\sigma}{\varepsilon}\,[MPa].$$

Given that in the stress–strain curve we can identify two main regions for soft tissues, Young's modulus is divided into E_0 and E_1, which represent the elastic and the viscoelastic behavior of the

sample, respectively. These regions correspond to a linear increase in the stress–strain curve.

2.6 SDS Residue Assay

The SDS amount in scaffold washing solutions was quantified using the Residual SDS Detection Kit (BioBasic Inc., Canada), following the manufacturer's protocol. Briefly, undiluted samples were mixed with solutions A and B, then vortexed for 30 s, left standing for 5 min at room temperature, and then centrifuged at 5,000 rpm for 5 min. The optical density of the sample supernatants and that of the standard solutions was measured at 499 nm using a Synergy HT microplate reader (Biotek, CA, United States). The final SDS concentration in the samples was obtained through a linear interpolation of the calibration curve derived from the optical density of standard SDS solutions. Each sample condition (after decellularization, 2-day wash, and 4-day wash) was an average of four different experiments, and the samples were tested in duplicates.

2.7 *In Vitro* Experiments

Human umbilical vein endothelial cells (HUVECs, PromoCell GmbH, Germany) and rat aorta endothelial cells (RAECs, obtained from the laboratory of Prof. Dahmen, Universitatklinikum Jena) were cultivated in Endothelial Cell Growth Medium (C-22010, PromoCell GmbH, Germany) and used at passages not higher than seven. Decellularized arteries after 2-day or 4-day washing (described in **Section 2.3**) were cut in half to expose the inner layer and then cut into smaller pieces (about 1 cm long). The scaffold pieces were placed in a 48-well plate, and 500 µl of cell suspension was dropped on the top of each sample at a seeding density of 10,000 cells/cm^2. The vessels were incubated in a humidified incubator at 37°C and 5% CO_2 for 24 h. Then, the samples were processed to assess cell viability using a Live/Dead Viability/Cytotoxicity kit (Invitrogen, L3224, MA, United States) according to the manufacturer's manual. For histochemical and immunofluorescence staining, the sample replicates were washed in phosphate-buffered saline (PBS), fixed in 4% formaldehyde (Bamed s.r.o., Czech Republic), and either embedded in paraffin for H&E staining (5 µm sections) or used as the whole sample for immunofluorescence staining for visualization of collagen I from the scaffold and cell cytoskeleton and DNA, as detailed in **Section 2.4**.

2.8 Statistical Analysis

The normality of individual data sets was tested using the Shapiro–Wilk's *W* test. Data sets with a normal distribution of values were analyzed using a two-way ANOVA test with Tukey's multiple comparison post-test. Data sets which did not pass the test for normality were analyzed using the Kruskal–Wallis test with Dunn's post-test to compare individual groups. GraphPad Prism 7.0 software (GraphPad Software Inc., CA, United States) was used for all statistical analyses. The decellularization score was analyzed using the Mann–Whitney test. The *p*-value representing a statistically significant difference was set at <0.05.

3. RESULTS

3.1 Decellularization

The decellularization was always performed by processing two vessels at the same time. The total time for achieving complete decellularization was 5 h and 10 min, with all the vessels turning white at this point (**Figure 1D**). Nevertheless, histological staining with H&E revealed that there were differences in the efficiency of decellularization. In some cases, the scaffold was completely decellularized, while in others, a specific area of the tunica media still contained nuclei. We introduced a scoring system based on the percentage of nuclei in the entire circular wall section. The score was set from 0 for completely decellularized up to 3 for more than 50% of the area still containing nuclei; for details, see **Supplementary Table 1**. Interestingly, arteries that were decellularized from the fresh tissue (FD) scored better in terms of complete or nearly complete decellularization (scores mainly 0 and 1), while vessels decellularized from the frozen tissue (CD) did not score that well (scores ranged between 0 – 3 with the majority of the values being 1 and 2). Statistical analysis revealed that this difference between CA decellularization protocols (fresh or frozen tissue used for decellularization) was significant, favoring the use of fresh tissue (**Supplementary Figure 2C**).

H&E and DAPI staining allowed us to visualize the nuclei and protein content in the native and decellularized carotids (**Figure 2A**). The variability among samples related to the different levels of decellularization is displayed in **Figures 2B,C**. There, the H&E staining shows the native artery section (left), a partially decellularized vessel that scored 2 (middle), and a completely decellularized scaffold scoring 0 (right). The purple-stained nuclei from H&E images corresponded with the DAPI-stained nuclei (**Figure 2D**). An overview of the CD and FD vessel scaffolds is given in **Supplementary Figures 2A and B**, respectively, highlighting the general morphological variability among animals.

The black color in Verhoeff's green trichrome staining evidenced the highly variable elastin content in decellularized samples (**Figure 3A**) and in native vessels. The elastin content of individual decellularized vessels corresponded to their native counterparts, meaning the decellularization protocol does not affect the presence of this protein. In contrast, it demonstrated the preservation of these fibers. We observed that elastic fibers were always present in the external elastic lamina and internal elastic lamina, while tunica media showed different amounts of elastic layers. Some samples were stained rather weakly (**Figure 3**, left column), while others showed strong staining of these multiple layers in parallel orientation (**Figure 3**, right column). To confirm the elastin presence, orcein staining was used to show elastin fibers in dark red (**Figure 3B**).

Collagen fibers were also mostly intact after the decellularization, as shown not only by pink color staining from H&E images (**Figures 2B and C**) but also by light green color in Verhoeff's green trichrome staining (**Figure 3**). Moreover, we used Picrosirius red staining imaged in polarized light to visualize birefringent collagen

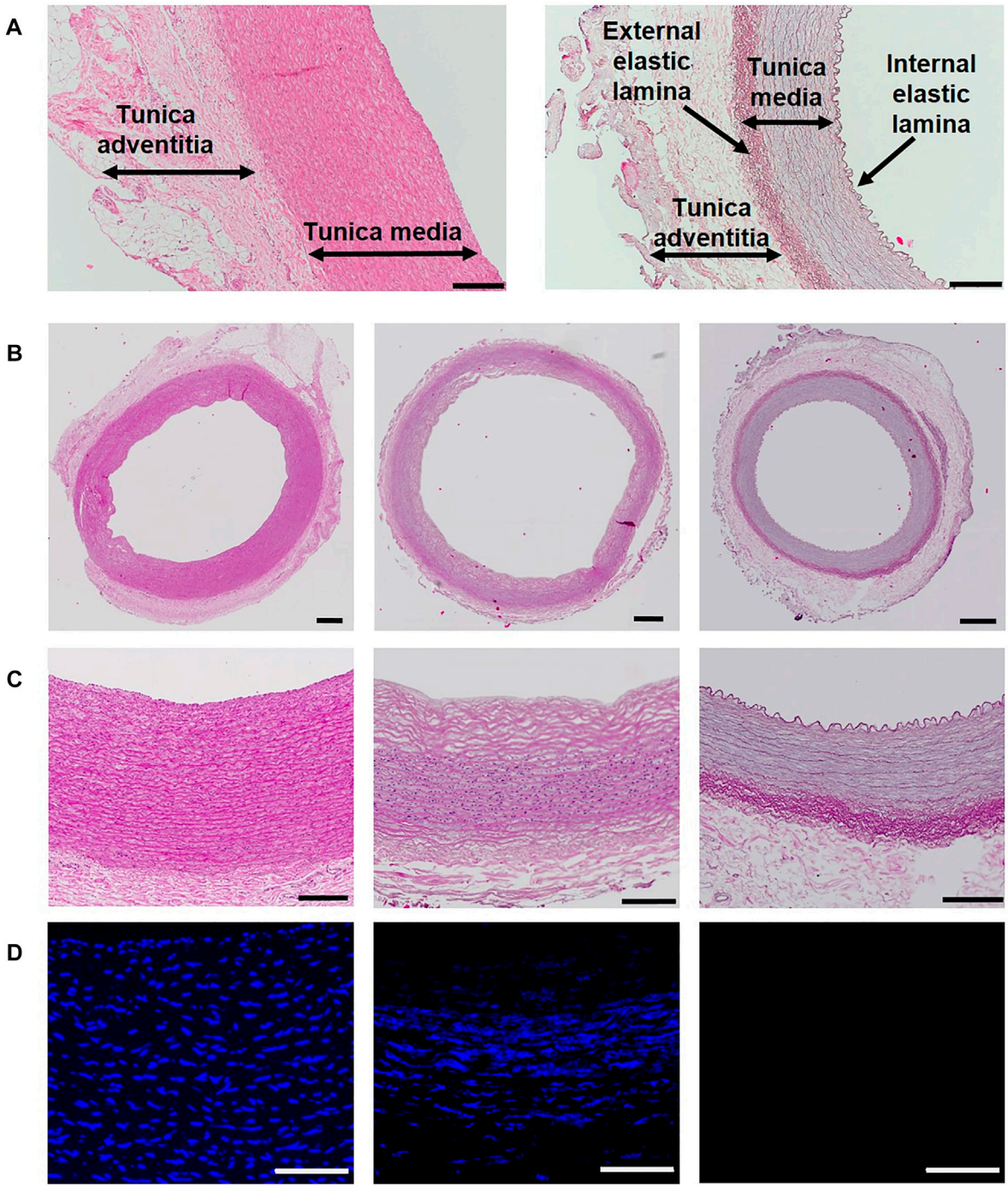

FIGURE 2 | Porcine coronary artery layers and evaluation of the decellularization efficacy: **(A)** detailed image of the native (left) and decellularized (right) carotid artery wall with the identification of the wall layers. It is evident that in the native vessel, the internal and external elastic laminas between each layer are indistinguishable, while they can be easily identified in the decellularized scaffold. The scale bar is 200 μm. **(B)** H&E staining of the entire section (native on the left, partially decellularized (score 2) in the middle and completely decellularized scaffold on the right) – scale bar is 500 μm; **(C)** details of the vessel wall from pictures in **(B)** to visualize the nuclei stained with hematoxylin – scale bar is 200 μm; **(D)** DAPI immunofluorescence at magnification ×40 showing nuclear loss in the middle picture and complete cell removal on the right side) scale bar is 100 μm.

molecules and reveal the presence of different collagen types in individual layers of the carotid artery (**Figure 4A**). The adventitia and external elastic lamina showed a strong yellow-red signal associated with collagen I, while tunica media had weaker staining with greenish color linked to collagen III (Junqueira et al., 1979).

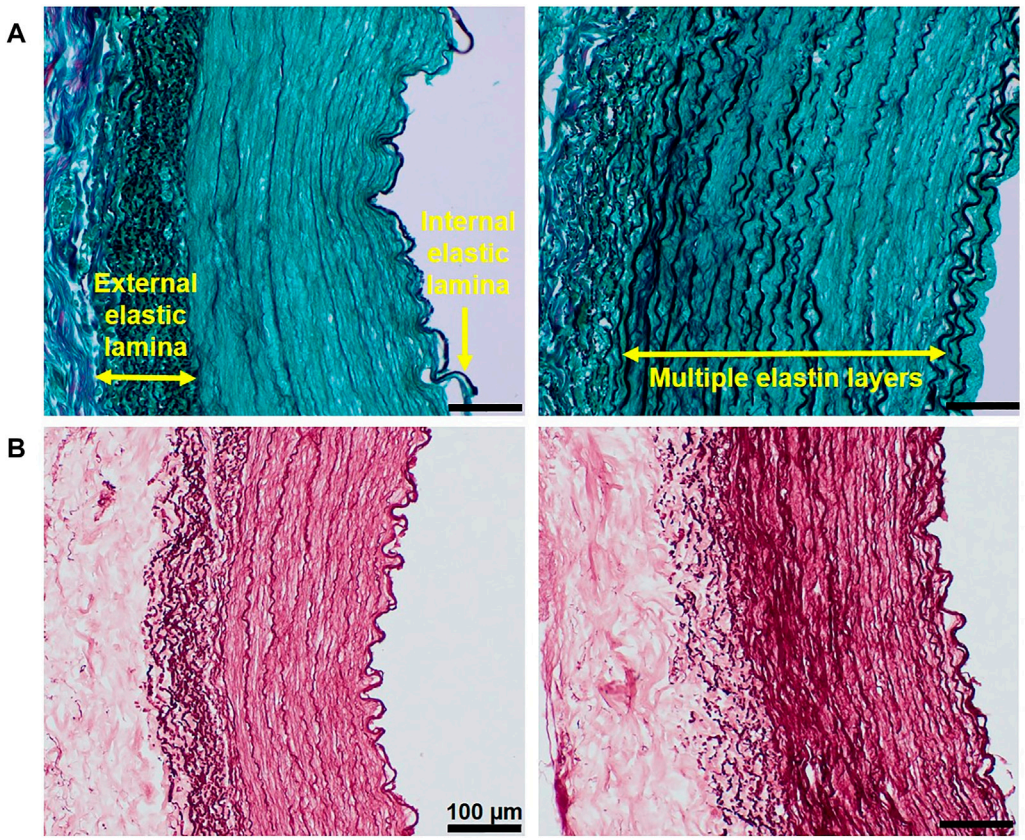

FIGURE 3 | Visualization of the highly variable presence of elastic fibers in decellularized arteries: Black color in Verhoeff's green trichrome–stained samples **(A)** and dark red color in orcein-stained samples **(B)** represent elastic fibers which are always present in external and internal elastic lamina; however, the amount of these fibers in tunica media is much lower in the sample on the left-hand side (weaker staining of elastic layers) than in the multiple elastic layers strongly stained in the sample on the right-hand side. The scale is the same for all the figures (100 µm).

In order to detect the presence of glycosaminoglycans (GAGs), which are important for non-structural functions of the ECM such as binding of various cytokines and growth factors (Gandhi and Mancera 2008), we used Alcian blue staining. The top image in **Figure 4B** shows a strong blue GAG staining in the tunica media of the native artery, whereas the adventitia contains almost no GAGs. The bottom image represents a typical example of a decellularized vessel and shows weaker GAG staining in the muscular tunica media in comparison to the native vessel. The loss of blue-stained GAGs after the decellularization can be associated with the removal of cells that have some GAGs bound on the membrane. We also cannot exclude that the detergents, particularly the SDS used for decellularization, could contribute to the reduction in GAG content in the ECM. Nevertheless, the level of blue staining in the decellularized vessel is still satisfactory to conclude that we have retention of some GAGs in the scaffold after decellularization.

To visualize specific ECM proteins such as collagen I, fibronectin, elastin, and laminin, we performed immunofluorescence staining. All four proteins were shown to withstand the decellularization procedure, as evidenced in the representative images of native and decellularized tissues in **Figures 5A-D**. Although collagen I is also stained by some of the abovementioned histological techniques, we still performed the extra IF staining for this protein. Histochemical collagen staining signals give more general information regarding the presence or absence of collagen but do not differentiate between the subtypes of collagen. In contrast, immunofluorescence visualizes individual specific collagen subtypes.

We also characterized the scaffold's ability to clear from detergent residues by SDS content assessment at different stages of washing. It is known that SDS detergent residues are cytotoxic for cells (Gilpin et al., 2014; Welch et al., 2021), with endothelial cells being particularly susceptible (Zvarova et al., 2016). As ECs are crucial for vessel repopulation, we analyzed the SDS concentration at the end of the decellularization procedure and after the application of several washing steps with PBS. As this scaffold characterization has a direct impact on cell culture, we show the SDS concentration data together with the *in vitro* results in **Section 3.3**.

3.2 Mechanical Testing

Maintaining the original mechanical properties is extremely important in the case of arterial grafts. Therefore, we paid

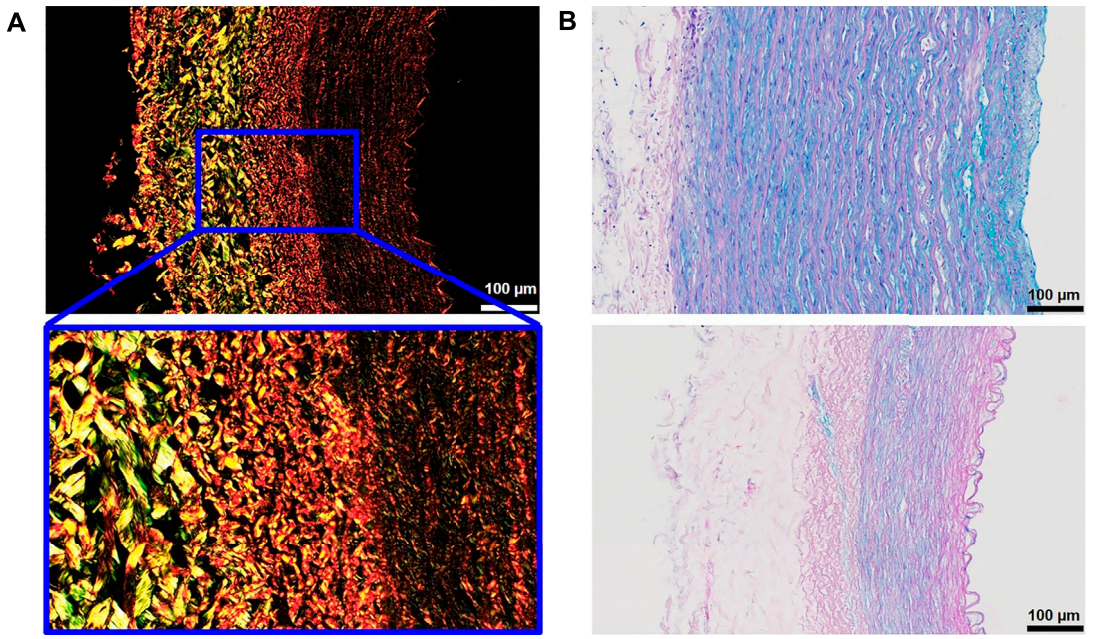

FIGURE 4 | Collagen and glycosaminoglycans (GAGs) in decellularized arteries. **(A)** Collagen fibers visualized by Picrosirius red staining in polarized light. **(B)** Alcian blue staining in native (top) and decellularized (bottom) tissue shows the presence of GAGs; the loss of blue staining in decellularized tissue can be caused by the removal of GAGs present within cells.

special attention to the mechanical testing of the vessel scaffolds. We compared the mechanical properties of native arteries with the decellularized ones. We tested both vessels and scaffolds processed either as fresh tissue or as thawed tissue after cryopreservation. Considering the different levels of decellularization of the vessels in this study, only fully decellularized or nearly fully decellularized scaffolds were analyzed (scores 0 and 1). Vessels scoring 2 and 3 were discarded from this analysis as the mechanical properties might be affected by the remaining cellular material. As shown by previous studies (Kochová et al., 2012; Tomášek et al., 2020), morphometric parameters and mechanical properties can significantly vary in different segments of the carotid artery; thus, we divided each vessel into three parts, namely, distal, middle, and proximal segments (**Figure 6A**). These segments were then tested and analyzed separately. In order to compare our results with other studies that did not consider variations between segments, we also analyzed the data obtained from individual arteries by merging the data from all three segments. **Supplementary Table 2** shows detailed values obtained during this analysis.

3.2.1 Determination of the Opening Angle

First, the opening angle test was performed for each vessel segment. A scheme of the experiment is shown in **Figure 6C**. As expected, the opening angle decreased with the decellularization procedure. Fresh native (FN) vessels and cryopreserved native (CN) arteries showed significantly larger opening angles than the freshly decellularized (FD) and cryopreserved decellularized (CD) tissues (**Figure 6D**). The opening angles varied neither between the native tissues (FN and CN) nor between the decellularized scaffolds (FD and CD). The mean angles were 60° ± 16 and 52° ± 23 for the native groups and 22° ± 18 and 24° ± 18 for the decellularized groups. Due to the data not passing the normality test, a nonparametric Kruskal–Wallis method with Dunn's post-test was used for statistical analysis.

Figure 6E shows the opening angle values for individual segments. The opening angle did not vary significantly between different regions (distal, middle, and proximal) within the same tested group. Values of 65° ± 19, 61° ± 17, and 55° ± 12 were obtained for FN segments in the three regions, respectively. In the same way, 46° ± 19, 44° ± 24, and 66° ± 22 were found for FS, 26° ± 5, 25° ± 23, and 12° ± 16 for FD, and 20° ± 12, 15° ± 17, and 37° ± 18 for SD. This set of data passed the normality test; thus, a two-way ANOVA test was used for statistical evaluation (using Tukey's multiple comparison post-test). These results from segment analysis were in agreement with the more general analysis of the opening angle values when all segments were analyzed together. The nonsignificant opening angles of the corresponding segments (native vs. decellularized) were most probably caused by the smaller number of individual measurements when analyzing the segments separately. Overall, the opening angle of tested tissues was not dependent on the individual region but rather on the analyzed group.

3.2.2 Determination of the Uniaxial Tensile Properties

Uniaxial tensile mechanical testing with the procedure depicted in **Figure 6B** showed a nonlinear behavior of the arteries as typical for biological tissues (Kubíková et al., 2017; Kochová et al.,

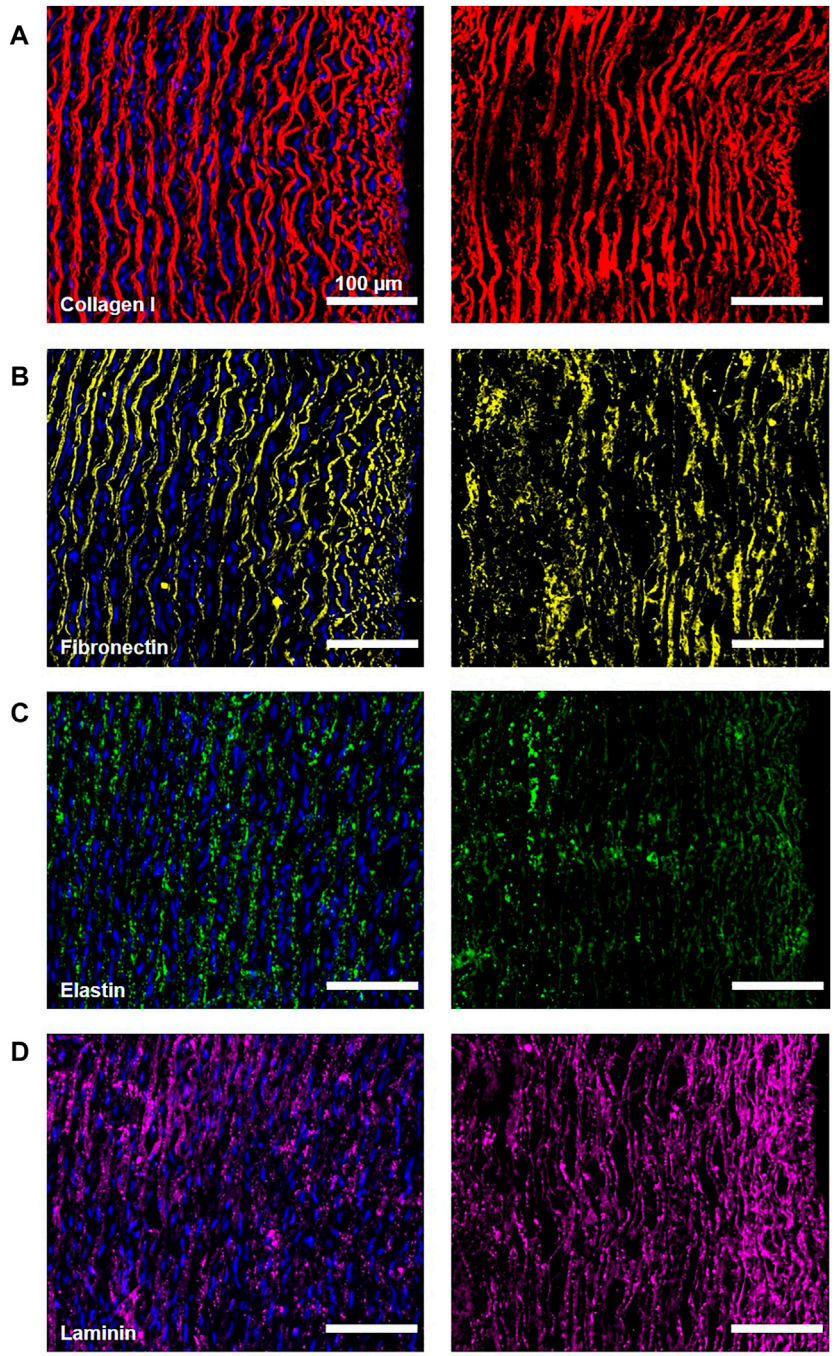

FIGURE 5 | ECM proteins in carotid arteries before (left) and after (right) the decellularization visualized by immunofluorescence. The vessel intima is always oriented on the right-hand side of the image. Collagen I is stained in red **(A)**, fibronectin in yellow **(B)**, elastin in green **(C)**, and laminin in magenta **(D)** (all artificially assigned colors). Blue DAPI shows nuclei in the native artery, while absence in decellularized tissue is indicative of complete cell removal. The scale bar is 100 µm for all the images.

2019). Representative examples of the stress–strain curves are given in **Figure 7A**, and examples for all the four groups divided between proximal, middle, and distal sections are shown in **Supplementary Figure 3**. In these curves, two linear regions can be identified for all samples: the small deformation region (elastic phase dominated by elastin, highlighted in blue) and the large deformation region (viscoelastic phase dominated by collagen, highlighted in red). While in the elastic phase, the material retains its initial properties, which can be restored if the load is removed; in the viscoelastic phase, the properties of the materials start to change until the ultimate stress is reached, and the sample is broken at the rupture point. For every sample, we

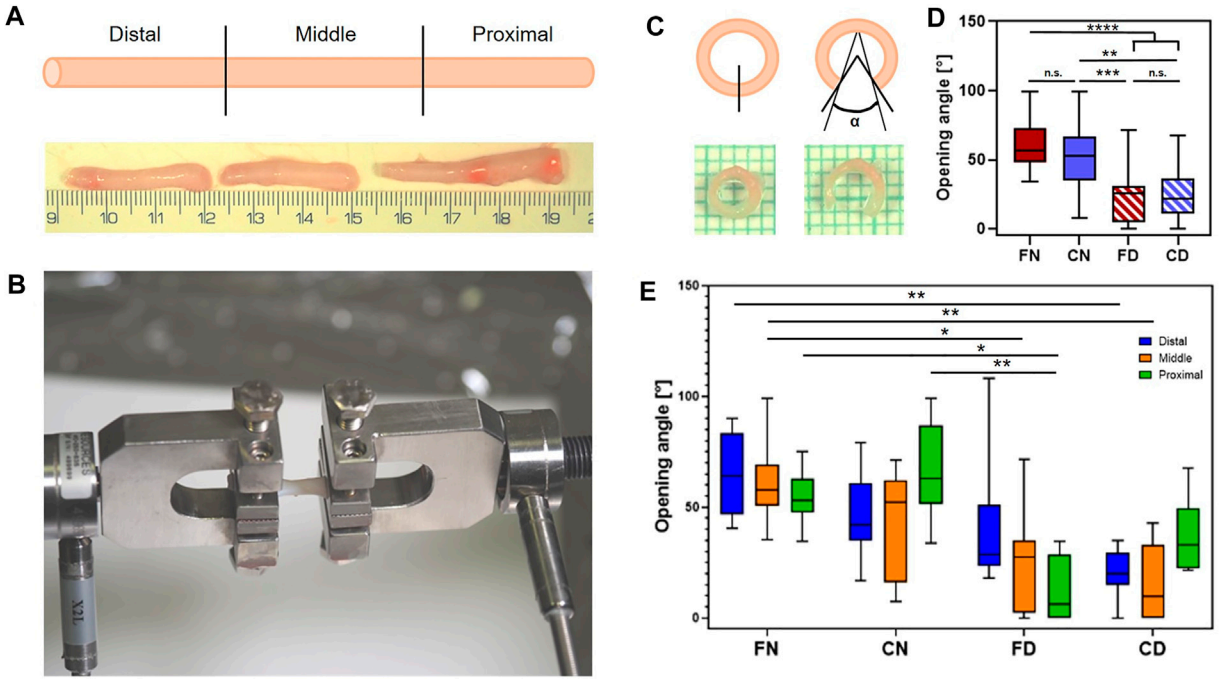

FIGURE 6 | Uniaxial tensile mechanical testing of native and decellularized vessels: **(A)** Scheme of the three sections of the artery (top) and image of a native artery after the division (bottom). **(B)** Image of the sample at the start of the load application (initial length is 10 mm); **(C)** scheme of the opening angle measurement (top) and image of the sample before (bottom left) and after (bottom right) incision; **(D)** boxplot of the opening angle for the four groups of fresh/frozen native artery or decellularized scaffold; **(E)** boxplot of the opening angle with a comparison between individual segments and the four groups. Abbreviations: FN, fresh native artery; CN, cryopreserved native artery; FD, freshly decellularized scaffold; CD, cryopreserved decellularized scaffold; level of significance is displayed as (*) for $p < 0.05$, (**) for $p < 0.01$, (***) for $p < 0.001$, and (****) for $p < 0,0001$.

obtained the following individual mechanical parameters: Young's modulus for both elastic phase (E_0) and viscoelastic phase (E_1) and ultimate stress and ultimate strain. These data were again analyzed for both the entire artery (**Figure 7B**) and three segments individually (**Figure 7C**).

3.2.2.1 Comparison of the Whole Vessel

In the general analysis of whole vessels, the datasets for Young's moduli E_0 and E_1 and for the ultimate stress did not have the normal Gaussian distribution; thus, the Kruskal–Wallis test was used for statistical evaluation. The ultimate strain dataset showed normal distribution and was analyzed by one-way ANOVA.

Young's modulus of the elastic phase (E_0) was significantly lower for scaffolds decellularized from fresh tissue (0.177 ± 0.181 MPa for FD and 0.264 ± 0.179 MPa for CD) than both groups of native arteries (0.403 ± 0.421 MPa for FN and 0.483 ± 0.556 MPa for CN), as visible in **Figure 7B** far left. This result suggests that some elastic components of the ECM might have been damaged during the decellularization procedure in this type of scaffold. However, this was not the case in scaffolds obtained from cryopreserved vessels. These scaffolds did not vary significantly from the native vessels, pointing out the good preservation of the elastic part of the ECM structure.

The values of Young's modulus of the viscoelastic phase (E_1) did not vary significantly between any sample groups, suggesting that the collagen structural components were not affected by the decellularization procedure (**Figure 7B**, middle-left). The values of 4.77 ± 3 MPa, 4.45 ± 3.55 MPa, 4.73 ± 3.93 MPa, and 6.09 ± 4.27 MPa were found for FN, CN, FD, and CD, respectively. The ultimate stress and ultimate strain resulted in similar values among the groups, with the only significant difference between cryopreserved samples CN and CD (with values of ultimate stress 1.38 ± 0.96 MPa for CN and 2.51 ± 1.46 MPa for CD and of ultimate strain 0.62 ± 0.32 for CN and 1.04 ± 0.37 for CD), as shown in **Figure 7B** middle-right and far-right. In these two cases, the values of ultimate stress and strain were surprisingly higher in decellularized samples than their native counterparts. The fact that the scaffold generated from cryopreserved tissue has slightly better mechanical properties than the native tissue that underwent a freeze–thaw cycle can be explained by a certain delay in the processing of the native vessel for the mechanical testing after thawing. The ECM of the CN vessel might be slightly damaged by enzymes released from the dead cells during the testing. The thawed vessels to be decellularized had always a shorter period of time between thawing and cell removal, leading to better preservation of the ECM. The ultimate stress and strain values of CD scaffolds actually

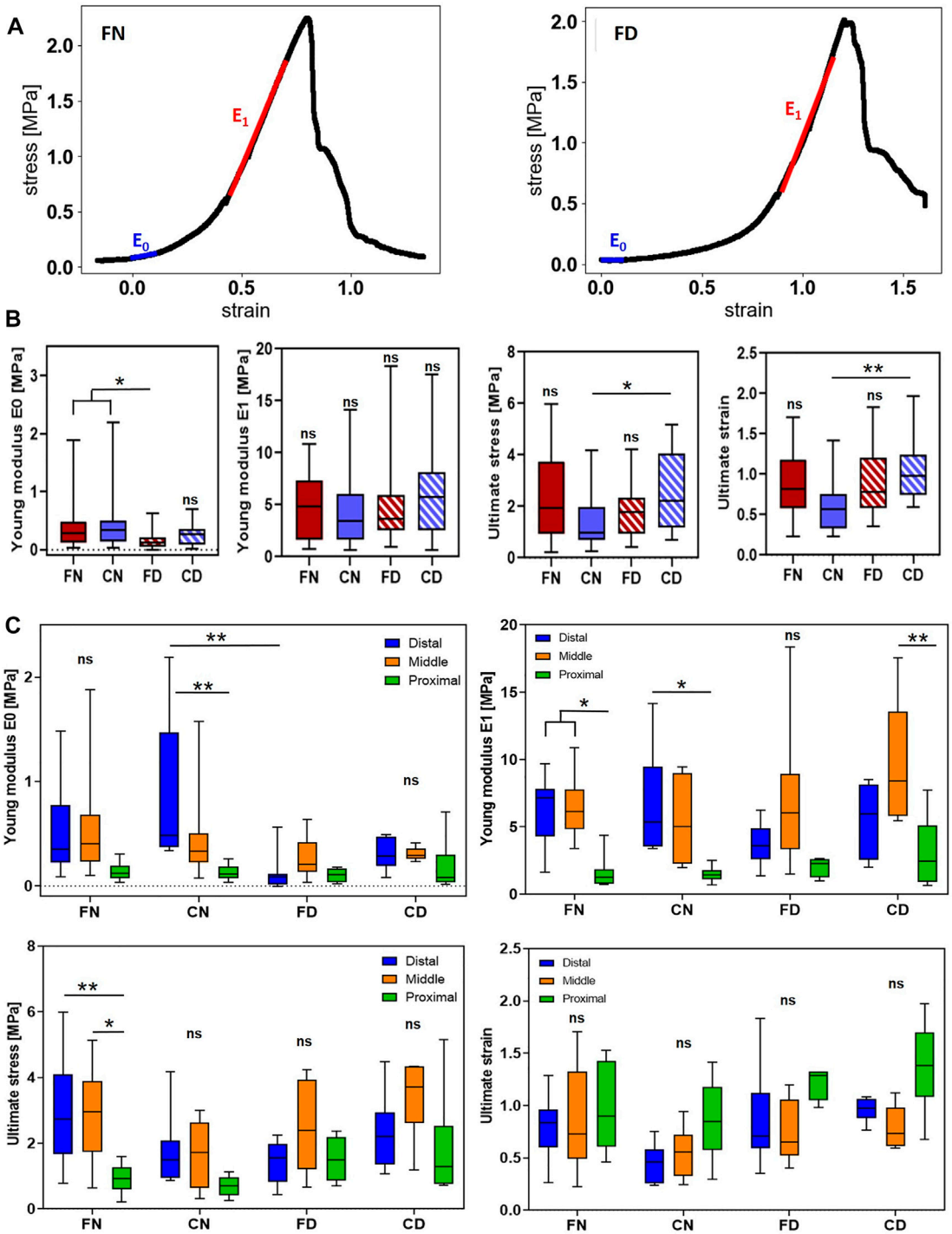

FIGURE 7 | Mechanical testing: **(A)** Typical stress–strain curves for the distal region of a native carotid (left) and a decellularized scaffold (right) in both curves. Young's modulus of elastic phase (E0) and the viscoelastic phase E1 and the rupture point (the highest value of stress reached) were easily identified. Boxplots of the mechanical test parameters are shown in **(B)** and **(C)**, where **(B)** represents parameters for the four main groups together, while **(C)** shows more detailed data of individual segments within the groups. FN, fresh native artery; CN, cryopreserved native artery; FD, freshly decellularized scaffold; CD, cryopreserved decellularized scaffold; level of significance is displayed as (*) for $p < 0.05$ and (**) for $p < 0.01$.

reach the values identified for the fresh vessels (FN), confirming a good quality of the scaffold being generated from the cryopreserved vessels.

3.2.2.2 Comparison of Specific Arterial Segments Among the Groups

The detailed analysis of the four mechanical parameters for individual arterial segments is shown in **Figure 7C**. Even with a reduced number of experimental data per condition, if compared with the evaluation of the four main groups together, it was still possible to perform the analysis. All the datasets passed the Shapiro–Wilk test for normality and were analyzed using a two-way ANOVA test. The comparison of the parameters identified in native vessel segments with parameters found in their decellularized counterparts revealed only one significant difference: Young's modulus E_0 of the proximal part of the native artery (CN, 0.128 ± 0.074 MPa) was significantly higher than E_0 of the proximal part of the decellularized vessel (FD, 0.105 ± 0.068 MPa) (**Figure 7C** top left). This confirms that the decellularization procedure does not affect the mechanical properties even on the level of individual segments, and it is also in line with the findings from the whole artery analysis considering E_0 and E_1. The interesting finding of ultimate stress and strain increase in the case of CN and CD samples was not confirmed here, most probably due to a smaller dataset used for this individual analysis.

3.2.2.3 Comparison of Arterial Segments Within the Groups

When comparing the different segments within the individual vessel groups, we observed significant differences between these segments in both fresh and cryoprotected native vessels (FN and CN). This confirmed the differences in porcine arteries that were reported earlier (Kochová et al., 2012). In particular, the mechanical parameters E_0, E_1, and ultimate stress for the proximal segment have a clear trend to be lower than the values of middle and distal segments (apart from the ultimate strain). This trend was found to be statistically significant for E_0 and E_1 values of proximal (0.128 ± 0.074 MPa and 1.47 ± 0.55 MPa, respectively) and distal (0.851 ± 0.702 MPa and 6.5 ± 3.89 MPa, respectively) parts of CN vessels; for E_1 values of proximal (1.54 ± 1.1 MPa), middle (6.48 ± 2.08 MPa), and distal (6.3 ± 2.46 MPa) parts of the FN vessels; and for the ultimate stress values of proximal (0.94 ± 0.43 MPa) middle (2.86 ± 1.42 MPa), and distal (2.97 ± 1.62 MPa) regions of the FN vessels. Moreover, we observed that these differences in native tissues can be transferred onto the decellularized scaffolds as in the case of Young's modulus E_1, where the value of the proximal part (3.08 ± 2.63 MPa) of the CD vessels was significantly lower than the E_1 of its middle region (9.67 ± 4.61 MPa). The only exception was E_0 in the FD group, where the mean value between the distal (0.125 ± 0.184 MPa) and proximal (0.105 ± 0.068 MPa) part was about the same.

Overall, the distal region presented higher values of E and ultimate stress and lower values of ultimate strain when compared to the proximal region due to lower elastin fiber content. If the elastin fibers are more abundant, the corresponding region of the artery, that is, the proximal part is more elastic and can reach a longer elongation. This is, in a way, supported by the ultimate strain values which were showing a trend of the proximal parts being higher than the other two parts, middle and distal (**Figure 7C**, bottom right). However, this trend was not proven to be significantly different. Young's modulus E is the ratio between the stress and strain. If we hypothetically consider an equal stress but higher strain for these proximal parts, then we would expect the E values to be lower as a consequence. This is, indeed, shown in the graphs for both E_0 and E_1 values of the proximal parts, in some cases being statistically significant (**Figure 7C**, top left and right, respectively).

3.3 *In Vitro* Experiments

The compatibility of vessel scaffolds with the cells was analyzed by culturing scaffold stripes for 24 h with HUVECs. We also tested scaffold compatibility with rat ECs (rECs). As the concentration of residual detergents was still too high immediately after decellularization (scaffold storage solution showed mild foaming after a vigorous shake), we applied an additional 2-day wash and seeded the cells. At the same time, residual SDS concentration was measured both in solution after decellularization and in washing solution after a 2-day wash, with the SDS concentration decreasing from 0.0057% ± 0.0012–0.0025% ± 0.0006 (**Figure 8A**). Nevertheless, the cells did not show viability on the scaffolds even at this low SDS concentration (data not shown). Thus, we applied additional washing steps to obtain the 4-day washed scaffolds, with SDS concentrations reaching values very close to zero (the average value for all vessels evaluated was 0.0004% ± 0.0003, **Figure 8A**). With scaffolds prepared this way, we performed several 1-day *in vitro* experiments. The samples were assessed for cell viability and stained for cell and ECM protein presence by H&E and IF, respectively. The live/dead assay revealed that only some cells were kept alive even on 4-day washed scaffolds as the cell viability was 19% ± 12 and 29% ± 5 for HUVECs and 46% ± 15 for rECs representing three independent experiments (**Figure 8B**). The difference between the two HUVEC experiments seemed to be again linked to the residual SDS concentrations, which were still quite variable. 0.0002% of SDS was detected for scaffolds entering the experiment with 19% HUVEC viability, and 0.00008% was shown for experiments with 29% HUVECs and 46% rECs viability (**Figure 8B**, detailed values in **Supplementary Table 3**). The best viability was, thus, shown for rat endothelial cells on scaffolds with 0.00008% residual SDS that kept about half of the cells alive.

HUVEC culture on arterial scaffolds was also monitored by H&E staining and IF. **Figure 8C** shows an H&E image of a vessel cross-section with few HUVECs adhered. A perpendicular view of the vessel intima surface is shown in **Figure 8D**, where collagen I fibers were stained by immunofluorescence in red, and the cells are depicted in green. Sparse distribution and partially rounded cell shape are likely related to residual SDS content which was around 0.0002% in this experiment.

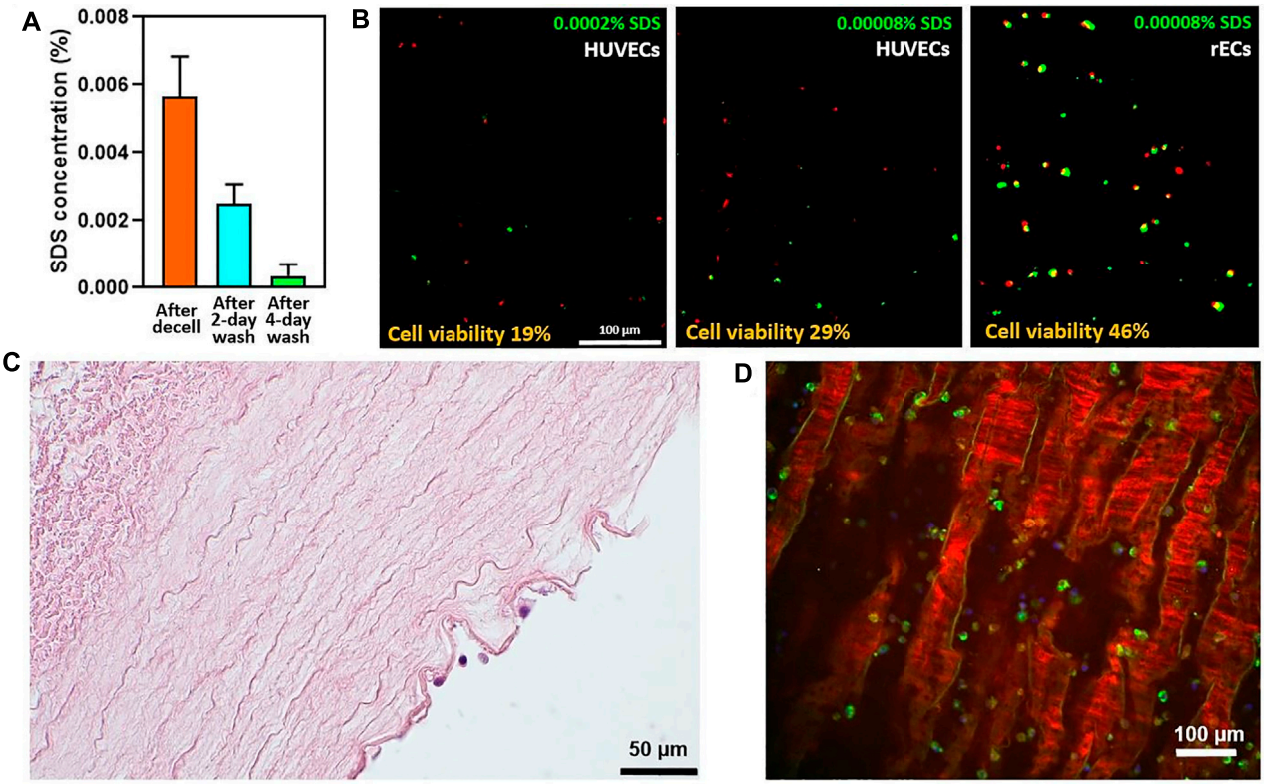

FIGURE 8 | Endothelial cell culture in arterial scaffolds after 1 day: **(A)** SDS concentration with successive PBS washes; **(B)** Live/Dead assay images of three different 1-day seeding with HUVECs and rECs at different SDS concentration; live cells are depicted in green and dead cells in red; **(C)** Cells (dark blue) adhered to the ECM of tunica intima (H&E staining, vessel cross-section); **(D)** Vessel scaffold surface with attached cells (blue for nuclei; green for cytoskeleton) imaged by fluorescence microscopy; red fibers represent collagen I from the scaffold.

4 DISCUSSION

The need for small-caliber vessel grafts and the problems of thrombogenicity related to the use of polymeric materials have led to the development of acellular xenogeneic grafts (Fayon et al., 2021). Protocols for decellularization of carotid arteries from different species have been developed; however, they last for more than 1 day, making it difficult to adapt these lengthy procedures for future clinical use where timing is essential (Dahl et al., 2003; Roy et al., 2005; Dahan et al., 2012; Sheridan et al., 2012; López-Ruiz et al., 2017; Wang et al., 2017; Gu et al., 2018; Cai et al., 2019; Cheng et al., 2019; Cai et al., 2020). Thus, we decided to contribute to this field by developing a procedure that would be faster than the ones currently used, while maintaining the scaffold well-preserved.

4.1 High Tissue Protection

First , we focused on careful tissue explantation to maintain the vessels as intact as possible for future processing. This was facilitated by two factors: 1) having a large animal house available just next to the laboratory, and 2) long-term collaboration with the team of surgeons working in the neighboring faculty hospital who performed the explantation.

We also compared scaffolds that were freshly decellularized with vessels that were stored for a period of time at −80°C in a cryoprotective solution to increase the immediate accessibility of tissues for the future. The decellularization of a fresh artery without any unnecessary delay has the advantage to obtain a scaffold that is the closest to the native ECM. Generally, prolonged cold storage of vessels prior to decellularization, for example, during transportation might result in the damage of the ECM proteins. The cryopreservation, on the other hand, would keep the vessel stored until it is needed. Our approach to cryoprotection might seem contradictory to many decellularization protocols that suggest using freeze/thaw cycles for an increase in decellularization efficacy (Porzionato et al., 2018; Cheng et al., 2019). Plain freezing and thawing can, indeed, help cell removal. However, if complete decellularization can be achieved without this step, the natural structure of the ECM can be better maintained as possible protein damage caused by enzymes released from cells during uncontrolled freezing and thawing can be prevented.

We considered the contact time of the tissue with the detergent to be of great importance. Recently, we developed a fast protocol for decellularization of porcine liver lasting around 3 h (Moulisová et al., 2020), where we particularly focused on

shortening the period of SDS perfusion. SDS is known for being very efficient but is also a harsh detergent, and thus some protocols for carotid arteries use a low SDS concentration (Cai et al., 2019; 2020) or completely avoid this reagent (Neff et al., 2011; Dahan et al., 2012; Sheridan et al., 2012). Nevertheless, using lower SDS concentrations or less efficient detergents results in much longer decellularization protocols, extending the time of arterial scaffold production, which takes 3 days and more (Neff et al., 2011; Dahan et al., 2012; Sheridan et al., 2012; Cai et al., 2019). Our approach is based rather on the strategy of shorter tissue contact with detergents as it seems to be better for the preservation of the scaffold's inner structure and provides the scaffold in shorter time.

4.2 Decellularization Efficiency

However, the efficiency of our fast protocol adapted from vein decellularization appeared to be lower for arteries. In the case of veins, all cells were always removed (Massaro et al., 2021a), while only a proportion of the arteries was completely decellularized. Naturally, when compared to the veins, the arterial vessel wall is much thicker and more compact due to the presence of elastic layers and much higher abundance of smooth muscle cells. Still, some of the arteries were decellularized completely, which could be related to the variable distribution of elastic fibers within the vascular wall as described by Espinosa et al. (2018). Our more detailed analysis revealed higher efficiency for arteries decellularized from fresh tissue. This can be possibly explained by mild tissue damage, particularly of endothelial cells caused by cold ischemia during the typical overnight storage period of these vessels prior to decellularization. This damage is considered minor in the case of vessel graft storage prior to implantation for up to 24 h, however depending strictly on the preservation solution (Neil et al., 2002). According to that study, saline (which we used as our storage solution in this study) did not produce such strong damage related to mitochondria, cytoplasm, and nuclear structure in endothelial cells of rat aortas (Neil et al., 2002). Still, in our case, this mild damage could have an effect on easier accessibility of detergents into cells than that of the cells of vessels that were cryopreserved immediately after explantation and fast-thawed to avoid cell damage by ice crystal formation (Amini et al., 2020). Moreover, we observed high variability in the content of elastic fibers between individual animals, which can also contribute to the different levels of decellularization, disregarding the storage conditions. The role of interindividual variability is also supported by a recent report describing a clear effect of heterogeneity between individuals on the decellularization outcome in the case of human cardiac tissue and related limitations of standardized protocols (Tenreiro et al., 2021).

4.3 Good Protein Maintenance

We put in a substantial effort on evaluating the quality of the scaffold with respect to the molecular composition. We also considered the relationship between the vascular layer, the segment of the vessel on the one hand, and the mechanical strength on the other hand.

All three different layers of the arterial wall (tunica intima, media, and adventitia, as shown in **Figure 2A**) were visualized by several microscopic techniques. Based on the evaluation of microscopic images of samples, both native and decellularized, we assume the protein composition of the ECM of these three layers does not change after the decellularization procedure. Cai et al. described a decrease in the biochemical properties of porcine carotid arteries after using 1% of Triton X-100 and 0.3% SDS solutions in a 4-day long decellularization protocol (lower collagen content and looser scaffold structure) (Cai et al., 2019). Our study, on the other hand, confirmed good maintenance of ECM proteins of high importance such as collagen, elastin, fibronectin, and laminin using a combination of classical histological staining such as H&E, Picrosirius red, Verhoeff's green trichrome, and orcein with specific immunofluorescence stainings. This implies that reasonable optimization of the protocol (increased SDS concentration, shortening the incubation time) can result in a high-quality scaffold to be used for cell repopulation. Other studies report that the protein content unchanged after the decellularization; however, the time to obtain these scaffolds is still longer than the one we report here (Sheridan et al., 2014; Cheng et al., 2019; Ilanlou et al., 2019).

4.4 Mild GAG Loss

Regarding the importance of GAGs for cytokine and growth factor retention in vessels [reviewed in (Lepedda et al., 2021)], we also included GAG staining in our study. We showed that native arteries have a high content in tunica media, while, basically, no GAGs are present in the adventitia. Based on histological staining, our decellularization protocol leads to a decrease in GAG content in tunica media, but still, some GAGs were preserved. A similar decrease has also been reported by other groups studying porcine carotid arteries (Cai et al., 2019; Cheng et al., 2019), while other groups did not monitor GAG presence at all (Sheridan et al., 2012). There are studies reporting that GAG loss is directly related to the SDS effect (Uygun et al., 2010) or to the effect of Triton X-100 (Mendoza-Novelo et al., 2011) decellularizing rat liver and bovine pericardium, respectively. However, considering the lower effectivity and prolonged decellularization procedure when other decellularization agents are used (Grandi et al., 2011; Kajbafzadeh et al., 2017), we assume the mild loss of GAGs could be an acceptable compromise when obtaining the scaffold faster and of high quality in other aspects such as protein content and mechanical strength. Nevertheless, whether this GAG decrease affects the repopulation procedure has to be investigated.

4.5 Retention of Mechanical Properties

Tunica media comprises mainly of smooth muscle cells and fibers of elastin and collagen. The decellularized ECM retains these structurally important fibers; thus, tunica media is the vessel part mainly responsible for the mechanical strength of the vessel. The external layer of the arterial wall, the adventitia, comprises fibroblasts and collagen fibers. Its role is to provide stability to the wall, and its presence depends on the type of artery (Holzapfel

et al., 2000). Importantly, carotid arteries have been shown to vary between proximal and distal parts in the percentage of collagen, elastin, and actin (Tomášek et al., 2020). The elastin content decreases in favor of the smooth muscle cells and collagen content from the proximal toward the distal part of the vessel wall and inevitably influences the mechanical properties of different vessel segments (Tomášek et al., 2020). This suggests that the mechanical properties of different parts of decellularized scaffolds can also be influenced. Our detailed analysis of each individual segment confirmed that proximal vessel segments showed a higher ultimate strain and thus lower stiffness (Young's modulus) than middle and distal segments that were also supported by some data from decellularized scaffolds. Thus, the segmentation of the scaffolds should be taken into account in future processing to ensure that a suitable segment is used, and random cutting of porcine carotid arteries in segments for the decellularization (Sheridan et al., 2012) should be avoided.

Previous studies reported weakened mechanical properties of porcine carotid artery scaffolds in comparison to native vessels and suggested different types of crosslinking to overcome this obstacle (Gu et al., 2018; Cai et al., 2019). Our work shows it is possible to obtain completely decellularized vessel scaffolds using a shorter protocol with mechanical properties maintained; thus, no additional complex modifications to restore the compromised quality are needed.

From the mechanical study, we only observed a difference between native and decellularized tissue in the case of opening angle values. The opening angle indicates the presence of residual stresses in the arterial wall that are mainly attributed to the smooth muscle cells (Rachev and Hayashi 1999). Thus, the loss of smooth muscle cells results in significant reduction of the circumferential stress. The results from both analyses and comparisons of opening angles of the whole arteries and individual segments are well-corresponding with this theoretical decrease of residual stress. Considering individual values, our results (56° for the native groups and 25° for the decellularized groups) are in line with those of Roy et al. that obtained opening angles around 69° in the native and 26° in the decellularized samples of porcine carotids (Roy et al., 2005).

Given that a decellularized vessel loses the cells in the process, we need to quantify if this loss influences its behavior. In order to increase our knowledge further, we decided to consider not only the differences between the native tissue, scaffold, and the single main regions of the artery but also include different storing conditions. We believe that for future translational use, the possibility to keep the native tissue and/or the scaffold stored would be beneficial in terms of the availability of the graft. Our findings evidenced that the decellularization procedure did not have an impact on the mechanical behavior in the longitudinal direction.

Looking at the vessels from the direction that is perpendicular to the longitudinal, Holzapfel et al. showed the influence of each layer of the arterial wall on the mechanical behavior of human coronary arteries (Holzapfel et al., 2005). They found out, by separating each layer, that the tunica adventitia can reach a stress of 1.3 MPa until rupture, while the tunica media and intima can only arrive at 0.4 MPa. Although we did not investigate the mechanical properties of each arterial layer separately in this study, we conclude it is important to keep all layers together for obtaining the scaffold which is as close to the native vessel as possible. Considering this aspect, we can state that our decellularized arteries present similar values as the native ones.

4.6 Compatibility With Cells

Tunica intima, the inner layer, is formed by endothelial cells to create a barrier between blood and the vessel wall. The endothelium is, thus, responsible for the antithrombogenicity of native blood vessels. There are studies successfully using endothelial cells for vessel scaffold repopulation to restore the intima (McFetridge et al., 2004; Quint et al., 2011; Dahan et al., 2012). It is important that the matrix stimulates cell adhesion and growth to reduce the risks of rejection and graft failure. In this work, we included a scaffold cytocompatibility experiment with two different cell types to test porcine scaffold compatibility with endothelial cells. We showed that both HUVECs and rECs can survive on the scaffold; nevertheless, we clearly showed that significant removal of residual detergents is absolutely necessary to keep the endothelial cells alive during repopulation. Our findings related to HUVEC sensitivity to residual SDS concentrations are in line with the publication of Zvarova et al. describing a very high susceptibility of endothelial cells, including HUVECs to low concentrations of this detergent (Zvarova et al., 2016). They report that endothelial cell types are affected by SDS concentrations as low as 0.00012%; at the same time, they show that other cell types are not so vulnerable, for example, hMSCs tolerate values around 0.002%. Apart from HUVECs, we also tested rat endothelial cells which were shown to be less susceptible than their human counterparts. Our results showing the high variation between cell viability of HUVECs and rECs on a matrix with comparable SDS residual content newly suggests different SDS sensitivity of endothelial cells from different species which has not yet been reported. At the same time, our findings highlight the importance of SDS residue monitoring in decellularized matrices. Provided that the SDS detergent residues are carefully removed from the scaffold, the cells would eventually be able to completely repopulate the scaffold and remodel the ECM for complete integration in the long term (Dahan et al., 2012).

5 CONCLUSION AND FUTURE PLANS

Our study showed that using our fast protocol, we could produce fully decellularized porcine carotid arteries with well-preserved ECM components and retain the mechanical characteristics of the native vessels. Although this protocol was not 100% efficient, it still brought the benefit of obtaining high-quality scaffolds. Moreover, we introduced a novel strategy of vessel cryopreservation using cryoprotective solution prior to the decellularization, which brings not only the benefit of the vessel available on demand but also better protection of the arterial ECM structure. We also confirmed the results of a previous study on the difference in mechanical properties in individual arterial segments and showed that this could be

transferred onto the decellularized scaffolds. Finally, the thorough removal of SDS residues from scaffolds was shown to be crucial for endothelial cell survival after seeding. The next steps we are planning in this area are to modify the protocol to increase the decellularization efficiency and perform a detailed study on the scaffold repopulation with primary cells with *in vivo* testing as the proof of concept. In parallel, we would like to expand the mechanical testing toward the analysis of the inflation-extension tests. As the arteries have a physiological pressure range in the circumferential direction corresponding to systolic and diastolic pressures, the knowledge of the maintenance of such mechanical properties in scaffolds and eventually recellularized grafts is crucial when the risk of aneurysm development is considered.

DATA AVAILABILITY STATEMENT

The original contributions presented in the study are included in the article/**Supplementary Material**, further inquiries can be directed to the corresponding author.

ETHICS STATEMENT

The animal study was reviewed and approved by the Ministry of Education, Youth and Sports of the Czech Republic, project approval MSMT-15629/2020-4.

AUTHOR CONTRIBUTIONS

MM and VM designed the experiments, analyzed the data, and wrote the manuscript; MM, PK, RP, JR, and LC performed the experiments and analyzed the data; UD, VL, and VM conceptualized and designed the study, interpreted the data, and edited the manuscript.

FUNDING

The authors received support from the European Regional Development Fund Project "AMTMI" (No. CZ.02.1.01/0.0/0.0/17_048/0007280) and grants START/MED/027 Start Program (No. CZ.02.2.69/0.0/0.0/19_073/00169 35, Ministry of Education, Youth and Sports of the Czech Republic), (GA United Kingdom stands for Grantova Agentura University Karlovy) Grant No. 462520 (Charles University), UNCE/MED006 Center of Excellence (Charles University "Center of Clinical and Experimental Liver Surgery", and Cooperation project "Surgical disciplines" (COOPERATION-207043, Charles University).

ACKNOWLEDGMENTS

The authors would like to acknowledge Mojmír Bohanes, Lucie Kepková, Pavel Krystl, Alexey Rozumnyi, Jan Ševčík, and Sima Šarčevič for their contribution in carotid artery explants and lab technicians Gabriela Suchá and Petra Šmolíková for help with histological staining.

SUPPLEMENTARY MATERIAL

The Supplementary Material for this article can be found online at: https://www.frontiersin.org/articles/10.3389/fbioe.2022.833244/full#supplementary-material

REFERENCES

Amini, M., Niemi, E., Hisdal, J., Kalvøy, H., Tronstad, C., Scholz, H., et al. (2020). Monitoring the Quality of Frozen-Thawed Venous Segments Using Bioimpedance Spectroscopy. *Physiol. Meas.* 41 (4), 044008. doi:10.1088/1361-6579/ab85b7

Cai, W.-W., Gu, Y. J., Wang, X.-N., and Chen, C.-Z. (2009). Heparin Coating of Small-Caliber Decellularized Xenografts Reduces Macrophage Infiltration and Intimal Hyperplasia. *Artif. Organs* 33 (6), 448–455. doi:10.1111/j.1525-1594.2009.00748.x

Cai, Z., Gu, Y., Cheng, J., Li, J., Xu, Z., Xing, Y., et al. (2019). Decellularization, Cross-Linking and Heparin Immobilization of Porcine Carotid Arteries for Tissue Engineering Vascular Grafts. *Cell Tissue Bank* 20 (4), 569–578. doi:10.1007/s10561-019-09792-5

Cai, Z., Gu, Y., Xiao, Y., Wang, C., and Wang, Z. (2020). Porcine Carotid Arteries Decellularized with a Suitable Concentration Combination of Triton X-100 and Sodium Dodecyl Sulfate for Tissue Engineering Vascular Grafts. *Cell Tissue Bank* 22, 277–286. doi:10.1007/s10561-020-09876-7

Carrabba, M., and Madeddu, P. (2018). Current Strategies for the Manufacture of Small Size Tissue Engineering Vascular Grafts. *Front. Bioeng. Biotechnol.* 6, 41. doi:10.3389/fbioe.2018.00041

Chandra, P., and Atala, A. (2019). Engineering Blood Vessels and Vascularized Tissues: Technology Trends and Potential Clinical Applications. *Clin. Sci.* 133 (9), 1115–1135. doi:10.1042/CS20180155

Chemla, E. S., and Morsy, M. (2008). Randomized Clinical Trial Comparing Decellularized Bovine Ureter with Expanded Polytetrafluoroethylene for Vascular Access. *Br. J. Surg.* 96 (1), 34–39. doi:10.1002/bjs.6434

Cheng, J., Wang, C., and Gu, Y. (2019). Combination of Freeze-Thaw with Detergents: A Promising Approach to the Decellularization of Porcine Carotid Arteries. *Bme* 30, 191–205. doi:10.3233/BME-191044

Conklin, B. S., Richter, E. R., Kreutziger, K. L., Zhong, D.-S., and Chen, C. (2002). Development and Evaluation of a Novel Decellularized Vascular Xenograft. *Med. Eng. Phys.* 24 (3), 173–183. doi:10.1016/S1350-4533(02)00010-3

Dahan, N., Zarbiv, G., Sarig, U., Karram, T., Hoffman, A., and MacHluf, M. (2012). Porcine Small Diameter Arterial Extracellular Matrix Supports Endothelium Formation and Media Remodeling Forming a Promising Vascular Engineered Biograft. *Tissue Eng. A* 18 (3–4), 411–422. doi:10.1089/ten.tea.2011.0173

Dahl, S. L. M., Koh, J., Prabhakar, V., and Niklason, L. E. (2003). Decellularized Native and Engineered Arterial Scaffolds for Transplantation. *Cel Transpl.* 12 (6), 659–666. doi:10.3727/000000003108747136

Fayon, A., Menu, P., and El Omar, R. (2021). Cellularized Small-Caliber Tissue-Engineered Vascular Grafts: Looking for the Ultimate Gold Standard. *Npj Regen. Med.* 6 (1), 46. doi:10.1038/s41536-021-00155-x

Gabriela Espinosa, M., Catalin Staiculescu, M., Kim, J., Marin, E., and Wagenseil, J. E. (2018). Elastic Fibers and Large Artery Mechanics in Animal Models of Development and Disease. *J. Biomech. Eng.* 140 (2), 0208031–02080313. doi:10.1115/1.4038704

Gandhi, N. S., and Mancera, R. L. (2008). The Structure of Glycosaminoglycans and Their Interactions with Proteins. *Chem. Biol. Drug Des.* 72 (6), 455–482. doi:10.1111/j.1747-0285.2008.00741.x

Gilpin, A., and Yang, Y. (20172017). Decellularization Strategies for Regenerative Medicine: From Processing Techniques to Applications. *Biomed. Res. Int.* 2017, 1–13. doi:10.1155/2017/9831534

Gilpin, S. E., Guyette, J. P., Gonzalez, G., Ren, X., Asara, J. M., Mathisen, D. J., et al. (2014). Perfusion Decellularization of Human and Porcine Lungs: Bringing the Matrix to Clinical Scale. *J. Heart Lung Transplant.* 33 (3), 298–308. doi:10.1016/j.healun.2013.10.030

Grandi, C., Baiguera, S., Martorina, F., Lora, S., Amistà, P., Dalzoppo, D., et al. (2011). Decellularized Bovine Reinforced Vessels for Small-Diameter Tissue-Engineered Vascular Grafts. *Int. J. Mol. Med.* 28 (3), 315–325. doi:10.3892/ijmm.2011.720

Gu, Y., Wang, F., Wang, R., Li, J., Wang, C., Li, L., et al. (2018). Preparation and Evaluation of Decellularized Porcine Carotid Arteries Cross-Linked by Genipin: The Preliminary Results. *Cell Tissue Bank* 19 (3), 311–321. doi:10.1007/s10561-017-9675-9

Holzapfel, G. A., Gasser, T. C., and Ogden, R. W. (2000). A New Constitutive Framework for Arterial Wall Mechanics and a Comparative Study of Material Models. *J. Elasticity* 61 (1–3), 1–48. doi:10.1023/A:1010835316564

Holzapfel, G. A., Sommer, G., Gasser, C. T., and Regitnig, P. (2005). Determination of Layer-specific Mechanical Properties of Human Coronary Arteries with Nonatherosclerotic Intimal Thickening and Related Constitutive Modeling. *Am. J. Physiology-Heart Circulatory Physiol.* 289 (5 58-5), H2048–H2058. doi:10.1152/ajpheart.00934.2004

Ilanlou, S., Khakbiz, M., Amoabediny, G., Mohammadi, J., and Rabbani, H. (2019). Carboxymethyl Kappa Carrageenan-modified Decellularized Small-diameter Vascular Grafts Improving Thromboresistance Properties. *J. Biomed. Mater. Res.* 107 (8), 1690–1701. doi:10.1002/jbm.a.36684

Junqueira, L. C. U., Bignolas, G., and Brentani, R. R. (1979). Picrosirius Staining Plus Polarization Microscopy, a Specific Method for Collagen Detection in Tissue Sections. *Histochem. J.* 11 (4), 447–455. doi:10.1007/BF01002772

Kajbafzadeh, A.-M., Khorramirouz, R., Kameli, S. M., Hashemi, J., Bagheri, A., and Amin, B. (2017). Decellularization of Human Internal Mammary Artery: Biomechanical Properties and Histopathological Evaluation. *BioResearch Open Access* 6 (1), 74–84. doi:10.1089/biores.2016.0040

Kochová, P., Cimrman, R., Jansová, M., Michalová, K., Kalis, V., Kubíková, T., et al. (2019). The Histological Microstructure and *In Vitro* Mechanical Properties of the Human Female Postmenopausal Perineal Body. *Menopause* 26 (1), 66–77. doi:10.1097/GME.0000000000001166

Kochová, P., Kuncová, J., Švíglerová, J., Cimrman, R., Miklíková, M., Liška, V., et al. (2012). The Contribution of Vascular Smooth Muscle, Elastin and Collagen on the Passive Mechanics of Porcine Carotid Arteries. *Physiol. Meas.* 33 (8), 1335–1351. doi:10.1088/0967-3334/33/8/1335

Kocová, J. (1970). Overall Staining of Connective Tissue and the Muscular Layer of Vessels. *Folia Morphologica* 18 (3), 293–295.

Kubíková, T., Kochová, P., Brázdil, J., Špatenka, J., Burkert, J., Králíčková, M., et al. (2017). The Composition and Biomechanical Properties of Human Cryopreserved Aortas, Pulmonary Trunks, and Aortic and Pulmonary Cusps. *Ann. Anat. - Anatomischer Anzeiger* 212, 17–26. doi:10.1016/j.aanat.2017.03.004

Lattouf, R., Younes, R., Lutomski, D., Naaman, N., Godeau, G., Senni, K., et al. (2014). Picrosirius Red Staining. *J. Histochem. Cytochem.* 62 (10), 751–758. doi:10.1369/0022155414545787

Lepedda, A. J., Nieddu, G., Formato, M., Baker, M. B., Fernández-Pérez, J., and Moroni, L. (2021). Glycosaminoglycans: From Vascular Physiology to Tissue Engineering Applications. *Front. Chem.* 9 (May), 1–21. doi:10.3389/fchem.2021.680836

Li, D., Xin, Z., Wan, J., Ma, X., Xin, Y., Gong, D., et al. (2016). Decellularized Sheep Internal Carotid Arteries as a Tissue-Engineered Small-Diameter Vascular Scaffold. *Int. J. Clin. Exp. Med.* 9 (6), 9983–9991.

Lindsey, P., Echeverria, A., Cheung, M., Kfoury, E., Bechara, C. F., and Lin, P. H. (2018). Lower Extremity Bypass Using Bovine Carotid Artery Graft (Artegraft): An Analysis of 124 Cases with Long-Term Results. *World J. Surg.* 42 (1), 295–301. doi:10.1007/s00268-017-4161-x

López-Ruiz, E., Venkateswaran, S., Perán, M., Jiménez, G., Pernagallo, S., Díaz-Mochón, J. J., et al. (2017). Poly(Ethylmethacrylate-Co-Diethylaminoethyl Acrylate) Coating Improves Endothelial Re-population, Bio-Mechanical and Anti-thrombogenic Properties of Decellularized Carotid Arteries for Blood Vessel Replacement. *Sci. Rep.* 7 (1), 1–14. doi:10.1038/s41598-017-00294-6

Massaro, M. S., Pálek, R., Rosendorf, J., Červenková, L., Liška, V., and Moulisová, V. (2021a). Decellularized Xenogeneic Scaffolds in Transplantation and Tissue Engineering: Immunogenicity versus Positive Cell Stimulation. *Mater. Sci. Eng. C* 127, 112203. doi:10.1016/j.msec.2021.112203

Massaro, M. S., Pálek, R., Rosendorf, J., Malečková, A., Červenková, L., Singh, R. K., et al. (2021b). Recellularization of Decellularized Porcine Caval Veins. *Biomed. Sci. Eng.* 4 (s1), 2–3. doi:10.4081/bse.2021.181

McFetridge, P. S., Daniel, J. W., Bodamyali, T., Horrocks, M., and Chaudhuri, J. B. (2004). Preparation of Porcine Carotid Arteries for Vascular Tissue Engineering Applications. *J. Biomed. Mater. Res.* 70A (2), 224–234. doi:10.1002/jbm.a.30060

Mendoza-Novelo, B., Avila, E. E., Cauich-Rodríguez, J. V., Jorge-Herrero, E., Rojo, F. J., Guinea, G. V., et al. (2011). Decellularization of Pericardial Tissue and its Impact on Tensile Viscoelasticity and Glycosaminoglycan Content. *Acta Biomater.* 7 (3), 1241–1248. doi:10.1016/j.actbio.2010.11.017

Moulisová, V., Jiřík, M., Schindler, C., Červenková, L., Pálek, R., Rosendorf, J., et al. (2020). Novel Morphological Multi-Scale Evaluation System for Quality Assessment of Decellularized Liver Scaffolds. *J. Tissue Eng.* 11, 204173142092112. doi:10.1177/2041731420921121

Nagaoka, Y., Yamada, H., Kimura, T., Kishida, A., Fujisato, T., and Takakuda, K. (2014). Reconstruction of Small Diameter Arteries Using Decellularized Vascular Scaffolds. *J. Med. Dent Sci.* 61 (1), 33–40. doi:10.11480/610105

Neff, L. P., Tillman, B. W., Yazdani, S. K., Machingal, M. A., Yoo, J. J., Soker, S., et al. (2011). Vascular Smooth Muscle Enhances Functionality of Tissue-Engineered Blood Vessels *In Vivo*. *J. Vasc. Surg.* 53 (2), 426–434. doi:10.1016/j.jvs.2010.07.054

Neil, D. A. H., Lynch, S. V., Hardie, I. R., and Effeney, D. J. (2002). Cold Storage Preservation and Warm Ischaemic Injury to Isolated Arterial Segments: Endothelial Cell Injury. *Am. J. Transplant.* 2 (5), 400–409. doi:10.1034/j.1600-6143.2002.20502.x

Parmaksiz, M., Dogan, A., Odabas, S., Elçin, A. E., and Elçin, Y. M. (2016). Clinical Applications of Decellularized Extracellular Matrices for Tissue Engineering and Regenerative Medicine. *Biomed. Mater.* 11 (2), 022003. doi:10.1088/1748-6041/11/2/022003

Porzionato, A., Stocco, E., Barbon, S., Grandi, F., Macchi, V., and De Caro, R. (2018). Tissue-Engineered Grafts from Human Decellularized Extracellular Matrices: A Systematic Review and Future Perspectives. *Ijms* 19 (12), 4117. doi:10.3390/ijms19124117

Quint, C., Kondo, Y., Manson, R. J., Lawson, J. H., Dardik, A., and Niklason, L. E. (2011). Decellularized Tissue-Engineered Blood Vessel as an Arterial Conduit. *Proc. Natl. Acad. Sci. U.S.A.* 108 (22), 9214–9219. doi:10.1073/pnas.1019506108

Rachev, A., and Hayashi, K. (1999). Theoretical Study of the Effects of Vascular Smooth Muscle Contraction on Strain and Stress Distributions in Arteries. *Ann. Biomed. Eng.* 27 (4), 459–468. doi:10.1114/1.191

Roy, S., Silacci, P., and Stergiopulos, N. (2005). Biomechanical Proprieties of Decellularized Porcine Common Carotid Arteries. *Am. J. Physiology-Heart Circulatory Physiol.* 289 (4 58-4), H1567–H1576. doi:10.1152/ajpheart.00564.2004

Schmidt, C. E., and Baier, J. M. (2000). Acellular Vascular Tissues: Natural Biomaterials for Tissue Repair and Tissue Engineering. *Biomaterials* 21 (22), 2215–2231. doi:10.1016/S0142-9612(00)00148-4

Seiffert, N., Tang, P., Keshi, E., Reutzel-Selke, A., Moosburner, S., Everwien, H., et al. (2021). *In Vitro* Recellularization of Decellularized Bovine Carotid Arteries Using Human Endothelial Colony Forming Cells. *J. Biol. Eng.* 15 (1), 1–15. doi:10.1186/s13036-021-00266-5

Sheridan, W. S., Duffy, G. P., and Murphy, B. P. (2012). Mechanical Characterization of a Customized Decellularized Scaffold for Vascular Tissue Engineering. *J. Mech. Behav. Biomed. Mater.* 8, 58–70. doi:10.1016/j.jmbbm.2011.12.003

Sheridan, W. S., Grant, O. B., Duffy, G. P., and Murphy, B. P. (2014). The Application of a Thermoresponsive Chitosan/β-GP Gel to Enhance Cell

Repopulation of Decellularized Vascular Scaffolds. *J. Biomed. Mater. Res.* 102 (8), 1700–1710. doi:10.1002/jbm.b.33138

Tenreiro, M. F., Almeida, H. V., Calmeiro, T., Fortunato, E., Ferreira, L., Alves, P. M., et al. (2021). Interindividual Heterogeneity Affects the Outcome of Human Cardiac Tissue Decellularization. *Sci. Rep.* 11 (1), 1–11. doi:10.1038/s41598-021-00226-5

Tomášek, P., Tonar, Z., Grajciarová, M., Kural, T., Turek, D., Horáková, J., et al. (2020). Histological Mapping of Porcine Carotid Arteries - an Animal Model for the Assessment of Artificial Conduits Suitable for Coronary Bypass Grafting in Humans. *Ann. Anat. - Anatomischer Anzeiger* 228, 151434. doi:10.1016/j.aanat.2019.151434

Uygun, B. E., Soto-Gutierrez, A., Yagi, H., Izamis, M.-L., Guzzardi, M. A., Shulman, C., et al. (2010). Organ Reengineering through Development of a Transplantable Recellularized Liver Graft Using Decellularized Liver Matrix. *Nat. Med.* 16 (7), 814–820. doi:10.1038/nm.2170

Wang, F., Zhang, J., Wang, R., Gu, Y., Li, J., and Wang, C. (2017). Triton X-100 Combines with Chymotrypsin: A More Promising Protocol to Prepare Decellularized Porcine Carotid Arteries. *Bme* 28 (5), 531–543. doi:10.3233/BME-171694

Welch, J., Wallace, J., Lansley, A. B., and Roper, C. (2021). Evaluation of the Toxicity of Sodium Dodecyl Sulphate (SDS) in the MucilAir Human Airway Model *In Vitro*. *Regul. Toxicol. Pharmacol.* 125 (April), 105022. doi:10.1016/j.yrtph.2021.105022

Zhou, M., Liu, Z., Wei, Z., Liu, C., Qiao, T., Ran, F., et al. (2009). Development and Validation of Small-Diameter Vascular Tissue from a Decellularized Scaffold Coated with Heparin and Vascular Endothelial Growth Factor. *Artif. Organs* 33 (3), 230–239. doi:10.1111/j.1525-1594.2009.00713.x

Zvarova, B., Uhl, F. E., Uriarte, J. J., Borg, Z. D., Coffey, A. L., Bonenfant, N. R., et al. (2016). Residual Detergent Detection Method for Nondestructive Cytocompatibility Evaluation of Decellularized Whole Lung Scaffolds. *Tissue Eng. C: Methods* 22 (5), 418–428. doi:10.1089/ten.tec.2015.0439

Conflict of Interest: The authors declare that the research was conducted in the absence of any commercial or financial relationships that could be construed as a potential conflict of interest.

Publisher's Note: All claims expressed in this article are solely those of the authors and do not necessarily represent those of their affiliated organizations, or those of the publisher, the editors, and the reviewers. Any product that may be evaluated in this article, or claim that may be made by its manufacturer, is not guaranteed or endorsed by the publisher.

Copyright © 2022 Massaro, Kochová, Pálek, Rosendorf, Červenková, Dahmen, Liška and Moulisová. This is an open-access article distributed under the terms of the Creative Commons Attribution License (CC BY). The use, distribution or reproduction in other forums is permitted, provided the original author(s) and the copyright owner(s) are credited and that the original publication in this journal is cited, in accordance with accepted academic practice. No use, distribution or reproduction is permitted which does not comply with these terms.

frontiers | Frontiers in Bioengineering and Biotechnology

TYPE Review
PUBLISHED 08 August 2022
DOI 10.3389/fbioe.2022.951644

Check for updates

OPEN ACCESS

EDITED BY
Kamal Hany Hussein,
Assiut University, Egypt

REVIEWED BY
Axel Haverich,
Hannover Medical School, Germany
Filippo Naso,
Biocompatibility Innovation Srl, Italy

*CORRESPONDENCE
Peter R. Corridon,
peter.corridon@ku.ac.ae

SPECIALTY SECTION
This article was submitted to Biomaterials, a section of the journal Frontiers in Bioengineering and Biotechnology

RECEIVED 24 May 2022
ACCEPTED 14 July 2022
PUBLISHED 08 August 2022

CITATION
Wang X, Chan V and Corridon PR (2022), Decellularized blood vessel development: Current state-of-the-art and future directions.
Front. Bioeng. Biotechnol. 10:951644.
doi: 10.3389/fbioe.2022.951644

COPYRIGHT
© 2022 Wang, Chan and Corridon. This is an open-access article distributed under the terms of the Creative Commons Attribution License (CC BY). The use, distribution or reproduction in other forums is permitted, provided the original author(s) and the copyright owner(s) are credited and that the original publication in this journal is cited, in accordance with accepted academic practice. No use, distribution or reproduction is permitted which does not comply with these terms.

Decellularized blood vessel development: Current state-of-the-art and future directions

Xinyu Wang[1,2], Vincent Chan[1] and Peter R. Corridon[2,3]*

[1]Biomedical Engineering and Healthcare Engineering Innovation Center, Khalifa University, Abu Dhabi, United Arab Emirates, [2]Department of Immunology and Physiology, College of Medicine and Health Sciences, Khalifa University, Abu Dhabi, United Arab Emirates, [3]Center for Biotechnology, Khalifa University, Abu Dhabi, United Arab Emirates

Vascular diseases contribute to intensive and irreversible damage, and current treatments include medications, rehabilitation, and surgical interventions. Often, these diseases require some form of vascular replacement therapy (VRT) to help patients overcome life-threatening conditions and traumatic injuries annually. Current VRTs rely on harvesting blood vessels from various regions of the body like the arms, legs, chest, and abdomen. However, these procedures also produce further complications like donor site morbidity. Such common comorbidities may lead to substantial pain, infections, decreased function, and additional reconstructive or cosmetic surgeries. Vascular tissue engineering technology promises to reduce or eliminate these issues, and the existing state-of-the-art approach is based on synthetic or natural polymer tubes aiming to mimic various types of blood vessel. Burgeoning decellularization techniques are considered as the most viable tissue engineering strategy to fill these gaps. This review discusses various approaches and the mechanisms behind decellularization techniques and outlines a simplified model for a replacement vascular unit. The current state-of-the-art method used to create decellularized vessel segments is identified. Also, perspectives on future directions to engineer small- (inner diameter >1 mm and <6 mm) to large-caliber (inner diameter >6 mm) vessel substitutes are presented.

KEYWORDS

decellularization, recellularization, bioartificial, blood vessel, vascular tissue engineering, vascular replacement therapy

1 Introduction

Vascular malfunctions often result in various maladies and are a leading cause of global mortality. Existing treatments include medications, rehabilitation, and surgical interventions. Medications have been developed to regulate cholesterol levels, ameliorate vasoconstriction, and control blood pressure. Alternatively, rehabilitation offers non-invasive approaches that incorporate active counseling, diet adjustments, and tailored

exercise to support significant lifestyle changes. In comparison, surgical options, which are the most invasive, include angioplasty and stenting, atherectomy, endarterectomy, thrombectomy, and vascular bypasses. Vascular bypass is often used to treat severe conditions in large- (inner vascular diameter >6 mm) to small-caliber arteries (inner vascular diameter >1 mm and <6 mm). This autologous form of vascular replacement therapy relies on harvesting vessels from a patient's arms, legs, chest, and abdomen to replace damaged vascular compartments (Crane and Cheshire, 2003).

Unfortunately, harvesting vessels from recipients can cause significant donor site morbidity, require expensive surgical procedures to repair lesions at the donor site, and often result in multiple post-surgery side effects like restenosis, aneurysms, infections, chronic paresthesia, dehiscence, and long-term pain (Thomas et al., 2013). The aesthetic outcomes of these surgical procedures may have severe social and psychological impacts on the patients, thus negatively impacting the patient's quality of life and introducing significant financial burdens if further corrective and cosmetic procedures are required. Besides, around one-third of patients do not have proper and sufficient vessels for replacement owing to pre-existing vascular diseases, vein stripping, and previous surgical interventions. These issues have called for the need to develop transplantable vascular substitutes.

An ideal vessel replacement or equivalent should be biocompatible and biodegradable, while it possesses integrative and functional properties to support normal *in vivo* physiologic conditions such as pulsatile high-pressure blood flow, be capable of growth, and be cost-affordable. Scientists and surgeons have developed artificial vessel substitutes for decades to address this issue. Traditional prosthetic vascular analogs have been designed using Dacron®, polyethylene terephthalate, and Goretex®, expanded polytetrafluoroethylene (ePTFE) (Peck et al., 2012), and polyurethane (Kakisis et al., 2017). These synthetic materials were proved inferior to autologous vessels due to their rapid-decreasing patency, limited durability after 2 to 5 years, lack of compliance between grafts and native anastomosis, and increased risk of thrombosis and inflammation (Lin et al., 2018). In comparison, tissue-engineered vascular grafts (TEVGs) devised from adaptive manufacturing technologies like 3D printing, electrospinning, hydrogelation, cell seeding, as well as the application of various acellular/cellular substrates have been used to create artificial/bioartificial vascular conduits. Overall, it has been challenging to develop vessel substitutes that meet all the requirements simultaneously.

Nevertheless, vascular decellularization technologies have shown promise in meeting these challenges in recent years. This process removes cellular components from the native tissues to create an extracellular matrix (ECM)-rich, non-immunogenic vascular scaffold. Like their original forms, these natural vascular templates are believed to maintain an ability to support vasculogenesis during the reseeding process. Previous studies have outlined endothelial cells (ECs) compatibility with ECM scaffolds. Such compatibility is crucial for cellular adhesion, proliferation, and migration needed to create a functional and intact endothelium bordering the inner lumen of replacement vascular segments (Xu et al., 2014).

Various sources, including human and animal cadavers, have been identified as the supply of native vessels for decellularization. However, allografting and xenografting techniques can reintroduce issues related to immunogenicity. These issues will, in turn, give rise to the rejection of allografts and xenografts by primitive multicellular organisms mediated by phagocytic cells, coagulation proteins, and possibly by complement-like proteins (Cohen et al., 2021). Beyond these issues, it is interesting to note that some decellularized vessel products are currently evaluated for clinical use. However, clinical outcomes are unsatisfactory because of the graft-related thrombosis, infection, and aneurysm compared with other alternatives such synthetic conduits. Research is also being conducted to eliminate genetic remnants that give rise to rejection by using advanced gene-editing tools.

This review outlines the native vascular structure and then transitions to decellularization approaches and mechanisms, including physical, chemical, biological, and combinational treatments used to create decellularized vascular segments. The current state-of-the-art approaches used to create decellularized vessel segments are identified. Challenges and future perspectives to engineer small- to large-caliber vascular substitutes are also presented. Additionally, this review discusses various mechanisms behind this technology and outlines a simplified model for a replacement vascular unit based on innovative approaches to reinforce the structure and enhance physiological functions.

2 The native vasculature structure

Blood vessels are mainly categorized as arteries, veins, and capillaries, which nourish tissues and organs to sustain homeostasis. Generally, blood vessels can be characterized by their caliber, i.e., inner diameter (ID), as macrovessels (ID > 6 mm), small vessels (1 < ID < 6 mm), and microvessels (ID < 1 mm). Vessels within each of these three categories differ in cell composition, histological organization, and physiological function. However, all three types of blood vessels contain heterogeneous but well-orchestrated networks of ECM that regulate cellular and tissue functions and maintain vascular structural integrity. Adjacent thin endothelial cell layers found in the inner lumen are known for their endocrine and metabolic functionalities (Forslund and Metsärinne, 1992;Baumgartner-Parzer and Waldhäusl, 2001). ECs secrete substances that regulate vascular relaxation and contraction, angiogenesis,

mitogenesis, blood clotting, platelet adhesion, and immune function.

The endothelium forms a crucial link between the cardiovascular and immune systems by expressing a range of innate pattern recognition receptors that allow ECs to respond to inflammatory stimulation, regulate immune cell recruitment, as well as extravasation into tissue targets. For example, ECs release endothelin, a potent vasoconstrictive polypeptide that exerts its major effects in both autocrine and paracrine regulations. This compound induces prolonged smooth muscle cell (SMC) contraction. Such secretions result in reduced blood flow, especially in renal and coronary circulations, and an increase in systemic blood circulation. Endothelin is also secreted in response to various biological stimuli, including vasoactive peptides such as angiotensin II, adrenaline, vasopressin, and thrombocytic products like transforming beta growth factor and thrombin.

SMC compartments within the vascular wall further control the vascular diameter, wall movement, and wall stiffness. From a classical perspective, these muscular regions can be divided into single- or multi-unit structures, as suggested by Bozler (Bozler, 1937;Bozler, 1970;Bozler, 1973). According to the Bozler model, single-unit (visceral) smooth muscle compartments are composed of cells electrically coupled by connexins through the formation of gap junctions. This unique conformation facilitates synchronous contraction, allowing the muscle layer to operate as an electrical syncytium. Whereas multi-unit smooth muscle layers, which are found in large blood vessels, lack, or rarely possess, gap junctions, differ from single-unit in that each smooth-muscle cell receives a synaptic input. This characteristic allows for the multi-unit smooth muscle to have much finer control. This division, which is based on motor nerve regulation and cellular electrical coupling, is predominately presented in the literature. However, this perspective does not fully describe the diversity of the tissue and is inconsistent with the experimental observations that have provided evidence of electrical coupling in all types of smooth muscles. A more recent division has been proposed to support phasic and tonic contractile responses that further outlines differences in cellular signaling and contractile kinetics.

The ECM is a microenvironment containing insoluble macromolecules that bind to its polymeric scaffold and soluble bioactive factors present in the liquid phase of this highly hydrated matrix, which regulate the behavior and functions of cells (Brown and Badylak, 2014). This microenvironment is an intricate multiphase network composed of an array of multidomain macromolecules organized in a cell/tissue-specific manner. Components of the ECM link or associate together to form a structurally stable composite, contributing to the mechanical properties of tissues and organs. At the same time, the ECM is a highly dynamic entity that is of vital importance, determining and controlling fundamental cellular functions, namely proliferation, adhesion, migration, polarity, differentiation, and apoptosis. Within these well-orchestrated networks are an abundance of glycoproteins, proteoglycans, glycosaminoglycans (GAGs), as well as structural proteins like collagen, elastin, and fibronectin, and laminin, which serves as the main component of the basal lamina (Davis and Senger, 2005; Hohenester and Yurchenco, 2013). These complexes define the two categories of molecules: glycosylated and fibrous proteins. Glycosylated proteins provide viscoelastic properties, support water retention, sustain osmotic pressures, and dictate proper fibrous protein organization (Iozzo and Schaefer, 2015). These qualities ensure tissue hydration that can withstand *in vivo* compressional forces (Yanagishita, 1993).

The fibrous extracellular networks of collagen and elastin provide the dominant mechanical responses of tissue. These two classes of fibrous proteins are secretory products from tissues and organs, and of these components, collagen is the most abundant fibrous protein and constitutes up to 30% of the total mass of mammalian proteins. Fibrous matrix proteins enable tissues to withstand high tensile and repetitive stresses without deformation or rupture. Collagen fibers have the greatest tensile strength and exhibit nonlinear responses when stretched, compared to elastin and fibronectin fibers, which are much more distensible (Williams et al., 2009). These structural ECM proteins work in tandem, whereby elastic fibers are tightly tethered to collagen fibrils to ensure that tissues resume their original shapes after compression or stretching. Moreover, during periods of extension, fibronectin fibers unfold to expose integrin-binding sites to facilitate cell adhesion. Such tension-activated cell-ECM adhesion is a central mechanism allowing cells to probe the mechanics of surrounding microenvironment (Merna et al., 2013). Once devoid of cells through decellularization, which isolates the extracellular matrix of the tissue from its native cells, it is hoped that the remaining matrices would offer a microenvironment naturally covered with molecular cues capable of initiating, for our purposes, vascular regeneration.

3 Decellularization approaches used to decellularize blood vessels

Decellularization offers a more efficient option to reduce the burdens of autologous grafting than other vascular tissue engineering (VTE) technologies, namely, those of a synthetic nature (Shakeel and Corridon, 2022). This approach generates far more accurate replicas of the ECM with superior bioactivity, immunogenicity, and biodegradability. This burgeoning technique relies on various physical, chemical, and biologic approaches or combinations of these individual approaches to rupture cellular membranes via immersive, agitative, and perfusive conditions.

TABLE 1 A systematic summary of decellularization methods, their mechanisms of actions, and related references.

Decellularization technique		Mechanisms of action	References
Physical treatments	Free-thaw cycle	Thermal shock generated from repeated freezing and thaw cycles ruptures membranes	Rabbani et al. (2021)
	High hydrostatic pressure	Cold isostatic pressure disrupts cellular membranes within tissues	Funamoto et al. (2010)
	Electroporation	Microsecond- durational electrical pulses to enhance the cellular membrane permeability drastically	Sano et al. (2010)
	Supercritical fluid	Gases/liquids exist above critical pressure/temperature eliminate cell compartments within tissues	Di Maio et al. (2021)
	Subcritical fluid	Liquefied (subcritical) DME extracts lipids of tissues	Kanda et al. (2021)
	Immersion and agitation	Immerse tissues in chambers with decellularizing agents, and agitate tissues with a magnetic plate, ultrasound source, shaker, or an agitator attached to the end of the chamber.	Syed et al. (2014)
	Perfusion	The fluid (agent solution) passage through the circulation system to tissues/organs	He and Callanan, (2013), Corridon et al. (2017), Xu et al. (2017)
Chemical treatments	Acids and bases	Bases hydrolyze proteins to promote cellular debasement and acids lead to denaturation and protein function loss	Mendoza-Novelo et al. (2011), Angelova et al. (2018)
	Surfactants (ionic, non-ionic and zwitterionic)	Lyse cell membranes through protein crystallization, destabilizing, denaturing, targeting lipid-lipid interactions	Koley and Bard (2010)
	Chaotropes	Chaotropic agents disrupt the hydrogen bonding networks, van der Waals forces, and hydrophobic effects	Salvi et al. (2005)
	Osmotic stress	Hypertonic/hypotonic solution-induced osmotic stress/shock responses disrupt cell stability and interfere with the interaction between DNA and proteins	Fu et al. (2014)
Biologic treatments	Enzymatic approach	Enzyme-based processes that disrupt the bonds and interactions between nucleic acids and interacting cells through the disruptions of neighboring proteins and other cellular components.	Rieder et al. (2004), Fu et al. (2014)
	Combination of physical/chemical/enzymatic treatments	Physical, chemical, and enzymatic treatments are combined to optimize vascular decellularization	Row et al. (2017)

Decellularization strategies vary widely based on distinct features of tissues, including structure, components, size, and thickness, as summarized in Table 1. Besides, antimicrobial treatments with penicillin, streptomycin, and amphotericin B are also applied to suppress antigen invasion (Jiménez-Gastélum et al., 2019). Theoretically, most cellular epitopes and antigens that trigger immune responses and contribute to implantation failure are ablated after vascular decellularization. As a result, decellularization leads to the optimized production of non-immunogenic vascular analogs that possess an ECM comparable to that of the native structure. Such an ECM scaffold can provide an environment conducive to cell integration/differentiation that is fit for *in vitro* vasculogenesis.

3.1 Physical treatments

Physical treatments involve thermal shock (freeze-thaw cycles), high hydrostatic pressures, supercritical fluids, pressure gradients, electroporation, ultrasound waves, vacuum technologies, immersion and agitation, and perfusion have been applied for decellularization (Rabbani et al., 2021).

3.1.1 Free-thaw cycle

Thermal shock generated from freeze-thaw cycles, ranging from −87° to 37°, is applied to rupture cell membranes. Repeated freezing and thawing cycles help ice to form within the cytoplasm and cellular membranes. Various studies have established that damage to the plasma membrane occurs post-thaw stage, but there has been a debate on when the damage occurs during the cycle (Rabbani et al., 2021). Current mechanisms related to intracellular ice formation identify the plasma membrane as the primary injury site. During freezing, ice first forms in the extracellular water. This thermal change increases the ionic concentration in extracellular fluid and establishes an unregulated osmotic pressure gradient across the plasma membrane. This osmotic pressure gradient supports water efflux and cytoplasm dehydration and cell dehydration, while ice formation supports a phase transition leading to both mechanical and non-mechanical cellular damage.

This method can effectively remove cellular contents but may lead to minor ECM degradation and mechanical instability (Keane et al., 2015). Interestingly, the number of freeze-thaw cycles and the rates of temperature variation have not significantly affected decellularization efficiency, structure, or mechanical properties. Regarding blood vessels, Cheng et al.

(2019). presented a study using freeze-thaw cycles to decellularize porcine carotid arteries, but this process was used in conjunction with chemical treatments of anionic and non-ionic surfactants. Microscopic and mechanical analyses unveiled well-maintained ECM morphology generated through the freeze-thaw cycles. Moreover, the resulting ECM was accompanied by the increase of arterial porosity after optimized use of both types of detergent. These results indicate that vascular scaffolds produced from the sequential use of freeze-thaw cycles and surfactants may serve as a promising option for VTE.

3.1.2 High hydrostatic pressure

High hydrostatic pressure (HHP) treatment is based on the generation of cold isostatic pressure on tissues immersed in saline to generate acellular scaffolds. The technique disrupts the cellular membranes within the tissue, and the resulting debris can be removed from the ECM scaffold after rinsing with saline solution (Funamoto et al., 2010). From another mechanistic perspective, reports have shown that HHP can induce mitochondrial damage, demonstrate the overproduction of ROS, and ultimately apoptosis (Le et al., 2020). This option relies on the fact that cell membranes are disrupted by pressures of 100 MPa, while the three-dimensional architecture of the ECM is maintained even at 980 MPa.

A study using HHP of 980 MPa for 10 min successfully decellularized porcine arteries. Generally, HHP-decellularization efficiently removed cellular components and debris, preserved tissue's mechanical properties, and suppressed structural damage. However, the amount of force applied must be precisely controlled in order to avoid nonideal structural alterations underlying the histological structure of the ECM. This process also supported xenogeneic transplantation, as HHP-decellularized arteries appeared to suppress immune responses and can be regenerated by recipient cell infiltration (Negishi et al., 2015). Allogenic transplantation showed that the acellular vascular scaffold endured arterial blood pressure and resisted luminal clot formation.

3.1.3 Electroporation

Electroporation, a non-thermal and irreversible decellularization treatment, applies electrical pulses of microsecond duration to drastically enhance the cellular membrane permeability, presumably *via* the induction of nanoscale pores within lipid bilayers (Sano et al., 2010). Studies have shown that this technique is capable of decellularizing large volumes of tissue when combined with organ perfusion. Unfortunately, this application may be limited by the relatively small size of the electrodes used to induce the micropore formation and their propensity for generating tissue inflammation. However, this inflammatory response of immune system could be suppressed if decellularization was performed *in vivo* (Crapo et al., 2011). It should be noted that *in vivo* decellularization can lead to off-target and unwanted tissue degradation if not well-controlled.

Another form of poration utilizes mechanical wave-based ultrasound pulses to cleave intermolecular bonds, disrupt the cell membrane, and eliminate innate cellularities. Nevertheless, sonication-derived cavitation can severely damage tissue structure. Such effects were observed by Azhim et al. while studying the coupling between sonication and one of the most prominent chemical decellularization agents, SDS. Additionally, the porcine aorta was successfully decellularized by sonication at the luminal side and compared well to the results derived from treatment with SDS. The physical changes induced by this detergent resulted in the effective removal of DNA content and the retention of native mechanical properties (Sano et al., 2010). However, in some cases, immersion treatments need additional mechanical support in order to eradicate immunogenic components better. Hydrodynamic fluid forces induced by perfusion and alterations in temperature have remarkably reduced DNA residual content while maintaining the integrative ECM structures for the perseverance of mechanical functions (Zager et al., 2016).

3.1.4 Supercritical and subcritical fluids

A supercritical fluid is a substance that can exist as a gas or liquid, and is used in a state above critical pressure and critical temperature when gases and liquids coexist (Di Maio et al., 2021). Supercritical fluids have also been used to eliminate cell compartments within tissues and to elute detergents from scaffolds after decellularization. Supercritical flow-based decellularization can impart minimal effect on tissue's mechanical properties, but the elevated pressure to create such fluids can impair certain ECM components (Keane et al., 2015). Commonly applied parameters in this technique are based on critical temperature of 31.1°C and pressure of 7.40 MPa achieved in supercritical carbon dioxide (SC-CO_2). This method is largely favored as no additional washing procedures are needed, and the intact structure and mechanical features are unchanged. For instance, porcine pericardial tissue, aortic and arterial tissues were decellularized with SC-CO_2-based approaches leading to the complete removal of lipids, including a notable decrease of pro-inflammatory fatty acids, as well as efficient DNA removal (Gil-Ramírez et al., 2020). This technique generated ECM scaffolds with essential proteins (collagen Type I, collagen Type III, collagen Type IV, elastin, fibronectin, and laminin) and pivotal biological and growth factors (GAG, VEGF). Yet, the complex and expensive apparatus required to generate these zero viscosity fluids may eventually limit its application.

Likewise, another surfactant-free decellularization technique has been identified, in this case, using a subcritical fluid. This method uses liquefied (subcritical) dimethyl ether (DME). DME dissolved in water is not toxic to microorganisms and exhibits resistance to autoxidation, and can be used to extract lipids from wet porcine tissues by using subcritical DME at 23°C with a DME pressure of

0.56 MPa. Afterwards, DME will evaporate from the aorta at room temperature due to its low boiling point. Interestingly, results from this study by Kanda et al. (2021) clarified that although subcritical DME inefficiently removes cell nuclei, it can be used in tandem with DNase and saline/ethanol washing treatments to remove cell nuclei. Hematoxylin and eosin staining, and DNA analyses confirmed that most cell nuclei were removed from the aorta roughly 1–3 days after the initial DME treatment. DNA analyses uncovered residual DNA content of 40 ng dsDNA per mg ECM dry weight in the aortic scaffold. This value is lower than the standard value of 50 ng dsDNA per mg ECM dry weight proposed by Crapo et al. as the minimal criteria to assess the efficacy of decellularization (Crapo et al., 2011; Bruyneel and Carr, 2017). Overall, these results have demonstrated that subcritical DME in conjunction with DNase eliminates the need to utilize surfactants.

3.1.5 Immersion and agitation

Immersive and agitative protocols are commonly used for hollow or less dense structures. This approach has been described for multiple tissue types, including blood vessels. The structure to be decellularized is immersed in chambers with decellularizing agents, and agitation is achieved with a magnetic plate, ultrasound source, shaker, or an agitator attached to the end of the chamber. It should be noted that the duration of the protocol of immersive/agitative approaches is a function of the tissue complexity, thickness, and density, as well as the detergent used, and the intensity and duration of applied treatment. Peristaltic pump-driven perfusion regimens can also be applied to enhance further the surface contact and homogeneity of the detergent-tissue interface (Syed et al., 2014).

3.1.6 Perfusion

Perfusion can be conducted in antegrade and retrograde patterns for homogenously distributing the lysing agents throughout the organ via its underlying vasculature. With this confirmation, it is crucial to define tissue-specific flow rates that will ideally support fluid distribution and limit the development of elevated levels of pressure, which can be detrimental to thinner-walled and less resistant microvessels. Large and small animal model protocols have also been defined for blood vessel decellularization by using porcine abdominal aortic and carotid segments (Xu et al., 2017), and rat coronary arteries (He and Callanan, 2013). In contrast, perfusion-based decellularization protocols are widely recommended for whole organs with intact arterial and venous connections and, in some instances, hollow structures like vessels that can directly support the passage of fluid (Corridon et al., 2017).

3.2 Chemical treatments

Several chemical treatments for decellularization have been proposed, including acids and bases, surfactants (single ionic, zwitterionic, and non-ionic forms), chelators, exogenous enzymes, and hyper-/hypotonic solutions. These decellularization solutions have varied effects in standalone applications or class combinations, resulting in ECM products with different compositions. Such heterogeneity is observed in diverse levels of cellular component denaturation.

3.2.1 Acids and bases

As an illustration, sodium hydroxide of sufficient strength can hydrolyze proteins in tissues to promote cellular debasement. Overall, alkaline treatments can introduce negative charges on the collagen molecules, which will create repulsive forces in tissues that drive substantial swelling suitable for pericardial decellularization (Mendoza-Novelo et al., 2011). Such treatment produced ECM scaffolds that possessed collagen structural networks, mechanical anisotropies, tensile moduli, tensile strengths, and strain maxima comparable to the native tissues. A study by Chuang et al. (2009) has also indicated that scaffolds generated by alkali-mediated decellularization efficiently removed native cells and DNA as revealed by histology and DNA analysis, respectively. This group aimed to develop tubular elastin scaffolds by using decellularization and removal of collagen from small-caliber porcine carotid arteries (diameters of approximately 5 mm). Alkaline extraction supported complete collagen removal while maintaining intact elastin and proteoglycans. Interestingly, the results from this study indicated that alkali-mediated decellularization is more conducive to cell repopulation than detergent-based methods.

Likewise, the combinations of reversible alkaline and nonionic surfactant (tridecyl alcohol ethoxylate) treatments retained general tissue structure and eliminated immunogenetic components. However, the inherent tissue swelling triggered a substantial loss of GAG content, and thus reduced viscoelasticity. Due to the acidic/basic properties of plasma membrane, pH directly affects membrane lipids, and substantial pH changes can induce lipid vesicle migration and extensive tissue deformation (Angelova et al., 2018). Acid oxidation can also lead to denaturation and loss of protein function. Specifically, acids can adversely alter protein stabilization by disrupting salt bridges and hydrogen bonds between the side chains, leading to denaturation. The process of protein oxidation frequently introduces new functional groups, such as hydroxyls and carbonyls, which contribute to altered biomolecular function and turnover.

For instance, peracetic acid has been used to create submillimeter-diameter vascular scaffolds. Yamanaka *et al.* decellularized rat tail arteries with an average inner diameter of 0.6 mm, using a combination of this acid and DNase I. Treatment with a 0.3% isotonic acid solution disrupted cell membranes and improved the decellularization efficiency in combination with the subsequent DNase treatment. A further illustration supporting combinative approaches outlined that the perfusion method was superior for cell removal compared to static immersion. However, histology showed that the perfusion

of the DNase solution decreased ECM thickness, and this approach was not necessarily optimal for very thin vascular tissue decellularization.

In vivo application suggested that the reduction in mechanical strength of the decellularized scaffolds even after their luminal modification with peptides composed of collagen-binding and endothelial progenitor cell-binding sequences. These allogeneic implants remained patent for 2 weeks but unexpectedly ruptured after that. As often realized, this method identified the compromise between effective cell removal and maintenance of the ECM nature and highlighted the complexity in defining universal decellularization methods, the need to define protocols according to the type of target tissue, and its intended applications (Yamanaka et al., 2020).

3.2.2 Surfactants

Surface-active agents such as surfactants, are widely used in biology for protein extraction from cell membranes for protein crystallization, as well as destabilizing, denaturing, and membrane permeabilizing agents (Koley and Bard, 2010). It can be argued that detergent-based decellularization is the most extensively applicable approach to induce cell lysis by disarranging the phospholipid membrane and uncontrolled membrane proration. Sodium dodecyl sulfate (SDS) and sodium deoxycholate (SD) are the most used anionic detergents. SDS is recommended for decellularization because of its efficient removal of cellular and genetic components and is well known for having strong electrostatic interactions with proteins, generated between aliphatic regions of the amino acids arginine and lysine and positively charged amino acids within primary protein structures supported by interactions of the hydrocarbon chains of the surfactant (Aguirre-Ramírez et al., 2021). Studies outlining the denaturing effect of SDS on globular proteins have identified that this process occurs at different stages depending on the concentration of the surfactant. Initially, SDS monomers bind to the protein to form groups up to a critical concentration for initiating denaturation. Further monomer binding alters the protein secondary structure. However, SDS is toxic and, damages tissues and organs' structure and mechanical properties, and efforts are needed to ensure its removal from scaffolds at the end of decellularization.

Concomitantly, SD can produce highly biocompatible scaffolds through the solubilization of cell membranes, resulting in decellularized matrices with better bioactivity, which is more suitable for cell seeding and growth. Although SD is less toxic, it can cause DNA agglutination on the surface of the scaffolds (Boccafoschi et al., 2017), reducing decellularization efficacy. On the other hand, cationic surfactants are more toxic than anionic surfactants and less effective as decellularization agents. Compared to anionic surfactants, cationic surfactants are positively charged and have a milder protein destabilization effect as they interact with negatively charged amino acid side chains, like aspartate (Peloso et al., 2015) and glutamate. Reports have shown that such interactions between cetyltrimethylammonium bromide, a popular cationic detergent, and lysozymes which are very hydrophobic and weakly electrostatic, do not cause a change in secondary protein structure but adversely alters the tertiary structure (Khan et al., 2015).

In contrast, nonionic surfactants targeting lipid-lipid interactions have minimum toxicity and are superior in preserving ECM architecture but inferior for removing DNA compared to anionic surfactants. Triton X-100 is one of the most widely used nonionic surfactants for lysing cells to extract proteins and other cellular organelles or permeabilize the living cell membrane for transfection. The nonionic surfactant Triton X-100 is frequently utilized to remove the remnant SDS in the perfusion process of organs (Corridon, 2021; Pantic et al., 2022). This surfactant has a disruptive effect on the polar head group as well as hydrogen bonds present within the lipid bilayer, altering the compactness and integrity of the lipid membrane. The insertion of a detergent monomer into the lipid membrane begins at low concentrations, which eventually disrupts cellular structures and eventually over permeabilizing the membrane as concentrations increase to support bilayer to micelle transitions. Aortic valvular scaffolds created using SD and Triton X-100 after formaldehyde fixation possessed mechanical properties close to those of the native valves (Singh et al., 2022). Combinations of Triton X-100 and SDS have also produced decellularized porcine carotid arteries with minimal destruction (Cai et al., 2021).

Zwitterionic constructs are ubiquitous in biological systems, from proteins to di-chain phospholipids within cellular membranes, and contain both positively and negatively charged chemical groups within their headgroups. Naturally occurring di-chain phospholipids are the main components of cell membranes. Such moieties generally show high solubility in water, broad isoelectric ranges, and high resistance to changes in the pH and ionic strength of the solution media, and their surfactants are known to form micelles in solution. Zwitterionic detergents exhibit the properties of both nonionic and ionic detergents and their tendency to denature proteins is more significant than that of nonionic detergents (Gratzer, 2019). However, the net-zero electrical charge on the hydrophilic groups of zwitterionic detergents protects the native state of proteins during the decellularization process (Keane et al., 2015). The molecule denoted by 3-[(3 cholamidopropyl) dimethylammonio]-1-propanesulfonate (CHAPS) is a notable zwitterionic surfactant that effectively eliminates protein-protein interactions and can match the cellular removal capacity of SDS (Keane et al., 2015).

Acellular scaffolds created by using CHAPS have better preserved ECMs, and lower remnant cell concentrations than non-ionic detergents (Gilpin and Yang, 2017). Explicitly, CHAPS-derived scaffolds retain more collagen, GAGs, and elastin than SDS ionic detergent while removing more than 95% of nuclear materials. It also revealed that CHAPS could

be used in both perfusion and immersion processes with excellent maintenance of ECM proteins and structure but incomplete removal of cellular debris like cytoplasmic proteins (Sullivan et al., 2012). Again, the results obtained using this powerful denaturing agent are concentration-dependent, as higher CHAPS concentrations can disrupt collagen networks and basement membrane integrity, similar to higher SDS concertation solutions. For the vasculature, CHAPS-treated arterial tissues have unaltered collagen and elastin morphologies, and the collagen content remains comparable to that of the native artery. Protocols using another zwitterionic surfactant, tributyl phosphate or tri-n-butyl phosphate (TNBP), revealed that it also has a decellularization capacity similar to that of SDS by adequately eliminating tissue cellularities and keeping the intact ECM (Meezan et al., 1975; Gilpin et al., 2014). Moreover, collagen matrix, GAGs, and biomechanical properties (including tensile strength and elasticity) were not significantly altered. Although residual cytoskeletal proteins (e.g., vimentin) were not wholly removed, TnBP is a viable option that warrants further study for other tissue types.

Simsa et al. (2018) performed a systematic comparison of SDS, SD, CHAPS, and TritonX-100 for decellularizing the porcine vena cava and found that all surfactants can efficiently decellularize blood vessels. They presented data that outlined the acellular scaffolds generated with ionic and zwitterionic surfactants retained appreciable and comparable mechanical strengths, level of collagen preservation, and ECM integrities, but TritonX-100-based treatment required additional and long-term DNase application for complete decellularization. This group also examined the *in vitro* potential of human umbilical vein endothelial cells to adhere and proliferate on the luminal decellularized surface. Interestingly, the non-ionic surfactant-derived scaffolds showed the most remarkable efficacy for recellularization. These results build up those obtained by Kuna et al. a year earlier in their report outlining the decellularization of the human saphenous vein by using Triton X-100, TnBP, and deoxyribonuclease (DNase) and subsequent recellularization by perfusion of the peripheral blood and the endothelial medium.

3.2.3 Chaotropes

Chaotropic agents disrupt the hydrogen bonding networks, van der Waals forces, and hydrophobic effects, specifically, non-covalent interactions in biological macromolecules, namely proteins (Salvi et al., 2005). Macromolecules attain more structural freedom that drives unfolding and destabilization through these agents while compromising the integrity of supramolecular assemblies (Hanai et al., 2020). Urea, a well-known chaotropic agent, denatures proteins and disrupts lipids and protein interactions to induce cell lysis, and chaotropic solubilization of proteins have prompted their evaluation of its potential as a decellularization agent (Wong et al., 2016). Over the years, urea has been used to produce ECM scaffolds from bovine umbilical veins (Wong et al., 2016).

3.2.4 Osmotic stress

Hypertonic or hypotonic solutions induce osmotic stress or shock responses that disrupt cell stability and interfere with the interaction between DNA and proteins. The osmotic shock lyses cells, but it does not remove the cellular residues that it releases into the matrix. In particular, waste derived from DNA is of paramount importance in all decellularization processes due to the tendency of the nuclear material to remain tethered to ECM proteins (Fu et al., 2014). As a result, endonucleases, exonucleases, and other kinds of DNA degrading enzymes are used in conjunction with this approach to guarantee the elimination of nuclear components from ECM (Mendibil et al., 2020). Agents that rely on tonicity have limited utility as a standalone decellularizer method but can be applied to enhance the action of detergents.

As an additive mechanism, this technique generally involves the initial application of a hypotonic solution to stimulate uncontrolled cellular swelling that results in osmotic lysis. The unregulated inward movement of water may also enhance the uptake of detergents into the cellular membrane. After that, a hypertonic solution is applied to expel water from the cell and induce cellular dehydration and shrinkage that helps cellular death and detachment from the ECM. Finally, an additional nuclease enzymatic digestion is used to remove residual DNA. Osmotic shock-based decellularization strategies have created acellular templates of blood vessels already.

3.3 Biologic treatments

3.3.1 Enzymatic approaches

Biologic treatments for decellularization are enzyme-based processes that disrupt the bonds and interactions between nucleic acids and interacting cells through the disruptions of neighboring proteins and other cellular components. Trypsin, nucleases (DNase and RNase), benzoase, and fetal bovine serum are widely used for decellularizing agents with low DNA, β-actin, and major histocompatibility complexes (MHC). These enzymatic agents are usually used with ethylenediaminetetraacetic acid (EDTA) or combined with surfactants to facilitate tissue or organ decellularization effectively (Rieder et al., 2004). These compounds have been widely investigated, and enzymatic treatments for decellularization can digest nucleic acids (DNA and RNA) and remove undesired ECM residues, as previously outlined for DNase activity (Rieder et al., 2004).

EDTA is a chelating agent that binds to calcium and prevents the integral proteins between cells from binding to one another. It is often used with trypsin, an enzyme that acts as a potent protease to cleave bonds between integral proteins of neighboring

cells within a tissue. For instance, trypsin combined with EDTA cleaves cell-matrix adhesions to eliminate cellular and genetic materials after 24 h of treatment. This relatively short period appears to be appropriate for immunogenetic component abatement and mechanical property as well as vital surface molecule maintenance. However, trypsin/EDTA treatments can decompose salt- and acid-soluble collagens due to their higher affinity towards iron ions that stabilize this essential ECM protein (Zhang et al., 2016).

Furthermore, collagenases, proteases, and lipases have been used to remove cells in conjunction with other approaches. Collagenase-based treatments may be applied in cases that do not require a fully intact ECM. A study aimed to develop acellular-based vascular grafts from rodent iliac arteries outlined the application of collagenase IV detached the endothelium, and its combined use with detergents facilitated effective decellularization and eliminated MHC class I and class II antigens (Dall'Olmo et al., 2014). Lipase, e.g., phospholipase A2, treatments can hydrolyze the phospholipid component of tissues (Keane et al., 2015), while dispase, a well-known protease, would have prevented undesired cell aggregation and cleaved connections between fibronectin and collagen I and collagen IV to dislodge cells from the ECM (Fernández-Pérez and Ahearne, 2019; Nouri Barkestani et al., 2021; Neishabouri et al., 2022). Likewise, proteases like dispase and thermolysin (metalloproteinases) and lipase activities are not effective enough for complete delipidation and deproteination of the relatively large tissues and whole organs.

3.3.2 Combined physical, chemical, and enzymatic treatments

Physical, chemical, and enzymatic treatments are combined to optimize vascular decellularization. This approach successfully developed functional, small vessels using a novel combination of zwitterionic, ionic detergents, and enzymatic treatments. Native samples were infused with CHAPS buffer followed by SDS solution. After that, to ablate unwanted cellular debris of these samples, they were incubated in a mixture of endothelial growth media-2 (EGM-2), 12% fetal bovine serum, and an enzymatic cocktail (Row et al., 2017). This innovative treatment has shown promising results for ECM retention, improved adhesion of HUVECs and SMCs *in vitro*, and reduced intimal hyperplasia (Gui et al., 2009). Apart from that, pressure gradients approach can adequately produce acellular templates from veins and other hollow structures in conjunction with an enzyme-mediated decellularizing process (Sierad et al., 2015).

Besides these treatments, decellularization processes have been developed to create large vessel scaffolds. The porcine abdominal aorta (approximately 20 mm in length) was decellularized with dichloroacetate DCA and DNase I, and the ECM was preserved to retain maximal tensile strength. Vessels harvested from the placenta were attached to a perfused capillary and assembled into a circulation system to lyse cells. Collagen and GAG retention facilitated EC attachment and mechanical property maintenance (Mancuso et al., 2014).

4 Current state-of-the-art for decellularized blood vessels

4.1 Commercially available grafts

Commercially available decellularized vascular products include Artegraft® (bovine carotid artery), Solcograft (bovine carotid artery), ProCol® (bovine mesenteric vein), SynerGraft® (bovine ureter), MatrACELL® (decellularized ECM), decellularized human iliac or mammary veins, and Synergraft-processed cadaver vein allograft, which are clinically available (Kumar et al., 2011). For instance, Artegraft® is applied for hemodialysis, lower extremity bypass, and the treatment of traumatic arteries, whose advantages are reduced thrombosis, long-term durability, naturally biocompatibility, non-immunogenicity, and flexibility in multi-sizes for matching various host vessels (Pashneh-Tala et al., 2016).

ProCol® is a vascular bioprosthesis designed to form a bridge graft for vascular access when the previous prosthetic grafts have failed. This product supports vascular hysteresis to amplify pulsatile blood flow and possesses appreciable strength, durability, anastomotic compliance, and biocompatibility (Sharp et al., 2004). ProCol® has shown promising outcomes when used as a hemodialysis access line. Similarly, SynerGraft® (bovine ureter) is a foundation for the next generation of implantable biological tissues. For example, pulmonary and cardiac tissues treated with SynerGraft® were implanted into patients' bodies without alloantibodies. Compared to standard cryopreserved allografts, SynerGraft® has excellent durability and better hemodynamics to suppress coagulation and maintain an integrative biological matrix.

This novel patented technology (SynerGraft®) created an underlying collagen matrix without epithelial cells, smooth muscle cells, and fibroblasts through denuding bovine ureters of cells by a series of hypotonic lysis and nuclease digestion (Das et al., 2011). These decellularized vascular products are processed by enzymatic/chemical methods, except for the SynerGraft® (bovine ureter) and SynerGraft®-processed cadaver vein allograft. Table 2 details the decellularization methods, indications, sizes, features, and other key properties of commercially available decellularized vascular products.

4.2 State-of-the-art *in vivo* applications

Successful examples of decellularized vascular conduits include multiscale components from diverse sources like carotid arteries from goats, and sheep, pulmonary aortas of sheep, rat abdominal/thoracic aortas, rat/porcine arteries, human umbilical arteries, porcine vena cava, saphenous/radial

TABLE 2 A summary of commercially available decellularized vascular products, their associated applications, and clinical performance.

Vascular product	Product information	Approved indications	Clinical applications	Product advantages/ Disadvantages
Artegraft®: bovine carotid artery(Harlander-Locke et al., 2014)	Decellularized steer's carotid artery through physical and chemical treatments; ID: 4–8 mm; length:15–50 cm	Distal/segmental aorta replacement, arterial bypass/ patch graft, arteriovenous shunt, and femoropopliteal bypass in lieu saphenous vein	Hemodialysis arteriovenous fistula grafting, salvage and repair, and lower extremity arterial trauma bypass	Reduced thrombus and patency rates compared to ePTFE, good saturability, and collagen matrix retains native cross-weave pattern with natural biocompatibility products available in multiple sizes to match host vessels
Cryovein®: human femoral vein (Fercana et al., 2014; Devillard and Marquette, 2021)	Small diameter grafts such as cryopreserved saphenous vein allografts	Saphenous veins, femoral veins, and femoral arteries for salvaging a localized prosthetic graft infection	Hemodialysis applications and extended lengths used to treat acutely ischemic limbs	Promising short-term, but extended thrombosis, poor 1-year patency, and aneurysmal degeneration led to rupture, calcification, and limited use
Cytograft, Lifeline™ (Carrabba and Madeddu, 2018)	Vascular graft is a living conduit with the properties of a native vessel	Self-assembled cell-sheet of human fibroblast in a shape of vascular conduit	Arteriovenous shunt for hemodialysis	ECs were seeded in graft after devitalization, and constructed using patient cells, void of synthetic or exogenous material, but requires 6–9-month production time
Humacyte® (Devillard and Marquette, 2021)	Polyglycolic acid biodegradable scaffold with SMCs from deceased organ and tissue donors	Resulting bioengineered vessel is then decellularized to create conduit	Conducted its phase II clinical trials in patients with end-stage renal disease	63% permeability 6 months after implantation (in 60 patients), absence of immune response and lower infection rate than ePTFE grafts, yet permeability rate was 18% (< than ePTFE)12 months after implantation
MatrACELL®: decellularized ECM (Porzionato et al., 2018)	Decellularized human pulmonary artery patch	Anionic detergent, N-Lauroyl sarcosinate, and endonuclease	Pulmonary valve replacement	Retained biomechanical properties, biocompatible, and able to support cellular and vascular in-growth
ProCol®: bovine mesenteric vein (Schmidli et al., 2004)	Glutaraldehyde cross-linked bovine mesenteric vein; ID: 6 mm; length: 10–40 cm	A bridge graft for vascular access	Synthetic vascular grafts for patients who have at least one-time failed graft access	Improve pulsatile forward flow, durability, anastomotic compliance, minimal bleeding, and good degree of biocompatible
Solcograft®: bovine carotid artery (Lin et al., 2018)	Decellularized carotid artery cross-linked with adipyl dichloride	Vascular conduits for pediatric and adult use	Aortic, aortoiliac, carotid and vena cava replacement	Increased biochemical properties, no aneurysm, reduced infection and early thrombosis, and homogenous structure before and after implantation
SynerGraft®: cadaver saphenous/ femoral veins (Pashneh-Tala et al., 2016)	Dimethyl sulfoxide-cryopreserved cadaver veins: Saphenous vein ID: 3–6 mm; length: 20–80 cm; Femoral vein ID: 6–15 mm; length: 10–30 cm	Saphenous vein bypass below knee in patients with infected fields that can't generate fistulas	Arteriovenous access line, and bypass below knees for patients with infected fields and/or at risk of infection	Excellent durability and hemodynamics, and virtually eliminates presence of allogenic donor cells to maintain matrix structural integrity and need for anticoagulation

arteries, jugular veins from dogs, bovine ureters, arterial tissues of sheep, SIS, as well as human amnion membrane (Bertanha et al., 2014). Due to the limited clinical success of decellularized vessels on the market, there are not many commercial products. Nevertheless, these decellularized vascular replacements offer better results than alternative synthetic conduits (Lin et al., 2018). This fact is also another reason that restricts their use. On the contrary, their potential to replace synthetic devices

supports the need for further research that can bring improved decellularized vascular segments to the market.

Endothelialization and SMCs repopulation can be observed in different layers of vessel structure within scaffolds. Acellular vascular grafts have been used in various models (e.g., sheep, goats, dogs, rats, mice, rabbits, and humans), providing patency rates of over 50% for at least 2 weeks. It is evident that the materials can vary according to their xenogeneic or non-xenogeneic nature, source locations within the cardiovascular system, and dimensions. Nevertheless, after generating decellularized ECM-derived scaffolds, some of those systems were reseeded with SMCs, ECs, and fibroblasts in different layers, while the others were implanted into anastomotic sites for endothelialization and remodeling. Histological results showed the most prolonged period for the convergence of the endothelialization is 8 weeks, and obvious recellularization happened at 6 weeks. During the remodeling process, no significant calcification, intima hyperplasia, graft dilation, rupture, or anastomotic aneurysm was detected (Bertanha et al., 2014).

In such cases, small-caliber (ID = 4 mm) decellularized ovine carotid arteries were grafted into 10 sheep and presented reendothelialization within 6 weeks with remarkably thicker neointima and apparent ECM reconstruction (Rijken et al., 2000). Besides, in 2013, decellularized rat thoracic aortas anastomosed to abdominal aortas maintained fully patent for 8 weeks, while only minute postoperative calcification was observed (Schneider et al., 2016). Similarly, Sakakibara and his colleagues implanted a decellularized rat artery (ID = 2–3 mm) to substitute the rat's abdominal aorta, which functioned for 14 months with complete ECs coverage after 5 weeks, contractile function at 12 months, and formation of tunica intima and media by the end of their study (Xiong et al., 2013).

ECM-mimicking human amnion membrane (ID = 3.2 mm) interposed the rabbit carotid artery and reached complete patency rate at 4 weeks without notable diameter and blood flow deduction but markedly thickened midpoint wall (Conklin et al., 2002). Moreover, the decellularized - SIS (ID =10 mm) successfully replaced the vena cava in canines (Kleinert et al., 1996). Regarding the decellularizing of the vena cava, remarkably few studies have reported successful transplantation. An example from a recent thesis presented decellularized porcine vena cava created by using a combination of detergents (SDS, SDC, Triton X-100, and CHAPS)(Simsa, 2020) and DNase, along with immersive/agitative-based incubation. Six pigs were implanted with a decellularized vena cava created by this technique, and the grafts were void of thrombus formation and intima hyperplasia during the 5-week observation period. Furthermore, the researchers observed vascular cells on the third-day post-implantation.

Apart from the aforementioned vascular replacements, which have been decellularized directly from tubular vessel structures, several vascular constructs have been decellularized indirectly by perfusing cardiovascular organs. An example of such an approach relied on first decellularizing rat hearts by coronary perfusion with ionic detergents (Ott et al., 2008). In that study, aortas were cannulated for retrograde heart perfusion resulting in acellular, perfusable vascular components. These scaffolds were then repopulated with cardiac and endothelial cells that remained intact for up to 28 days. Additionally, other scientists have applied decellularization methods to intact pulmonary/systemic arteries to generate heart valves for transplantation. At the same time, they also obtained decellularized vascular analogs (Boccafoschi et al., 2017) with the hopes of defining clinical products.

With current models, clinical translation of vascular-derived grafts must originate from preclinical trials. Thus, it is essential to examine the feasibility of decellularized vascular constructs for *in vivo* applications during these periods. As for large-ID blood vessel replacements, commercial synthetic vascular conduits such as ePTFE and Dacron® are currently preferred and widely used compared to decellularized vascular grafts (Matsuzaki et al., 2019). Commercially available decellularized vascular grafts have limited performance due to the lack of cellularity upon implantation (Spark et al., 2008) and high production costs (Pashneh-Tala et al., 2016). Yet, synthetic vessel analogs on the market have been raising concerns because of unsatisfactory clinical outcomes resulting from graft-related thrombosis, infection, and aneurysm, which are even worse in small-ID vessel grafts (Sharp et al., 2004). Therefore, decellularized products may provide a viable alternative to creating small ID vascular replacements in the future.

According to a meta-analysis performed by Skovrind et al. on preclinical trials related to small-diameter tissue-engineered vascular grafts, the patency of these segments is significantly affected by recellularization, TEVG length/diameter, surface modification, and preconditioning (Skovrind et al., 2019). At the same time, the scaffold type was less impactful. Specifically, their analyses showed that TEVGs with a median ID of 3 mm, 4 mm, and 5 mm showed patencies of 63.5%, 89%, and 100%, respectively. Besides that, they also indicated that this measure was not enhanced through recellularization using SMCs, ECs, nor affected by the endothelial origin. The patency was most likely improved by the long-term (46–240 h) recellularization. Likewise, data analyses presented that the median TEVG length (5 cm) and median follow-up time (56 days) for *in vivo* decellularized analogs may lack the capacity for future direct clinical translation. In comparison, small-caliber (ID = 4 mm) decellularized ovine carotid arteries presented reendothelialization within 6 weeks (Rijken et al., 2000). These decellularized rat thoracic aortas anastomosed to abdominal aortas maintained complete patency for 8 weeks (Schneider et al., 2016) and appeared suitable as a clinical translation model. The potential of analogous decellularized rat arterial segments (ID = 2–3 mm) to substitute for the rat's abdominal

aorta and be functional for 14 months (Xiong et al., 2013) is further highlighted by such results. Overall, these evaluations have been established on preliminary preclinical data, and the precise requirements to support the transition to the clinic remain ambiguous. Nevertheless, this reminds us that future studies on TEVGs should incorporate endothelial recellularization and bioreactor preconditioning. We also recommend more detailed and precise guidelines for testing and reporting TEVGs in large animals. Meanwhile, to generate robust and reproducible outcomes and clinical translation, interstudy comparisons and multiple factors that affect the efficiency of vascular grafts should also be conducted (Skovrind et al., 2019).

4.3 Advances with *in vitro* models

Several achievements have been made using *in vitro* models. For example, such models have shown that decellularized biological scaffolds possess a propensity to be reengineered with ECs, SMCs, HUVECs, human iliac artery endothelial cells, fibroblasts, myofibroblasts, adhesion, and growth factors (Xiong et al., 2013). The scaffolds vary widely and include umbilical arteries, saphenous arteries, aortas, placenta vessel matrices, umbilical veins, and small intestinal submucosa (Xiong et al., 2013). After reseeding with various types of cells as mentioned above, these decellularized 3D matrices can provide an appropriate biological plateau to investigate vascular remodeling *in vitro*. Some examples of results obtained using these conduits are presented below.

Dahl *et al.* created flexible decellularized SMCs-based conduits with ID ≥ 6 mm or between 3 and 4 mm seeded using ECs, while Gui et al. re-endothelialized decellularized umbilical arteries with HUVECs(Gui et al., 2009). In addition, porcine pulmonary ECs can be grown on the decellularized porcine saphenous artery (ID ≈ 2 mm). These studies also showed that decellularized vascular scaffolds could regain appreciable function and reduce thrombogenicity by supporting cell regrowth, adhesion, migration, and differentiation (Fitriatul et al., 2017). Similar work also revealed that small-caliber acellular vascular grafts (ID < 4 mm) produced from portions of the placenta network could support HUVEC-based reendothelialization and phenotypic maintenance (Schneider et al., 2016). Uzarski et al. also discovered a way to drive the recellularization of human umbilical veins by using diverse groups of ECs (Dahan et al., 2017). SIS-derived scaffolds can also retain various angiogenic growth factors (such as basic fibroblast growth factor (bFGF) and vascular endothelial growth factor (VEGF) that proved to facilitate some degree of human EC retention, yet approaches to support a complete endothelium needs further exploration (Bader et al., 2000).

As for large–caliber veins, porcine and leporine vena cava (ID ≈13 mm) are commonly decellularized *in vitro*. For instance, researchers have used a combination of 1% Triton X-100, 1% TnBP, and DNase under three physical conditions: static immersion, agitation, and perfusion, and concluded that agitation or low-velocity perfusion with detergents are preferable for obtaining integrative and functional vena cava. The rabbit vena cava has also been decellularized with agitated SDS and SD incubation at a rate of 160 rpm at 37 °C, illustrating that both detergents produced effective results (Bader et al., 2000). These studies emphasize the potential for scaffold development that may ultimately drive neovascularization.

5 Future directions for decelluarizing vessels

Decellularization technologies have demonstrated an outstanding potential for developing bioartificial vascular substitutes based on ECM composition, ability to support remodeling, and propensity to minimize immunogenicity. Nonetheless, this technology still faces challenges and needs profound improvements to optimize structure, function, safety, and functionality. From a preclinical view, present decellularization methods may adversely alter the mechanical integrity of vessels and retain cellular and antigenic components that can induce immunogenicity. The inherent difficulty in accurately mimicking vascular structure is highlighted by the fact that we are still awaiting approaches that can generate complete tunica that can withstand *in vivo* conditions. In this case, strengthening the viscoelasticity and mechanical features within the decellularized wall with hydrogel-based approaches may be useful.

From a clinical perspective, most decellularized vascular grafts are used as larger-diameter replacements in hemodialysis or peripheral arterial bypasses with disappointing outcomes due to graft thrombosis, infection, and aneurysms (Bertanha et al., 2014). Apart from that, calcification and other forms of damage are present in patients after vessel replacement/repairment surgeries. Moreover, the autologous decellularized vascular grafting approaches are scarcely utilized, which drives the need for cadaveric allograft- and xenograft-derived templates, which still need to show their ability to present consistent clinical advantages over widely available and cost-effective synthetic counterparts (Khan et al., 2017).

Regarding the future directions of decellularized vasculature, researchers are inclined to combine other techniques such as hydrogelation, 3D printing/electrospinning, bioreactors, and decellularization/recellularization techniques to generate highly biomimetic scaffolds matching personalized regimens with high efficiency. It is currently difficult to generate an ideal

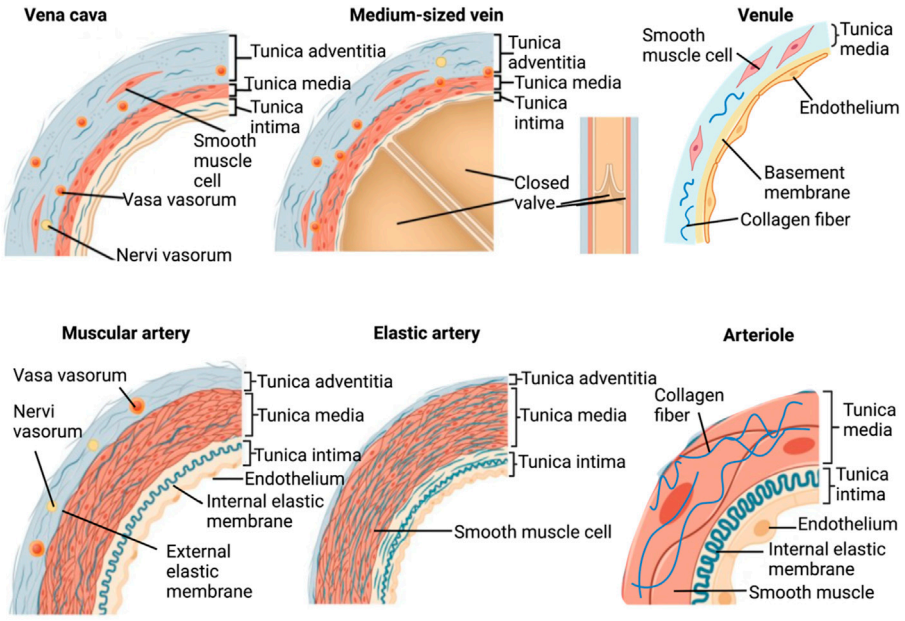

FIGURE 1
Structures of major native small- to large-caliber blood vessels.

decellularized scaffold by applying a single agent or technique from previous research. Therefore, it is believed that combinational technique-based decellularized techniques are the best way forward to facilitate VTE. For instance, hydrogels containing decellularized ECM (dECM) have been investigated and show a remarkable capacity for vascular cell reseeding compared to dECM scaffolds. Such cells can be primarily encapsulated in the hydrogel structure, facilitating recellularization. Also, these hydrogels can be used to create 3D printed or electrospun vasculature segments (Amirazad et al., 2022). 3D printing or electrospinning processes may coat the dECM with ECs and SMCs, and embed various factors like VEGF and platelet-derived growth factors (PDGF) to support vasculogenic multiscale substitutes development.

Reliable sources to obtain various cell types, ways to improve cell culture, and processes that drive differentiation and widescale recellularization are still needed. Efforts should be continued to enhance and potentially automate bioreactor systems with artificial intelligence to supervise regenerative processes, record morphological changes and functional performance of scaffolds, and continuously adjust the nutrient delivery and waste removal regimens (Wang et al., 2021). Finally, emerging organoid technologies can also be leveraged to provide insight into models that share complexity and scale with the microvasculature and provide a platform for examining vascular integration and interactions between vessels and tissues/organs via vascularization on a chip approach.

6 Simplified models for generating decellularized vascular units

Malone was the first investigator to demonstrate the potential of decellularized vessels for clinical application by showing that small-caliber arterial scaffolds grafted into canines could remain patent for roughly 3 months without an immune response (Sicari et al., 2014; Reis, 2019). Numerous studies have been conducted to define decellularization methods within the past 4 to 5 decades since these pioneering studies conducted by Malone presented the benefits of this technique in 1983. Since then, various other pioneering studies outlined above have supported decellularized vessel development, yet substantial gaps in knowledge still limit the extensive commercialization of decellularization-based VTE. As a result, further studies are required to support optimization techniques and ways to engineer small- to large-caliber vascular substitutes that truly mimic their native counterparts as shown in Figure 1. Therefore, we propose to define some essential components of acellular vascular graft models and approaches that may support the development of enhanced clinical substitutes in the near future.

The current state-of-the-art approach in the production of commercially available conduits highlights the limited

structural composition of acellular compartments compared to native vessels. Native vessels possess diverse, complex, and well-defined layers, namely the tunica intima, tunica media, and tunica adventitia (or externa), with each having its own sub-layers/compartments which provide various structural and physiological functions. One can argue that instead of directly focusing on recrafting each independent layer, efforts within this field have been directed toward creating vascular walls that possess sufficient characteristics to support recellularization and *in vivo* pulsatile flow. Such research can simultaneously work to inhibit immune responses and thrombosis and, as technologies progress, help to realize the aim of extending this approach beyond the capabilities of synthetic grafts.

This simplified approach outlines vascular walls that rely on innate ECM-derived mechanical properties from the decellularized tunicas to support sufficient epithelial/endothelial cell regrowth, matrix stabilization, and functionalization. It is well known that the outmost layer of vessels is mainly composed of collagen-rich ECM. The functions of ECM provide signals that induce, define, and stabilize vascular phenotypes (Wagenseil and Mecham, 2009). Such characteristics must be maintained in the decellularized vessels since an intact, potent, and active ECM has a high potential for supporting long-term implantation. Furthermore, by using various decellularization methods, this model can be tuned to reinforce the structure and sustain adequate gas diffusion gradients and blood flow relative to the underlying contents and integrities of ECM fibers and glycoproteins. Perhaps such revised morphological and physiological properties are sufficient since the reduced cellular complexity no longer requires vasa vasorum to support additional nutrient and waste transport within the deeper layers of the vascular wall. There are two types of vasa vasorum: vasa vasorum externa and vasa vasorum interna. When the thickness extends beyond 1 mm, vasa vasorum are needed to support waste and nutrient exchange (Majesky et al., 2012). The former is found in the adventitia at its border with the media, and the latter originates from the luminal surface or the media and branches into the adjacent artery wall (Majesky et al., 2012).

Based on diffusion properties and considering what can be argued as the most complex vascular structure, the aorta, the existence of vasa vasorum makes diffusion more efficient by increasing surface area and reducing thickness, which Fick's law of diffusion can be valid. This law states, $\dot{V} = \frac{DA\Delta P}{\Delta x}$, which describes the time course of gas transfer ($\dot{V}$), with respect to its partial pressure, (ΔP) and diffusion coefficient (D), as well as the surface area (A), and thickness ($x\Delta$) of the membrane facilitating solute transfer. However, with decellularization, it is unknown how well the structural components remain within the vasa vasorum. This issue can be further complicated across different species, as mice and other mammals with ≤29 elastic lamellar do not have vasa vasorum (Wagenseil and Mecham, 2009; Billaud et al., 2018), which indicates that choosing decellularizing sample species plays a vital role. Thus, larger mammals with >29 medial lamellar are preferable for exploring the vasa vasorum, and it might be generated through 3D printing and electrospinning since these two technologies focus on the microvasculature and can be investigated with powerful vascular *in vivo* modalities like micro-computed tomography (Zagorchev et al., 2010) and intravital microscopy (Eriksson, 2011; Corridon et al., 2021). Furthermore, this issue may be counteracted by the increased degree of ECM porosity that can be achieved with decellularization to support nutrient exchange with reseeding models.

It is also essential to consider various versatile molecules within the native ECM, such as GAGs (Dewey et al., 2021) and VEGF (Liang et al., 2001), for promoting vasculogenesis. GAG chains are attached to proteoglycans which, based on the physicochemical characteristics of the glycosaminoglycan component, provide hydration and swelling capacities that allow tissues to withstand compressional forces (Yanagishita, 1993). The large proteoglycans interact with hyaluronic acid, forming an extensive, interconnected polymeric network in the extracellular space (Davison et al., 1995). The types and amount of GAG chains linked to proteoglycans can affect the matrix assembly (Berry and Greenwald, 1976) and porosity (Corridon et al., 2006). Meanwhile, growth factors like VEGF can support the regrowth and differentiation of endothelium, as observed in decellularized models (Lin et al., 2018) and VEGF-coated stents to accelerate re-endothelialization (Swanson et al., 2003). These two factors may ultimately enhance the structural and functional abilities of the aggregated decellularized tunica.

Autonomic innervation also plays a vital role under a complex homeostatic mechanism observed within native blood vessels that helps to regulate vascular diameter. For example, in addition to the intrinsic vessels (vasa vasorum), the adventitia houses collections of nerve fibers called nervi vasorum, i.e., nerves of the vessel, which modulate vascular vasodilatative and vasoconstrictive capacities through the incorporation of SMCs. These muscular cells within the tunica media of the native aorta (and in media and adventitia of vena cava) deposit collagen and elastin fibers that account for tensile strength and distensibility, respectively. Previous studies suggest that less than 10% of collagen bears physiological pressure, while once the pressure rises, the collagen fibers are recruited to support the passive wall tension and limit aortic distention, making vessels progressively distensible (Davis, 1993). However, as pressures exceed the standard physiological threshold, collagen fibers automatically realign to limit radial expansion, and help elastic fibers recoil. This tightly regulated mechanism is lost in denervated decellularized

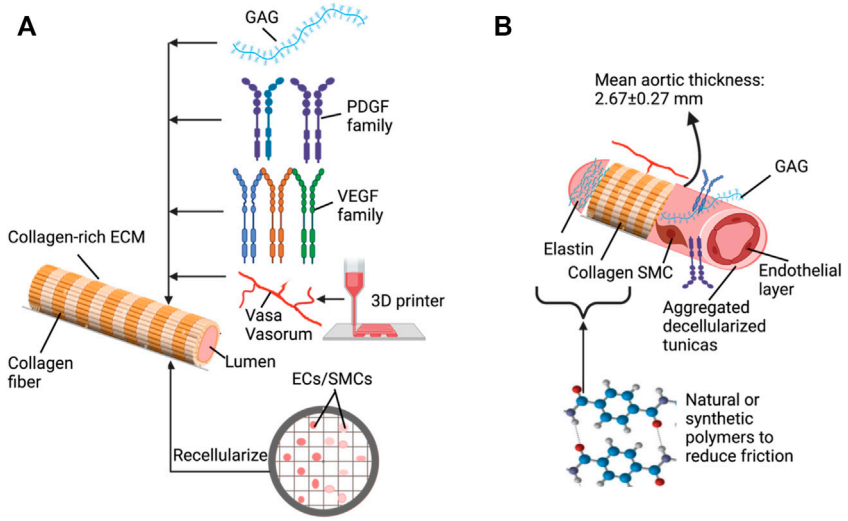

FIGURE 2
Key elements and approaches to support the development of decellularized vascular grafts: **(A)** basic decellularization vessel model that can be tuned with various additives **(B)** using combinative approaches to generate improved vascular substitutes.

vessels. As a result, retaining ECMs with optimal collagen and elastin fiber networks for vascular structures now devoid of nervi vasorum, SMCs, and thus, their innate regulatory capacities (Corridon, 2021).

Finally, ensuring that the anticoagulant nature of the decellularized vascular lumen mimics what is produced by the native endothelium will aid in preventing thrombosis. The endothelium achieves this by providing a surface that discourages the attachment of cells and clotting proteins (Yau et al., 2015). This layer also modulates vascular tone, blood cell aggregation, and deformability (Simmonds et al., 2014). Such traits impact the release of endothelial mediators in response to chemical (production of oxygen free radicals and nitric oxide that alter vascular tone) and physical (changes in blood viscosity that alter shear stress) stimuli (Forconi and Gori, 2013). These effects can be described by the Hagen-Poiseuille's law, which states, $Q = \frac{\pi r^4 \Delta P}{8l\eta}$, where the rate of blood flow (Q) is influenced by blood pressure (ΔP) and viscosity (η), as well as vessel length (l) and radius (r). We have recently used this relationship to describe flow rates through the decellularized renal artery and vein under normothermic and hypothermic conditions in a whole decellularized organ model with controlled pressures and varying viscosities (Corridon, 2021). Thus, this relationship may provide a way to optimize the replacement graft diameter and length for a given grafting procedure. Another aspect that can stem from this approach is the inability to regulate the wall thickness of decellularized vessel products. The overall approach, as summarized in Figure 2, may identify the necessary and sufficient decellularized wall components capable of supporting gas diffusion and withstanding debilitating blood viscosities using global mean aortic widths, 2.67 ±0.27 mm (Liu et al., 2015), as a starting point. In particular, the model may also support combinative decellularization technologies to tune luminal surfaces with natural or synthetic polymers to reduce friction between moving blood and stationary acellular walls in large- to small-caliber replacement vessels.

7 Conclusion

This review discussed different methods for decellularizing multiscale blood vessels. Theoretically, all of these methods can create acellular templates. Different decellularization strategies generate vessel substitutes with viable mechanical features, structures, and levels of patency, and combinational treatments have so far provided the best results. Ideally, scientists have to minimize immunogenicity and maximize physiological performance. So far, we have gained tremendous insight into how decellularizing agents impact native structures, which has led to successful cadaveric transplantation and xenotransplantation models, some of which have been translated to the clinical applications. These achievements, in turn, have spawned interest in generating commercially available vascular substitutes derived from natural materials to replace existing synthetic devices. However, several challenges must still be overcome to support this progression, including identifying unified decellularization and recellularization protocols and improving the basic tenets needed to support long-term

implantation. Perhaps solutions to these major challenges may come from other combinative approaches that utilize emerging strategies. Altogether, the future appears promising as we strive to develop the state-or-the-art in VTE using decellularization technologies.

Author contributions

PC conceived the project. PC and XW drafted the manuscript. XW, VC, and PC critically revised the manuscript and approved the final version.

Funding

This study was supported by funds from Khalifa University of Science and Technology, Grant Nos. FSU-2020-25 and RC2-2018-022 (HEIC), and the College of Medicine and Health Sciences.

Acknowledgments

The author would like to acknowledge Ms. Raheem Khan for reviewing the manuscript.

Conflict of interest

The authors declare that the research was conducted in the absence of any commercial or financial relationships that could be construed as a potential conflict of interest.

Publisher's note

All claims expressed in this article are solely those of the authors and do not necessarily represent those of their affiliated organizations, or those of the publisher, the editors and the reviewers. Any product that may be evaluated in this article, or claim that may be made by its manufacturer, is not guaranteed or endorsed by the publisher.

References

Aguirre-Ramírez, M., Silva-Jiménez, H., Banat, I. M., and Díaz De Rienzo, M. A. (2021). Surfactants: Physicochemical interactions with biological macromolecules. *Biotechnol. Lett.* 43, 523–535. doi:10.1007/s10529-020-03054-1

Amirazad, H., Dadashpour, M., and Zarghami, N. (2022). Application of decellularized bone matrix as a bioscaffold in bone tissue engineering. *J. Biol. Eng.* 16, 1. doi:10.1186/s13036-021-00282-5

Angelova, M. I., Bitbol, A.-F., Seigneuret, M., Staneva, G., Kodama, A., Sakuma, Y., et al. (2018). pH sensing by lipids in membranes: The fundamentals of pH-driven migration, polarization and deformations of lipid bilayer assemblies. *Biochimica Biophysica Acta (BBA) - Biomembr.* 1860, 2042–2063. doi:10.1016/j.bbamem.2018.02.026

Bader, A., Steinhoff, G., Strobl, K., Schilling, T., Brandes, G., Mertsching, H., et al. (2000). Engineering of human vascular aortic tissue based on a xenogeneic starter matrix. *Transplantation* 70, 7–14.

Baumgartner-Parzer, S. M., and Waldhäusl, W. K. (2001). The endothelium as a metabolic and endocrine organ: Its relation with insulin resistance. *Exp. Clin. Endocrinol. Diabetes* 109, S166–S179. doi:10.1055/s-2001-18579

Berry, C. L., and Greenwald, S. E. (1976). Effects of hypertension on the static mechanical properties and chemical composition of the rat aorta. *Cardiovasc. Res.* 10, 437–451. doi:10.1093/cvr/10.4.437

Bertanha, M., Moroz, A., Jaldin, R. G., Silva, R. A., Rinaldi, J. C., Golim, M. A., et al. (2014). Morphofunctional characterization of decellularized vena cava as tissue engineering scaffolds. *Exp. Cell. Res.* 326, 103–111. doi:10.1016/j.yexcr.2014.05.023

Billaud, M., Hill, J. C., Richards, T. D., Gleason, T. G., and Phillippi, J. A. (2018). Medial hypoxia and adventitial vasa vasorum remodeling in human ascending aortic aneurysm. *Front. Cardiovasc. Med.* 5, 124. doi:10.3389/fcvm.2018.00124

Boccafoschi, F., Botta, M., Fusaro, L., Copes, F., Ramella, M., Cannas, M., et al. (2017). Decellularized biological matrices: An interesting approach for cardiovascular tissue repair and regeneration. *J. Tissue Eng. Regen. Med.* 11, 1648–1657. doi:10.1002/term.2103

Bozler, E. (1970). Action potentials of visceral smooth muscles and their relation to mechanical activity. *Nihon Heikatsukin Gakkai Zasshi* 6, 63–65.

Bozler, E. (1937). Physiological evidence for the syncytial character of smooth muscle. *Science* 86, 476. doi:10.1126/science.86.2238.476

Bozler, E. (1973). Smooth muscle physiology, past and future. *Philos. Trans. R. Soc. Lond. B Biol. Sci.* 265, 3–6. doi:10.1098/rstb.1973.0003

Brown, B. N., and Badylak, S. F. (2014). "Chapter 25 - the role of the host immune response in tissue engineering and regenerative medicine," in *Principles of tissue engineering*. Editors R. Lanza, R. Langer, and J. Vacanti. Fourth Edition (Boston: Academic Press), 497–509.

Bruyneel, A. a. N., and Carr, C. A. (2017). Ambiguity in the presentation of decellularized tissue composition: The need for standardized approaches. *Artif. organs* 41, 778–784. doi:10.1111/aor.12838

Cai, Z., Gu, Y., Xiao, Y., Wang, C., and Wang, Z. (2021). Porcine carotid arteries decellularized with a suitable concentration combination of Triton X-100 and sodium dodecyl sulfate for tissue engineering vascular grafts. *Cell. Tissue Bank.* 22, 277–286. doi:10.1007/s10561-020-09876-7

Carrabba, M., and Madeddu, P. (2018). Current strategies for the manufacture of small size tissue engineering vascular grafts. *Front. Bioeng. Biotechnol.* 6, 41. doi:10.3389/fbioe.2018.00041

Cheng, J., Wang, C., and Gu, Y. (2019). Combination of freeze-thaw with detergents: A promising approach to the decellularization of porcine carotid arteries. *Biomed. Mat. Eng.* 30, 191–205. doi:10.3233/bme-191044

Chuang, T. H., Stabler, C., Simionescu, A., and Simionescu, D. T. (2009). Polyphenol-stabilized tubular elastin scaffolds for tissue engineered vascular grafts. *Tissue Eng. Part A* 15, 2837–2851.

Cohen, S., Partouche, S., Gurevich, M., Tennak, V., Mezhybovsky, V., Azarov, D., et al. (2021). Generation of vascular chimerism within donor organs. *Sci. Rep.* 11, 13437. doi:10.1038/s41598-021-92823-7

Conklin, B. S., Richter, E. R., Kreutziger, K. L., Zhong, D. S., and Chen, C. (2002). Development and evaluation of a novel decellularized vascular xenograft. *Med. Eng. Phys.* 24, 173–183. doi:10.1016/s1350-4533(02)00010-3

Corridon, P., Ascázubi, R., Krest, C., and Wilke, I. (2006). "Time-domain terahertz spectroscopy of artificial skin," in *Proceedings - society of photo-optical instrumentation engineers*.

Corridon, P. R. (2021). *In vitro* investigation of the impact of pulsatile blood flow on the vascular architecture of decellularized porcine kidneys. *Sci. Rep.* 11, 16965. doi:10.1038/s41598-021-95924-5

Corridon, P. R., Karam, S. H., Khraibi, A. A., Khan, A. A., and Alhashmi, M. A. (2021). Intravital imaging of real-time endogenous actin dysregulation in proximal and distal tubules at the onset of severe ischemia-reperfusion injury. *Sci. Rep.* 11, 8280. doi:10.1038/s41598-021-87807-6

Corridon, P. R., Ko, I. K., Yoo, J. J., and Atala, A. (2017). Bioartificial kidneys. *Curr. Stem Cell. Rep.* 3, 68–76. doi:10.1007/s40778-017-0079-3

Crane, J., and Cheshire, N. (2003). Recent developments in vascular surgery. *BMJ Clin. Res. ed.)* 327, 911–915. doi:10.1136/bmj.327.7420.911

Crapo, P. M., Gilbert, T. W., and Badylak, S. F. (2011). An overview of tissue and whole organ decellularization processes. *Biomaterials* 32, 3233–3243. doi:10.1016/j.biomaterials.2011.01.057

Dahan, N., Sarig, U., Bronshtein, T., Baruch, L., Karram, T., Hoffman, A., et al. (2017). Dynamic autologous reendothelialization of small-caliber arterial extracellular matrix: A preclinical large animal study. *Tissue Eng. Part A* 23, 69–79. doi:10.1089/ten.tea.2016.0126

Dall'Olmo, L., Zanusso, I., Di Liddo, R., Chioato, T., Bertalot, T., Guidi, E., et al. (2014). Blood vessel-derived acellular matrix for vascular graft application. *BioMed Res. Int.* 2014, 1–9. doi:10.1155/2014/685426

Das, N., Bratby, M. J., Shrivastava, V., Cornall, A. J., Darby, C. R., Boardman, P., et al. (2011). Results of a seven-year, single-centre experience of the long-term outcomes of bovine ureter grafts used as novel conduits for haemodialysis fistulas. *Cardiovasc. Interv. Radiol.* 34, 958–963. doi:10.1007/s00270-011-0096-z

Davis, E. C. (1993). Smooth muscle cell to elastic lamina connections in developing mouse aorta. Role in aortic medial organization. *Lab. Invest.* 68, 89–99.

Davis, G. E., and Senger, D. R. (2005). Endothelial extracellular matrix. *Circulation Res.* 97, 1093–1107. doi:10.1161/01.res.0000191547.64391.e3

Davison, I. G., Wright, G. M., and Demont, M. E. (1995). The structure and physical properties of invertebrate and primitive vertebrate arteries. *J. Exp. Biol.* 198, 2185–2196. doi:10.1242/jeb.198.10.2185

Devillard, C. D., and Marquette, C. A. (2021). Vascular tissue engineering: Challenges and requirements for an ideal large scale blood vessel. *Front. Bioeng. Biotechnol.* 9, 721843. doi:10.3389/fbioe.2021.721843

Dewey, M. J., Kolliopoulos, V., Ngo, M. T., and Harley, B. a. C. (2021). Glycosaminoglycan content of a mineralized collagen scaffold promotes mesenchymal stem cell secretion of factors to modulate angiogenesis and monocyte differentiation. *Mater. (Oxf)* 18, 101149. doi:10.1016/j.mtla.2021.101149

Di Maio, E., Iannace, S., and Mensitieri, G. (2021). "Chapter 4 - supercritical fluids," in *Supercritical fluid science and technology*. Editors E. Di Maio, S. Iannace, and G. Mensitieri (Elsevier), 55–68.

Eriksson, E. E. (2011). Intravital microscopy on atherosclerosis in apolipoprotein e-deficient mice establishes microvessels as major entry pathways for leukocytes to advanced lesions. *Circulation* 124, 2129–2138. doi:10.1161/circulationaha.111.030627

Fercana, G., Bowser, D., Portilla, M., Langan, E. M., Carsten, C. G., Cull, D. L., et al. (2014). Platform technologies for decellularization, tunic-specific cell seeding, and *in vitro* conditioning of extended length, small diameter vascular grafts. *Tissue Eng. Part C. Methods* 20, 1016–1027. doi:10.1089/ten.tec.2014.0047

Fernández-Pérez, J., and Ahearne, M. (2019). The impact of decellularization methods on extracellular matrix derived hydrogels. *Sci. Rep.* 9, 14933. doi:10.1038/s41598-019-49575-2

Fitriatul, N., Sha'ban, M., and Azhim, A. (2017). Evaluation of recellularization on decellularized aorta scaffolds engineered by ultrasonication treatment. *Annu. Int. Conf. IEEE Eng. Med. Biol. Soc.* 2017, 2072–2075. doi:10.1109/EMBC.2017.8037261

Forconi, S., and Gori, T. (2013). Endothelium and hemorheology. *Clin. Hemorheol. Microcirc.* 53, 3–10. doi:10.3233/ch-2012-1571

Forslund, T., and Metsärinne, K. (1992). The endothelial cell as an endocrine organ--endothelin. *Tidsskr. Nor. Laegeforen.* 112, 648–652.

Fu, R. H., Wang, Y. C., Liu, S. P., Shih, T. R., Lin, H. L., Chen, Y. M., et al. (2014). Decellularization and recellularization technologies in tissue engineering. *Cell. Transpl.* 23, 621–630. doi:10.3727/096368914x678382

Funamoto, S., Nam, K., Kimura, T., Murakoshi, A., Hashimoto, Y., Niwaya, K., et al. (2010). The use of high-hydrostatic pressure treatment to decellularize blood vessels. *Biomaterials* 31, 3590–3595. doi:10.1016/j.biomaterials.2010.01.073

Gil-Ramírez, A., Rosmark, O., Spégel, P., Swärd, K., Westergren-Thorsson, G., Larsson-Callerfelt, A.-K., et al. (2020). Pressurized carbon dioxide as a potential tool for decellularization of pulmonary arteries for transplant purposes. *Sci. Rep.* 10, 4031. doi:10.1038/s41598-020-60827-4

Gilpin, A., and Yang, Y. (2017). Decellularization strategies for regenerative medicine: From processing techniques to applications. *BioMed Res. Int.* 2017, 1–13. doi:10.1155/2017/9831534

Gilpin, S. E., Guyette, J. P., Gonzalez, G., Ren, X., Asara, J. M., Mathisen, D. J., et al. (2014). Perfusion decellularization of human and porcine lungs: Bringing the matrix to clinical scale. *J. Heart Lung Transpl.* 33, 298–308. doi:10.1016/j.healun.2013.10.030

Gratzer, P. F. (2019). "Decellularized extracellular matrix," in *Encyclopedia of biomedical engineering*. Editor R. Narayan (Oxford: Elsevier), 86–96.

Gui, L., Muto, A., Chan, S. A., Breuer, C. K., and Niklason, L. E. (2009). Development of decellularized human umbilical arteries as small-diameter vascular grafts. *Tissue Eng. Part A* 15, 2665–2676. doi:10.1089/ten.tea.2008.0526

Hanai, H., Jacob, G., Nakagawa, S., Tuan, R. S., Nakamura, N., Shimomura, K., et al. (2020). Potential of soluble decellularized extracellular matrix for musculoskeletal tissue engineering – comparison of various mesenchymal tissues. *Front. Cell. Dev. Biol.* 8, 581972. doi:10.3389/fcell.2020.581972

Harlander-Locke, M., Jimenez, J. C., Lawrence, P. F., Gelabert, H. A., Derubertis, B. G., Rigberg, D. A., et al. (2014). Bovine carotid artery (Artegraft) as a hemodialysis access conduit in patients who are poor candidates for native arteriovenous fistulae. *Vasc. Endovasc. Surg.* 48, 497–502. doi:10.1177/1538574414561231

He, M., and Callanan, A. (2013). Comparison of methods for whole-organ decellularization in tissue engineering of bioartificial organs. *Tissue Eng. Part B Rev.* 19, 194–208. doi:10.1089/ten.teb.2012.0340

Hohenester, E., and Yurchenco, P. D. (2013). Laminins in basement membrane assembly. *Cell. adhesion Migr.* 7, 56–63. doi:10.4161/cam.21831

Iozzo, R. V., and Schaefer, L. (2015). Proteoglycan form and function: A comprehensive nomenclature of proteoglycans. *Matrix Biol.* 42, 11–55. doi:10.1016/j.matbio.2015.02.003

Jiménez-Gastélum, G. R., Aguilar-Medina, E. M., Soto-Sainz, E., Ramos-Payán, R., and Silva-Benítez, E. L. (2019). Antimicrobial properties of extracellular matrix scaffolds for tissue engineering. *BioMed Res. Int.* 2019, 1–7. doi:10.1155/2019/9641456

Kakisis, J. D., Antonopoulos, C., Mantas, G., Alexiou, E., Katseni, K., Sfyroeras, G., et al. (2017). Safety and efficacy of polyurethane vascular grafts for early hemodialysis access. *J. Vasc. Surg.* 66, 1792–1797. doi:10.1016/j.jvs.2017.06.083

Kanda, H., Ando, D., Hoshino, R., Yamamoto, T., WahyudionoSuzuki, S., Shinohara, S., et al. (2021). Surfactant-free decellularization of porcine aortic tissue by subcritical dimethyl ether. *ACS omega* 6, 13417–13425. doi:10.1021/acsomega.1c01549

Keane, T. J., Swinehart, I. T., and Badylak, S. F. (2015). Methods of tissue decellularization used for preparation of biologic scaffolds and *in vivo* relevance. *Methods* 84, 25–34. doi:10.1016/j.ymeth.2015.03.005

Khan, S., Villalobos, M. A., Choron, R. L., Chang, S., Brown, S. A., Carpenter, J. P., et al. (2017). Fibroblast growth factor and vascular endothelial growth factor play a critical role in endotheliogenesis from human adipose-derived stem cells. *J. Vasc. Surg.* 65, 1483–1492. doi:10.1016/j.jvs.2016.04.034

Khan, T. A., Mahler, H.-C., and Kishore, R. S. K. (2015). Key interactions of surfactants in therapeutic protein formulations: A review. *Eur. J. Pharm. Biopharm.* 97, 60–67. doi:10.1016/j.ejpb.2015.09.016

Kleinert, L. B., Hoying, J. B., and Williams, S. K. (1996). The neointima formed in endothelial cell sodded ePTFE vascular grafts results from both cellular-hyperplasia and extracellular-hypertrophy. *Cell. Transpl.* 5, 475–482. doi:10.1016/0963-6897(96)00024-3

Koley, D., and Bard, A. J. (2010). Triton X-100 concentration effects on membrane permeability of a single HeLa cell by scanning electrochemical microscopy (SECM). *Proc. Natl. Acad. Sci. U. S. A.* 107, 16783–16787. doi:10.1073/pnas.1011614107

Kumar, V. A., Brewster, L. P., Caves, J. M., and Chaikof, E. L. (2011). Tissue engineering of blood vessels: Functional requirements, progress, and future challenges. *Cardiovasc. Eng. Technol.* 2, 137–148. doi:10.1007/s13239-011-0049-3

Le, T. M., Morimoto, N., Ly, N. T. M., Mitsui, T., Notodihardjo, S. C., Munisso, M. C., et al. (2020). Hydrostatic pressure can induce apoptosis of the skin. *Sci. Rep.* 10, 17594. doi:10.1038/s41598-020-74695-5

Liang, D., Chang, J. R., Chin, A. J., Smith, A., Kelly, C., Weinberg, E. S., et al. (2001). The role of vascular endothelial growth factor (VEGF) in vasculogenesis, angiogenesis, and hematopoiesis in zebrafish development. *Mech. Dev.* 108, 29–43. doi:10.1016/s0925-4773(01)00468-3

Lin, C. H., Hsia, K., Ma, H., Lee, H., and Lu, J. H. (2018). *In vivo* performance of decellularized vascular grafts: A review article. *Int. J. Mol. Sci.* 19, 2101. doi:10.3390/ijms19072101

Liu, C. Y., Chen, D., Bluemke, D. A., Wu, C. O., Teixido-Tura, G., Chugh, A., et al. (2015). Evolution of aortic wall thickness and stiffness with atherosclerosis: Long-term follow up from the multi-ethnic study of atherosclerosis. *Hypertension* 65, 1015–1019. doi:10.1161/hypertensionaha.114.05080

Majesky, M. W., Dong, X. R., Hoglund, V., Daum, G., and Mahoney, W. M., Jr. (2012). The adventitia: A progenitor cell niche for the vessel wall. *Cells Tissues Organs* 195, 73–81. doi:10.1159/000331413

Mancuso, L., Gualerzi, A., Boschetti, F., Loy, F., and Cao, G. (2014). Decellularized ovine arteries as small-diameter vascular grafts. *Biomed. Mat.* 9, 045011. doi:10.1088/1748-6041/9/4/045011

Matsuzaki, Y., John, K., Shoji, T., and Shinoka, T. (2019). The evolution of tissue engineered vascular graft technologies: From preclinical trials to advancing patient care. *Appl. Sci. (Basel).* 9, 1274. doi:10.3390/app9071274

Meezan, E., Hjelle, J. T., Brendel, K., and Carlson, E. C. (1975). A simple, versatile, nondisruptive method for the isolation of morphologically and chemically pure

basement membranes from several tissues. *Life Sci.* 17, 1721–1732. doi:10.1016/0024-3205(75)90119-8

Mendibil, U., Ruiz-Hernandez, R., Retegi-Carrion, S., Garcia-Urquia, N., Olalde-Graells, B., Abarrategi, A., et al. (2020). Tissue-specific decellularization methods: Rationale and strategies to achieve regenerative compounds. *Int. J. Mol. Sci.* 21, 5447. doi:10.3390/ijms21155447

Mendoza-Novelo, B., Avila, E. E., Cauich-Rodríguez, J. V., Jorge-Herrero, E., Rojo, F. J., Guinea, G. V., et al. (2011). Decellularization of pericardial tissue and its impact on tensile viscoelasticity and glycosaminoglycan content. *Acta Biomater.* 7, 1241–1248. doi:10.1016/j.actbio.2010.11.017

Merna, N., Robertson, C., La, A., and George, S. C. (2013). Optical imaging predicts mechanical properties during decellularization of cardiac tissue. *Tissue Eng. Part C. Methods* 19, 802–809. doi:10.1089/ten.tec.2012.0720

Negishi, J., Funamoto, S., Kimura, T., Nam, K., Higami, T., Kishida, A., et al. (2015). Porcine radial artery decellularization by high hydrostatic pressure. *J. Tissue Eng. Regen. Med.* 9, E144–E151. doi:10.1002/term.1662

Neishabouri, A., Soltani Khaboushan, A., Daghigh, F., Kajbafzadeh, A.-M., and Majidi Zolbin, M. (2022). Decellularization in tissue engineering and regenerative medicine: Evaluation, modification, and application methods. *Front. Bioeng. Biotechnol.* 10, 805299. doi:10.3389/fbioe.2022.805299

Nouri Barkestani, M., Naserian, S., Uzan, G., and Shamdani, S. (2021). Post-decellularization techniques ameliorate cartilage decellularization process for tissue engineering applications. *J. Tissue Eng.* 12, 204173142098356. doi:10.1177/2041731420983562

Ott, H. C., Matthiesen, T. S., Goh, S.-K., Black, L. D., Kren, S. M., Netoff, T. I., et al. (2008). Perfusion-decellularized matrix: Using nature's platform to engineer a bioartificial heart. *Nat. Med.* 14, 213–221. doi:10.1038/nm1684

Pantic, I. V., Shakeel, A., Petroianu, G. A., and Corridon, P. R. (2022). Analysis of vascular architecture and parenchymal damage generated by reduced blood perfusion in decellularized porcine kidneys using a gray level Co-occurrence matrix. *Front. Cardiovasc. Med.* 9, 797283. doi:10.3389/fcvm.2022.797283

Pashneh-Tala, S., Macneil, S., and Claeyssens, F. (2016). The tissue-engineered vascular graft-past, present, and future. *Tissue Eng. Part B Rev.* 22, 68–100. doi:10.1089/ten.teb.2015.0100

Peck, M., Gebhart, D., Dusserre, N., Mcallister, T. N., and L'heureux, N. (2012). The evolution of vascular tissue engineering and current state of the art. *Cells Tissues Organs* 195, 144–158. doi:10.1159/000331406

Peloso, A., Ferrario, J., Maiga, B., Benzoni, I., Bianco, C., Citro, A., et al. (2015). Creation and implantation of acellular rat renal ECM-based scaffolds. *Organogenesis* 11, 58–74. doi:10.1080/15476278.2015.1072661

Porzionato, A., Stocco, E., Barbon, S., Grandi, F., Macchi, V., De Caro, R., et al. (2018). Tissue-engineered grafts from human decellularized extracellular matrices: A systematic review and future perspectives. *Int. J. Mol. Sci.* 19, 4117. doi:10.3390/ijms19124117

Rabbani, M., Zakian, N., and Alimoradi, N. (2021). Contribution of physical methods in decellularization of animal tissues. *J. Med. Signals Sens.* 11, 1. doi:10.4103/jmss.jmss_2_20

Reis, R. L. (2019). *Encyclopedia of tissue engineering and regenerative medicine*.

Rieder, E., Kasimir, M. T., Silberhumer, G., Seebacher, G., Wolner, E., Simon, P., et al. (2004). Decellularization protocols of porcine heart valves differ importantly in efficiency of cell removal and susceptibility of the matrix to recellularization with human vascular cells. *J. Thorac. Cardiovasc. Surg.* 127, 399–405. doi:10.1016/j.jtcvs.2003.06.017

Rijken, P. F., Bernsen, H. J., Peters, J. P., Hodgkiss, R. J., Raleigh, J. A., Van Der Kogel, A. J., et al. (2000). Spatial relationship between hypoxia and the (perfused) vascular network in a human glioma xenograft: A quantitative multi-parameter analysis. *Int. J. Radiat. Oncology*Biology*Physics* 48, 571–582. doi:10.1016/s0360-3016(00)00686-6

Row, S., Santandreu, A., Swartz, D. D., and Andreadis, S. T. (2017). Cell-free vascular grafts: Recent developments and clinical potential. *Technol. (Singap World Sci.* 5, 13–20. doi:10.1142/S2339547817400015

Salvi, G., De Los Rios, P., and Vendruscolo, M. (2005). Effective interactions between chaotropic agents and proteins. *Proteins.* 61, 492–499. doi:10.1002/prot.20626

Sano, M. B., Neal, R. E., 2nd, Garcia, P. A., Gerber, D., Robertson, J., Davalos, R. V., et al. (2010). Towards the creation of decellularized organ constructs using irreversible electroporation and active mechanical perfusion. *Biomed. Eng. OnLine* 9, 83. doi:10.1186/1475-925x-9-83

Schmidli, J., Savolainen, H., Heller, G., Widmer, M. K., Then-Schlagau, U., Baumgartner, I., et al. (2004). Bovine mesenteric vein graft (ProCol) in critical limb ischaemia with tissue loss and infection. *Eur. J. Vasc. Endovasc. Surg.* 27, 251–253. doi:10.1016/j.ejvs.2003.12.001

Schneider, K. H., Aigner, P., Holnthoner, W., Monforte, X., Nürnberger, S., Rünzler, D., et al. (2016). Decellularized human placenta chorion matrix as a favorable source of small-diameter vascular grafts. *Acta Biomater.* 29, 125–134. doi:10.1016/j.actbio.2015.09.038

Shakeel, A., and Corridon, P. R. (2022). Mitigating challenges and expanding the future of vascular tissue engineering–are we there yet? Available at SSRN: https://ssrn.com/abstract=4039050 (Accessed February 20, 2022).

Sharp, M. A., Phillips, D., Roberts, I., and Hands, L. (2004). A cautionary case: The SynerGraft vascular prosthesis. *Eur. J. Vasc. Endovasc. Surg.* 27, 42–44. doi:10.1016/j.ejvs.2003.09.015

Sicari, B. M., Londono, R., and Badylak, S. F. (2014). "Chapter 5 - extracellular matrix as a bioscaffold for tissue engineering," in *Tissue engineering*. Editors C. a. V. Blitterswijk and J. De Boer. Second Edition (Oxford: Academic Press), 149–175.

Sierad, L. N., Shaw, E. L., Bina, A., Brazile, B., Rierson, N., Patnaik, S. S., et al. (2015). Functional heart valve scaffolds obtained by complete decellularization of porcine aortic roots in a novel differential pressure gradient perfusion system. *Tissue Eng. Part C. Methods* 21, 1284–1296. doi:10.1089/ten.tec.2015.0170

Simmonds, M. J., Detterich, J. A., and Connes, P. (2014). Nitric oxide, vasodilation and the red blood cell. *Biorheology* 51, 121–134. doi:10.3233/bir-140653

Simsa, R. (2020). "Decellularization as a method to generate a new generation of vascular grafts," in *Doctor of philosophy (medicine)* (University of Gothenburg. Sahlgrenska Academy).

Simsa, R., Padma, A. M., Heher, P., Hellström, M., Teuschl, A., Jenndahl, L., et al. (2018). Systematic *in vitro* comparison of decellularization protocols for blood vessels. *PLOS ONE* 13, e0209269. doi:10.1371/journal.pone.0209269

Singh, M., Park, C., and Roche, E. T. (2022). Decellularization following fixation of explanted aortic valves as a strategy for preserving native mechanical properties and function. *Front. Bioeng. Biotechnol.* 9, 803183. doi:10.3389/fbioe.2021.803183

Skovrind, I., Harvald, E. B., Juul Belling, H., Jørgensen, C. D., Lindholt, J. S., Andersen, D. C., et al. (2019). Concise review: Patency of small-diameter tissue-engineered vascular grafts: A meta-analysis of preclinical trials. *Stem Cells Transl. Med.* 8, 671–680. doi:10.1002/sctm.18-0287

Spark, J. I., Yeluri, S., Derham, C., Wong, Y. T., and Leitch, D. (2008). Incomplete cellular depopulation may explain the high failure rate of bovine ureteric grafts. *Br. J. Surg.* 95, 582–585. doi:10.1002/bjs.6052

Sullivan, D. C., Mirmalek-Sani, S. H., Deegan, D. B., Baptista, P. M., Aboushwareb, T., Atala, A., et al. (2012). Decellularization methods of porcine kidneys for whole organ engineering using a high-throughput system. *Biomaterials* 33, 7756–7764. doi:10.1016/j.biomaterials.2012.07.023

Swanson, N., Hogrefe, K., Javed, Q., Malik, N., and Gershlick, A. H. (2003). Vascular endothelial growth factor (VEGF)-eluting stents: *In vivo* effects on thrombosis, endothelialization and intimal hyperplasia. *J. Invasive Cardiol.* 15, 688–692.

Syed, O., Walters, N. J., Day, R. M., Kim, H. W., and Knowles, J. C. (2014). Evaluation of decellularization protocols for production of tubular small intestine submucosa scaffolds for use in oesophageal tissue engineering. *Acta Biomater.* 10, 5043–5054. doi:10.1016/j.actbio.2014.08.024

Thomas, L. V., Lekshmi, V., and Nair, P. D. (2013). Tissue engineered vascular grafts — preclinical aspects. *Int. J. Cardiol.* 167, 1091–1100. doi:10.1016/j.ijcard.2012.09.069

Wagenseil, J. E., and Mecham, R. P. (2009). Vascular extracellular matrix and arterial mechanics. *Physiol. Rev.* 89, 957–989. doi:10.1152/physrev.00041.2008

Wang, P., Sun, Y., Shi, X., Shen, H., Ning, H., Liu, H., et al. (2021). 3D printing of tissue engineering scaffolds: A focus on vascular regeneration. *Biodes. Manuf.* 4, 344–378. doi:10.1007/s42242-020-00109-0

Williams, C., Liao, J., Joyce, E. M., Wang, B., Leach, J. B., Sacks, M. S., et al. (2009). Altered structural and mechanical properties in decellularized rabbit carotid arteries. *Acta Biomater.* 5, 993–1005. doi:10.1016/j.actbio.2008.11.028

Wong, M. L., Wong, J. L., Horn, R. M., Sannajust, K. C., Rice, D. A., Griffiths, L. G., et al. (2016). Effect of urea and thiourea on generation of xenogeneic extracellular matrix scaffolds for tissue engineering. *Tissue Eng. Part C. Methods* 22, 700–707. doi:10.1089/ten.tec.2015.0552

Xiong, Y., Chan, W. Y., Chua, A. W., Feng, J., Gopal, P., Ong, Y. S., et al. (2013). Decellularized porcine saphenous artery for small-diameter tissue-engineered conduit graft. *Artif. Organs* 37, E74–E87. doi:10.1111/aor.12014

Xu, S., Lu, F., Cheng, L., Li, C., Zhou, X., Wu, Y., et al. (2017). Preparation and characterization of small-diameter decellularized scaffolds for vascular tissue engineering in an animal model. *Biomed. Eng. OnLine* 16, 55. doi:10.1186/s12938-017-0344-9

Xu, Y., Yan, M., Gong, Y., Chen, L., Zhao, F., Zhang, Z., et al. (2014). Response of endothelial cells to decellularized extracellular matrix deposited by bone marrow mesenchymal stem cells. *Int. J. Clin. Exp. Med.* 7, 4997–5003.

Yamanaka, H., Morimoto, N., and Yamaoka, T. (2020). Decellularization of submillimeter-diameter vascular scaffolds using peracetic acid. *J. Artif. Organs* 23, 156–162. doi:10.1007/s10047-019-01152-0

Yanagishita, M. (1993). Function of proteoglycans in the extracellular matrix. *Pathol. Int.* 43, 283–293. doi:10.1111/j.1440-1827.1993.tb02569.x

Yau, J. W., Teoh, H., and Verma, S. (2015). Endothelial cell control of thrombosis. *BMC Cardiovasc. Disord.* 15, 130. doi:10.1186/s12872-015-0124-z

Zager, Y., Kain, D., Landa, N., Leor, J., and Maor, E. (2016). Optimization of irreversible electroporation protocols for iIn-vivo myocardial decellularization. *PLoS One* 11, e0165475. doi:10.1371/journal.pone.0165475

Zagorchev, L., Oses, P., Zhuang, Z., Moodie, K., Mulligan-Kehoe, M., Simons, M., et al. (2010). Micro computed tomography for vascular exploration. *J. angiogenesis Res.* 2, 7. doi:10.1186/2040-2384-2-7

Zhang, J., Hu, Z. Q., Turner, N. J., Teng, S. F., Cheng, W. Y., Zhou, H. Y., et al. (2016). Perfusion-decellularized skeletal muscle as a three-dimensional scaffold with a vascular network template. *Biomaterials* 89, 114–126. doi:10.1016/j.biomaterials.2016.02.040

frontiers | Frontiers in Bioengineering and Biotechnology

TYPE Original Research
PUBLISHED 13 September 2022
DOI 10.3389/fbioe.2022.895735

Check for updates

OPEN ACCESS

EDITED BY
Kamal Hany Hussein,
Assiut University, Egypt

REVIEWED BY
Stathis Michalopoulos,
Biomedical Research Foundation of the Academy of Athens (BRFAA), Greece
Carlo Tremolada,
Manchester Metropolitan University, United Kingdom
Edoardo Raposio,
Plastic Surgery Chair, Italy

*CORRESPONDENCE
Paul Girard,
paul.girard@hotmail.fr
Nicolas Bertheuil,
nicolas.bertheuil@chu-rennes.fr

SPECIALTY SECTION
This article was submitted to Biomaterials, a section of the journal Frontiers in Bioengineering and Biotechnology

RECEIVED 14 March 2022
ACCEPTED 17 August 2022
PUBLISHED 13 September 2022

CITATION
Girard P, Dulong J, Duisit J, Mocquard C, Le Gallou S, Chaput B, Lupon E, Watier E, Varin A, Tarte K and Bertheuil N (2022), Modified nanofat grafting: Stromal vascular fraction simple and efficient mechanical isolation technique and perspectives in clinical recellularization applications. *Front. Bioeng. Biotechnol.* 10:895735. doi: 10.3389/fbioe.2022.895735

COPYRIGHT
© 2022 Girard, Dulong, Duisit, Mocquard, Le Gallou, Chaput, Lupon, Watier, Varin, Tarte and Bertheuil. This is an open-access article distributed under the terms of the Creative Commons Attribution License (CC BY). The use, distribution or reproduction in other forums is permitted, provided the original author(s) and the copyright owner(s) are credited and that the original publication in this journal is cited, in accordance with accepted academic practice. No use, distribution or reproduction is permitted which does not comply with these terms.

Modified nanofat grafting: Stromal vascular fraction simple and efficient mechanical isolation technique and perspectives in clinical recellularization applications

Paul Girard[1,2,3]*, Joelle Dulong[2,3], Jerome Duisit[1], Camille Mocquard[1,2,3], Simon Le Gallou[2,3], Benoit Chaput[4,5], Elise Lupon[4], Eric Watier[1], Audrey Varin[5], Karin Tarte[2,3] and Nicolas Bertheuil[1,2,3]*

[1]Department of Plastic, Reconstructive and Aesthetic Surgery, CHU Rennes, University of Rennes I, Rennes, France, [2]INSERM U1236, University of Rennes I, Rennes, France, [3]SITI Laboratory, CHU Rennes, Rennes, France, [4]Department of Plastic, Reconstructive and Aesthetic Surgery, Rangueil Hospital, CHU Toulouse, Toulouse, France, [5]INSERM U1031 STROMALab, Toulouse, France

Background: Nanofat grafting (NG) is a simple and cost-effective method of lipoaspirates with inter-syringe passages, to produce stromal vascular fraction (SVF) and isolate adipose-derived stem cells (ASCs). This represents a tremendous interest in the future clinical needs of tissue engineering. In this study, we optimized the NG technique to increase the yield of ASC extractions.

Methods: We analyzed three groups of SVF obtained by 20, 30, and 40 inter-syringe passages. The control group was an SVF obtained by enzymatic digestion with Celase. We studied their cell composition by flow cytometry, observed their architecture by confocal microscopy, and observed immunomodulatory properties of the ASCs from each of the SVFs by measuring inflammatory markers of macrophages obtained by an ASC monocyte co-culture.

Results: We have established the first cell mapping of the stromal vascular fraction of adipose tissue. The results showed that SVF obtained by 20 inter-syringe passages contains more statistically significant total cells, more cells expressing the ASC phenotype, more endothelial cells, and produces more CFU-F than the SVF obtained by 30 and 40 passages and by enzymatic digestion. Confocal microscopy showed the presence of residual adipocytes in SVF obtained by inter-syringe passages but not by enzymatic digestion. The functional study indicates an orientation toward a more anti-inflammatory profile and homogenization of their immunomodulatory properties.

Conclusion: This study places mechanically dissociated SVF in the center of approaches to easily extract ASCs and a wide variety and number of other

progenitor cells, immediately available in a clinical setting to provide both the amount and quality of cells required for decellularized tissues.

KEYWORDS

mechanical isolation, adipose tissue, SVF, recellularization, clinical applicability, adipose derived stem cells, nanofat, immunomodulatory properties

Introduction

Among current tissue engineering strategies to produce high-quality scaffolds, the so-called decellularization technique is the only technique yet to fulfill this goal (Badylak, 2002). Natural tissue-derived extracellular matrix (ECM), thus, brings the most complex 3D architecture, extensive components, and associated growth factors, with applications to a wide variety of simple to complex tissues, and organs (Crapo et al., 2011). The recellularization aspect, however, remains a huge challenge in order to reach clinical relevance, due to several limiting factors: the type and number of cells to be cultured, the cost of personalized medicine, and associated regulatory issues. As stated by Badylak (2016), the most realistic and applicable approach would be to use the human body's regenerative potential. Identification of adipose stromal cells (ASCs) (Zuk et al., 2002) within the adipose tissue (AT) made it valuable for clinical regenerative purposes (Wang et al., 2013). However, isolation and expansion of ASCs remain a long and expensive process, with the need for a laboratory step before its use back in a patient. This is the reason why stromal vascular fraction (SVF), a direct and easy source of ASCs and various cells types—like endothelial progenitor cells, smooth muscle cells, pericytes, M2 monocytes/macrophages, and regulatory T cells—appears to be a particularly promising aspect in the field. With already several examples of recellularization strategies based on SVF (Scarritt et al., 2015; Duisit et al., 2018; Tan et al., 2019; Gentile et al., 2020), SVF obtention and clinical handling have already been extensively studied in the field of plastic surgery, in particular through the nanofat grafting (NG) technique (Tonnard et al., 2013). The reference method to isolate SVF is enzymatic digestion (Aronowitz and Ellenhorn, 2013; Raposio et al., 2014). Some commercial devices are now available to produce SVF inside an operating room, but the process remains time-consuming and expensive (Aronowitz and Ellenhorn, 2013). Mechanical isolation of SVF with current devices represents a seducing alternative to the operating room, faster and cheaper than enzymatic digestion (Tonnard et al., 2013; Raposio et al., 2016; Mashiko et al., 2017). Chaput et al. (2016) showed that ASCs produced by mechanical isolation matched Dominici's criteria (Dominici et al., 2006; Bertheuil et al., 2015, 2019) and were able to inhibit T-cell proliferation (Chaput et al., 2016). Since this study, it is now clear that the most interesting technique in a clinical setting is the NG technique (Tonnard et al., 2013), performing an AT emulsification through 30 intersyringe passages. It is a simple, reproducible, and cheaper procedure, but the scientific evidence that ASC yield was improved had not been given yet. Furthermore, Tonnard et al. (2013) initially stated that SVF resulting from the NG technique contained no adipocytes later; Lo Furno et al. (2017) showed that nanofat contains fewer adipocytes instead of none. Due to the very high potential of SVF as a cell reservoir for regenerative medicine and recellularization purposes, we focused on extending the scientific roundness of its bedside extracting techniques. The objectives of this study are as follows: 1) to optimize the NG technique and determine, with flow cytometry, the closest number of intersyringe passages to maximize SVF cellular composition and functionality; 2) to compare SVF architectural changes between mechanical and enzymatic digestions, as well as the presence of adipocytes, by confocal microscopy; 3) to study, by co-culture and flow cytometry, the immunomodulatory properties of different SVF-isolated ASCs toward macrophages, key players in tissue regeneration, especially the M2 anti-inflammatory type.

Material and methods

Between March and July 2018, we included nine female patients undergoing an abdominoplasty procedure in the Department of Plastic Surgery of the University Hospital of Rennes, France. This study was approved by the Institutional review board and performed in accordance with the principles of the Declaration of Helsinki (1964, and the French bioethics laws of July 7th, 2011, after written informed consent from all patients. The mean age of patients was 42.7 years (±12.9 SD), and the mean BMI was 26.35 kg/m^2 (±3.2 SD). AT was manually harvested using 4-mm-diameter cannulas with a 400-mmHg vacuum, before starting the abdominoplasty procedure. We aimed at comparing the group of mechanically extracted SVF to a control group of enzymatically isolated SVF.

Management of AT

For each group, a 10 g sample of AT was processed into SVF, according to its designated technique. The final product was washed with a phosphate-buffered saline (PBS, 14,040, Life Technologies, California, United States) solution and centrifuged at 680 g for 5 min. Cell pellets were collected to count the number of cells in each sample. We normalized the count of cells of each SVF per gram of initial AT.

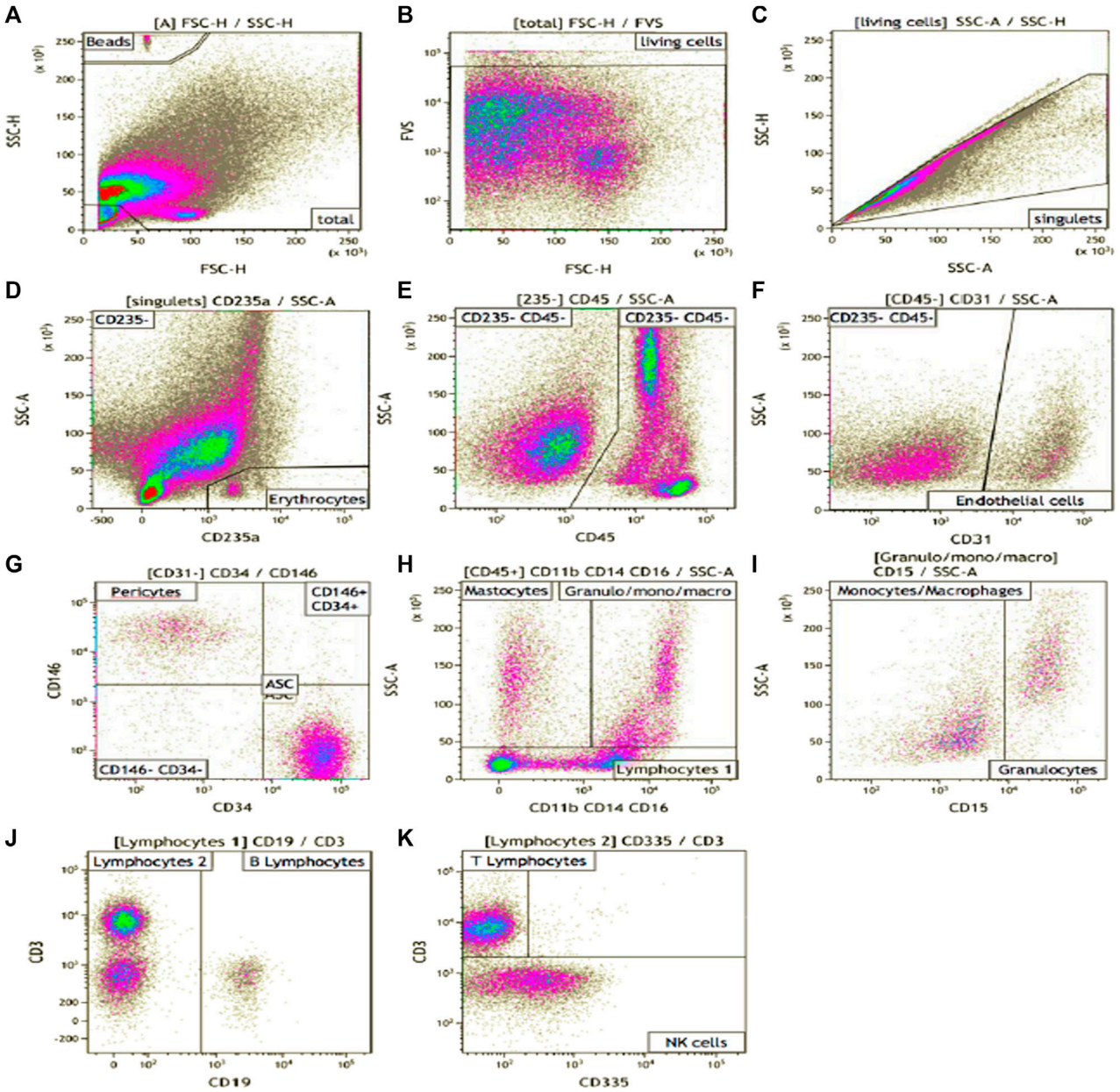

FIGURE 1
SVF phenotype gating strategy. Manual analysis on Kalooza software. **(A)** showed the gating of beads count. FVS-780 was the viability marker **(B)**. **(C)** eliminate the doublets. CD235a stained erythrocytes **(D)**. CD45 was expressed by hematopoietic cells **(E)**. CD31 was expressed by endothelial cells **(F)**. CD146 stained pericytes (on $CD45^{-}$ $CD31^{-}$cells) **(G)**. CD34 stained AUCs after an adapted gating strategy **(G)**. CD11b, CD14, and CD16 **(H)** were pooled in a cocktail of antibodies on the same filter and stained myeloid cells. CD15 stained granulocytes **(I)**. CD19 stained B cells **(J)**, CD3 stained the T cells **(K)**. CD335 stained NK cells **(K)**.

Mechanical isolation

The AT sample was transferred into a 10-ml syringe with a Luer lock nozzle connected to an identical syringe, with a 3-way connector (Connecta Luer Lock, ref 394,601, Becton Dickinson, New Jersey, United States). AT was emulsified by 20 (P20), 30 (P30), or 40 (P40) intersyringe passages, but with no filtration at 500 µm, contrary to Tonnard's original technique (Tonnard et al., 2013). Mechanically isolated SVF suspensions were stored in 50-ml tubes until further processing.

Enzymatic digestion

AT was digested with 1 ml of PBS and 18 µl of Celase® (final concentration of 0.09 mg/ml) per gram of tissue for 25 min at 37°C, as recommended. The enzyme was neutralized with PBS, and the digested tissue was filtered through a 100-µm Steriflip® unit (SCNY00100 Merck Millipore, Massachusetts, United States), and it was then centrifuged at 680 g at ambient temperature for 10 min.

Conditioning of samples before analysis

In order to precisely analyze cell composition and avoid a bias between the two isolation processes, an additional extensive enzymatic digestion process was applied to the two groups: the objective was to obtain a fully digested cellular suspension, to be analyzed by flow cytometry after filtration. Thus, each sample from mechanically isolated SVF and enzymatically isolated SVF was digested for 45 min at 37°C on a shaker using a solution with 10 ml α-MEM (32,561, Life Technologies), 100 UI/mL, and 100 µg/ml penicillin/streptomycin (15140122, Life Technologies), 200 UI/mL, 100 UI/mL, and 100 µg/ml penicillin/streptomycin (15140122, Life Technologies), 200 UI/mL of type IV CLS-4 collagenase (rLS00189, Worthington), 1.6 UI/mL dispase (LS02104, Worthington), 10 UI/ml DNase (Pulmozyme, ref 10139247, Roche, Basel, Switzerland), and 5 mM MgCl, (magnesium chloride, ref AM95306, Ambion, Thermo Fisher Scientific, Massachusetts, United States). At the end of the digestion process, all samples were washed with PBS and filtered at 100 µm, as before, and the pellet was transferred in a PBS and 10 U/ml of DNase solution, with a volume of 1 ml per gram of freshly harvested tissue.

Immunophenotypic analysis

Each SVF sample was then centrifuged, and cell pellets were re-suspended in 300 µl of 1% PBS–albumin (ref BE17-512 F Lonza, Basel, Switzerland). Samples were incubated for 10 min at 4°C with FVS-780 (ref 565,388, BD Biosciences, United States) to study viability and then incubated with brilliant staining buffer (ref 563794, BD) in order to prevent any interference between Brilliant Violet and Brilliant Ultra Violet fluorochromes. Cells were incubated at 4°C for 25 min using the following antibodies: anti-CD146-BUV395 (ref 564326), anti-CD3⁻ BUV496 (ref 564810), anti-CD45-BUV805 (ref 564916), anti-CD335-BV711 (ref 563043 BD), anti-CD11b-PE (ref PN IM25181U), anti-CD235a-FITC (ref PN IM2212U), anti-CD19-PC7 (ref IM328 Beckmann Coulter, CA, United States) anti-CD14-PE (ref R0864), anti-CD16- PE (ref R7012, Dako Agilent Technologies, California, United States), anti-CD15-PB (ref 323022, BioLegend CA, United States), anti-CD31=PerCP eF710 (ref 46-0319-42 eBioscience Thermo Fisher Scientific MA, United States), and anti-CD34-APC (ref 130-090-954, Miltenyi Biotec, Germany). After labeling, we performed erythrocyte lysis (ref S2364, Dako), and after a final wash, cell pellets were re-suspended in 240 µl of 1% PBS–albumin with 10 µl of DNAse and 50 µl of beads for counting (ref 424902, Beads Comp, BioLegend). Acquisitions were performed on a multicolor flow cytometer (BD, Fortessa X20, BD Biosciences).

Clonogenicity

The presence of colony forming unit fibroblasts (CFU-F) was assessed in SVF. Cells were seeded at 8 cells/cm^2 in 25 cm^2 plates with 5 ml of culture medium made of αMEM, fetal calf serum 10% (ref FB-1101/500 Bioserra), and penicillin-streptomycin (20 UI/mL final, ref 15140-122 Gibco, Thermo Fisher Scientific). The culture medium was initially replaced after 24 h and then twice a week. Staining took place on day 14 with a MCDH kit (ref 313590–313570 – 313560–313600, RAL Diagnostics, France). Colonies of more than 50 cells were considered CFU-F. The count of ASCs was defined as the number of CFU-F divided by the number of cells initially seeded.

Confocal microscopy

The objective was to detect residual intact mature adipocytes in mechanically isolated SVF. Adipocytes were stained with BODIPY 558/568 1/50 dilution (Invitrogen, Thermo Fisher Scientific), endothelial cells with Alexa Fluor 488-Isolectin 1/50 dilution (I21411 Invitrogen, Thermo Fisher Scientific), and cellular nucleus with DAPI 1/50 dilution (D9542-1 MG Sigma Life Science, Missouri, United States). We used a "whole-mount staining" protocol based on a technique described by Mashiko et al. (2017). Preparations were fixed with 4% paraformaldehyde with shaking for 10 min then rinsed three times with PBS. Then, preparations were incubated for 1 h with a saturation solution of PBS, saponin 0.01% final (S7900, Quillaja Bark Sigma life science), 2% bovine serum albumin (A3294 Sigma Life Science), and 4% donkey serum (CO6SB, Bio-Rad, California, United States). Staining was performed on approximately 500 µl of tissue for 30 min at room temperature while shaking. Tissue was placed on a microscopic slide using the "thick smear" technique. After a 12-h drying process, slides were observed by confocal fluorescent SP8 microscopy (Leica, Germany).

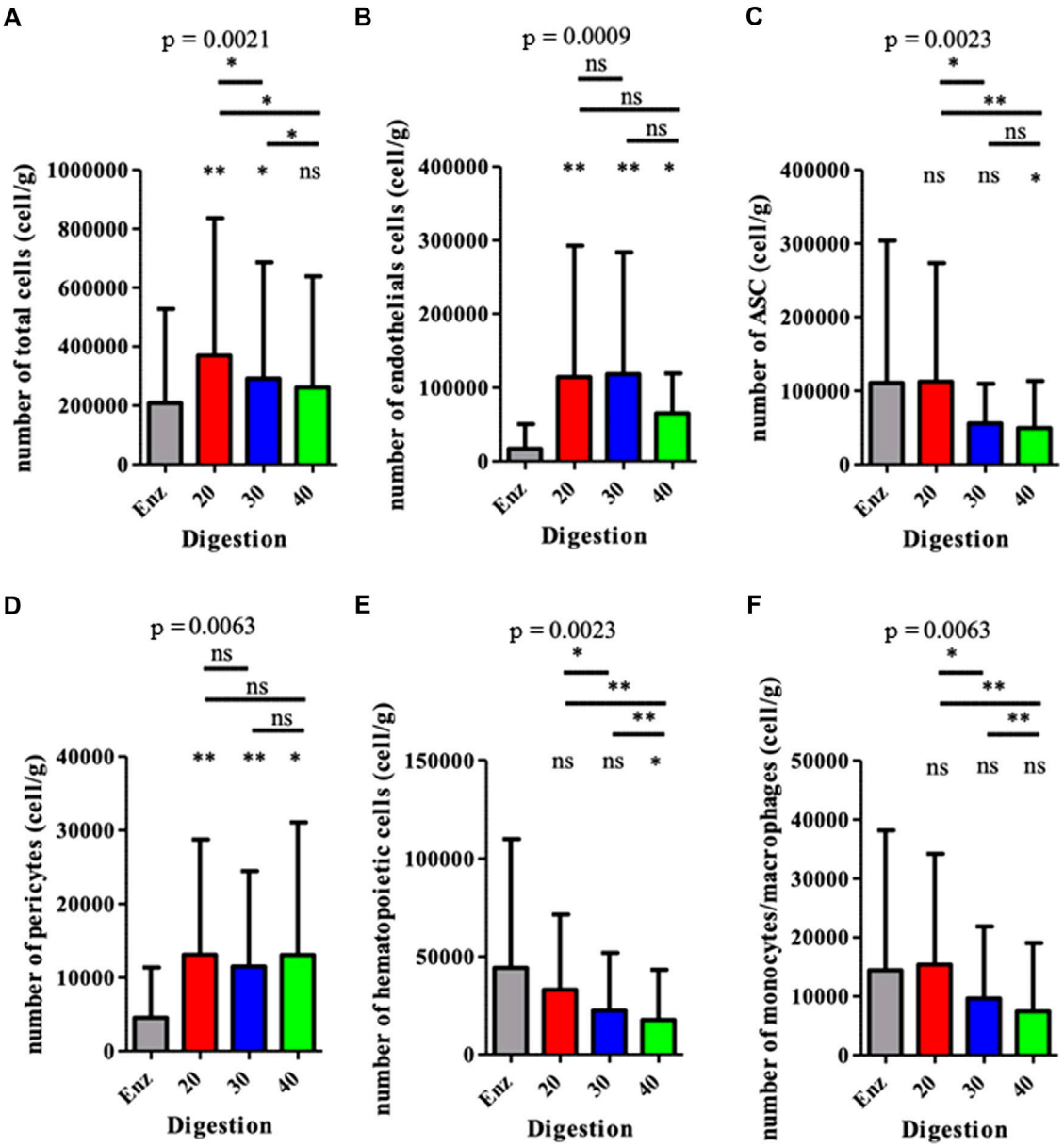

FIGURE 2
Analysis of the cell populations from each SVF obtained for various methods. The results are expressed as the number of cells per gram of the initial fresh tissue. *$p < 0.05$, **$p < 0.001$, and ***$p < 0.0001$; ns: not significant. SVF: stromal vascular fraction.

Immunomodulatory assay

The objective was to assess the *in vitro* functional ability of SVF-derived ASCs to polarize macrophages. The monocytes used were, therefore, stored in liquid nitrogen, obtained by elutriation of leuko-platelet concentrate from discarded banked human blood. At the end of passage 0, ASCs were co-cultured with monocytes at a ratio of 4:1 in RPMI (ref 61870-010, Life Technologies), fetal calf serum (ref FB-1101/500, Bioserra), penicillin-streptomycin 20 UI/mL final (ref 15140-122, Gibco), and M-CSF 100 ng/ml final (ref 216-MC-005 R&D Systems, Minnesota, United States). After 5 days, cocultures were stopped, and cells were stained with anti-CD45^{-} BUV395 (ref 56379 BD), anti-CD73-BV786 (ref 7423635 BD), anti-CD206-APC (ref 550889 BD), anti-CD163-PE (ref 556018 BD), and anti-HLA-DR-BV605 (ref

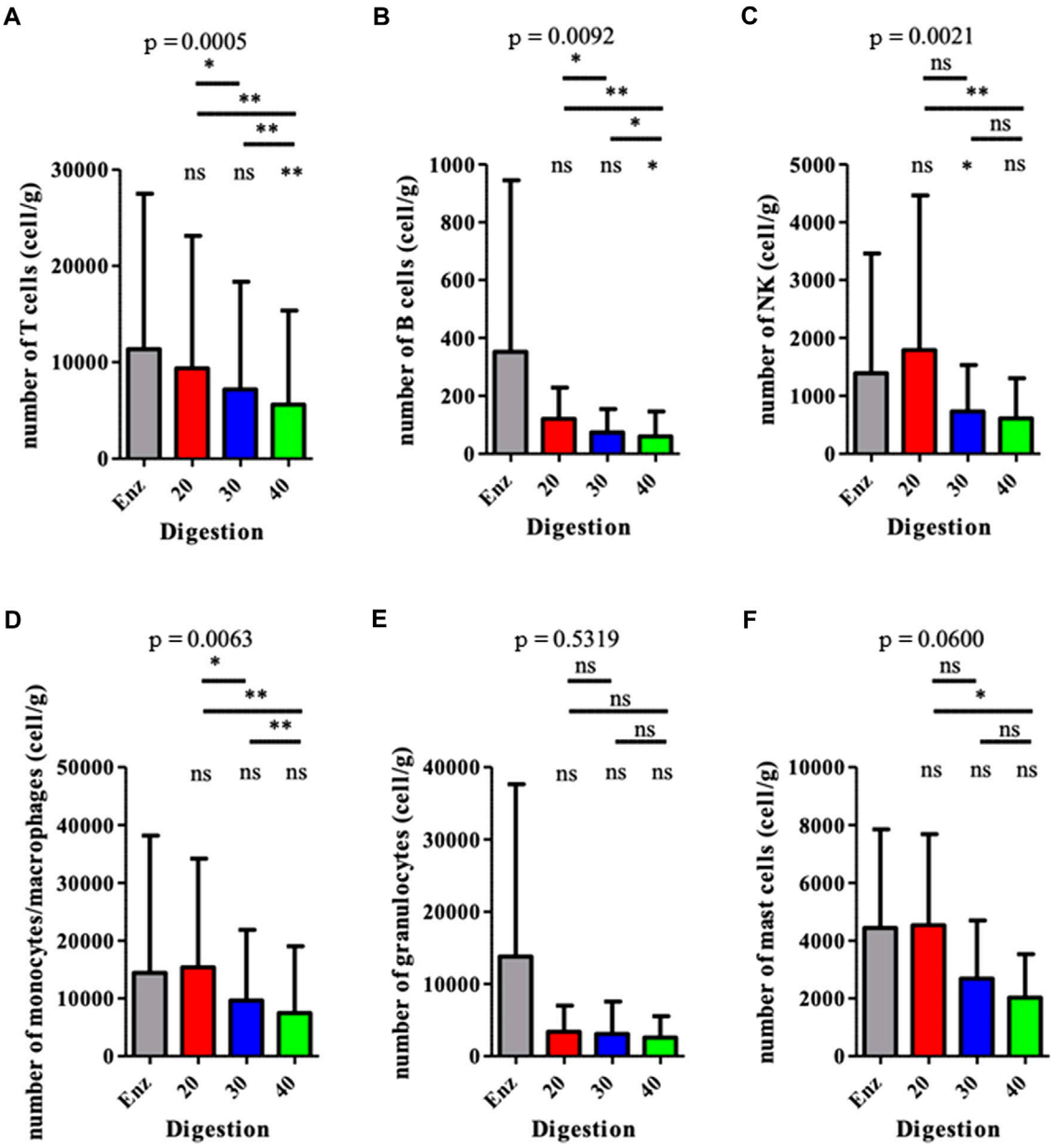

FIGURE 3
Analysis of the hematopoietic (CD45pos) populations from the SVFs. Results are expressed as a percentage of the total number of cells, for each population. *$p < 0.05$, **$p < 0.001$, and ***$p < 0.0001$; ns: not significant. SVF: stromal vascular fraction.

562844 BD). Cells were analyzed in a multicolor flow cytometer. The control group was defined for M1/M2 differentiation: in order to create a reference scale of macrophage polarization, we performed an M1 and M2 differentiation *in vitro*, on the same batch of monocytes we used for the co-culture experiments. To promote differentiation, we added cytokines to the culture medium: GM-CSF (granulocyte macrophage colony-stimulating factor; 200 ng/ml) for M1 wells and M-CSF (200 ng/ml) for M2 wells. The plate was placed at 37°C for 5 days. On day 5, the culture medium of M1 macrophages received IFNg (40 ng/ml) and LPS (200 ng/ml), and the culture medium of M2 macrophages received IL4 (40 ng/ml), IL10 (40 ng/ml) and IL13 (40ng/ml). The plates were placed at 37°C for additional 3 days. The analysis took place on day 8 using the same panel we used in the co-culture. The

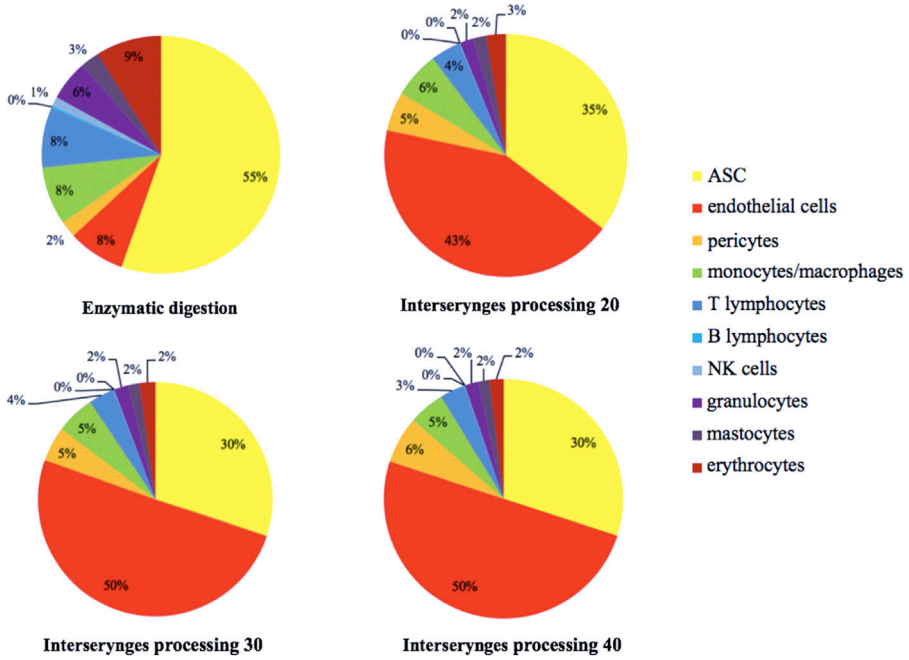

FIGURE 4
Estimated distribution of the different SVF cell populations, distributed according to the color code indicated. The percentage represents the proportion of each cellular sub-population. SVF: stromal vascular fraction.

mean fluorescence intensity of CD206, CD163, and HLA-DR of Fluorescence Minus One (FMO) tubes and TEST tubes was calculated on a monoparametric diagram.

Statistics

Statistical analysis was performed by GraphPad Prism 7.04 (GraphPad Software, GSL Biotech LLC, CA, United States). We used a one-factor variance analysis test (one-way ANOVA) for comparison of conditions with one parameter and a Wilcoxon *t*-test for comparison of two versus two conditions. Results are shown with their standard deviations (SD). Graphic representation is shown with scatter plots. Dispersion is represented by the mean standard deviation (meanSD).

Results

Flow cytometry

The exhaustive cartography of adipose-derived SVF, of mechanically isolated SVF compared to enzymatically isolated SVF samples (Figure 1), showed important differences between the two groups. However, mechanical M20, M30, and M40 groups presented the same distribution for each cell population, regardless of the number of intersyringe passages. Mechanically isolated SVF with P20 and P30 passages contained a higher number of cells than the enzymatically isolated SVF control group: 369 557 cpg (cells per gram of 167 initial tissue) ± 466 220 (p = 0.0078), 291 272 cpg ± 394 588 p = 0.0117), and 208 575 cpg ±318 774, respectively (Figure 2A). Mechanically isolated SVF contained more endothelial cells and pericytes than enzymatically isolated SVF (Figures 2B,D). Mechanically isolated SVF P20 had the highest number of cells expressing an ASC phenotype ($CD45^-$ $CD31^-$ $CD34^+$) (Figure 2C). There was no difference between the two groups regarding the number of hematopoietic cells, but within the mechanically isolated SVF group, more intersyringe passages decreased their amount (Figure 2E); the same observation was made for the number of monocytes/macrophages (Figure 2F). There was no difference between the two groups regarding the number of hematopoietic subpopulation cells (Figure 3). An increase in intersyringe passages reduced the number of small cells (LT, LB, and NK) (Figures 3A–C) but had no effect on the bigger granulocytes and mastocytes (Figures 3D–F). The proportion of endothelial cells in enzymatically isolated SVF (8.02% ± 6.11) was significantly lower than that in mechanically isolated SVF and following passages: P20 with 43.77% (± 16.49, p = 0.0039), P30 with 50.09% (± 16.42, p = 0.0039), and

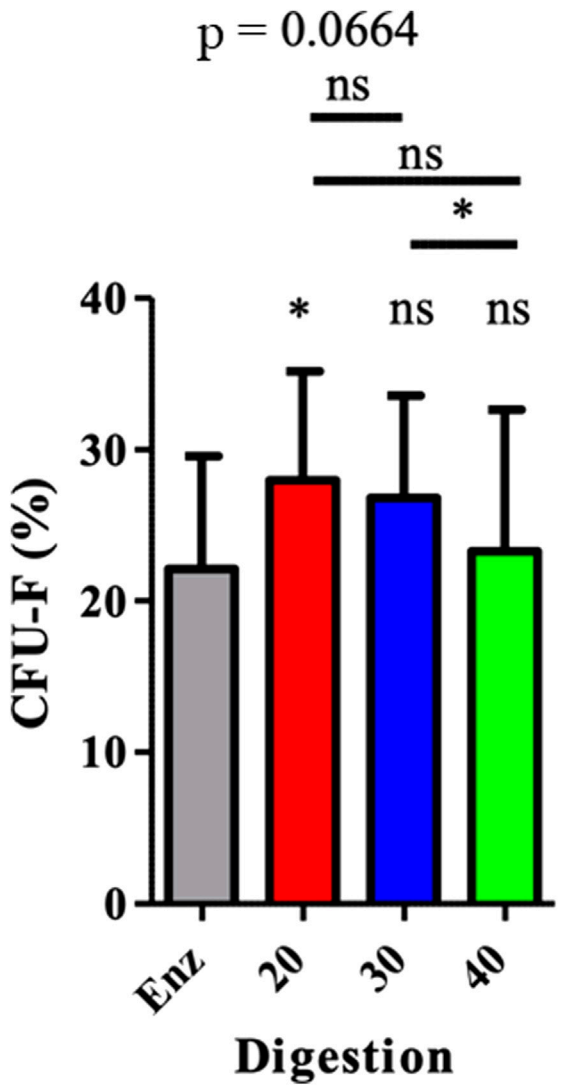

FIGURE 5
ASC (CFU-F) representation in SVF. The results are expressed as a percentage of CFU-F. It was obtained by the number of CFU-F counted in relation to the number of cells sown. *$p < 0.05$, **$p < 0.001$, and ***$p < 0.0001$; ns = not significant. ASCs: adipose-derived mesenchymal stem cells; CFU-F: colony-forming unit–fibroblast; SVF: stromal vascular fraction.

P40 with 51.81% (± 20.33, $p = 0.0039$), relying to the proportional increase of other cell populations. Mechanically isolated SVF subgroups had similar repartition of their cell populations (Figure 4).

Clonogenicity

Mechanically isolated SVF P20 had a significantly higher rate of ASCs than enzymatically isolated SVF of 27.97% (± 7.18) compared to 22.11% (± 7.44) and $p = 0.0243$. (Figure 5).

Confocal microscopy

In the enzymatically isolated SVF group, confocal microscopic observation with BODIPY staining demonstrated the absence of any intact mature adipocytes. However, in mechanically isolated SVFs, all types of adipocytes (Figure 6) were detected, and the overall number of adipocytes decreased for P20–P40 passages. As expected, vascular structures were altered after a mechanical dissociation.

Immunomodulatory properties on monocytes and macrophages

Macrophages co-cultured with ASCs from all the different SVFs significantly increased their expression of the CD206 marker, compared to the control group. The RMFI values were the following: for the control group 15.87 (± 10.99); for the enzymatically isolated SVF 54.06 (± 34.70, $p = 0.0156$); and for the mechanically isolated SVF group 50.32 (± 33.4, $p = 0.0156$), 48.47 (± 32.80, $p = 0.0156$), and 52.87 (± 43.80, $p = 0.0156$) for P20, P30, and P40, respectively. No difference was observed between the different co-culture conditions. However, the expression of the HLA-DR marker was significantly decreased for all conditions, compared to that of the monocyte control group. We found an RMFI of 76.66 (± 6.71) for monocytes alone; 46.69 (± 27.91, $p = 0.0343$); and in the enzymatically isolated SVF group; 51.48(± 31.65, $p = 0.0343$), 37.25 (± 23.69, $p = 0.0223$), and 40.02 (± 23.50; $p = 0.0223$) for P20, P30, and P40 mechanically isolated SVF subgroups, respectively. However, like for CD206 and CD163, there was no difference between the ASCs from the different methods of SVF isolation. The expression level increased for CD206 and decreased for HLA-DR, and co-cultured ASCs and monocytes tend to lead to an M2 phenotype. There was no difference between ASCs of different mechanically isolated SVF and enzymatically isolated SVF samples, regarding the polarization level of monocytes/macrophages (Figure 7). This means that a greater number of intersyringe passages increased the ECM destruction, as demonstrated by a progressive diminution of residues in the filter (Supplementary material S1), and did not release more cells as we thought it would but instead proportionally destroyed more of it.

Discussion

The use of adipose tissue in surgery is both an ancient practice and a growing concept. Initially used as a filler substance, the discovery of ASCs by Zuk et al. (2002) and then the development of knowledge of this tissue, the cells that make it up and their properties have multiplied the medical indications. Seeking to concentrate the cells and

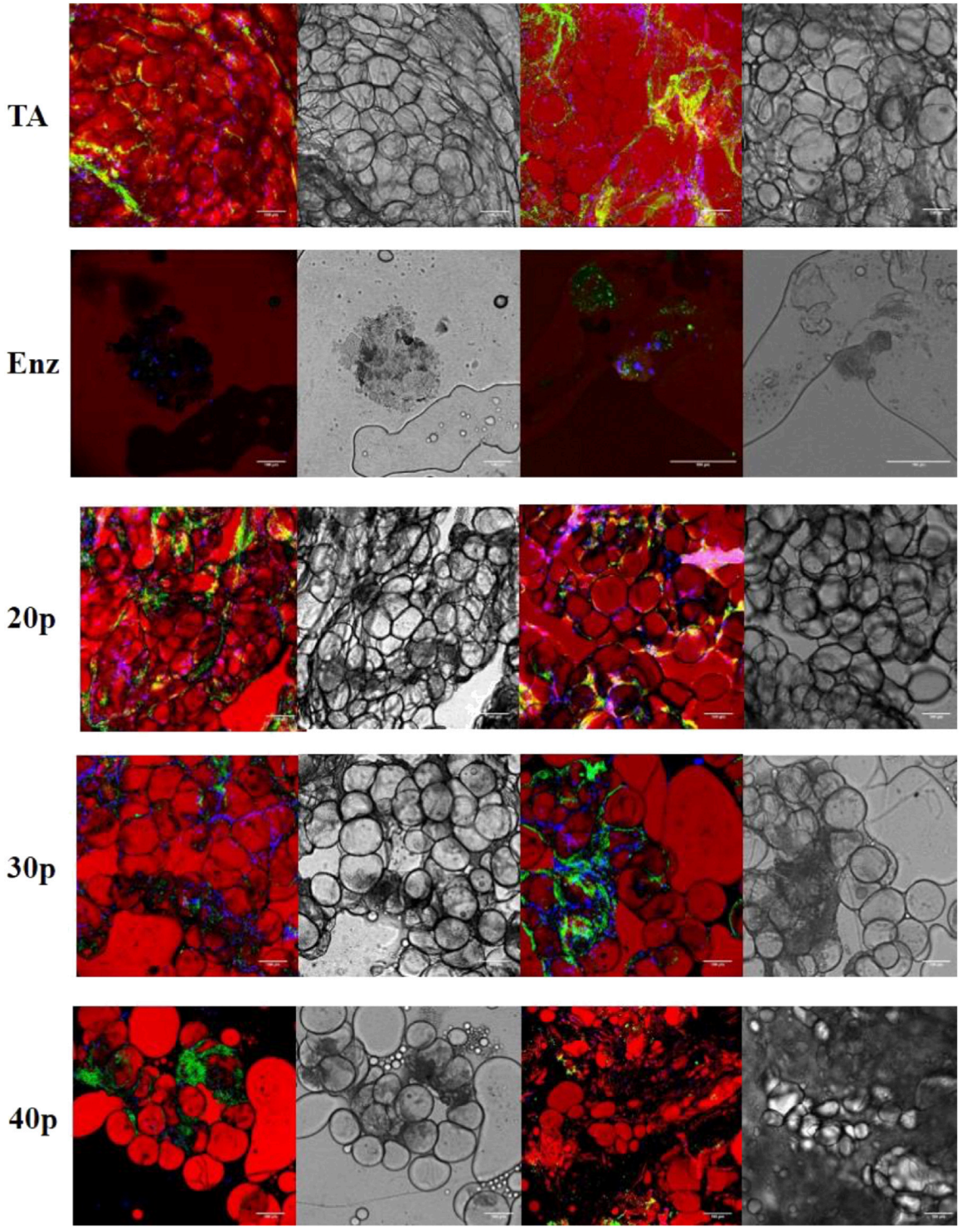

FIGURE 6
Immunofluorescence by confocal microscopy of the different SVFs. In red, adipocytes are stained by BODIPY; in green, endothelial cells are stained by isolectin coupled with Alexa Fluor 488, and in blue, nucleated cells are stained by DAPI. Shades of gray: transmission electron microscopy imaging of the same section. * False positive, lipid vacuole. SVF: stromal vascular fraction.

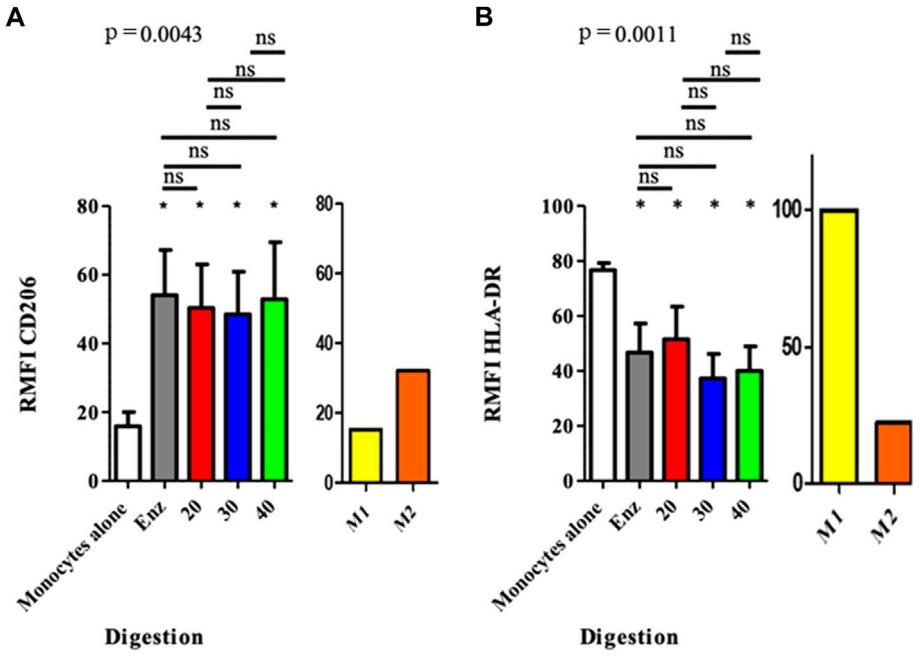

FIGURE 7
Polarization of macrophages after co-culture with ASCs at the end of P0. The results are expressed as the fluorescence ratio of the TEST tube/FMO tube, obtained by mono parametric test. If the ratio is < 1, the marker is not expressed; between 1 and 2, the expression of the marker cannot be concluded, and 2 the marker is expressed. *$p < 0.05$, **$p < 0.001$, and ***$p < 0.0001$; ns: not significant. ASCs: adipose-derived mesenchymal stem cells.

purify the substrate for reinjection, several techniques have followed one another to optimize the grafting of adipose tissue. The Coleman technique is the most commonly used in current practice, allowing clean adipose tissue to be reinjected, and washed from this waste, to optimize engraftment. With a view to performing tissue regeneration, the objective is to overcome the filler effect of TA to concentrate the cells of interest (ASC, macrophages, and endothelial cells). Other techniques such as Microfragmented adipose tissue or LIPOGEMS® can reduce sub-millimeter adipocyte clusters (Bianchi et al., 2013). They have been shown to produce a reinjection substrate containing ASCs (Maioli et al., 2014) endothelial cells, pericytes, and anti-inflammatory and anti-angiogenic properties (Ceserani et al., 2016; Bouglé et al., 2018; Ragni et al., 2022). The indications are very promising for intra-tissue reinjection (Tremolada et al., 2016; Naldini et al., 2018; Ceresa et al., 2022), especially intra-articular injection (Cattaneo et al., 2018; Filardo et al., 2022), where the reinjected product combines the functionality of the cells of interest with a mechanical effect. However, from the perspective of tissue engineering, an SVF seems even more interesting because it further reduces the clusters and the filler effect of adipocytes by concentrating the cells of interest. An SVF obtained with the least possible manipulation, directly in the operating room and at a lower cost is of capital interest in current clinical practice and opens the door to new perspectives in the laboratory because of the number of cells obtained and their functionality.

We optimized the NG technique and demonstrated that the increase of intersyringe passages reduced the SVF final number of cells, adjusted per gram of AT, along with a reduction of ASC phenotypes and clonogenic cells (CFU-F). Interestingly, compared to enzymatically isolated ones, there were more cells in mechanically isolated SVFs. This was quite unexpected, compared to previous findings (Shah et al., 2013; Markarian et al., 2014; Chaput et al., 2016). It could be explained by the fact that, in order to perform flow cytometry on SVF, we had to use a 100-µm strainer to avoid clogging the cytometer. Second, enzymatic digestion had been described by Van Dongen et al., 2016 and by Mashiko et al. (2017) with only one collagenase. The cocktail was made of type IV collagenase, dispase, and DNase to avoid cellular aggregates and magnesium chloride, which acted as an enzymatic activator. This cocktail enabled us to analyze more thoroughly the composition of each SVF. Other studies compared the enzymatic activator to mechanical dissociation after straining for cytometric analyses (Tonnard et al., 2013; Aronowitz et al., 2015; Chaput et al., 2016; Mashiko et al., 2017), without taking

into account this inherent bias. It should be noted that, unlike its original description, intersyringe emulsification was not filtered through a 500-µm sterile nylon: indeed, the pore size (500 µm) is too large to retain different cell populations of AT and would only retain fibrous and vascular structures not eliminated after digestion, as we previously demonstrated (Bertheuil et al., 2016). The number of cells per gram of initial AT (cpg), obtained after enzymatic digestion in our study (208 575 cpg ± 318774), was lower than Chaput's (600 000 cpg) (Chaput et al., 2016) and Yoshimura's (1 310 000 cpg) (Yoshimura et al., 2006). However, even with the same collagenase, the number of cells remains higher than that of Aronowitz and Ellenhorn, 2013 (101 061 cpg) who used the Cytori device. Chaput obtained fewer cells than we did (40 000 vs. 291,272 cpg) (Chaput et al., 2016) as Tonnard (19750 cpg) (Tonnard et al., 2013) without enzymatic digestion of mechanically isolated SVF. In contrast, Mashiko found more cells (around 600 000 cpg) with additional enzymatic digestion (Mashiko et al., 2017). This demonstrates the necessity of an additional enzymatic digestion step, in order to get a better representation of the isolated cell population and amount. Regarding the number of ASCs per gram of initial AT, our results found 55 643 ± 54 049 cpg with the M30 technique. In order to compare these results with the literature, we used the same gating strategy as Chaput (Chaput et al., 2016) and Mashiko (Mashiko et al., 2017). From their work, we can consider CD45neg CD31neg CD34pos cells as ASCs. Preliminary unpublished results of our laboratory (Bertheuil, 2017) confirmed these CD45neg CD31neg CD34pos also express CD73, CD90, and CD105 specific markers of MSCs. (Supplementary material S2). Mashiko et al. (2017) found more cells (150 000 cpg) but used a smaller syringe of 2.5 vs. 10 ml, which could have had an impact on the pressure put on the cells, when they are pushed through the connector. Through second enzymatic digestion, we found 57.58% ± 11.38 of ASCs in SVF which is more than what is described in the literature: 21.45% ± 2.52 (Chaput et al., 2016); 10.68% (Aronowitz and Ellenhorn, 2013), same enzyme but using the Celution device for digestion; 14% (Güven et al., 2012), with Sepax device. With mechanically isolated SVF obtained with P30, we found 30,52% ± 13.09 ASCs, which is in line with Mashiko's findings of near 35% (Mashiko et al., 2017) and with Chaput's findings of 38.11% ± 5.14 (Chaput et al., 2016) using a similar ASC gating strategy. It is interesting to note that Tonnard only found 5% (Tonnard et al., 2013) with ASC staining with only $CD34^+$. We found an 8.02% ± 6.11 rate of endothelial cells with our enzymatic digestion, comparable to that of Chaput (7.64% ± 1.50) (Chaput et al., 2016). Although, unlike us, collagenase was used alone in that study, which means that enzymatic digestion had few impacts upon the vascular network. Sundarraj's rate of 3% ± 1 is in line with our findings (SundarRaj et al., 2015). On the other hand, with P30 passages, we found 51.09% ± 16.42 of endothelial cells, which is much higher than that of Guven (25%) (Güven et al., 2012), Mashiko (25%–30%) (Mashiko et al., 2017), or Chaput (Chaput et al., 2016) studies. Interestingly, regarding CFU-F, enzymatically isolated SVF had a lower ASC rate (22.11% ± 7.44) than P20 and P30 mechanically isolated SVF. These results are the opposite of Chaput's results of 36.74% ± 4.96 after enzymatic digestion and 17.79% ± 4.29 after mechanical dissociation, possibly due to the absence of second enzymatic digestion and an underestimation of mechanically isolated SVF content (Chaput et al., 2016). Aronowitz et al. (2015)found only 16% of CFU-F with the Celution device (Aronowitz et al., 2015). In our study, with regards to the overall number of cells per gram of initial tissue and the number of ASCs, the P20 technique was superior to the P30 and P40 mechanically isolated SVF. It means that a greater number of passages between syringes increases the extracellular matrix disruption, as observed with fewer residues in the filter and not releasing as many cells as expected, but instead destroying these cells. In his work, Tonnard et al. (2013) claimed that there were no adipocytes in the reinjected product because of the absence of viable adipocytes, as assessed by direct fluorescence microscopy, after AM-calcein and DAPI staining. Here, we demonstrated the presence of adipocytes after mechanical dissociation, regardless of the number of passages between the syringes. This major difference is probably related to the confocal microscopy technique which, unlike fluorescence microscopy, is more precise and allows the visualization of a cell. Immunomodulatory properties of MSCs are well known but those of ASCs are less well documented, especially when obtained by mechanical dissociation (Mallis et al., 2021). A previous study (Chaput et al., 2016) showed that mechanically isolated SVF isolated ASCs presented a similar inhibition of proliferation of activated T-lymphocytes after one culture passage, compared to ASCs from enzymatically isolated SVF. We also assessed if ASCs from mechanically isolated SVF and enzymatically isolated SVF had similar immunomodulatory properties on macrophages, key players in tissue regeneration processes. When SVF is directly reinjected in a tissue, the immunomodulatory effect of ASCs on macrophages seems more relevant for regenerative purposes**.** We determined the effect of each ASC group based on the phenotype modifications of cocultured monocyte cells. The expression of three markers (CD206, CD163, and HLA-DR) was used to determine the polarization state of cells, allowing us to conclude that macrophages from mechanically isolated SVF had the same M2 orientated profile as those from enzymatic isolated SVF. M2-orientated polarization documented here is an additional element to comfort the application of the NG technique, with mechanically isolated SVF to seed engineered tissues and promote *in vivo* regeneration. Regarding immunomodulatory properties of ASCs, depending on the type of isolation methodology, a previous study showed that the mechanically isolated ASCs demonstrated a similar inhibition of proliferation of activated T lymphocytes in CFSE, after one culture passage (Chaput et al., 2016), as it is known for MSCs (Mallis et al., 2021). This is particularly interesting for cell therapy purposes. However, when directly

reinjecting SVF in a tissue, meaning without any laboratory step between clinical procurement and mechanical processing, the immunomodulatory effect of ASCs on macrophages seems more relevant. In this work, it was difficult to get an exhaustive profile demonstrating a pro-inflammatory (M1) or anti-inflammatory (M2) environment, especially *in vivo* where a control group is difficult to achieve. This determination is based on the cell's phenotype, its phagocytosis ability, and its secretory profiles. We used a shortcut commonly described in studies that analyzes only surface markers of macrophages. The variation in the intensity of expression of three markers (CD206, CD163, and HLA-DR) was used to determine the polarization state of cells. We wanted to look at the macrophage's status within the reinjected SVF and the immunomodulatory effect of ASCs after one passage in culture on macrophages *in vitro*. First of all, the *in vivo* marking (CD206, CD163, and HLA-DR) on myeloid sub-populations allowed us to conclude that macrophages from mechanically isolated SVF had a more anti-inflammatory profile than those from enzymatic isolated SVF. Nevertheless, we could not conclude their polarization without measuring the specific cytokines as explained previously. This is in line with the literature where it is now clearly accepted that MSCs promote a macrophage M2 profile. Dong et al. (2013) showed that CD206 and CD163 increases in PCR, when adipose tissue is cultured with SVF in mice, tend to show that ASCs give macrophages an M2 profile. Moreover, Kim and Hematti (2009) also demonstrated that co-cultured macrophages and ASCs have a higher expression of CD206 and an increased secretion of IL-10 and IL-6, as long as reduced secretion of TNF alpha and IL-12. Adutler-Lieber et al. (2013) showed that in a co-culture of monocytes and ASCs, there is an increased expression of CD-206 and CD-163, increased secretion of IL-13, IL-4, VEGF, and IL-10, and reduced secretion of IL-1, IL-12, TNF alpha, IL-17, and INF gamma. Rybalko et al. (2017) showed a proportional increase of CD-206 within the ASC coculture when the macrophage/ASC ratio reached 5:1. Our findings are not statistically significant even though we used a 4/1 ratio in culture. However, immunomodulatory properties of ASCs obtained by mechanical dissociation are not known. We, therefore, preferred to initiate a co-culture with non-oriented monocytes in case these types of ASCs orient macrophages toward an M1 profile. The demonstration of their capacity to orient macrophages toward an M2 profile would have been strengthened if the same results had been demonstrated on macrophages pre-oriented toward an M1 profile instead of neutral monocytes. Nevertheless, the M2 polarization of ASCs obtained by mechanical dissociation seems interesting for regenerating tissues. Moreover, *in vivo*, there are no M1 or M2 macrophages which are laboratory creations but a continuum of macrophages going from M1 to M2.

Conclusion

The SVF use represents a major strategy in the clinical ECM recellularization approach: a large source of autologous progenitor cells, both in cell types and number, being easily harvested with the minimal morbidity of liposuction or lipectomies—classically used in plastic and aesthetic surgery—as well as an easy and cost-efficient extraction. The so-obtained SVF can then be processed to cellularize engineered constructs, either directly in an operating theater, or to be used in a bioreactor. The great advantage is also to avoid all the regulatory constraints as cells are autologous and with very limited manipulation. Our work is the first to precisely detail this human adipose-derived SVF composition and optimize the mechanical technique, compared to the enzymatic approach. It gives an exhaustive listing of the different cellular actors involved. However, interaction mechanisms between the different cell sub-populations and host tissues are still to define. This work suggests modifying the existing NG technique with 20 intersyringe passages is optimal. For regenerative purposes in the operating room, mechanical SVF will play an important role in the therapeutic arsenal of the regenerative surgeon because of the M2 macrophages' anti-inflammatory and pro-angiogenic abilities, which are true architects of regeneration. It is undeniable that there is a clinical benefit when mechanical SVF contains myeloid cells with an anti-inflammatory profile and the same overall number of cells as enzymatic SVF. Moreover, mechanically isolated SVF has a greater number of endothelial cells, which promotes a pro-angiogenic environment and a greater number of immunomodulatory/anti-inflammatory ASCs, with greater clonogenicity. Given its low cost of production, especially compared to enzymatic digestion in a laboratory or use of the Celution device (2400$ for one dissociation) (Aronowitz and Ellenhorn, 2013), mechanical SVF after 20 passages between two syringes appears as a very efficient and affordable technique. Furthermore, their clonogenicity ability is not altered after P0 culture which means mechanically isolated SVF could also become a reference to produce ASCs for cell therapy.

Data availability statement

The raw data supporting the conclusion of this article will be made available by the authors, without undue reservation.

Ethics statement

The studies involving human participants were reviewed and approved by the Ethics committee, University of Rennes I, Rennes, France. The patients/participants provided their written informed consent to participate in this study.

Author contributions

PG: conception and design of the study, processing sampling and performing the experiment, interpretation of the data, and drafting of the manuscript. JD: conception and design of the study. JD: extensive revision of the article. CM: translation and revision of the article. AV, KT, and BC: conception of drawing. EW and EL: revision of the article. SL: development of the flow cytometry matrix. NB: conception and design of the study, drafting of the manuscript, and final approval of the version to be published.

Acknowledgments

The authors thank Menard Cedric for his support in flow cytometry analysis at the Cytometry and Cell Sorting Platform (INSERM/UPS-UMR1048). They also thank Isabelle Bezier, Maelle Latour, and Nadège Bescher for the education of experimentation techniques and Marion Guirriec for assistance in confocal microscopy. Salary of the first author was financed by "bourse année recherche CHU de Rennes" .All experience was financed by "bourse projet CORECT CHU de Rennes".

Conflict of interest

The authors declare that the research was conducted in the absence of any commercial or financial relationships that could be construed as a potential conflict of interest.

Publisher's note

All claims expressed in this article are solely those of the authors and do not necessarily represent those of their affiliated organizations, or those of the publisher, the editors, and the reviewers. Any product that may be evaluated in this article, or claim that may be made by its manufacturer, is not guaranteed or endorsed by the publisher.

Supplementary material

The Supplementary Material for this article can be found online at: https://www.frontiersin.org/articles/10.3389/fbioe.2022.895735/full#supplementary-material

References

Adutler-Lieber, S., Ben-Mordechai, T., Naftali-Shani, N., Asher, E., Loberman, D., Raanani, E., et al. (2013). Human macrophage regulation via interaction with cardiac adipose tissue-derived mesenchymal stromal cells. *J. Cardiovasc. Pharmacol. Ther.* 18, 78–86. doi:10.1177/1074248412453875

Aronowitz, J. A., and Ellenhorn, J. D. I. (2013). Adipose stromal vascular fraction isolation: A head-to-head comparison of four commercial cell separation systems. *Plastic Reconstr. Surg.* 132, 932e–9e. doi:10.1097/PRS.0b013e3182a80652

Aronowitz, J. A., Lockhart, R. A., and Hakakian, C. S. (2015). Mechanical versus enzymatic isolation of stromal vascular fraction cells from adipose tissue. *SpringerPlus* 4, 713. doi:10.1186/s40064-015-1509-2

Badylak, S. F. (2002). The extracellular matrix as a scaffold for tissue reconstruction. *Semin. Cell Dev. Biol.* 13, 377–383. doi:10.1016/s1084952102000940

Badylak, S. (2016). Perspective: Work with, not against, biology. *Nature* 540, S55. doi:10.1038/540S55a

Bertheuil, N., Chaput, B., Berger-Müller, S., Ménard, C., Mourcin, F., Watier, E., et al. (2016). Liposuction preserves the morphological integrity of the microvascular network: Flow cytometry and confocal microscopy evidence in a controlled study. *Aesthet. Surg. J.* 36, 609–618. doi:10.1093/asj/sjv209

Bertheuil, N., Chaput, B., Ménard, C., Varin, A., Garrido, I., Grolleau, J. L., et al. (2015). Adipose-derived stromal cells: History, isolation, immunomodulatory properties and clinical perspectives. *Ann. Chir. Plast. Esthet.* 60, 94–102. doi:10.1016/j.anplas.2014.09.014

Bertheuil, N., Chaput, B., Ménard, C., Varin, A., Laloze, J., Watier, E., et al. (2019). Adipose mesenchymal stromal cells: Definition, immunomodulatory properties, mechanical isolation and interest for plastic surgery. *Ann. Chir. Plast. Esthet.* 64, 1–10. doi:10.1016/j.anplas.2018.07.005

Bertheuil, N. (2017). Le tissu adipeux : Approfondissement des connaissances fondamentales du tissu et de son compartiment vasculaire stromal, intérêt clinique pour la chirurgie plastique. Available at: https://www.theses.fr/2017REN1B051 (Accessed July 9, 2022).

Bianchi, F., Maioli, M., Leonardi, E., Olivi, E., Pasquinelli, G., Valente, S., et al. (2013). A new nonenzymatic method and device to obtain a fat tissue derivative highly enriched in pericyte-like elements by mild mechanical forces from human lipoaspirates. *Cell Transpl.* 22, 2063–2077. doi:10.3727/096368912X657855

Bouglé, A., Rocheteau, P., Hivelin, M., Haroche, A., Briand, D., Tremolada, C., et al. (2018). Micro-fragmented fat injection reduces sepsis-induced acute inflammatory response in a mouse model. *Br. J. Anaesth.* 121, 1249–1259. doi:10.1016/j.bja.2018.03.032

Cattaneo, G., De Caro, A., Napoli, F., Chiapale, D., Trada, P., and Camera, A. (2018). Micro-fragmented adipose tissue injection associated with arthroscopic procedures in patients with symptomatic knee osteoarthritis. *BMC Musculoskelet. Disord.* 19, 176. doi:10.1186/s12891-018-2105-8

Ceresa, C., Borrone, A., Fracchia, L., Rinaldi, M., Marchetti, A., Tremolada, C., et al. (2022). Lipoaspirate shows *in vitro* potential for wound healing. *Pharmaceutics* 14, 447. doi:10.3390/pharmaceutics14020447

Ceserani, V., Ferri, A., Berenzi, A., Benetti, A., Ciusani, E., Pascucci, L., et al. (2016). Angiogenic and anti-inflammatory properties of micro-fragmented fat tissue and its derived mesenchymal stromal cells. *Vasc. Cell* 8, 3. doi:10.1186/s13221-016-0037-3

Chaput, B., Bertheuil, N., Escubes, M., Grolleau, J.-L., Garrido, I., Laloze, J., et al. (2016). Mechanically isolated stromal vascular fraction provides a valid and useful collagenase-free alternative technique: A comparative study. *Plastic Reconstr. Surg.* 138, 807–819. doi:10.1097/PRS.0000000000002494

Crapo, P. M., Gilbert, T. W., and Badylak, S. F. (2011). An overview of tissue and whole organ decellularization processes. *Biomaterials* 32, 3233–3243. doi:10.1016/j.biomaterials.2011.01.057

Dominici, M., Le Blanc, K., Mueller, I., Slaper-Cortenbach, I., Marini, F., Krause, D., et al. (2006). Minimal criteria for defining multipotent mesenchymal stromal cells. The International Society for Cellular Therapy position statement. *Cytotherapy* 8, 315–317. doi:10.1080/14653240600855905

Dong, Z., Peng, Z., Chang, Q., and Lu, F. (2013). The survival condition and immunoregulatory function of adipose stromal vascular fraction (SVF) in the early stage of nonvascularized adipose transplantation. *PLoS ONE* 8, e80364. doi:10.1371/journal.pone.0080364

Duisit, J., Amiel, H., Wüthrich, T., Taddeo, A., Dedriche, A., Destoop, V., et al. (2018). Perfusion-decellularization of human ear grafts enables ECM-based scaffolds for auricular vascularized composite tissue engineering. *Acta Biomater.* 73, 339–354. doi:10.1016/j.actbio.2018.04.009

Filardo, G., Tschon, M., Perdisa, F., Brogini, S., Cavallo, C., Desando, G., et al. (2022). Micro-fragmentation is a valid alternative to cell expansion and enzymatic digestion of adipose tissue for the treatment of knee osteoarthritis: A comparative preclinical study. *Knee Surg. Sports Traumatol. Arthrosc.* 30, 773–781. doi:10.1007/s00167-020-06373-y

Gentile, P., Sterodimas, A., Pizzicannella, J., Dionisi, L., De Fazio, D., Calabrese, C., et al. (2020). Systematic review: Allogenic use of stromal vascular fraction (SVF) and decellularized extracellular matrices (ECM) as advanced therapy medicinal products (ATMP) in tissue regeneration. *Int. J. Mol. Sci.* 21, E4982. doi:10.3390/ijms21144982

Güven, S., Karagianni, M., Schwalbe, M., Schreiner, S., Farhadi, J., Bula, S., et al. (2012). Validation of an automated procedure to isolate human adipose tissue-derived cells by using the Sepax® technology. *Tissue Eng. Part C. Methods* 18, 575–582. doi:10.1089/ten.TEC.2011.0617

Kim, J., and Hematti, P. (2009). Mesenchymal stem cell-educated macrophages: A novel type of alternatively activated macrophages. *Exp. Hematol.* 37, 1445–1453. doi:10.1016/j.exphem.2009.09.004

Lo Furno, D., Tamburino, S., Mannino, G., Gili, E., Lombardo, G., Tarico, M. S., et al. (2017). Nanofat 2.0: Experimental evidence for a fat grafting rich in mesenchymal stem cells. *Physiol. Res.* 66, 663–671. doi:10.33549/physiolres.933451

Maioli, M., Rinaldi, S., Santaniello, S., Castagna, A., Pigliaru, G., Delitala, A., et al. (2014). Radioelectric asymmetric conveyed fields and human adipose-derived stem cells obtained with a nonenzymatic method and device: A novel approach to multipotency. *Cell Transpl.* 23, 1489–1500. doi:10.3727/096368913X672037

Mallis, P., Michalopoulos, E., Chatzistamatiou, T., and Giokas, C. S. (2021). Interplay between mesenchymal stromal cells and immune system: Clinical applications in immune-related diseases. *Explor. Immunol.* 1, 112–139. doi:10.37349/ei.2021.00010

Markarian, C. F., Frey, G. Z., Silveira, M. D., Chem, E. M., Milani, A. R., Ely, P. B., et al. (2014). Isolation of adipose-derived stem cells: A comparison among different methods. *Biotechnol. Lett.* 36, 693–702. doi:10.1007/s10529-013-1425-x

Mashiko, T., Wu, S.-H., Feng, J., Kanayama, K., Kinoshita, K., Sunaga, A., et al. (2017). Mechanical micronization of lipoaspirates: Squeeze and emulsification techniques. *Plastic Reconstr. Surg.* 139, 79–90. doi:10.1097/PRS.0000000000002920

Naldini, G., Sturiale, A., Fabiani, B., Giani, I., and Menconi, C. (2018). Micro-fragmented adipose tissue injection for the treatment of complex anal fistula: A pilot study accessing safety and feasibility. *Tech. Coloproctol.* 22, 107–113. doi:10.1007/s10151-018-1755-8

Ragni, E., Viganò, M., Torretta, E., Perucca Orfei, C., Colombini, A., Tremolada, C., et al. (2022). Characterization of microfragmented adipose tissue architecture, mesenchymal stromal cell content and release of paracrine mediators. *J. Clin. Med.* 11, 2231. doi:10.3390/jcm11082231

Raposio, E., Caruana, G., Bonomini, S., and Libondi, G. (2014). A novel and effective strategy for the isolation of adipose-derived stem cells: Minimally manipulated adipose-derived stem cells for more rapid and safe stem cell therapy. *Plastic Reconstr. Surg.* 133, 1406–1409. doi:10.1097/PRS.0000000000000170

Raposio, E., Caruana, G., Petrella, M., Bonomini, S., and Grieco, M. P. (2016). A standardized method of isolating adipose-derived stem cells for clinical applications. *Ann. Plast. Surg.* 76, 124–126. doi:10.1097/SAP.0000000000000609

Rybalko, V., Hsieh, P.-L., Ricles, L. M., Chung, E., Farrar, R. P., and Suggs, L. J. (2017). Therapeutic potential of adipose-derived stem cells and macrophages for ischemic skeletal muscle repair. *Regen. Med.* 12, 153–167. doi:10.2217/rme-2016-0094

Scarritt, M. E., Pashos, N. C., and Bunnell, B. A. (2015). A review of cellularization strategies for tissue engineering of whole organs. *Front. Bioeng. Biotechnol.* 3, 43. doi:10.3389/fbioe.2015.00043

Shah, F. S., Wu, X., Dietrich, M., Rood, J., and Gimble, J. M. (2013). A non-enzymatic method for isolating human adipose tissue-derived stromal stem cells. *Cytotherapy* 15, 979–985. doi:10.1016/j.jcyt.2013.04.001

SundarRaj, S., Deshmukh, A., Priya, N., Krishnan, V. S., Cherat, M., and Majumdar, A. S. (2015). Development of a system and method for automated isolation of stromal vascular fraction from adipose tissue lipoaspirate. *Stem Cells Int.* 2015, 1–11. doi:10.1155/2015/109353

Tan, Y., Landford, W. N., Garza, M., Suarez, A., Zhou, Z., and Coon, D. (2019). Complete human penile scaffold for composite tissue engineering: Organ decellularization and characterization. *Sci. Rep.* 9, 16368. doi:10.1038/s41598-019-51794-6

Tonnard, P., Verpaele, A., Peeters, G., Hamdi, M., Cornelissen, M., and Declercq, H. (2013). Nanofat grafting: Basic research and clinical applications. *Plastic Reconstr. Surg.* 132, 1017–1026. doi:10.1097/PRS.0b013e31829fe1b0

Tremolada, C., Colombo, V., and Ventura, C. (2016). Adipose tissue and mesenchymal stem cells: State of the art and Lipogems® technology development. *Curr. Stem Cell Rep.* 2, 304–312. doi:10.1007/s40778-016-0053-5

van Dongen, J. A., Stevens, H. P., Parvizi, M., van der Lei, B., and Harmsen, M. C. (2016). The fractionation of adipose tissue procedure to obtain stromal vascular fractions for regenerative purposes. *Wound Repair Regen.* 24, 994–1003. doi:10.1111/wrr.12482

Wang, L., Johnson, J. A., Zhang, Q., and Beahm, E. K. (2013). Combining decellularized human adipose tissue extracellular matrix and adipose-derived stem cells for adipose tissue engineering. *Acta Biomater.* 9, 8921–8931. doi:10.1016/j.actbio.2013.06.035

Yoshimura, K., Shigeura, T., Matsumoto, D., Sato, T., Takaki, Y., Aiba-Kojima, E., et al. (2006). Characterization of freshly isolated and cultured cells derived from the fatty and fluid portions of liposuction aspirates. *J. Cell. Physiol.* 208, 64–76. doi:10.1002/jcp.20636

Zuk, P. A., Zhu, M., Ashjian, P., De Ugarte, D. A., Huang, J. I., Mizuno, H., et al. (2002). Human adipose tissue is a source of multipotent stem cells. *Mol. Biol. Cell* 13, 4279–4295. doi:10.1091/mbc.e02-02-0105

frontiers | Frontiers in Bioengineering and Biotechnology

TYPE Original Research
PUBLISHED 23 September 2022
DOI 10.3389/fbioe.2022.896269

Check for updates

OPEN ACCESS

EDITED BY
Laura Iop,
University of Padua, Italy

REVIEWED BY
Marie-José Goumans,
Leiden University Medical Center (LUMC), Netherlands
Mohamed Fizur Nagoor Meeran,
United Arab Emirates University, United Arab Emirates

*CORRESPONDENCE
Artur Lichtenberg,
artur.lichtenberg@med.uni-duesseldorf.de

SPECIALTY SECTION
This article was submitted to Biomaterials, a section of the journal Frontiers in Bioengineering and Biotechnology

RECEIVED 14 March 2022
ACCEPTED 30 August 2022
PUBLISHED 23 September 2022

CITATION
Aubin H, Rath L, Vey A, Schmidt V, Barth M, Weber E, Lichtenberg A and Akhyari P (2022), Ventricular stabilization with a customized decellularized cardiac ECM-based scaffold after myocardial infarction alters gene expression in a rodent LAD-ligation model.
Front. Bioeng. Biotechnol. 10:896269.
doi: 10.3389/fbioe.2022.896269

COPYRIGHT
© 2022 Aubin, Rath, Vey, Schmidt, Barth, Weber, Lichtenberg and Akhyari. This is an open-access article distributed under the terms of the Creative Commons Attribution License (CC BY). The use, distribution or reproduction in other forums is permitted, provided the original author(s) and the copyright owner(s) are credited and that the original publication in this journal is cited, in accordance with accepted academic practice. No use, distribution or reproduction is permitted which does not comply with these terms.

Ventricular stabilization with a customized decellularized cardiac ECM-based scaffold after myocardial infarction alters gene expression in a rodent LAD-ligation model

Hug Aubin[1,2], Lenard Rath[2], Alexandra Vey[2], Vera Schmidt[1,2], Mareike Barth[1,2], Elvira Weber[1,2], Artur Lichtenberg[1,2]* and Payam Akhyari[1,2]

[1]Department of Cardiac Surgery, Medical Faculty and University Hospital Düsseldorf, Heinrich-Heine-University Düsseldorf, Duesseldorf, Germany, [2]Research Group 3D Cardiovascular Regenerative Medicine and Tissue Engineering (CURE 3D), Department of Cardiac Surgery, Medical Faculty and University Hospital Düsseldorf, Heinrich-Heine-University Düsseldorf, Düsseldorf, Germany

Objectives: Decellularized extracellular matrix (dECM) is increasingly used in a wide range of regenerative medicine applications and may also offer the potential to support injured myocardium. Here, we evaluated the myocardial gene expression pattern after myocardial infarction (MI) in a standardized rodent LAD-ligation model with and without ventricular stabilization with a customized, cardiac dECM-based scaffold (cdECM).

Methods: MI was induced in male Wistar rats by standard LAD-ligation and confirmed 14 days post-intervention by echocardiographic parameters (FAS<40%). Cardiac ECM from donor rats was used to generate individual cdECM-scaffolds (tissue engineered myocardial sleeve, TEMS), which were epicardially implanted after confirmed MI for ventricular stabilization. After 4 and 8 weeks heart function was assessed by echocardiography, rats were sacrificed and explanted hearts were analyzed. In addition to histological analysis, standardized anterior left ventricular wall myocardial tissue samples were assessed by quantitative real-time PCR evaluating the specific gene expression pattern for immunomodulatory (IL-10, TGFBR2, TNFα), pro-angiogenic (VEGFA, FGF2, PGF, PDGFB), pro-survival (HGF, SDF1, IGF1, AKT1), remodeling-associated (TIMP1, MMP2, MMP9) and infarction-specific (NPPA, NPPB) markers.

Results: Ventricular stabilization led to integration of the TEMS-scaffold into the myocardial scar with varying degrees of cellular infiltration, as well as significantly improved echocardiographic parameters demonstrating attenuation of maladaptive cardiac remodeling. Further, TEMS implantation after MI altered the myocardial gene expression pattern. Differences in gene expression were most striking after 4 weeks with significantly reduced expression of NPPA (0.36 ± 0.26 vs 0.75 ± 0.40; $p < 0.05$), NPPB

(0.47 ± 0.25 vs 0.91 ± 0.429; $p < 0.01$), TGFBR2 (0.68 ± 0.16 vs 0.90 ± 0.14; $p < 0.01$) and PDGFB (0.81 ± 0.13 vs 1.06 ± 0.14; $p < 0.01$) as well as increased expression of IL-10 (5.93 ± 5.67 vs 1.38 ± 0.60; $p < 0.05$), PGF (1.48 ± 0.38 vs 1.09 ± 0.25; $p < 0.05$) and IGF1 (1.67 ± 0.70 vs 1.03 ± 0.42; $p < 0.05$). However, after 8 weeks differences in the gene expression patterns of remodeling-associated, and pro-angiogenic markers could still be observed between groups.

Conclusion: Ventricular stabilization via TEMS implantation after MI did not only led to biological integration of the cdECM-scaffolds into the host tissue and improved functional cardiac parameters, but also altered 4 and 8 week gene expression of infarcted myocardium, possibly contributing to reducing chronic deteriorating effects while increasing the potential for myocardial regeneration.

KEYWORDS

myocardial infarction, decellularized extracellular matrix, gene expression, tissue engineering, cardiac regeneration

Introduction

Decellularized extracellular matrix (dECM) based scaffolds are increasingly used in a wide range of regenerative medicine applications, as they maintain the complex microarchitecture and ultracomposition of native tissues and hence provide ideal cues for tissue regeneration (Taylor et al., 2018). In the cardiovascular field, dECM based scaffolds have already been successfully employed in many pre-clinical and clinical models, with decellularized heart valves being at the verge of changing paradigms of heart valve therapy (Horke et al., 2020). Decellularized ECM scaffolds may also offer great potential for regeneration and repair of damaged myocardium, as composition and organization of cardiac ECM - critical for cell support and tissue function–can be reproduced by decellularization of cardiac ECM (Bejleri and Davis, 2019). Although whole-heart tissue engineering approaches have impressively shown the prospects of cardiac-based ECM scaffolds, the generation of a bioartificial heart replacement is still very far afield due to biological and technical complexity (Tang-Quan et al., 2018). Hence, efforts in the field should concentrate on exploring strategies to support, repair and/or regenerate the damaged myocardium instead of replacing it. Such therapies are strongly warranted, as for today, the only viable options for the treatment of end-stage heart failure (HF) consist in the implantation of a permanent mechanical assist device or heart transplantation (McDonagh et al., 2021). Other surgical and experimental approaches that have been explored in the past, such as surgical cardiomyoplasty or stem cell therapy, have been mostly abandoned due to disappointing outcomes (Hetzer et al., 2021).

Here, we introduce a new therapy concept using a customized, decellularized cardiac ECM-based scaffold (cdECM-scaffold) in form of a tissue engineered myocardial sleeve (TEMS) for ventricular stabilization after myocardial infarction, hypothesizing that this might stimulate myocardial regeneration, hinder adverse cardiac remodeling and improve cardiac hemodynamics. This proof-of-concept study focuses on the effect on myocardial gene-expression after ventricular stabilization via TEMS in a standardized rodent LAD-ligation *in vivo* model.

Materials and methods

All animal experiments and surgical procedures were performed in compliance with the Guide for the Care and Use of Laboratory Animals as published by the US National Institutes of Health (NIH Publication 85-23, revised 1996) and approved by the local animal care committees (Registration No. 84-01.04.2012. A335).

Whole-heart decellularization

Donor hearts of Wistar rats (male, 350–450 g) were explanted and perfusion based *in toto* heart decellularization was performed via standardized automated software-controlled coronary perfusion with decellularization agents as previously described (Akhyari et al., 2011). Briefly, decellularization protocol consisted of perfusion with 0.5% sodium dodecyl sulfate (SDS; CarlRoth) and 0.5% desoxycholic acid (DCA; Amresco) for 48 h with subsequent perfusion with deionized water and phosphate-buffered saline (PBS; Gibco) for 24 and 72 h, respectively. Decellularized whole-hearts were stored in PBS supplemented with penicillin/streptomycin at 4°C before further processing.

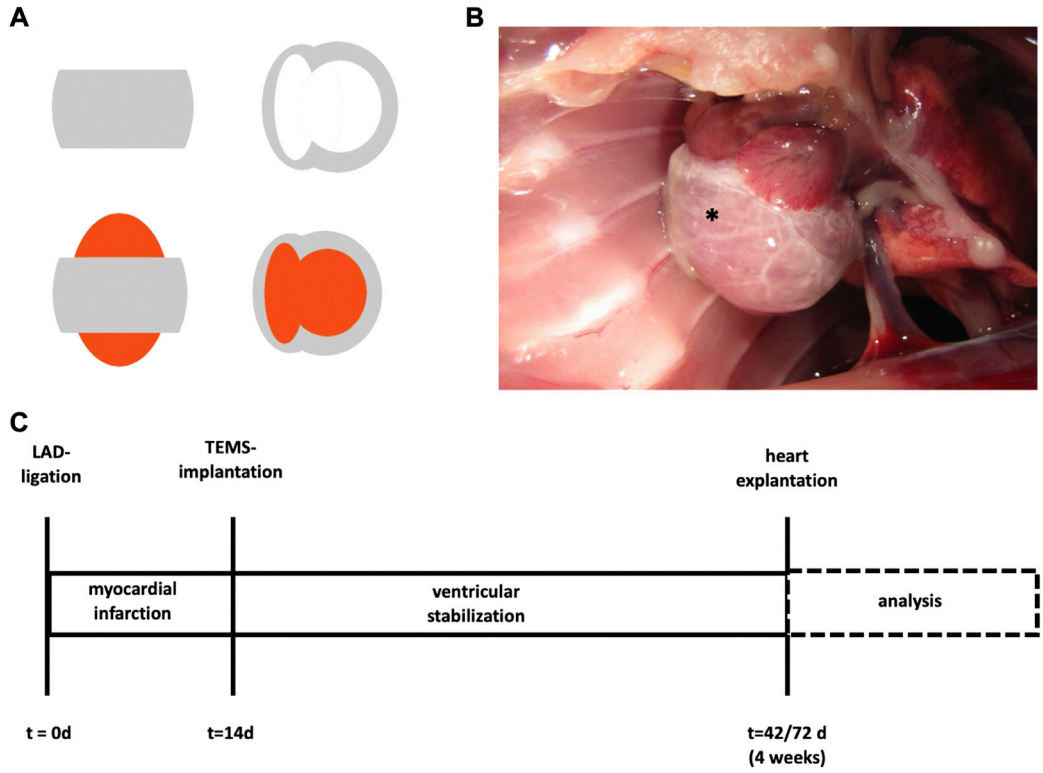

FIGURE 1
TEMS schematics and timeline surgical protocol. **(A)** Schematics of ventricular stabilization via TEMS. Grey, cdECM scaffold; red, native heart. **(B)** Macroscopic image of ventricular stabilization via TEMS in rodent model. *, TEMS. **(C)** Myocardial infarction was induced by LAD-ligation in a standard rodent model and after 14 days ventricular stabilization via TEMS implantation was performed. Hearts were explanted and analyzed after 4 or 8 weeks. LAD, left anterior descending; TEMS, tissue engineered myocardial sleeve.

Tissue engineered myocardial sleeve

Customized, decellularized cardiac ECM-based scaffolds (cdECM-scaffolds) where obtained through standardized microsurgical dissection of the decellularized whole-hearts. Therefore, the atria including the atrioventricular heart valves, the septum and the apex of the decellularized whole-heart were removed, leaving a myocardial sleeve consisting of the free walls of the right and left ventricle (TEMS; tissue engineered myocardial sleeve) (Figure 1A). Dissected tissue was analyzed for removal of cellular components and degree of ECM conservation, as already previously published (Aubin et al., 2013a). TEMS were stored in PBS supplemented with penicillin/streptomycin at 4°C before further processing.

Surgical protocol

In order to evaluate the biological effects of ventricular stabilization with a cdECM-scaffold after myocardial infarction we used a standard rodent LAD (left anterior descending coronary artery)-ligation model with Wistar rats (from an in-house breed of the local animal care facility) as animal model. Fourteen days after LAD-ligation the cdECM-scaffold in form of a TEMS was then epicardially implanted and left *in situ* for either 4 or 8°weeks, after which the experimental animal was euthanized, the heart explanted and analyzed (Figure 1C).

LAD-ligation induced myocardial infarction was confirmed by standard echocardiographic parameters (Galrinho et al., 2015).

TABLE 1 Experimental groups, timepoints and rationale.

Experimental group[a]	timepoints	rationale
-LAD/-TEMS	4/8 weeks	control (native heart)
-LAD/+TEMS	4/8 weeks	effect TEMS on healthy heart
+LAD/-TEMS	4/8 weeks	control (infarcted heart)
+LAD/+TEMS	4/8 weeks	effect TEMS on infarcted heart

[a]-LAD, respective sham operation; +LAD, myocardial infarction via LAD-ligation; -TEMS, respective sham operation; +TEMS, ventricular stabilization via TEMS, implantation.

Only animals which presented with a FAS (fractional area shortening) of the left ventricle <40% 14 days after LAD-ligation entered the LAD-ligation group. In cases where FAS remained >40% after LAD-ligation or the explantation timepoint was not reached due to mortality or morbidity experimental animals dropped out of further analysis. As control groups respective sham operations for the LAD-ligation and the TEMS implantation were performed, hence, experimental groups as shown in Table 1 were analyzed.

Rodent LAD-ligation model

For induction of myocardial infarction, a standard LAD-ligation model was used (Gao et al., 2010). Wistar rats (male, 200–250 g), fed *ad libitum* with standard rat chow, were used as a rodent animal model. For LAD-ligation, rats were anesthetized with 2.0–2.5% isoflurane, orotracheally intubated and machine ventilated with room air supplemented with oxygen using a small animal ventilator (tidal volume, 10 ml/kg). The respiratory rate was adjusted to maintain the partial pressure of CO_2 within physiological limits. Body temperature was maintained at 37°C–37.5°C with a heating pad. Baseline echocardiographic parameters were recorded, and afterwards a lateral left-sided thoracotomy was performed. After pericardiotomy, the heart was exposed, the left anterior descending coronary artery (LAD) was identified and a 10–0 monofilament non-absorbable polypropylene suture (Prolene, Ethicon, Norderstedt, Germany) was looped around the LAD and ligated. Coronary artery occlusion was immediately verified by blanching and cyanosis of the myocardial area at risk (experimental group: +LAD). After LAD-ligation the thoracotomy was closed in layers. For LAD-ligation sham operation (experimental group: LAD) the suture was only looped around a major branch of the LAD and removed, without ligation.

TEMS implantation

TEMS were implanted 14 days after LAD-ligation (or sham operation). Therefore, rats were anesthetized, orotracheally intubated and machine ventilated as described above. Echocardiographic parameters were recorded in order to evaluate efficacy of prior LAD-ligation. Afterwards thoracotomy was performed using the surgical access site from the prior operation in order to expose the heart. The TEMS was slipped over a copped 2 ml syringe (B. Braun, Melsungen, Germany), whose opening was used to apply gentle suction force on the apex, luxate the heart ventrally and pull the TEMS over the native heart. TEMS was aligned anatomically correct (left and right ventricle aligned accordingly) and fixated with four stitches using 10-0 Prolene suture (Ethicon, Raritan, NJ, US) so that it covered most of the surface of both ventricles (experimental group: +TEMS) (Figure 1B). After implantation, the thoracotomy was closed again in layers. For TEMS implantation sham operation (experimental group: TEMS) the native heart was luxated and four holding sutures were placed accordingly.

Heart explantation

Four and 8 weeks after TEMS implantation or sham operation experimental animals were narcotized and echocardiographic parameters were recorded. After euthanasia the heart was explanted via median sternotomy and processed depending on subsequent tissue analysis.

Echocardiographic assessment

Echocardiographic assessment was performed on anesthetized animals at baseline, 14, 42 and 70 days, according to the experimental protocol, using a Philips HDX11 ultrasonography system equipped with a 15- MHz probe (Philips, Hamburg, Germany). Following parameters were evaluated in a standardized analysis: left ventricular end-diastolic diameter (LVEDD), ejection fraction (EF) and fractional area shortening (FAS) of the left ventricle (Galrinho et al., 2015).

Tissue analysis

Histology

For orientating histological analysis, explanted hearts were dissected into standardized slices, fixed in a 4% buffered formaldehyde solution (Roth, Karlsruhe, Germany) and processed via cryo-sectioning (CM 1950; Leica, Wetzlar, Gemany) using standard protocols. Frozen sections of 6 mm were then stained with hematoxylin and eosin (H&E) and Movat's pentachrom staining according to standard protocols, and then visualized using a transmission light microscope (DM 2000; Leica, Wetzlar, Gemany).

Gene expression

For evaluation of gene expression, freshly explanted hearts were dissected into standardized probes separating the TEMS from the native heart (heart: anterior and posterior wall of the left ventricle; TEMS in projection to the anterior wall of the native heart). Probes were then snap-frozen in liquid nitrogen and pulverized. RNA was isolated of processed tissue samples using the RNeasy Mini Kit (Quiagen, Hilden, Germany) according to the manufacturer's protocol. RNA quality was analyzed by automated electrophoresis (Agilent 2100 Bioanalyzer (Agilent, Santa Clara, California, United States). Isolated RNA was subjected to cDNA synthesis using the QuantiTect Reverse Transcription Kit (Quiagen, Hilden, Germany) according to the manufacturer's protocol using a real time cycler (StepOne Plus, Applied Biosystems, Foster City, United States). Synthesized cDNA samples then underwent real-time-polymerase chain reaction (qRT-PCR) to assess the expression

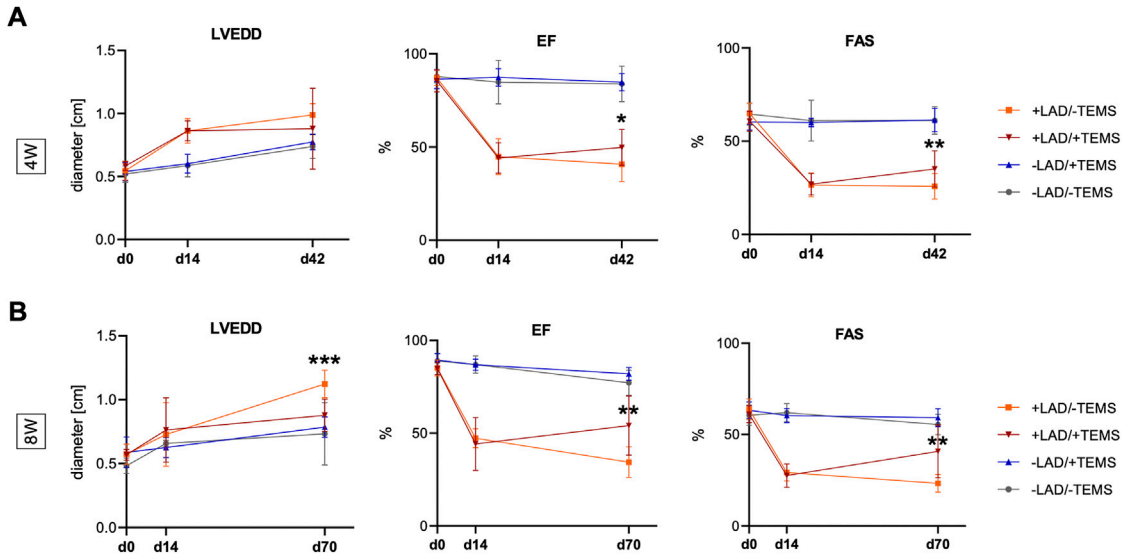

FIGURE 2
Echocardiographic parameters. Additional TEMS-implantation 14 days after LAD-ligature decreased LVEDD (left ventricular end-diastolic diameter) and improved left ventricular EF (ejection fraction) and FAS (fractional area shortening) after 4 and 8 weeks. **(A)** LVEDD, EF and FAS 14 days after LAD-ligature (+LAD) and 4 weeks after TEMS-implantation (+TEMS) or respective shame operations (-LAD; -TEMS), showing significantly improved EF and FAS in the +LAD/+TEMS as compared to the +LAD/-TEMS-group, and no significant differences between the -LAD/-TEMS and -LAD/+TEMS group. **(B)** LVEDD, EF and FAS 14 days after LAD-ligature and 8 weeks after TEMS-implantation or respective shame operations, showing significantly reduced LVEDD as well as improved EF and FAS in the +LAD/+TEMS-group as compared to the +LAD/-TEMS group, and no significant differences between the–LAD/-TEMS and–LAD/+TEMS group. Experimental groups: LAD/-TEMS, grey; -LAD/+TEMS, blue; +LAD/-TEMS, orange; +LAD/+TEMS, red. Data presented as mean ± SD; *, $p < 0.05$; **, $p < 0.01$; ***, $p < 0.001$).

levels of specific immunomodulatory (IL 10, TGFBR2, TNFα), pro-angiogenic (VEGFA, FGF2, PGF, PDGFB), pro-survival (HGF, SDF1, IGF1, AKT1), remodeling-associated (TIMP1, MMP2, MMP9) and infarction-specific (NPPA, NPPB) genes using top2b as well as beta2-microglobulin as respective housekeeping genes. Primers were selected from the National Center for Biotechnology Information (NCBI) database (Supplementary Table S1). Recorded values were processed and analyzed using the ΔΔCT method, representing relative increase or decrease of expression levels directly by evaluating the ratios between experimental samples and their corresponding controls. For the 4 weeks experimental groups at least eight biological replicates and for the 8 week experimental group at least six biological replicates were used. Data are presented for both housekeeping genes.

Statistics

All values are presented as mean −/+ standard deviation of the mean for all continuous variables. For direct group comparisons at one single time point, Student's t-tests with or without Welch's correction or Mann–Whitney U tests were performed. Statistical significance was assumed if p-values were lower than 0.05. Data analysis was conducted with GraphPad Prism v5.04 (GraphPad Software, San Diego, CA).

Results

Surgical outcome

Ventricular stabilization with a cdECM-based scaffold via TEMS-implantation either with or without LAD-ligature was performed in 56 animals. Peri- and postoperative mortality was 35.7% and mostly due to perioperative complications either related to the anaesthesia or the surgical procedure. Mortality after successful TEMS implantation was neglectable, with 36 animals (64.3%) reaching the end of the experiment after 4 or 8 weeks. Together with the respective sham control groups 86 animals reached the endpoint and were analysed.

Echocardiographic parameters

As expected LAD-ligature led to a significant decrease in EF (84.8 ± 3.3% vs. 44.9 ± 9.2%, $p < 0.0001$) and a significant increase in LVEDD (0.59 ± 0.09 cm vs 0.86 ± 0.09 cm, $p < 0.0001$) after 14 days, as compared to the sham control group (Figure 2). Mean FAS in LAD-ligature animals entering the experimental groups was 26.5 ± 6.1%. Animals subsequently receiving an additional TEMS-implantation 14 days after LAD-ligature had by trend smaller LV diameters (0.88 ± 0.04 cm vs 0.99 ± 0.08 mm, $p = 0.13$)

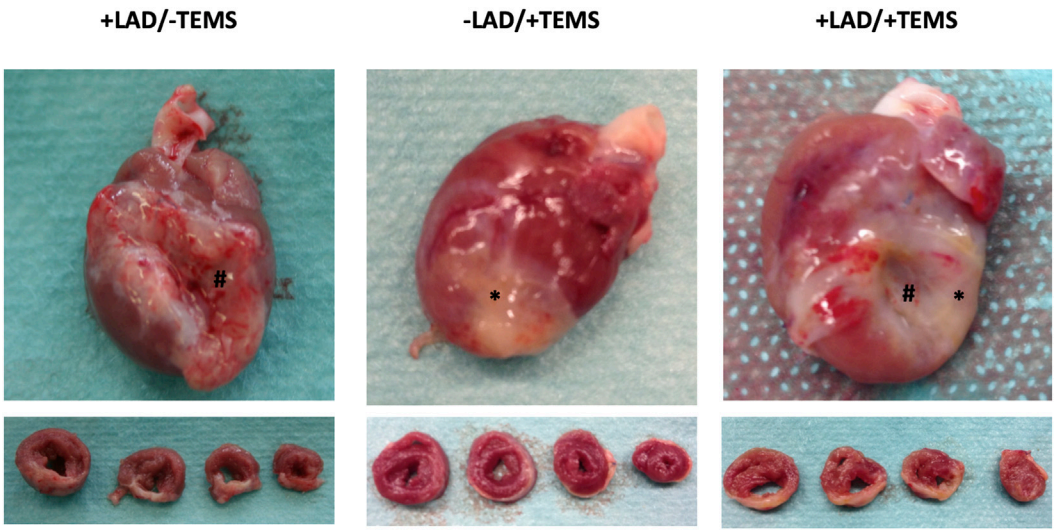

FIGURE 3
Macroscopic appearance of explanted heart specimens after LAD-ligation and TEMS implantation. Representative images of explanted whole heart and sliced specimens 4 weeks after either LAD-ligation, TEMS implantation and LAD-ligation plus TEMS-implantation. Region of myocardial infarction as wells TEMS scaffold was clearly distinguishable in all specimens. #, region of myocardial infarction; *, TEMS scaffold.

with however significant improved EF (49.8 ± 9.2% vs. 40.8 ± 9.0%, $p < 0.05$) as well as FAS (35.1 ± 9.1% vs. 25.8 ± 6.5%, $p < 0.01$), as compared to the respective shame control group (+LAD/-TEMS) after 4 weeks (Figure 2A). Eight weeks after TEMS-implantation LV diameters were significantly smaller (0.88 ± 0.12 cm vs 1.12 ± 0.10 mm, $p < 0.0001$) with further increase in EF (54.1 ± 14.7% vs. 34.4 ± 7.8%, $p < 0.01$) as well as LV-FAS (40.8 ± 13.3% vs. 23.3 ± 4.5%, $p < 0.01$), as compared to the respective shame control group (+LAD/-TEMS) (Figure 2B). TEMS-implantation in animals without myocardial infarction did not have any significant impact on LVEDD, EF nor FAS after 4 or 8 weeks, as compared to their respective sham control group (-LAD/-TEMS) (Figures 2A,B).

Macroscopic appearance

Representative images of explanted heart specimens 4 weeks after TEMS-implantation are shown in Figure 3. The area of myocardial infarction was clearly distinguishable in animals with LAD-ligature with aneurysm and scar tissue formation. In the explanted hearts the cdECM-based scaffold of the TEMS was still largely intact and could be identified around the whole circumference of the heart. After 4 and 8 weeks *in vivo* the TEMS scaffold had adhered to the epicardium and seemed to be especially integrated to the native tissue in the infarct area. TEMS scaffolds could however be mechanically removed from the heart for further analysis.

Orientating histological analysis

LAD-ligature led to classical histological findings after myocardial infarction with formation of granulation tissue, neovascularization and decreased cellularity (data not show). Ventricular stabilization via TEMS implantation led to biological integration of the TEMS scaffold to the native myocardium with native cells infiltrating the TEMS scaffold (Figure 4). As opposed to the non-infarcted hearts where the TEMS scaffold could still be clearly differentiated from the native myocardium on the left anterior wall, in hearts with prior LAD-ligature TEMS scaffolds highly integrated into the infarcted region without distinguishable boundaries between native myocardium and implanted tissue. Cellular infiltration into the TEMS scaffold was highly increased at the interface between native tissue and the cdECM, with areas of very high degree of cellular infiltration especially within the infarcted myocardial area. There were no gross differences in the histological analysis of hearts explanted either 4 or 8 weeks after TEMS implantation (data not shown).

RNA concentration

Evaluation of TEMS tissue prior to implantation revealed no detectable RNA in the cdECM scaffolds. However, due to the *in vivo* cellular infiltration, the explanted TEMS tissue contained high degrees of RNA, ranging between 40% and 70% of the RNA concentration in the adjacent native myocardial tissue. In the

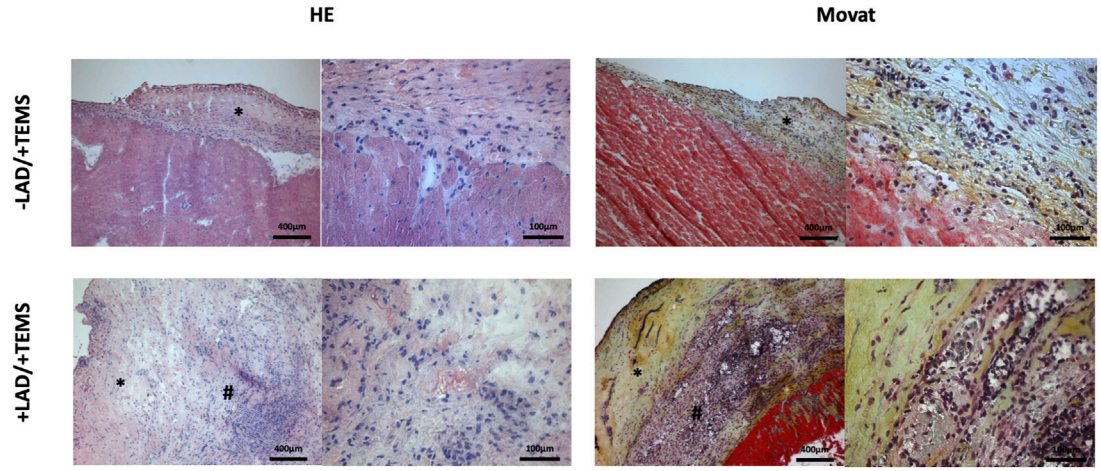

FIGURE 4
Orientating histological analysis. Representative images of HE and MOVAT staining of explanted hearts 4 weeks after ventricular stabilization via TEMS implantation with and without prior myocardial infarction via LAD-ligature, showing high degree of cellular infiltration of the TEMS scaffold (*) as well as integration of the TEMS scaffold into the infarcted zone (#) of the heart.

TABLE 2 Relative changes in gene expression of the anterior left ventricular myocardial wall after ventricular stabilization via TEMS-implantation following myocardial infarction.

Gene group		relative changes in gene expression*			
		4 weeks		8 weeks	
housekeeping		TOP2B	β2M	TOP2B	β2M
immunomodulatory	IL 10	↑*	↑*	↑	↑
	TNF α	↑	↓	↑	↑
	TGFBR2	↓	↓**	↓	↑
pro-angiogenic	VEGFA	↓	↓	↑	↑
	FGF2	↑	↓	↓**	↓*
	PGF	↑	↑*	↑	↑
	PDGFB	↓**	↓	↑*	↑
pro-survival	HGF	↑	↑	↓	↑
	SDF1	↑	↓	↓	↓
	IGF1	↑*	↑*	↓	↓
	AKT1	↓	↓	↑	↑
remodeling-associated	MMP2	↑	↓	↓	↑
	MMP9	↑	↓	↑	↑*
	TIMP1	↑	↓	↓	↓
infarction-specific	NPPA	↓	↓*	↓	↑
	NPPB	↓*	↓*	↑	↑

Relative changes to anterior left ventricular myocardial wall of respective sham control group. *, $p < 0.05$; **, $p < 0.01$; ***, $p < 0.001$.

TEMS tissue adjacent to the infarcted region of the heart, RNA concentration was 238.5 ± 102.8 ng/µl after 4 weeks and 161.04 ± 92.65 ng/µl after 8 weeks *in vivo*, as compared to 354.2 ± 92.0 ng/µl and 331.8 ± 128.5 ng/µl in the respective adjacent anterior wall of the LV.

Gene expression

Myocardial tissue

As expected, myocardial infarction via LAD-ligation did significantly changed the expression pattern of the analyzed

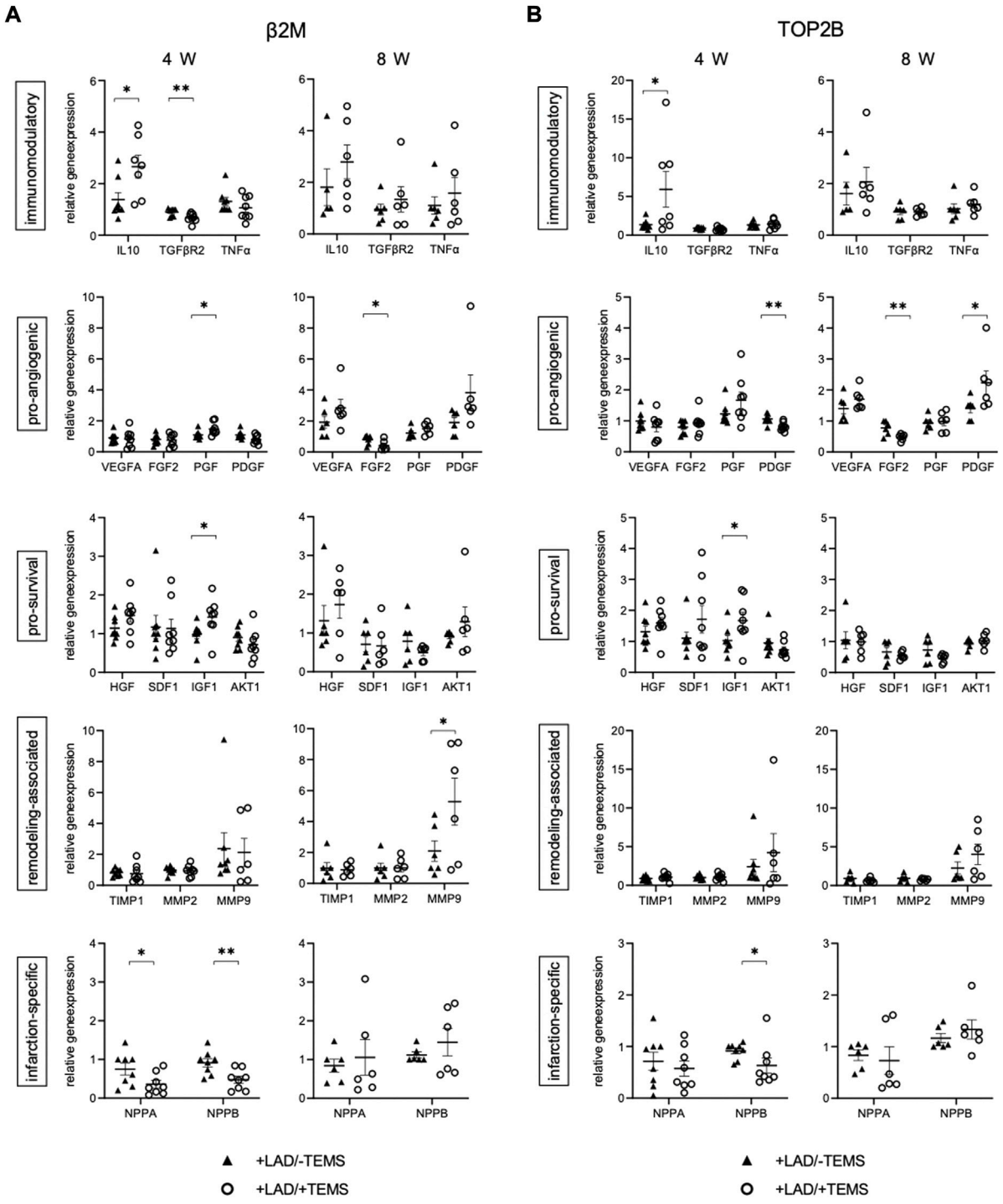

FIGURE 5
Gene expression after myocardial infarction with and without ventricular stabilization via TEMS implantation. Relative gene expression patterns of left anterior wall myocardial tissue samples after myocardial infarction via LAD-ligation (+LAD) and either 4 or 8 weeks of ventricular stabilization via TEMS implantation (+TEMS) or respective sham control (-TEMS). **(A)** Gene expression relative to β2M housekeeping gene. **(B)** Gene expression relative to TOP2B housekeeping gene. Data presented as mean ± SD; *, $p < 0.05$; **, $p < 0.01$; ***, $p < 0.001$.

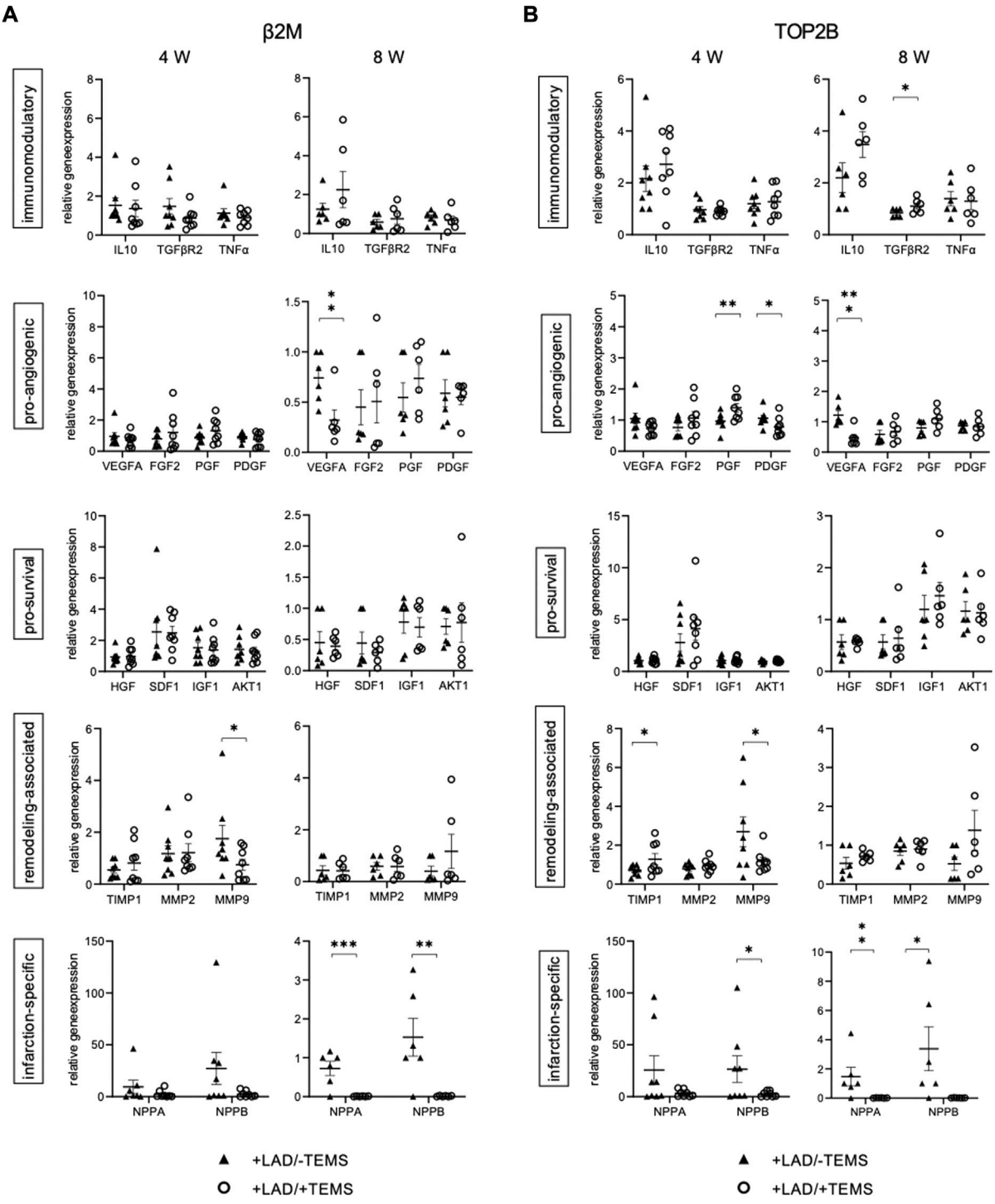

FIGURE 6
Gene expression of cells infiltrating the TEMS scaffold. Relative gene expression patterns of TEMS samples removed from the native myocardium after either 4 or 8 weeks *in vivo* after myocardial infarction via LAD-ligation (+LAD) or respective sham control (-TEMS). **(A)** Gene expression relative to β2M housekeeping gene. **(B)** Gene expression relative to TOP2B housekeeping gene. Data presented as mean ± SD; *, $p < 0.05$; **, $p < 0.01$; ***, $p < 0.001$.

genes in the infarcted myocardial area of the left anterior ventricular wall after 4 as well as 8 weeks, as compared to the respective sham control group (-LAD) (Supplementary Table S2). In the adjacent, non-infarcted myocardial regions, LAD-ligation had no influence in the gene expression patterns (data not shown).

Gene expression of the myocardial tissue within the infarcted region was further altered after ventricular stabilization via TEMS-implantation, as compared to the respective sham control group (+LAD/-TEMS) (Table 2, Figure 5). Differences in gene expression were most striking after 4 weeks with significantly reduced infarction-related expression of NPPA (0.36 ± 0.26 vs 0.75 ± 0.40; β2m; $p < 0.05$) and NPPB (0.47 ± 0.25 vs 0.91 ± 0.429; β2m; $p < 0.01$), increased expression of immunomodulatory IL-10 (5.93 ± 5.67 vs 1.38 ± 0.60; top2b; $p < 0.05$) and reduced TGFBR2 (0.68 ± 0.16 vs 0.90 ± 0.14; β2m; $p < 0.01$), increased expression of pro-angiogenic PGF (1.48 ± 0.38 vs 1.09 ± 0.25; β2m; $p < 0.05$) and reduced PDGFB (0.81 ± 0.13 vs 1.06 ± 0.14; top2b; $p < 0.01$) as well as increased expression of pro-survival IGF1 (1.67 ± 0.70 vs 1.03 ± 0.42; top2b; $p < 0.05$) after LAD-ligation and TEMS implantation as compared to LAD-ligation alone (Figures 5A,B). However, significant changes in the gene expression pattern could still be seen 8 weeks after TEMS implantation following LAD-ligature with reduced expression of pro-angiogenic FGF2 (0.48 ± 0.10 vs. 0.78 ± 0.21; top2b; $p < 0.01$) and increased PDGFB (2.24 ± 0.86 vs 1.41 ± 0.32; top2b; $p < 0.05$) as well as increased expression of remodeling-associated MMP9 (5.29 ± 3.41 vs 2.10 ± 1.47; β2m; $p < 0.05$) as compared to the respective control (Figures 5A,B).

TEMS scaffold

Interestingly, cells in the TEMS scaffold had a different gene expression pattern depending on whether the cdECM scaffold was placed on healthy or infarcted myocardium (Supplementary Table S3, Figure 6). After 4 weeks *in situ* the TEMS scaffold on infarcted myocardium showed significantly increased expression of pro-angiogenic PGF (1.40 ± 0.36 vs 0.97 ± 0.25; top2b; $p < 0.05$) and reduced PDGFB (0.78 ± 0.29 vs 1.06 ± 0.24; top2b; $p < 0.04$), increased expression of remodeling-associated TIMP1 (1.28 ± 0.78 vs 0.71 ± 0.24; top2b; $p < 0.05$) and reduced expression of MMP9 (1.18 ± 0.54 vs 2.70 ± 2.04; top2b; $p < 0.05$) as well as reduced infarction-related expression of NPPB (2.41 ± 2.44 vs 26.42 ± 34.14; top2b; $p < 0.05$), as compared to the TEMS scaffold placed on non-infarcted myocardium (Figures 6A,B). After 8 weeks *in situ* the TEMS scaffold on infarcted myocardium showed significantly increased expression of immunomodulatory TGFBR2 (0.68 ± 0.16 vs 0.84 ± 0.15; top2b; $p < 0.05$), decreased expression of pro-angiogenic VEGFA (0.02 ± 0.01 vs 1.22 ± 0.33; top2b; $p < 0.001$), as well as reduced infarction-related expression of NPPA (2.41 ± 2.44 vs 1.47 ± 1.41; top2b; $p < 0.05$) and NPPB (0.02 ± 0.01 vs 3.38 ± 3.39; top2b; $p < 0.05$), as compared to the TEMS scaffold placed on non-infarcted myocardium (Figures 6A,B).

Discussion

This proof-of concept study demonstrates that ventricular stabilization after myocardial infarction with a customized, decellularized cardiac ECM-based scaffold (TEMS) significantly alters myocardial gene expression in a rodent LAD-ligation model. Further, orientating analysis shows improved functional echocardiographic parameters as well as biological integration of the TEMS scaffold after 4 and 8 weeks of ventricular stabilization *in vivo*.

In the past, different surgical and experimental approaches have used the concept of cardiomyoplasty in terms of functional left ventricular restoration in order to treat end-stage heart failure. This concept was first introduced in 1985 by Carpentier and Chaques as dynamic cardiomyoplasty, by wrapping the M. latissimus dorsi circumferentially around the heart in order to support systolic contraction (Carpentier and Chachques, 1985). Another surgical approach was the implantation of a mesh-like woven polyester jacket circumferentially around the heart (Acorn CorCap cardiac support device, Acorn Cardiovascular, Inc., St Paul, Minn.) to provide support during diastole (Starling and Jessup, 2004). Although those surgical cardiomyoplasty approaches were used in thousands of patients, they were ultimately abandoned, as outcomes were disappointing with questionable improvement of cardiac hemodynamics and concerns regarding adverse effects such as pericardial constrictions (Acker, 1999; Power et al., 2001). However, one of the main effects of surgical cardiomyoplasty was its ability to prevent adverse left ventricular remodeling, such as attenuation of cardiac enlargement and specific reduction of left ventricular end-diastolic dimensions.

As shown in this study ventricular stabilization via TEMS implantation prevents progressive left ventricular dilatation after myocardial infarction. Rats with supported ventricles via TEMS implantation after LAD-ligation did not only present with significantly smaller LVEDDs after 8 weeks as compared to their controls, but also showed LVEDDs comparable to the values at the time-point of TEMS implantation 14 days after myocardial infarction. Together with the other functional echocardiographic parameters, this demonstrates the potential of the TEMS concept to prevent adverse cardiac remodeling. It is still unclear what triggers this effect. Decellularized cardiac ECM still has a certain stiffness which might offer passive mechanical support during diastole (Brazile et al., 2021), leading to similar effects as with above-mentioned Acorn CorCap device. However, as demonstrated by the orientating histological analysis the TEMS scaffold is not only largely infiltrated by host cells, but also seems to integrate into the scar zone after myocardial infarction. Hence, a biological interaction with the host tissue is likely to play a mechanistic role.

The alteration of the gene expression pattern of the infarcted myocardium depending on whether the LV was supported by

TEMS implantation or not, as well as the different gene expression pattern of the cells infiltrating the TEMS scaffold depending on whether it was placed on healthy or infarcted myocardium, seem to demonstrate a high degree of biological interdependency. TEMS implantation seemingly inhibited an up-regulation of infarction-related NPPA and NPPB, while promoting a down-regulation of pro-angiogenic PDGFB and immunomodulatory TGFBR2 and an up-regulation of pro-survival IGF1 and immunomodulatory IL-10 after 4 weeks of ventricular stabilization. Multiple pathophysiological factors converge after myocardial infarction leading to adverse remodeling and ischemic cardiomyopathy (Prabhu and Frangogiannis, 2016). Alteration of gene expression, as shown in this study, might enhance the post myocardial infarction regenerative process attenuating deteriorative effects of cardiac remodeling. For instance, platelet-derived growth factors as well as transforming growth factor-beta are involved in the negative inflammatory and fibrogenic response in the infarcted myocardium (Myocardial Remodeling, 2011; Dobaczewski et al., 2011) while IL-10 is a potent anti-inflammatory agent suppressing the synthesis of proinflammatory cytokines (Fiorentino et al., 1991), and activation of IGF-1 protects from the detrimental effects of myocardial infarction (Troncoso et al., 2014). On the other hand, down-regulation of NPPB, which is mainly secreted by the myocardium due to increased transmural pressure or volume overload and is considered a hallmark for maladaptive LV remodeling, could be a consequence of the TEMS capacity to prevent LV dilatation 4 weeks after myocardial infarction (Fu et al., 2018). Further, significant differences in gene expression could still be demonstrated 8 weeks after TEMS implantation with an up-regulation of remodeling-associated MMP9 and pro-angiogenic PDGFB and down-regulation of FGF2. Together with the echocardiographic findings demonstrating improved functional parameters and a further decrease in LV dimensions, our results advocate for beneficial long-term effects of ventricular stabilization via a cdECM scaffold.

Since in this proof-of-concept study only an orientating histological analysis of the explanted TEMS specimens was conducted, it remains unclear which cells infiltrate the TEMS scaffold and what role they play in the observed effects with regards to cardiac remodeling and improved cardiac function. Interestingly though, gene expression patterns of those cells significantly varied depending on whether the TEMS was placed on infarcted or healthy myocardium. During implantation the TEMS scaffold is only loosely placed on the epicardium, therefore the cdECM-scaffold seems to inherently attract resident cells, which possess the ability to integrate the scaffold into the myocardial tissue especially in the region of infarcted myocardium. Recent research efforts are increasingly demonstrating the importance of epicardial-myocardial signaling and epicardial stem cells in cardiac repair (Pellegrini et al., 2020). Therefore, a cdECM scaffold such as the TEMS might provide an ideal environment for recruitment, activation and differentiation of epicardial cells, which might enhance the regenerative capacity of the heart (Moroni and Mirabella, 2014). Targeted biofunctionalization of cdECM with specific biological cues, could further modulate TEMS-cell interaction by specific cell recruitment and activation enhancing the TEMS effects (Aubin et al., 2016).

Further, cardiac-derived decellularized ECM scaffolds can be repopulated *ex vivo* offering the possibility to enhance the TEMS concept with appropriate pro-regenerative cell populations potentially further increasing cardiac repair (Aubin et al., 2013b; Hülsmann et al., 2013). This would follow the cellular cardiomyoplasty approach, which aims at employing stem cell technologies in order to induce cardiac repair (Lamb et al., 2013). Although in the past cellular cardiomyplasty has shown the potential to decrease fibrosis of infarcted myocardium, to prevent adverse post-ischemic remodeling and to some extent improve systolic cardiac function, clinical outcomes have been disappointing so far, with low rates of cell survival and shortage of donor cells limiting further translation into the routine clinical practice (Broughton et al., 2018). Here, the TEMS platform could offer a promising delivery strategy that could be combined with induced pluripotent stem cell (iPSC) technology, which now allows for the derivation of large numbers of autologous cardiomyocytes from patient-specific iPSCs (Duran et al., 2018). In fact, engineered heart tissue patches generated from fibrinogen-thrombin and human iPSCs have already shown potential for remuscularization and improvement of cardiac function in a pre-clinical large animal model (Querdel et al., 2021).

In conclusion, ventricular stabilization of the heart via a cdECM-scaffold in form of a TEMS stimulates myocardial regeneration, attenuates cardiac remodeling and improves cardiac hemodynamics in a rodent model. Hence, the TEMS approach might be a promising therapy strategy for inducing cardiac regeneration in diseased hearts following a novel bioactive cardiomyoplasty concept. However, further studies are warranted in order to confirm those findings and translate the concept into a clinical setting.

Limitations

As this is a first proof-of-concept study several limitations remain. Cardiac functional parameters are based solely on echocardiographic parameters and need to be validated with more sensitive analysis such as MRI or invasive catherization. Although gene expression analysis was mostly consistent between both housekeeping genes, there is still a large biological variability within the reduced sample size. Further analysis in order to elucidate on the mechanism behind the observed biological effects and to characterize infiltrating cells are warranted. As this study was conducted in a rodent animal

model, results should be considered with caution when applied to humans.

Data availability statement

The original contributions presented in the study are included in the article/supplementary material, further inquiries can be directed to the corresponding author.

Ethics statement

The animal study was reviewed and approved by Landesamt für Natur, Umwelt und Verbraucherschutz Nordrhein-Westfalen.

Author contributions

HA, AL and PA contributed to conception and design of the study. HA, LR, AV and MB conducted the experiments. HA, MB and VS. analysed the data and performed the statistical analysis. HA wrote the first draft of the manuscript. EW and VS. wrote sections of the manuscript. All authors contributed to manuscript revision, read, and approved the submitted version.

Funding

This study was funded by the Research Committee (ReCo) of the medical faculty of the Heinrich-Heine-University Düsseldorf.

Acknowledgments

The authors thank Gisela Müller (Department of Cardiac Surgery, University Hospital Düsseldorf, Heinrich-Heine-University Düsseldorf) as well as Jörn Hülsmann for technical support. The generous support of the S. Bunnenberg Foundation to the Cardiovascular Research Facilities at the Heinrich Heine University Düsseldorf is greatly appreciated.

Conflict of interest

The authors declare that the research was conducted in the absence of any commercial or financial relationships that could be construed as a potential conflict of interest.

Publisher's note

All claims expressed in this article are solely those of the authors and do not necessarily represent those of their affiliated organizations, or those of the publisher, the editors and the reviewers. Any product that may be evaluated in this article, or claim that may be made by its manufacturer, is not guaranteed or endorsed by the publisher.

Supplementary material

The Supplementary Material for this article can be found online at: https://www.frontiersin.org/articles/10.3389/fbioe.2022.896269/full#supplementary-material

References

Acker, M. A. (1999). Dynamic cardiomyoplasty: At the crossroads. *Ann. Thorac. Surg.* 68 (2), 750–755.

Akhyari, P., Aubin, H., Gwanmesia, P., Barth, M., Hoffmann, S., Huelsmann, J., et al. (2011). The quest for an optimized protocol for whole-heart decellularization: A comparison of three popular and a novel decellularization technique and their diverse effects on crucial extracellular matrix qualities. *Tissue Eng. Part C. Methods* 17 (9), 915–926.

Aubin, H., Kranz, A., Hülsmann, J., Lichtenberg, A., and Akhyari, P. (2013). Decellularized whole heart for bioartificial heart. *InCellular Cardiomyoplasty* 1036, 163–178. doi:10.1007/978-1-62703-511-8_14

Aubin, H., Kranz, A., Hülsmann, J., Pinto, A., Barth, M., Fomin, A., et al. (2013). A novel native derived coronary artery tissue-flap model. *Tissue Eng. Part C. Methods* 19 (12), 970–980.

Aubin, H., Mas-Moruno, C., Iijima, M., Schütterle, N., Steinbrink, M., Assmann, A., et al. (2016). Customized interface biofunctionalization of decellularized extracellular matrix: Toward enhanced endothelialization. *Tissue Eng. Part C. Methods* 22 (5), 496–508.

Bejleri, D., and Davis, M. E. (2019). Decellularized extracellular matrix materials for cardiac repair and regeneration. *Adv. Healthc. Mater.* 8 (5).1801217

Brazile, B. L., Butler, J. R., Patnaik, S. S., Claude, A., Prabhu, R., Williams, L. N., et al. (2021). Biomechanical properties of acellular scar ECM during the acute to chronic stages of myocardial infarction. *J. Mech. Behav. Biomed. Mater.* 116. 104342.

Broughton, K. M., Wang, B. J., Firouzi, F., et al. (2018). Mechanisms of cardiac repair and regeneration. *Circ. Res.* 122, 1151–1163.

Carpentier, A., and Chachques, J. C. (1985). Myocardial substitution with a stimulated skeletal muscle: First successful clinical case [letter]. *Lancet* 1, 1267.

Dobaczewski, M., Chen, W., and Frangogiannis, N. G. (2011). Transforming growth factor (TGF)-β signaling in cardiac remodeling. *J. Mol. Cell. Cardiol.* 51 (4), 600–606.

Duran, A. G., Reidell, O., Stachelscheid, H., Klose, K., Gossen, M., Falk, V., et al. (2018). Regenerative medicine/cardiac cell therapy: Pluripotent stem cells. *Thorac. Cardiovasc. Surg.* 7 (01), 053–062.

Fiorentino, D. F., Zlotnik, A., Mosmann, T. R., Howard, M., and O'Garra, A. (1991). IL-10 inhibits cytokine production by activated macrophages. *J. Immunol.* 147 (11), 3815–3822.

Fu, S., Ping, P., Wang, F., Luo, L., Zhao, W., Zhao, T., et al. (2018). Synthesis, secretion, function, metabolism and application of natriuretic peptides in heart failure. *J. Biol. Eng.* 12 (1), 1–21. Platelet-derived growth factor.

Galrinho, R. D., Ciobanu, A. O., Rimbas, R. C., Manole, C. G., Leena, B. M., and Vinereanu, D. (2015). New echocardiographic protocol for the assessment of experimental myocardial infarction in rats. *Maedica* 10 (2), 85.

Gao, E., Lei, Y. H., Shang, X., Huang, Z. M., Zuo, L., Boucher, M., et al. (2010). A novel and efficient model of coronary artery ligation and myocardial infarction in the mouse. *Circulation Res.* 107 (12), 1445–1453.

Hülsmann, J., Aubin, H., Kranz, A., Godehardt, E., Munakata, H., Kamiya, H., et al. (2013). A novel customizable modular bioreactor system for whole-heart cultivation under controlled 3D biomechanical stimulation. *J. Artif. Organs* 16 (3), 294–304.

Hetzer, R., del Maria Javier, M. F., Wagner, F., Loebe, M., and Delmo, E. M. (2021). Organ-saving surgical alternatives to treatment of heart failure. *Cardiovasc. diagnosis Ther.* 11 (1), 213.

Horke, A., Tudorache, I., Laufer, G., Andreas, M., Pomar, J. L., Pereda, D., et al. (2020). Early results from a prospective, single-arm European trial on decellularized allografts for aortic valve replacement: The ARISE study and ARISE registry data. *Eur. J. Cardio-Thoracic Surg.* 58 (5), 1045–1053.

Lamb, E. K., Kao, G. W., and Kao, R. L. (2013). Cellular cardiomyoplasty: Its past, present, and future. *Cell. Cardiomyoplasty* 1036, 1–7. doi:10.1007/978-1-62703-511-8_1

McDonagh, T. A., Metra, M., Adamo, M., Gardner, R. S., Baumbach, A., Böhm, M., et al. (2021). ESC Guidelines for the diagnosis and treatment of acute and chronic heart failure: Developed by the Task Force for the diagnosis and treatment of acute and chronic heart failure of the European Society of Cardiology (ESC) with the special contribution of the Heart Failure Association (HFA) of the ESC. *Eur. heart J.* 42 (36), 3599–3726.

Moroni, F., and Mirabella, T. (2014). Decellularized matrices for cardiovascular tissue engineering. *Am. J. stem cells* 3 (1), 1.

Myocardial Remodeling (2011). Involvement in myocardial remodeling following infarction. *J. Mol. Cell. Cardiol.* 51 (5), 830–838.

Pellegrini, L., Foglio, E., Pontemezzo, E., Germani, A., Russo, M. A., and Limana, F. (2020). Cardiac repair: The intricate crosstalk between the epicardium and the myocardium. *Curr. Stem Cell Res. Ther.* 15 (8), 661–673.

Power, J. M., Buxton, B. F., Clif Alferness, B. S., and Hare, D. (2001). The mid-term results of ventricular containment (ACORN WRAP) for end-stage ischemic cardiomyopathy. *Ann. Thorac. Cardiovasc Surg.* 7 (5).

Prabhu, S. D., and Frangogiannis, N. G. (2016). The biological basis for cardiac repair after myocardial infarction: From inflammation to fibrosis. *Circulation Res.* 119 (1), 91–112.

Querdel, E., Reinsch, M., Castro, L., Köse, D., Bähr, A., Reich, S., et al. (2021). Human engineered heart tissue patches remuscularize the injured heart in a dose-dependent manner. *Circulation* 143 (20), 1991–2006.

Starling, R. C., and Jessup, M. (2004). Worldwide clinical experience with the CorCap™ cardiac support device. *J. cardiac Fail.* 10 (6), S225–S233.

Tang-Quan, K. R., Mehta, N. A., Sampaio, L. C., and Taylor, D. A. (2018). Whole cardiac tissue bioscaffolds. *Card. Extracell. Matrix* 1098, 85–114. doi:10.1007/978-3-319-97421-7_5

Taylor, D. A., Sampaio, L. C., Ferdous, Z., Gobin, A. S., and Taite, L. J. (2018). Decellularized matrices in regenerative medicine. *Acta biomater.* 74, 74–89.

Troncoso, R., Ibarra, C., Vicencio, J. M., Jaimovich, E., and Lavandero, S. (2014). New insights into IGF-1 signaling in the heart. *Trends Endocrinol. Metabolism* 25 (3), 128–137.

frontiers | Frontiers in Bioengineering and Biotechnology

TYPE Original Research
PUBLISHED 18 January 2023
DOI 10.3389/fbioe.2023.957458

Check for updates

OPEN ACCESS

EDITED BY
Hasan Uludag,
University of Alberta, Canada

REVIEWED BY
Chih Hsun Lin,
Taipei Veterans General Hospital, Taiwan
Peter Crapo,
Becton Dickinson, United States

*CORRESPONDENCE
Sotirios Korossis,
s.korossis@lboro.ac.uk

†These authors share senior authorship

SPECIALTY SECTION
This article was submitted to Biomaterials, a section of the journal Frontiers in Bioengineering and Biotechnology

RECEIVED 31 May 2022
ACCEPTED 02 January 2023
PUBLISHED 18 January 2023

CITATION
Zia S, Djalali-Cuevas A, Pflaum M, Hegermann J, Dipresa D, Kalozoumis P, Kouvaka A, Burgwitz K, Andriopoulou S, Repanas A, Will F, Grote K, Schrimpf C, Toumpaniari S, Mueller M, Glasmacher B, Haverich A, Morticelli L and Korossis S (2023), Development of a dual-component infection-resistant arterial replacement for small-caliber reconstructions: A proof-of-concept study.
Front. Bioeng. Biotechnol. 11:957458.
doi: 10.3389/fbioe.2023.957458

COPYRIGHT
© 2023 Zia, Djalali-Cuevas, Pflaum, Hegermann, Dipresa, Kalozoumis, Kouvaka, Burgwitz, Andriopoulou, Repanas, Will, Grote, Schrimpf, Toumpaniari, Mueller, Glasmacher, Haverich, Morticelli and Korossis. This is an open-access article distributed under the terms of the Creative Commons Attribution License (CC BY). The use, distribution or reproduction in other forums is permitted, provided the original author(s) and the copyright owner(s) are credited and that the original publication in this journal is cited, in accordance with accepted academic practice. No use, distribution or reproduction is permitted which does not comply with these terms.

Development of a dual-component infection-resistant arterial replacement for small-caliber reconstructions: A proof-of-concept study

Sonia Zia[1], Adrian Djalali-Cuevas[1], Michael Pflaum[1], Jan Hegermann[2], Daniele Dipresa[1], Panagiotis Kalozoumis[1], Artemis Kouvaka[1], Karin Burgwitz[1], Sofia Andriopoulou[1], Alexandros Repanas[3], Fabian Will[4], Karsten Grote[5], Claudia Schrimpf[6], Sotiria Toumpaniari[7,8], Marc Mueller[3], Birgit Glasmacher[1,3], Axel Haverich[1,6], Lucrezia Morticelli[1†] and Sotirios Korossis[1,6,7,8*†]

[1]Lower Saxony Centre for Biomedical Engineering Implant Research and Development, Hannover Medical School, Hannover, Germany, [2]Institute of Functional and Applied Anatomy, Research Core Unit Electron Microscopy, Hannover Medical School, Hannover, Germany, [3]Institute for Multiphase Processes, Leibniz University Hannover, Hannover, Germany, [4]LLS ROWIAK LaserLabSolutions GmbH, Hannover, Germany, [5]Cardiology and Angiology, Philipps-University Marburg, Marburg, Germany, [6]Department of Cardiothoracic, Transplantation and Vascular Surgery, Hannover Medical School, Hannover, Germany, [7]Cardiopulmonary Regenerative Engineering Group (CARE), Centre for Biological Engineering, Loughborough University, Loughborough, United Kingdom, [8]Wolfson School of Mechanical, Electrical and Manufacturing Engineering, Loughborough University, Loughborough, United Kingdom

Introduction: Synthetic vascular grafts perform poorly in small-caliber (<6mm) anastomoses, due to intimal hyperplasia and thrombosis, whereas homografts are associated with limited availability and immunogenicity, and bioprostheses are prone to aneurysmal degeneration and calcification. Infection is another important limitation with vascular grafting. This study developed a dual-component graft for small-caliber reconstructions, comprising a decellularized tibial artery scaffold and an antibiotic-releasing, electrospun polycaprolactone (PCL)/polyethylene glycol (PEG) blend sleeve.

Methods: The study investigated the effect of nucleases, as part of the decellularization technique, and two sterilization methods (peracetic acid and γ-irradiation), on the scaffold's biological and biomechanical integrity. It also investigated the effect of different PCL/PEG ratios on the antimicrobial, biological and biomechanical properties of the sleeves. Tibial arteries were decellularized using Triton X-100 and sodium-dodecyl-sulfate.

Results: The scaffolds retained the general native histoarchitecture and biomechanics but were depleted of glycosaminoglycans. Sterilization with peracetic acid depleted collagen IV and produced ultrastructural changes in the collagen and elastic fibers. The two PCL/PEG ratios used (150:50 and 100:50) demonstrated differences in the structural, biomechanical and antimicrobial properties of the sleeves. Differences in the antimicrobial activity were also found between sleeves fabricated with antibiotics supplemented in the electrospinning solution, and sleeves soaked in antibiotics.

Discussion: The study demonstrated the feasibility of fabricating a dual-component small-caliber graft, comprising a scaffold with sufficient biological and biomechanical functionality, and an electrospun PCL/PEG sleeve with tailored biomechanics and antibiotic release.

KEYWORDS

small-caliber vascular graft, tibial artery, decellularized scaffold, polymeric sleeve, biomechanics, antimicrobial activity

1 Introduction

The incidences of occlusive coronary and peripheral arterial disease, and lower extremity chronic deep venous insufficiency are increasing worldwide (Fowkes et al., 1991), whereas the failure rate for arterio-venous fistulas for hemodialysis is .95 fistulas per patient per year (Lemson et al., 2000). Vascular grafting is one of the most performed surgical procedures for treating atherosclerotic, aneurysmal and stenotic blood vessels. The gold standard for grafting involves the use of autologous internal thoracic artery, long saphenous vein, internal mammary artery, radial, gastroepiploic or tibial artery for coronary (Gaudino et al., 2015), infrainguinal, or other peripheral revascularization (Klinkert et al., 2004), and for the creation of arterio-venous fistulas in hemodialysis patients (Pisoni et al., 2002). However, there is no suitable autologous vessel available for grafting in 10%–40% of patients due to trauma, disease and/or previous operations (Derham et al., 2008). Even though prosthetic (synthetic) grafts, such as Dacron® and expanded polytetrafluoroethylene, perform well in large diameter vessels (>6 mm), they perform poorly in low-flow small-caliber (<6 mm) anastomoses due to intermediate-term failure from intimal hyperplasia and thrombosis, caused by the lack of a thromboresistant blood-contacting surface, adverse haemodynamics and compliance mismatch between the prosthesis and the host vessel, that lead to a 10-year patency rate of approximately 50% (Lemson et al., 2000; Yow et al., 2006; Gaudino et al., 2015). Vascular homografts and bioprosthetic (chemically treated) xenografts have been used as alternatives to autologous conduits. However, these have demonstrated aneurysmal degeneration and rupture, whereas bioprostheses with cell remnants and xenoantigens will calcify, become rigid and degenerate, and homografts are associated with limited availability and immunogenicity (Dardik et al., 2002).

In contrast to prosthetic, bioprosthetic and homograft conduits that cannot regenerate in the patient, decellularized grafts have been reported to recellularize *in vitro* and *in vivo* and have the potential to remodel and regenerate (Yow et al., 2006; Derham et al., 2008; Katsimpoulas et al., 2015; Ma et al., 2017). Decellularized animal or human tissues offer natural 3D histoarchitecture and constitution, with appropriate physical and biological cues for tethering cell colonization, and reduced immunogenicity, providing that decellularization can remove xenoepitopes from animal tissues (Luo et al., 2014). Most previous studies on decellularized vascular conduits have focused on the use of carotid (Böer et al., 2013), coronary (Campbell et al., 2012), radial (Meiring et al., 2017), umbilical (Rodríguez-Rodríguez et al., 2018) and femoral (Meiring et al., 2017) arteries, iliac (Olausson et al., 2012), inferior vena cava (Teebken et al., 2000), great saphenous (Teebken et al., 2009), jugular (Mogaldea et al., 2017) and umbilical (Rodríguez-Rodríguez et al., 2018) veins, as well as abdominal aorta (Katsimpoulas et al., 2015) and ureter (Yow et al., 2006; Derham et al., 2008). To the best of the authors' knowledge there have been no reports on the decellularization of the tibial artery. Tibial artery is widely used for lower extremity reconstructions (Kawarada et al., 2014) and presents a good-size match to coronary arteries (Benjacholamas et al., 2002; Telang et al., 2016), whereas its arterial nature makes it a favorable choice over venous counterparts for coronary reconstructions (Benjacholamas et al., 2002).

Regardless of the specific vascular condition, conventional vascular grafting is also confronted with increased susceptibility to infection, with a relatively high incidence at the implantation site. Graft infection carries a high rate of mortality and amputation, and has a reported incidence of between 1%–8%, depending on the implantation site, indication for primary intervention, underlying disease, and host defense mechanism (Young et al., 2012). Such infections are more common after emergency procedures for ruptured aneurysms and for peripheral and abdominal prosthetic graft implantation (Young et al., 2012). Systemic antibiotic therapy has been reported to be unable to reach a sufficient local concentration to suppress bacterial adhesion on the graft. In order to induce antimicrobial activity at the site of implantation, studies have reported on the pre-soaking/coating of prosthetic grafts with antimicrobial agents (Bisdas et al., 2012), fibrin sealant/antibiotic compounds (Kuehn et al., 2010) and antibiotic-releasing polymers (Grafmiller et al., 2016). However, such direct treatments on biological grafts might induce changes in their biomechanics and function and might also interfere with any potential cellularization of decellularized scaffolds *in vivo*.

This overview indicates a major clinical need for novel and smarter solutions, encompassing implants that can fully integrate and regenerate with the patient, whilst providing postoperative antimicrobial prophylaxis. The aim of the present study was to develop a dual-component graft for small-caliber arterial reconstructions, comprising a decellularized tibial artery scaffold and an antibiotic-releasing, electrospun PCL/PEG blend outer sleeve. The overarching approach of this study is presented in graphical form in the Supplementary Figure S1 in the Supplement. Although porcine tibial arteries (PTAs) were used as a model of tibial artery homografts, decellularized PTAs could be potentially used clinically, providing that they are free of immunogenic xenoepitopes. PCL is semi-crystalline highly hydrophobic polymer that has gained FDA approval for clinical use. PCL can be easily solubilized in most organic solvents and can be easily electrospun, whereas it has good miscibility and demonstrates good mechanical stability and prolonged degradation. PEG is a water-soluble biocompatible polyether with a wide range of molecular weights, which has been used in hydrogels, and as a surface modification and adhesion molecule (Repanas et al., 2015). The diverse properties of PCL and PEG make them ideal

candidates for tailoring PCL/PEG blends that exhibit a combination of properties. The objectives of the study were to i) conduct an in-depth assessment of the effect of a modified version of the in-house decellularisation protocol on the morphological, biological and biomechanical properties of the produced small-caliber PTA scaffolds, ii) quantify the effect of nuclease enzymes, as part of the decellularization technique, on DNA removal, iii) assess two commonly used sterilization methods (peracetic acid and γ-irradiation) on the biological and biomechanical integrity of the PTA scaffolds, and iv) investigate two different PCL/PEG ratios on the antimicrobial, biological and biomechanical properties of the polymer blend sleeve.

2 Materials and methods

2.1 Tissue procurement, disinfection, decellularisation, and sterilization

Porcine legs were obtained from 6-month-old German Landrace pigs from the local abattoir and the PTAs were isolated within 4 h of animal slaughter. The adventitial surface of PTAs was scraped with a scalpel blade and washed in phosphate-buffered saline (PBS) to remove excess connective tissue and blood. The PTAs were tested immediately after dissection (Native), or placed in 150 mL square Schott bottles and disinfected in 100 mL of antibiotics solution [0.2 mg/mL polymyxin B sulfate, Sigma-Aldrich; .05 mg/mL vancomycin hydrochloride hydrate (VAN), Sigma-Aldrich; 0.5 mg/mL gentamicin sulfate (GEN); Biochrom] in PBS (pH7.2) at 37°C for 1 h. The PTAs were then decellularized according to a modified version of the in-house protocol (Theodoridis et al., 2016). Specifically, the PTAs were placed in 150 mL square Schott bottles and treated 2 × 12 h with hypotonic buffer (10 mM Tris, 2.7 mM EDTA), before they were treated 2 × 12 h with .5% (w/v) Triton X-100 (Roth) in distilled water (DW) and then 2 × 12 h with .5% (w/v) sodium dodecyl sulfate (SDS; Roth) in DW, at room temperature (RT). The samples were then rinsed 6 × 12 h in PBS. Following decellularization, the PTA scaffolds were split into two groups. The first group (method 1; M1) was sterilized straight after decellularization by either immersion in .1% (v/v) peracetic acid (PAA; Sigma-Aldrich) in PBS (pH7.3) for 3 h, followed by 3 × 30 min washes in PBS (M1-PAA) (Morticelli et al., 2013; Granados et al., 2017), or by 150 Gy of γ-irradiation (M1-γ), and stored in PBS at 4°C until testing. The second group (method 2; M2) was incubated with nucleic acid digestion solution (50.35 mM Tris, 21 mM MgCl2, pH 7.5–7.7), containing 50 U/mL DNase (Sigma-Aldrich) and 1 U/mL RNase (Sigma-Aldrich) for 3 h at 37°C, followed by 3 × 30 min washes in PBS. The PTAs were then sterilized with PAA (M2-PAA) or γ-irradiation (M2-γ), and stored in PBS at 4°C until testing. All decellularization and sterilization steps were carried out under aseptic conditions and agitation (180 rpm) in an elliptical shaker (GFL 3031), whereas all solutions were autoclaved or filtered sterilized. The sterility of the treated PTAs was assessed by incubating 24 mL of the final washing solution with 6 mL of Soy-Casein medium (Roth X938.1) in filter-cap falcon tubes for 14 days at 37°C. The negative control was 24 mL of sterile PBS incubated with 6 mL Soy-Casein medium. Contamination was assessed by the medium turbidity; contaminated samples were eliminated from further assessment.

2.2 Polymer sleeve fabrication and sterilization

Tubular polymer blend sleeves with two different PCL/PEG ratios, with or without antibiotics, were fabricated by electrospinning. Polymer blend solutions were prepared by dissolving PCL (Mn 70,000–90000; Sigma-Aldrich) and PEG (Mr 3,500–4,500; Fluka) in 2,2,2-trifluroethanol (TFE; abcr GmbH) under constant stirring (300 rpm) for 18 h at RT, in order to achieve homogenous mixtures. The total polymer concentration was either 200 mg/mL (150 mg/mL PCL and 50 mg/mL PEG; group 150:50) or 150 mg/mL (100 mg/mL PCL and 50 mg/mL PEG; group 100:50), rendering PCL/PEG mass ratios of 3:1 and 2:1, respectively. The concentrations of PCL and PEG were selected based on previous studies (Repanas et al., 2015; Repanas et al., 2016) and preliminary experiments, considering the ease of electrospinning of the solutions and the solubility of the polymers in TFE. In addition, solutions with the same polymer concentrations and mass ratios, but supplemented with 5 mg/mL VAN and 5 mg/mL GEN were also prepared (groups 150:50A and 100:50A). Electrospinning was conducted according to Repanas et al. (2015), Repanas et al. (2016). Specifically, the polymer blend solutions were transferred to 10 mL syringes (Omnifix), which were fitted with disposable blunt-tipped 0.6 mm-inner-diameter needles (21G Nordson EFD) and used as reservoirs. The flow rate of the solution was maintained at 4 mL/h with an applied voltage of 25 kV, whereas the distance between the needle tip and the grounded cylindrical collector was set at 25 cm. During electrospinning, the collector (5 mm × 50 mm) was covered with an aluminum foil and rotated at 1000 rpm. The electrospinning was performed under stable conditions of RT (21°C ± 1.5°C) and relative humidity (30% ± 5%) for 30 min per sample. The samples were removed from the collector and left to dry in vacuum overnight. The sleeves were then sterilized with either ethylene oxide (EtO) gas in vacuum, for the case of the samples used in the antimicrobial assessment, or PAA, as described for PTAs, for biocompatibility and biomechanical assessment. Sleeve sterility was assessed as described for the PTAs.

2.3 Histological and immunohistochemical assessment

Native and decellularized PTAs were assessed histologically and immunohistochemically, in order to evaluate the effect of decellularization and sterilization on extracellular matrix (ECM) histoarchitecture and presence of collagen IV and galactose-α-1,3-galactose-β-1,4-GlcNAc-R (α-gal), respectively. PTA samples were fixed in either 10% (v/v) neutral buffered formalin (NBF; histology), or zinc fixative (9.97 mM Tris, 2.84 mM calcium acetate, 36.68 mM zinc chloride and 22.78 mM zinc acetate dihydrate in DW, pH 7.4; immunohistochemistry) at 4°C for 24 h. The samples were dehydrated, embedded in paraffin and sectioned in 5 μm-thick slices. The sections were transferred to Superfrost Plus microscope slides (Thermo Fisher; histology), or Superfrost Ultra Plus slides (Thermo Fisher; immunohistochemistry). The sections were dewaxed, rehydrated, stained, rehydrated, mounted with coverslips, using Eukit mounting medium (Fluka), and dried overnight. For histology, sections were stained using either H&E, Roti-Mount FluorCare DAPI (Roth), Masson's Trichrome (Sigma-Aldrich), Elastica van Gieson's (Merck Miilipore), or Alcian Blue/PAS (Thermo Fisher), according to the manufacturers' guidelines. Immunohistochemistry was performed using the labeled polymer

technique according to the EnVision Dual Link System-HRP (DAB+) kit (Dako). The primary monoclonal antibodies used were anti-collagen IV (1:100 dilution; Dako M0785) and anti-α-gal (Enzo ALX-801-090-1; clone M86; 1:10 dilution). IgG1 (1: 200 dilution) and IgM (1:60 dilution) were used as isotype controls for negative collagen IV and α-gal staining, respectively, together with omission of the primary antibody (labelled polymer-HRP). Antibodies and isotypes were diluted in .1% (v/v) bovine serum albumin (BSA; VW) in tris-buffered saline (TBS; 50 mM Tris, 150 mM NaCl, pH 7.6). Stained sections were visualized with a Nikon Eclipse TE300 microscope and images were captured with a Nikon DS-Fi1C camera.

2.4 Electron and multiphoton laser microscopy

Native and decellularized PTAs were assessed under TEM, whereas the polymeric sleeves were assessed under SEM, according to the method described by Rudat et al. (2014). Native and decellularized PTAs treated with PAA and γ-irradiation were cut transversely and fixed in a solution containing 1.5% (v/v) paraformaldehyde, 1.5% (v/v) glutaraldehyde, and 150 mM HEPES at pH 7.35 for 30 min at RT, followed by dehydration in increasing concentrations of acetone (30%, 50%, 70%, 90% & 100%) for 10 min each time, and embedding in Epon. Sections of 50 nm were post-stained with uranyl acetate and lead citrate, and observed under a Morgagni TEM (FEI). Images were captured with a side-mounted Veleta CCD camera. The structural and morphological characteristic of the polymeric sleeves were assessed under SEM. Sleeve samples were sputtered with an ultrathin gold layer (Polaron E5000S SEM Coating System) and images were captured using a Philips SEM-505 (Philips), at 10 kV with 1,000× magnification and 50 nm spot size. PTA scaffolds (M1-PAA & M1-γ) were further assessed under multiphoton microscopy. The multiphoton imaging was performed using a CellSurgeon multiphoton microscope (MPM; LLS-ROWIAK). The MPM comprised a femtosecond mode-locked near infrared 705–980 nm Ti:Sapphire laser (Chameleon XR, Coherent) and a microscope. The samples were visualized using a 40×/1.3 NA apochromatic oil (Carl Zeiss) or a 25×/.95 W (Leica) objective lens, and images were acquired with a voxel size of .22 × .24 × 1 μm or .42 × .44 × 1 μm, respectively, and a field of view of 700 × 700 pixels, using the built-in CellSurgeon acquisition software (LLS-ROWIAK). Collagen was visualized using two-photon excitation at 880 nm that produced a second harmonic generation signal at 440 nm. Elastin in the elastic fibers was visualized using two-photon excitation at 780 nm. Emitted light was filtered with a shortpass (E680sp-2p; Chroma Technology Corp.) or a bandpass (512-25: 512/25; BrightLine HC) filter. In total, 100 images were acquired per sample.

2.5 Biochemical assessment

Native and decellularized PTA samples (n = 6 in all cases), were minced and frozen to −80°C. The samples were lyophilized overnight using a vacuum concentrator (Christ RVC 2-33 CD Plus) and weighed. DNA was extracted from ≈25 mg of wet tissue using a DNeasy Blood and Tissue Kit (Qiagen). Following elution, the DNA concentration was measured using a NanoDrop spectrophotometer (Thermo Fisher) at 260 nm. Collagen quantification was carried out by measuring the hydroxyproline (HYP) content, according to Edwards and O'Brien (Edwards and O'Brien, 1980). For this purpose, ≈15 mg from each lyophilized sample was hydrolyzed in 4 mL HCl (6 N) at 121°C overnight. The samples were incubated at 96°C until evaporation was completed, before they were reconstituted in buffer solution (13.3 g citric acid, 32 g sodium acetate, 9.1 g sodium hydroxide, 3.2 mL glacial acetic acid, 8 mL 1-propanol in 400 mL of DW; pH6.0–6.5). Trans-4-hydroxy-L-proline (Sigma-Aldrich) was diluted in buffer solution to create standard solutions (30, 25, 20, 15, 10, 8, 6, 4, 2, 1.5, 1, 0.5 μg/mL). 50 μL of each of the standard and test solutions were aliquoted into wells (n = 3) of 96-well plates (Nunc F) and incubated with 100 μL 1.4% (w/v) chloramine T solution (.05 mol/L; Sigma-Aldrich) for 5 min under gentle agitation. 100 μL of Ehrlich's reagent (7.5 g 4-dimethyl-amino-benzaldehyde, 30 mL propan-1-ol, 13 mL of 62% (v/v) perchloric acid, 7 mL DW) was added to each well and incubated at 60°C for 45 min. Absorbance was measured at 570 nm with a multimode microplate reader (Biotek Synergy 2). HYP content was determined by interpolation from the trans-4-hydroxy-L-proline standard curve. Total collagen content was calculated by a HYP: collagen ratio of 1:7.14 (Harding and Wesley, 1968). Denatured HYP (dHYP) quantification was carried out according to Bank et al. (Bank et al., 1997), using α-chymotrypsin to cleave denatured collagen. Specifically, ≈15 mg of each lyophilized sample was incubated with 5 mL of α-chymotrypsin solution, containing 5 mg/mL α-chymotrypsin (Sigma-Aldrich) in digestion buffer (1.21 g Tris, .15 g CaCl2 in 100 mL DW, pH7.8), at 37°C for 24 h. The samples were centrifuged for 10 min at 600 g, and 2 mL of the supernatants were added to 2 mL of HCl (6 N) and used for dHYP quantification as in the case of HYP. Sulfated glycosaminoglycan (sGAG) content was measured according to Farndale et al. (1986). Briefly, ≈15 mg from each lyophilized sample was incubated with 5 mL papain solution containing 7 U/mL papain (Sigma-Aldrich) in digestion buffer (5 mM L-cysteine, 5 mM EDTA in PBS; pH6.0-6.1) for 24 h at 60°C under agitation. Chondroitin sulphate (CS B amino acid; Sigma-Aldrich) was diluted in assay buffer (137 mL 0.1 M sodium di-hydrogen phosphate solution, 63 mL of 0.1 M di-sodium hydrogen phosphate solution; pH6.8) to create standard solutions (30, 25, 12.5, 6.25, 3.125 μg/mL). 40 μL of each standard and test solution was aliquoted in a 96-well plate in triplicates, and 250 μL of dimethyl-methylene blue (DMB) dye solution (16 mg 1,9-dimethylene-methylene blue zinc, 2 g sodium formate, 5 mL 99.5% ethanol, 2 mL formic acid, 1 L DW; pH 3.0-3.1) was added to each well and incubated for 5 min. Absorbance was measured at 525 nm with a microplate reader; the GAG content was determined by interpolation from the CS B standard curve.

2.6 Biocompatibility assessment

The biocompatibility of the decellularized PTAs and polymeric sleeves was assessed under contact and extract cytotoxicity assays, according to ISO 10993-5. Both assays were performed with L929 murine fibroblasts (DSMZ ACC2), cultured in RPMI 1640 medium (Merck), supplemented with 10% (v/v) fetal bovine serum (FBS; Biochrom) and 1% (v/v) penicillin/streptomycin (P/S; Lonza), at 37°C and 5% (v/v) CO2 in air. For the contact cytotoxicity,

5 mm^2 samples ($n = 3$) were isolated from the decellularized PTAs and polymeric sleeves, fabricated with the two PCL/PEG ratios and sterilized with PAA. Each PTA and polymer sample, together with a collagen gel (negative control; Cultrex 3D Culture Matrix Rat Collagen I; R&D Systems) and a cyanoacrylate glue (positive control; UHU) sample, were placed in individual wells of a 6-well plate, seeded with 4 × 105 cells/well L929 murine fibroblasts and cultured for 24 h at 37°C and 5% (v/v) CO2. The cells were fixed with 10% (v/v) NBF and stained with Giemsa stain (Sigma-Aldrich). Cell morphology and distribution were examined with a Nikon Eclipse TE300 microscope and images were captured with a Nikon DS-Fi1C camera.

For the extract assay, extracts were prepared by finely mincing 100 mg (wet weight) samples ($n = 6$) from the decellularized PTAs and 6 cm^2 samples from polymeric sleeves fabricated with the two PCL/PEG ratios. The minced samples were incubated in Eppendorf tubes with 1 mL RPMI 1640 medium (with 10% (v/v) FBS and 1% (v/v) P/S) at 37°C under agitation for 72 h. After extraction, the tubes were centrifuged for 15 min at 19,000 g, and the supernatants were collected. L929 murine fibroblasts were seeded in a 96-well plate at a density of 10,000 cells/well and incubated for 24 h at 37°C in 5% (v/v) CO2 in air. The medium was replaced by 100 µL of double-strength cell culture medium (RPMI 1640, with 20% FBS and 2% P/S), together with 100 µL of each extract, or 80% (v/v) dimethyl-sulfoxide (DMSO; AppliChem) in RPMI 1640 (positive control), or RPMI 1640 (negative control), in replicates of six, and incubated for 48 h. The cells were lysed and the ATP activity was measured using an ATP-Lite kit (PerkinElmer). Luminescence was measured using a multimode microplate reader and the results were expressed as relative luminescence units (RLU).

2.7 Biomechanical assessment

Native ($n = 6$) and decellularized PTAs were subjected to uniaxial tensile loading to failure in order to assess the effect of the two decellularization and two sterilization methods ($n = 6$ in all cases) on the scaffolds' integrity. Non-sterilized and PAA-sterilized polymeric sleeves fabricated with the two PCL/PEG ratios ($n = 6$ in all cases) were also subjected to uniaxial loading. Native and decellularized PTAs were tested along their axial direction only, since their small diameter did not allow for sufficiently-long circumferential specimens to be reliably tested. The sleeves were tested along their axial and circumferential direction. Testing was conducting according to Korossis et al. (2002). Samples measuring 20 × 5 mm (15 × 3 mm for the circumferential sleeve samples) were isolated from the PTAs and sleeves, and their thickness was measured using a Mitutoyo thickness gauge and averaged. The samples were mounted to a bespoke holder, which allowed sample mounting under zero stress and a sample gauge length of 10 mm (6 mm for the circumferential sleeve samples), prior to mounting them to an Instron tester (5,967 Dual Column Series; Instron) with a 100 N load cell. Testing was conducted in PBS at 37°C. During testing, the samples were preloaded to .01 N and preconditioned for 60 cycles at a strain rate 10 mm/min (PTA samples only), and then loaded to failure at the same strain rate. Failure was taken at the first decrease in the recorded load during extension. The load-extension response of each sample was converted to engineering stress-engineering strain. The biomechanical parameters calculated for the PTA samples included the elastic and collagen phase slopes, transition stress and strain, failure strain and ultimate tensile strength (UTS), whereas for the sleeve samples included the primary and secondary phase slopes, failure strain and UTS.

Native ($n = 6$) and decellularized PTAs were subjected to burst pressure testing in order to assess the effect of the two decellularization and two sterilization methods ($n = 6$ in all cases) on the burst pressure characteristics of the scaffolds. In addition, PAA-sterilized polymeric sleeves, fabricated with the two PCL/PEG ratios, were fitted on the outside of equal-length PTA scaffolds, prepared with the two decellularisation and two sterilization methods ($n = 6$ in all cases), and subjected to burst pressure testing as a dual-component graft. For this testing, decellularised PTA scaffolds with an outer diameter between 4–4.5 mm (after decellularisation) were selected and fitted with the polymeric sleeves that were manufactured with an internal diameter of 5 mm. The scaffolds with and without the polymeric sleeves, measuring 15 cm in length, were clamped on one end using adjustable stainless-steel clamps, filled with saline, and then mounted on the other end to the bottom of a pressure vessel. The pressure vessel, which could accommodate one graft at a time, was connected to a pressurized air supply at the top through an analogue pneumatic regulator and a Vivitro® Labs precision digital manometer at the bottom. The pressure vessel was half-filled with saline and then sealed from the atmosphere, before the manometer was zeroed and the air pressure was increased at a rate of 100 mmHg/s. Following failure of the graft, the maximum pressure achieved was recorded in mmHg.

2.8 Antibacterial efficacy

The antimicrobial activity of antibiotics-impregnated polymeric sleeves was assessed with VAN and GEN against three facultative anaerobic bacteria, including *Staphylococcus Aureus* (*S. Aureus*; Gram positive; 20231 DSMZ) and *Staphylococcus Epidermidis* (*S. Epidermidis*; Gram positive; 20,044 DSMZ), as common skin bacteria, and against *Escherichia Coli* (*E. Coli*; Gram negative; 1103 DSMZ), over a period of 7 days. VAN is effective against Gram positive strains, whereas GEN is mostly effective against Gram negative strains, but also against *Staphylococcus*. The bacteria strains were subcultured in sterile TSB-medium, containing 30 g/L tryptone soya broth powder (TSB; OXOID CM0 129) and 3 g/L yeast extract powder (Carl Roth) in DW (pH7.4), at 37°C for 24 h under shaking. The suspensions were then adjusted to an optical density (OD; measured at 600 nm) of approximately .20, measured by a BioPhotometer spectrophotometer (Eppendorf), before they were used to inoculate the samples. This OD corresponded to 1 × 106 colony-forming units (CFUs)/ml for *S. epidermidis*, 1 × 108 CFU/mL for *S. aureus*, and 1 × 107 CFU/mL for *E. coli*.

Samples measuring 1 cm^2 were isolated aseptically from the EtO-sterilized polymeric sleeves and M2-PAA scaffolds, and impregnated with antibiotics by immersing them in varying concentrations of VAN and GEN in PBS (pH7.2), and for different durations, in 50 mL Falcon tubes at RT. Specifically, samples from the 150:50 ($n = 3$ for each bacterial strain) and 100:50 ($n = 3$ for each bacterial strain) polymer blend groups were treated with 5 mg/mL VAN and 5 mg/mL GEN for either 1 h or 24 h, or with 5 mg/mL VAN and 8 mg/mL GEN for 24 h, whereas samples from PAA-sterilized PTA scaffolds ($n = 3$ for each bacterial strain) were treated with 5 mg/mL VAN and 8 mg/mL GEN for 24 h. Moreover, 1 cm^2 samples were also isolated aseptically from the EtO-sterilized 150:50A and 100:50A sleeves ($n = 3$ for each bacterial strain in both cases) and used in the assessment without any further antibiotic treatment. Three additional 1 cm^2 samples for

each bacterial strain were isolated from 150:50 sleeves and used without any antibiotic treatment as a positive control for bacteria growth. The samples were transferred aseptically in individual wells of 6-well plates and inoculated with 4 mL of either the *S. Aureus*, *S. Epidermidis* or *E. Coli* suspensions, and incubated at 37°C and 5% (v/v) CO2 for 7 days. Wells with 1 cm^2 samples isolated from 150:50 polymeric sleeves (n = 3), and incubated with 4 mL of TSB-medium only, without bacteria, were used as negative controls, whereas wells with 4 mL of TSB-medium only (n = 3) were used to assess medium sterility. After 24 h, 500 µL of bacterial suspension was sampled from each well and placed in standard rectangular cuvettes for measuring the OD of the bacterial suspensions. Each well was then supplemented with 500 µL of fresh TSB-medium. The sampling and OD measuring procedure was repeated every 24 h for 7 days. The daily recorded OD of each sample and bacteria strain was averaged over the number of samples in each group and plotted against time.

Moreover, a disk diffusion assay was performed in order to assess the diffusion of the antibiotics, released by the antibiotics-impregnated sleeves, through solid agar to inhibit bacterial growth. Samples measuring 1 cm^2 were isolated aseptically from EtO-sterilized 150:50 and 100:50 sleeves, and M2-PAA scaffolds (n = 3 for each bacterial strain in all cases), which were impregnated with antibiotics by immersion in an solution, containing 5 mg/mL VAN and 8 mg/mL GEN in PBS (7.2), for 24 h in 50 mL Falcon tubes at RT. The choice of the concentrations of the antibiotics and treatment duration was based on the favorable results observed in the bacteria growth testing described above. Following the antibiotic treatment, the samples were placed onto bacteria lawns grown onto Muller Hinton agar (MHA) plates, which had been inoculated with either *S. Aureus*, *S. Epidermidis* or *E. Coli*. 150:50 and 100:50 sleeve and scaffold samples without antibiotics were used as negative controls of bacterial inhibition (n = 3 for each case and bacterial strain). The agar plates were incubated at 37°C and 5% (v/v) CO2 for 24 h, and then photographed. The bacteria inhibition area formed by each sample was calculated using ImageJ (v1.51j8; Wayne Rasband National Instituted of Health), and the results were averaged over the number of samples in each group and for each bacterial strain.

2.9 Data analysis

The data was analyzed in Microsoft Excel and GraphPad Prism [v6.0 (GraphPad Software Inc.)]. The results were expressed as means ± 95% confidence intervals (CI). One-way analysis of variance (ANOVA), followed by the Tukey test, was used to determine statistically significant differences between the means at the .05 level.

3 Results

3.1 Histological and immunohistochemical assessment

The histological and immunohistochemical results of the native and decellularized PTAs are shown in Figures 1, 2, respectively. As evidenced by all stains used, all decellularized scaffolds appeared to be void of cells and cellular debris, throughout their thickness, and preserved the trilaminar structure of the native tissue. The DAPI staining also verified the absence of cell nuclei in the scaffolds. The Alcian Blue/PAS staining indicated that the scaffolds were depleted of acid mucosubstances (GAGs) and proteoglycans, but not of neutral polysaccharides. The decellularized tissue also presented a generally preserved network of collagen and elastic fibers, albeit seemingly disrupted due the voids generated by cell removal. The scaffolds also demonstrated a preserved internal (IEL) and external (EEL) elastic laminae. The immunohistochemical staining demonstrated high presence of the α-gal xenoepitope in the scaffolds, although it was reduced compared to the native tissue. The M2-PAA scaffolds presented the least α-gal staining, with a prevalent signal only in the media. Immunohistochemical staining for collagen IV demonstrated a clearly defined collagen IV layer in the basal lamina of the luminal surface and medial layer of the native PTA. Collagen IV was strongly present in the basal lamina and media of the γ-irradiated scaffolds, but not in the PAA-sterilized ones.

3.2 Electron and multiphoton laser microscopy

The TEM results at low, medium and high magnification of the cross-sectioned native and decellularized PTAs are shown in Figure 3. The native PTA (Figures 3A1–3E1) revealed a clearly distinguishable intima and media, containing well-organized and aligned elastic and collagen fibers, and a clearly visible internal elastic lamina (IEL) and healthy-looking cells, dispersed within a continuous collagen network. No intact cells could be identified in any of the decellularized scaffolds, whereas the organization of their collagen and elastic fibers networks, together with their IEL, seemed to be unaffected compared to the native tissue. At higher magnification, the typical cross-striation of longitudinally cut collagen fibrils could be observed throughout the decellularized scaffold, which did not differ in their ultrastructural appearance from the native tissue (Figures 3E1–3E5). In general, decellularization with (M2) or without (M1) nucleases did not generate any differences in the ultrastructural properties of the scaffolds. Both Methods resulted in completely decellularized scaffolds, with grossly preserved collagen and elastic fiber networks. However, in the PAA-treated scaffolds, the surface of the elastic fibers seemed to be different compared to the native and γ-irradiated samples. While in the native tissue and γ-irradiated samples the surface of elastic fibers was decorated with thin fibrils (Figures 3E1, E3, E5 nested), these were generally absent in the PAA-treated scaffolds (Figures 3E2, E4, nested), indicating a degradation effect by PAA. In addition, thin structures, probably representing tropocollagensssssss and collagen fibrils, were evident between and around the collagen fibers (Figures 3F1–3F5 nested). These structures appeared clearly diminished in the PAA-treated scaffolds (Figures 3F2, F4, nested).

The laser microscopy results included *en face* micrographs of the IEL (imaging plane ≈20 µm below lumen surface) and media (imaging plane ≈60 µm below lumen surface) of the M1-PAA and M1-γ scaffolds (Figure 4). The multiphoton images demonstrated a clearly disrupted IEL in the PAA-treated scaffolds (Figure 4E), with a shredded-like morphology, whereas the γ-irradiated scaffolds demonstrated a less-disrupted and more compact IEL (Figure 4G), with a sheet-like morphology. However, the fibrillar collagen histoarchitecture of the media did not present any significant differences between the two sterilization treatments (Figure 4G). The sleeves were assessed under SEM, to assess the effect of the two PCL/PEG mass ratios (2:1 and 3:1) on sleeve ultrastructure. These results are shown in Figure 7, for the non-sterilized 100:50 (Figure 7E)

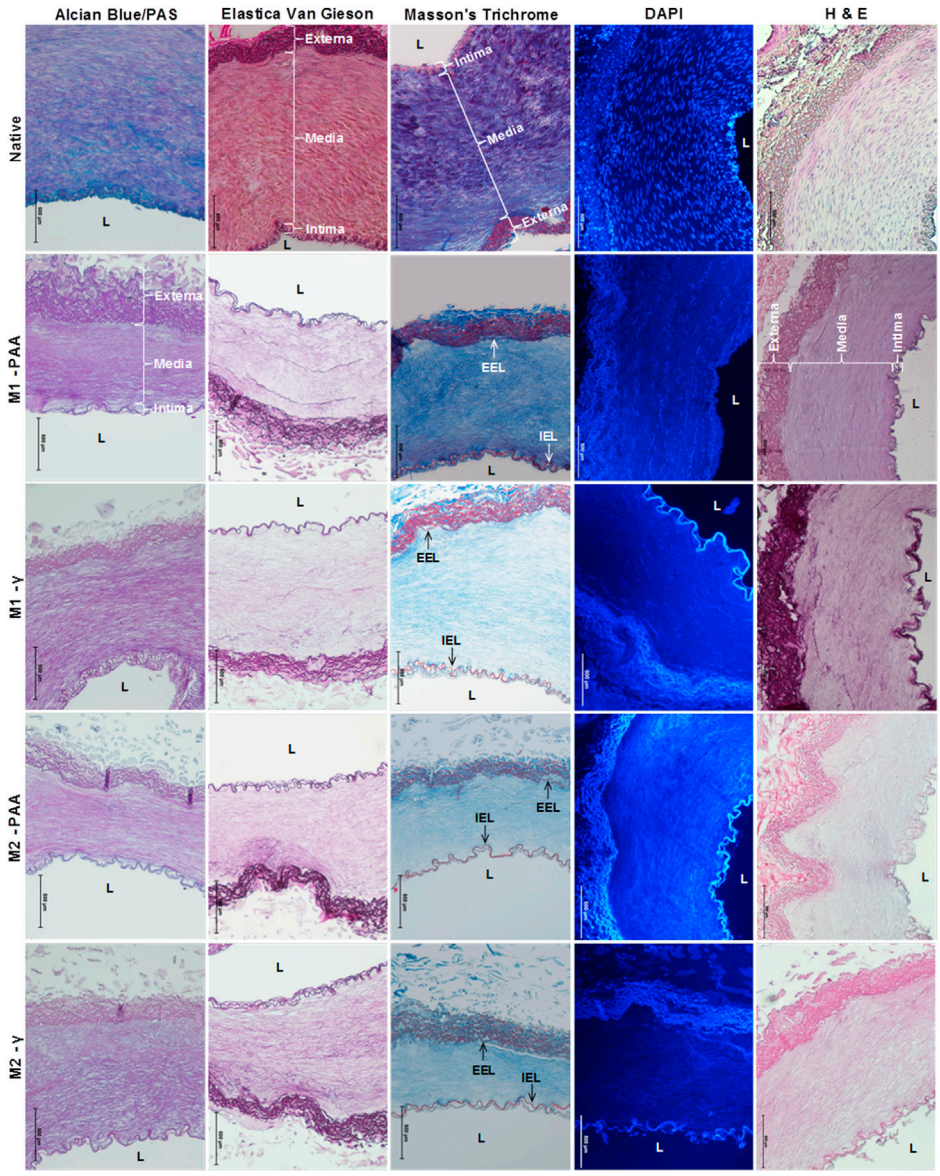

FIGURE 1
Alcian Blue/PAS, Elastica Van Gieson, Masson's Trichrome, DAPI and H&E staining of native PTA and decellularized PTA scaffolds treated with (M2) or without (M1) RNase/DNase and sterilized with either PAA or γ–irradiation. Alcian Blue/PAS stained nuclei dark blue, acid mucosubstances (GAGs) and proteoglycans blue, and neutral polysaccharides magenta; Elastica Van Gieson stained nuclei black/brown, cytoplasm yellow/pink, elastic fibers purple and collagen light purple; Masson's Trichrome stained nuclei dark blue/black, cytoplasm bright red, elastic fibers red and collagen fibers blue; DAPI stained nuclei blue and fluorescent under UV light; H&E stained nuclei blue/beep purple, cytoplasm red and collagen pale pink. Media: tunicae media; Intima: tunicae interna; Externa: tunicae externa; L: lumen; IEL: internal elastic lamina; EEL: external elastic lamina. All decellularized scaffolds appeared to be void of cell and cellular debris and preserved the trilaminar structure of the native tissue. It also appeared to be depleted of acid mucosubstances whilst its ECM fibers conserved their sugar moieties (Alcian Blue/PAS). The decellularized tissue also presented a well-preserved network of collagen and elastic fibers, as well as IEL and EEL. Scale bars indicate 500 μm.

and 150:50 (Figure 7F) sleeves. The 150:50 sleeves, demonstrated larger pores and thicker more uniform fibers compared to the 100:50 sleeves, which showed variable-thickness and thinner fibers.

3.3 Biochemical assessment

The DNA, sGAG, HYP and dHYP contents of the native and decellularized PTAs are illustrated in Figures 4A–D, respectively. The DNA content of the scaffolds treated both with (M2) and without (M1) nucleases was significantly reduced compared to the native tissue ($p = .000$; MSD = 4.6). However, the reduction in the detectable DNA content was greater in the scaffolds treated with nucleases (93.6% and 93.7% for M2-PAA and M2-γ, respectively) than in the scaffolds treated without nucleases (83.0% and 86.7% for M1-PAA and M1-γ, respectively). The difference between the M1 groups and their corresponding M2 counterparts was statistically significant.

No statistically significant difference was observed between the two M1 or the two M2 groups. A reduction was also observed in sGAGs, with all scaffolds demonstrating significantly reduced

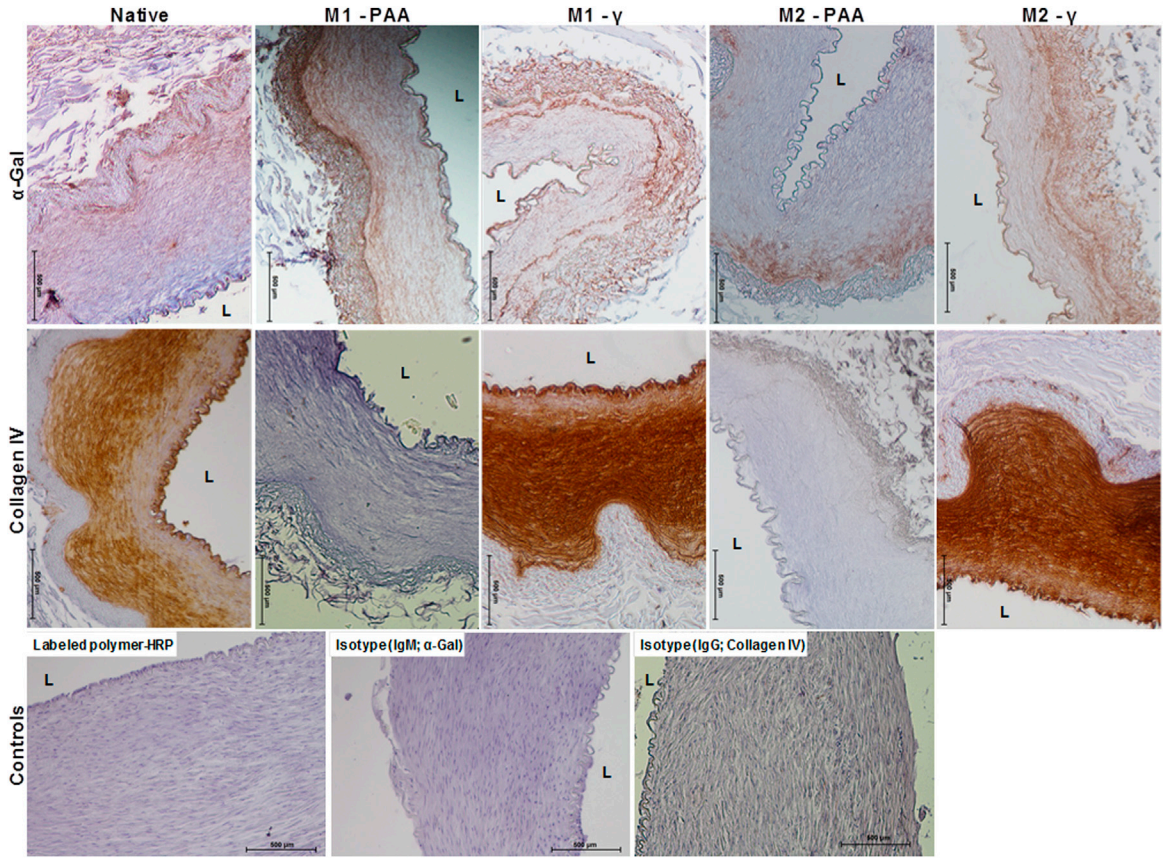

FIGURE 2
Immunohistochemical staining against α-gal and collagen IV of native PTA and decellularized PTA scaffolds treated with (M2) or without (M1) RNase/DNase and sterilized with either PAA or γ-irradiation, also showing the HRP and isotype controls. Tissue positive against the α-gal epitope was stained light brown, whereas tissue positive to collagen IV was stained dark brown. All decellularized scaffolds expressed α-gal, albeit in a reduced amount compared to the native control. Collagen IV was expressed throughout the media, intima and basement membrane of the native PTA and the decellularized PTA scaffolds that were sterilized with γ-irradiation. No staining against collagen IV could be observed in the decellularized scaffolds that were sterilized with PAA. Scale bars indicate 500 μm.

contents compared to the native control (p = .000; MSD = 3.26), in accordance with the Alcian Blue/PAS staining results. There were no significant differences in the sGAG content between the scaffolds decellularized and sterilized with the different methods. In contrast, the HYP content of all scaffolds was increased compared to the native control. The increase was statistically significant for all scaffold groups, except the M1-γ group (p = .002; MSD = 23.00). A statistically significant increase was also observed in the case of the dHYP, with all scaffold groups demonstrating higher contents compared to the native control (p = .000; MSD = 1.77). In addition, the dHYP content of the M2-γ group was significantly increased compared to the other decellularized scaffold groups.

3.4 Biocompatibility assessment

The contact cytotoxicity results of the scaffolds (Figures 5A–D) and 100:50 (Figure 5E) and 150:50 (Figure 5F) sleeves indicated that there were no cytotoxic effects on the seeded cells, which appeared confluent, growing up to and in contact with the tested materials. Similar results were observed for the case of the negative control (collagen gel; Figure 5H), but no cells survived in contact with the positive control (cyanoacrylate glue; Figure 5G). The ATP quantification indicated that both the scaffold (Figure 5I) and polymer sleeve samples (Figure 5J) achieved significantly higher ATP levels compared to the positive control (80% (v/v) DMSO) (p = .000, MSD = 1,375 and p = .000, MSD = 1,061, for the scaffolds and polymers, respectively). There was no statistically significant difference between the test and negative control (RPMI 1640) for the polymer groups. Significant differences were found between the negative control and the M1-PAA, M2-PAA and M1-γ scaffold groups, which were reduced compared to the former.

3.5 Biomechanical assessment

The mean axial biomechanical parameters for the native and groups are presented in Figure 6, whereas the corresponding results for the sleeves are shown in Figure 7. No significant differences were found in the elastic (Figure 6A; p = .750; MSD = .09) or collagen (Figure 6A; p = .271; MSD = 3.43) phase slopes, transition stress (Figure 6B; p = .647; MSD = .26) or ultimate tensile strength (Figure 6B; p = .211; MSD = 1.62) of the scaffold groups, compared to the native control, or compared to each other.

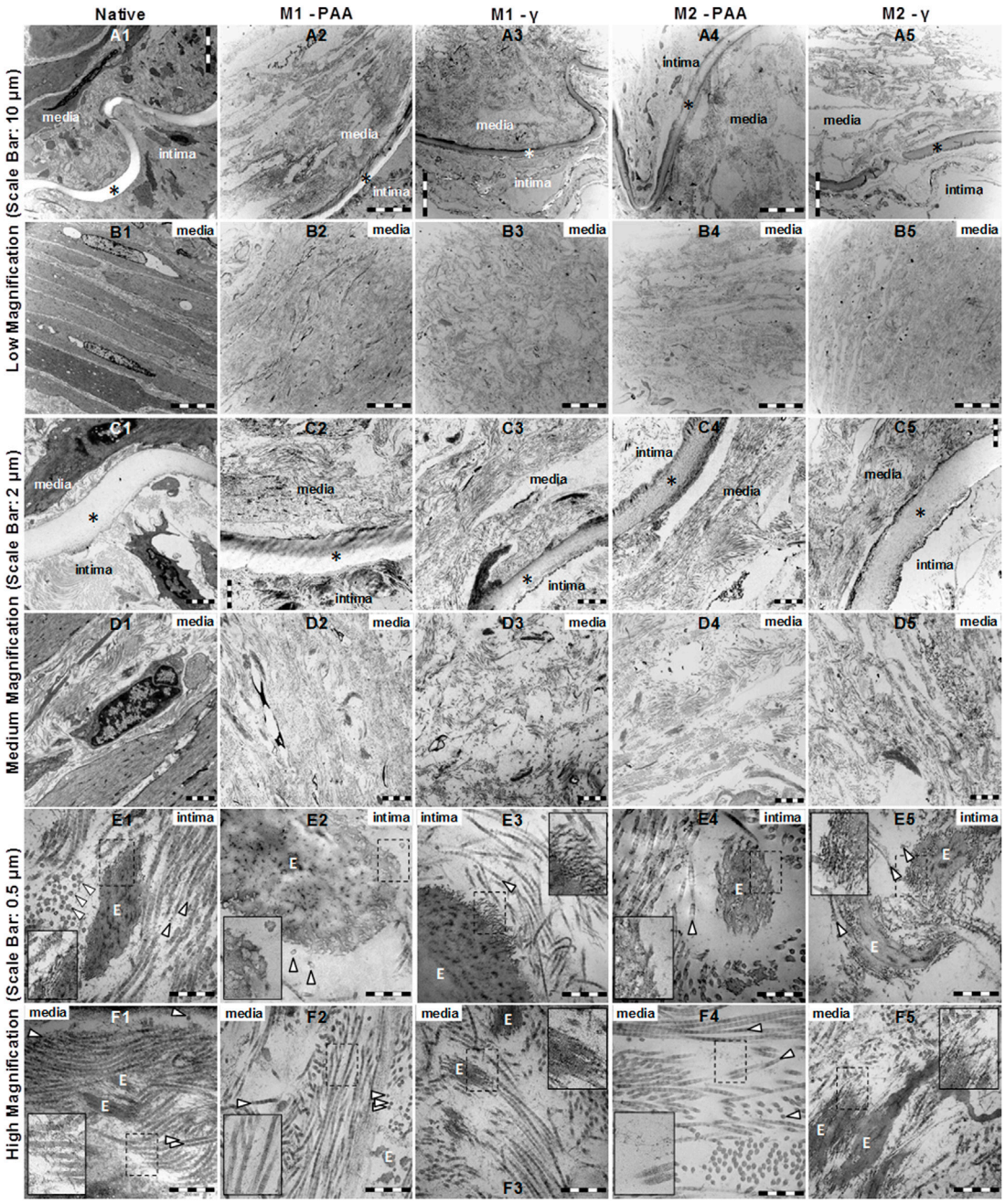

FIGURE 3
TEM imaging at low **(A1–B5)**, medium **(C1–D5)** and high **(E1–F5)** magnification of native PTA **(A1, B1, C1, D1, E1, F1)** and decellularized PTA scaffolds treated with **(M2; A4, B4, C4, D4, E4, F4, and A5, B5, C5, D5, E5, F5)** or without **(M1; A2, B2, C2, D2, E2, F2, and A3, B3, C3, D3, E3, F3)** RNase/DNase and sterilized with either PAA **(A2, B2, C2, D2, E2, F2, and A4, B4, C4, D4, E4, F4)** or γ–irradiation **(A3, B3, C3, D3, E3, F3, and A5, B5, C5, D5, E5, F5)**. Media: tunicae media; Intima: tunicae interna; È: elastic fibers; ▷ collagen fibers; ∗ interna elastic lamina. All scaffolds appeared to be completely decellularized, containing collagen and elastic fibers. Although no differences could be observed between M1 and M2, the elastic fibers of the PAA-treated scaffolds (E2, E4 nested) appeared to be cleaved of the thin fibrils that decorated the native tissue (E1 nested) and the γ-irradiated scaffolds (E3, E5 nested). In all samples, tropocollagen and collagen fibrils were evident between and around the collagen fibers (F1, F2, F3, F4, F5 nested), which were rather reduced in the case of the PAA-treated scaffolds (F2, F4, nested).

Significant differences were only observed in the transition (Figure 6C; p = .010; MSD = .27) and failure (Figure 6C; p = .001; MSD = .36) strains, and thickness (Figure 6D; p = .000; MSD = .08). Specifically, all scaffold groups demonstrated significant reduced thickness compared to the native control. Moreover, the M2-treated groups demonstrated significantly reduced thickness compared to the M1-PAA and M1-γ (M2-PAA only) groups. The transition strain of the M1-γ group was significantly increased compared to the native and M1-PAA groups, whereas the failure strains of the M2-PAA, M1-γ and M2-γ were significantly increased compared to the native control. The increased transition and failure strains are indicative of an increased extensibility of these scaffolds. The typical stress-strain behavior of the sleeve

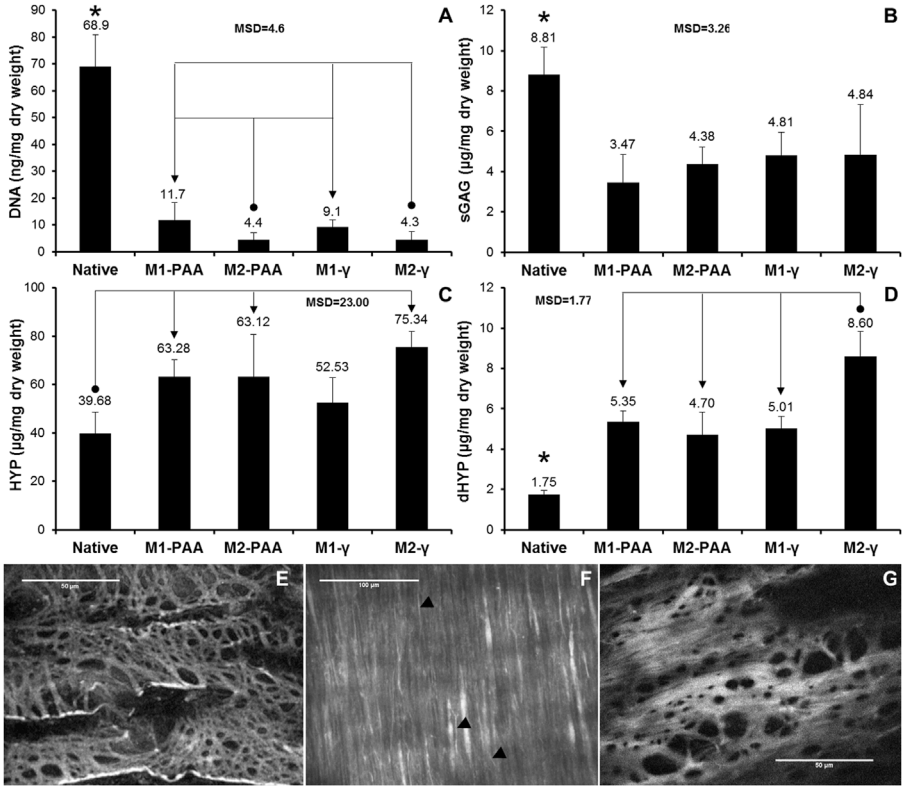

FIGURE 4
Mean DNA **(A)**, sGAG **(B)**, HYP **(C)** and dHYP **(D)** content per dry weight of native PTA and decellularized PTA scaffolds treated with (M2) or without (M1) RNase/DNase and sterilized with either PAA or γ-irradiation. Data was expressed as means (n = 6); error bars indicate 95% C.I.; MSD: minimum significant difference; indicates significant difference between the native and the decellularized groups. Connectors indicate significant difference between the originator and end arrow group. **(E–G)** Characteristic *en face* multiphoton images of the lumen of decellularized PTAs, treated with M1 and sterilized with either PAA **(E,F)** or γ-irradiation **(G)**, showing the elastic fiber network of internal elastic lamina (E, G; imaging plane was approximately 20 μm below lumen surface) and the collagen fibers of tunica media (F; imaging plane was about 60 μm below lumen surface). Black arrow heads (►) show elastic fibers. Scale bars indicate 100 μm **(E,F)** or 50 μm **(G)**.

samples is illustrated in Figure 7D. In order to assess this type of behavior, three distinct phases were identified, including a primary, secondary and failure phase. The primary and secondary phases were characterized by their slope, whereas the failure phase by the failure strain and UTS.

The mean biomechanical parameters for the sleeve groups tested along their axial and circumferential directions are shown in Figures 7A–C. Significant differences were found in all parameters apart from thickness (Figure 7C; p = .585, MSD = .13 and p = .704, MSD = .09 for axial and circumferential groups, respectively). No significant differences were found between the circumferential and axial directions of the two sleeve groups, indicating that they were rather isotropic. PAA sterilization did not affect sleeve biomechanics, since there were no significant differences in any of the parameters between the PAA-sterilized and non-sterilized sleeve groups. Significant differences were found between the two polymer blend ratios. Specifically, both 100:50 groups (with and without PAA sterilization) demonstrated statistically significant decreased primary phase slope (Figure 7A) compared to their 150:50 counterparts, along both the axial (p = .003; MSD = 11.3) and circumferential (p = .000; MSD = 6.5) directions, indicating that in this phase the 100:50 sleeves were more compliant. This was reversed in the case of the secondary slope (Figure 7A), with the 100:50 groups demonstrating significant increased values compared to their 150:50 counterparts, along both the axial (p = .000; MSD = .7) and circumferential (p = .000; MSD = .7) directions, indicating that in this phase the 100:50 sleeves were stiffer. In terms of the failure strain (Figure 7B), both 100:50 groups demonstrated significantly decreased means compared to the 150:50 groups, along both the axial (p = .011; MSD = 2.5) and circumferential (p = .000; MSD = 1.5) directions, indicating that the 100:50 groups were less extensible than their 150:50 counterparts. The 100:50 groups also demonstrated increased UTS compared to their 150:50 counterparts. The difference was statistically significant only along the circumferential direction (p = .001; MSD = 1.5).

Burst pressure testing was conducted to assess the effect of the two decellularisation methods and two sterilization techniques on the integrity of the decellularised PTAs, as well as to assess the burst pressure characteristics of the dual-component graft, comprising the PTA scaffold and polymeric sleeve. These results are presented in Figure 7G. No statistically significant differences were found among the PTA scaffold groups (without the polymeric sleeve), decellularised with M1 and M2, and sterilized with PAA and γ-irradiation, or between the PTA scaffold groups and the native control (p = .110; MSD = 235). This was also the case for the PTA scaffolds that were ensheathed with the PAA-sterilised polymeric sleeves. Specifically, there was no statistically significant difference between the PTA

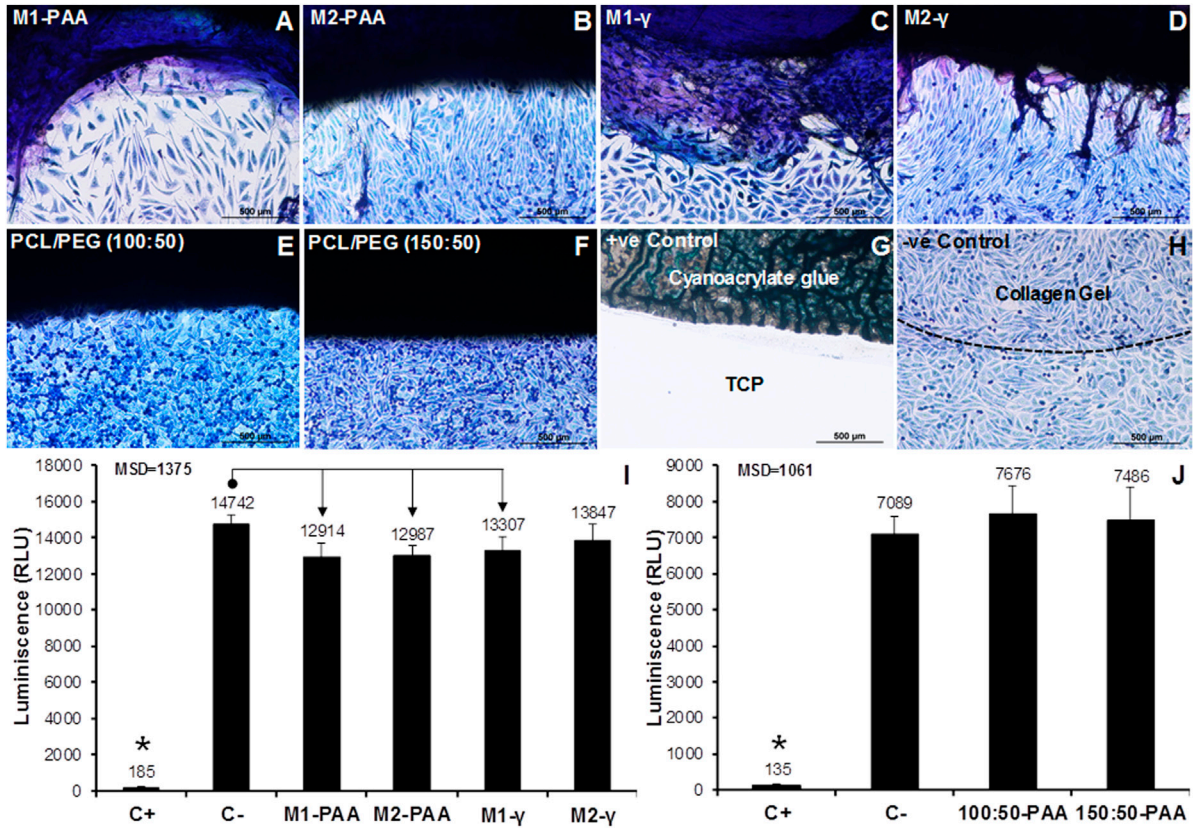

FIGURE 5
Contact **(A–H)** and extract **(I,J)** cytotoxicity results of the decellularized PTA scaffolds treated with (M2; **(B,D,I)** or without (M1; **(A,C,I)** RNase/DNase and sterilized with either PAA **(A,B,I)** or γ-irradiation **(C,D,I)**, together with the corresponding results for the 150:50 **(E,J)** and 100:50 **(F,J)** electrospun polymeric sleeves sterilized with PAA. The contact cytotoxicity **(A–H)** was performed with L929 murine fibroblasts, which were stained with Giemsa. Cyanoacrylate glue and collagen gel served as the positive (+ve) and negative (-ve) control, respectively. Scale bars indicate 100 μm. No contact cytotoxicity effects were observed with either the decellularized scaffolds or polymeric sleeves. The extract cytotoxicity assay **(I,J)** was also performed with L929 murine fibroblasts with 80% (v/v) DMSO and RPMI 1640 medium serving as positive (C+) and negative (C–) controls, respectively. Luminescence was expressed as means (n = 6); error bars indicate 95% C.I.; MSD: minimum significant difference; indicates significant difference between the native and decellularized groups. Connectors indicate significant difference between originator and end arrow group.

scaffold groups fitted with the 100:50 polymer blend sleeve, or between those groups and the native control (p = .648; MSD = 225). Similarly, there was no statistically significant difference between the PTA scaffold groups fitted with the 150:50 polymer blend sleeve, or between those groups and the native control (p = .424; MSD = 249). Further analysis showed that there were no statistically significant differences among the PTA scaffold groups (with and without the polymeric sleeve) treated with each of the four decellularisation/sterilization protocol combinations, or between them and the native control (M1-PAA: p = .023, MSD = 229; M2-PAA: p = .084, MSD = 255; M1-γ: p = .297, MSD = 208; M2-γ: p = .052, MSD = 216; Figure 7G), except for the case of the M1-PAA groups and between the PTA scaffold group (no sleeve) and the PTA scaffold group fitted with the 100:50 polymer blend sleeve (Figure 7G), with the latter demonstrating increased burst pressure.

3.6 Antibacterial efficacy

The antibacterial activity of sleeve (100:50, 150:50, 100:50A, 150:50A) and scaffold (M2-PAA) samples, impregnated with varying concentrations of VAN and GEN for different periods, was assessed in terms of the population growth of *S. Aureus*, *S. Epidermidis* and *E. Coli* over a period of 7 days. These results are shown in Figure 8A–J, together with the corresponding results of the 150:50 polymer sleeve samples, which were not treated with any antibiotics, and used as a as a positive control (150:50-W/O; Figure 8I). Groups 100:50A (Figure 8A) and 150:50A (Figure 8B), which were fabricated with 5 mg/mL VAN and 5 mg/mL GAN supplemented in the electrospinning solution, were able to produce a certain degree of bacterial inhibition compared to the positive control (150:50-W/O), especially for the *S. Epidermis* and *E. Coli* strains. However, all strains were able to proliferate and sharply increase their OD after 24 h, reaching a plateau that was maintained after 7 days. A similar bacterial growth behavior was observed for the 100:50 and 150:50 samples, which were incubated with 5 mg/mL VAN and 5 mg/mL GEN for 1 h (100:50-5V/5G-1H, Figure 8C; 150:50-5V/5G-1H; Figure 8D). Increasing the incubation time of the 100:50 and 150:50 samples with the same concentration of VAN and GEN to 24 h (100:50-5V/5G-24H, Figure 8E; 150:50-5V/5G-24H; Figure 8F), the polymer samples were able to inhibit the growth of *S. Epidermis* and *S. Aureus*, and even completely suppress *S.*

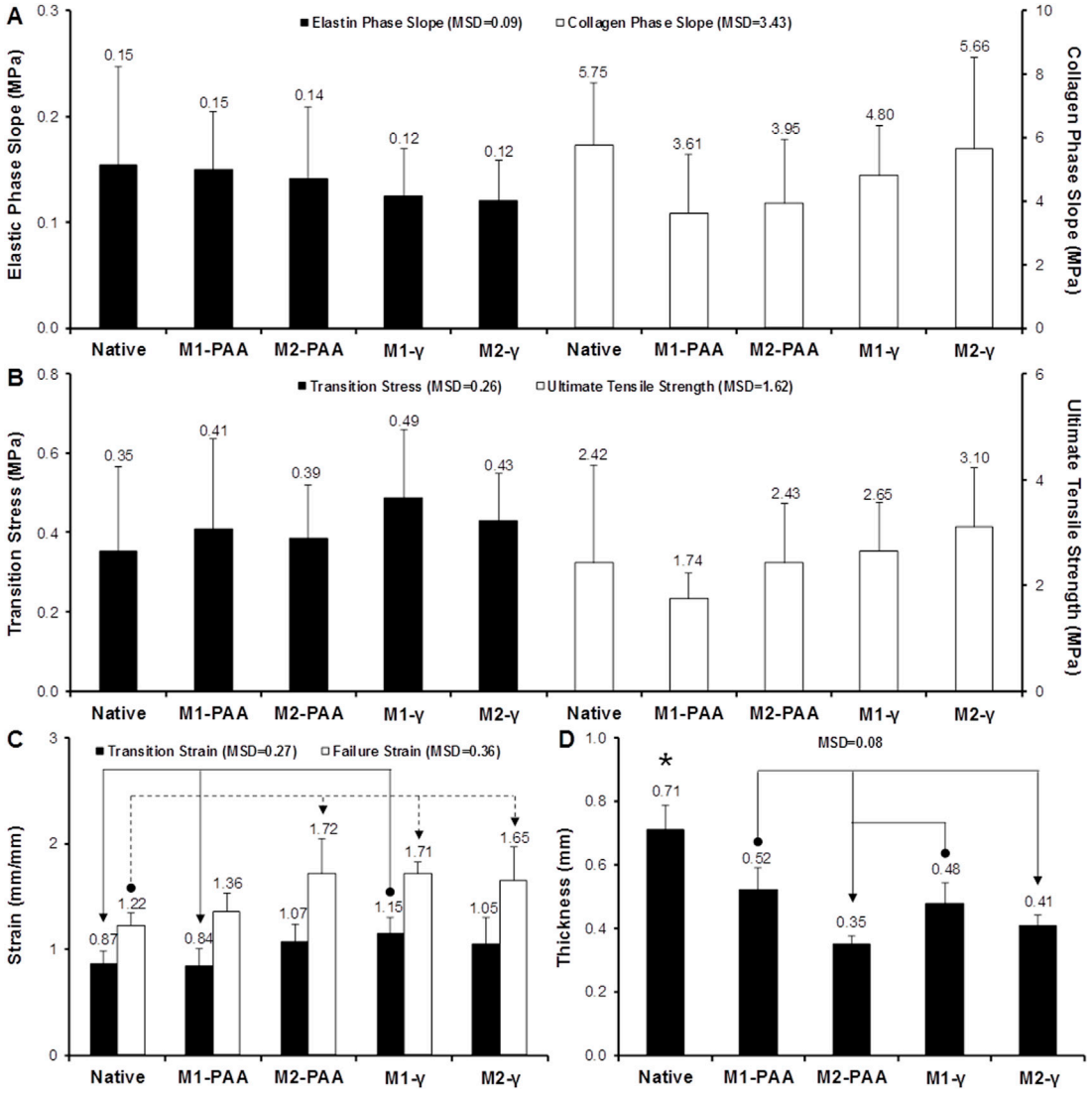

FIGURE 6
Biomechanics of native PTA and decellularized PTA scaffolds treated with (M2) or without (M1) RNase/DNase and sterilized with either PAA or γ-irradiation, tested axially. **(A)** Elastic and collagen phase slope; **(B)** transition stress and ultimate tensile strength; **(C)** transition and failure strain; **(D)** sample thickness. Data shows means (n = 6); error bars indicate 95% C.I.; MSD: minimum significant difference; indicates significant difference between the native and the decellularized groups. Connectors indicate significant difference between originator and end arrow group.

Epidermis, whereas the 150:50-5V/5G-24H group was also able to completely suppress *S. Aureus*. Neither of the 100:50-5V/5G-24H and 150:50-5V/5G-24H groups was able to effectively inhibit *E. Coli* growth, although they reduced it compared to the 150:50-W/O group.

In order to increase bacterial inhibition, the polymer samples were incubated with 5 mg/mL VAN and 8 mg/mL GEN for 24 h (100:50-5V/8G-24H, Figure 8G; 150:50-5V/8G-24H; Figure 8H). Both groups were able to completely suppress all three strains after 7 days, with the 150:50-5V/8G-24H group producing a faster suppression compared to the 100:50-5V/8G-24H. The scaffolds that were incubated with 5 mg/mL VAN and 8 mg/mL GEN for 24 h (Decel-PTA-5V/8G-24H; Figure 8J) also showed a prominent bacterial inhibition. However, complete bacterial suppression could not be achieved after 7 days. The three best performing groups (100:50-5V/8G-24H, 150:50-5V/8G-24H, Decel-PTA-5V/8G-24H) were used in the disk diffusion assay (Figure 8K). The 150:50-5V/8G-24H group demonstrated increased inhibition areas compared to the 100:50-5V/8G-24H and Decel-PTA-5V/8G-24H, for all three strains. The increase was statistically significant only for *S. Epidermis* (p = .011; MSD = 4.86) and *E. Coli* compared to the 100:50-5V/8G-24H group (p = .034; MSD = 3.27).

4 Discussion

To the best of the authors' knowledge, this was the first study on the development of a dual-component infection-resistant arterial replacement for small-caliber reconstructions, comprising a decellularized porcine tibial artery scaffold and an antibiotic-releasing polymeric outer sleeve. Previously, there have been two studies by Gong et al. (2016) and Yang et al. (2019), reporting on the development of a dual-component small-caliber graft, using a similar approach to the

10.3389/fbioe.2023.957458

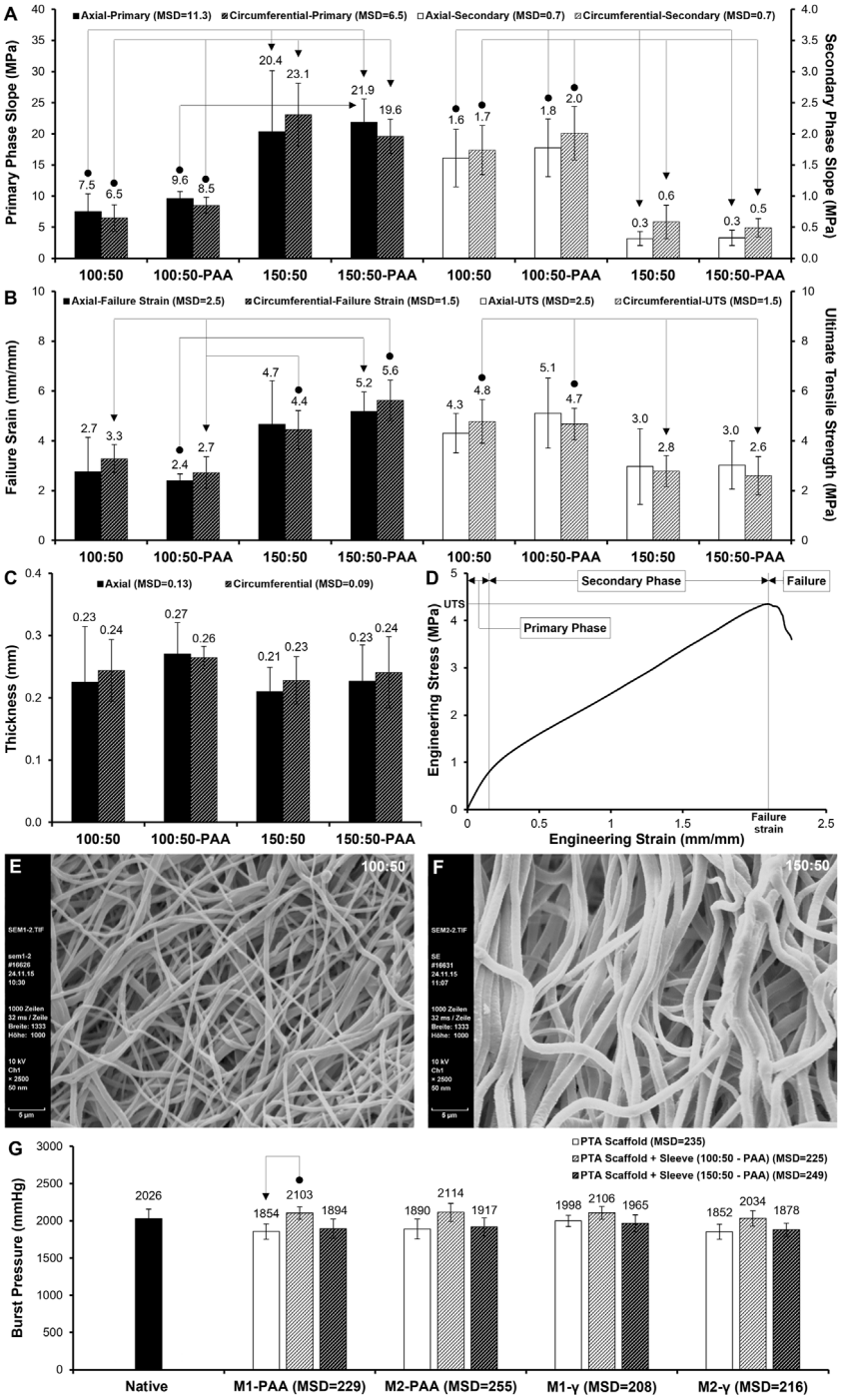

FIGURE 7
(A–C) Biomechanics of non-sterilized and PAA-sterilized 100:50 and 150:50 polymeric sleeves, tested axially and circumferentially. **(A)** Primary and secondary phase slope; **(B)** failure strain and ultimate tensile strength (UTS); **(C)** sample thickness. Data shows means (n = 6); error bars indicate 95% C.I.; MSD: minimum significant difference. Connectors indicate significant difference between originator and end arrow group. **(D)** Sample stress-strain behavior of sleeve, showing primary, secondary and failure phases. **(E,F)** SEM of 100:50 **(E)** and 150:50 **(F)** sleeves (non-sterilized). Note the increased fiber thickness and pore size of 150:50 blend. Scale bars indicate 5 μm. **(G)** Burst pressure of PTA scaffolds treated with (M2) or without (M1) RNase/DNase and sterilized with either PAA or γ-irradiation, with and without PAA-sterilized 100:50 and 150:50 polymeric sleeves. Data shows means (n = 6); error bars indicate 95% C.I.; MSD: minimum significant difference. Connector indicates significant difference between originator and end arrow group.

present study. Both studies, which were conducted by the same group, utilized rodent (rat) abdominal aortas, which were decellularised using a detergent-based protocol, combined with vacuum freeze-drying. The rat abdominal aorta has little relevance in the clinical setting for the development of a small-caliber vascular graft due to its short length, whilst it cannot be used as a model of the human abdominal aorta since the latter cannot be used as a small-caliber vascular graft in the clinical setting. The present study developed and characterized a tibial artery

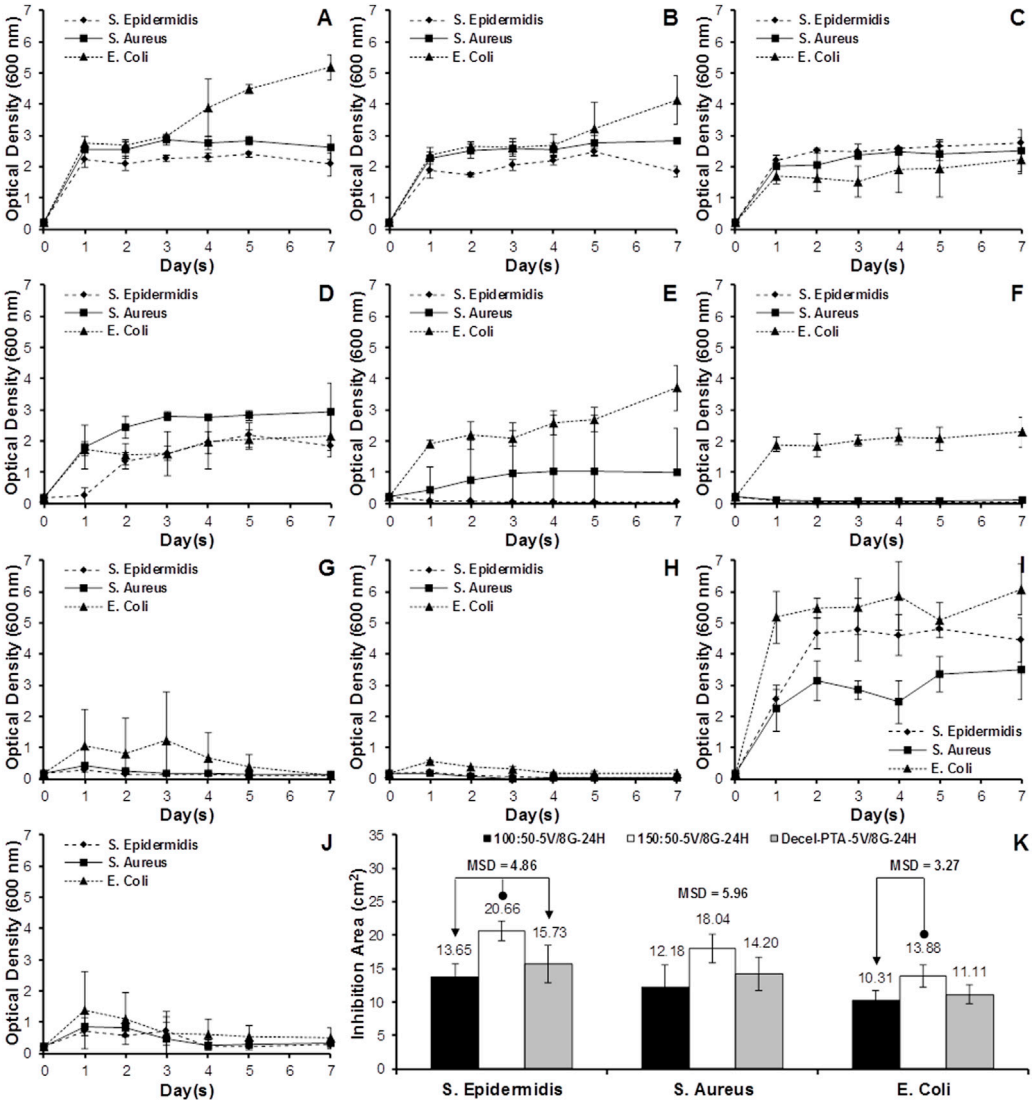

FIGURE 8
Bacteria growth curves for the polymer blends **(A–I)** and decellularized PTA **(J)**, inoculated with *S. Aureus*, *S. Epidermidis* or *E. Coli*. **(A)** 100:50A (5 mg/mL VAN and 5 mg/mL GEN supplemented in electrospinning solution); **(B)** 150:50A (5 mg/mL VAN and 5 mg/mL GEN supplemented in electrospinning solution); **(C)** 100:50-5V/5G-1H (100:50 soaked in 5 mg/mL VAN and 5 mg/mL GEN for 1 h); **(D)** 150:50-5V/5G-1H (150:50 soaked in 5 mg/mL VAN and 5 mg/mL GEN for 1 h); **(E)** 100:50-5V/5G-24H (100:50 soaked in 5 mg/mL VAN and 5 mg/mL GEN for 24 h); **(F)** 150:50-5V/5G-24H (150:50 soaked in 5 mg/mL VAN and 5 mg/mL GEN for 24 h); **(G)** 100:50-5V/8G-24H (100:50 soaked in 5 mg/mL VAN and 8 mg/mL GEN for 24 h); **(H)** 150:50-5V/8G-24H (150:50 soaked in 5 mg/mL VAN and 8 mg/mL GEN for 24 h); **(I)** 15:50-W/O (150:50 without antibiotics); **(J)** Decel-PTA-5V/8G-24H (M2-PAA decellularized PTA soaked in 5 mg/mL VAN and 8 mg/mL GEN for 24 h). **(K)** Mean bacteria inhibition area for the 100:50-5V/8G-24H, 150:50-5V/8G-24H and Decel-PTA-5V/8G-24H groups, inoculated with *S. Aureus*, *S. Epidermidis* or *E. Coli*, and cultured for 24 h in the disk diffusion assay. Data expressed as means (n = 3); error bars indicate 95% C.I.; MSD: minimum significant difference. Connectors indicate significant difference between originator and end arrow group.

scaffold, which was decellularized according to a modified version of the in-house protocol, with and without nucleases, and sterilized by either PAA or γ-irradiation. The present study utilized PTA as a model of the human tibial artery, which can be used clinically as a homologous small-caliber arterial replacement. In addition, decellularized PTAs could be potentially used in the clinical setting, providing that they are free of immunogenic xenoepitopes, especially α-gal. Furthermore, the decellularisation protocol that was utilized in the previous studies demonstrated significantly inferior performance in terms of DNA removal, which is a potent marker of decellularization efficacy. Specifically, the reduction of the DNA content in the decellularised scaffolds compared to the native tissue that was reported in those studies was 70% (Gong et al., 2016), whereas in the present study the reduction in the DNA content in the developed scaffolds compared to the native tissues was up to 93.7%. Both previous studies utilized polycaprolactone (PCL) fibers that were electrospun directly on the outer surface of the decellularized rat aorta. In contrast, the approach followed in the present study was to manufacture the decellularised scaffold and polymeric sleeve separately, giving significant flexibility in both the fabrication of the polymeric sleeve and the storage of the two components (decellularised scaffold and polymeric sleeve) of the dual-component arterial graft, which would most probably require different long-term storage conditions for their off-the-self availability and the successful clinical application of the dual-component graft.

Moreover, the electrospun PCL sleeve that was developed in the study by Gong et al. (2016) was used purely for the mechanical support of the decellularised scaffold, which demonstrated a significant reduction in strength compared to its native counterpart (Gong et al., 2016). In the subsequent study by the same group, the PCL nanofibers were blended with rapamycin to fabricate a dual-component graft with a drug delivery function to prevent intimal hyperplasia (Yang et al., 2019). On the other hand, the present study developed an antimicrobial mechanism for tackling the high rate of infections, associated with vascular grafting. To the best of the authors' knowledge, the antimicrobial mechanism proposed in the present study has not been investigated before. The work developed and characterized electrospun polymer blend tubular sleeves, fabricated with two PCL/PEG mass ratios, for engaging the scaffold and providing a local antibiotic-releasing mechanism at the site of implantation. Polymeric sleaves fabricated with PCL/PEG blends have the potential to better tailor drug release *in situ* after implantation, in order to control the antimicrobial activity induced by the graft. The antibiotics were loaded onto the sleeves by either fabricating them with antibiotics supplemented in the electrospinning solution, or by soaking them in antibiotics solution after electrospinning. Moreover, the effect of PAA-sterilization on the cytotoxicity and biomechanics of the polymer sleeves was also assessed, as a simple benchtop technique that could be applied for the treatment of the dual-component graft incorporating both the decellularized scaffold and polymer sleeve, without any specialized equipment.

PAA and γ-irradiation are two commonly used sterilization methods for biological tissues (Qiu et al., 2011). PAA has been reported to be bactericidal at .001% (v/v), fungicidal at .003% (v/v) and sporicidal at .3% (v/v) (Crow, 1992). In the present study, PAA was used at a concentration of .1% (v/v), which was sufficient to sterilize the PTAs and polymer sleeves. In the case of γ-sterilization, a dose of 25 kGy has been routinely applied for medical devices and biological tissues (da Silva Aquino, 2012). However, recent studies have reported that bovine decellularized pericardium (Guhathakurta et al., 2016) and human tendon, tracheal, skin and amnion (Harrell et al., 2018) treated with 25 kGy demonstrated a significant mechanical and biological deterioration, whereas porcine aortic heart valves treated with as low as 1 kGy demonstrated significant biomechanical and ultrastructural changes *in vitro*, and significant deterioration after only 2 months *in vivo* (Helder et al., 2016). In the present study, a dosage of 150 Gy was sufficient to sterilize the decellularized PTAs, as assessed by sterility testing. However, it should be noted that following isolation, and prior to decellularization, the PTAs were disinfected by incubation with an antibiotics solution. This would have reduced the bioburden of the PTA scaffolds prior to sterilization with either PAA or γ-irradiation.

Histology confirmed that the scaffolds, regardless of whether they were treated with (M2) or without (M1) nucleases, or sterilized by PAA or γ-irradiation, were void of cells, nuclei and cellular debris, and generally preserved the trilaminar structure of the native tissue, with a seemingly well-preserved networks of collagen and elastic fibers. Some disruption in the ECM was observed, but this was due to the voids generated by the cell removal. However, the scaffolds were also depleted of acidic mucins, indicating depletion of GAGs, although neutral polysaccharides were retained in the ECM. This has also been reported by previous studies that used detergent-based decellularization (Luo et al., 2014; Granados et al., 2017). The scaffolds also demonstrated a preserved IEL and EEL elastic laminae, with the former being an important feature for endothelial cell attachment and resistance to thrombus formation (Wilshaw et al., 2012). Nevertheless, under multiphoton microscopy, and whilst the γ-irradiation scaffolds demonstrated a IEL with a sheet-like morphology, resembling that of native arteries that was reported in previous studies (Neufeld et al., 2013), the IEL of the PAA-treated scaffolds was found to be significantly disrupted, demonstrating a shredded-like morphology. However, multiphoton microscopy showed that the collagen histoarchitecture in the media was similar between the two sterilization treatments. Detrimental effects in the PAA-treated samples could also be observed under TEM. Although at low magnification all scaffolds were void of cells and cellular debris, with well-maintained collagen and elastic fiber networks, at high magnification the surface of the elastic fibers of the PAA-treated scaffolds seemed to be depleted of thin fibrils that decorated the native and γ-irradiated samples. Similar differences were observed in the collagen, with the PAA-treated scaffolds lacking thin structures, probably representing tropocollagen and collagen fibrils, which were present in the native and γ-irradiated samples.

Immunohistochemical staining showed that collagen IV was strongly present in the basal lamina, intima and media of the native, M1-γ and M2-γ samples, but not in the PAA-sterilized scaffolds, in which collagen IV staining was completely absent. This indicated that the PAA-treated scaffolds were either depleted of collagen IV, or the collagen IV structure was altered by the PAA treatment and rendered unrecognizable by the anti-collagen IV antibody. Collagen IV presence has been suggested to promote scaffold endothelialization (Brown et al., 2006). However, decellularized pulmonary valves treated with trypsin/EDTA, which was shown to remove the basement membrane, were successfully re-endothelialized *in vitro* (Cebotari et al., 2002). The immunohistochemical staining also demonstrated a high presence of the α-gal xenoepitope in the scaffolds treated with both M1 and M2, albeit reduced compared to the native tissue. The M2-PAA scaffolds presented the least α-gal staining, present only in the media of the scaffolds. Successful clinical translation of xenogeneic scaffolds necessitates the effective removal of xenoantigens, especially α-gal, which has been identified as responsible for hyperacute xenograft rejection in humans (Simon et al., 2003). It has been suggested that apart from cellular membranes, α-gal is also present on ECM proteins and proteoglycans of xenogeneic tissues. As such, complete removal of α-gal might not be possible by decellularization alone (Galili, 2015). This xenoepitope could be selectively removed by α-galactosidase, or α-gal-knockout pig tissue could be used for scaffold development. In animal tissue, however, additional xenoantigens, such as N-glycolylneuraminic acid, are present that have been linked to chronic and systemic inflammation (Samraj et al., 2015).

In addition, decellularized scaffolds should be void of DNA, since they have been linked to inflammatory responses (Keane et al., 2012), whereas large DNA fragments could potentially act as nucleation sites for calcification (Wilshaw et al., 2012). DNA reduction is an important measure of the effectiveness of a decellularization protocol, whereas absence of a substantial DNA content in a scaffold is highly desirable for clinical application (Wilshaw et al., 2012). The DNA content of both the M1-and M2-treated scaffolds was significantly reduced compared to the native tissue, with the reduction being significantly greater in the scaffolds treated with nucleases than those treated without. Gilbert and colleagues used the PicoGreen

assay to quantify double-stranded DNA in commercially available biological scaffolds, and found small amounts of residual DNA in most of them. Based on this, residual DNA lengths of less than 300 bp, and DNA contents of less than 50 ng/mg of dry tissue have been considered acceptable (Gilbert et al., 2009). The residual amount of DNA obtained with the Nanodrop spectrophotometer in the present study for the M2-PAA and M2-γ scaffolds was 4.4 ± 2.6 and 4.3 ± 3.2 ng/mg, respectively (Figure 4A). Similar values of residual DNA have been reported for decellularized human common femoral arteries (7 ± 1 ng/mg) (Wilshaw et al., 2012) and human aortas (5 ± 1.5 ng/mg) (Aldridge et al., 2018). The DNA amount measured for the native PTAs was 68.9 ± 11.9 ng/mg, which corresponds relatively well to the DNA values of 273 ± 72 ng/mg and 88 ± 43.4 ng/mg, reported previously for the native human common femoral artery (Wilshaw et al., 2012) and native human aorta (Aldridge et al., 2018), respectively. It should be noted that unlike the PicoGreen assay, which is more sensitive, but limited to only detecting double-stranded DNA, the spectrophotometric method used in the present study was able to detect both single- and double-stranded DNA, giving a better quantification of the DNA content.

With regards to HYP, the mean content measured for the native PTAs was 39.68 ± 8.80 μg/mg of dry tissue. Considering that HYP constitutes 1/7.14 of collagen, the content measured corresponds to a collagen content of 283.34 ± 62.83 μg/mg of dry native tissue. This value corresponds well to the collagen contents of 173.6 ± 29.4 μg/mg and 259.18 ± 21.42 μg/mg, reported previously for the native human aorta (Aldridge et al., 2018) and native porcine pulmonary artery (Luo et al., 2014). Similar comparability was found in the mean dHYP and sGAG content of the native PTA, with the values obtained in the present study (1.75 ± .18 and 8.81 ± 1.36 μg/mg of dry tissue, respectively) corresponding well to the mean dHYP and sGAG content of native porcine pulmonary artery (2.8 ± .3 and 9.7 ± 1.2 μg/mg of dry tissue, respectively), reported by Luo et al. (2014). The mean HYP and dHYP contents of all scaffolds were significantly increased compared to the native control. No significant difference was found between the decellularized groups, except for the case of the mean dHYP content of M2-γ group, which was significantly increased compared to the other scaffold groups, indicating a possible damaging effect of the M2-γ treatment on the collagen fibers. The increase in the HYP and dHYP contents of the decellularized compared to the native PTAs was most probably due to the loss of tissue components during decellularization, which affected the overall constitution of the scaffolds. Specifically, and in addition to the removal of the cellular mass, the scaffolds were also depleted of a significant amount of their GAG content, as evidenced both by the Alcian Blue/PAS staining and the biochemical results, which showed that the mean sGAG content of all decellularized groups was significantly reduced, compared to the native control. The loss of these components increased the relative amount of HYP per unit mass of the scaffolds. The decrease in the GAG and the increase in the HYP content following decellularization, has been reported by previous studies with detergent-based decellularization (Korossis et al., 2002; Wilshaw et al., 2012; Luo et al., 2014; Granados et al., 2017). No significant differences were observed in the sGAG content between the scaffolds decellularized and sterilized with the different protocols.

Previous studies have suggested that the loss of GAGs contributes to changes in the mechanical properties of the tissues through disruption of their interaction with other ECM components (Sacks et al., 2011; Luo et al., 2014). GAGs interact with collagen and elastic fibers and cells, and form proteoglycans, which have been reported to contribute to collagen assembly and crimping, and mediate the formation of mature collagen fibers. It has been suggested that fibrillogenesis of collagen I is regulated by GAGs, which are entrapped within the collagen fiber network (Yoon and Halper, 2005). GAGs have been reported to confer increased stiffness to and attract water into the ECM, giving the tissue turgor (Sacks et al., 2011). The biomechanical analysis in the present study indicated a trend of reduced elastic and collagen phase slope (indicating increased scaffold extensibility) for the γ-irradiated and PAA-treated scaffold groups, respectively. However, these decreases were not statistically significant. Nevertheless, it should be noted that the thickness of the decellularized PTA groups was significantly decreased compared to the native control, most probably due to the GAG loss, which made the samples more compressible by the thickness measuring device. Taking this into account and calculating the elastic and collagen phase slopes of the force-strain plots (instead of the stress-strain plots) of the native and decellularized PTA samples, in terms of the force generated per unit strain (N/mm/mm), statistically significant differences were found between the native and decellularized PTA groups. Specifically, the mean values calculated for the elastic phase slope of the native, M1-PAA, M2-PAA, M1-γ and M2-γ groups were .55 ± .24N, .38 ± .12N, .24 ± .11N, .29 ± .10N, and .25 ± .08N, respectively, whereas the corresponding values for the collagen phase slope were 20.58 ± 8.07N, 9.19 ± 4.07N, 6.94 ± 3.77N, 11.29 ± 3.30N and 11.86 ± 7.08N, respectively. With regards to the elastic phase slope, the mean values of the M2-PAA, M1-γ and M2-γ groups were significantly decreased compared to the native control (p = .002; MSD = .23), whereas in the case of the collagen phase slope, only the PAA-treated groups (M1-PAA and M2-PAA) demonstrated significantly decreased values compared to the native control (p = .002; MSD = 9.35). Similar significant differences were also found in the case of the transition and failure strains (not a function of the thickness of the sample, but only of its length). These findings indicated that the decellularized groups were more extensible compared to the native control in both the elastic and collagen phases. The increased extensibility of the scaffold groups in the elastic phase could be potentially attributed to the GAG and proteoglycan loss, which allowed the ECM to deform more freely. The GAG and proteoglycan loss could also have caused the increased extensibility in the collagen phase of the PAA-treated samples, which they also showed the highest GAG reduction, together with collagen IV loss. No significant differences or trends were found between the decellularized groups and the native control in the transition stress and ultimate tensile strength. The latter was also reflected in the burst pressures of the PTA scaffolds. Specifically, none of the decellularisation/sterilization protocol combinations produced and significant changes in scaffolds compared to the native PTA control (Figure 7G).

The contact cytotoxicity assessment of the decellularized PTA scaffolds and the polymer sleeves indicated that there were no cytotoxic effects on the seeded L929 fibroblasts. However, in the case of the extract cytotoxicity with the PTA scaffolds, and even though their ATP levels was significantly higher than the positive control [80% (v/v) DMSO], a cytotoxic effect was observed in the case of the M1-PAA, M2-PAA, and M1-γ groups, whose ATP levels were significantly reduced compared to the negative control (RPMI 1640). This could be potentially indicative of residual detergents in the scaffolds, and the need for increased washing cycles for effectively removing detergent residues. No cytotoxic effects were observed in the

extract cytotoxicity assessment with the sleeve samples. Moreover, under SEM the 150:50 sleeves, demonstrated a more uniform structure with thicker fibers and larger pores, compared to the 100:50 sleeves, which showed a variable fiber thickness and generally thinner fibers. These differences could potentially have an effect on the degradation rates of the polymer sleeves. The increased porosity of the 150:50 sleeves could have potentially increased the intake of antibiotic solution during soaking, which, in turn, caused a higher release of antibiotics. In addition, the increased fiber thickness of the 150:50 blend indicated an increase in the specific area of the fibers, which would have increased the amount of antibiotics that physically bound to the polymer during soaking. These features of the 150:50 sleeves could have potentially contributed to their superior antimicrobial performance.

The differences found in the structure of the sleeves fabricated with the two polymer blends were manifested in their mechanical properties. Both polymer blends demonstrated biphasic stress-strain behaviors, with a primary high-modulus linear phase and a secondary low-modulus linear region. The 150:50 group demonstrated significantly higher primary phase slope and failure strain, and significantly reduced secondary phase slope and ultimate tensile strength, compared to the 100:50 group, demonstrating the "tailorability" of the biomechanics of the sleeve using different PCL/PEG mass ratios. The biomechanical assessment did not demonstrate significant differences between the axial and circumferential directions of the two polymer blends, indicating that they were quite isotropic. Moreover, the PAA treatment did not affect the biomechanics of the polymer groups, whereas there were no differences in the thickness between any of the groups tested, indicating the high repeatability of the electrospinning technique. Comparing the physical properties of the two components, the thickness of the sleeves was about half the thickness of the PTA scaffolds. This can be considered an advantage, given the limited space at the implantation site and the minimal disturbance that needs to be imposed on the surrounding tissues. However, there was a significant modulus mismatch between the scaffolds and the sleeves along their axial direction, especially in the case of the 150:50 sleeves, with the sleeves demonstrating higher slopes (less compliant) at low strains (primary phase) than the scaffolds at low strains (elastic phase). On the other hand, the axial collagen phase slope (high strains) of the scaffolds was higher than the axial secondary phase slope of the sleeves, indicating that at higher strains the sleeves would impose little resistance to scaffold dilation under the *in vivo* pulsatility. The scaffolds and the 100:50 sleeves demonstrated comparable axial strains to failure, whereas both the 100:50 and 150:50 sleeves demonstrated higher axial ultimate tensile strengths compared to the PTA scaffolds.

Comparison of the biomechanical behavior of the scaffolds and polymer sleeves along their circumferential direction is more important for understanding their functional mismatch/compatibility under pulsatile flow and subsequent graft dilation *in vivo*. In the present study, only the axial direction of the scaffolds was tested, since it was not possible to assess the biomechanics of the PTAs along their circumferential direction, due to their small diameter. Nevertheless, previous studies have shown that the circumferential direction of the blood vessels, which is the main alignment direction of the collagen fibers in the media, is considerably stiffer than the axial direction. Korossis et al. (2005) reported mean elastic phase slopes of .16MPa and .29 MPa for the axial and circumferential direction, respectively, and mean collagen phase slopes of 1.26 MPa and 3.78 MPa for the axial and circumferential direction, respectively, for the native porcine aorta. Luo et al. (2014) reported mean elastic phase slopes of .03 MPa and .04 MPa for the axial and circumferential direction, respectively, and mean collagen phase slopes of .51 MPa and .79 MPa for the axial and circumferential direction, respectively, for the native porcine pulmonary artery. Therefore, it can be safely concluded that the circumferential direction of both the native and decellularized PTAs would demonstrate higher elastic and collagen phase slopes compared to their axial direction. This would reduce the modulus mismatch between the scaffolds and sleeves at low strains. Moreover, the decellularized PTAs in the present study demonstrated increased extensibility compared to their native state. This has also been reported by several previous studies, for both the axial and circumferential direction of blood vessels decellularized with detergents (Korossis et al., 2005; Luo et al., 2014). Considering this, and although a reduced distensibility of the sleeve might be regarded problematic in restricting scaffold dilation *in vivo*, a modulus mismatch between the sleeve and the scaffold might actually be beneficial in preventing potential aneurysmatic behavior of the scaffold. In any case, and since the predominant function of the polymer sleeve would be to induce antimicrobial activity *in situ*, a setup could be considered in which the polymer sleeve is sized so that its internal diameter is larger than the outer diameter of the PTA scaffold, so that the former does not obstruct the dilation of the latter. Alternatively, the sleeve could be incised axially, so that to minimize the circumferential resistance imposed on scaffold dilation. In terms of the burst pressure characteristics of the dual-component graft, comprising the PTA scaffold and polymeric sleeve, none of the four scaffold decellularisation/sterilization combinations (M1-PAA, M2-PAA, M1-γ, M12-γ), and none of the two polymeric sleeves (100:50 or 150:50) affected the burst pressure of the dual-component graft significantly, compared to the native control or to each other. The dual-component graft groups comprising the 100:50 polymer blend sleeve for all scaffold decellularisation/sterilization combinations demonstrated a trend for increased burst pressures compared to all other groups and the native PTA control, but this increase was not statistically significant, except for the case of the M1-PAA-treated scaffold group, fitted with the 100:50 polymer blend sleeve, for which the increase was statistically significant compared to the M1-PAA-treated scaffold group without a sleeve (Figure 7G). These findings indicated that the dual-component graft can withstand similar burst pressures to the native PTA. However, further testing would be required to assess the dilation characteristics of the dual-component graft under physiological/pathological pressure conditions, with a view to assessing any potential aneurysmatic behaviour of the graft *in vivo*.

With regards to the antibacterial activity of the antibiotics-loaded sleeve and decellularized PTA, the sleeves that were fabricated with antibiotics supplemented in the electrospinning polymer blend solution (100:50A and 150:50A) were not able to suppress bacterial growth, most probably due to minimal release of the entrapped antibiotics, which, in turn, could have been due to the minimal degradation of these polymer blends over the 7-day period. Similar behavior was also observed with the sleeve samples that were soaked in antibiotic solutions for 1 h (100:50-5V/5G-1H and 150:50-5V/5G-1H). In this case, the antibiotic uptake by the polymers within 1 h, and the subsequent antibiotic release over 7 days, was not sufficient to suppress the growth of the strains

tested. By increasing the incubation time to 24 h (100:50-5V/5G-24H and 150:50-5V/5G-24H), the polymers were able to suppress the growth of *S. Epidermis* and *S. Aureus*, but not *E. Coli*. The polymer samples that were incubated with 5 mg/mL VAN and 8 mg/mL GEN for 24 h (100:50-5V/8G-24H and 150:50-5V/8G-24H) demonstrated the best antibacterial activity, with both groups completely suppressing all three strains after 7 days. Overall, the 150:50-5V/8G-24H demonstrated the best performance, with a faster and complete antimicrobial suppression, which was also superior to the decellularized PTA group (Decel-PTA-5V/8G-24H) that could not achieve complete bacterial suppression after 7 days. The superior performance of the 150:50-5V/8G-24H group was confirmed in the disk diffusion assay, with this group demonstrating the largest inhibition area compared to the other two groups tested (100:50-5V/8G-24H and Decel-PTA-5V/8G-24H). The improved antimicrobial performance of the 150:50 polymer groups could be attributed to their structure, which demonstrated larger pores and thicker fibers that allowed higher impregnation by the antibiotics solutions and higher specific area for antibiotics binding, respectively, which in turn produced faster and increased release of antibiotics compared to the 100:50 sleeves.

5 Conclusion

This study assessed the biological, biomechanical, ultrastructural and antimicrobial performance of the components of a dual-component graft, comprising a decellularized PTA scaffold and an antibiotic-impregnated PCL/PEG blend sleeve. The inclusion of nuclease enzymes in the decellularization protocol reduced the amount of residual DNA in the scaffolds, as expected, without further affecting the other biological or biomechanical properties of the scaffold. Although the decellularization treatment was not able to effectively remove the α-gal xenoepitope, it could be used for the decellularization of human or α-gal-knockout small-caliber arterial grafts. Among the two sterilization treatments investigated, γ-irradiation with 150Gy produced the least detrimental effects, whereas treatment with 1% (v/v) PAA caused degradation of the collagen IV content of the scaffolds, and ultrastructural changes in the collagen and elastic fibers, and IEL. The assessment of the polymer sleeves, which were fabricated with two different PCL/PEG mass ratios, demonstrated that it is possible to tailor the biomechanical properties of the sleeve, so that it does not interfere with the dilation of the decellularized graft *in vivo*, or indeed to restrict any potential aneurysmatic behavior. Furthermore, the antimicrobial assessment demonstrated that it is also possible to tailor the antibiotics-releasing properties of the sleeve. Owing to the encouraging results obtained in this study, future work will focus on assessing the short- and long-term degradation rates of the PCL/PEG blend sleeve, as well as its antibiotics uptake and release kinetics, and any potential biofilm formation. In the case of the decellularized PTA scaffold, further studies will quantify potential detergent residues in the scaffold and will optimize the decellularization protocol in terms of more effective detergent and α-gal removal. Moreover, the biomechanical, haemodynamic and haemocompatibility function of the dual-component graft will be assessed *in vitro*, followed by *in vivo* testing in a large animal model.

Data availability statement

The raw data supporting the conclusion of this article will be made available by the authors, without undue reservation.

Author contributions

Conceptualization, SK, MM, and BG; methodology, SK, LM, and MP; biomechanical testing, DD, PK, and SZ; electrospinning, AR and MM; multiphoton laser microscopy, FW and AK; investigation, SZ, AD-C, KB, and SA; formal analysis, SK and LM; resources, CS; data curation, SK and LM; writing (original draft preparation), SK and SZ; writing (review and editing), SK, SZ, and ST; TEM and SEM, JH; supervision, SK, LM, KG, BG, and KB; project administration, SK; funding acquisition, SK and AH. All authors have read and agreed to the published version of the manuscript.

Funding

This research was funded by the People Programme (Marie Curie Actions) of the EU seventh Framework Programme FP7/2007–2013/ under the TECAS-ITN (317512), the German Research Foundation through the Cluster of Excellence REBIRTH (EXC 62), the Engineering and Physical Sciences Research Council (EPSRC, UK; EP/D073618/1), and the German Academic Exchange Service (DAAD).

Conflict of interest

FW was employed by LLS ROWIAK LaserLabSolutions GmbH.

The remaining authors declare that the research was conducted in the absence of any commercial or financial relationships that could be construed as a potential conflict of interest.

Publisher's note

All claims expressed in this article are solely those of the authors and do not necessarily represent those of their affiliated organizations, or those of the publisher, the editors and the reviewers. Any product that may be evaluated in this article, or claim that may be made by its manufacturer, is not guaranteed or endorsed by the publisher.

Supplementary material

The Supplementary Material for this article can be found online at: https://www.frontiersin.org/articles/10.3389/fbioe.2023.957458/full#supplementary-material

References

Aldridge, A., Desai, A., Owston, H., Jennings, L. M., Fisher, J., Rooney, P., et al. (2018). Development and characterisation of a large diameter decellularised vascular allograft. *Cell Tissue Bank.* 19 (4), 287–300. doi:10.1007/s10561-017-9673-y

Bank, R. A., Krikken, M., Beekman, B., Stoop, R., Maroudas, A., Lafebers, F. P. J. G., et al. (1997). A simplified measurement of degraded collagen in tissues: Application in healthy, fibrillated and osteoarthritic cartilage. *Matrix Biol.* 16, 233–243. doi:10.1016/s0945-053x(97)90012-3

Benjacholamas, V., Jindarak, S., and Buddhari, W. (2002). Myocardial revascularization with the posterior tibial artery. *Ann. Thorac. Surg.* 73, 1312–1314. doi:10.1016/s0003-4975(01)03239-8

Bisdas, T., Beckmann, E., Marsch, G., Burgwitz, K., Wilhelmi, M., Kuehn, C., et al. (2012). Prevention of vascular graft infections with antibiotic graft impregnation prior to implantation: *In vitro* comparison between daptomycin, rifampin and nebacetin. *Eur. J. Vasc. Endovasc. Surg.* 43, 448–456. doi:10.1016/j.ejvs.2011.12.029

Böer, U., Spengler, C., Jonigk, D., Klingenberg, M., Schrimpf, C., Lützner, S., et al. (2013). Coating decellularized equine carotid arteries with ccn1 improves cellular repopulation, local biocompatibility, and immune response in sheep. *Tissue Eng. Part a.* 19, 1829–1842. doi:10.1089/ten.tea.2012.0558

Brown, B., Lindberg, K., Reing, J., Stolz, D. B., and Badylak, S. F. (2006). The basement membrane component of biologic scaffolds derived from extracellular matrix. *Tissue Eng.* 12, 519–526. doi:10.1089/ten.2006.12.519

Campbell, E., Cahill, P., and Lally, C. (2012). Investigation of a small-diameter decellularised artery as a potential scaffold for vascular tissue engineering; biomechanical evaluation and preliminary cell seeding. *J. Mech. Behav. Biomed. Mater.* 14, 130–142. doi:10.1016/j.jmbbm.2012.06.001

Cebotari, S., Mertsching, H., Kallenbach, K., Kostin, S., Repin, O., Batrinac, A., et al. (2002). Construction of autologous human heart valves based on an acellular allograft matrix. *Circulation* 106, I63–I68. doi:10.1161/01.cir.0000032900.55215.85

Crow, S. (1992). Peracetic acid sterilization: A timely development for a busy healthcare industry. *Infect. Control Hosp. Epidemiol.* 13, 111–113. doi:10.1086/646483

da Silva Aquino, K. A. (2012). "Sterilization by Gamma Irradiation," in *Gamma Radiation [Internet]*. Editors F. Adrovic (London: InTech). doi:10.5772/34901

Dardik, H., Wengerter, K., Qin, F., Pangilinan, A., Silvestri, F., Wolodiger, F., et al. (2002). Comparative decades of experience with glutaraldehyde-tanned human umbilical cord vein graft for lower limb revascularization: An analysis of 1275 cases. *J. Vasc. Surg.* 35, 64–71. doi:10.1067/mva.2002.121053

Derham, C., Yow, H., Ingram, J., Fisher, J., Ingham, E., Korrosis, S. A., et al. (2008). Tissue engineering small-diameter vascular grafts: Preparation of a biocompatible porcine ureteric scaffold. *Tissue Eng. Part a.* 14, 1871–1882. doi:10.1089/ten.tea.2007.0103

Edwards, C. A., and O'Brien, W. D. (1980). Modified assay for determination of hydroxyproline in a tissue hydrolyzate. *Clin. Chim. Acta.* 104, 161–167. doi:10.1016/0009-8981(80)90192-8

Farndale, R. W., Buttle, D. J., and Barrett, A. J. (1986). Improved quantitation and discrimination of sulphated glycosaminoglycans by use of dimethylmethylene blue. *BBA - Gen. Subj.* 883, 173–177. doi:10.1016/0304-4165(86)90306-5

Fowkes, F. G., Housley, E., Cawood, E. H., Macintyre, C. C., V Ruckley, C., and Prescott, R. J. (1991). Edinburgh artery study: Prevalence of asymptomatic and symptomatic peripheral arterial disease in the general population. *Int. J. Epidemiol.* 20, 384–392. doi:10.1093/ije/20.2.384

Galili, U. (2015). Avoiding detrimental human immune response against mammalian extracellular matrix implants. *Tissue Eng. Part B Rev.* 21, 231–241. doi:10.1089/ten.teb.2014.0392

Gaudino, M., Taggart, D., Suma, H., Puskas, J. D., Crea, F., and Massetti, M. (2015). The choice of conduits in coronary artery bypass surgery. *J. Am. Coll. Cardiol.* 66, 1729–1737. doi:10.1016/j.jacc.2015.08.395

Gilbert, T. W., Freund, J., and Badylak, S. F. (2009). Quantification of DNA in biologic scaffold materials. *J. Surg. Res.* 152, 135–139. doi:10.1016/j.jss.2008.02.013

Gong, W., Lei, D., Li, S., Huang, P., Qi, Q., Sun, Y., et al. (2016). Hybrid small-diameter vascular grafts: Anti-expansion effect of electrospun poly ε-caprolactone on heparin-coated decellularized matrices. *Biomaterials* 76, 359–370. doi:10.1016/j.biomaterials.2015.10.066

Grafmiller, K. T., Zuckerman, S. T., Petro, C., Liu, L., von Recum, H. A., Rosen, M. J., et al. (2016). Antibiotic-releasing microspheres prevent mesh infection *in vivo*. *J. Surg. Res.* 206, 41–47. doi:10.1016/j.jss.2016.06.099

Granados, M., Morticelli, L., Andriopoulou, S., Kalozoumis, P., Pflaum, M., Iablonskii, P., et al. (2017). Development and characterization of a porcine mitral valve scaffold for tissue engineering. *J. Cardiovasc. Transl. Res.* 10, 374–390. doi:10.1007/s12265-017-9747-z

Guhathakurta, S., Balasubramanian, V., Tata, B. V. R., and Ponraju, S. (2016). Is gamma irradiation as a secondary sterilization procedure required for decellularized xenogenic tissue material? *Curr. Sci.* 110, 337–344. doi:10.18520/cs/v110/i3/337-344

Harding, J. J., and Wesley, J. M. (1968). The purification and amino acid composition of human uterus collagens, rheumatoid-arthritis-nodule collagen and ox tendon collagen. *Biochem. J.* 106, 749–757. doi:10.1042/bj1060749

Harrell, C. R., Djonov, V., Fellabaum, C., and Volarevic, V. (2018). Risks of using sterilization by gamma radiation: The other side of the coin. *Int. J. Med. Sci.* 15, 274–279. doi:10.7150/ijms.22644

Helder, M. R. K., Hennessy, R. S., Spoon, D. B., Tefft, B. J., Witt, T. A., Marler, R. J., et al. (2016). Low-dose gamma irradiation of decellularized heart valves results in tissue injury *in vitro* and *in vivo*. *Ann. Thorac. Surg.* 101, 667–674. doi:10.1016/j.athoracsur.2015.07.080

Katsimpoulas, M., Morticelli, L., Michalopoulos, E., Gontika, I., Stavropoulos-Giokas, C., Kostakis, A., et al. (2015). Investigation of the biomechanical integrity of decellularized rat abdominal aorta. *Transpl. Proc.* 47, 1228–1233. doi:10.1016/j.transproceed.2014.11.061

Kawarada, O., Yasuda, S., Nishimura, K., Sakamoto, S., Noguchi, M., Takahi, Y., et al. (2014). Effect of single tibial artery revascularization on microcirculation in the setting of critical limb ischemia. *Circ. Cardiovasc. Interv.* 7, 684–691. doi:10.1161/circinterventions.113.001311

Keane, T. J., Londono, R., Turner, N. J., and Badylak, S. F. (2012). Consequences of ineffective decellularization of biologic scaffolds on the host response. *Biomaterials* 33, 1771–1781. doi:10.1016/j.biomaterials.2011.10.054

Klinkert, P., Post, P. N., Breslau, P. J., and van Bockel, J. H. (2004). Saphenous vein versus PTFE for above-knee femoropopliteal bypass. A review of the literature. *Eur. J. Vasc. Endovasc. Surg.* 27, 357–362. doi:10.1016/j.ejvs.2003.12.027

Korossis, S. A., Booth, C., Wilcox, H. E., Watterson, K. G., Kearney, J. N., Fisher, J., et al. (2002). Tissue engineering of cardiac valve prostheses II: Biomechanical characterization of decellularized porcine aortic heart valves. *J. Heart Valve Dis.* 11, 463–471.

Korossis, S. A., Wilcox, H. E., Watterson, K. G., Kearney, J. N., Ingham, E., and Fisher, J. (2005). *In-vitro* assessment of the functional performance of the decellularized intact porcine aortic root. *J. Heart Valve Dis.* 14, 408–421.

Kuehn, C., Graf, K., Mashaqi, B., Pichlmaier, M., Heuer, W., Hilfiker, A., et al. (2010). Prevention of early vascular graft infection using regional antibiotic release. *J. Surg. Res.* 164, e185–e191. doi:10.1016/j.jss.2010.05.029

Lemson, M. S., Tordoir, J. H. M., Daemen, M. J. A. P., and Kitslaar, P. J. E. H. M. (2000). Intimal hyperplasia in vascular grafts. *Eur. J. Vasc. Endovasc. Surg.* 19, 336–350. doi:10.1053/ejvs.1999.1040

Luo, J., Korossis, S. A., Wilshaw, S.-P., Jennings, L. M., Fisher, J., and Ingham, E. (2014). Development and characterization of acellular porcine pulmonary valve scaffolds for tissue engineering. *Tissue Eng. Part a.* 20, 2963–2974. doi:10.1089/ten.tea.2013.0573

Ma, X., He, Z., Li, L., Liu, G., Li, Q., Yang, D., et al. (2017). Development and *in vivo* validation of tissue-engineered, small-diameter vascular grafts from decellularized aortae of fetal pigs and canine vascular endothelial cells. *J. Cardiothorac. Surg.* 12, 101. doi:10.1186/s13019-017-0661-x

Meiring, M., Khemisi, M., Laker, L., Dohmen, P. M., and Smit, F. E. (2017). Tissue engineered small vessel conduits – the anti-thrombotic effect of re-endothelialization of decellularized baboon arteries: A preliminary experimental study. *Med. Sci. Monit. Basic Res.* 23, 344–351. doi:10.12659/msmbr.905978

Mogaldea, A., Goecke, T., Theodoridis, K., Haverich, A., Cebotari, S., and Hilfiker, A. (2017). Tissue engineering of vein valves based on decellularized natural matrices. *Cells Tissues Organs* 204, 199–209. doi:10.1159/000477776

Morticelli, L., Thomas, D., Roberts, N., Ingham, E., and Korossis, S. (2013). Investigation of the suitability of decellularized porcine pericardium in mitral valve reconstruction. *J. Heart Valve Dis.* 22, 340–353.

Neufeld, E. B., Lucotte, B. M., and Balaban, R. S. (2013). "Multiphoton excitation imaging of the arterial vascular bed," in *Second harmon. Gener. Imaging*. Editors Pavone F. S. and Campagnola P. J. (Boca Raton, FL: CRC Press), 289–308.

Olausson, M., Patil, P. B., Kuna, V. K., Chougule, P., Hernandez, N., Methe, K., et al. (2012). Transplantation of an allogeneic vein bioengineered with autologous stem cells: A proof-of-concept study. *Lancet* 380, 230–237. doi:10.1016/s0140-6736(12)60633-3

Pisoni, R. L., Young, E. W., Dykstra, D. M., Greenwood, R. N., Hecking, E., Gillespie, B., et al. (2002). Vascular access use in europe and the United States: Results from the DOPPS. *Kidney Int.* 61, 305–316. doi:10.1046/j.1523-1755.2002.00117.x

Qiu, Q. Q., Sun, W. Q., and Connor, J. (2011). "Sterilization of biomaterials of synthetic and biological origin," in *Compr. Biomater.* (Elsevier), 127–144.

Repanas, A., Al Halabi, F., Andriopoulou, S., Korossis, S., and Glasmacher, B. (2016). PCL/PEG coaxially spun fibers as a drug delivery system for anti-thrombotic pharmaceutical agents. *Sch. Acad. J. Biosci.* 4 (2), 149–153. doi:10.4172/2161-1459.1000192

Repanas, A., Wolkers, W. F., Gryshkov, O., Kalozoumis, P., Mueller, M., Zernetsch, H., et al. (2015). Coaxial electrospinning as a process to engineer biodegradable polymeric scaffolds as drug delivery systems for anti-inflammatory and anti-thrombotic pharmaceutical agents. *Clin. Exp. Pharmacol.* 5 (5), 1–8. doi:10.4172/2161-1459.1000192

Rodríguez-Rodríguez, V. E., Martínez-González, B., Quiroga-Garza, A., Reyes-Hernández, C. G., de la Fuente-Villarreal, D., de la Garza-Castro, O., et al. (2018). Human umbilical vessels: Choosing the optimal decellularization method. *ASAIO J.* 64 (5), 1. doi:10.1097/mat.0000000000000715

Rudat, C., Grieskamp, T., Hr, C. R., Airik, R., Wrede, C., Hegermann, J., et al. (2014). Upk3b is dispensable for development and integrity of urothelium and mesothelium. *PLoS One* 9, e112112. doi:10.1371/journal.pone.0112112

Sacks, M. S., Wognum, S., Stella, J., Joyce, E., and D'Amore, A. (2011). "The mechanics of native and engineered cardiac soft tissues," in *Compr. Biomater.* (Elsevier), 113–132.

Samraj, A., Pearce, O., Läubli, H., Crittenden, A., Bergfeld, A., Banda, K., et al. (2015). A red meat-derived glycan promotes inflammation and cancer progression. *Proc. Natl. Acad. Sci.* 112, 542–547. doi:10.1073/pnas.1417508112

Simon, P., Kasimir, M. T., Seebacher, G., Weigel, G., Ullrich, R., Salzer-Muhar, U., et al. (2003). Early failure of the tissue engineered porcine heart valve SYNERGRAFT™ in pediatric patients. *Eur. J. Cardio-Thoracic Surg.* 23, 1002–1006. doi:10.1016/s1010-7940(03)00094-0

Teebken, O. E., Bader, A., Steinhoff, G., and Haverich, A. (2000). Tissue engineering of vascular grafts: Human cell seeding of decellularised porcine matrix. *Eur. J. Vasc. Endovasc. Surg.* 19, 381–386. doi:10.1053/ejvs.1999.1004

Teebken, O. E., Puschmann, C., Breitenbach, I., Rohde, B., Burgwitz, K., and Haverich, A. (2009). Preclinical development of tissue-engineered vein valves and venous substitutes using re-endothelialised human vein matrix. *Eur. J. Vasc. Endovasc. Surg.* 37, 92–102. doi:10.1016/j.ejvs.2008.10.012

Telang, A. V., Lone, M., and Natarajan, M. (2016). A study of the internal diameter of popliteal artery, anterior and posterior tibial arteries in cadavers. *Indian J. Clin. Anat. Physiol.* 3, 287–290. doi:10.5958/2394-2126.2016.00065.7

Theodoridis, K., Müller, J., Ramm, R., Findeisen, K., Andrée, B., Korossis, S., et al. (2016). Effects of combined cryopreservation and decellularization on the biomechanical, structural and biochemical properties of porcine pulmonary heart valves. *Acta Biomater.* 43, 71–77. doi:10.1016/j.actbio.2016.07.013

Wilshaw, S. P., Rooney, P., Berry, H., Kearney, J. N., Homer-Vanniasinkam, S., Fisher, J., et al. (2012). Development and characterization of acellular allogeneic arterial matrices. *Tissue Eng. Part a.* 18, 471–483. doi:10.1089/ten.tea.2011.0287

Yang, Y., Lei, D., Zou, H., Huang, S., Yang, Q., Li, S., et al. (2019). Hybrid electrospun rapamycin-loaded small-diameter decellularized vascular grafts effectively inhibit intimal hyperplasia. *Acta Biomater.* 97, 321–332. doi:10.1016/j.actbio.2019.06.037

Yoon, J. H., and Halper, J. (2005). Tendon proteoglycans: Biochemistry and function. *J. Musculoskelet. Neuronal Interact.* 5, 22–34.

Young, M. H., Jr, G. R. U., and Malani, P. N. (2012). Vascular graft infections. *Infect. Dis. Clin. North Am.* 26, 41–56. doi:10.1016/j.idc.2011.09.004

Yow, K. H., Ingram, J., Korossis, S. A., Ingham, E., and Homer-Vanniasinkam, S. (2006). Tissue engineering of vascular conduits. *Br. J. Surg.* 93, 652–661. doi:10.1002/bjs.5343

Frontiers in
Bioengineering and Biotechnology

Accelerates the development of therapies, devices, and technologies to improve our lives

A multidisciplinary journal that accelerates the development of biological therapies, devices, processes and technologies to improve our lives by bridging the gap between discoveries and their application.

Discover the latest Research Topics

See more →

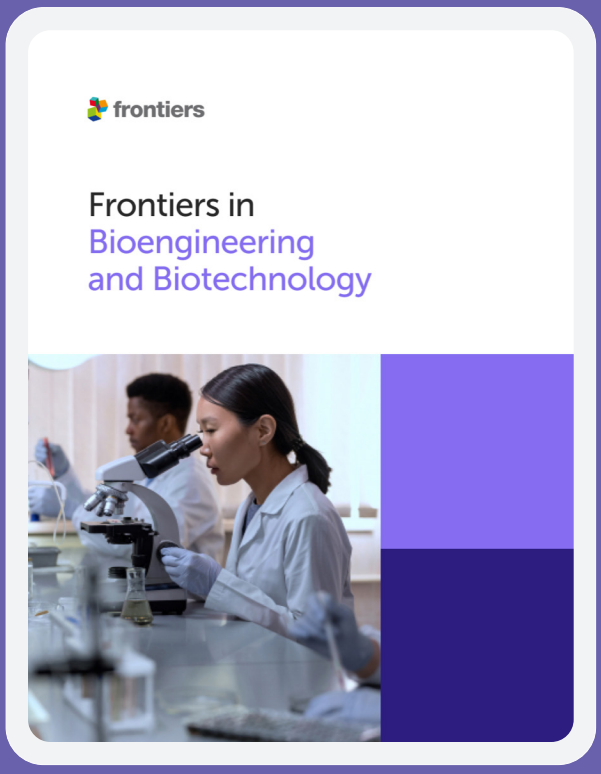

Frontiers

Avenue du Tribunal-Fédéral 34
1005 Lausanne, Switzerland
frontiersin.org

Contact us

+41 (0)21 510 17 00
frontiersin.org/about/contact